Experimental and Theoretical Investigation of Glass Ceramics: The Transparent Ferroelectric Nanocomposite $LaBGeO_5$

by

Alexander Liam Paterson

Submitted in partial fulfillment of the requirements
for the degree of Doctor of Philosophy

at

Dalhousie University
Halifax, Nova Scotia
December 2018

To Zoë, for making this journey with me

Table of Contents

List of Tables

List of Figures

Abstract

The $LaBGeO_5$ glass-ceramic composite is a transparent ferroelectric nanocomposite (TFN) material that has come under attention for its ferroelectric properties. $LaBGeO_5$ crystals-in-glass can be formed through controlled devitrification of the glass, as well as through laser irradiation. While structural models of the glass have been proposed, they have only considered differences in the borate environment between the glass and the crystal.

Understanding the structure of the $LaBGeO_5$ glass is an important first step towards understanding the formation of the crystals-in-glass. To study the structure of the $LaBGeO_5$ glass, we made use of a combination of nuclear magnetic resonance (NMR) spectroscopy, neutron diffraction, density functional theory (DFT) calculations, and several other techniques. These techniques provided complementary data on both local order within the glass, as well as connectivity between different local structural units.

^{11}B NMR spectroscopy was used to establish the presence of both trigonal and tetrahedral borate units, and to identify the trigonal borate species. $^{11}B\{^{10}B\}$ heteronuclear NMR spectroscopy was used to probe the connectivity between the borate units. Neutron diffraction was used to provide evidence of the presence of high-coordinate germanate units, as well as evidence of changes in the lanthanum–oxygen coordination number between the glass and the crystal. ^{139}La NMR spectroscopy was applied to glasses for the first time in order to provide data on the La – O environment. The use of ^{17}O NMR spectroscopy provided data regarding the connectivity of all local structural units. The ^{17}O NMR data support a highly interconnected structure for the $LaBGeO_5$ glass, and indicated that the glass network is homogeneous.

DFT calculations were carried out to probe the stress environment in laser-written $LaBGeO_5$ crystals-in-glass. Our calculations support an anisotropic stress environment with both tensile and compressive stresses being present.

Our results support a model of the structure of the $LaBGeO_5$ glass that is radically different than the crystal structure. The new structural model should inform future studies of the $LaBGeO_5$ laser-written crystals-in-glass. Our data suggest that the nucleation mechanism in the $LaBGeO_5$ glass is heterogeneous, and we propose future work to test this hypothesis.

List of Abbreviations and Symbols Used

3QMAS triple quantum magic angle spinning

a the first unit cell length

A symmetric non-degenerate phonon modes

A the quadrupole product prefactor; the correlation function peak area

$\bar{b}$ the coherent scattering length

b the second unit cell length

BO bridging oxygen

c the third unit cell length; the speed of light in vacuum; the atomic fraction; the crystallite fraction

C the elastic stiffness tensor; the Raman intensity prefactor

CN coordination number

CPMG Carr-Purcell Meiboom-Gill

C_{Q} the quadrupolar coupling constant

CSA chemical shift anisotropy

$\mathrm{C_z}$ a MQMAS referencing convention

d the lattice plane distance

D the dipolar coupling constant

d_{avg} the average La−O bond length

DFPT density functional perturbation theory

DFT density functional theory

$d_{\max}$ the maximum La–O bond length

$d_{\min}$ the minimum La–O bond length

$D(r)$ the differential neutron correlation function

DSC differential scanning calorimetry

e the elementary charge

E doubly-degenerate phonon modes

E the elastic modulus; the energy

e_a the shortest semi-major axis of a coordination ellipsoid

EA elemental analysis

e_b the intermediate semi-major axis of a coordination ellipsoid

EBS electrostatic bond strength

e_c the longest semi-major axis of a coordination ellipsoid

EC ellipsoid character

EDS energy dispersive spectroscopy

EFG electric field gradient

EMPA electron microprobe analysis

f the quadrupolar REDOR calibration factor

FWHM full-width at half-maximum

G glass

G the shear modulus

g^0 the atom number density

$G^{(0)}$ the zeroth rotational invariant

$G^{(1)}$ the first rotational invariant

$G^{(2)}$ the second rotational invariant

GEM GEneral Materials Diffractometer

GGA generalized gradient approximation

GIPAW gauge-including projector augmented-wave

h the Planck constant

$\hbar$ the reduced Planck constant

I the nuclear spin number

I the indirect nuclide

ICSD Inorganic Crystal Structure Database

$I_{\parallel}^{\text{powder}}$ the parallel Raman intensity

$I_{\perp}^{\text{powder}}$ the perpendicular Raman intensity

$i(Q)$ the distinct scattering

IR infrared

$I^{\text{S}}(Q)$ the neutron self-scattering

$I_{\text{Total}}^{\text{powder}}$ the total Raman intensity

JTH Jollet, Torrent, and Holzwarth

k the MQMAS echo position factor; the force constant

K the bulk modulus

k_B the Boltzmann constant

L linear

LA-ICP-MS laser ablation inductively coupled plasma mass spectrometry

LBG $LaBGeO_5$

LDA local-density approximation

LO longitudinal optic

$\boldsymbol{M}$ the reduced dielectric polarization vector

M_2^{IS} the van Vleck heteronuclear dipolar second moment

MAS magic angle spinning

MQ multiple quantum

$M(Q)$ the modification function

MQMAS multiple quantum magic angle spinning

n the coordination number; the number of atoms

N the WURST exponent

NBO non-bridging oxygen

NCPP norm-conserving pseudopotential

NMR nuclear magnetic resonance

$n(\omega)$ the Bose-Einstein factor

NSERC Natural Sciences and Engineering Research Council of Canada

Ø bridging oxygen

O_{666} oxygen triply coordinated to ^6Ge

O_b bridging oxygen

O_{nb} non-bridging oxygen

ONCVPSP Optimized Norm-Conserving Vanderbilt Pseudopotential

P the isotropic stress

$\parallel$ parallel

PAW projector augmented-wave

PBE Perdew, Burke, and Ernzerhof

PDF probability distribution function

PDF powder diffraction file

$\perp$ perpendicular

p_Q the Czjzek probability distribution function

P_Q the quadrupolar product

pXRD powder X-ray diffraction

$\mathbf{q}$ the phonon wavevector

$\hat{\boldsymbol{q}}$ the unit vector of the direction of propagation

$\boldsymbol{q}$ the incoming wavevector

Q the nuclear electric quadrupole moment; the momentum transfer; the degree of polymerization of a phosphate bonding unit

Q_{max} the maximum momentum transfer

r the internuclear distance; the correlation function peak position

R the ratio of lanthanum oxide to boron and germanium oxides

R^2 the coefficient of determination

$r_{\alpha\tau}$ the atomic displacement

REAPDOR rotational-echo adiabatic passage double-resonance

REDOR rotational-echo double-resonance

RF radio frequency

RMS root mean square

r_s the average distance between the centroid of a coordination polyhedron and its ligands

s the strain tensor; the electrostatic bond strength

S the observed nuclide

S the REDOR intensity of the observed nuclide with I irradiation

S_0 the REDOR intensity of the observed nuclide without I irradiation

SEM scanning electron microscopy

SHG second harmonic generation

ssNMR solid-state nuclear magnetic resonance

t the time

$t_{ii'}(r)$ the partial correlation function

T the temperature

$T^0(r)$ the average density contribution

t_1 the multiple quantum coherence evolution time

T_1 the longitudinal, or spin-lattice, relaxation time

T_2 the transverse, or spin-spin, relaxation time

TFN transparent ferroelectric nanocomposite

T_{g} the glass transition temperature

TGA thermogravimetric analysis

T_{gr} the reduced glass transition temperature

THF tetrahydrofuran

T_{m} the melting temperature

TO transverse optic

$T(r)$ the total correlation function

T_{r} the rotor spinning period

u the neutron peak width

$u_{\alpha\tau}$ the phonon eigenvector

V the electric field gradient tensor

V volume

v_{L} the longitudinal velocity of sound

V_{M} the molar volume

VOCS variable offset cumulative spectrum

v_{T} the transverse velocity of sound

V_{xx} the xx component of the electric field gradient tensor

V_{yy} the yy component of the electric field gradient tensor

V_{zz} the zz component of the electric field gradient tensor

W^* the work of nucleation

WCPMG WURST Carr-Purcell Meiboom-Gill

WDS wavelength dispersive spectroscopy

W the weight

WURST wideband, uniform rate, smooth truncation

X crystal

XC exchange-correlation

z the cation valence

Z the atomic number

α the first Euler angle; the coefficient of thermal expansion; the ratio of BO_3 and $[B\emptyset_4]^-$ in the $LaBGeO_5$ glass

β the second Euler angle; the Raman susceptibility tensor

γ the gyromagnetic ratio; the third Euler angle

Γ the Brillouin zone centre

Δ the WURST sweep width

δ_{11} the 11 component of the chemical shielding tensor

δ_{22} the 22 component of the chemical shielding tensor

δ_{33} the 33 component of the chemical shielding tensor

$\delta_{G1-z}^{\text{obs}}$ the centre of gravity in the isotropic dimension

δ_{G2}^{obs} the centre of gravity in the MAS dimension

ΔG_x the free energy of crystallization

δ_{ij} the Kronecker delta

$\delta_{\mathrm{iso}}^{\mathrm{CS}}$ the isotropic chemical shift

δ^{MQ} the shift of the isotropic axis

Δ_{offset} the Czjzek position parameter

$\Delta S/S_0$ the normalized REDOR intensity

ϵ the ellipsoid span

ϵ_0 the vacuum permittivity

ϵ_∞ the dielectric constant

ϵ_{ij}^{∞} the high-frequency dielectric

$\epsilon_\infty^{\parallel}$ the parallel component of the dielectric constant

$\epsilon_\infty^{\perp}$ the perpendicular component of the dielectric constant

η_{Q} the quadrupolar asymmetry parameter

θ the scattering angle; the tip angle; the phonon wavevector angle;

θ_{m} the magic angle

κ the chemical shift skew

λ the wavelength

μ_0 the vacuum permeability

μ_{m} the reduced mass

ν the Poisson's ratio

ν_0 the classical vibrational frequency

ν_{off} the offset frequency

ν_{Q} the quadrupolar frequency

ν_{rf} the RF pulse power

ρ the density

σ the surface energy of the nucleation interface; the stress tensor; the Czjzek breadth parameter; the chemical shielding tensor; the scattering cross-section

Σ the sphericity; the electrostatic bond strength sum

σ_{iso} the isotropic chemical shielding

σ_{ref} the reference isotropic chemical shielding

σ_{r_s} the standard deviation of the distance between the centroid of a coordination polyhedron and its ligands

τ_{w} the pulse duration

ϕ the WURST phase

Φ the heterogeneous nucleation factor

χ_{ij} the electric polarizability tensor

ω the radio frequency amplitude; the phonon mode frequency

Ω the chemical shift span; the solid angle; the unit cell volume

ω_{cf} the spectrometer carrier frequency

ω_i the transverse phonon frequency of mode i

ω_{L} the laser frequency

Acknowledgements

I've been a graduate student at Dalhousie University since the Fall term of 2013. This project started in earnest in the Fall term of 2014. Over these last five years I've been lucky to have the help and support of so many people, all of whom deserve thanks (though there's only space to thank them once).

To begin with, I could not have completed this degree without the guidance and support of Joe Zwanziger and Ulli Werner-Zwanziger. They have positively influenced every aspect of my time at Dalhousie. It has been an absolute pleasure to work with both of you. Thank you!

I would like to thank my committee members, Mark Obrovac and Daniel Boyd, for their supervision and contributions as members of my committee. Their critical contributions were valuable in reminding me to keep the bigger picture in mind.

I've had the pleasure of working with many people, at Dalhousie and elsewhere, without whom I would have struggled much more than I did. My co-authors, Alex Hannon, Emma Power, and Margaret Hanson, all of who wrote alongside me. The staff and scientists at Dalhousie (Andy George; Cathy Ryan; Dan MacDonald; Mike Boutilier; Mike Johnson; Mike Lumsden; Tim Hatchard; Todd Carter) played an important role in my time here, and they have taught me, trained me, and enabled my success. Special thanks to Alex Speed for vital help in synthesizing isotopically enriched samples, where there is little room for error.

The members of the Zwanziger group, both past and present, deserve some recognition. To the graduate students of the past (Courtney Calahoo, Justine Galbraith, Michał Plucinski), thank you for your mentorship and patience, as well as for making my arrival in Halifax a soft landing. To the postdocs (Mounesha Garaga Nagendrachar and Tsanka Todorova), thank you for showing me new perspectives on science. And to the new graduate students (Chris Sutherland and Milad Rezazadeh) and the undergraduate students (Jocelyn Sinclair, Miaad Fadami, and Trevor Law), it's been a pleasure to be part of your time at Dal.

To my friends and colleagues, within the department and without. There are too many of you to list here, but you've all worked together to make my time at Dalhousie not only productive, but actually fun. Be it board games, beers, or listening to me #$@&%, you've helped keep me (mostly) sane. It's very appreciated.

Finally, a thank you to my family, for their ongoing support in my studies and in my life. A special thank you to my partner Zoë, for so very much. Her caring, support, and patience has kept me going, especially in the sprint to the end. Zoë, I couldn't have done this without you.

Chapter 1

Introduction

This dissertation focuses on the study of the $LaBGeO_5$ glass and glass-ceramic system. The $LaBGeO_5$ glass-ceramic system has provoked interest as a potential transparent ferroelectric nanocomposite (TFN) material [1]. Furthermore, single-crystal $LaBGeO_5$ lines can be induced to form in the glass via laser-writing with a femtosecond laser [2]. This transition from amorphous glass to highly-ordered single crystal represents a profound change in the long-range order of the system; however, there is no model for the atomistic changes during laser writing. This is in part due to a lack of understanding of the structure of the glass.

The current structural model suggests that the glass is divided into two different regions: "crystal-like" regions, where the structure of the glass is largely similar to that of the crystal; and regions where the structure is considerably more amorphous. The data presented in support of this conclusion are insufficient to support this model. Hence, in order to support the study of the formation of $LaBGeO_5$ single-crystal lines in the glass, we ask the following question: *what is the structure of the* $LaBGeO_5$ *glass?*

This dissertation contains nine chapters, including this introduction.

The second chapter, Chapter 2, is a description of the study of the structure of oxide glasses, a literature review for the $LaBGeO_5$ system, and why the $LaBGeO_5$ system has drawn our interest. It also contains the stated goals of this work in Section 2.5.

The third chapter, Chapter 3, describes the theory and technical underpinnings of the techniques used in this work. Particular focus is given to glass synthesis, advanced nuclear magnetic resonance (NMR) spectroscopy, neutron diffraction, and density functional theory calculations. It does not contain specific experimental details, as these are reported in the appropriate chapters.

The development of a model relating ^{139}La NMR spectral parameters to the

structure of lanthanum oxide-based crystals is presented in Chapter 4. This model is refined and applied to the ^{139}La NMR spectra of lanthanum oxide-based glasses in Chapter 5. However, it is not obviously possible to extract the NMR observable used in the crystalline model from the ^{139}La NMR spectra of glass. Instead, ^{139}La NMR spectroscopy of glasses is better suited to assessing changes in the disorder surrounding La^{3+}.

Chapter 6 presents a combined neutron diffraction and ^{11}B NMR spectroscopy study of lanthanum borogermanate glasses, including $LaBGeO_5$. The neutron diffraction results support the presence of high-coordinate germanium species in the $LaBGeO_5$ glass.

The connectivity of glass bonding units is probed in Chapter 7. A combination of ^{17}O NMR spectroscopy and $^{11}B\{^{10}B\}$ heteronuclear NMR spectroscopy establish the presence (and absence) of various connectivities in $LaBGeO_5$ glass. The ^{17}O and ^{11}B NMR results also support a correction to the literature regarding the determination of the crystallite fraction of $LaBGeO_5$ glass-ceramic composites via high-resolution ^{11}B NMR spectroscopy.

The Raman spectral response of the $LaBGeO_5$ crystal to isotropic and anisotropic stress is determined via density functional perturbation theory (DFPT). The results are presented in Chapter 8, and compared to micro-Raman data from the literature. A qualitative model for the residual internal stresses in the $LaBGeO_5$ glass-ceramic composite is presented in the context of the anisotropic linear thermal expansion coefficients of the $LaBGeO_5$ crystal.

Finally, the results of the overall work are discussed in Chapter 9. The "data chapters" described above (Chapters 4 to 8) were either published, or prepared to be published, as journal articles prior to the completion of this work; hence they stand largely independent from one another. Chapter 9 presents the overall conclusions that can be drawn from the combination of these chapters, as well as their limitations, and proposals for future work.

There are several appendices at the end of this work that contain supporting information for the data chapters (where applicable), details of the computational work important for reproducibility, as well as copyright permissions. The final appendix contains the bibliography.

Chapter 2

Background

> Each of us is carving a stone, erecting a column, or cutting a piece of stained glass in the construction of something much bigger than ourselves.
>
> (Adrienne Clarkson)

Glass is ubiquitous in modern life. Glass is in our homes, our cars, our phones; it is on our bodies, and sometimes in our bodies; and in the form of the fibre-optic cables which make up the backbone of the internet, it ties us all together. When glass is mentioned in common conversation, it is the former uses which generally come to mind, the soda-lime-silicate glass used in buildings. However, the term glass encompasses a wide range of material compositions, some with many different properties and uses beyond construction.

2.1 What is a Glass?

For a material to be considered a glass, it must possess two characteristics. First, a glass is *amorphous*, and hence structurally isotropic: it does not possess any long-range, periodic arrangement of atoms, and as such has the same properties in all directions. It is possible to break this long-range isotropy by surface treatments (*e.g.*, tempering, ion-exchange), but in the absence of external influences or internal stresses, glasses are essentially isotropic [3]. Second, a glass exhibits a *glass transition* within a composition-dependent temperature range. The glass transition involves a continuous change in volume with a dramatic change in physical properties such as viscosity and thermal expansion. Both these characteristics must be present in a material for it to be considered a glass, and contribute to some of the special properties of glasses [3, 4].

Many categories of materials can exhibit these characteristics. Some examples which influence everyday life are metallic glasses — such as Metglas, typically a iron-based alloy used in electric transformers [5] — and certain plastics — such as

polycarbonate, used in applications ranging from water bottles to military aircraft [6]. The eponymous example of a glass, however, is the silicate glass. Silicate glasses are an example of the broader *oxide glass* family of materials. Oxide glasses are wholly or primarily composed of the oxides of metals or metalloids, such as Na_2O, SiO_2, or B_2O_3 [3]. Many oxide glasses share structural similarities across compositions, and share few with metallic or organic glasses. The particular focus of this work, $LaBGeO_5$, is an oxide glass. Hence this work is focused on the study of oxide glasses.

2.2 Glasses and Glass-Ceramics

2.2.1 The Structure of Oxide Glasses

Perhaps the oldest useful model of glass structure is that put forward by Zachariasen [7]. His 1932 work serves as the foundation of the *random network model*, though it is worth noting that a glass network cannot be truly random, as there are physical constraints on the internuclear distances of the atoms composing the network. Consider a compound consisting of a cation A and oxygen anion O with formula A_nO_m. Zachariasen proposed that glass formation may occur in the A_nO_m system if the following conditions are met:

1. the oxygen-cation coordination number is two or less;
2. the cation-oxygen coordination number is small, *i.e.*, 3 or 4;
3. the cation-oxygen polyhedra share corners, not edges; and
4. at least three corners of the cation-oxygen polyhedra are shared.

Under these four conditions, Zachariasen predicted the following: that oxides with the formula A_2O or AO will not form glasses under any conditions; that oxides with the formula A_2O_3 will form a glass if the A−O coordination number is three (*e.g.*, Fig. 2.1); and that oxides with the formulas AO_2 or A_2O_5 will form glasses if the A−O coordination number is four. These rules serve to describe some of the *glass network former* oxides, which are capable of forming a glass as the pure material. Typically, the glass network formers are considered to be B_2O_3, SiO_2, GeO_2, and P_2O_5, though this list is not exhaustive [3, 4]. These oxides can form a glass via the melt-quench

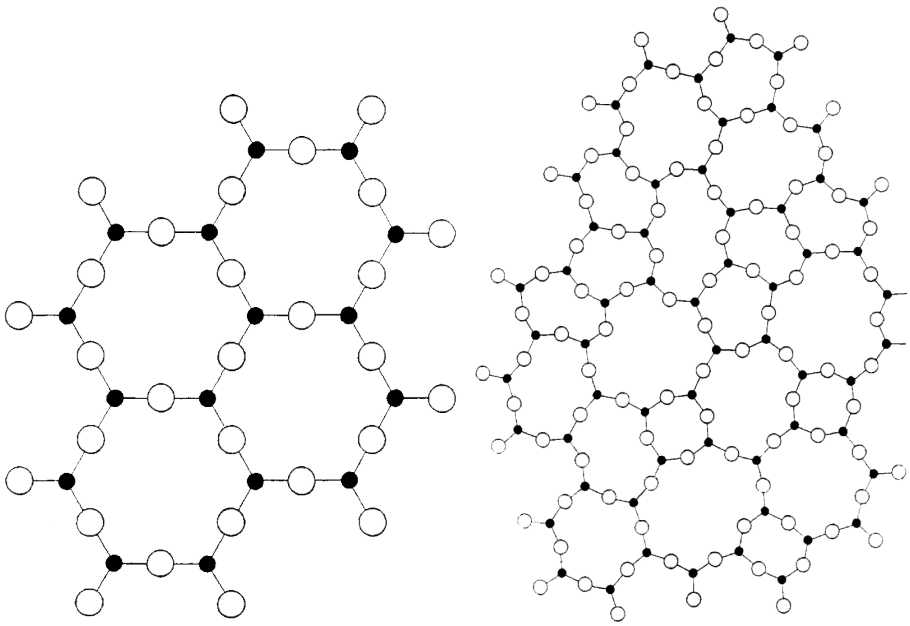

(a) The crystal lattice. (b) The glass network.

Figure 2.1: A schematic representation of the hypothetical two-dimensional compound A_2O_3. Figure 2.1a represents the periodic, crystalline arrangement, while Fig. 2.1b represents the glass network of the same compound. Note that while both have similar short-range order, the long-range behaviour of the glass and crystal are entirely different. Reprinted (adapted) with permission from W. H. Zachariasen, The Atomic Arrangement in Glass, J. Am. Chem. Soc. 54 (10) (1932) 3841–3851 [7]. Copyright 1932 American Chemical Society.

synthesis approach (Section 3.1). It is important to note that Zachariasen's conditions are not absolute; for example, SnO_2 is at best considered a network modifier, and often simply precipitates from the glass, while SnO can form the majority of a glass composition [8].

Beyond the glass network formers, there are two other broad classes of oxides which can be part of the glass network. The *glass network modifiers* are oxides which are unable to form a glass on their own, but can be incorporated into a glass composed primarily of a network former [3]. The prototypical example of a glass network modifier is Na_2O, which (among other effects) can dramatically decrease the melting point of a silicate glass. Many physical properties of a glass can be modified with the addition of an appropriate glass modifier oxide. Glass network modifiers often have the chemical formula A_2O or AO, though A_2O_3 is not uncommon.

The final class of oxides are known as the *glass network intermediates*. As the name implies, the network intermediates have properties which are intermediate between those of the formers and the modifiers. In structural terms, this often manifests in behaviour which is sometimes more modifier-like, and sometimes more former-like [3]. The best-known network intermediates are perhaps Al_2O_3 and PbO, though there are others (*e.g.*, Bi_2O_3, SnO) which qualify. The line between network modifier and network intermediate is poorly defined; the line between intermediate and former is only slightly clearer. For further discussion of the varying technical definitions of these three classes, see Ref. [3].

In oxide glasses, oxygen can generally be found in one of two broad categories [3]. The first is the bridging oxygen (BO) environment, which is indicated in this work by Ø. Bridging oxygen are oxygen which link two glass former (or former-like intermediate) cations. The bridged elements can be homogeneous or heterogeneous. For example, B–O–B oxygen are considered bridging, as would Ge–O–B. The second is the non-bridging oxygen (NBO) environment, frequently indicated by O^-. Non-bridging oxygen are bonded to a single glass former, as well as a network modifier (or modifier-like intermediate). B–O–Na would be an example of a non-bridging oxygen. There is technically a third possible environment, known as *free oxygen*, which consists of oxygen bonded to two network modifiers (*e.g.*, Ca–O–Ca); however, free oxygen is not necessarily present in a glass, and if it is it tends to be present in low concentrations [9].

As a general principle, the bonding of bridging oxygen tends to be more covalent, while the bonding of non-bridging oxygen is more ionic [3].

Coordination numbers are the focus of much of the discussion in this work. As mentioned above, Zachariasen predicted that glass formers were expected to have coordination numbers of three or four [7]. In practice, this is generally true; the A-O coordination numbers of pure B_2O_3, SiO_2, GeO_2, and P_2O_5 at standard pressures are three, four, four, and four, respectively. The addition of network modifiers and intermediates introduces species with greater coordination numbers. Modifiers typically have higher coordination numbers than formers; A−O coordination numbers of six to nine are not uncommon [10–13]. Intermediates often have coordination numbers between three and six; the Al−O coordination number again is a classic example, with Al−O coordination numbers of four, five, and six all coexisting in a single glass [14, 15].

The glass formers also have the potential of showing higher coordination numbers. Six-coordinate Si−O polyhedra have been shown to exist in glasses quenched at high pressures [16]. Two of the most studied examples of network formers exhibiting higher coordination are alkali borate and alkali germanate glasses, both of which show changes in coordination in response to the addition of modifier oxide. Both alkali borate and alkali germanate glasses exhibit an "anomaly", in which various physical properties undergo non-linear changes in response to the addition of alkali oxide [17–19].

The cause of the borate anomaly has been attributed to the changes in boron-oxygen coordination which occurs with the addition of alkali oxide [20]. Pure B_2O_3 glass is composed of threefold-coordinate BO_3 units, with a substantial fraction arranged into "boroxol rings" [21]. As network modifier oxide is introduced into the glass, the BO_3 units will convert to fourfold-coordinate $[B\emptyset_4]^-$ units, dramatically increasing the level of connectivity within the glass network [22]. As the modifier oxide concentration is increased further, $B\emptyset_2O^-$ units will form, and as it is increased further still even more depolymerized BO_3 species will appear. The different possible borate structural units are presented in Fig. 2.2.

The evolution of borate units is quite well understood, in no small part due to the amenable NMR properties of the ^{11}B nuclide. The same cannot be said for the evolution of germanate structural units. Like borates, alkali germanate glasses show

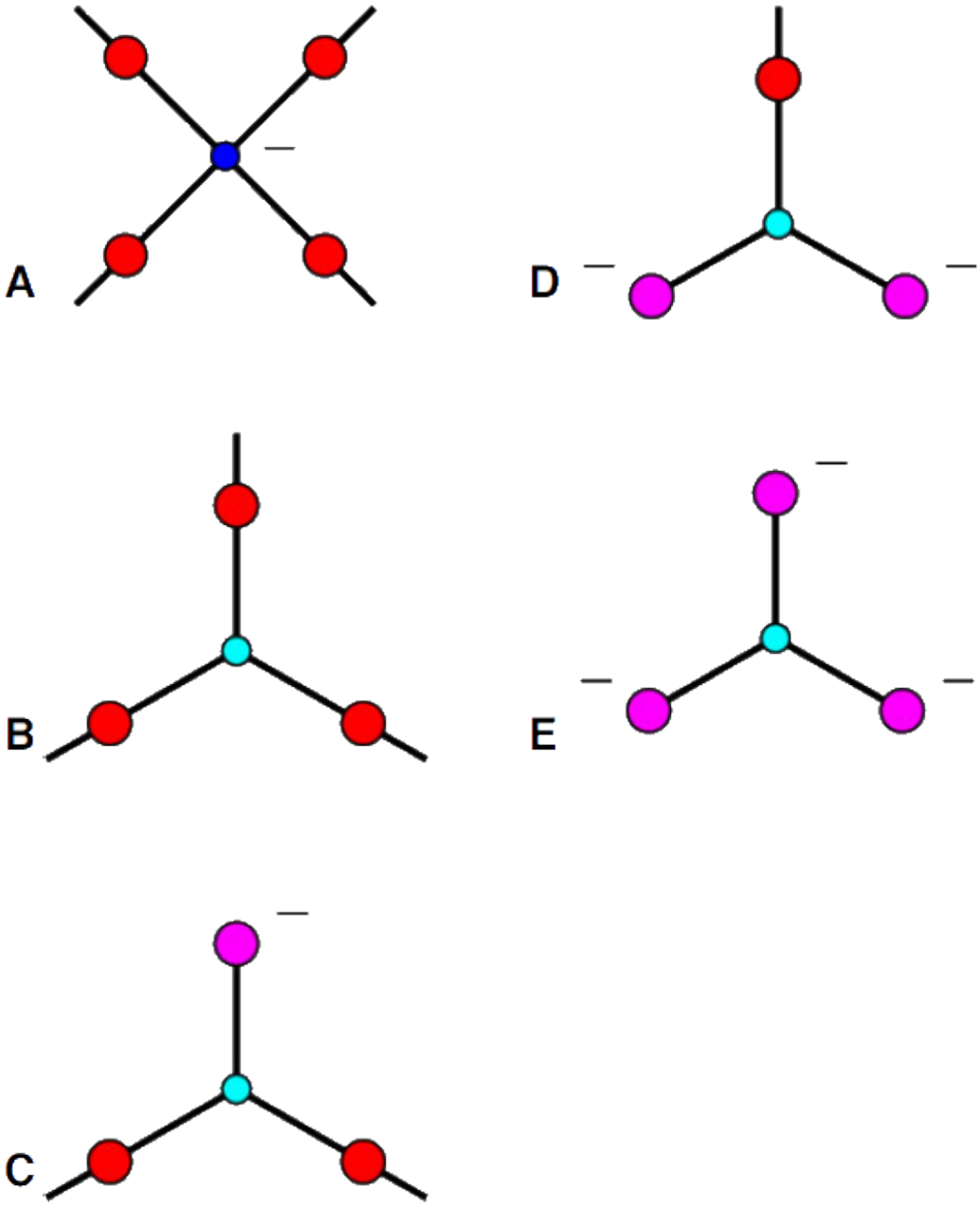

Figure 2.2: Schematic representation of the basic borate structural units. A) $[B\emptyset_4]^-$. B) $B\emptyset_3$. C) $B\emptyset_2O^-$. D) $B\emptyset\,O_2{}^{2-}$. E) $BO_3{}^{3-}$. In the figure, the blue circle represents tetrahedral boron, while cyan represents trigonal boron. Red circles indicate bridging oxygen ($\emptyset$), while magenta represent non-bridging oxygen (O^-). Reprinted with permission from A. C. Wright, My Borate Life: An Enigmatic Journey, Int. J. Appl. Glass Sci. 6 (1) (2015) 45-63 [20]. Copyright 2015 John Wiley and Sons.

non-linear evolution of properties with the addition of modifier oxide [23, 24]. This was termed the germanate anomaly. The study of the germanate anomaly is not as straightforward as the borate anomaly, in no small part due to the poor NMR properties of the ^{73}Ge nuclide [19, 25]. The precise nature of the structural rearrangements which cause the germanate anomaly have not been decisively determined, but it is generally accepted that it involves the presence of high-coordinate germanate units, *i.e.*, GeO_5 and/or GeO_6 [19, 26, 27]. Since GeO_5 and GeO_6 are not obviously differentiable in glasses via neutron diffraction, high-coordinate germanium is frequently labelled as $^{5/6}$Ge rather than one or the other [26, 28]. As the presence of $^{5/6}$Ge can potentially impact the physical properties of the glass, any structural model of a germanate glass must at least consider the presence of $^{5/6}$Ge.

2.2.2 Glass-Ceramics

Chemically, there are no distinctions between "glass elements" and "crystal elements"; a glass and a crystal can share the same composition, *e.g.*, SiO_2, GeO_2, B_2O_3. The primary distinction between a crystal and a glass is the presence or absence of long-range order. At short length scales, a bond between a silicon atom and an oxygen atom in a crystal is indistinguishable from the same in a glass. It should not come at a surprise, then, that it possible for crystals and glasses to simultaneously exist in the same material. When small crystalline domains, or *crystallites*, exist within a glass matrix, the resulting material is known as a glass-ceramic composite.

Crystallites most often occur in a glass when the liquid glass melt is cooled too slowly [3]. The crystalline form of a material is generally the thermodynamically stable form, whereas the glass is better described as being kinetically stable. When the temperature of the glass is above the glass transition temperature (T_g), the atoms composing the glass have enough energy to form nuclei. Here, nuclei are extremely small periodic collections of atoms that are the precursors of larger crystallites [3].

Nuclei can form in two different ways. The first is *homogeneous* nucleation. In homogeneous nucleation, nuclei form spontaneously and stochastically. The chance of homogeneous nucleation is the same everywhere in the glass. The second is *heterogeneous* nucleation. In heterogeneous nucleation, there is some surface or substrate which increases the probability of the formation of nuclei. Heterogeneous

nucleation sites include the surface of the glass, internal cracks or bubbles, or in some cases insoluble precipitates.

The formation of nuclei is governed by two considerations [3]. The first is the energetic barrier of the interface between the glass and the nucleus, which represents the change in structure between the two environments. The second is the change in the total free energy of the system. The crystal-like arrangement of the nucleus lowers the volume free energy of the system, but the introduction of a second environment results in an increase in the surface energy. The first condition imposes a minimum energy requirement on the formation of crystal nuclei; this often manifests as nucleation taking place at or near to the glass transition temperature T_{g}. The second condition affects the likelihood that a given nucleus survives to become a proper crystallite. For small nuclei, the surface energy term dominates, making nucleation energetically unfavourable. For large nuclei, the volume energy term dominates, and nuclei growth is favourable.

The work of nucleation W^*, for both heterogeneous and homogeneous nucleation, is given by

$$W^* = \frac{16\pi}{3}\frac{\sigma^3}{\Delta {G_x}^2}\Phi. \tag{2.1}$$

Here, σ is the surface energy of the interface between the nucleus and the glass, ΔG_x is the change in free energy from transforming a unit volume of the glass to a unit volume of the crystal (*i.e.*, the free energy of crystallization), and Φ is the so-called heterogeneous nucleation factor [3]. Φ can range from 0 to 1 depending on the contact angle between the nucleus and the substrate. When $\Phi = 1$, there is no difference between the heterogeneous and homogeneous nucleation cases. When $\Phi = 0$, there is no energetic barrier to nucleation. Hence, heterogeneous nucleation is either energetically comparable or favourable when compared to homogeneous nucleation.

Both heterogeneous and homogeneous nucleation exhibit behavioural dependencies on the reduced glass transition temperature (T_{gr}). T_{gr} is defined as $T_{\mathrm{gr}} = T_{\mathrm{g}}/T_{\mathrm{m}}$, where T_{m} is the melting temperature of the composition under consideration [29]. James and Zanotto suggest that when $T_{\mathrm{gr}} \geq 0.6$, only heterogeneous nucleation is possible, whereas when $T_{\mathrm{gr}} < 0.6$, both heterogeneous and homogeneous nucleation are possible [30, 31]. These predictions have been experimentally verified for silicate glasses [32].

The maximum nucleation rate is dependent on T_{gr}, as well as Φ. Figure 2.3 shows how maximum nucleation rate can vary depending on Φ. All else being equal, heterogeneous nucleation can occur at greater values of T_{gr} than homogeneous nucleation, significantly expanding the range of compositions which can be induced to crystallize.

For the vast majority of systems undergoing heterogeneous nucleation, the maximum nucleation rate will occur at lower temperatures than the maximum crystalline growth rate. This is particularly advantageous for the synthesis of glass-ceramics, as this allows for the semi-independent control of the number of crystallites and their size. The examples in Fig. 2.3 show why this control is only semi-independent: for all cases, the crystallite growth rate overlaps the maximum nucleation rate. It is not generally possible to induce nucleation without at least some growth, nor to grow crystallites without inducing further nucleation. This only becomes a problem, however, if the maxima are at quite similar temperatures.

Two-phase nucleation and growth has been observed in the $LaBGeO_5$ system [33, 34]. The type of nucleation mechanism which is most likely has been hypothesized to be related to structural similarities or differences between the glass and the crystallites [35, 36]. As will be discussed below, the structural differences between the glass and crystal forms of the $LaBGeO_5$ system are a central question of this work, and hence any link between structure and nucleation is of interest. The discussion of nucleation and growth in this work is mostly qualitative due to the difficulty of probing the interface between the nuclei and the glass, which is extremely small in both length and volume. For a more rigorous discussion of the crystallization of glasses, the interested reader is directed to the literature [37–39].

2.3 How Can We Study Glass Structure?

There are many techniques used for the study of the structure of glass, but the three predominant categories are NMR spectroscopy, vibrational spectroscopy, and X-ray and/or neutron diffraction. They each provide complimentary data regarding the structure of a glass. The theory of the techniques used in this study are provided in Chapter 3; the specific technical details are presented in the chapters where they are used. This section provides context on the use of these techniques, and examples of

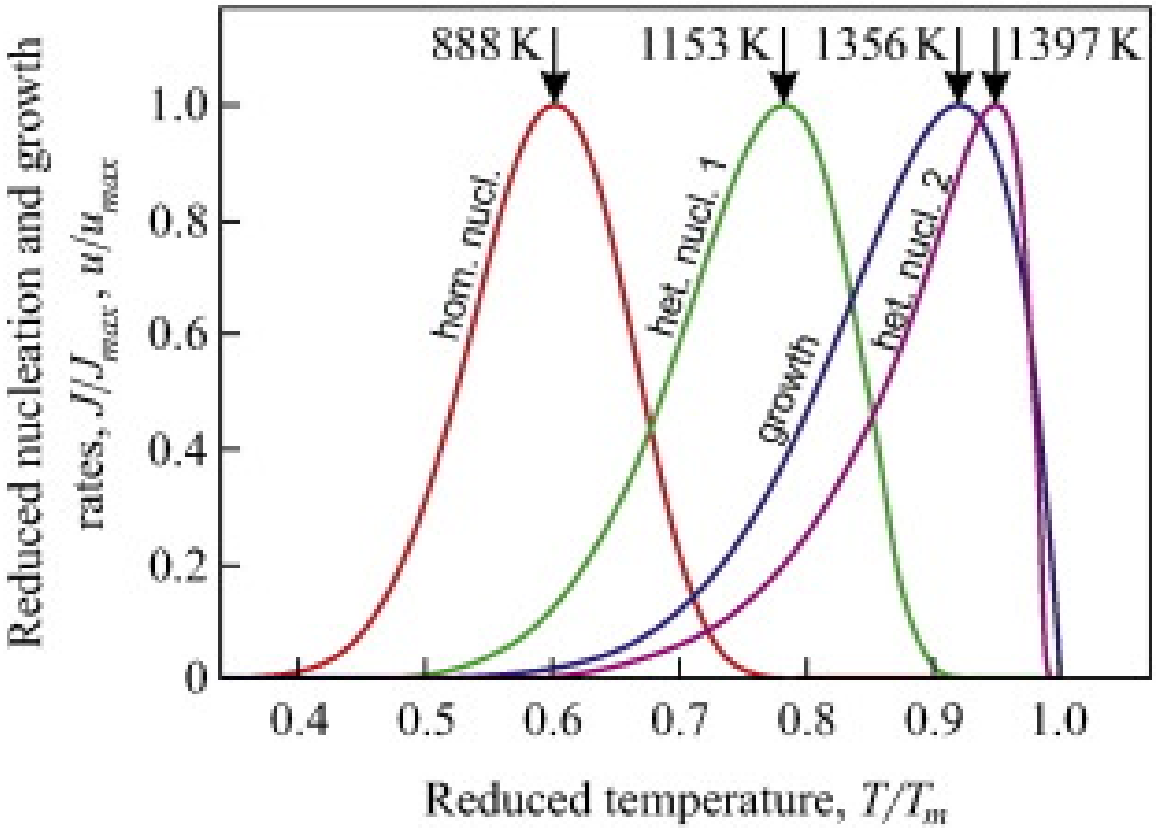

Figure 2.3: Possible nucleation maxima temperatures for homogeneous and heterogeneous nucleation. For both examples of heterogeneous nucleation, the maximum nucleation rate occurs at a temperature greater than that of the homogeneous nucleation rate. For example 1, $\Phi = 0.1$; for example 2, $\Phi = 0.001$. The difference between the heterogeneous and homogeneous cases is expected to be less dramatic for greater values of Φ. Reprinted from Journal of Non-Crystalline Solids, 429, Jürn W.P. Schmelzer, Alexander S. Abyzov, Vladimir M. Fokin, Christoph Schick, Edgar D. Zanotto, *Crystallization of Glass-Forming Liquids: Maxima of Nucleation, Growth, and Overall Crystallization Rates*, 24–32, Copyright (2015), with permission from Elsevier [29].

the conclusions that can be drawn from their use.

2.3.1 NMR Studies of Glass

NMR spectroscopy is a powerful technique for the study of glasses. It has been used to elucidate glass structure for both short-range and intermediate-range scales [40–46]. The specific details of the application and interpretation of NMR spectroscopy substantially depend on the nuclide under investigation. Therefore, rather than attempting to provide a comprehensive overview of how NMR spectroscopy is applied to all nuclides potentially present in glass, this section describes how the elements present in $LaBGeO_5$, *i.e.*, La, B, Ge, and O, interact with NMR spectroscopy.

Boron NMR spectroscopy is a long-standing technique for the study of borate glasses. It was first applied by Silver and Bray in 1958 to identify $[B\emptyset_4]^-$ units in sodium borate glasses [40]. There are two NMR-active boron nuclides, with very distinct spectroscopic properties [47]. ^{11}B is a quadrupolar nuclide with half-integer nuclear spin $I = 3/2$. It composes 80 % of natural abundance boron. The other NMR-active boron nuclide is ^{10}B. ^{10}B is also quadrupolar, but has integer nuclear spin $I = 3$. It composes 20 % of natural abundance boron. The most commonly used nuclide is ^{11}B. It has the greater sensitivity — due to the greater abundance and gyromagnetic ratio — and greater resolution — due to a lesser nuclear quadrupole moment and half-integer spin.

The study of borate glass structure by use of ^{11}B NMR spectroscopy typically involves the use of magic angle spinning (MAS) and multiple quantum magic angle spinning (MQMAS) NMR experiments. As discussed in Section 2.2.1, borate glasses often contain a variety of borate species. BO_3 and $[B\emptyset_4]^-$ species can usually be wholly resolved by use of MAS NMR, but separating BO_3 species frequently requires the use of MQMAS. The presence and identity of multiple coexisting BO_3 species can be determined, providing insight into the nature and degree of the network polymerization [48, 49]. Additionally, ^{11}B can detect changes in the connectivity of $[B\emptyset_4]^-$ unit via changes in its chemical shift [50, 51]. ^{10}B is not generally useful for NMR studies of glass, as the BO_3 environment is effectively unobservable; however, as ^{10}B and ^{11}B are chemically identical but spectroscopically distinct, the use of $^{11}B\{^{10}B\}$ heteronuclear NMR can provide boron-boron connectivity information [52].

Although oxygen is the majority atomic constituent of oxide glasses, oxygen NMR is not routinely applied to the study of glass. There is a single NMR-active oxygen nuclide, ^{17}O, with nuclear spin $I = 5/2$ and natural abundance 0.037 %. Effective ^{17}O NMR spectroscopy requires that the sample under investigation be enriched with ^{17}O, typically by hydrolysis of a halide or alkoxide of the appropriate cation. However, typically samples require at least 20 % ^{17}O enrichment, which in turn requires water of greater ^{17}O concentration; and water highly enriched with ^{17}O is expensive, in the range of 500 CAD g^{-1} to 2000 CAD g^{-1}. The high cost of ^{17}O enrichment makes ^{17}O NMR spectroscopy less feasible than NMR spectroscopy of other nuclides.

^{17}O NMR spectroscopy, when conducted on an enriched sample, can provide substantial information regarding the connectivity of the glass network. Bridging oxygen and non-bridging oxygen can frequently be resolved and quantified. Homonuclear (X-O-X) and heteronuclear (X-O-Y) bridges usually have different spectral properties, allowing for the investigation of network homogeneity or segregation [53]. Furthermore, different network polyhedra can sometimes be observed via ^{17}O MAS or MQMAS NMR, which has been used to establish the presence of high-coordinate germanium in alkali germanate glasses [54–56].

Lanthanum NMR spectroscopy has not been widely applied in the literature. Natural abundance lanthanum is 100 % ^{139}La, with $I = 7/2$. The nuclear quadrupole moment of ^{139}La is quite large [57], leading to extremely broad spectra. Only a single lanthanum-based oxide ($LaAlO_3$) has been collected under MAS conditions, and spectral collection typically requires significant signal enhancement [58–60].

Germanium is even less accessible via NMR spectroscopy than lanthanum. The only NMR-active germanium isotope is ^{73}Ge, with low natural abundance (7.76 %), a large quadrupole moment, and a low gyromagnetic ratio. While ^{73}Ge NMR spectra of germanate glasses have been collected, the experiments were both prohibitively lengthy as well as being unable to provide insight into the structure of the glass [25]. As ^{73}Ge NMR spectroscopy is not a viable option for the study of the Ge−O environment in glasses, we instead turn to neutron diffraction, which has been used to study germanate glasses to good effect [12, 42, 61, 62].

2.3.2 Neutron Diffraction Studies of Glass

X-ray and neutron diffraction are valuable tools for determining the structure of crystalline materials. The theory behind their use is described in Sections 3.3 and 3.8. The application of diffraction-based techniques to glasses is somewhat more complex than for crystals. In crystals, the inherent long-range order produces sharp diffraction peaks which are used to determine unit cell dimensions and ionic positions. Unit cell dimension and ionic positions are not well-founded concepts in glasses, and cannot be determined. Instead, diffraction data is used to produce correlation functions, from which bond distributions can be extracted. X-ray diffraction and neutron diffraction are complimentary techniques, as X-ray diffraction is based around the number of electrons in the system, while neutron diffraction is a function of the nuclides present. Neutron diffraction was used in this work in order to leverage the existing literature on germanate glasses [27, 28, 42, 61–67]. It is important to note that for this particular application of X-ray diffraction generally requires a synchrotron X-ray source, and is functionally distinct from powder X-ray diffraction (pXRD). While pXRD was used in this work, no synchrotron X-ray diffraction was carried out.

Neutron diffraction is well-suited for the structural study of glasses due to its high real-space resolution of mean bond lengths. For example, this property has allowed for the detection of the two different P−O bond lengths in phosphate glasses [42, 68]. In principle, if differing germanium coordination environments (*i.e.*, GeO_4, GeO_5, GeO_6) existed in a germanate glass, they would be expected to possess different bond lengths. However, what is observed in alkali germanate glasses is not distinct peaks corresponding to discrete bond length distributions, but a broad tail beginning at the GeO_4 peak and extending to longer bond lengths [28, 64]. This is generally understood to indicate a distribution of long Ge−O bonds that are not well-localized [12]. It is useful to note that neutron diffraction can quantify coordination number via integration, and does not require strict resolution of like bonds [27, 69]. Hence the mean coordination number of germanium can be determined without requiring to distinguish between the three possible units [26].

2.3.3 Vibrational Spectroscopy Studies of Glass

Infrared (IR) spectroscopy and Raman spectroscopy have both been applied to the study of glasses. However, Raman spectroscopy tends to provide more valuable information regarding the study of glasses due to the increased resolution of Raman modes as compared to IR modes [70]. In glasses, observable Raman modes are typically the various vibrational modes of the glass network forming polyhedra. Both X–O stretching modes and X–O–X bending modes can be observed, and with very careful experimental considerations, quantified [71]. Certain structures can have extremely distinctive Raman modes, *e.g.*, the sharp peak at $\approx 805\,\mathrm{cm}^{-1}$ associated with the boroxol ring breathing mode [72]. The vibrational modes of network modifiers are less frequently observed, as their bonding is more ionic and they tend to be heavier, both factors which will tend towards lower vibrational frequencies.

Raman spectroscopy is particularly pertinent to the study of $LaBGeO_5$ glass for two factors: the first is that Raman spectroscopy is frequently applied to the study of germanate glasses, and its use has the potential to provide meaningful data [73]; the second is that much of the current structural understanding of the $LaBGeO_5$ glass stems from Raman spectroscopy [74, 75].

The first structural model of the $LaBGeO_5$ glass, reported by Kratochvilova *et al.* in 2000, relied on Raman data to conclude that "...short range order in [the $LaBGeO_5$ glass] is the same as in the crystals...", *i.e.*, $[B\emptyset_4]^-$, GeO_4, and LaO_9 units [74]. This was shown to be incorrect by Gupta *et al.* in 2004 by the use of ^{11}B NMR spectroscopy [34]. The ^{11}B NMR spectrum of $LaBGeO_5$ glass unambiguously shows the coexistence of both BO_3 and $[B\emptyset_4]^-$ units in the glass. The peak associated with BO_3 in the Raman spectra of the $LaBGeO_5$ glass is subtle, but its presence was observable in the spectra reported by Kratochvilova *et al.*, and was confirmed by Sigaev *et al.* in 2010 [75]. However, determination of coordination number by Raman spectroscopy is not always straightforward, and in particular it is difficult to definitively establish the presence or absence of high-coordinate germanium in glasses via Raman spectroscopy [19]. As such, we used Raman spectroscopy only sparingly in our study of the $LaBGeO_5$ glass.

2.3.4 DFT Studies of Materials

Density functional theory (DFT) calculations are widely used in materials science, and allow for the calculation of a wide variety of physical properties [76]. In this work, DFT is used to calculate NMR parameters of a variety of crystal structures, as well as Raman spectra of the $LaBGeO_5$ crystal. DFT can often be used to probe systems which would be difficult to test experimentally. However, while DFT calculations of crystalline materials are generally straightforward to run, it is difficult to extend these to amorphous materials such as glasses.

Most DFT calculations of solids take advantage of periodic boundary conditions, which effectively impose perfect long-range order. As glasses have no long-range order at all, let alone perfect long-range order, this complicates the application of periodic boundary conditions to amorphous systems. The typical method of compensating for this imposed long-range order is to use a very large simulation "box" containing hundreds or thousands of atoms. This allows for the sampling of a large number of atoms that are effectively in a disordered environment, but has two main pitfalls. The first is that for large systems, DFT computational costs scale with the cube of the size of the system; anecdotally, the structural optimization for a simple sodium silicate glass can require several core-years of calculations. The second is that the structures used for DFT calculation of glass must be rigorously validated to ensure that the model is accurately describing the physical system under investigation. This too is very computationally expensive.

To summarize, while DFT calculations on crystals are relatively straightforward, the computational costs of applying DFT calculations to amorphous materials makes the latter beyond the scope of this work.

2.4 Which Glass is Studied in this Work?

The glass (and crystal) which are the primary research target of this work have the composition $LaBGeO_5$. This lanthanum borogermanate composition is a synthetic analogue of the stillwellite mineral (Fig. 2.4). Named in 1955 by McAndrew and Scott, natural stillwellite has the composition $(Ce, La, Ca)BSiO_5$, depending somewhat on its origin [77]. The system itself is chemically flexible, and generally follows the

Figure 2.4: An example of natural stillwellite. Sample is from the mineralogy collection of the Natural History Museum of London. Photo is of the sample on display on 2016-03-26.

formula $(Ln^{3+}, M^{2+})B(Si, Ge, Al, P)(O, OH, F)_5$. There are two synthetic examples of the stillwellite structure that have garnered particular attention in the literature: $LaBSiO_5$ and $LaBGeO_5$. For reasons which will be discussed below, this work focuses primarily on $LaBGeO_5$.

2.4.1 Crystal Structure and Properties

$LaBSiO_5$ and $LaBGeO_5$ are isostructural with space group $P3_1$ [78, 79]. Part of the interest in these crystals stems from the fact are that they are ferroelectric, *i.e.*, they possess a permanent electric dipole moment which can be changed by an electric field [80, 81]. Ferroelectricity is named in analogy to ferromagnetism, though while ferromagnetism is an asymmetry in electronic spin, ferroelectricity arises from an asymmetry of charge [82]. Both ferromagnetism and ferroelectricity are dependent on both the chemical composition of a crystal and also its space group. Ferroelectric materials, in particular, can only arise in *polar* space groups [80]. Polar space groups are defined by their ability to support a permanent electric dipole moment, and will posses at least one Cartesian direction which differs from the others [80]. In the $P3_1$ space group, this is the c axis. By the necessity of symmetry, ferroelectric materials are potentially pyroelectric and piezoelectric, and by definition all are noncentrosymmetric.

The crystal structure of $LaBGeO_5$ is displayed in Fig. 2.5; the structure of $LaBSiO_5$ is very nearly identical [78, 79, 83]. It has a single crystallographic La^{3+} site, B^{3+} site, and Ge^{4+} site, and five distinct O^{2-} sites. The ferroelectricity of the $LaBGeO_5$ and $LaBSiO_5$ are thought to originate in the $[B\emptyset_4]^-$ helix which is parallel to the crystallographic c axis [79, 84, 85]. The c axis is the 3_1 screw axis of the crystal. Ferroelectric materials undergo a phase transition at a critical temperature (known as the Curie temperature) to a paraelectric phase. The ferroelectric-paraelectric phase transition can be: displacive, where ionic positions are substantially changed; order-disorder, where the crystal structure loses the long-range order necessary to maintain a permanent dipole moment; or some combination of the two [82]. The phase transition in $LaBGeO_5$ is a combination of the two. The high-temperature ($T \gtrapprox 530\,^\circ\mathrm{C}$) phase of $LaBGeO_5$ is of space group $P3_121$ [79]. In the phase transition, the La^{3+} and Ge^{4+} ions move to a twofold rotation axis, while the B^{3+} ion (and one O^{2-} ion) move towards one of two positions near, but not on, the twofold axis. The

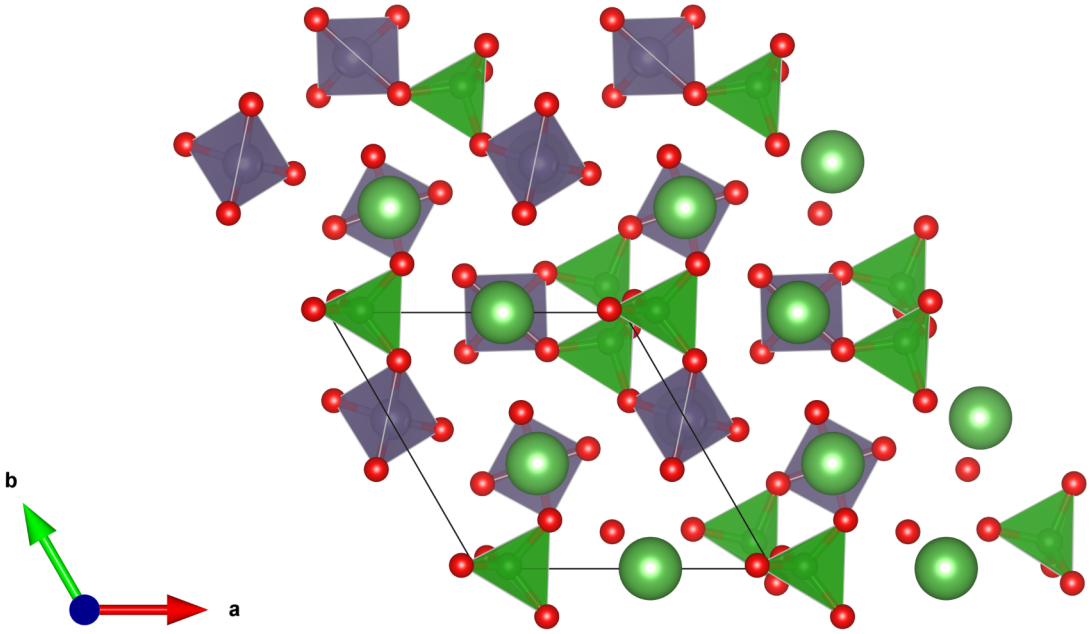

Figure 2.5: The room-temperature crystal structure of $LaBGeO_5$ [78]. The presented view is down the crystallographic c axis with a $2 \times 2 \times 2$ supercell. $[B\emptyset_4]^-$ tetrahedra are coloured dark green, while $Ge\emptyset_2O_2{}^{2-}$ tetrahedra are purple. LaO_9 polyhedra are omitted for clarity. Lanthanum ions are light green.

B^{3+} and corresponding O^{2-} site are half-occupancy, and this half-occupancy disrupts the periodic development of the $[B\emptyset_4]^-$ helix, hence contributing to the order-disorder nature of the phase transition [79].

The spontaneous polarization of the $LaBGeO_5$ crystal has not been precisely determined. Measurements and simulations by various different techniques have returned a range of values from $2.7\,\mu C\,cm^{-2}$ to $12\,\mu C\,cm^{-2}$ [85–88].

The optical properties of $LaBGeO_5$ also are a source of scientific interest. $LaBGeO_5$ has non-linear optical properties, and in particular is capable of second harmonic generation (SHG) [89]. SHG involves the process known equivalently as frequency doubling or wavelength halving: two photons with the same frequency interact within the crystal structure, and a photon of half the original frequency is emitted [90]. The largest SHG tensor component of the $LaBGeO_5$ crystal is $0.76\,pm\,V^{-1}$, comparing favourably to quartz ($0.3\,pm\,V^{-1}$) and lithium triborate ($0.84\,pm\,V^{-1}$) [91–93]. The SHG properties of $LaBGeO_5$ have lead to interest in its use as a potential optical waveguide, or as a self-doubling laser [94].

2.4.2 Our Interest

Our interests in the $LaBGeO_5$ system are primarily structural. As displayed in Fig. 2.5, the crystal structure of $LaBGeO_5$ is known; and as discussed above, many physical properties have been measured and are understood [78, 79, 91, 95, 96]. The glass has also been subject to investigation, and some of its properties (*e.g.*, T_g, shear modulus G, linear coefficient of thermal expansion α_L) have been previous reported [96]. Our interest, however, stems from the formation of $LaBGeO_5$ glass-ceramic composites by laser writing of the glass.

Glass-ceramics are partially-crystallized glasses which share properties of both the crystal and the glass. In the $LaBGeO_5$ system in particular, it is the ferroelectric properties of the crystal which are desirable. The glass cannot be ferroelectric (as it is disordered on long length scales), but it is substantially more straightforward to synthesize the $LaBGeO_5$ glass than a single $LaBGeO_5$ crystal. By inducing crystallisation of the glass, a $LaBGeO_5$ glass-ceramic is formed. $LaBSiO_5$ has also been targeted as a glass-ceramic; however, recent results show that pure $LaBSiO_5$ glass cannot be formed [97]. Literature reports on $LaBSiO_5$ glass samples typically are the

result of Al_2O_3 contamination of the glass from synthesis in Al_2O_3 crucibles [97, 98].

There are two aspects of $LaBGeO_5$ glass-ceramics which have received interest in the literature. The first is that $LaBGeO_5$ can form a TFN material. The $LaBGeO_5$ glass is optically transparent, and if the crystallites are sufficiently small (less than approx. 40 nm) they will not significantly impede the transmission of light [1]. Many studies have been carried out with the intent of optimizing crystallite growth via heating of the bulk $LaBGeO_5$ glass [33, 34, 99, 100].

The second interesting aspect of the $LaBGeO_5$ glass is that crystallisation of the glass can be induced via laser irradiation. First reported in $LaBGeO_5$ by Gupta *et al.* in 2007, laser-induced crystallisation has been performed using both continuous-wave and femtosecond lasers of a variety of wavelengths [2, 101–104]. Recent work has focused on the use of fs lasers to produce $LaBGeO_5$ crystal "lines" which appear to be a single crystal [2, 103–108]. These lines can be written into complex geometries, including forking paths, without observed grain boundaries which would indicate a polycrystalline sample [107]. The nature of the change from the disorder of the glass form to the extreme order of the single-crystal form is an interesting question.

Despite many studies concerning the formation of these laser-written $LaBGeO_5$ glass-ceramics, several important questions remain unanswered. First among them is "what are the atomistic changes in the glass during the crystallisation process?" Answering this question requires an understanding of both the crystal structure, which is well-known, and the glass structure, which is not.

The current structural model, proposed by Sigaev *et al.*, divides the $LaBGeO_5$ glass into two different types of "nanoregions": the first with a high concentration of four-coordinated boron in "'crystal-similar' fragments"; and the second being considerably more disordered, with the boron being threefold coordinate [75]. Both germanium and lanthanum are expected to have the same coordination behaviour in the glass as in the crystal [75]. The current structural data available in the literature are the Raman spectra presented by Sigaev *et al.* and the ^{11}B NMR spectra presented by Gupta *et al.* [34, 74, 75]. Both are consistent with the presence of both BO_3 and $[B\emptyset_4]^-$ units. However, neither speak to the connectivity of BO_3–$[B\emptyset_4]^-$units. Furthermore, ^{11}B NMR by its nature cannot provide direct information regarding the local structure of La or Ge. In principle Raman spectroscopy can provide information regarding both

La−O bonds and Ge−O bonds, but in practice the observation of La−O vibrations is impractical. GeO_6 can be observed in crystalline rutile-type GeO_2, but whether GeO_5 or GeO_6 can be detected in glasses via Raman spectroscopy was not clear at the time that the model of Sigaev *et al.* was reported [19, 73, 75]. In short, there are insufficient data available in the literature to produce a comprehensive model of the $LaBGeO_5$ glass structure, a problem that this work rectifies.

A second lingering question is the stress environment of the laser-written $LaBGeO_5$ lines. The thermal evolution of $LaBGeO_5$ during the laser-writing process is complex, but generally involves a portion of the glass being liquefied at high temperature, cooling sufficiently to crystallise (expected to occur above T_g), passing through T_g(at which point the glass network ceases to easily deform), passing through the phase transition at $T \gtrapprox 530\,°C$, and then cooling to room temperature [103]. This process induces enough stress in the sample that it cannot be carried out at room temperature; instead crystallisation is carried out with the bulk sample pre-heated to 400 °C [103, 108]. The complex thermal evolution, as well as the anticipated mismatch between the thermal expansion coefficients of the glass and the crystal, would likely lead to residual internal stress on the glass-ceramic composite material. The residual stress on the laser-written crystal has the potential to affect both its ferroelectric and optical properties, the two primary potential applications of the $LaBGeO_5$ TFN material [1, 108]. As such, it is important to understand the stress environment of laser-written $LaBGeO_5$ composites.

2.5 The Central Goals of this Work

The primary goal of this work is to develop a model of the short- and intermediate-range structure of the $LaBGeO_5$ glass, and thereby allow for future investigations into the crystallization mechanism of the laser-written $LaBGeO_5$ glass-ceramic composite. To this end, both the local environments of La, B, Ge, and O, as well as the connectivity of the glass network must be probed.

The first structural model of the $LaBGeO_5$ glass assumed that all local structure in the glass was the same as the crystal, *i.e.*, $[B\emptyset_4]^-$, GeO_4, and LaO_9 [74]. However, the boron-oxygen coordination number undergoes a dramatic change between the crystal (entirely $[B\emptyset_4]^-$) and the glass (both BO_3 and $[B\emptyset_4]^-$) [34]. The current structural model of the $LaBGeO_5$ glass acknowledges this change, but concludes that only the

borate environment is changing [75]. With the knowledge that the germanium-oxygen coordination number can in principle be greater than four, there is no *a priori* reason to discount the possibility of the presence of high-coordinate germanium in the $LaBGeO_5$ glass, and so the possible presence of $^{5/6}Ge$ must be investigated. There is no data whatsoever on the behaviour of lanthanum in the $LaBGeO_5$ glass; however, given the established changes in the boron environment, it is entirely possible that there will be significant differences here as well. Hence, to create a model of the short- and intermediate-range structure of the $LaBGeO_5$ glass, new data must be acquired.

The data which need to be acquired can be grouped into two categories: short-range order, concerning cation-oxygen coordination; and intermediate-range order, concerning the connectivity of network unit polyhedra. In the chapters that follow, the short-range order of La, B, and Ge in the $LaBGeO_5$ glass is probed by the use of a combination of NMR spectroscopy and neutron diffraction.

The change in B coordination number has been established in the literature, but the identity (or identities) of the BO_3 unit (or units) has not been determined [34]. Through the use of ^{11}B MAS and MQMAS NMR spectroscopy, the BO_3 environment can be characterized. This will provide data on the degree of polymerization of the borate network in the $LaBGeO_5$ glass.

As ^{73}Ge NMR is not an effective method for characterizing germanium in glasses, we turn to neutron diffraction. Neutron diffraction provides confirmatory data regarding the boron-oxygen coordination number, but most importantly is a direct probe of the distribution of bond lengths in the germanium-oxygen polyhedra. As high-coordinate germanium is expected to have substantially greater bond lengths than four-coordinate germanium, the observation of long germanium-oxygen bond lengths would support the hypothesis that the germanium environment in the glass is significantly different than the crystal.

Neutron diffraction can, in principle, probe the lanthanum-oxygen environment in $LaBGeO_5$ glass, but given the length scales of typical La–O bonds (approx. 2.4 Å to 2.8 Å) there is the possibility of substantial peak overlap in a glass as chemically complex as $LaBGeO_5$. ^{139}La NMR spectroscopy offers the potential to characterize the lanthanum-oxygen environment without interference from the rest of the glass network, but to date there have been no ^{139}La NMR spectra of lanthanum-containing

glasses reported in the literature.

In order to make use of ^{139}La NMR for the study of the $LaBGeO_5$ glass, we must first create a model of the response of ^{139}La NMR properties to changes in structure in crystalline materials. With a working crystal model of ^{139}La NMR behaviour, we can begin to interpret ^{139}La NMR spectra of glasses. This will provide data regarding the lanthanum-oxygen coordination number in the $LaBGeO_5$ glass, which can then be compared to that in the $LaBGeO_5$ crystal.

The approach described above provides data regarding the short-range order of the cation components of the glass, but provides limited information regarding the intermediate-range order. The intermediate-range order of the glass network formers (*i.e.*, boron and germanium) is more interesting than that of lanthanum, as the order of the former can be used to deduce the latter. The structural model proposed by Sigaev *et al.* proposes a network where three-coordinate boron is substantially segregated from four-coordinate boron [75]. To probe the intermediate-range order of the glass, we turn to ^{17}O NMR spectroscopy and ^{11}B$\{^{10}$B$\}$ heteronuclear NMR spectroscopy. Both have been used to probe the connectivity of glass networks; in particular, the latter allows for a direct test of the model proposed by Sigaev *et al.* [52]. If the ^{11}B$\{^{10}$B$\}$ heteronuclear NMR provides data suggesting BO_3–$[B\emptyset_4]^-$ avoidance, then the model of Sigaev *et al.* becomes more plausible. However, if the data suggests that BO_3–$[B\emptyset_4]^-$ units are substantially connected, then this would contradict the Sigaev *et al.* model.

An additional point of interest in the $LaBGeO_5$ system is the mechanism of crystallization. It has been hypothesized that if the structures of the crystal and glass forms are similar, homogeneous nucleation is more likely [35, 36]. Conversely, if the structures of the crystal and glass forms are dissimilar, heterogeneous nucleation is more likely. Observing heterogeneous nucleation in the $LaBGeO_5$ system would support a structural model where the structure of the glass is dissimilar to the structure of the crystal.

Finally, the stress environment of a laser-written $LaBGeO_5$ sample is evaluated via the use of DFT calculations. Previous literature studies on the stress environment in laser-written $LaBGeO_5$ samples concluded that the stress was isotropically compressive, and 0.75 GPa in magnitude [108]. However, the determination of both the magnitude

and direction of the stress were based upon Raman spectral data from a $LaBGeO_5$ crystal which was isotropically compressed, which may not reflect the complex geometry of the system [109]. We conduct DFT calculations to provide insight into the response of the $LaBGeO_5$ crystal to stress, and re-evaluate the available literature data.

In summary, the goals of the work described in this document are as follows:

- obtain data on the short-range structure of boron in the $LaBGeO_5$ glass via ^{11}B NMR spectroscopy;
- probe for the presence of high-coordinate germanium in the glass via neutron diffraction;
- develop a model relating ^{139}La NMR parameters to short-range lanthanum structure in crystalline materials;
- apply this crystalline model to ^{139}La NMR spectrum of the $LaBGeO_5$ glass to determine the lanthanum-oxygen environment;
- probe the connectivity of the $LaBGeO_5$ glass via ^{17}O NMR spectroscopy;
- test the Sigaev model directly via $^{11}B\{^{10}B\}$ heteronuclear NMR spectroscopy;
- examine the mechanism of crystallization of the $LaBGeO_5$ glass-ceramic composite;
- and evaluate the stress on laser-written $LaBGeO_5$ glass-ceramics via DFT calculations.

Chapter 3

Theory and Methods

The characterization of the structure and properties of oxide glasses and crystals can require a wide variety of different methods and techniques, as no single technique can provide all requisite data on a given material. As such, a wide variety of experimental and theoretical approaches are described in this document. The following chapter focuses on the theoretical underpinnings of the techniques used in later chapters. Specific experimental details are generally found within the applicable chapters.

3.1 Sample Preparation

All glasses produced for this work were produced using the melt-quench approach. The melt-quench approach generally involves three to five steps:

1. Glass reagents (often metal/metalloid oxides) are intimately mixed in stoichiometric amounts.

2. The combined reagents are calcined at a temperature lower than the melting temperature in order to drive off gaseous by-products.

3. The combined reagents are brought to a sufficiently high temperature to melt them.

4. The glass melt is "quenched" via rapid cooling through the glass transition temperature.

5. The quenched glass is annealed at a temperature near, but lower than, the glass transition temperature (T_g).

The first, third, and fourth steps are the fundamental steps of the melt-quench method of glass synthesis. The second and fifth steps are often useful, but are not necessary for certain applications.

The choice of reagents for glass synthesis depends on a number of factors, including stability, cost, and by-products (in particular gasses released during melting) [4]. Metal or metalloid oxides (or their precursors) are combined in stoichiometric amounts, melted at high temperature, and then "quenched" via rapid cooling of the melt. This rapid cooling of the melt passes through the T_g quickly enough that the formation of crystal nuclei is inhibited, and a glass is formed [3]. The precise rate of cooling can have observable effects on the structure of the glass, but for the investigations within this work it is sufficient that the rate of cooling is high enough to prevent crystallization. The oxide reagents or oxide precursors were combined as powders, and intimately mixed using a porcelain mortar and pestle. Glass precursors composed solely of oxide reagents (such as La_2O_3, B_2O_3, and GeO_2) can be placed directly into a furnace of the appropriate temperature to melt the mixture.

If the glass precursor requires the use of a reagent that will be converted to the desired oxide (*e.g.*, H_3BO_3, $NH_4H_2PO_4$), it can be beneficial to add a calcining step at an intermediate temperature prior to melting [4]. This calcining step allows for by-product gases (*e.g.*, H_2O, NH_3, CO_2) to be removed, in order to prevent their incorporation into the glass. For glasses containing components that are volatile, or have volatile by-products, limiting the length of time spent at high temperatures can mitigate mass loss.

During glass melting, the choice of crucible becomes important. An ideal crucible is stable at the melting temperature of the glass, does not interact chemically with the glass, and is minimally wet by the glass (to aid in pouring for quenching). Crucibles are commonly produced from alumina, silica, or various metals. For glasses where the tolerance for impurities is low, it is wise to use platinum or platinum-alloy crucibles. Both Pt and Pt/Au crucibles were used in this work, as alumina contamination in lanthanum borogermanate and lanthanum borosilicate compositions has particularly severe consequences [97, 98].

Quenching can be accomplished by a variety of means, including pouring into moulds, pressing flat between metal plates or rollers, dipping the bottom of the crucible into water, or directly pouring the melt into water. The details of quenching are not explored in this work; for further details on quenching refer to the literature [3]. Glasses described herein were quenched either by pouring onto a brass plate (typically

preheated to near 400 °C), or in the case of particularly viscous glasses, by dipping the bottom of the crucible into water.

After quenching, it is usually valuable to immediately anneal the glass at a temperature near to, but below, T_g. Annealing the glass allows for residual thermal stresses to relax. If residual thermal stresses are allowed to persist, it is possible that the glass will fracture upon cooling to room temperature. Even if the glass is stable at room temperature, the forces introduced by *e.g.*, cutting and polishing can interact with the residual stress and cause cracking. For the preparation of glasses for optical measurements, or for elemental analysis (Section 3.4) annealing is a recommended step. However, for analysis by techniques that do not depend on a flat surface (*e.g.*, NMR spectroscopy, neutron diffraction) it is not strictly required.

For certain applications (*e.g.*, neutron diffraction, ^{17}O NMR) it may become important to isotopically enrich the sample. Enrichment with ^{11}B is straightforward, as $^{11}B_2O_3$ ($\geq 99\%$ ^{11}B) is commercially available. Enrichment with ^{17}O is somewhat more complicated, as ^{17}O is typically sold as $^{17}O_2$(g) or $H_2{}^{17}O$(l). The precise method of introducing the ^{17}O to the glass will vary with composition, but a common method is via hydrolysis of an appropriate metal halide or alkoxide [55]. Borane in solution is also acceptable for enrichment of borates, avoiding the by-product of hydrofluoric acid. The hydrolysis typically takes place in a double displacement reaction. For example, for the production of ^{17}O-enriched GeO_2:

$$Ge(OCH_2CH_3)_4(l) + 2\,H_2{}^{17}O\,(l) \longrightarrow Ge^{17}O_2(s) + 4\,CH_3CH_2OH\,(l).$$

In this work $Ge^{17}O_2$ and $H_3B^{17}O_3$ were produced with the assistance of Prof. Alex Speed of the Dalhousie University Department of Chemistry.

3.2 Physical Properties

3.2.1 Density

Density is a particularly important physical property for the study of glass structure, as it is a quantity frequently required in the measurements of other properties (*e.g.*, neutron diffraction, Section 3.8). The mass density of the glass samples were determined via two methods: via use of Archimedes' principle, and via helium pycnometry.

The use of Archimedes' principle is an elegant means of determining the density of a sample of arbitrary shape [110]. Its working equation is straightforward and requires the knowledge of only a few simple properties. Determining the density of a sample (ρ_{sample}) requires only measuring the weight of the sample in air (W_{air}), the weight of the sample in a working liquid (W_{liquid}), and the density of the working liquid (ρ_{liquid}). ρ_{sample} is then calculated by

$$\rho_{\text{sample}} = \rho_{\text{liquid}} \left(\frac{W_{\text{air}}}{W_{\text{air}} - W_{\text{liquid}}} \right) \tag{3.1}$$

Sample weights are typically straightforward to determine accurately, only requiring an analytical balance. The density of the working liquid may present a source of error, as it has the potential to change with temperature or with time (*e.g.*, for hygroscopic liquids). In this work the working liquid was absolute ethanol, and its density was varied as a function of the temperature at the time of measurement. Measurements were reproducible to within $\leq 1\,\%$. Accuracy was calibrated via measurement of a piece of fused quartz, which has a reliable density of $2.20\,\text{g}\,\text{cm}^{-3}$.

For applications which are significantly affected by the accuracy of the density (*e.g.*, the determination of coordination number via neutron diffraction), or for powdered samples, helium pycnometry can be used instead of Archimedes' principle [110]. In helium pycnometry, a sample of known mass but unknown volume is inserted into a chamber of known volume. The chamber is then filled with a known volume of helium. The pressure of helium in the sample chamber can then be used to calculate the volume of the sample. Calculating the density of the sample is then straightforward. Measurements were generally reproducible to within $\leq 0.2\,\%$.

The density of the sample is closely related to the molar volume (V_{M}) of the material [110]. The molar volume is the ratio between the molar mass of the glass and its density. Determination of the molar mass of a sample requires accurate knowledge of both its density (as above) and its composition (see Section 3.4). The advantage of molar volume is that it removes the mass term from the density, which can make comparisons between differing compositions more straightforward.

3.2.2 Thermal Analysis

Both thermogravimetric analysis (TGA) and differential scanning calorimetry (DSC) were used occasionally in this work; however, they were not the focus of any particular portion. The description of their operation will be brief; for further detail the reader should refer to reference [110].

In TGA, the weight of a sample is recorded as it undergoes changes in temperature. The sample is placed on a precision balance inside of a furnace. As the temperature is increased, mass changes can indicate a number of different phenomenon. Adsorbed water may be released, or phase transitions can release gases (*e.g.*, H_2O, CO_2) that were previously incorporated in the crystal structure. In this work TGA was used to determine the temperatures of several decompositions, for example

$$LaPO_4 \cdot nH_2O \longrightarrow LaPO_4 + nH_2O.$$

In DSC, the temperature of the sample (contained within a pan of known mass and thermal properties) is held at the same temperature of an empty reference pan. The difference in power provided to the pans is plotted as a function of temperature. Thermal events, such as phase changes, crystallization, decomposition, and importantly the glass transition can be observed, and their temperatures quantified, by careful analysis of the DSC curve. In this work T_g was taken as the inflection point of the glass transition event.

3.2.3 Elastic Properties

The linear elastic behaviours of materials are described by the elastic stiffness tensor, C_{ij} [111]. The elastic stiffness tensor is defined as

$$\sigma_{ij} = C_{ijkl} s_{kl} \tag{3.2}$$

where σ is the stress applied to the system and s is strain experienced by the system. For small values of σ, the amount of strain is proportional to the applied stress, and is described by C_{ij}. The elastic stiffness tensor is generally sufficiently symmetric that its order can be reduced via Voigt notation [112]. For isotropic materials such as glasses,

many of the elements are zero, and most others are related by symmetry. All non-zero elements can be fully described by three terms, only two of which are independent:

$$C_{44} = \frac{1}{2}(C_{11} - C_{12}). \tag{3.3}$$

Furthermore, the elastic moduli (in this case the Young's modulus E, the bulk modulus K, the shear modulus G, and the Poisson's ratio ν) of glasses are interrelated such that there are only two independent values. With the knowledge of any two, the other two can be calculated exactly [3]. The elastic moduli can be related to C_{ij} via the following relations:

$$C_{11} = \frac{E(1-\nu)}{(1+\nu)(1-2\nu)} \tag{3.4}$$

$$C_{12} = \frac{E\nu}{(1+\nu)(1-2\nu)} \tag{3.5}$$

$$C_{44} = G = \frac{E}{2(1+\nu)}. \tag{3.6}$$

The elastic moduli can be measured via a variety of means, but for glasses the ultrasonic method is particularly convenient [3]. The ultrasonic method relies upon two facts: the first is that glasses are isotropic, and hence have no directionally-dependent properties; the second is that for isotropic materials, the elastic moduli can be related to the speeds of sound in that material. There are two speeds of sound: the longitudinal velocity v_{L}; and the transverse (or shear) velocity v_{T}. They can both be measured in a similar fashion with only a change in transducer.

In the ultrasonic method, a transducer propagates a pulse through a glass sample of known thickness. The time required for the pulse-echo to be observed is used to calculate the velocity of the pulse. With both the longitudinal and ultrasonic velocities,

the various elastic moduli can be calculated:

$$\nu = \frac{1 - 2\left(\frac{v_T}{v_L}\right)^2}{2 - 2\left(\frac{v_T}{v_L}\right)^2} \tag{3.7}$$

$$G = {v_T}^2 \rho \tag{3.8}$$

$$K = \rho\left({v_L}^2 - \frac{4}{3}{v_T}^2\right) \tag{3.9}$$

$$E = \frac{\rho {v_T}^2 (3{v_L}^2 - 4{v_T}^2)}{{v_L}^2 - {v_T}^2} \tag{3.10}$$

The density is a term for the calculation of almost all of the moduli, and hence a precise determination of the elastic moduli requires good knowledge of the density (see Section 3.2.1). Accurate measurement of the velocities requires a homogeneous glass sample that is free of cracks or bubbles. The reliability of the method is greatest when the glass sample is prepared with parallel sides.

3.3 Powder X-Ray Diffraction

PXRD is a widely-used technique in the field of materials science. Typical applications include the identification of crystalline phases, the measurement of crystallite sizes in polycrystalline samples, and the quantification of samples of mixed phase [113]. As will be discussed below, the direct application of pXRD to amorphous materials (*e.g.*, oxide glasses) is difficult due to their disordered nature. However, as oxide glasses are typically produced using polycrystalline reagents, pXRD is nevertheless a valuable tool in the synthesis and study of glassy materials.

The fundamental equation governing pXRD is known as Bragg's law. Bragg's law describes the diffraction of radiation of wavelength λ by a series of atomic planes separated by a distance d. Figure 3.1 shows the diffraction from such a pair of parallel planes. Incident X-rays will be diffracted from the planes regardless of geometry. However, if the difference in path length between reflections from neighbouring planes is an integer multiple of the wavelength of the X-rays, they will interfere constructively. Hence Bragg's law is stated as

$$n\lambda = 2d\sin\theta \tag{3.11}$$

where θ is the scattering angle and n is an integer [114].

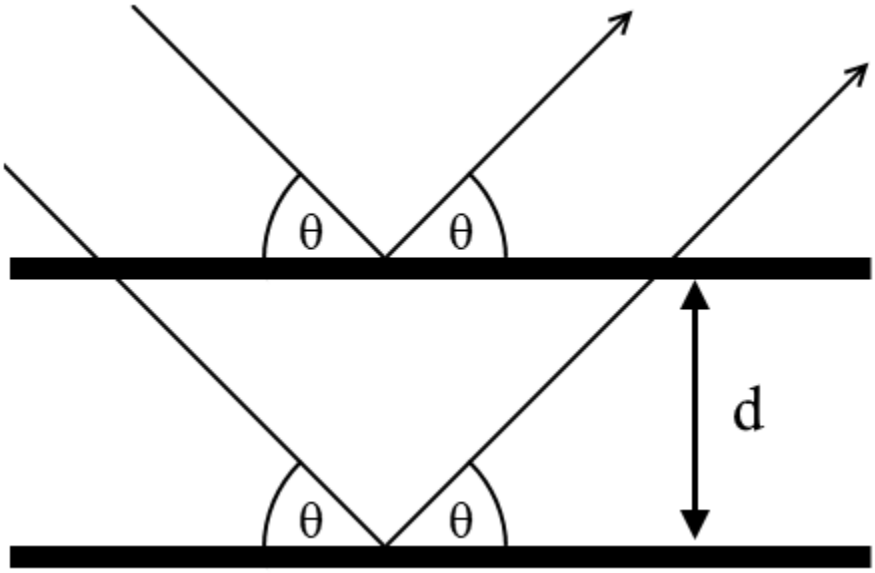

Figure 3.1: A schematic of Bragg's law for a pair of parallel planes. The X-ray beams constructively interfere when the path length difference between them is an integer multiple of the wavelength, a value which is equal to $2d \sin\theta$.

As presented in Fig. 3.1, it is straightforward to visualize the effects of Eq. (3.11) for a simple pair of parallel planes. However, the atomic structure of a crystal can lead to a set of distinct and varied planes which depend on not only the relative magnitude and orientation of the lattice vectors, but also on the identity of the atoms making up the crystal. This makes X-ray diffraction a powerful tool for the determination of crystal structures. Additionally, as the X-ray diffraction pattern is characteristic of both the identity of the atoms and their relative position within the crystal structure, pXRD can be used to identify the composition and phase of unknown materials.

Typically the identification of a sample involves comparison of the experimental diffraction pattern to a database of previously reported diffraction patterns, rather than determining the structure *de novo* for each sample. These databases are sometimes proprietary (*e.g.*, the International Centre for Diffraction Data's Powder Diffraction File) and sometimes open-source (*e.g.*, the Crystallography Open Database). In either case, phase identification is typically based primarily upon the position of the diffraction peaks, and then by their intensity. A basic knowledge of the likely composition of the sample can be quite beneficial, in order to narrow the set of possible

matches.

The effectiveness of Eq. (3.11) is conditional on a number of factors. The incident X-ray beam must be both collimated and monochromatic to ensure only reflections corresponding to a particular lattice spacing are observed. Similarly, consistent lattice spacings (*i.e.*, long-range structural order) must exist for constructive interference to occur [113]. This latter condition severely restricts the application of pXRD to glasses, which by definition are disordered on long length scales.

With no consistent lattice spacings over long ranges, well-defined Bragg peaks are absent from X-ray diffraction patterns of glasses. Instead, broad and featureless distributions are observed when conducting pXRD of amorphous samples. It is technically possible to extract statistical information regarding the glass structure from pXRD of glasses, but this typically requires exacting experimental conditions and detailed modelling [113]. Other techniques (*e.g.*, NMR spectroscopy, Raman spectroscopy) are frequently better suited to the restrictions imposed by the disordered structure of glass. However, pXRD has one particularly important application in the study of glasses. As Bragg diffraction peaks of crystallites are generally quite narrow (and substantially narrower than any glassy distribution), the presence of even small amounts of crystallites in a glass can be observed via pXRD. PXRD is therefore an important technique for confirming the amorphous nature of a glass sample prior to further study.

X-ray diffraction can be run on a variety of different types of instruments (varying X-ray sources, sample geometry, and detectors), and a comprehensive discussion of their relative features and merits is beyond the scope of this work [113]. A brief description of the type of instrument used in this work follows; a schematic is presented in Fig. 3.2. X-rays are generated via a Cu Kα source: low-energy electrons are emitted from a filament (typically tungsten), accelerated towards a copper anode via a strong electric field (on the order of tens of keV), and upon impacting the anode trigger the release of X-rays. The X-rays are collimated by a divergence slit, which ensures that the X-ray beam that diffracts off of the sample is reasonably parallel. The diffracted beam passes through a receiving slit (minimizing spurious reflections), and the diffracted beam is ensured to be monochromatic by passing it through a monochromator prior to detection. For X-ray diffraction, a monochromator is typically a single crystal with

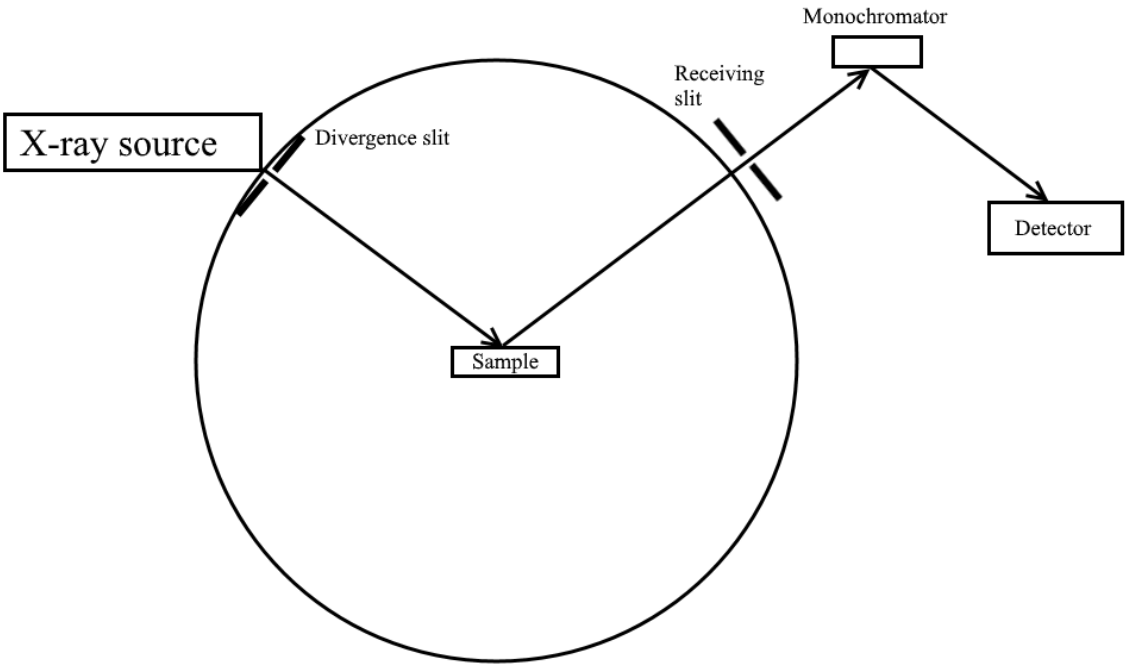

Figure 3.2: A schematic of a Bragg-Brentano powder X-ray diffractometer. X-rays are collimated by a divergence slit and diffract off the sample. Diffracted X-rays are collimated by a receiving slit prior to being diffracted by a monochromator. The monochromatic, parallel beam of X-rays then reaches the detector. The scattering angle is varied by moving the X-ray source and the detector assembly (receiving slit, monochromator, detector).

well-known d-spacing, allowing for particular wavelengths to be selected via Eq. (3.11). The diffracted X-rays corresponding to a given scattering angle are detected via a scintillation detector. The scattering angle is controlled via simultaneous movement of the X-ray source and the detector, in a configuration known as the Bragg-Brentano geometry. With this configuration, the incident X-rays are collimated, and the detected X-rays are monochromatic, thus fulfilling the requirements of Bragg diffraction.

3.4 Elemental Analysis

Characterization of the composition of a given sample — typically termed elemental analysis (EA) — is an important part of understanding the structure and properties of the sample. Without careful EA, it can be difficult to derive trends based upon compositional changes, as there are a number of effects which can alter the composition of a glass as it is melting.

One common source of contamination is the crucible that the sample is prepared in. Typical crucibles for the production of glasses are made of silica, alumina, or a platinum alloy (*e.g.*, Pt, Pt/Au, or Pt/Rh). Silica and alumina are particularly troublesome as sources of contamination, as both SiO_2 and Al_2O_3 are easily incorporated into many glass compositions. Platinum-based crucibles are generally effective at mitigating contamination, as Pt is not easily incorporated into oxide glasses.

Another frequent source of differences between nominal and actual composition is oxide volatility. Many oxides and their derivatives (*e.g.*, P_2O_5, B_2O_3, Cs_2O) are known to become volatile at high temperatures [115]. Depending on the composition of the glass, it may not be possible to mitigate these losses by melting at lower temperatures. Hence EA is an important aspect of understanding the system under investigation.

There are a number of different EA techniques that are commonly used to characterize the composition of glasses. Briefly, they can be categorized into two categories: "wet" techniques, where the sample is dissolved via an appropriate solvent (frequently an acid), and the solution is characterized by common analytical methods; and "dry" techniques, where the sample is non-destructively characterized.

Most glass samples in this thesis are either $LaBGeO_5$ or a close relative. $LaBGeO_5$ is quite chemically durable, and we found it difficult to dissolve directly. It is common to use a flux to enhance the solubility of the sample: the analysed glass is melted

with a water-soluble glass, and the resulting mixed glass is analysed. However, the fluxes used in this method are typically borates; given that $LaBGeO_5$ glasses are substantially composed of boron, have high melting temperatures, and are known to have concerns regarding borate volatility, we were concerned about the reliability of this approach for our particular system. We turned instead to two dry techniques: wavelength dispersive spectroscopy (WDS) and laser ablation inductively coupled plasma mass spectrometry (LA-ICP-MS).

3.4.1 Electron Microprobe Analysis

Electron microprobe analysis (EMPA) is a common method of characterizing the elemental composition of glasses. As with many techniques, an electron microprobe can be coupled to different detectors. The two EMPA detectors in common use allow for energy dispersive spectroscopy (EDS) and WDS. We first discuss the operation of the electron microprobe, and then the differences in physics and application between EDS and WDS.

Both EMPA detectors operate by analysing characteristic X-rays released by the sample [116]. In order to generate the X-rays, the sample must be bombarded by free electrons. The free electrons are generally produced by heating a tungsten filament to high temperatures. The tungsten filament produces a large number of low-energy electrons that are not directionally-oriented. For EMPA to be useful, the electron beam must be both high-energy and well-collimated. Both are achieved by applying a strong ($\sim$15 keV) positive voltage to a metal plate with an aperture. The low-energy electrons are drawn to the plate (increasing their kinetic energy), and only those with appropriate directionality pass through the aperture (improving the collimation of the beam). The collimation is further improved by a series of magnetic lenses. The beam diameter at the focal point (typically the surface of the sample) is on the order of 1 to 10 µm.

Upon impacting the sample, the electron beam scatters in various ways. For EMPA, the important scattering occurs in the core electrons of the atoms in the sample. The incident high-energy electron displaces a core electron, producing a vacancy. This vacancy is filled with an electron from a higher energy level. An electron moving from a higher energy level to a lower energy level releases energy in the form of a photon.

For the core electrons, this photon is an X-ray. The precise energy of the X-ray is dependent on the electronic structure of the atom in question. As such, each element has a characteristic set of X-ray emissions in EMPA, and hence EMPA can be used to identify the elements present in a sample.

A common detection method for EMPA is EDS. In EDS, all X-rays emitted by the sample are detected nearly simultaneously, and separated based upon their energy [116]. The detector is a semiconductor block which determines the energy of an incoming X-ray by counting the number of electrons that it causes to enter the conduction band. Some of the advantages of EDS detection (as opposed to WDS detection) are that EDS collection is extremely fast, and can detect a significant number of elements simultaneously. However, the elemental specificity of an arbitrary EDS peak is not necessarily straightforward. While the set of X-ray photons emitted by an atom are characteristic of a particular element, an X-ray of a given energy (or equivalently, wavelength) could indicate one of many elements. An element will emit X-rays of a variety of energies, which are often quite disparate. This can cause substantial peak overlap between EDS peaks of different elements, hindering accurate quantification.

An additional complication of EDS is that it is frequently conducted with detectors equipped with beryllium windows. The beryllium of the window is notionally X-ray transparent, but will in fact attenuate X-rays produced by the lighter elements ($Z \leq 11$, *i.e.*, sodium or lighter) [116]. If so equipped, EDS is then not suitable for the analysis of borate glasses.

For analysis of the lighter elements, WDS is preferred. Whereas EDS separates the characteristic X-rays of the sample by energy, WDS separates them by wavelength [117]. While the wavelength of the X-ray is related to its energy by the Planck-Einstein relation (*i.e.*, $E = hc/\lambda$), it is usually easier to effect changes in X-ray geometry than in detector physics. By working in wavelengths, we can take advantage of Bragg's Law (see Eq. (3.11)).

In WDS, the characteristic X-rays are generated in the same fashion as in EDS. Rather than collecting all X-rays simultaneously, however, specific X-ray wavelengths are selected. The details of X-ray collection are similar to the operation of a powder X-ray diffractometer (See Section 3.3). The important differences between WDS and EDS come from the X-ray selectivity enabled by fine control of the detector geometry.

The wavelength resolution of WDS is far superior to the energy resolution of EDS, enabling both elemental selectivity and decreasing the limit of detection. However, as different elements cannot be analysed simultaneously, WDS collection times are generally significantly greater than EDS collection times [117].

Despite the technical ability of WDS to analyse light elements, such as boron, accurate and precise quantitative determination of these elements can be quite challenging. Boron is particularly difficult to quantify reliably, as its characteristic X-rays are very low-energy, and are frequently absorbed by heavier elements present in the sample (*e.g.*, La, Ge). It is possible to apply matrix effect corrections to attempt to compensate for the resulting low intensity of boron characteristic X-rays, but substantial uncertainties can remain despite the best efforts of the experimenter. This is an inherent complication to quantification of borate glasses present in any X-ray-based technique.

3.4.2 LA-ICP-MS

An alternative method for elemental analysis of glasses is LA-ICP-MS. In LA-ICP-MS, a laser is used to remove small amounts of material from the sample ("ablation"). The ablated material is conveyed to an argon plasma torch, heated to high temperatures by time-varying magnetic fields ("induction"). The highly-energetic argon particles in the torch ionize the constituent atoms of the sample material. The resulting ions are then directed to a mass spectrometer, which separates the ions based upon their atomic mass. A schematic of the instrument is presented in Fig. 3.3.

As a non-X-ray technique, LA-ICP-MS does not face particular challenges when quantifying light elements such as boron. However, due to potential variation in the ablation of the sample from the laser, effective use of LA-ICP-MS requires significant effort to optimize the performance of the laser for a given sample. Furthermore, accurate quantification in LA-ICP-MS is best achieved with reference materials which match the sample matrix, and with established external calibration standards [118]. $LaBGeO_5$ is a particularly difficult target in this context, as it is dissimilar to the geological or common industrial glasses that receive the most attention for standardization. Matrix effects are quite likely, as commercial glass are typically silicates; and even in glasses which contain lanthanum, boron, and germanium, $LaBGeO_5$ will

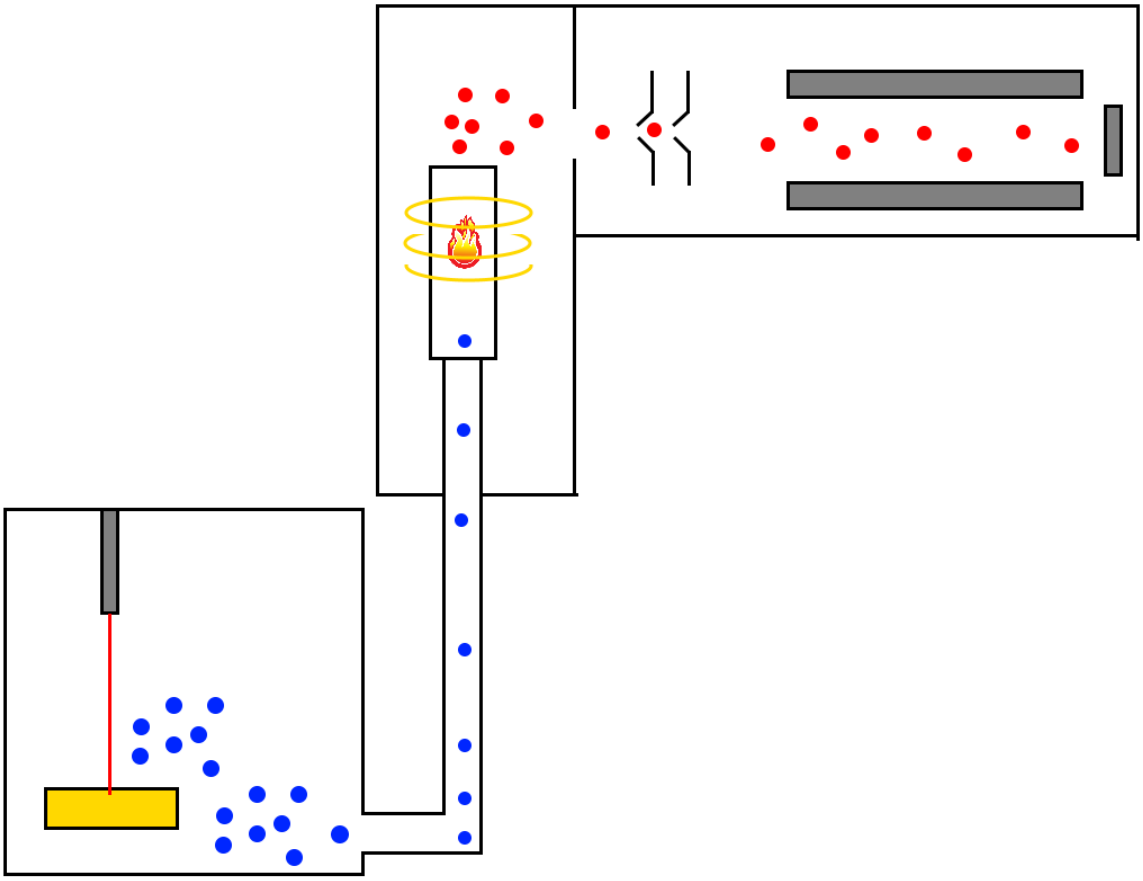

Figure 3.3: A schematic of a LA-ICP-MS instrument. A laser impacts the sample, which causes particles to be released from the surface. The particles are drawn to an inductively coupled argon plasma torch, which atomizes the particles and ionizes the atoms. The ions are drawn into a mass spectrometer, which separates them based on their mass and charge. The atoms can be identified based upon the time taken to pass through the mass spectrometer. The entire procedure is carried out under varying levels of vacuum. No part of the diagram is to scale.

contain substantially greater fractions of each. Hence WDS and LA-ICP-MS are best considered complimentary techniques, with WDS providing a reliable La/Ge ratio and LA-ICP-MS providing an overall approximation of the composition.

3.5 Nuclear Magnetic Resonance Spectroscopy

NMR spectroscopy is an incredibly useful technique in the field of chemistry. While solution-state NMR is of particular use to synthetic chemists, in part due to the spectroscopic properties of ^{1}H, solid-state nuclear magnetic resonance (ssNMR) has been extensively applied to the studies of crystals and glasses. The particular utility of ssNMR when applied to amorphous materials such as glasses comes from two fundamental aspects of NMR spectroscopy. The first is that NMR spectroscopy is practically nuclide-selective. While certain nuclides can have resonances which overlap at certain field strengths (*e.g.*, ^{137}Ba and $^{35/37}$Cl [119]), for most investigations a given spectrum arises from the target nuclide. This selectivity is particularly valuable in chemically complex glasses. The second useful aspect of NMR spectroscopy for the study of glasses is that NMR spectroscopy primarily (though not exclusively) probes *local* order. As opposed to pXRD, which requires substantial long-range order, NMR spectroscopy can provide useful information regarding the local environments of crystals, glasses, intermediate states, and composites.

NMR spectroscopy, whether carried out on solution-state or solid-state samples, is a mature technique. Rather than rehashing the fundamentals of NMR spectroscopy from first principles, the novice reader is directed to one of many introductory textbooks on the subject [47, 120, 121]. The contents of this section focus on the aspects of ssNMR that have particular relevance to the work contained in later chapters, and assume a base level of experience with NMR principles.

3.5.1 Magic Angle Spinning

MAS is a fundamental technique for ssNMR. The technique involves packing a sample (typically powdered) inside a cylindrical rotor, and then spinning the rotor on a bed of air at high speeds at an angle to the magnetic field. The “magic angle” is approximately

$\theta_m = 54.74°$ [122]. Its origin is the root of the second Legendre polynomial,

$$P_2(\cos\theta_m) = \frac{1}{2}\left(3\cos^2\theta_m - 1\right) = 0. \tag{3.12}$$

In a rotating system, many NMR interactions contain the second Legendre polynomial, and hence rotating at the solution of Eq. (3.12) will effectively negate these interactions. This results in a substantial narrowing of the peaks, enhancing their resolution. Interactions which contain the second Legendre polynomial include the first-order (but not the second-order) quadrupolar broadening, the chemical shift anisotropy, and the dipolar coupling.

It is important to note that MAS is only effective at mitigating an interaction when the rotation speed is comparable to the magnitude of the interaction (in Hz) [47]. Spinning speeds in excess of 130 kHz have been reported in the literature, but typical spinning speeds are substantially lower, typically between 4 kHz and 30 kHz. The physical maximum spinning speed of a rotor depends on its material (typically ZrO_2) and its diameter, with narrower rotors more capable of higher speeds. However, narrow rotors can only contain small amounts of sample. Hence rotor choice is typically governed by the amount of sample required for timely acquisition, and not simply the highest available speed.

Even the highest available MAS speeds can prove to be wholly insufficient when applied to nuclides with extremely large quadrupole moments. For example, fully narrowing the ^{139}La NMR spectrum of $LaBGeO_5$ would require MAS spinning speeds in excess of 440 kHz at a field strength of 16.4 T. For such broad peaks, instead of attempting MAS the spectra are collected under static (*i.e.*, non-spinning) conditions. Sensitivity enhancement techniques are frequently used as well.

3.5.2 Wideband, Uniform Rate, Smooth Truncation Pulses

Wideband, uniform rate, smooth truncation (WURST) pulses were first introduced by Kupče and Freeman in 1995 [123, 124]. While the full name is an accurate description for the shape and behaviour of the pulse, it is likely a "backronym"; the pulses typically resemble sausages (*i.e.*, rounded-end cylinders). WURST pulses are intended to provide uniform adiabatic inversion of the bulk magnetization over a wide

bandwidth. The time-dependent amplitude ($\omega_1(t)$) of a WURST-N pulse is given by

$$\omega_1(t) = \omega_{\max}\left(1 - \left|\cos\left(\frac{\pi t}{\tau_{\mathrm{w}}}\right)\right|^N\right) \tag{3.13}$$

where $\omega_{\max}$ is the maximum radio frequency (RF) amplitude and τ_{w} is the duration of the pulse. The exponent N determines the overall shape of the pulse. At low values of N, the maximum RF amplitude is reached only briefly, and a WURST-2 pulse is similar to a hyperbolic secant pulse. At large values of N, the WURST pulse resembles a square pulse, with sharp truncations. Intermediate values of N are required for the WURST pulse to have both smooth truncation and significant time spent at maximum RF amplitudes. WURST-80 pulses are a commonly used compromise between these two competing requirements [125].

The phase (ϕ) of a WURST pulse is described by

$$\phi(t) = \pm 2\pi\left\{\left(\nu_{\mathrm{off}} + \frac{\Delta}{2}\right)t - \left(\frac{\Delta}{2\tau_{\mathrm{w}}}\right)t^2\right\}. \tag{3.14}$$

Δ is the sweep width of the WURST pulse. ν_{off} is the offset frequency of the centre of the sweep. This phase modulation allows for the linear progression of the effective frequency of the pulse, and contributes to its wideband character. It also allows for the frequency to be swept in both positive direction (*i.e.*, low to high frequencies) and negative direction (*i.e.*, high to low frequencies). To ensure homogeneous excitation, it is typically advisable to run two experiments, one with each sweep direction, rather than using one or the other.

Empirically, the WURST pulses used in this work provided fairly homogeneous excitation over a range of approximately 80% of Δ, consistent with literature reports [125]. The maximum Δ that could be achieved on the spectrometer available was 1 MHz. However, $\Delta = 500$ kHz was found to generally provide more homogeneous spectra when considering the peak breadth, sensitivity, and response to changing sweep direction. WURST pulses often provide lower absolute signal-to-noise ratios than square pulses of equivalent power, but due to their greater bandwidth the resulting overall intensity is greater.

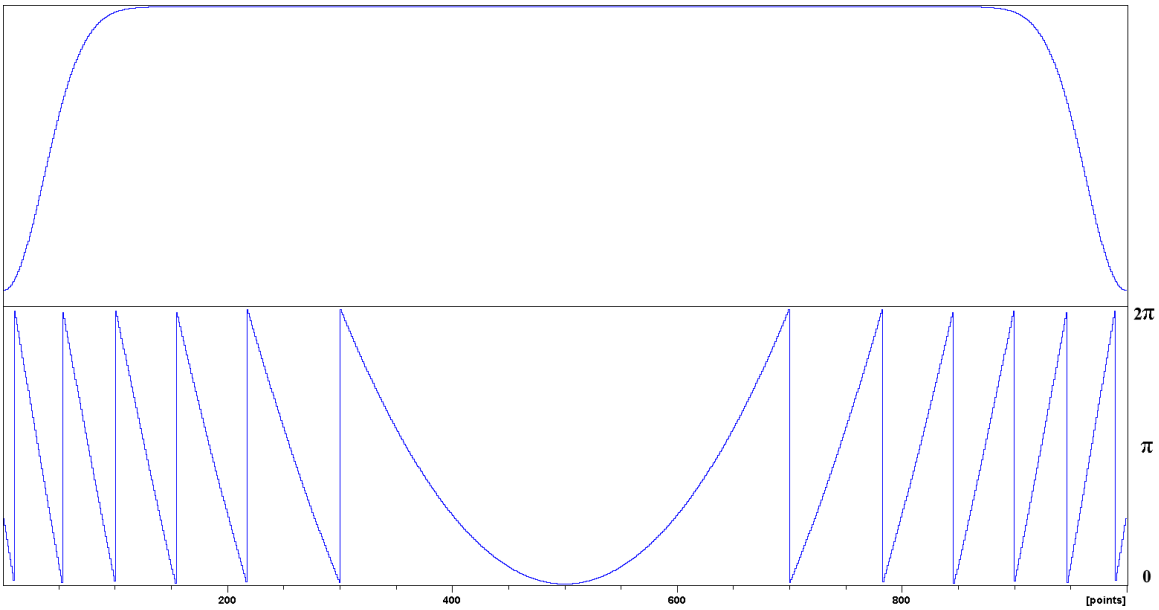

Figure 3.4: The amplitude (top) and phase (bottom) of a WURST-80 pulse. The pulse displayed uses 1000 points and has a Δ of 1 MHz, and is similar to what was used in this work. The phase of the pulse is displayed over a [0,2π] interval.

3.5.3 The WCPMG Pulse Sequence

Even with the substantial bandwidth provided by WURST pulses, many NMR line widths are so broad to prohibit their collection within a single spectral window. For example, for the spectrometers used in this work, the maximum frequency window which can be collected is 1 MHz, while the ^{139}La NMR spectrum of $LaBGeO_5$ spans more than 1.2 MHz at 16.4 T (Chapter 4) [126]. To collect these "ultra-wide" spectra, it is typically necessary to generate a variable offset cumulative spectrum (VOCS) [127, 128]. VOCS involves collecting multiple spectra ("slices") at various transmitter frequencies (chosen to ensure homogeneous excitation of the linewidth), summing them, and analysing the resulting spectrum. As multiple experiments must be carried out, for practical acquisition the time required for each slice must be minimized. An effective signal-enhancement method for this task is the WURST Carr-Purcell Meiboom-Gill (WCPMG) pulse sequence [123–125, 129–131]. The WCPMG pulse sequence is the combination of the well-known Carr-Purcell Meiboom-Gill (CPMG) sequence with WURST pulses.

The CPMG pulse sequence is an excitation pulse followed by a series of refocusing pulses [130, 131]. The refocusing pulses result in a "train" of echoes which persists

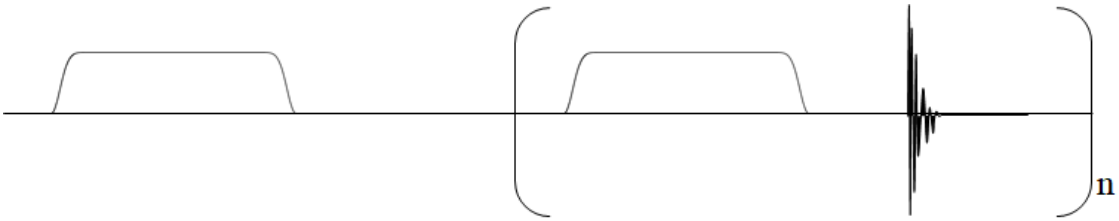

Figure 3.5: The WCPMG pulse sequence [129].

until coherence is lost due to transverse relaxation. When this echo train is Fourier transformed, it results in a spectrum composed of "spikelets". The intensity manifold of these spikelets reproduce the powder lineshape of the spectrum. The density of the spikelets depends on the spacing of the echoes. A greater delay between echoes leads to more densely packed spikelets, allowing for greater resolution of spectral features. However, the greater delay between echoes reduces the total number of echoes collected, reducing the level of signal enhancement. The choice of echo spacing is therefore a balance between signal and resolution. However, even small numbers of collected echoes can lead to a substantial signal enhancement as compared to a Hahn-echo experiment. The spikelets are centred on the excitation frequency of the VOCS slice, and hence the position of the centre spikelet contains no information. This is in contrast to a MAS experiment, where the spinning speed determines the position of the spinning sidebands relative to an isotropic peak, the position of which is independent of the excitation frequency.

The above paragraph deals with the CPMG pulse sequence. The only difference between the CPMG sequence and the WCPMG sequence is that the latter uses WURST pulses, rather than "square" pulses. The WCPMG pulse sequence was first reported by O'Dell and Schurko in 2008 [129], and is displayed in Fig. 3.5. The effects of using WURST pulses in the CPMG echo train are: that the bandwidth of the experiment is increased, as per Section 3.5.2; and that the absolute number of echoes which can be collected are slightly decreased, due to the typically longer pulse lengths of WURST pulses. However, the net integrated intensity of WCPMG is generally greater than that of CPMG using square pulses. The net result in the context of VOCS acquisition is that WCPMG slices require less time to collect, and fewer are required, which together greatly decrease total experimental time for homogeneous spectral collection.

3.5.4 Multiple Quantum Magic Angle Spinning

MQMAS is an invaluable technique in ssNMR of quadrupolar nuclei. Developed in 1995 by Medek *et al.*, MQMAS is a two-dimensional NMR experiment which has been widely applied to both crystalline and amorphous materials [132]. The primary advantage of the MQMAS experiment is the dramatic increase in resolution in spectra with multiple environments which overlap in the MAS experiment. There are a large number of variations and developments upon the basic MQMAS pulse sequence, but the fundamental experiment involves four steps [133]:

1. Multiple quantum (MQ) coherences are excited by RF pulses;
2. The MQ coherences are allowed to evolve;
3. The MQ coherences are reconverted to single quantum coherences via additional RF pulses; and
4. The signal is detected.

The evolution of the MQ coherences causes the second-order quadrupolar interactions to be averaged, resulting in very sharp half-integer quadrupole resonances. The theory behind MQ coherences is beyond the scope of this work; the reader is directed to the literature for further details.

The practical considerations of MQMAS follow [47]. Split-t_1 MQMAS spectra are two-dimensional NMR with a MAS axis and an "isotropic" axis. The projection of the MAS axis is generally extremely similar to a single-pulse MAS experiment, subject to lineshape distortions introduced in the MQMAS experiment. The projection of the isotropic axis is free of anisotropic quadrupolar and chemical shift contributions. Peaks in the isotropic axis are generally quite narrow (in well-ordered materials), leading the isotropic axis to also be referred to as the "high-resolution" axis. The position of a peak in the MQMAS spectrum is dependent on both its isotropic chemical shift ($\delta_{\mathrm{iso}}^{\mathrm{CS}}$) and its quadrupole parameters (C_{Q}, η_{Q}). Hence peaks which may be poorly resolved in the MAS experiment (which separates based upon $\delta_{\mathrm{iso}}^{\mathrm{CS}}$) can be fully resolved in MQMAS.

Resolution limits in MQMAS generally arise from one of two causes. The first is spectral. The number of data points which can be collected is restricted by the T_2

relaxation of the environments present in the sample. If the relaxation is fast, only a limited number of points can be collected, and hence the resolution of the isotropic axis cannot be improved. The second cause is structural. The isotropic average is free of anisotropic quadrupole and chemical shift interactions. However, if there exists a distribution of environments with similar chemical shift and quadrupole parameters (as in, for example, a glass) they will result in a relatively broad peak. Both fast relaxation and structural broadening are common in glasses, and as such MQMAS spectra of glasses are rarely as sharp and well-resolved as in crystalline materials.

Beyond providing qualitative evidence of the existence of multiple environments in a sample, MQMAS spectra can provide quantitative values for $\delta_{\text{iso}}^{\text{CS}}$and for P_{Q}. The centres of gravity of a peak in the MAS and isotropic dimensions can be used to calculate the values of $\delta_{\text{iso}}^{\text{CS}}$ and P_{Q} for said peak, with the precise formula depending on the referencing convention used [134]. In this work all MQMAS spectra are referenced with the C_z convention [132, 134]. In the C_z convention, the isotropic chemical shift and quadrupole product are calculated as follows:

$$\delta_{\text{iso}}^{\text{CS}} = \frac{10}{27}\delta_{G2}^{\text{obs}} + k_{\text{Gz}}\delta_{G1-z}^{\text{obs}} \tag{3.15}$$

$$P_{\text{Q}} = A\sqrt{k_{\text{Gz}}\left(\delta_{G1-z}^{\text{obs}} - k_{1\text{z}}\delta_{G2}^{\text{obs}}\right)}. \tag{3.16}$$

k_{Gz} and $k_{1\text{z}}$ are factors affecting the position of the MQMAS echo, and depend on the spin of the nuclide under investigation (I), as well as the MQ transition being excited. Their values are tabulated by Millot and Man [134]. $\delta_{G1-z}^{\text{obs}}$ and δ_{G2}^{obs} are the centres of gravity of the peak in the isotropic and MAS dimensions, respectively. A is a spin- and frequency-dependent prefactor required for calculating P_{Q}, and is

$$A = I(2I-1)\frac{\omega_{\text{cf}}}{2\pi}\sqrt{\frac{40}{3\left[I(I+1) - \frac{3}{4}\right]}}. \tag{3.17}$$

These equations are valid for both crystalline and amorphous materials, though in the latter they are better understood as means of a distribution, rather than as precise values. The consequences of distributions of quadrupole parameters are discussed in further detail in Section 3.5.5.

3.5.5 The Czjzek Model

Glasses are disordered materials. Rather than the well-defined bond lengths and angles present in a crystal, in glasses these properties are distributed over a range of possible values. Similarly, the electric field gradient (EFG) tensor, and its elements, will also be subject to this statistical disorder. An analytical expression for describing statistical disorder in quadrupolar environments was first formulated by Czjzek in the context of Mössbauer spectroscopy [135]. Czjzek's model has been extended to NMR studies of quadrupolar nuclei in disordered materials via the efforts of Le Caër, Brand, Massiot, and many others [136–139]. It is known under several names, including the Czjzek model and the Gaussian Isotropic Model. A straightforward derivation of the Czjzek model is provided by by de Lacaillerie *et al.*; rather than repeat the derivation, a summary of the important experimental considerations are provided [139].

The Czjzek model is a joint probability distribution function (PDF) of ν_Q and η_Q, where ν_Q is

$$\nu_Q = \frac{3eQ}{2I(2I-1)h} V_{zz}. \tag{3.18}$$

The analytical expression of the joint PDF is

$$p_Q(\nu_Q, \eta_Q) = \frac{1}{\sqrt{2\pi}\sigma^5} {\nu_Q}^4 \eta_Q \left(1 - \frac{\eta_Q}{9}\right) \exp\left[-\frac{{\nu_Q}^2\left(1 + \frac{{\eta_Q}^2}{3}\right)}{2\sigma^2}\right]. \tag{3.19}$$

Here, σ is the standard deviation of the five independent elements of the EFG tensor. This distribution analytically describes the asymmetric lineshape of disordered quadrupolar environments in NMR spectra, and is particularly useful for quantitatively fitting partially resolved environments (*e.g.*, ^{27}Al NMR spectra of glasses). The validity of this PDF relies on four assumptions, quoted from de Lacaillerie *et al.* [139]:

1. the structural elements contribute additively to the EFG;
2. the sets of random variables defining the structural elements constitute independent random variables;
3. the number of structural elements contributing to the EFG is "sufficiently" large;
4. the ensemble of structural elements responsible for the EFG constitute a statistically isotropic solid.

The practical consequences of these assumptions are twofold. The first is that the Czjzek model is only meaningful for systems which are disordered on length scales exceeding that of the range of the quadrupole interaction. Oxide glasses easily fulfil this requirement. The second consequence is due to the third assumption; empirically, "sufficiently large" has been found to mean a coordination number of four or greater [139]. This prevents the meaningful application of the Czjzek model to ^{11}B or ^{17}O NMR spectra, as the coordination numbers of these nuclides are typically lower than four. In this work, the Czjzek model is only applied to ^{139}La NMR spectra.

The Czjzek model has been widely applied to NMR studies of glasses, encompassing many quadrupolar nuclei. However, it is less straightforward to extract meaningful structural information from the Czjzek model than it is from fitting well-defined crystalline lineshapes. The Czjzek model has a single breadth parameter, σ, which is the common standard deviation of the distributions of the independent elements of the EFG tensor. The mean value of C_Q (and equivalently P_Q and ν_Q) in the Czjzek model is zero, while the mean value of η_Q is a constant with approximate value of 0.610. σ can, however, be related to the standard deviations of C_Q and P_Q by proportionality constants. It can also be related to the most probable values of C_Q and P_Q. Hence, while σ cannot be meaningfully related to the well-defined C_Q or P_Q values of crystals, it can be used as a quantitative descriptor of the disorder surrounding a given nuclide.

The utility of the Czjzek model comes primarily from its ability to analytically fit disordered quadrupolar NMR lineshapes, and not the value of σ. Once such a lineshape has been fit, in principle both σ and $\delta_\mathrm{iso}^\mathrm{CS}$ values can be extracted. The σ values can be compared between glass samples, while the $\delta_\mathrm{iso}^\mathrm{CS}$ values can be compared between both glass and crystalline samples. However, care must be taken that the Czjzek position parameter, Δ_offset, actually corresponds to $\delta_\mathrm{iso}^\mathrm{CS}$; a simple check of this is fitting spectra of the same sample collected at different magnetic field strengths.

3.5.6 Rotational-Echo Double-Resonance

First reported in 1989 by Gullion and Schaefer, the rotational-echo double-resonance (REDOR) pulse sequence is designed to reintroduce the dipolar coupling between nuclei that has been removed via MAS [140]. Dipolar coupling is the interaction between two magnetic dipoles (*e.g.*, nuclear spins), and can occur in both homonuclear

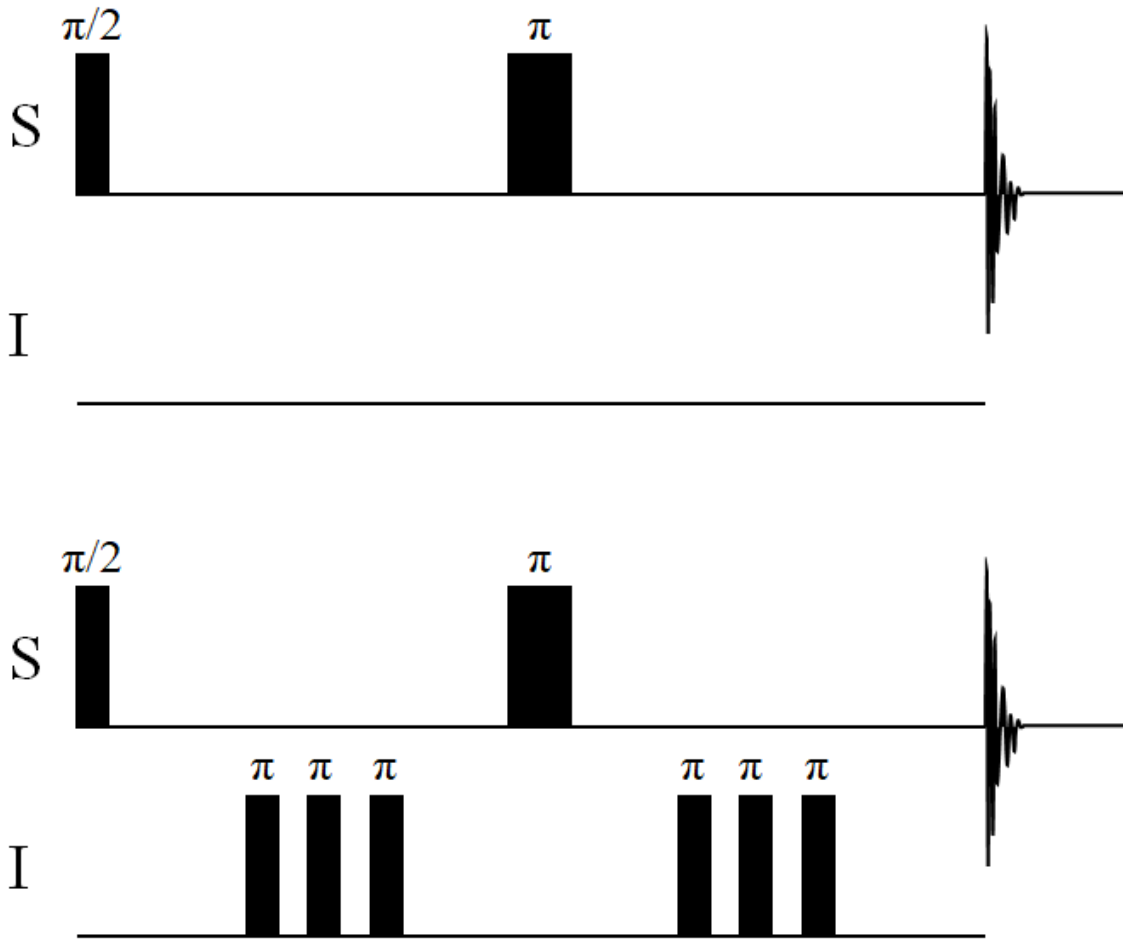

Figure 3.6: The REDOR pulse sequence [140].

and heteronuclear cases. Homonuclear dipolar coupling can be a significant source of spectral broadening in systems where the nuclide in question is abundant (*e.g.*, ^{1}H, ^{11}B), and it is typically desirable to remove this interaction via MAS when possible. Mitigating the substantial dipolar coupling of ^{1}H, often on the order of 50 kHz, is a major drive towards faster MAS speeds [47]. In nuclei pertinent to glasses, the dipolar coupling is usually sufficiently small to be mitigated by modest MAS spinning rates.

The REDOR experiment reintroduces the dipolar coupling between an observe nuclide (S) and an indirect nuclide (I). In the REDOR experiment, two spectra are collected under near-identical experimental conditions. Their pulse sequences are displayed in Fig. 3.6. The first experiment is a Hahn-echo of nuclide S. The second experiment is a Hahn-echo of nuclide S with π pulses applied to nuclide I during the evolution period. The π pulses on nuclide I invert the sign of the S-I dipolar

coupling interaction, preventing it from being averaged out during MAS, and allow for the interaction to be refocussed by the Hahn-echo pulse. The magnitude of the dipolar coupling constant can be measured by evaluating the difference in intensity of the Hahn-echo experiment without I irradiation (S_0) and the experiment with I irradiation (S). This difference is typically normalized to the S_0 intensity, and is written as $\Delta S/S_0$.

The heteronuclear dipolar coupling constant, D, is a function of the internuclear distance between spins. It is given by

$$D = \frac{\mu_0}{4\pi}\frac{\gamma_\mathrm{I}\gamma_\mathrm{S}\hbar}{2\pi r^3}. \tag{3.20}$$

μ_0 is the vacuum permeability, γ_S is the gyromagnetic ratio of the observed nuclide, γ_I is the gyromagnetic ratio of the unobserved nuclide, and r is the internuclear distance between S and I [47]. Equation (3.20) allows for the internuclear distance between two spins to be determined, making it a valuable tool for structure determination. However, it has several limitations. It is well-defined only for isolated spins, and not for large ensembles. It requires a well-defined π pulse length for complete inversion, which can prove difficult to achieve with quadrupolar nuclei [141].

For REDOR experiments on quadrupolar nuclei within crystals and glasses, rather that calculating the exact distance between isolated spins, the van Vleck heteronuclear dipolar second moment is calculated [142]. The van Vleck heteronuclear dipolar second moment M_2^IS is defined as

$$M_2^\mathrm{IS} = \frac{4}{15}\left(\frac{\mu_0}{4\pi}\right)^2 \gamma_\mathrm{I}^2\gamma_\mathrm{S}^2\hbar^2 I(I+1)\sum_\mathrm{I}\left\langle r_\mathrm{IS}^{-6}\right\rangle \tag{3.21}$$

where I is the nuclear spin quantum number of nuclide I [143]. The author would like to take a moment to apologize for the duplicate use of so many symbols, but is adhering to the conventions of the literature. The van Vleck second moment does not allow for precise distances to be extracted, but does allow for quantitative comparisons of the relative distances between spins S and I in systems with unknown structure. M_2^IS can be related to the REDOR observable via

$$\Delta S/S_0 = \frac{f}{I(I+1)\pi^2}(NT_\mathrm{r})^2 M_2^\mathrm{IS}. \tag{3.22}$$

T_r is the rotation period of the MAS rotor, and N is the number of rotor cycles it has undergone [142]. It is this NT_r parameter which is under experimental control. f is a calibration factor accounting for the imperfect excitation which occurs when both the S and I nuclides are quadrupolar. It must be calibrated by comparing the experimentally determined value of M_2^{IS} to the theoretical value from a known crystal structure [41, 52].

The van Vleck second moment is useful in glasses because, for small values of $\Delta S/S_0$, the curve of $\Delta S/S_0$ with respect to NT_r is independent of geometry [144]. A "small" value of $\Delta S/S_0$ is typically between $0 \leq \Delta S/S_0 \leq 0.2$ [41]. Due to the complicated interactions present in systems where both S and I are quadrupolar, it is generally most informative to compare unknown samples to closely related model compounds, and to be cognizant about the (at best) semi-quantitative nature of the comparisons [141].

3.5.7 Quantification in Solid-State NMR Spectroscopy

Many quantities can be derived from ssNMR spectroscopy. For glasses, two are particularly relevant: chemical shift and coordination number. Chemical shift values rarely require consideration beyond the quality of the chemical shift referencing and the quality of the fit. Mean coordination numbers in well-resolved systems (*e.g.*, ^{11}B NMR of borate glasses) are typically derived from integrated intensities. When comparing integrated intensities of different environments, care must be taken to ensure that their response to the RF pulse is homogeneous. Briefly, three factors must be considered: T_1 relaxation; sensitivity-dependence; and processing effects.

T_1 relaxation is perhaps the most straightforward factor which affects the quantification of intensities. In short, all environments in a spectrum must be fully relaxed between scans to allow for quantitative relative intensities [47]. This can be ensured by determining effective T_1 times for each environment (*e.g.*, via a saturation-recovery experiment), and setting the recycle delay appropriately for the longest time. The use of short tip angles serves to generally reduce the recycle delay required [145].

The sensitivity of an environment can vary substantially depending on the experiment being conducted. In this work, four different types of experiments are reported, all on quadrupolar nuclei: single-pulse; MQMAS; WCPMG; and REDOR. They are

considered in order. For single-pulse experiments, for a given environment the pulse length corresponding to maximum intensity (*i.e.*, the 90° or $\pi/2$ pulse length) depends on C_Q. Hence two environments with widely differing C_Q values cannot be simultaneously maximized with a single pulse length. Rather than attempting to maximize every environment simultaneously, it is best to exploit that for short pulse lengths, the sensitivity of an environment is independent of C_Q [146–148]. The maximum tip angle corresponding to this homogeneous response region is spin-dependent, and can be calculated by

$$\theta = \frac{90}{3(I + 1/2)} \tag{3.23}$$

The $\pi/2$ pulse length can generally be determined from a reference sample with a highly-symmetric environment (*e.g.*, $NaBH_4$). Conveniently, reducing the tip angle also reduces the required recycle delay [145].

In MQMAS experiments, the intensity of the site is similarly dependent on C_Q [132]. However, the pulse lengths cannot be altered to allow for C_Q-independent excitation. Hence MQMAS intensities are not generally considered to have quantitative intensities.

REDOR experiments are not generally quantitative in the relative intensities between environments, and are typically conducted with pulse lengths striking a compromise with overall maximum intensity. However, this does not pose an issue to the interpretation of the experiment. The important value derived from REDOR experiment is the ratio of the change in intensity with the re-introduction of dipolar coupling. As long as the pulse lengths are consistent within a set of experiments, the ratios are not dependent on the pulse length.

WCPMG provides signal enhancement by the refocusing of large numbers of echoes. The number of echoes which can be refocused depends substantially on T_2. Hence, sites with significantly different T_2 values will experience different amounts of signal enhancement. As the T_2 of an environment within a sample cannot be known *a priori*, WCPMG spectra generally have non-quantitative relative intensities.

The final factor which can affect the reliability of integrated intensities is the processing required to obtain the final spectrum. This particularly concerns ^{11}B single-pulse ssNMR spectra, as the MAS stator contributes a substantial background signal. Both background subtraction and phasing can affect the reported intensities of the peaks. Even with substantial care being taken during phasing and background

subtraction, errors in the integrated intensities are often on the order of 5 %.

3.6 Raman Spectroscopy

Raman spectroscopy is a common technique for the study of glass structure [71]. It is (comparatively) inexpensive and technologically mature. In Raman spectroscopy, monochromatic light (typically from a moderately-powered laser) passes through some volume of a material and is scattered in all directions [149]. Much of the light is elastically scattered, and contains no pertinent structural information. Similarly, some light is absorbed and converted to heat. The balance is inelastically scattered. Inelastically scattered light has two separate frequency ranges: the Brillouin range, containing light scattered by acoustic vibrations within the sample; and the Raman range, containing light scattered by so-called "optic vibrations" [150].

Both types of inelastic scattering involve interactions with the quasiparticles known as phonons. Phonons are the quantization of collective movement (or vibration) of atoms within a crystal structure. Like photons (and indeed all particles) phonons can be modelled as a wave, a particle, or both, depending on circumstance. Phonons are grouped into two categories: acoustic, named due to their resemblance to sound waves; and optic, named such due to their interactions with visible light. It is optic phonons which interact with the laser light in Raman scattering.

In molecules, the vibrational motion of atoms can be well defined, often involving only two atoms. This allows for the use of the classical vibration equation

$$\nu_0 = \frac{1}{2\pi}\sqrt{\frac{k}{\mu_\mathrm{m}}} \tag{3.24}$$

where ν_0 is the vibrational frequency, k is the force constant of the bond between the two atoms, and μ_m is the reduced mass of the two atoms [149]. In crystals and glasses, both of which are highly interconnected, vibrations often involve the motion of many atoms, and Eq. (3.24) cannot be used directly. However, its key insights still apply: atoms which are tightly bound will tend to have higher frequencies; and atoms which are heavy will tend to have lower frequencies.

In molecules, the point group symmetry determines whether a particular vibration will be Raman-active. In crystals, it is the space group which restricts the activity

of a given vibrational mode. In glasses, all modes possible for the composition are active to at least some degree, due to the absence of long-range symmetry and the disorder present even at short ranges. However, the bonds in the glass are essentially the same as the bonds present in the crystal — for example, in GeO_2 a Ge–O bond is essentially the same regardless of whether the GeO_2 is in crystalline or vitreous form. The Raman spectra of crystalline materials can therefore be used to assist in the interpretation of Raman spectra of glasses.

When high-quality data is coupled with structural modelling (*e.g.*, force fields, molecular clusters, DFPT), the structural origin of a given Raman mode can be deduced. With knowledge of the structural origins of a mode in a control sample, changes in the frequency, intensity, or presence of modes in the Raman spectrum of an unknown can be attributed to structural changes. Structural changes which can be visible in Raman spectra include changes in atomic coordination (*e.g.*, BO_3 vs. BO_4) and changes in next-nearest neighbour (*e.g.*, Si–O–Si vs. Si–O–Na).

3.7 Density Functional Theory Calculations

The use of DFT calculations to complement experimental data is a common practice in the fields of both chemistry and physics. In this work the results of DFT calculations were used to validate the reliability of experimental crystal structures, assist in interpreting poorly-resolved NMR spectra, and to probe the response of Raman spectra to stress. The theoretical underpinnings of these calculations are complex and too lengthy to reproduce here, and the interested reader is directed to the literature [151, 152]. The following discussion focuses on some practical aspects of the use of DFT calculations as applied to the study of crystals. Calculations on glassy structures were not attempted, as a proper DFT handling of amorphous systems is well beyond the scope of this work.

3.7.1 A Brief Description of DFT Calculations

In a DFT calculation on an ordered crystal, an appropriate unit cell is constructed. The crystal is treated as an infinite periodic set composed of repeated unit cells. These periodic boundary conditions are amenable to being modelled by plane-wave functions. By increasing the maximum energy of the set of plane waves used, the variance of

any given term decreases. Periodic plane-waves are well equipped to model long-range phenomenon, but require extremely high energies to reproduce aperiodic interactions, *e.g.*, those close to the nucleus of an atom. To reduce the maximum plane-wave energies, the rapidly-varying atomic wavefunctions are replaced by a smoothly-varying function which matches the behaviour of the atom at long range, but is easier to model at short ranges. The details of this approximation are described in Section 3.7.2.

Rather than carrying out the calculation over all space, a set of discrete points sample the response of the plane-waves. This set of points is used for a three-dimensional integration of the response over the whole cell. These points are called k-points. The number of k-points that are required to reliably calculate a given parameter will vary with the needs of the calculation. In general, the number of k-points required to model a system are inversely proportional to the volume of the unit cell. The only detriment to increasing the number of k-points is the corresponding increase in computational time (which can be prohibitive). For the sake of expediency, it is important to test the number of k-points required for property convergence and to not overdo things.

3.7.2 Pseudopotentials and PAW Datasets

Modelling the behaviour of electronic states close to the nucleus is costly, due to their rapidly fluctuating nature. An effective means of reducing this cost is the use of pseudopotentials [153]. Pseudopotentials approximate the behaviour of electronic states contained within some arbitrary cut-off radius. Outside the cut-off radius, the atomic wavefunction is identical to that from an all-electron calculation. Inside the cut-off radius, the oscillating all-electron wavefunction is replaced by a smoothly-varying "pseudized" wavefunction. The cut-off radius is set such that the valence electrons (which account for the vast majority of chemically-relevant interactions) are outside the cut-off radius, while the core electrons (which are not generally chemically interesting) are inside the cut-off radius. The use of pseudopotentials has the effect of significantly reducing the computational cost of a given DFT calculation, but does not allow for the modelling of nuclear properties (*i.e.*, NMR properties).

In order to model nuclear properties while still retaining the computational efficiency of pseudopotentials, we turn to the projector augmented-wave (PAW) method. The

PAW method is superficially quite similar to the use of pseudopotentials, but is rather more complex. The details of PAW can be found in the literature [154, 155]. The practical implications of the use of PAW over pseudopotentials lie in the fact that in PAW the electronic behaviour near the core is handled explicitly. By handling the core behaviour explicitly, nuclear interactions can now be modelled.

An important factor affecting PAW is the choice of cut-off radius. The PAW formalism is only strictly correct if the cut-off radii of all PAW datasets are chosen such that there is no overlap of the resulting PAW spheres. It is not uncommon for "default" PAW datasets to have some PAW sphere overlap for an arbitrary structure. In oxide-based materials, X−O overlap is particularly common. The effects of PAW overlap range from being unnoticeable to significantly affecting the results, being particularly severe for large overlaps and nuclear properties [155]. Hence all PAW datasets used in this work were checked for overlap on the relevant structures; and custom datasets were used where overlap occurred.

3.7.3 Computation of NMR Observables

As the EFG is a strict ground-state property of the electron density, it may be computed accurately within the PAW framework. The calculation of the EFG tensor is computationally trivial, requiring only the calculation of the second spatial derivatives of the electrostatic potential. The electrostatic potential is routinely calculated in a DFT calculation, and is readily available. The EFG tensor, V, is a diagonal traceless second-rank tensor, and hence can be expressed as $V_{xx} + V_{yy} + V_{zz} = 0$, where V_{xx}, V_{yy}, and V_{zz} are the diagonal tensor elements. The elements are ranked such that $|V_{zz}| \geq |V_{yy}| \geq |V_{xx}|$. The quadrupolar symmetry parameter, η_{Q}, can be derived directly from the tensor elements, and is defined as

$$\eta_{\mathrm{Q}} = \frac{V_{yy} - V_{xx}}{V_{zz}}. \tag{3.25}$$

The other EFG NMR observable, the quadrupolar coupling constant C_{Q}, is defined as

$$C_{\mathrm{Q}} = \frac{eQV_{zz}}{h}. \tag{3.26}$$

While η_{Q} can be calculated using only the EFG tensor elements, calculation of C_{Q} requires knowledge of the nuclear quadrupole moment Q. These values are determined experimentally, and can be found in the work of Pyykkö [57]. Calculating C_{Q} can be a quick check on the validity of the input crystal structure prior to more detailed calculations: while DFT-derived C_{Q} values are often overestimated, on the order of 10%, substantial differences from experiment (*e.g.*, 50%) can indicate an error in the crystal structure.

Calculation of the chemical shielding tensor requires taking account of an external magnetic field, which is a subtle and difficult problem. The gauge-including projector augmented-wave (GIPAW) method, developed by Pickard and Mauri in 2001, provides one approach to this problem [156]. It allows for the calculation of the chemical shielding tensor σ for all atoms in a given unit cell. The mathematical derivation of the GIPAW method is beyond the scope of this work, and the interested reader is directed to the literature for the details [156–158]. The practical considerations of the GIPAW method in this work follow.

The calculation of the chemical shielding tensor by GIPAW is computationally quite expensive, and scales poorly with the number of atoms in the unit cell. However, calculating the chemical shielding of the system is the only way to obtain the chemical shift. The chemical shift is (very well) approximated by the difference in shielding between the target sample and a reference composition [158]. However, as both the target system and the reference system are calculated in DFT, GIPAW results must be interpreted critically; beyond the common DFT concerns regarding input structure and exchange-correlation effects, it is possible for many subtle interactions to affect the calculated chemical shifts [157].

The chemical shielding tensor is a diagonal second-rank tensor which is not traceless. In its principal axis system, there are three unique chemical shielding tensor elements: σ_{xx}, σ_{yy}, and σ_{zz}. There are multiple notations used for describing the shielding (and equivalently, shift) tensors; the different notations and their relative advantages are discussed in the literature [159]. In this work all chemical shielding and chemical shift anisotropy (CSA) parameters are described in the Herzfeld-Berger (a.k.a. Maryland)

notation [160]. In this notation, the tensor elements are defined as

$$\sigma_{11} \leq \sigma_{22} \leq \sigma_{33}. \tag{3.27}$$

The isotropic shielding is clearly

$$\sigma_{\text{iso}} = \frac{1}{3}\left(\sigma_{11} + \sigma_{22} + \sigma_{33}\right). \tag{3.28}$$

Two additional parameters are required to describe the tensor. These are the span (Ω) and the skew (κ), with the following definitions:

$$\Omega = \sigma_{33} - \sigma_{11} \tag{3.29}$$

$$\kappa = \frac{3(\sigma_{\text{iso}} - \sigma_{22})}{\Omega}. \tag{3.30}$$

Ω is effectively a breadth parameter, while κ describes the axial symmetry of the tensor. κ will vary from $+1$, where it describes a prolate ellipsoid, to -1, where it describes an oblate ellipsoid.

3.7.4 DFT Software Used in This Work

A variety of software programs were used in this work for the purpose of carrying out DFT calculations on a variety of systems. A brief description of the software used, and the justification for their use, follows.

For pseudopotential and PAW DFT calculations, the Abinit and Quantum ESPRESSO software packages were used [161–163]. Both are open-source plane-wave DFT software, and are broadly comparable in capabilities and scope. Abinit was used for many calculations in this work due to familiarity with the software. Quantum ESPRESSO was used when chemical shielding calculations were required. Currently, chemical shielding calculations are typically carried out using the GIPAW method. A GIPAW module is implemented in Quantum ESPRESSO, but not in Abinit.

Norm-conserving pseudopotentials (NCPPs) were generated using the Optimized Norm-Conserving Vanderbilt Pseudopotential (ONCVPSP) code [164]. NCPPs were used for the DFPT calculations of the Raman spectra of the $LaBGeO_5$

crystal (Chapter 8); the code required to run the same calculations using PAW has not yet been enabled in ABINIT. PAW datasets were used for all other calculations, as all other calculations were to obtain NMR properties. PAW datasets were generated using the ATOMPAW software [165]. ATOMPAW can generate PAW datasets for both ABINIT and QUANTUM ESPRESSO. Custom PAW datasets were validated using the ELK all-electron DFT package (http://elk.sourceforge.net/).

3.8 Neutron Diffraction

Neutron diffraction is a valuable technique for both crystallography and for the study of glass structure [69]. As a diffraction-based experiment, it shares many aspects in common with X-ray diffraction, described above (Section 3.3). The greatest difference between a neutron diffraction experiment and a X-ray diffraction experiment is the nature of the diffracting beam. Whereas X-rays interact with the electron cloud surrounding each atom, neutrons interact directly with the atomic nucleus. As such, neutrons are capable of diffracting off of light elements such as H, He, or Li. However, neutron beams are much less straightforward to produce than X-ray beams. A brief description of the neutron source and detector used in this work follows. It is accompanied by a brief description of the approach for data processing.

Neutrons beams for diffraction experiments can only be generated with sufficient neutron flux via two sources: nuclear reactors and time-of-flight spallation sources. For this work, neutron diffraction was carried out at the ISIS spallation neutron source at the Rutherford Appleton Laboratory in Oxfordshire, United Kingdom. At the ISIS source, protons are accelerated by a synchrotron, which periodically collides bunches of protons with a tungsten target (Fig. 3.7). Neutrons are "spalled" from the target and channelled into several beamlines. Detectors are placed upon these beamlines, and samples placed within. The detector used for this work is the GEneral Materials Diffractometer (GEM) (Fig. 3.8), which allows for the detection of scattering over a wide range of scattering angles. Further information regarding the specifics of ISIS and GEM can be found in reference [166].

In a neutron scattering experiment, the quantity which is determined is the differential cross-section

$$\frac{\mathrm{d}\sigma}{\mathrm{d}\Omega} = I^{\mathrm{S}}(Q) + i(Q). \tag{3.31}$$

Figure 3.7: The ISIS neutron source. Displayed is the containment structure of the tungsten target from which neutrons are produced. For scale, see the ladder on the right of the image. The sample access port of the GEM detector can be observed in the bottom right.

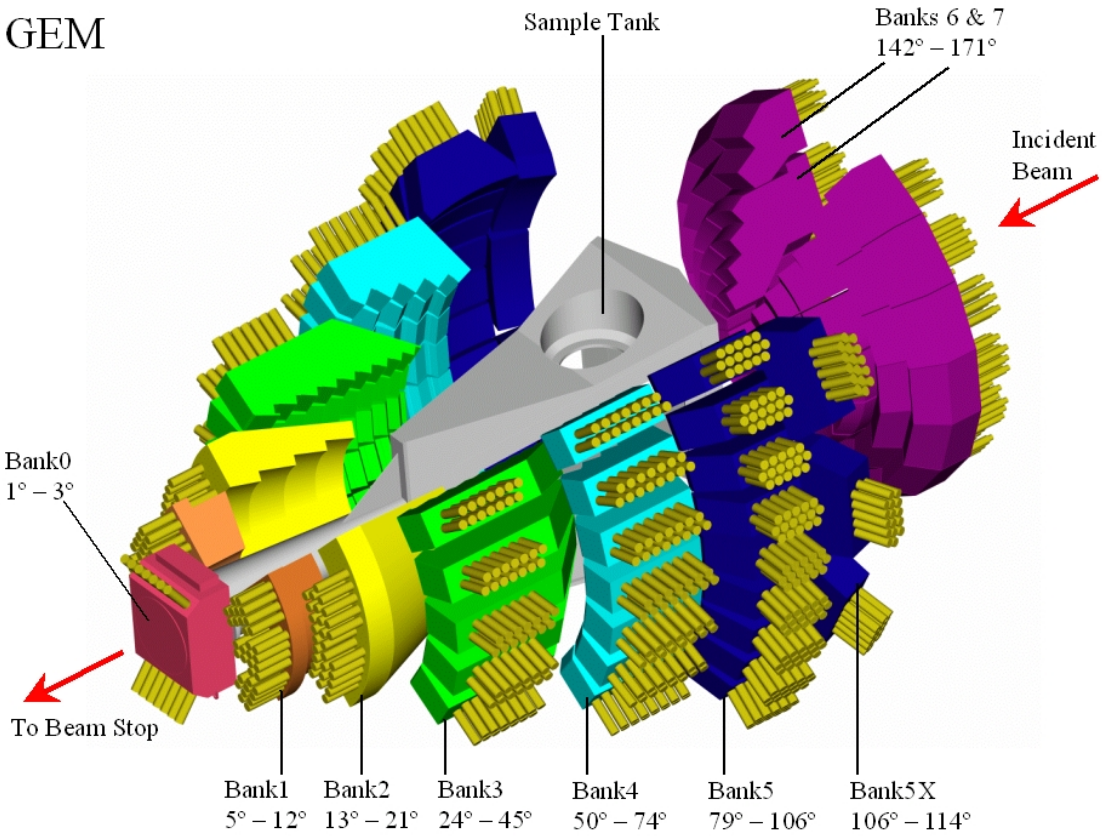

Figure 3.8: The GEM neutron detector. It is composed of eight detector banks with ZnS/^{6}Li scintillation detectors. The detector banks are structured to allow for the detection of scattering from a wide range of scattering angles. This image is provided courtesy of Dr. Alex C. Hannon, and is used with permission.

$\hbar Q = 4\pi\hbar \sin(\theta)/\lambda$ is the magnitude of the momentum transferred during the scattering event, where θ is the angle of the scattering [69, 166]. $I^{\mathrm{S}}(Q)$ is the self-scattering of the sample, and can be approximated with a knowledge of the composition of the sample and the various properties of the detector [167]. $i(Q)$ is the distinct scattering of the sample, and is the function which contains the structurally interesting information regarding the sample. The distinct scattering can be determined by subtracting the approximation of $I^{\mathrm{S}}(Q)$ from the differential cross-section.

To obtain structural information from the distinct scattering, it is subjected to a Fourier transformation which returns the total correlation function $T(r)$:

$$T(r) = T^0(r) + \frac{2}{\pi}\int_0^\infty Qi(Q)M(Q)\sin(rQ)Q\,\mathrm{d}Q. \tag{3.32}$$

$M(Q)$ is a modification function introduced to mitigate the effects of truncation of $i(Q)$. Like in NMR spectroscopy, the finite nature of $i(Q)$ can lead to ripples in $T(r)$; this can be mitigated through a large maximum value of Q ($Q_{\max}$), and by the use of an appropriate modification function, which will be discussed below. $T^0(r)$ is the average density contribution to $T(r)$, and is defined as

$$T^0(r) = 4\pi r g^0 \left(\sum_i^N c_i \bar{b}_i\right)^2. \tag{3.33}$$

g^0 is the atomic number density. c is the atomic fraction of element i, and $\bar{b}$ is its coherent neutron scattering length. The summation over i runs over the N elements present in the sample. $T(r)$ is a weighted sum of the pairwise partial correlation functions of each element pair $t_{ii'}(r)$:

$$T(r) = \sum_{i,i'} c_i \bar{b}_i \bar{b}_{i'} t_{ii'}(r) \tag{3.34}$$

In this work, two modification functions are used. The first is the simple "step" function, with

$$M(Q) = \begin{cases} 1, & \text{if } Q \leq Q_{\max} \\ 0, & \text{otherwise.} \end{cases} \tag{3.35}$$

The step modification function is mathematically trivial, and allows for the maximum

real-space resolution in $T(r)$. However, it will almost always lead to significant ripples on either side of real peaks in $T(r)$, due to the truncation of Q during the Fourier transform [166]. These ripples can cause difficulties in fitting peaks, either from peak overlap or misidentification. To mitigate truncation effects, the Lorch modification function is commonly used (and indeed was used in this work). The Lorch function is defined as

$$M(Q) = \begin{cases} \frac{\sin(\Delta r Q)}{\Delta r Q}, & Q \leq Q_{\max}, \Delta r = \pi / Q_{\max}, \\ 0, & Q > Q_{\max}. \end{cases} \tag{3.36}$$

The Lorch modification function dramatically decreases the intensity of truncation ripples, allowing for more accurate peak fitting and identification [63]. There is some loss of real-space resolution from using the Lorch function instead of the step function; however, with $Q_{\max} = 50\,\text{Å}^{-1}$, the difference is only 0.04 Å.

Once $T(r)$ is calculated, much information can be derived from its constituent peaks. As per Eq. (3.34), the peaks in $T(r)$ are due to scattering from various elemental pairs. A peak maximum in $T(r)$ corresponds to the mean interaction distance between the element pair. In many cases — in oxides, typically the first X–O peak — this distance corresponds to a mean bond length. The first-order peaks typically correspond to local order, *e.g.*, distinguishing between BO_3 trigonal planes and $[B\O_4]^-$ tetrahedra. The second-order peaks can contain valuable information regarding intermediate-range order. For example, the B–B distance in borate glasses can be used to infer information regarding the presence of superstructural units [20].

The position of a peak and its area can together be used to determine the coordination number of the element pair producing the peak. The equation describing the coordination number of a peak is

$$n_{ij} = \frac{r_{ij} A_{ij}}{(2 - \delta_{ij}) c_i \bar{b}_i \bar{b}_j}. \tag{3.37}$$

Here r_{ij} is the position of the peak of the interaction of the elements i and j [12, 69]. A_{ij} is the area of the peak. δ_{ij} is the Kronecker delta, and accounts for self-interaction for a peak resulting from homonuclear scattering. As above, c_i is the atomic fraction of element i, and $\bar{b}$ are the coherent scattering lengths. While both elements i and j contribute to the peak, only element i is required to obtain the i–j coordination

number. n_{ij} and n_{ji} are related by

$$n_{ji} = n_{ij}\frac{c_i}{c_j} \tag{3.38}$$

Hence n_{ij} and n_{ji} are related but distinct values.

It is important to note how the values obtained via neutron diffraction are dependent on the composition and density of the sample under investigation. The differential cross-section measured from the sample does not depend on the knowledge of the composition (atomic and isotope fractions) nor the density. However, every subsequent processing step requires both the composition in terms of both elemental composition (in the c terms) and isotopic composition (in the $\bar{b}$ terms). The c and $\bar{b}$ terms obviously are contained within Eq. (3.37), but the A_{ij} term is also dependent on the composition and density. Errors in the composition primarily affect the vertical scale of $T(r)$, and consequently the area of the peaks. Similarly, errors in the composition and density affect $T^0(r)$, which in turn affects the vertical scaling of $T(r)$. Hence an accurate set of values for the elemental and isotopic composition of the sample, as well as its density, are required to obtain accurate coordination numbers using neutron diffraction. The methods of obtaining these values are described in Section 3.4 and Section 3.2.1. Conveniently, r is not significantly affected by errors in composition or density, and hence can be analysed independently.

When considering neutron diffraction, the isotopic composition of each sample must be carefully considered. For some elements (*e.g.*, La) there is only one naturally abundant isotope. For others (*e.g.*, Ge) there are many isotopes, but all are amenable for diffraction (though some are more concerning than others when considering radiation safety), and scattering parameters can be taken as averages. Boron rates special consideration in the context of neutron diffraction. Two boron isotopes are naturally occurring: ^{10}B and ^{11}B, with natural abundances of 20 % and 80 %, respectively. ^{10}B is an excellent neutron absorber, with an absorption cross-section of 3835 fm^2. For comparison, the absorption cross-sections of natural abundance La, Ge, and O are 8.93 fm^2, 2.2 fm^2, and 0.000 19 fm^2, respectively [168]. The presence of ^{10}B in a sample intended for analysis by neutron diffraction can significantly reduce the intensity of the detected neutron flux, and hence it is typically desirable to enrich samples intended for neutron diffraction analysis with ^{11}B. Thankfully, this enrichment

does not typically affect other analyses: ^{10}B and ^{11}B are chemically identical in glass; EA techniques used in this work are either isotope-agnostic, or capable of quantifying the isotopes independently; and ^{11}B NMR is not deleteriously affected by the absence of ^{10}B. $^{11}B_2O_3$ ($\geq 99\,\%$ ^{11}B) is commercially available at reasonable prices ($47\,\mathrm{CAD\,g^{-1}}$ from Sigma-Aldrich ISOTEC at time of writing), making ^{11}B enrichment of borate glasses straightforward.

Chapter 4

Relating ^{139}La Quadrupolar Coupling Constants to Polyhedral Distortion in Crystalline Structures

4.1 Context

One of the central goals of this work is to obtain information on the differences (or lack thereof) in the La−O environment between the $LaBGeO_5$ glass and crystal forms. NMR spectroscopy is frequently applied to the study of amorphous materials such as oxide glasses, as it is primarily a probe of local structure, and does not require the presence of long-range order. However, ^{139}La NMR spectra of glasses have not been reported in the literature, in no small part because of the large nuclear quadrupole moment of lanthanum. In order to interpret ^{139}La NMR spectra of glasses, we must first construct a model describing the relationship between spectral properties and chemical structure in lanthanum-containing crystals. This chapter assesses the state of ^{139}La spectroscopy in the literature, and combines novel data with data from the literature to construct a model relating ^{139}La C_Q and $\delta_\mathrm{iso}^\mathrm{CS}$ to various structural features of lanthanum oxide-based crystals.

This chapter was originally published as Paterson, A.L., Hanson, M.A., Werner-Zwanziger, U., and Zwanziger, J.W., Relating ^{139}La Quadrupolar Coupling Constants to Polyhedral Distortion in Crystalline Structures, *J. Phys. Chem. C* 119 (45) (2015) 25508–25517 [126]. Copyright 2015 American Ceramic Society. The content below has been reproduced from the preprint version of the article, with minor modifications for style and clarity. Copyright permissions for this use are contained in Appendix E. The contributions of the authors to the text are as follows: ALP collected all experimental data, performed the analyses, and wrote the manuscript. MAH assisted with NMR technical support and data collection. UWZ provided substantial NMR technical support, including the implementation of WCPMG and validation of the technique. UWZ also collaborated on the analysis and review of the manuscript. JWZ collaborated

on the analysis of the results and the review of the manuscript.

4.2 Abstract

A broad series of crystalline lanthanum oxide-based materials has been investigated through high-field ^{139}La ssNMR spectroscopy and *ab initio* DFT calculations. The ^{139}La ssNMR spectra of $LaBGeO_5$, $LaBSiO_5$, $LaBO_3$, $LaPO_4 \cdot 1.8\,H_2O$, $La_2(SO_4)_3 \cdot 9\,H_2O$, and $La_2(CO_3)_3 \cdot 8\,H_2O$ are reported for the first time. Both newly reported and literature values of ^{139}La quadrupolar coupling constants C_Q are related to various quantitative expressions of polyhedral distortion, including the sphericity (Σ) and ellipsoid span (ϵ). The compounds were separated into two groups based upon their polyhedral distortion behaviour: compounds with the general formula $LaMO_3$, where M is a trivalent cation; and compounds with different general formulae. The ^{139}La C_Q of the $LaMO_3$ family was found to correlate best with ϵ. The ^{139}La C_Q of non-$LaMO_3$ compounds correlates adequately to ϵ, but is better described by Σ. The ^{139}La isotropic chemical shift (δ_{iso}^{CS}) of the non-$LaMO_3$ compounds is negatively correlated with the lanthanum coordination number (CN); there is insufficient data from the $LaMO_3$ compounds to draw conclusions relating to chemical shift. DFT calculations of NMR parameters prove to be a sensitive probe of the quality of input geometry, with predicted parameters agreeing with experiment except in cases where the crystal structure is suspect.

4.3 Introduction

Lanthanum compounds have a wide variety of applications, including nickel-metal hydride batteries [169], transparent ferroelectric nanocomposites [34], medical glass-making [170], and both medical and environmental phosphate sequestration [171, 172]. Many of these applications involve amorphous materials, complicating the characterization of the lanthanum environment. SsNMR is an effective probe of local coordination in non-periodic solids, but has not yet been applied to ^{139}La in amorphous lanthanum compounds. In order to increase the utility of ^{139}La ssNMR as a structural characterization tool, we investigate the relationship between observable ^{139}La ssNMR properties and the distortion of the lanthanum sites in lanthanum oxide-based materials.

The primary NMR-active nucleus of lanthanum, ^{139}La, has several attractive nuclear properties including a complete natural abundance (100 %), a nuclear spin of $I = 7/2$, and a moderate gyromagnetic ratio ($\gamma = 3.801 \times 10^{-7}\,\mathrm{rad\,T^{-1}\,s^{-1}}$), all of which contribute to a high receptivity (1.61×10^2 as compared to ^{29}Si). A moderately high nuclear electric quadrupole moment ($Q = 20\,\mathrm{fm}^2$)[57] has been the primary barrier to the ssNMR study of ^{139}La. Until the advent of the WCPMG pulse sequence [129], the breadth of many spectra prevented their timely acquisition, restricting investigations into relatively high symmetry compounds which yield narrow spectra [58, 59, 173]. The WCPMG pulse sequence, in conjunction with VOCS collection, has recently been put to good use in the investigation of a number of both coordination and inorganic lanthanides [174–176], including $LaScO_3$ [177] and $LaPO_4$ [172].

The lineshape of ^{139}La NMR spectra is primarily due to interactions of the nucleus with the EFG tensor. Two parameters describe this interaction: the C_Q, and the η_Q

$$C_\mathrm{Q} = \frac{eQV_{zz}}{h} \tag{4.1}$$

$$\eta_\mathrm{Q} = \frac{V_{yy} - V_{xx}}{V_{zz}} \tag{4.2}$$

where Q is the electric quadrupole moment of the nucleus, h is the Planck constant, e is the elementary charge, and $|V_{zz}| \geq |V_{yy}| \geq |V_{xx}|$ are the principal components of the EFG tensor. The magnitude of the quadrupolar coupling constant has commonly been used to infer qualitative deviations from spherical symmetry while the asymmetry parameter provides information regarding axial symmetry [25, 58, 60]. An additional influence on the lineshape of NMR spectra is CSA. The CSA tensor is defined similarly to the EFG tensor, with principal components $\delta_{11} \geq \delta_{22} \geq \delta_{33}$. This work uses the Herzfeld-Berger convention [160] for describing the influence of CSA on NMR lineshapes.

Note that the principal directions of the CSA tensor need not coincide with those of the EFG tensor, and neither need coincide with "obvious" crystallographic directions unless satisfying the symmetry requirements of the unit cell. Nevertheless, if correlations between these tensors and crystal structures can be established for a class of materials, then extension to structurally uncharacterised samples is possible.

Indeed, many studies have attempted to link the above NMR properties to structural features: for example, Pan *et al.* used ^{6}Li MAS NMR to probe the presence of Cr^{3+} in the lithium coordination sphere [178]; ^{11}B MAS NMR is routinely used to quantify relative proportions of three- and four-coordinate boron; Willans *et al.* were able to establish a link between ^{139}La isotropic chemical shift and lanthanum CN in organic lanthanum coordination compounds using ssNMR;[176] and Michaelis and Kroeker investigated the possibility of relating ^{73}Ge C_{Q} to octahedral and tetrahedral distortion parameters [25].

While tetrahedral and octahedral distortion parameters are effective in describing differences between real and ideal polyhedra, it is difficult to generalize the method used by Michaelis and Kroeker to polyhedra with higher CN. Balić Žunić and Makovicky devised a method involving least-squares fitting of a sphere to the ligands of the coordination polyhedron [179] which provides a novel means of measuring distortion. Various distortion parameters are derived from the relationship between a circumscribed sphere and the ideal polyhedral shape [180]. These parameters have been successfully used to predict the coefficient of thermal expansion in $A_2M_3O_{12}$ materials [181, 182]. However, modelling the EFG tensor requires a parameter more sensitive to the specific distortion from spherical symmetry.

Balić Žunić and Makovicky [179] define the Σ of the coordination polyhedron as

$$\Sigma = 1 - \frac{\sigma_{r_s}}{r_s} \tag{4.3}$$

where r_s is the average distance between the centroid of the coordination polyhedron and the ligands, and σ_{r_s} is the standard deviation of the same. The centroid of coordination is the point with minimal variation of position with regards to the oxygen ligands, and frequently, but not always, coincides with the position of the La^{3+} cation. The sphericity describes the deviation of the ligand distances from the average distance, which models the general deviation from spherical symmetry.

Beyond considering the isotropic deviation from spherical symmetry, we also consider the anisotropy of the distortion. To this end, we fit the coordination polyhedron with a triaxial ellipsoid (Fig. 4.1). The resulting ellipsoid is defined by its three semi major axes $e_a \leq e_b \leq e_c$. The level of anisotropy of the ellipsoid is described by two parameters derived from the semi major axes: the ϵ, defined by Balić Žunić and

Makovicky [183] as

$$\epsilon = \frac{e_c - e_a}{\frac{e_a + e_b + e_c}{3}} \tag{4.4}$$

and the ellipsoid character (EC), which describes how close in length e_b is to the other semi major axes. More precisely, the ellipsoid character is defined in analogy to the optical character [183]. The ellipsoid character is the cosine of the angle between the normals of the two unique circular cross-section of the ellipsoid fitting the polyhedron, as bisected by the longest major axis. Practically, the ellipsoid character ranges from -1, describing an oblate spheroid, to +1, describing a prolate spheroid, while intermediate values indicate that the ellipsoid is triaxial. ϵ will range from 0 when the ellipsoid is spherical, and will approach 3 when $e_c \gg e_a$.

In this work we use ^{139}La ssNMR in conjunction with DFT calculations to construct an empirical model relating the distortion of the lanthanum coordination polyhedra to the observed ^{139}La C_Q values. We establish that the ^{139}La C_Q of compounds with the general formula $LaMO_3$ (M = B^{3+}, Al^{3+}, Sc^{3+}, Ti^{3+}, Cr^{3+}, Co^{3+}) is dependent primarily on the ellipsoid span, while the ^{139}La C_Q of other compounds is related to both the ellipsoid span and the sphericity parameter. Experimental data is reported for crystalline samples of La_2O_3, $LaPO_4 \cdot 1.8\,H_2O$, $LaPO_4$, $LaBO_3$, $LaBGeO_5$, $LaBSiO_5$, $La_2(SO_4)_3 \cdot 9\,H_2O$, and $La_2(CO_3)_3 \cdot 8\,H_2O$. The results of DFT calculations on La_2O_3, $LaPO_4 \cdot 0\,H_2O$, $LaPO_4$, $LaBO_3$, $LaBGeO_5$, $LaBSiO_5$, $La_2(SO_4)_3 \cdot 9\,H_2O$, $La(OH)_3$, $LaAlO_3$, $LaCoO_3$, $LaCrO_3$, $LaScO_3$, and $LaNbO_4$ are included.

4.4 Experimental

4.4.1 Synthesis and Characterization

Samples of La_2O_3 ($\geq$ 99.9 %), $LaBO_3$ (99.9 %), $La_2(CO_3)_3 \cdot nH_2O$ (99.9 %), and $La_2(SO_4)_3 \cdot 9\,H_2O$ ($\geq$ 99.99 %) were purchased from Sigma-Aldrich. $LaPO_4 \cdot nH_2O$ (99.99 %) was purchased from Alfa Aesar. The above samples were used without further purification. $LaPO_4$ was produced by heating $LaPO_4 \cdot nH_2O$ at 750 °C for 21 h in air. Crystalline $LaBGeO_5$ was produced via devitrification of a glass sample. $LaBGeO_5$ glass was produced by grinding stoichiometric amounts of La_2O_3, B_2O_3 (99 %, Sigma-Aldrich), and GeO_2 (99.998 %, Sigma-Aldrich) in a ceramic mortar and

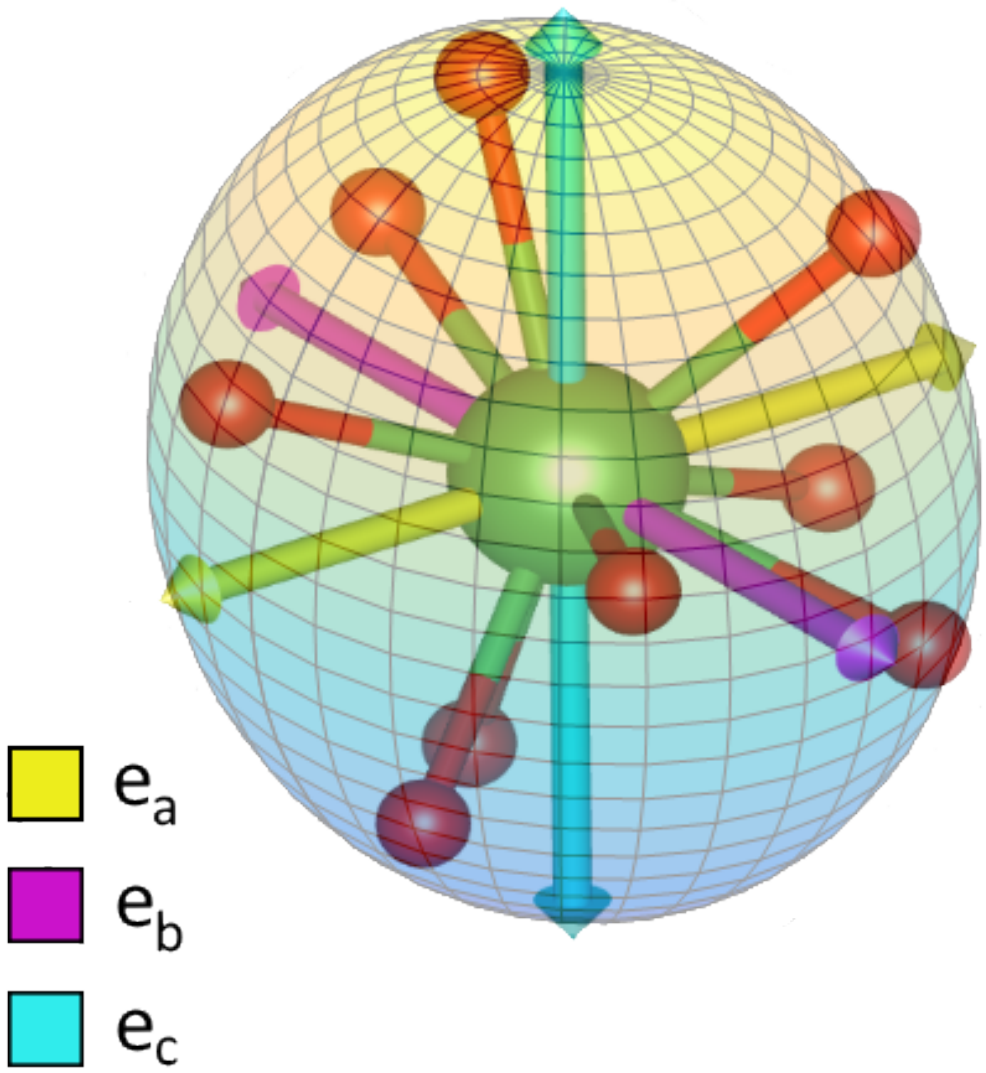

Figure 4.1: Schematic diagram of a triaxial ellipsoid fit to the LaO_9 polyhedron of $LaBGeO_5$.

pestle and heating at 1300 °C for 30 min in a platinum crucible in air. The resulting glass was poured into a glass mold pre-heated to 400 °C, and held at 400 °C for 24 h. Crystallization was induced by heating the glass at 950 °C for 12 h. The resulting ceramic was ground to powder in an agate mortar and pestle. $LaBSiO_5$ powder was produced by grinding stoichiometric amounts of La_2O_3, B_2O_3, and SiO_2 (Analytical, Sigma-Aldrich) in a ceramic mortar and pestle and heating from 900 °C to 1300 °C over 5 h in a platinum crucible in air. Identities of both commercial and synthesized samples were confirmed using pXRD. X-ray diffraction experiments were conducted using a Rigaku Ultima IV X-ray diffractometer using a copper anode X-ray tube with a diffracted beam monochromator and a scintillation detector. X-ray diffractograms are available in the supporting information. TGA was used to characterize the level of hydration of $LaPO_4 \cdot 1.85H_2O$ and $La_2(SO_4)_3 \cdot 9\,H_2O$ (Fig. B.8). The level of hydration of $La_2(CO_3)_3 \cdot nH_2O$ was not determined experimentally as the ^{139}La NMR spectrum was not used.

4.4.2 NMR Spectroscopy

^{139}La NMR spectra were collected on 9.4 T (56.54 MHz ^{139}La frequency) and 16.4 T (98.91 MHz ^{139}La frequency) Bruker Avance NMR spectrometers. Samples were finely ground in an agate mortar and pestle and packed into either 4 mm (16.4 T) or 7 mm (9.4 T) outer diameter ZrO_2 rotors. All spectra were collected under static conditions. The WCPMG pulse sequence [129] was used with WURST-80 (16.4 T) or WURST-20 (9.4 T) pulses [123] of 50 µs duration, sweeping across 500 kHz at a rate of 10 MHz ms^{-1} to ensure homogeneous excitation. The number of echoes collected varied from 60 to 250 according to the T_2 relaxation of the sample. Spectral slices were collected with a transmitter offset of either approximately 100 kHz or 200 kHz, with the exact value set to an integer multiple of the spikelet separation. The number of slices depended on the breath of the spectral peak. The number of scans per slice varied between 16 and 3192, dependent on sensitivity of the sample. Optimized recycle delays of 0.1 s to 5 s were used. Total experimental time was uniformly less than 2 h. ^{139}La chemical shifts were referenced to a 1.0 mol dm^{-3} aqueous solution of $LaCl_3$. Spectra were fit using DMFit v20110512 [184], WSolids v1.19.226 [185], and QUEST v1.1.527 [186].

4.4.3 DFT Calculations

Density functional theory calculations were carried out using the ABINIT code [187–190] using the PAW method [154]. The PAW datasets used varied depending on the structure being investigated. When possible, Jollet, Torrent, and Holzwarth (JTH) PAW datasets were used without alteration [191]. In systems where there was significant PAW sphere overlap, custom datasets were used to avoid this problem. Details on the datasets used for each structure are available in the supporting information (Table B.1). All calculations were performed using the Perdew, Burke, and Ernzerhof (PBE) generalized gradient approximation (GGA) exchange-correlation functional [192].

Calculations were conducted on crystal structures taken from the Inorganic Crystal Structure Database (ICSD) [193] Optimized plane-wave cutoff energies were used, typically between 30 and 45 hartree, with PAW fine grid cutoff energies generally between 90 and 150 hartree. K-point grids were optimized for each structure, but typically had a grid spacing of 0.03 Å^{-1}. Specific values for each structure are available in the supporting information (Table B.2). EFG parameters were calculated on experimental geometries. Calculations were performed using the WestGrid Grex research facility, with Intel Xeon X6560 2.66 GHz cores. Between 4 and 24 cores were used depending on the fineness of the k-point grid.

4.4.4 Distortion Parameters

Distortion parameters were calculated using the IVTON software [183]. Input structures were obtained from the ICSD [193], and were also used for DFT calculations. Uncertainties in distortion parameters were either determined through propagation of error or estimated from least-squares variance.

4.5 Results

^{139}La NMR spectroscopic parameters, computational results, and distortion parameters are reported in Table 4.1, Table 4.2, and Table 4.3, respectively. The presentation of the results for $LaBGeO_5$ and $LaScO_3$ are discussed as representative of the non-$LaMO_3$ and $LaMO_3$ compounds, respectively. The full results and discussion for all other

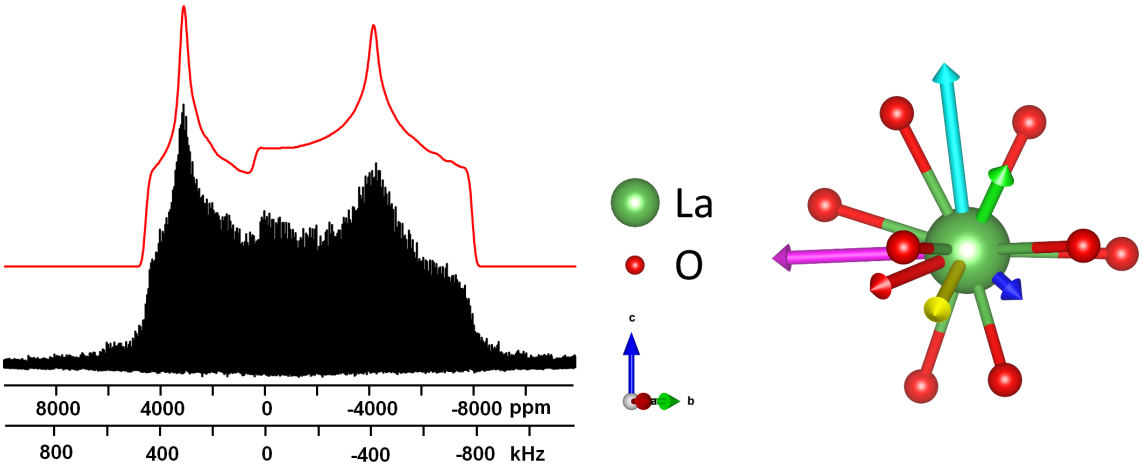

Figure 4.2: Left: Static ^{139}La NMR spectrum of $LaBGeO_5$ at 16.4 T. Analytical simulation is show in red. The EFG parameters used are reported in Table 4.1. Right: First coordination sphere of LaO_9 in $LaBGeO_5$. The V_{xx}, V_{yy}, and V_{zz} components are displayed as blue, green, and red, respectively. The e_a, e_b, and e_c semi major axes are in yellow, magenta, and teal respectively.

compounds of interest are included in Appendix B.

4.5.1 Lanthanum Borogermanate

$LaBGeO_5$ is an example of the stillwellite rare earth mineral [77] that has been extensively studied for its ferroelectric properties [75, 195, 196]. It is a remarkably efficient glass former, given its high lanthanum content. $LaBGeO_5$ glass is an effective TFN material, due to the shared stoichiometry between crystalline and glassy phases [34]. $LaBGeO_5$ has been previously studied using Raman spectroscopy [197], computational methods [198], and ^{11}B MAS NMR spectroscopy [34], but as of yet has not been investigated using ^{139}La NMR. As a member of the stillwellite family, $LaBGeO_5$ is of trigonal space group $P3_1$, with three formula units per unit cell. The environment of the single lanthanum site in $LaBGeO_5$ is ninefold coordinate to oxygen, with contributions from both the GeO_4 and BO_4 tetrahedra. La−O bond lengths range from 2.41 Å to 2.74 Å, with an average of 2.60 Å. There are no obvious symmetry elements present within the lanthanum polyhedron.

The ^{139}La ssNMR spectrum of $LaBGeO_5$ acquired at 16.4 T is presented in Fig. 4.2. The spectrum is extremely broad, spanning approximately 12 000 ppm. It is fit using a C_Q of (85.5 ± 0.5) MHz and η_Q of (0.30 ± 0.02) The spectrum is overwhelmingly

Table 4.1: Summary of the experimental ^{139}La NMR parameters. Values with a reference were taken from the respective source.

	$\lvert C_\mathrm{Q}\rvert$ / MHz	η_Q	$\delta_\mathrm{iso}^\mathrm{CS}$ / ppm	Ω / ppm	κ	α / °	β / °	γ / °
La_2O_3	58.6 ± 0.3	0.00 ± 0.02	620 ± 30	500 ± 50 [60]	-1.0 ± 0.1 [60]	150 ± 30 [60]	90 ± 10 [60]	180 ± 10 [60]
$LaPO_4 \cdot 1.8\,H_2O$	33 ± 1	1.00 ± 0.05	400 ± 20					
$LaPO_4$	46.7 ± 1.0 [172]	0.75 ± 0.03 [172]	36 ± 4 [172]					
$LaBO_3$	23.4 ± 0.4	0.68 ± 0.05	230 ± 10	350 ± 30	0.3 ± 0.1	15 ± 5	0 ± 5	165 ± 10
$LaBGeO_5$	85.5 ± 0.5	0.30 ± 0.02	200 ± 25	400 ± 200	0.8 ± 0.3	75 ± 75	15 ± 5	0 ± 10
$LaBSiO_5$	90.0 ± 0.5	0.35 ± 0.02	225 ± 50					
$La_2(SO_4)_3 \cdot 9\,H_2O$								
La(1)	52.5 ± 0.5	0.00 ± 0.02	-175 ± 25					
La(2)	36.5 ± 0.5	0.00 ± 0.03	-75 ± 25					
$La(OH)_3$	22.0 ± 0.5 [60]	0.05 ± 0.02 [60]	260 ± 20 [60]	80 ± 7 [60]	0.0 ± 0.1 [60]	80 ± 7 [60]	10 ± 10 [60]	0 ± 10 [60]
$LaAlO_3$	6 *[58]	0 *[58]	375 ± 5 [58]					
$LaCoO_3$	23.8 *[59]	0 *[59]	4230 *[59]					
$LaCrO_3$	48 *[59]	0.15*[59]	442.5 *[59]					
$LaTiO_3$	53.2 *[194]	0.6*[194]	N.D.					
$LaScO_3$	61.6 ± 0.5 [177]	0.10 ± 0.02 [177]	600 ± 50 [177]					
$LaNbO_4$	36 ± 2 [60]	0.44 ± 0.05 [60]	295 ± 25 [60]	255 ± 10 [60]	0.40 ± 0.04 [60]	90 ± 5 [60]	50 ± 5 [60]	270 ± 10 [60]

* These values were provided without uncertainties; discussion of the reliability of these values is found in the Supporting Information.

Table 4.2: Summary of the calculated ^{139}La NMR parameters.

	C_Q / MHz	η_Q
La_2O_3	60.61	0
$LaPO_4 \cdot 0\,H_2O$	−136.18	0.5
$LaPO_4$	53.67	0.56
$LaBO_3$	−28.79	0.57
$LaBGeO_5$	−89.03	0.32
$LaBSiO_5$	−109.95	0.05
$La_2(SO_4)_3 \cdot 9\,H_2O$		
La(1)	−59.1	0
La(2)	−36.46	0
$La(OH)_3$	−29.49	0
$LaAlO_3$	8.44	0
$LaCoO_3$	20.99	0
$LaCrO_3$	−47.22	0.32
$LaScO_3$	−65.17	0.08
$LaNbO_4$	39.46	0.5

quadrupolar in character, with only a minor influence from CSA. Using spectra collected at 9.4 T and 16.4 T we fit the spectra with CSA values of $\Omega = (400 \pm 200)$ ppm, $\kappa = 0.8 \pm 0.3$, $\alpha = (75 \pm 75)°$, $\beta = (15 \pm 5)°$, and $\gamma = (0 \pm 10)°$. When fitting the spectrum acquired at the lower field strength (9.4 T), the high-field approximation is less valid due to the extreme breadth of the peak; as such, we must fit it exactly, rather than through perturbation theory [186].

DFT calculations on the experimental $LaBGeO_5$ geometry [78] yield a ^{139}La C_Q of −89 MHz and η_Q of 0.32. This is in excellent agreement with the experimental results ($C_Q = (85.5 \pm 0.5)$ MHz and $\eta_Q = 0.30 \pm 0.02$). The V_{zz} component of the EFG tensor is not directed toward any specific structural feature, but is generally aligned with GeO_4 tetrahedra. The La−O bond closest to the V_{zz} vector links a GeO_4 tetrahedron with two LaO_9 polyhedra, but the bond and the vector are not parallel (Fig. 4.2).

The ellipsoid fit to the LaO_9 polyhedron is triaxial, with $e_a = (2.359 \pm 0.001)$ Å, $e_b = (2.713 \pm 0.001)$ Å, and $e_c = (2.744 \pm 0.001)$ Å. The shortest semi major axis, e_a, is in close proximity to the V_{zz} component. The ellipsoid is significantly distorted from spherical symmetry, with $\epsilon = 0.148 \pm 0.001$. The ellipsoid is oblate in nature, with an EC of -0.87 ± 0.01.

Table 4.3: Collected distortion parameters.

	CN	Σ	e_a / Å	e_b / Å	e_c / Å	ϵ	EC
La_2O_3	7	0.960 ± 0.005	2.481 ± 0.002	2.481 ± 0.002	2.731 ± 0.002	0.098 ± 0.002	1.00 ± 0.01
$LaPO_4 \cdot 0\,H_2O$	9	0.965 ± 0.002	2.415 ± 0.001	2.574 ± 0.001	2.796 ± 0.001	0.147 ± 0.001	0.05 ± 0.01
$LaPO_4$	9	0.963 ± 0.001	2.331 ± 0.001	2.721 ± 0.001	2.741 ± 0.001	0.157 ± 0.001	-0.92 ± 0.01
$LaBO_3$	9	0.951 ± 0.002	2.359 ± 0.001	2.713 ± 0.001	2.744 ± 0.001	0.148 ± 0.001	-0.87 ± 0.01
$LaBGeO_5$	10	0.943 ± 0.004	2.350 ± 0.001	2.713 ± 0.001	2.808 ± 0.001	0.175 ± 0.001	-0.67 ± 0.01
$LaBSiO_5$							
$La_2(SO_4)_3 \cdot 9\,H_2O$	12	0.960 ± 0.002	2.463 ± 0.001	2.837 ± 0.001	2.837 ± 0.001	0.138 ± 0.001	-1.00 ± 0.01
La(1)	9	0.9927 ± 0.0001	2.514 ± 0.001	2.514 ± 0.001	2.585 ± 0.001	0.028 ± 0.001	1.00 ± 0.01
La(2)	9	0.9927 ± 0.0001	2.551 ± 0.001	2.551 ± 0.001	2.620 ± 0.001	0.027 ± 0.001	1.00 ± 0.01
$La(OH)_3$	12	0.963 ± 0.001	2.67 ± 0.01	2.70 ± 0.01	2.70 ± 0.01	0.01 ± 0.01	-1.00 ± 0.01
$LaAlO_3$	12	0.931 ± 0.005	2.67 ± 0.04	2.78 ± 0.04	2.78 ± 0.04	0.04 ± 0.03	-1.00 ± 0.01
$LaCoO_3$	12	0.909 ± 0.009	2.58 ± 0.06	2.81 ± 0.06	3.03 ± 0.06	0.16 ± 0.05	-0.15 ± 0.01
$LaCrO_3$	8	0.956 ± 0.003	2.384 ± 0.001	2.462 ± 0.001	2.872 ± 0.001	0.190 ± 0.001	0.60 ± 0.01
$LaScO_3$	8	0.935 ± 0.006	2.334 ± 0.001	2.432 ± 0.001	3.032 ± 0.001	0.269 ± 0.001	0.61 ± 0.01
$LaNbO_4$	8	0.9877 ± 0.0004	2.419 ± 0.001	2.478 ± 0.001	2.606 ± 0.001	0.075 ± 0.001	0.32 ± 0.01

4.5.2 Lanthanum Scandate

$LaScO_3$ is the lanthanum perovskite most recently studied by ^{139}La ssNMR spectroscopy, and the only one published to date that has been studied by WCPMG [177]. $LaScO_3$ is in the $Pbnm$ space group with four formula units per unit cell. The lanthanum environment is eightfold, with La–O bonds ranging from 2.40 Å to 2.88 Å, with an average bond length of 2.62 Å [177]. Like $LaTiO_3$, the LaO_8 polyhedron is best described as a distorted square antiprism.

Johnston *et al.* fit the ^{139}La WCPMG ssNMR spectrum of $LaScO_3$ with a C_Q of (61.6 ± 0.5) MHz and an η_Q of 0.10 ± 0.02 [177], and carried out DFT calculations on the $LaScO_3$ structure reported by Liferovich and Mitchell [199]. In order to obtain the principal components of the EFG tensor, we conducted our own DFT calculations on the experimental geometry reported by Johnston *et al.* [177]; our calculations yielded a C_Q of -65.2 MHz and an η_Q of 0.08. The V_{xx} component is parallel to both the crystallographic c axis and the ellipsoid e_c axis, hence the V_{yy} and V_{zz} components are in the plane defined by the a and b crystallographic axes. Our computed value of η_Q is comparable with the computed value reported by Johnston *et al.* (0.08 vs. 0.13) as well as with their experimental value (0.08 vs. 0.10 ± 0.02), but our computed value of C_Q is significantly different than their computed value (-65.17 MHz vs. -51.66 MHz) [177]. Our computed value of the ^{139}La C_Q is in good agreement with the experimental value reported by Johnston *et al.* (-65.17 MHz vs. (61.6 ± 0.5) MHz) [177]. This difference is likely due to the difference in initial starting geometries; where we used the structure reported by Johnston *et al.* [177], they began from the structure reported by Liferovich and Mitchell [199].

The ellipsoid used to fit the LaO_8 polyhedron is significantly distorted, with $e_a = (2.334 \pm 0.001)$ Å, $e_b = (2.432 \pm 0.001)$ Å, and $e_c = (3.032 \pm 0.001)$ Å (Fig. 4.3). The ellipsoid is generally prolate, with an EC of 0.61 ± 0.01, and shows the greatest distortion of all ellipsoids modelled in this study, with a ϵ value of 0.269 ± 0.001. The largest semi major axis e_c is aligned with the crystallographic c axis, while the other two semi major axes are slightly angled from La–O_1 bonds (as labelled by Johnston *et al.* [177]). The shortest semi major axis is very nearly parallel with a La–O bond of length 2.532 Å, while the e_b axis is displaced from a La–O bond of length 2.396 Å by the same angle. Similar behaviour is observed in the isostructural $LaTiO_3$.

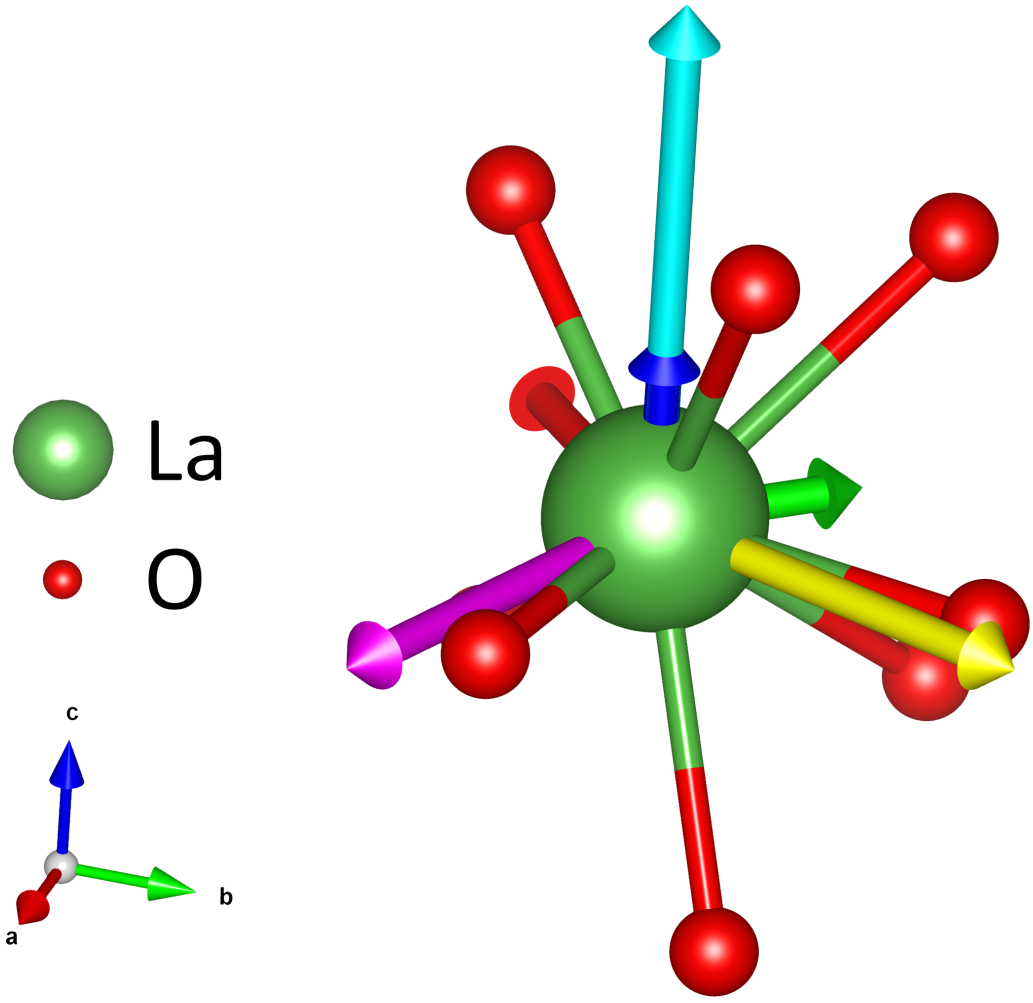

Figure 4.3: First coordination sphere of LaO_8 in $LaScO_3$. The V_{xx}, V_{yy}, and V_{zz} components are displayed as blue, green, and red, respectively. The e_a, e_b, and e_c semi major axes are in yellow, magenta, and teal respectively.

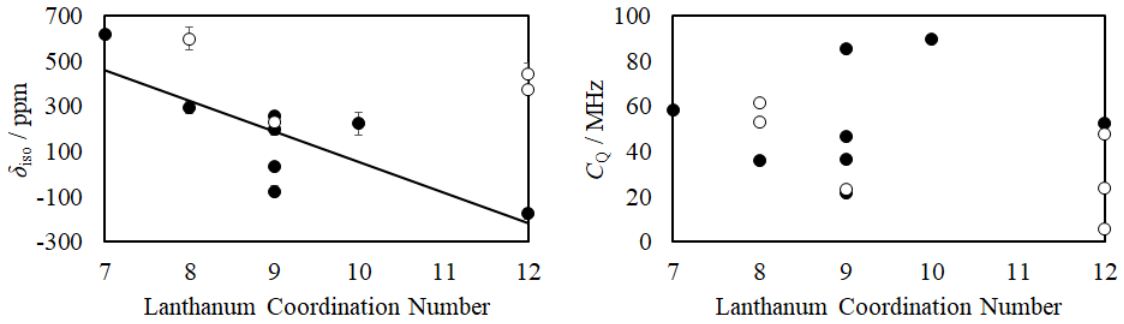

Figure 4.4: Relationship between the La CN and the ^{139}La isotropic chemical shifts (left) and quadrupolar coupling constants (right). Filled circles indicate compounds of the non-$LaMO_3$ family, while open circles indicate $LaMO_3$ compounds. The solid line in the left plot shows the relationship between La CN and ^{139}La δ_{iso}^{CS}, with $\delta_{iso}^{CS} = -135\,\text{ppm} \cdot CN + 1405\,\text{ppm}$ ($R^2 = 0.63$) for the non-$LaMO_3$ compounds. Error bars may be obscured by the datum symbol.

4.6 Discussion

4.6.1 Coordination Number

The relationship between lanthanum CN and ^{139}La NMR properties has previously been investigated by Willans *et al.* [176]. They found no correlation between La CN and C_Q or Ω, but they did find a strong relationship between the La CN and ^{139}La δ_{iso}^{CS}. When analysing our data, we were unable to establish a generally strong relationship between the coordination number and δ_{iso}^{CS} ($R^2 = 0.11$). The quality of the fit improves dramatically ($R^2 = 0.63$) when considering compounds of general formula $LaMO_3$ (M = B^{3+}, Co^{3+}, Cr^{3+}, Sc^{3+}, Ti^{3+}) separately from the other lanthanum compounds (Fig. 4.4). The isotropic chemical shift of the non-$LaMO_3$ compounds decreases as coordination number increases, consistent with the observations of Willans *et al.* It is difficult to conclusively evaluate the trend of δ_{iso}^{CS} in the $LaMO_3$ compounds due to insufficient data, as the δ_{iso}^{CS} of $LaTiO_3$ has not been reported and the δ_{iso}^{CS} of $LaCoO_3$ is anomalously high; this is proposed to be caused by transferred hyperfine interactions [59]. The coordination number alone is clearly insufficient to relate the ^{139}La isotropic chemical shift to local structure, but it is nonetheless useful in assigning NMR peaks in structures with multiple lanthanum sites (*e.g.*, $La_2(SO_4)_3 \cdot 9\,H_2O$). The range of δ_{iso}^{CS} reported in this study is approximately 900 ppm, while the range of chemical shifts reported in the literature spans approximately 1200 ppm (excluding

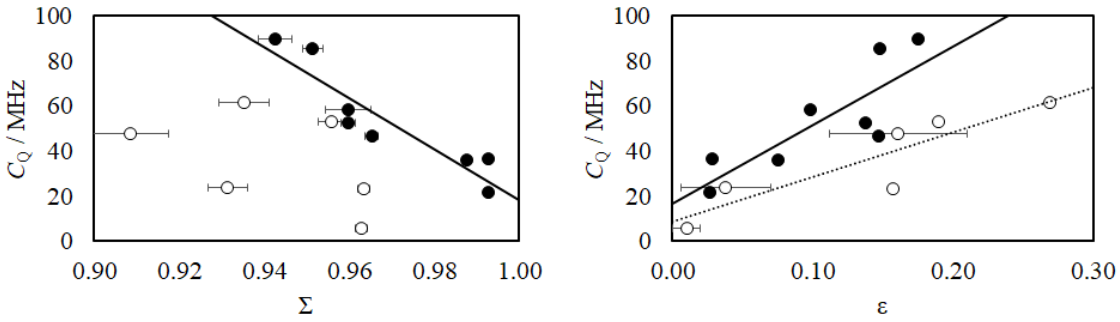

Figure 4.5: Filled circles indicate compounds of the non-$LaMO_3$ family, while open circles indicate $LaMO_3$ compounds. Left: the relationship between ^{139}La C_Q and Σ. Right: the relationship between ^{139}La C_Q and ϵ. The solid lines indicate the relationship between ^{139}La C_Q and the respective distortion parameter of the non-$LaMO_3$ compounds, with: left, $C_Q = -1133\,\text{MHz} \cdot \Sigma + 1151\,\text{MHz}$ ($R^2 = 0.85$); right, $C_Q = 349\,\text{MHz} \cdot \epsilon + 17\,\text{MHz}$ ($R^2 = 0.68$). The dotted line indicates the relationship between ^{139}La C_Q and ϵ of the $LaMO_3$ compounds, with $C_Q = 198\,\text{MHz} \cdot \epsilon + 9\,\text{MHz}$ ($R^2 = 0.80$). Error bars may be obscured by the datum symbol.

samples affected by hyperfine interactions, *e.g.*, $LaCoO_3$) [200]. ^{139}La ssNMR peaks are often broadened past this chemical shift range, limiting the potential effects of CSA in ultrawide compounds. Like Willans *et al.*, no relationship was found between the lanthanum coordination number and ^{139}La C_Q (Fig. 4.4).

4.6.2 Chemical Shielding Anisotropy

The quadrupolar interaction is clearly the primary influence on the lineshape of ^{139}La spectra. However, it is clear that CSA can have significant impact, as seen with the spectra of $LaBO_3$, $LaScO_3$, and La_2O_3. Many lanthanum compounds have only been investigated at a single field strength, preventing the collection of accurate CSA parameters. While we have investigated a few samples at two field strengths, the still too small number of data points and their considerable uncertainties render it impossible to draw any conclusions about the relationship between crystal structure and ^{139}La CSA at this time.

4.6.3 Quadrupolar Coupling Constant

The relationships between ^{139}La C_Q values and selected polyhedral distortion parameters are shown in Fig. 4.5. As with the isotropic chemical shift, it is valuable to

examine the non-$LaMO_3$ and $LaMO_3$ compounds separately.

Non-$LaMO_3$ Compounds

The non-$LaMO_3$ compounds show a strong negative correlation with the sphericity distortion parameter, with C_Q increasing as sphericity decreases. The uncertainty in the sphericity is relatively low for the non-$LaMO_3$ compounds as compared to the $LaMO_3$ compounds; this is attributed to a wider range of bond lengths present in most $LaMO_3$ compounds.

The quality of the fit of the relationship between the ϵ and C_Q for the non-$LaMO_3$ compounds ($R^2 = 0.68$) is lower than both that of the $LaMO_3$ compounds ($R^2 = 0.79$) and the relationship between Σ and C_Q for the non-$LaMO_3$ compounds ($R^2 = 0.86$). The ellipsoid span is primarily dependent on the shortest and longest semi major ellipsoid axes, e_a and e_c. There is a moderate correlation between C_Q and e_a for the non-$LaMO_3$ compounds (Fig. B.30, $R^2 = 0.69$), but not between C_Q and e_c. As such, ϵ is not as good of a descriptor of distortion for the non-$LaMO_3$ compounds, but has the advantage of being generally useful for both non-$LaMO_3$ and $LaMO_3$ compounds.

In an attempt to relate C_Q to specific structural features, the various distortion parameters are plotted against the longest and shortest La–O bonds (d_{max} and d_{min}, respectively). The most relevant plots are presented in Fig. 4.6; the rest can be found in Appendix B. The distortion parameters that best correlate to the C_Q of the non-$LaMO_3$ compounds are generally dependent on d_{max}, suggesting that the C_Q of the non-$LaMO_3$ compounds might be similarly dependent. Unfortunately, this is not the case, as the relationship between C_Q and d_{max} of the non-$LaMO_3$ compounds is less reliable than the relationship between C_Q and either Σ or ϵ (R^2 values of 0.58, 0.85, and 0.68, respectively) for the non-$LaMO_3$ compounds. The quadrupolar coupling constants of the non-$LaMO_3$ compounds seem to be dependent on both d_{min} and d_{max}, and are better fit by a combination of d_{min} and d_{max} than by either alone. The difference between the average La–O bond length (d_{avg}) and the shortest La–O bond length (Fig. 4.7) is the structural parameter which best predicts the ^{139}La C_Q for non-$LaMO_3$ compounds ($R^2 = 0.92$).

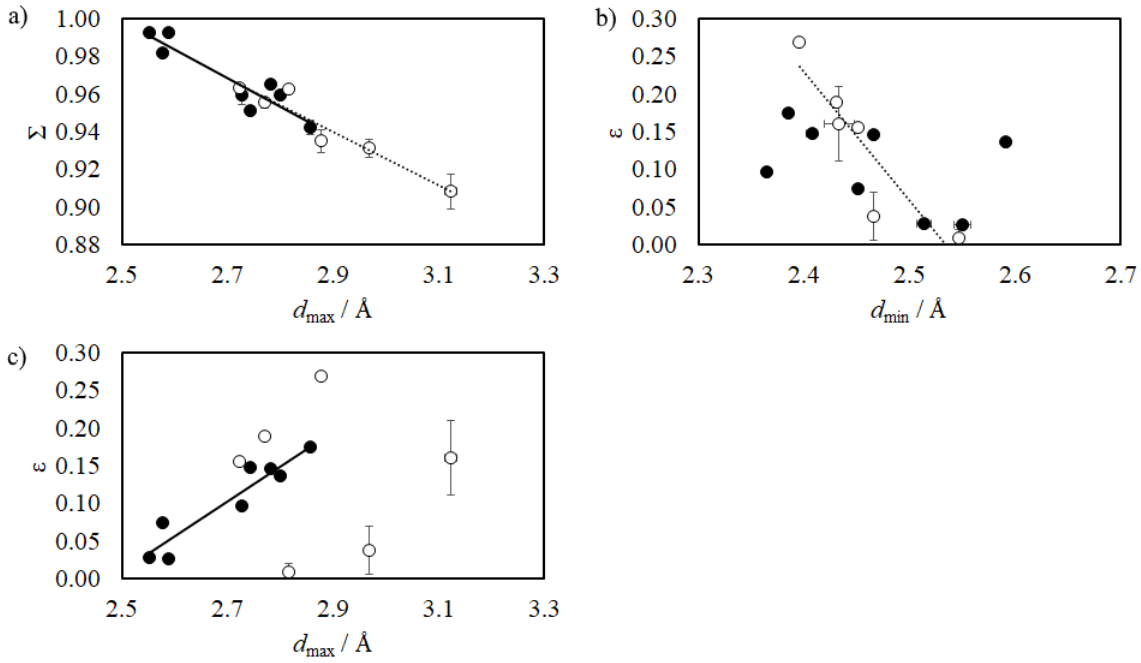

Figure 4.6: Filled circles indicate compounds of the non-$LaMO_3$ family, while open circles indicate $LaMO_3$ compounds. a) Relationship between Σ and $d_{\max}$. The solid line indicates the relationship between Σ and $d_{\max}$ for the non-$LaMO_3$ compounds, with $\Sigma = -5.71\,\text{Å}^{-1} \cdot d_{\max} + 8.23$ ($R^2 = 0.86$). The dashed line indicates the relationship between between Σ and $d_{\max}$ for the $LaMO_3$ compounds, with $\Sigma = -6.49\,\text{Å}^{-1} \cdot d_{\max} + 9.00$ ($R^2 = 0.92$). b) Relationship between ϵ and $d_{\min}$. The dashed line indicates the relationship between between ϵ and $d_{\min}$ for the $LaMO_3$ compounds, with $\epsilon = -0.48\,\text{Å}^{-1} \cdot d_{\min} + 2.52$ ($R^2 = 0.82$). c) Relationship between ϵ and $d_{\max}$. The solid line indicates the relationship between between ϵ and $d_{\max}$ for the non-$LaMO_3$ compounds, with $\epsilon = 1.92\,\text{Å}^{-1} \cdot d_{\max} + 2.5$ ($R^2 = 0.89$). Error bars may be obscured by the datum symbol.

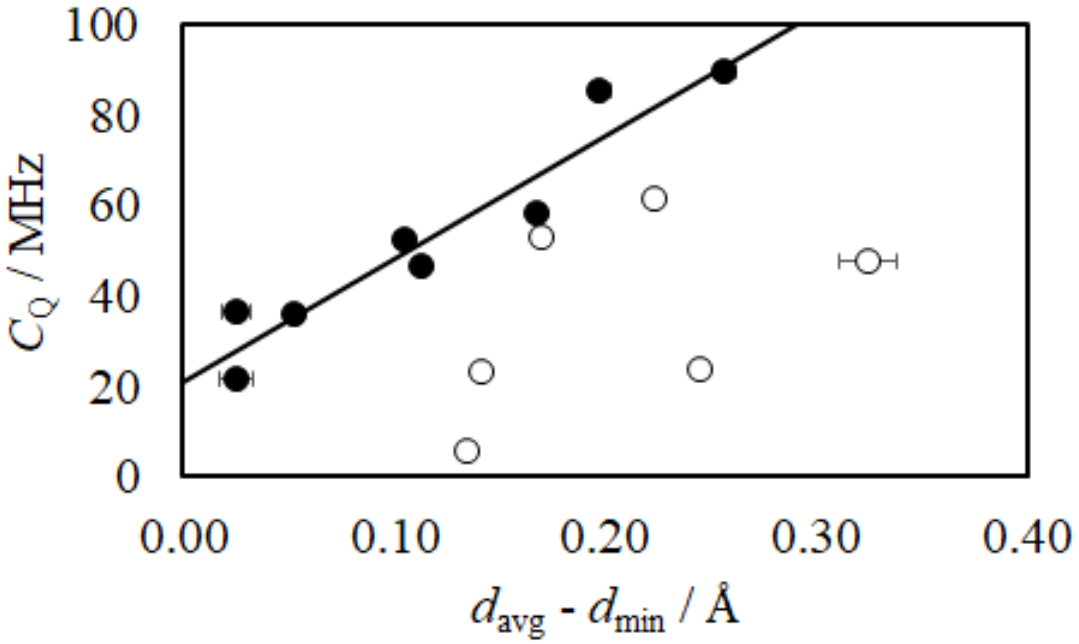

Figure 4.7: Relationship between C_Q and the difference of d_{avg} and d_{min} Filled circles indicate compounds of the non-$LaMO_3$ family, while open circles indicate $LaMO_3$ compounds. The solid line indicates the relationship between the bond length difference and C_Q for the non-$LaMO_3$ compounds, with $C_Q = 272\,\text{MHz}\,\text{Å}^{-1} + 21\,\text{MHz}$ ($R^2 = 0.92$) Error bars may be obscured by the datum symbol.

$LaMO_3$ Compounds

In contrast to the strong relationship seen in the non-$LaMO_3$ compounds, the $LaMO_3$ compounds do not show a significant dependence of C_Q on Σ ($R^2 = 0.22$). The compounds that are most likely affecting the relationship between C_Q and Σ for the $LaMO_3$ compounds are $LaCoO_3$ and $LaCrO_3$. As discussed in their respective sections in the supporting information, the $LaCoO_3$ and $LaCrO_3$ coordination polyhedra are cuboctohedra with a large difference between d_{min} and d_{max}; furthermore, the positioning of the longest and shortest La−O bonds in these structures ensures that it is difficult to fit a sphere to the oxygen positions.

The use of the ellipsoid span to relate ^{139}La C_Q and distortion is more effective than the use of Σ for the $LaMO_3$ compounds, though it is difficult to reliably fit an ellipsoid to the lanthanum polyhedra of $LaCrO_3$ and $LaCoO_3$ for the same reasons that it is difficult to fit a sphere; this is reflected in the large uncertainties of ϵ for these compounds. The individual influences of e_a and e_c are examined for the $LaMO_3$ compounds, with e_c having a much stronger relationship with C_Q than e_a. This behaviour is the mirror image of the non-$LaMO_3$ compounds, and indicates the difference between the two families.

Figure 4.6 highlights additional differences between the $LaMO_3$ and non-$LaMO_3$ compounds. While the sphericity of both families is highly dependent on d_{max}, the ellipsoid span of the $LaMO_3$ compounds is not dependent on d_{max}, but instead on d_{min}. As such, we examine the relationship between C_Q and d_{min} for the $LaMO_3$ compounds (Fig. 4.8). The fit of the relationship between C_Q and d_{min} is comparable in quality to the relationship between C_Q and ϵ (R^2 of 0.84 and 0.80, respectively). The C_Q of the $LaMO_3$ compounds is effectively independent of d_{max}, with an R^2 of 0.06. While the C_Q values of the $LaMO_3$ compounds cannot be explained solely by the shortest La−O bond lengths, they are much more dependent on this parameter than the non-$LaMO_3$ compounds. The differing influences of individual structural parameters also explains why the sphericity poorly relates to $LaMO_3$ C_Q: Σ is strongly dependent on d_{max}, while the C_Q values of $LaMO_3$ compounds are not dependent on d_{max}. We attribute the differences in the behaviour of the $LaMO_3$ and non-$LaMO_3$ compounds with regards to our model parameters primarily due to structural differences between the two compounds. The shortest La−O bonds in the $LaMO_3$ compounds form either

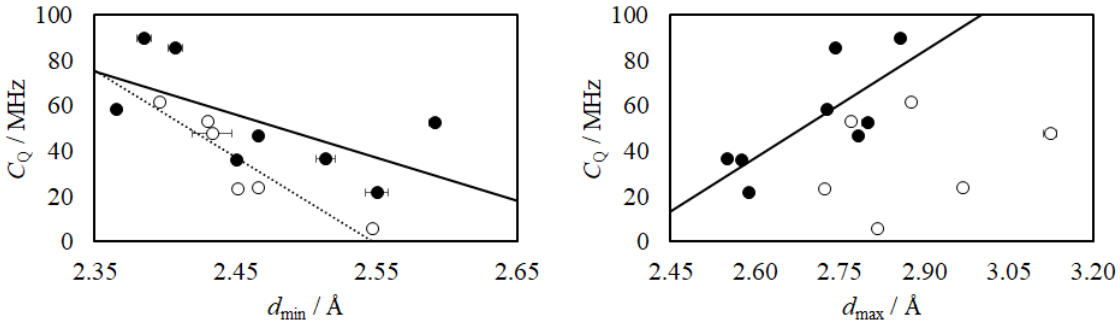

Figure 4.8: Relationship between minimum and maximum La–O bond lengths and experimental ^{139}La C_Q. Filled circles indicate compounds of the non-$LaMO_3$ family, while open circles indicate $LaMO_3$ compounds. Left: relationship between d_{min} and ^{139}La C_Q. The solid line indicates the relationship between d_{min} of the non-$LaMO_3$ compounds and C_Q, with $C_Q = -191\,\text{MHz}\,\text{Å}^{-1} \cdot d_{min} + 523\,\text{MHz}$ ($R^2 = 0.41$), while the dotted line indicates the relationship between d_{min} of the $LaMO_3$ compounds and C_Q, with $C_Q = -382\,\text{MHz}\,\text{Å}^{-1} \cdot d_{min} + 974\,\text{MHz}$ ($R^2 = 0.84$). Right: relationship between d_{max} and ^{139}La C_Q. The solid line indicates the relationship between d_{max} of the non-$LaMO_3$ compounds and C_Q, with $C_Q = 157\,\text{MHz}\,\text{Å}^{-1} \cdot d_{max} - 372\,\text{MHz}$ ($R^2 = 0.58$). Error bars may be obscured by the datum symbol.

ideal or slightly distorted trigonal prisms, whereas this substructure is generally absent from the non-$LaMO_3$ coordination polyhedra. This substructure, when considered in the context of the remaining atoms in the coordination polyhedron, is difficult to fit with either a sphere or an ellipsoid, limiting the generalizability of our models.

The most generally applicable distortion parameter is the ellipsoid span, adequately relating the C_Q to distortion for both the $LaMO_3$ and non-$LaMO_3$ compounds. The distortion of the non-$LaMO_3$ compounds is better described by the sphericity parameter. The C_Q values of both $LaMO_3$ and non-$LaMO_3$ compounds can be related to specific structural features. The C_Q of a given $LaMO_3$ compound is related to the length of the shortest La–O bond, while the C_Q of a given non-$LaMO_3$ compound is related to the difference between the average La–O bond length and the shortest La–O bond length.

4.6.4 DFT Calculations

The quadrupolar coupling constants calculated with ABINIT generally show good agreement with those determined experimentally (Fig. 4.9), with deviations typically

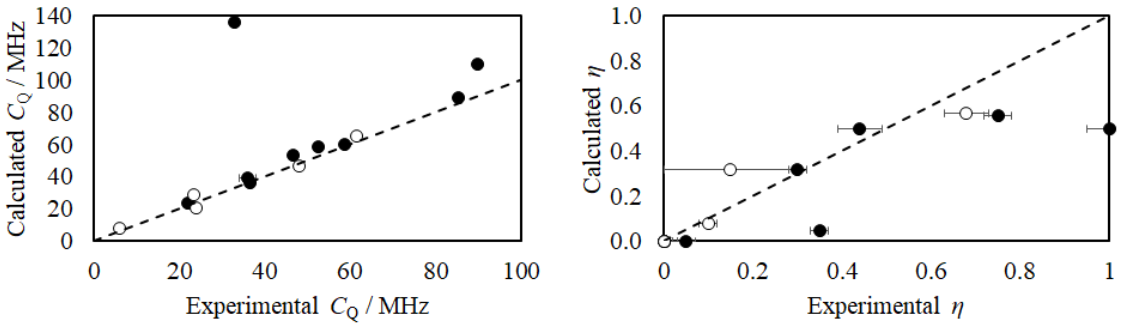

Figure 4.9: Relationship between experimental and calculated ^{139}La C_Q values (left) and η_Q values (right). Filled circles indicate compounds of the non-$LaMO_3$ family, while open circles indicate $LaMO_3$ compounds. The dashed line indicates a 1:1 relationship between computational results and experimental results. Error bars may be obscured by the datum symbol.

less than either 15 % or 3 MHz absolute, depending on the magnitude of C_Q. There are two notable exceptions to this trend: the calculated C_Q values of $LaBSiO_5$ and $LaPO_4 \cdot nH_2O$ are significantly greater than the experimental values, $LaBSiO_5$ by 22 % (20.0 MHz) and $LaPO_4 \cdot nH_2O$ by 312 % (103.2 MHz). In both of these cases, the difference between experimental and *ab initio* results are largely attributed to errors in the experimental structure. An example of the sensitivity of C_Q to crystal structure is $LaBO_3$: calculations carried out on a different $LaBO_3$ structure [201] returned a C_Q of -84 MHz and η_Q of 0.05, with only slight structural differences from the structure used in this study. The error in the calculated C_Q of $LaPO_4 \cdot nH_2O$ has two possible explanations: firstly, the structure used in our calculations does not account for the presence of interstitial water; secondly, as discussed above, there is some debate over the structure of rare earth phosphate hydrates. The C_Q predicted by the sphericity of the lanthanum site in $LaPO_4 \cdot nH_2O$ is 107.8 MHz, consistent with the *ab initio* results.

If the two results with the greatest absolute error ($LaPO_4 \cdot nH_2O$ and $LaBSiO_5$) are excluded from the fit, the relationship between experimental and calculated C_Q is very nearly 1:1, with most computational values being slightly overestimated.

The calculations of the asymmetry parameter suffer the same problems as the calculations of the quadrupolar coupling constant: the values of η_Q for $LaPO_4 \cdot nH_2O$ and $LaBSiO_5$ are extremely low as compared to experiment. The large deviation in η_Q is also attributed to errors in the experimental geometry used for the DFT calculations.

The values of η_Q for the other systems that were studied are more reliable. Most are constrained to $\eta_Q = 0$ by symmetry, which is reflected by the DFT calculations. The few that are not constrained by symmetry generally have calculated values which are reasonably close to experiment.

4.6.5 Differences Between $LaMO_3$ and non-$LaMO_3$ Compounds

There are no obvious differences between the $LaMO_3$ and non-$LaMO_3$ compounds aside from their general formulae. The coordination numbers of the $LaMO_3$ compounds range from 8 to 12, and examples can be found in the non-$LaMO_3$ compounds which share the same coordination numbers. A mirror plane can be found in the lanthanum polyhedra of most, but not all, $LaMO_3$ compounds, and can also be found in non-$LaMO_3$ compounds. The presence of a threefold rotation axis is not a unifying factor, as some $LaMO_3$ compounds possess this symmetry element, while others do not. Given the complex relationship between the EFG and crystal structure, it is likely that there is no single distinguishing structural feature between the $LaMO_3$ and non-$LaMO_3$ compounds, but instead a combination of features.

4.7 Conclusions

In this work we relate two numerical measures of the distortion of coordination polyhedra from spherical symmetry to ^{139}La C_Q. The ^{139}La WCPMG NMR spectra of $LaBO_3$, $LaPO_4 \cdot 1.8\,H_2O$, $LaBGeO_5$, $LaBSiO_5$, $La_2(SO_4)_3 \cdot 9\,H_2O$ and $La_2(CO_3)_3 \cdot 8\,H_2O$ are reported for the first time, and used to supplement existing literature reports of ^{139}La NMR parameters in solid state oxide materials. When examining a broad range of compounds, we find that the behaviour of the ^{139}La C_Q in response to deviations from spherical symmetry divides the examined materials into two families: compounds with the general formula $LaMO_3$, and the rest. The ellipsoid span, ϵ, is effective in relating C_Q to polyhedral distortion for both families of compounds. Non-$LaMO_3$ compounds are better described by the sphericity parameter Σ. Both families of compounds can be related to direct structural features, with the C_Q of $LaMO_3$ compounds being strongly dependent on the shortest La–O bond length and non-$LaMO_3$ compounds exhibiting a more complex relationship. Isotropic chemical shifts of the non-$LaMO_3$ compounds are found to move to lower frequencies with higher coordination number, while there

are insufficient data to draw a similar conclusion for the $LaMO_3$ compounds. *Ab initio* calculations of EFG parameters provide values that generally agree with experiment, with the exceptions of $LaBO_3$, $LaBSiO_5$, and $LaPO_4 \cdot nH_2O$; the failure of *ab initio* calculations to return values consistent with experiment is attributed to errors in the reported crystal structures.

4.8 Acknowledgements

Financial support from the Natural Sciences and Engineering Research Council of Canada (NSERC) (Canada Grant RGPIN 261978) is gratefully acknowledged. We appreciate the assistance of Dr. M. Obrovac (TGA and pXRD) and Dr. C. Romao (IVTON). This research was enabled in part due to support provided by WestGrid (https://www.westgrid.ca/).

Chapter 5

Application of ^{139}La NMR Spectroscopy to Lanthanum Oxide-Based Glasses

5.1 Context

The previous chapter developed a model describing the relationship between various ^{139}La spectral parameters and the local structure of lanthanum oxide-based crystals. This chapter focuses on applying that model to two lanthanum oxide-based glass series: lanthanum borogermanates and lanthanum phosphates. These series were chosen for several reasons. The lanthanum borogermanate series includes the $LaBGeO_5$ composition, which is the primary target of this dissertation. The lanthanum phosphate series forms a glass over a wide range of La_2O_3 concentrations, allowing for the possibility of a wide range of La−O coordination numbers (n_{LaO}). Both the lanthanum borogermanate and lanthanum phosphate series have n_{LaO} values that have been determined via diffraction-based techniques; this is an important check on the predictive power of the crystal model, allowing for the model to be empirically tested. Finally, both $LaBGeO_5$ and LaP_3O_9 compositions have congruent crystal and glass forms. This potentially allows for the direct comparison of n_{LaO} between the crystal and glass.

The work described in this chapter was completed by collaboration of ALP, UWZ, and JWZ. ALP synthesized most of the samples, collected the pXRD and NMR data, conducted much of the analysis, and wrote the majority of the manuscript. UWZ provided technical support in the collection of the NMR data and provided important contributions to the analysis of the ^{139}La NMR spectra of the glass samples in particular. UWZ also provided editorial contributions. JWZ contributed to the understanding of the Czjzek distribution, contributed text describing the physical background of the distribution, and editorial input to the manuscript.

5.2 Abstract

Understanding the local environment of rare-earth ions in glasses is useful for designing effective optical glasses and functional nuclear waste glasses. Lanthanum is a particularly appealing target for NMR spectroscopy as it is both diamagnetic and chemically similar to the other lanthanide elements. However, due to its large quadrupole moment, to date ^{139}La NMR spectroscopy has not been applied to the study of lanthanum-containing glasses. We present ^{139}La nuclear magnetic resonance spectra of a variety of lanthanum oxide-based crystalline samples and glasses, including the $LaBGeO_5$ transparent ferroelectric composite. Our results suggest that the breadth of the ^{139}La quadrupole distribution is indicative of the disorder in the second-neighbour shell around La. We relate the ^{139}La isotropic chemical shift ($\delta_{\text{iso}}^{\text{CS}}$) of crystalline materials to La–O coordination numbers. Our results suggest that the change in chemical shift with respect to change in CN is consistent within chemical species (with a value of $-130\,\text{ppm}\,\text{CN}^{-1}$). Unfortunately, we find that the ^{139}La $\delta_{\text{iso}}^{\text{CS}}$ values appear to be masked by other broadening mechanisms in the glass samples, so we are unable to extract additionally coordination numbers by this method.

5.3 Introduction

Glasses containing rare-earth oxides are of significant scientific and industrial interest. Rare-earth oxide-based glasses have optical applications in lasers and optical amplifiers [202–205], and are a potential method for sequestering radioactive lanthanides and actinides produced in the nuclear fuel cycle [206, 207]. For many of these applications, an understanding of the local environment of the rare-earth ions in the glass is an important tool in tailoring the composition of the glass to obtain the desired set of properties.

Of the methods typically used for the characterization of the local structure of glasses (*i.e.*, vibrational spectroscopy, NMR spectroscopy, neutron and/or X-ray diffraction), diffraction-based techniques have been the most widely used for the study of the environment of rare-earth ions. The cause for this is the high atomic weight of the lanthanides and actinides (restricting vibrational spectroscopy), and generally undesirable NMR properties of most rare-earth nuclides. Most rare-earth ions are

paramagnetic, precluding their direct study by NMR spectroscopy. Only three (*i.e.*, ^{45}Sc, ^{89}Y, ^{139}La) are reliably diamagnetic, and hence most NMR spectroscopy of rare-earth compounds have been of these nuclides.

^{45}Sc, ^{89}Y, and ^{139}La NMR spectra of crystalline materials have been reported in the literature [47, 126, 208, 209]. However, to date only ^{45}Sc and ^{89}Y NMR spectroscopy have been applied to glasses [210, 211]. The reason for this is the large nuclear quadrupole moment of ^{139}La ($Q = (20.0 \pm 0.6)\,\mathrm{fm}^2$ [57]), which results in spectra that are typically quite broad, requiring step-wise collection and signal enhancement techniques to allow for timely acquisition [126]. In crystalline environments with well-defined crystallographic sites, it is nevertheless possible to separate overlapping environments via NMR lineshape fitting. This approach is less tractable in amorphous materials, where well-defined quadrupolar features are broadened and may be completely obscured by structural disorder [25].

One lanthanide oxide of particular interest is the $LaBGeO_5$ transparent ferroelectric glass-ceramic. The $LaBGeO_5$ glass crystallizes congruently, *i.e.*, the glass and crystal share the same stoichiometry. However, there are significant differences in the local structure between the glass and the crystal. In particular, both the boron–oxygen and germanium–oxygen coordination numbers have been shown to vary [34, 212]. We have estimates of the mean La–O coordination number (n_{LaO}) in the $LaBGeO_5$ glass from our analysis of our neutron diffraction data, but these estimates are limited by the complex O–O coordination resulting from the distribution of Ge–O coordinations. This is a concern that is present in any amorphous system containing distributions of coordination numbers, multiple rare-earth elements, or small amounts of the element of interest (*e.g.*, optically-relevant doping).

The extension of ^{139}La NMR spectroscopy to lanthanum oxide-containing glasses would allow for a useful tool in the analysis of the local environment of La^{3+}. As NMR spectroscopy is nuclide-specific, it allows for the characterization of local environments even in a complex system. This is particularly applicable to lanthanide or actinide glasses, where La_2O_3 is frequently used as a proxy for paramagnetic or radioactive oxides [206]. Furthermore, NMR spectroscopy is typically more accessible than neutron diffraction, which requires either a nuclear reactor or a spallation neutron source, available at only a few places in the world.

In this contribution we expand on our previous work on ^{139}La NMR of crystalline materials [126], reporting the spectra of several additional crystals, and extend this work to lanthanum oxide-containing glasses. We present ^{139}La spectra of various lanthanum borogermanate and lanthanum phosphate glasses. We are able to make structural inferences about the relative disorder around the lanthanum sites in the glasses. Unfortunately, it proves difficult to extract the isotropic chemical shift of lanthanum in the presence of the strong, disorder-broadened quadrupole interactions, so application of the crystal-based correlation found in Chapter 4 to extract coordination numbers is not possible.

5.4 Methods

5.4.1 Sample Preparation

Three glass sample series were produced:
xLaBG ($x\mathrm{La_2O_3}$–(100-x)(0.33 $\mathrm{B_2O_3}$–0.67 $\mathrm{GeO_2}$)), with x = 20, 25, and 30; yLaP ($y\mathrm{La_2O_3}$–(100-y)$\mathrm{P_2O_5}$), with y =10, 15, 20, 25, and 30; and
25LaB (25 $\mathrm{La_2O_3}$–75 $\mathrm{B_2O_3}$). The synthesis and description of the xLaBG samples has been reported previously [212], and correspond to the samples labelled 20LaBG, 25LaBG-1, and 30LaBG-1 described therein. The yLaP and 25LaB glasses were produced in a similar fashion. All reagents were sourced from Sigma-Aldrich. Stoichiometric amounts of the appropriate reagents [($\mathrm{La_2O_3}$, 99.99 %), ($\mathrm{NH_4H_2PO_4}$, $\geq$ 98 %), ($\mathrm{B_2O_3}$, $\geq$ 98 %)] were thoroughly ground in a porcelain mortar and pestle, and then placed in a platinum crucible. The yLaP samples were first heated to approximately 400 °C for several hours, to allow for the conversion of $\mathrm{NH_4H_2PO_4}$ to $\mathrm{P_2O_5}$, before being placed into a furnace preheated to temperatures between 850 °C to 1300 °C, depending on $\mathrm{La_2O_3}$ content. The 25LaB sample was placed directly into a box furnace preheated to 1300 °C and allowed to melt for 30 min. The yLaP and 25LaB glasses were quenched by pouring onto room-temperature brass plates.

In addition to the glasses, $\mathrm{LaB_3O_6}$, $\mathrm{LaP_3O_9}$, and $\mathrm{La_2Sn_2O_7}$ crystalline powders were synthesized. The $\mathrm{LaB_3O_6}$ crystalline powder was synthesized by combining stoichiometric amounts of $\mathrm{La_2O_3}$ and $\mathrm{B_2O_3}$ and heating in a platinum crucible for 12 h

at 850 °C in air. The LaP_3O_9 crystalline powder was synthesized by combining stoichiometric amounts of La_2O_3 and solid H_3PO_4 (99.999 %) under nitrogen atmosphere for 60 h at 400 °C. The $La_2Sn_2O_7$ crystalline powder was synthesized by combining stoichiometric amounts of La_2O_3 and SnO_2 (99.9 %) and heating in a platinum crucible for 4 d at 1250 °C in air.

All diffraction measurements were made using a Rigaku Ultima IV X-ray diffractometer equipped with a Cu anode X-ray tube and a diffracted beam monochromator. Diffraction measurements used angular steps of 0.05°, and dwell times of 1 s.

5.4.2 NMR Spectroscopy

All ^{139}La NMR spectra were collected using the WCPMG pulse sequence [129], which combines WURST pulses [123, 124] with CPMG loops [130, 131]. Spectra were collected on a 16.4 T Bruker Avance spectrometer using 4 mm ZrO_2 rotors, and on a 9.4 T Bruker Avance spectrometer using custom-made 9 mm glass tubes. The spectra were collected under static conditions. 50 µs WURST-80 pulses were swept across 500 kHz at a rate of 10 MHz ms^{-1}. Most spectra were too broad to allow for collection in one spectral window (1 MHz). To allow for the entire spectrum of the central transition to be collected, the VOCS method was employed [127, 128]. The transmitter was moved in VOCS steps of 100 kHz. The number of steps required was dependent on the breadth of the spectrum, with collection proceeding until either no significant signal could be observed, or until the signal consisted of nothing but a flat line (indicative of the satellite transitions). The number of scans per step varied between 16 and 32 768, depending on the La_2O_3 content of the sample, as well as the number of echoes collected per scan. The number of echoes collected per scan ranged from 5 to 100 depending on the sample, with the crystalline samples generally allowing for a greater number than the glass samples. The recycle delay was optimized for each sample, with times of 1 s proving sufficient for full relaxation in all cases. ^{139}La NMR spectra were referenced to a 1 mol dm^{-3} aqueous solution of $LaCl_3$ (0 ppm). Spectra were fit using DMFIT version 20150521 [184]. The Czjzek model, as implemented in DMFIT, was used to fit the ^{139}La NMR spectra of the glass samples [135, 136, 138, 139]. For the glass samples, the position parameter (Δ_{offset}) and the standard deviation of the electric field gradient tensor elements from the Czjzek fit (σ) are reported. For

the crystalline compounds, fits were performed with the usual chemical shift and quadrupole parameters, and the quadrupolar coupling constant (C_Q), quadrupolar asymmetry parameter (η_Q), and isotropic chemical shift (δ_{iso}^{CS}) are reported as per standard conventions [159]. We report the CSA parameters using the Herzfeld-Berger convention, where Ω is the chemical shift span and κ is the chemical shift skew [160]. Some spectra are presented as the Fourier transform of the summed WCPMG echoes, which returns a continuous lineshape that is equivalent to the intensity profile of the spikelet manifold. This allows for least-squares fitting of the lineshape using DMFIT.

5.5 Results

5.5.1 X-Ray Diffraction

The results of our powder X-ray diffraction experiments are presented in Fig. 5.1.

The diffraction patterns indicate that the samples are primarily composed of the structure of interest. The top diffraction pattern is consistent with that calculated from the reported crystal structure of $La_2Sn_2O_7$ (powder diffraction file (PDF) 88-0446) [213]. We observe small impurity peaks consistent with the presence of cassiterite SnO_2 (PDF 72-1147). The middle diffraction pattern is consistent with the diffraction pattern of LaB_3O_6 reported in the literature (PDF 13-0246) [214]. There are minor impurity peaks identified as a trace amount of $LaBO_3$ (PDF 12-0762). The bottom diffraction pattern is consistent with literature reports of LaP_3O_9 (PDF 33-0717) [215]. There is an impurity peak at approximately 23° which we have been unable to identify conclusively. The impurity is tentatively attributed to PtP_2O_7, which could have formed through the reaction of the H_3PO_4 with the platinum crucible. However, we cannot be confident in the exact identification of the impurity based upon only one unique diffraction peak.

For the purposes of ^{139}La NMR, these samples are sufficiently pure. As NMR is isotopically selective, the presence of impurities which do not contain ^{139}La do not affect the ^{139}La NMR spectrum. Hence, the presence of SnO_2 does not affect the ^{139}La NMR spectrum of $La_2Sn_2O_7$. We have previously reported the ^{139}La NMR spectrum of $LaBO_3$, and its influence on the spectrum of LaB_3O_6 can be accounted for [126]. While we cannot identify the impurity in the LaP_3O_9 sample, it is inconsistent with

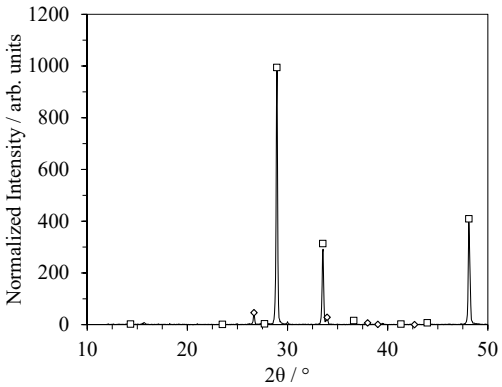

(a) $La_2Sn_2O_7$ (PDF 88-0446, squares) and SnO_2 (PDF 72-1147, diamonds).

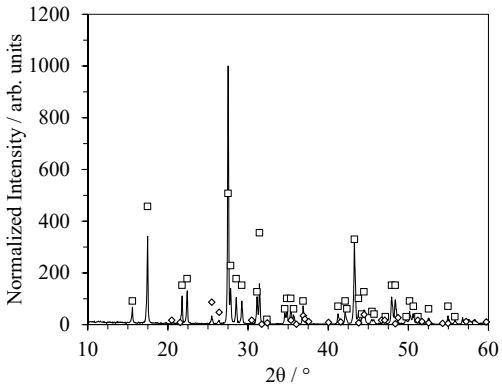

(b) LaB_3O_6 (PDF 13-0246, squares) and $LaBO_3$ (PDF 12-0762, diamonds).

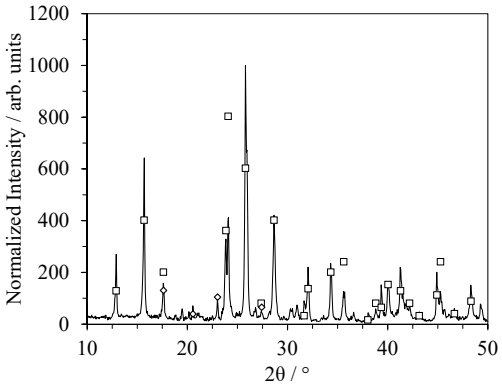

(c) LaP_3O_9 (PDF 33-0717, squares) and PtP_2O_7 (PDF 33-0980, diamonds). Only the major peaks of PtP_2O_7 are presented.

Figure 5.1: X-ray diffraction patterns of the crystalline compounds studied in this work. Intensities are presented on a linear scale, and are normalized such that the most intense peak has a value of 1000. The primary compounds are indicated by squares, while impurity phases are indicated with diamonds. The vertical position of a marker is indicative of its reported intensity. All reference patterns are obtained from the literature, and citations are provided in the text.

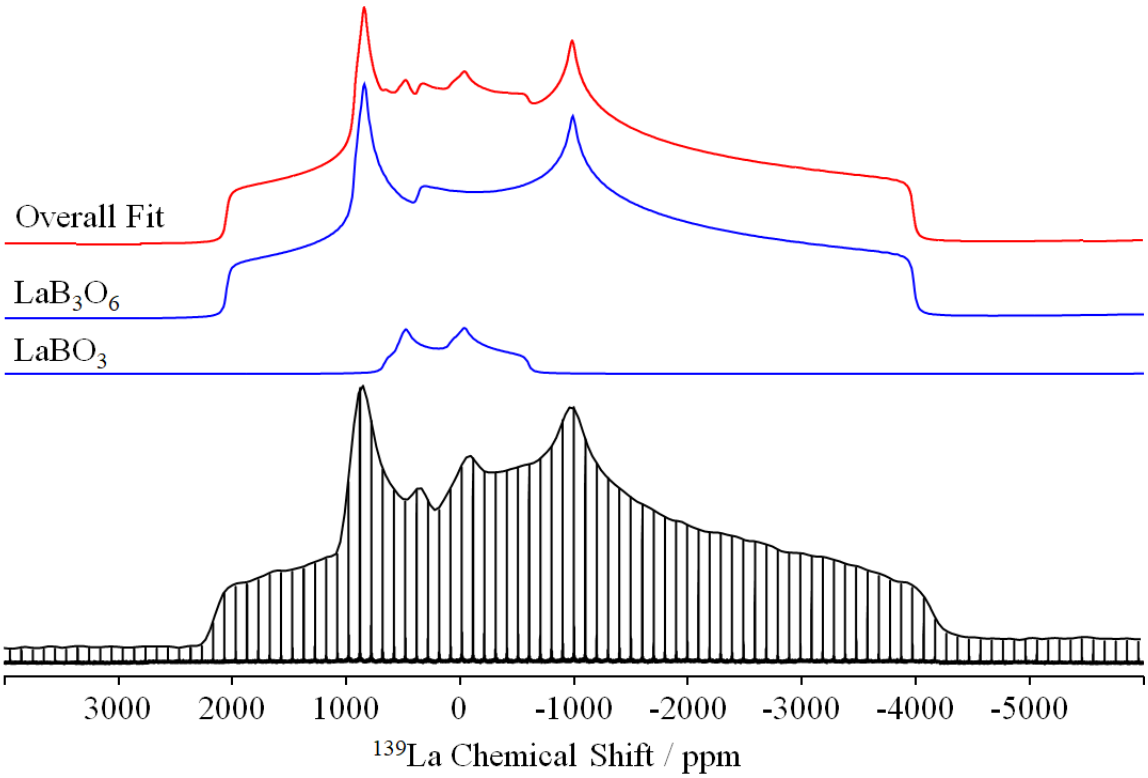

Figure 5.2: The ^{139}La WCPMG NMR spectrum of LaB_3O_6 at 16.4 T. The LaB_3O_6 parameters used to generate the fit are reported in the text. The parameters used for the $LaBO_3$ contribution have been previously reported [126].

the presence of any known La-based crystals, and we thus neglect it.

5.5.2 ^{139}La NMR Spectroscopy of Crystalline Compounds

We have previously reported on the relationship between various ^{139}La NMR parameters and structural distortion in lanthanum-based oxide crystalline materials [126]. In this work we show the spectra of three additional lanthanum-based oxide crystalline materials, two of which have congruent glass forms.

We present the ^{139}La NMR spectrum of our crystalline LaB_3O_6 sample, and our fit to the spectrum, in Fig. 5.2. The LaB_3O_6 crystal structure has a single La site, and hence we expect to fit the spectrum with a single lineshape [216]. In agreement with our X-ray results, an adequate fit of the spectrum requires the inclusion of a $LaBO_3$ peak, the ^{139}La NMR parameters of which we have previously reported [126]. We neglect the CSA parameters in our fit, as their influence is

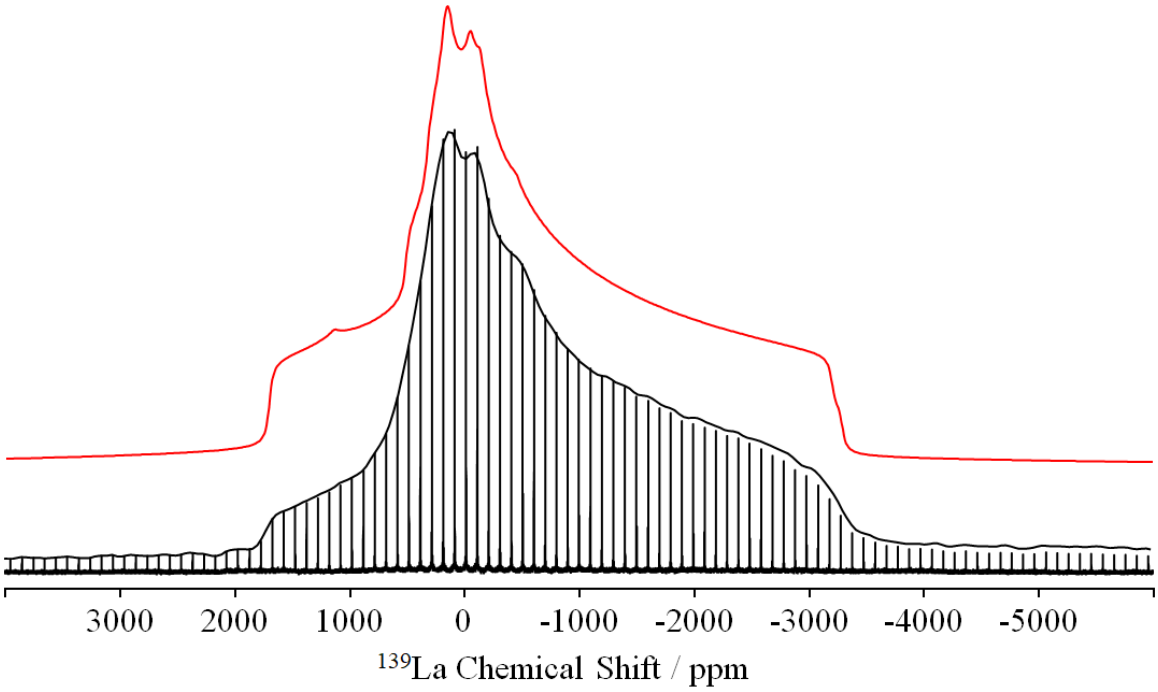

Figure 5.3: The ^{139}La WCPMG NMR spectrum of LaP_3O_9 at 16.4 T. The spectral parameters used to generate the fit are reported in the text.

expected to be small compared to the quadrupolar parameters. Our fit for the LaB_3O_6 portion of the spectrum yields $\delta_{iso}^{CS} = (46 \pm 50)$ ppm, $C_Q = (54.4 \pm 0.5)$ MHz, and $\eta_Q = 0.58 \pm 0.03$. WCPMG experiments are inherently non-quantitative in relative intensities, as the signal enhancement is dependent on the spin-spin relaxation of the respective crystallographic sites. It is our experience that the La site in $LaBO_3$ is particularly enhanced by WCPMG. However, the amount of $LaBO_3$ intensity required for a reasonable fit of the spectrum is less than 5 %, consistent with the X-ray diffraction data (Fig. 5.1).

The ^{139}La NMR spectrum of the crystalline LaP_3O_9 sample is presented in Fig. 5.3. The crystal structure of LaP_3O_9 has a single La site. We fit the spectrum with a single quadrupolar lineshape, with $\delta_{iso}^{CS} = (26 \pm 25)$ ppm, $C_Q = (43.8 \pm 0.5)$ MHz, and $\eta_Q = 0.95 \pm 0.04$. There is no indication of any La-based impurity such as La_2O_3 or $LaPO_4$.

The ^{139}La NMR spectra of $La_2Sn_2O_7$ at 16.4 T and 9.4 T are presented in Fig. 5.4. The crystal structure of $La_2Sn_2O_7$ has a single axially symmetric La site, which restricts η_Q to be 0 or near-0 [213]. Unlike LaB_3O_6 and LaP_3O_9, a good fit of $La_2Sn_2O_7$ can only

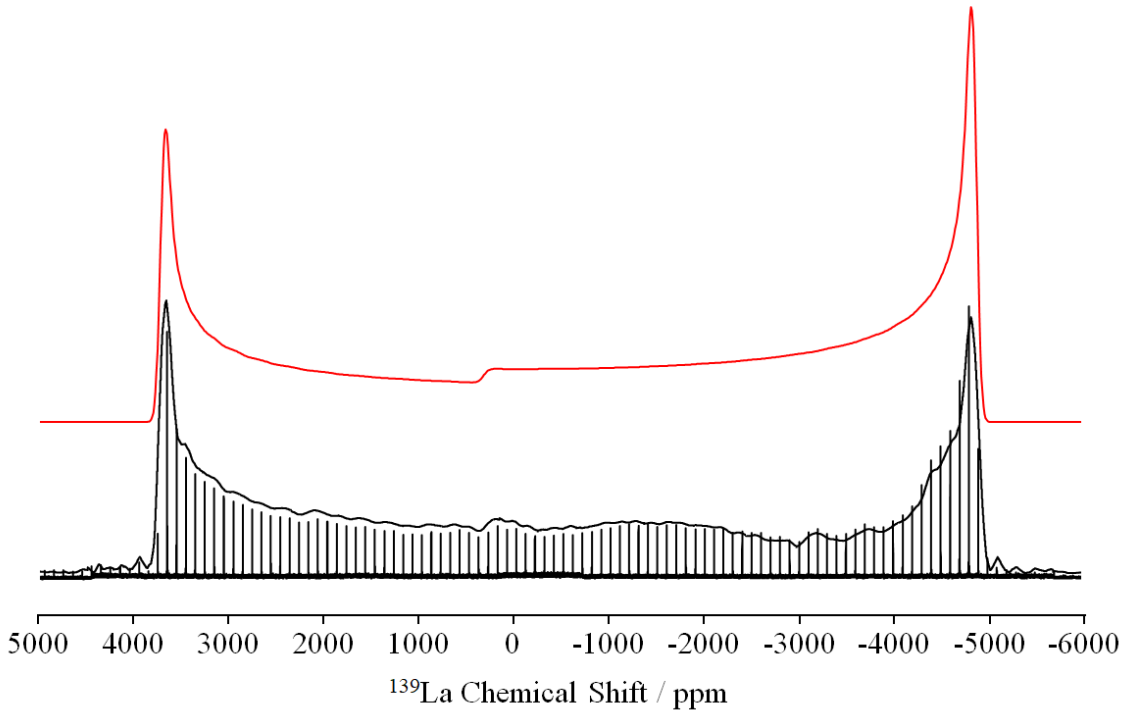

(a) 16.4 T.

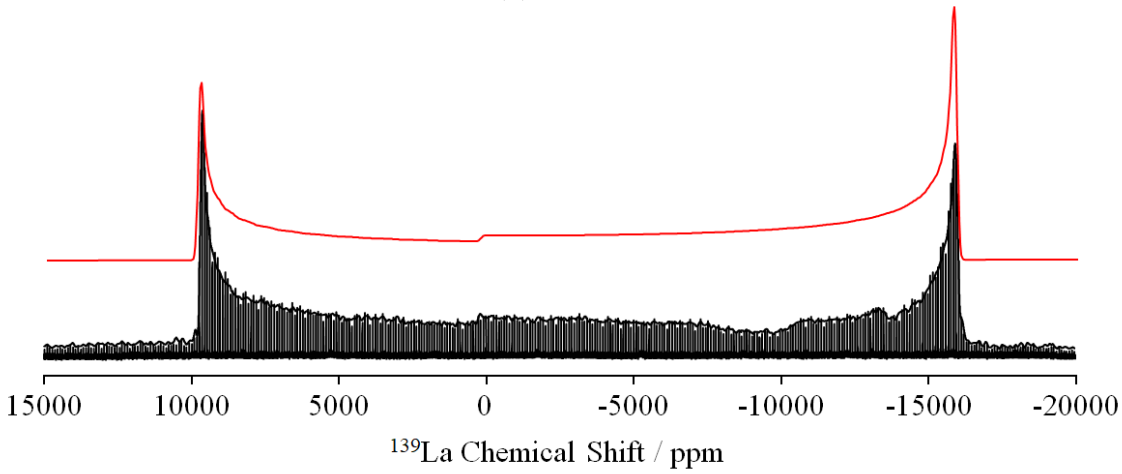

(b) 9.4 T.

Figure 5.4: The ^{139}La WCPMG NMR spectra of $La_2Sn_2O_7$ at a) 16.4 T and b) 9.4 T. The spectral parameters used to generate the fit are reported in the text. The same set of parameters is used at both field strengths.

by obtained by including the effects of CSA, requiring collecting spectra at two NMR field strengths. We fit the $La_2Sn_2O_7$ spectrum with the following parameters: $C_Q = (78.3 \pm 0.3)$ MHz; $\eta_Q = 0.00 \pm 0.02$; $\delta_{iso}^{CS} = (540 \pm 100)$ ppm; $\Omega = (375 \pm 100)$ ppm; $\kappa = 1.00 \pm 0.03$. The EFG and CSA tensors are coaxial, consistent with the crystal structure and density functional theory calculations (not shown). The consideration of the CSA parameters is required for the accurate positioning of the step discontinuity; if the CSA parameters are neglected, the quadrupolar horns and the step discontinuity cannot be fit simultaneously.

The ^{139}La isotropic chemical shift (δ_{iso}^{CS}) values from this work are included in our overall dataset of known ^{139}La NMR parameters and structural information, which is presented in Table 5.1. We restricted our dataset to compounds where the crystal

Table 5.1: ^{139}La δ_{iso}^{CS} values and n_{LaO} coordination numbers of the crystalline compounds considered in this study. Values in parentheses indicate uncertainties. For values reported for the first time in this work, uncertainties are derived from least-squares fitting of the ^{139}La spectra.

Compound	n_{LaO}	δ_{iso}^{CS} / ppm	δ_{iso}^{CS} Source	Structure Source
$La(OH)_3$	9	260 ± 20	[60]	[217]
$La_2(SO_4)_3 \cdot 9\,H_2O$ (1)	12	-175 ± 25	[126]	[218]
$La_2(SO_4)_3 \cdot 9\,H_2O$ (2)	9	-75 ± 25	[126]	[218]
La_2O_3	7	620 ± 10	[126]	[219]
$La_2Sn_2O_7$	8	540 ± 100	This work	[213]
LaB_3O_6	10	45 ± 50	This work	[216]
$LaBGeO_5$	9	225 ± 25	[126]	[78]
$LaBSiO_5$	10	225 ± 50	[126]	[220]
$LaNbO_4$	8	295 ± 25	[60]	[221]
LaP_3O_9	8	26 ± 25	This work	[222]
$LaPO_4$	9	36 ± 10	[172]	[223]

structure is well-known, the La−O coordination numbers are well-defined, the ^{139}La NMR peaks are unambiguously fit and assigned, and which do not fall into the $LaMO_3$ family of compounds which we have previously discussed [126]. The relationship between the ^{139}La δ_{iso}^{CS} and the n_{LaO} coordination number is presented in Fig. 5.5. The data are fit using a linear regression, with a slope of (-130 ± 40) ppm CN^{-1} and intercept of (1400 ± 400) ppm ($R^2 = 0.51$). The lanthanum phosphates (*i.e.*, $LaPO_4$, LaP_3O_9) and the lanthanum sulfate nonahydrate samples have δ_{iso}^{CS} values that are

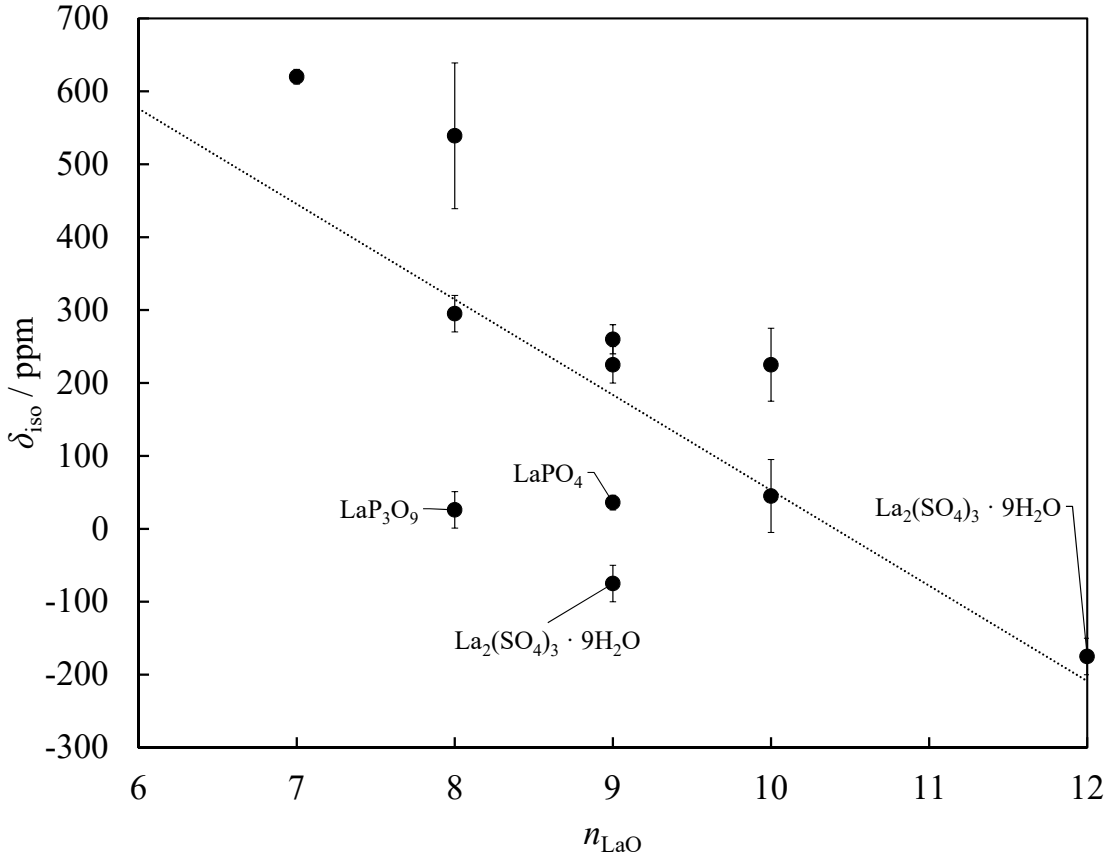

Figure 5.5: The relationship between ^{139}La δ_{iso}^{CS} and La–O coordination number in crystalline compounds. The data used to construct this figure are reported in Table 5.1. The line indicates a linear fit to the data, with slope of (-130 ± 40) ppm CN^{-1} and intercept of (1400 ± 400) ppm ($R^2 = 0.51$). The phosphate and sulphate species are highlighted.

substantially lower than the trendline. Figure 5.5 shows a moderate correlation between La−O coordination number and ^{139}La $\delta_{\text{iso}}^{\text{CS}}$, but the deviation of the phosphates and sulfate from the trendline suggests that the relationship may be affected by composition.

5.5.3 ^{139}La NMR Spectroscopy of Glasses

We present ^{139}La WCPMG NMR spectra of three glass series: xLaBG, with composition $x\text{La}_2\text{O}_3-(100\text{-}x)(0.33\,\text{B}_2\text{O}_3-0.67\,\text{GeO}_2)$; yLaP, with composition $y\text{La}_2\text{O}_3-(100\text{-}y)\text{P}_2\text{O}_5$; and 25LaB, with composition $25\,\text{La}_2\text{O}_3-75\,\text{B}_2\text{O}_3$. ^{11}B MAS NMR and neutron diffraction data from the xLaBG samples have been previously reported in the literature [212]. The spectra of the glass samples are presented in Fig. 5.6. The spectra are extremely broad; the narrowest spectrum has a full width at half maximum of approx. 1500 ppm. This is due in large part to the large quadrupole moment of the ^{139}La nucleus, but also due to the structural disorder inherent in glasses. As the spectra are universally too broad to successfully narrow using MAS, they are collected under static conditions. The xLaBG spectra have similar shapes, with each spectrum showing an asymmetric tail to low frequencies and a noticeable increase in width at the greatest La_2O_3 content. The yLaP spectra show greater variation in breadth. They are markedly narrower than the xLaBG spectra, and also show a significant increase in width with added La_2O_3. The asymmetric shape of the ^{139}La spectra of the glass samples are indicative of a distribution of quadrupolar parameters, that is, of electric field gradients.

In order to fit spectra with distributions of EFG parameters, we employ the Czjzek distribution [135, 136, 138, 139]. This model assumes that the values of each of the five independent elements of the EFG tensor (C_{Q} , η_{Q}, and the Euler angles α, β, and γ) are normally distributed, with mean zero and standard deviation σ (the same σ is used for all five elements). These assumptions are typically valid for quadrupolar nuclei in disordered environments with relatively large coordination numbers, and so are reasonable to apply to the ^{139}La case. From a Czjzek fit, the size of σ may be correlated with the extent of disorder. In addition, the spectra show overall composition-dependent changes in chemical shift, but our tests comparing the shifts in different field strengths indicate that this shift is not due just to the isotropic chemical shift. It likely includes contributions from other interactions as well,

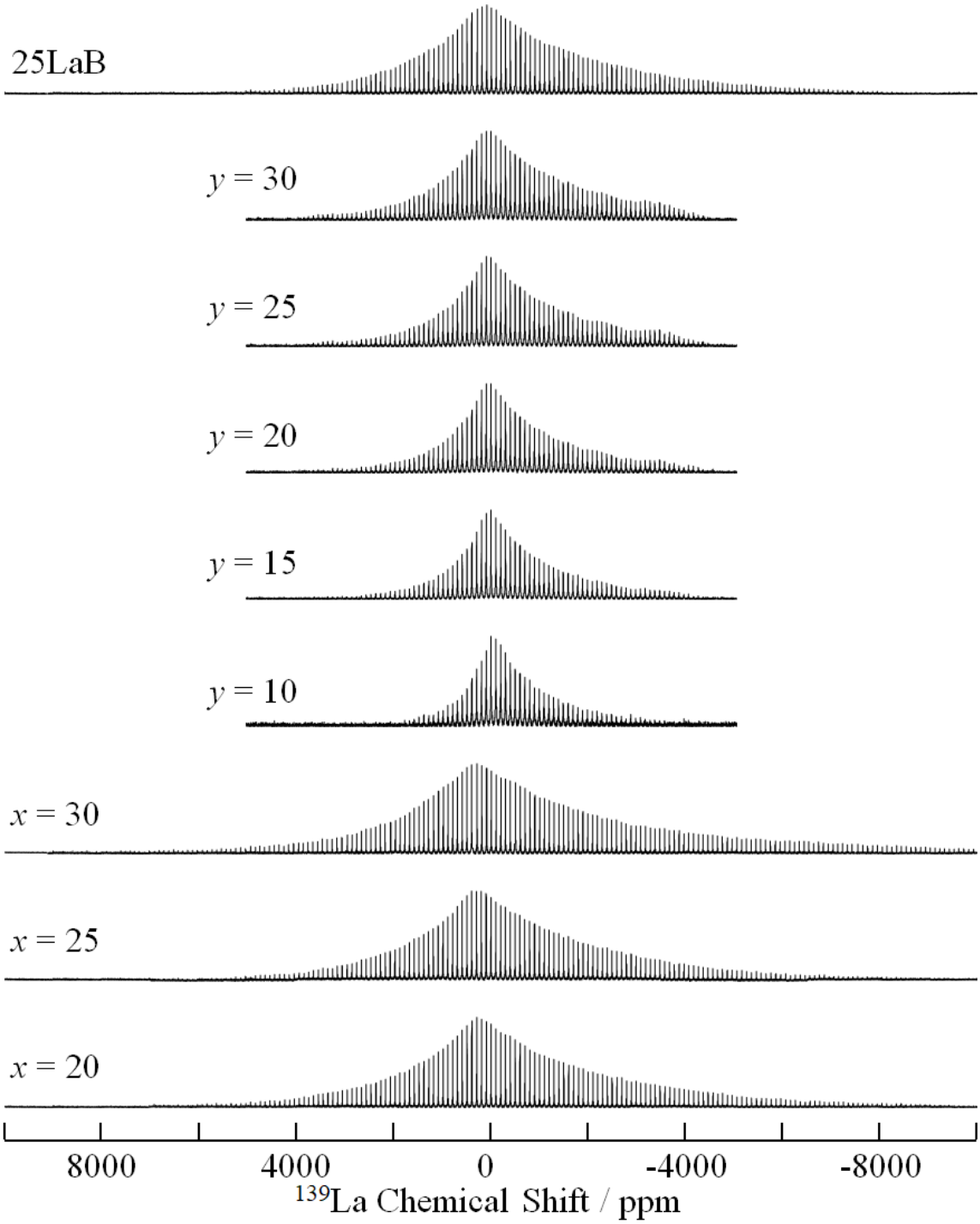

Figure 5.6: ^{139}La WCPMG NMR spectra of the glass series xLaBG and yLaP, and of 25LaB. The xLaBG spectra are presented on the bottom; the yLaP spectra are in the middle; and the 25LaB spectrum is on the top. The spectra are presented as WCPMG spikelet patterns with normalized intensities. The parameters used to fit these spectra are reported in Table 5.2.

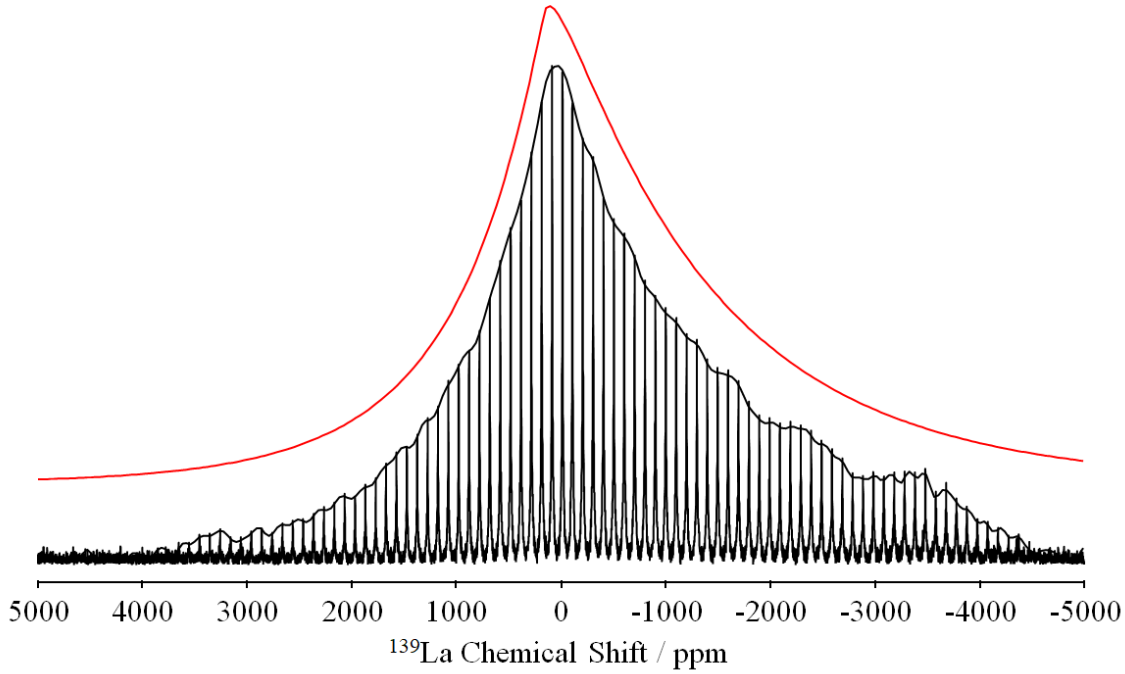

Figure 5.7: ^{139}La WCPMG NMR spectrum of the 25LaP glass. The parameters used for the fit are reported in Table 5.2. This fit is representative of the fits of all glass samples reported here.

which we cannot quantify at this time. An example of the fit produced by applying the Czjzek distribution to our ^{139}La NMR spectra is presented in Fig. 5.7, where we present the fit of the 25LaP sample.

The fitted ^{139}La NMR parameters of all glass samples are presented in Table 5.2.

The greatest σ value in the xLaBG samples occurs at the greatest La_2O_3 content. In the yLaP sample series, the σ values are notably smaller than in the xLaBG samples, and increase linearly with y. Both observations are in line with the compositional dependence of the spectral widths noted above.

5.6 Discussion

5.6.1 The Applicability of the Crystalline Model to Glasses

Based upon the data presented in Table 5.1, we calculate a linear relationship between ^{139}La chemical shift and La–O coordination number. This relationship is presented in Fig. 5.5. The linear fit has a slope of (-130 ± 40) ppm and an intercept of (1400 ± 400) ppm ($R^2 = 0.51$). This model does not effectively describe the behaviour

Table 5.2: ^{139}La Δ_{offset} and σ values for the glass samples. Values are provided at two field strengths for the xLaBG samples. Uncertainties are indicated by parentheses.

		Δ_{offset} / ppm		σ / MHz	
Sample	La_2O_3 Content / mol%	9.4 T	16.4 T	9.4 T	16.4 T
10LaP	10		3 ± 25		2.9 ± 0.2
15LaP	15		109 ± 25		3.1 ± 0.2
20LaP	20		132 ± 25		3.3 ± 0.2
25LaP	25		148 ± 25		3.4 ± 0.2
30LaP	30		178 ± 25		3.6 ± 0.2
20LaBG	20	968 ± 50	431 ± 25	4.3 ± 0.2	4.1 ± 0.2
25LaBG-1	25	942 ± 50	448 ± 25	4.4 ± 0.2	4.0 ± 0.2
30LaBG-1	30	1030 ± 50	473 ± 25	4.4 ± 0.2	4.4 ± 0.2
25LaB	25		308 ± 25		4.0 ± 0.2

of the lanthanum phosphate samples included in the dataset (*i.e.*, $LaPO_4$ and LaP_3O_9). The most likely cause for this discrepancy is a dependence of the ^{139}La chemical shift range on the second-nearest-neighbour of lanthanum.

Second-nearest-neighbour effects on chemical shifts are well-known in NMR spectroscopy of other elements, in both crystals and glasses. For example, Dupree *et al.* reported that the ^{43}Ca $\delta_{\text{iso}}^{\text{CS}}$ values of calcium silicates, carbonates, and oxides depend on the mean Ca–O bond length [224]. However, while all compounds were found to have the same dependence of $\delta_{\text{iso}}^{\text{CS}}$ on bond length, the shifts were offset depending on the nature of the second neighbour. Thus, the second neighbour type provided an additive constant to the shifts, while for a given neighbour type, the shifts changed with bond length in the same way.

We hypothesize that the same type of effect is operative in the ^{139}La shifts, namely, that all glasses show the same linear change in shift with first-neighbour oxygen coordination number, and that this linear change will be offset by different amounts, depending on the nature of the second neighbour. Hence any potential model relating ^{139}La $\delta_{\text{iso}}^{\text{CS}}$ to coordination number must account for composition effects. However, it is not clear how to obtain the true ^{139}La $\delta_{\text{iso}}^{\text{CS}}$ of the glass.

From our previous work, as well as a matter of general principles, we expect the ^{139}La $\delta_{\text{iso}}^{\text{CS}}$ of the glass to be related to the mean La–O coordination number of the glass [126, 225, 226]. In Table 5.2 we present the position parameters of the Czjzek model as implemented in DMFIT, which we label Δ_{offset}, as well as the σ values, of the

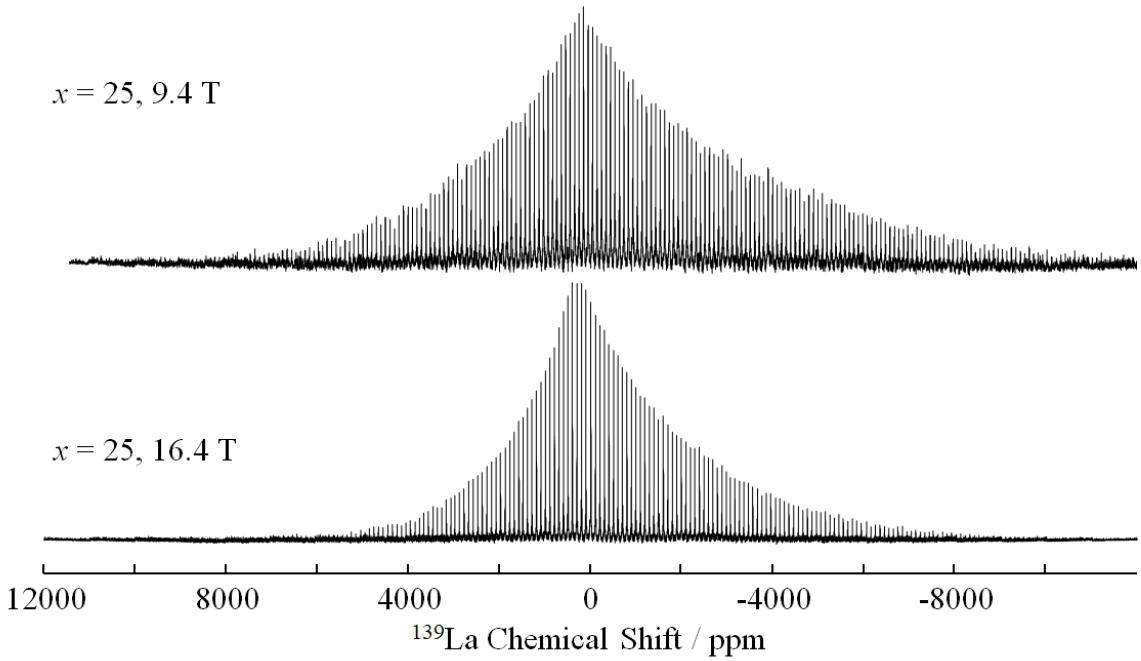

Figure 5.8: The ^{139}La WCPMG NMR spectra of the 25LaBG sample at two field strengths. Top, spectrum at 9.4 T. Bottom, spectrum at 16.4 T. Parameters used to fit these spectra are reported in Table 5.2. Note that while the maxima of the spectra occur at approximately the same chemical shift value, the Δ_{offset} values are quite different.

glasses. Using the Δ_{offset} values from our 16.4 T data with our fit from Fig. 5.5 yields reasonable predicted coordination numbers for the xLaBG samples, consistent with those estimated from neutron diffraction (Section 6.6.2) [212]. This is coincidence. When the Δ_{offset} values at 16.4 T for the yLaP sample series are passed through the fit presented in Fig. 5.5, the predicted coordination numbers range between 9 and 11. From diffraction data reported by Hoppe *et al.*, we would expect coordination numbers between 6.1 ± 0.3 and 8.2 ± 0.3 for the yLaP samples [10]. However, there is a more fundamental concern in applying Δ_{offset} to our crystalline model.

Spectra for the xLaBG samples were collected at multiple field strengths (9.4 T and 16.4 T). A comparison of the spectra of the $x = 25$ sample is presented in Fig. 5.8. Their Δ_{offset} values at the two field strengths do not agree. If Δ_{offset} was truly the isotropic chemical shift of this system (*i.e.*, $\delta_{\text{iso}}^{\text{CS}}$), its value should be independent of field strength. As the value of Δ_{offset} is not independent of field strength, it cannot be $\delta_{\text{iso}}^{\text{CS}}$, and hence cannot be meaningfully compared to the $\delta_{\text{iso}}^{\text{CS}}$ values of the crystalline

samples, or the model described in Fig. 5.5. There are many possible interactions which could account for the discrepancy between the Δ_{offset} values at different field strengths, and there are insufficient data to allow for the determination of which interactions are responsible.

While the fit procedure outlined above yields interesting structural information about the relative disorder around the La sites, the fact that the fit parameter Δ_{offset} does not appear to be a faithful representation of $\delta_{\text{iso}}^{\text{CS}}$ means that we cannot extract coordination numbers by this method. We can speculate that Δ_{offset} contains not only the isotropic chemical shift, but also effects due to disorder broadened chemical shift anisotropy, higher-order quadrupole effects, and so forth. More detailed data will be required to test these suggestions.

5.6.2 Quadrupolar Interactions

While crystalline La-oxide compounds typically show La sites with significant electric field gradient interactions, the glass ^{139}La NMR spectra are all well-fit by the Czjzek distribution. Recall that the Czjzek distribution results in a single parameter fit, assuming only that the electric field gradient tensor component values are normally distributed with mean zero and standard deviation σ [135, 139]. This distribution thus implies that the *average* quadrupole interaction for ^{139}La in the glasses is zero. However, as has been discussed elsewhere, it can be shown that this distribution also yields standard deviations in quantities like the quadrupole product P_{Q} and the quadrupolar frequency ν_{Q}, as well as the most probable values of P_{Q} and ν_{Q} , that are non-zero [139]. There is no inconsistency here, as the EFG interaction is a signed quantity: in a disordered solid, for sites with many local interactions, it is reasonable that the average over all sites will yield both positive and negative interactions, leading to a zero mean but non-zero variance and standard deviation, just as the Czjzek model predicts. We also note that the standard deviations of P_{Q} and ν_{Q} , as well as their most probable values, are all proportional to the single fit parameter σ, with constants of proportionality of order 1 [139]. Therefore, to avoid the confusion of using symbols familiar from the crystalline context to describe the glasses, we will discuss the quadrupole interactions for ^{139}La in glasses only in terms of the standard deviation of the EFG tensor elements σ. The meaning of this quantity is clear: an

increase in σ implies an increase in the disorder in the neighbourhood of the nucleus probed.

In the LaP glass series, the increase in σ with added La_2O_3 (Table 5.2) indicates an increase in disorder around the La sites. As the first coordination sphere is certainly oxygen, the origin of this disorder is likely due to the second neighbour distribution. As La^{3+} acts as a modifier, we would expect that the increasing La_2O_3 content would be accompanied by a depolymerization of the phosphate network, and in fact the production of a variety of phosphate Q^n species. Thus we interpret the increase in σ as signalling an increase in the diversity of Q^n species with added La_2O_3. This result is in agreement with the Raman spectra obtained by Brow and co-workers [227]. They concluded that as La_2O_3 content increases, the cross-linked Q^3 PO_4 tetrahedra are replaced by chain-like Q^2 tetrahedra. Furthermore, they observe the simultaneous existence of Q^1, Q^2, and Q^3 species, increasing the degree of structural disorder surrounding the La^{3+} ion.

An additional potential contributor to disorder in the second coordination sphere of La^{3+} is the presence of multiple chemical species. In binary lanthanum phosphates, both Brow *et al.* and Hoppe *et al.* conclude that at moderate La_2O_3 concentrations, La^{3+} will begin to cluster — *i.e.*, there will be La–O–La neighbours [10, 61, 227]. We would expect that the presence of multiple second nearest neighbour species would lead to greater variance in the EFG distribution. Likewise, the larger values of σ observed in the LaBG glasses probably arises from the fact that both borate and germanate species appear in the second neighbour shell, which would give stronger disorder interactions than just the phosphate groups alone. This finding is in agreement with our previous work based on ^{11}B NMR spectroscopy and neutron diffraction [212].

5.7 Conclusions

We present ^{139}La WCPMG NMR data of a range of lanthanum oxide-based crystalline materials and glasses. The ^{139}La NMR spectra of $La_2Sn_2O_7$, LaP_3O_9, and LaB_3O_6, and their associated fits, are reported. The ^{139}La WCPMG NMR spectra of lanthanum oxide-based glasses are presented for the first time. The glass spectra can be well-fit using the Czjzek model, which accounts for the distribution of quadrupole parameters in disordered solids.

We find that the breadth parameter of the Czjzek model, σ, increases with increasing La_2O_3 content in the glasses. This is correlated with an increase in disorder surrounding the La^{3+} environment. In the lanthanum phosphate glasses, the change in the disorder is attributed to changes in the Q^n species of the phosphate units. In the lanthanum borogermanate glasses, the change in the disorder is attributed to both changes in the local order of the borate and germanate units, as well as potential changes in the proportion of neighbouring borate and germanate units.

The position parameter of the Czjzek fit, Δ_{offset}, is found to be different from the isotropic chemical shift, $\delta_{\text{iso}}^{\text{CS}}$. As such, it is not clear how to extract $\delta_{\text{iso}}^{\text{CS}}$ values for the glass samples, and thus the correlations found from crystal models are not applicable at this point.

Our results show that ^{139}La WCPMG NMR spectroscopy has a complimentary role in the study of lanthanum oxide-based glasses. However, rather than obtaining coordination numbers, ^{139}La WCPMG NMR spectroscopy is better suited to assessing changes in disorder around the La^{3+} environment.

5.8 Acknowledgements

Financial support from NSERC (Canada Grant Number RGPIN 261987) is gratefully acknowledged. Dr. Mark Obrovac is thanked for access to an X-ray diffractometer. Ms. Jocelyn Sinclair is thanked for synthesizing the $La_2Sn_2O_7$ sample.

Chapter 6

Structural Differences between the Glass and Crystal Forms of the Transparent Ferroelectric Nanocomposite $LaBGeO_5$, from Neutron Diffraction and NMR Spectroscopy

6.1 Context

The previous two chapters (Chapters 4 and 5) were concerned with determining the mean La−O coordination number in the $LaBGeO_5$ glass via ^{139}La NMR spectroscopy. It is also possible to determine mean coordination numbers for glass modifiers in glasses via neutron diffraction, and Chapter 5 referred to estimates based on the data contained within this chapter. Furthermore, for some nuclei, NMR is not feasible while neutron diffraction is; germanium is such a case. The primary goal of the work contained within this chapter was to assess the possibility of the presence of high-coordinate germanium species (*i.e.*, GeO_5 and/or GeO_6) within the $LaBGeO_5$ glass. Neutron diffraction has been used extensively in the literature to establish the presence of high-coordinate germanium species in alkali germanate, alkaline earth germanate, and germanophosphate glasses, making it a suitable technique for testing the $LaBGeO_5$ glass system [12, 28, 42].

An additional goal of this work was to identify the BO_3 species present in the $LaBGeO_5$ glass. While the presence of some kind of BO_3 in the $LaBGeO_5$ glass is known from the literature, the precise nature of the BO_3 species are present had not been determined [34]. High-resolution ^{11}B MAS and MQMAS NMR spectroscopy was applied to a lanthanum borogermanate glass series to examine the change in the BO_3 environment as the amount of lanthanum oxide was varied.

This chapter was originally published as Paterson, A.L., Hannon, A.C., Werner-Zwanziger, U., and Zwanziger, J.W., Structural Differences between the Glass and

Crystal Forms of the Transparent Ferroelectric Nanocomposite $LaBGeO_5$, from Neutron Diffraction and NMR Spectroscopy, *J. Phys. Chem. C* 122 (36) (2018) 20963–20980 [212]. Copyright 2018 American Chemical Society. The content below has been reproduced from the preprint version of the article, with minor modifications for style and clarity. Copyright permissions for this use are contained in Appendix E. The contributions of the authors to the text are as follows. ALP synthesized all samples, collected all experimental data, performed the analyses, and wrote the majority of the manuscript. ACH provided substantial technical support in the collection of the neutron diffraction data, reviewed the neutron diffraction analysis performed by ALP, and provided additional analysis relating to the La–O coordination number (Section 6.6.2). ACH also contributed to the editorial review of the manuscript. UWZ assisted in the collection and interpretation of the NMR results, as well as contributing to the electrostatic bond strength (EBS) analysis (Section 6.6.4). JWZ assisted in the collection of the neutron diffraction data, and provided significant editorial contributions to the manuscript.

6.2 Abstract

A combination of pulsed neutron diffraction and high-field ^{11}B NMR spectroscopy was used to obtain structural information on the $x La_2O_3 \cdot (1\text{-}x)(0.33\,B_2O_3 - 0.67\,GeO_2)$ ($x = 0.00, 0.20, 0.25, 0.30$) glass system, as well as a crystallized sample of composition $LaBGeO_5$. $LaBGeO_5$ is of interest as a ferroelectric nanocomposite, as it crystallizes isochemically from the glass. The crystal structure is comprised of 4-coordinated boron and germanium, together with 9-coordinated lanthanum. Our results support a model for the glass structure that is substantially different: both NMR and neutron diffraction show that the glasses contain large fractions of 3-coordinated boron as well as 4-coordinated boron, and the neutron diffraction results show clear evidence for a significant fraction of germanium with a coordination number greater than four. Moreover, the La coordination number in the glasses is estimated as 7.4, with a typical La–O bond length of 2.52 Å, based on detailed modelling of the neutron correlation function. The composition-dependence of the boron and germanium coordination numbers provides evidence that both boron and germanium undergo non-monotonic changes in coordination similar to those observed in the "borate anomaly"

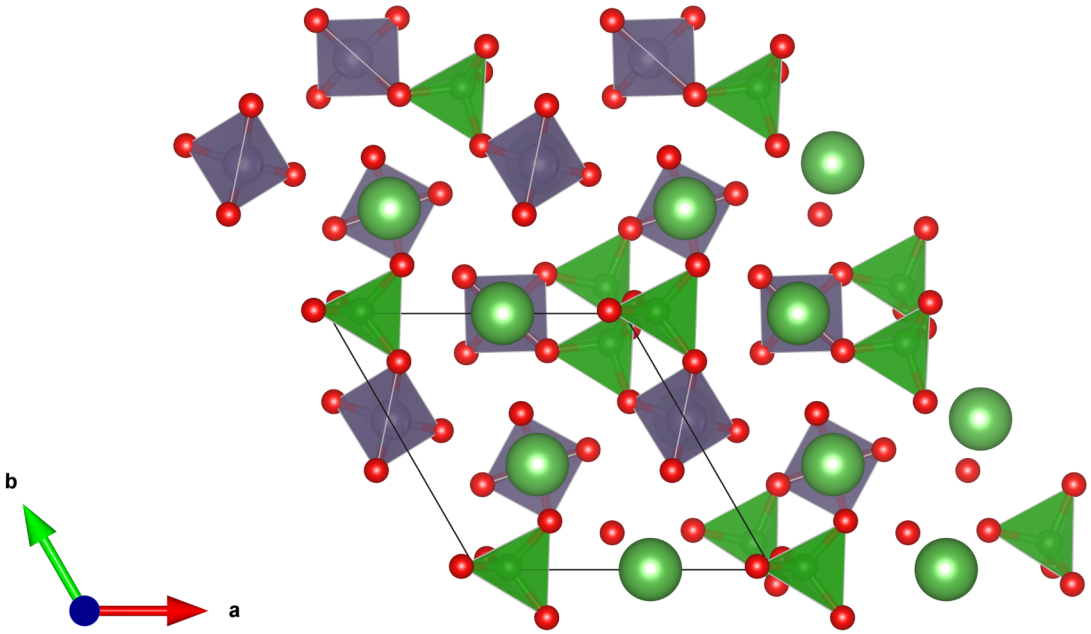

Figure 6.1: The room-temperature crystal structure of $LaBGeO_5$ [78]. The presented view is down the crystallographic c axis. $[B\emptyset_4]^-$ tetrahedra are coloured dark green, while $Ge\emptyset_2O_2^{2-}$ tetrahedra are purple. LaO_9 polyhedra are omitted for clarity. Lanthanum ions are light green.

and "germanate anomaly".

6.3 Introduction

TFN materials are optically interesting materials combining the excellent nonlinear optical properties of ferroelectric crystals with the ease of formability of glasses. These glass-ceramic composites have been the subject of much study over the last two decades, with a variety of compositions having been examined [1, 228–231]. One particularly interesting material is the synthetic stillwellite $LaBGeO_5$ (LBG). The LBG system is a valuable subject for the study of TFN materials, as the glass and crystal phases share the same stoichiometry. As such, the LBG system has been well-characterized, including its crystal structure [78, 79] (Fig. 6.1), second harmonic generation [232, 233], glass transition temperature [100], and Curie temperature [79, 234].

When LBG is crystallized via laser irradiation, the crystals can be made to grow in a highly directed fashion [105]. Understanding this technologically attractive

crystallization behaviour requires a knowledge of the glass structure. However, there is not a comprehensive model of the structure of the LBG glass phase. Previous structural models [74] assumed that the basic structural units present in the glass would be the same as those in the LBG crystal structure, *i.e.*, GeO_4 and $[B\emptyset_4]^-$ tetrahedra and LaO_9 polyhedra. Through the use of ^{11}B MAS NMR, Gupta *et al.* established a change in the boron–oxygen coordination environment, with roughly equal proportions of BO_3 and $[B\emptyset_4]^-$ in the glass phase [34], where BO_3 indicates a non-specific three-coordinate boron species (Fig. 6.2). Ø indicates a bridging oxygen, *i.e.*, in this case an oxygen bonded to at least two B and/or Ge atoms. The most recent direct structural investigation of the LBG glass phase concluded that while the boron-oxygen coordination environment underwent a change between the glass and crystalline phases, the germanium-oxygen coordination environment in the glass was not substantially different from that of the crystal [75]. However, there is no fundamental reason to assume that the Ge–O and La–O environments are unchanged between the LBG glass and crystal phases. Most of the structural data on the LBG glass comes from Raman and ^{11}B NMR spectroscopies. The lanthanum environment is difficult to probe using Raman spectroscopy, due to very low resonant frequencies, while the interpretation of Raman data with regards to the germanium environment is an active point of discussion in the literature [19, 26]. While we have had some success with the application of ^{139}La NMR spectroscopy to glassy systems, ^{73}Ge NMR is not currently a useful tool in investigating the structure of germanate glasses [25]. In order to probe directly the nature of the germanium-oxygen coordination in LBG glass, we made use of neutron diffraction. Neutron diffraction has been successfully used in the literature to probe the structure of binary germanates [27, 28, 64], borates [235, 236], and lanthanoid glasses [67, 237]. As a direct probe of the length scale of bonding interactions, neutron diffraction serves as an effective means of studying the coordination environment of many glass formers. We combine the use of high-field ^{11}B NMR spectroscopy and neutron diffraction to investigate the structural changes in lanthanum borogermanate glasses as a function of lanthanum content with the goal of producing a comprehensive structural model of the $LaBGeO_5$ glass composition.

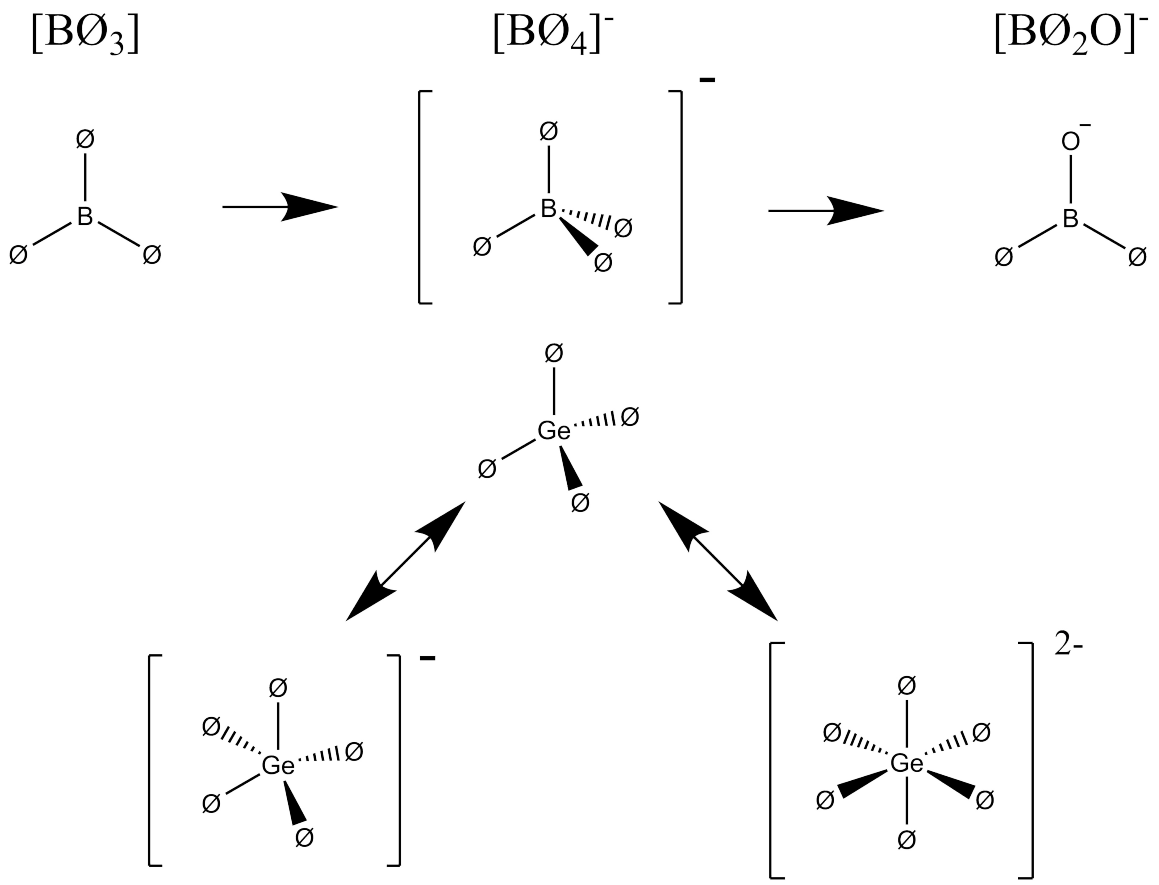

Figure 6.2: Possible structural units under consideration in the $La_2O_3-B_2O_3-GeO_2$ glass composition. Top: the conversion of $B\emptyset_3$ to $[B\emptyset_4]^-$ to $B\emptyset_2O^-$ with the addition of modifier oxide. Bottom: possible configurations of GeO_4, $[GeO_5]^-$, and $[GeO_6]^{2-}$.

6.4 Experimental Procedures

6.4.1 Sample Synthesis

Glass formation has previously been reported for compositions between 20 mol% to 28 mol% La_2O_3 [238], and glasses of composition $x La_2O_3 \cdot (1\text{-}x)(0.33\, B_2O_3 \cdot 0.67\, GeO_2)$ ($x = 0.00, 0.20, 0.25, 0.30$) were prepared using a conventional melt-quench approach (Section 3.1). Powders of La_2O_3 (99.99 %), GeO_2 ($\geq$ 99.99 %), and isotopically-enriched $^{11}B_2O_3$ (99.62 atom % ^{11}B) were obtained from Sigma-Aldrich and used without further purification. ^{11}B enrichment is required to mitigate the effects of the high neutron absorption cross section of ^{10}B. Weighed powders were thoroughly ground in a porcelain mortar and pestle in air before melting. Some excess of B_2O_3 was added to account for known issues with borate volatility [98, 239]. The amount of excess B_2O_3 was varied based on preliminary elemental analysis results. The 25LaBG-X sample used 100.36 % of the nominal B_2O_3 mass. The 0LaBG, 20LaBG, 25LaBG-1, and 30LaBG-1 samples used 116 % of the nominal B_2O_3 mass. The 25LaBG-2 and 30LaBG-2 samples used 133 % of the nominal B_2O_3 mass. The mixed powders were melted in covered platinum crucibles in a box furnace in air at 1300 °C for 30 min. Glasses were quenched by dipping the bottom of the crucible into room-temperature water. Significant mass loss during melting was observed; potential causes are discussed below. Mass loss was determined by comparing the masses of the reagents and crucible prior to melting with the mass of the resulting glass and crucible after quenching. The crystalline sample of $LaBGeO_5$, 25LaBG-X, was produced by devitrification of a quenched glass. The composition of the crystal $LaBGeO_5$ is equivalent to the $x = 0.25$ glass. The sample was heated at 950 °C for 4 h. The crystalline phases within the sample were probed using pXRD (Fig. C.3). X-ray diffraction measurements were made using a Rigaku Ultima IV X-ray diffractometer with a Cu anode X-ray tube and a diffracted beam monochromator.

6.4.2 Sample Characterization

The elemental compositions of the samples were determined by LA-ICP-MS. The laser used a spot size of 30 µm, with a repetition rate of 7 Hz and an energy density of 3 J cm^{-2}. 5 spots were analysed per sample to test for homogeneity. The observed

analytes were ^{11}B, ^{72}Ge, and ^{139}La, with corrections made for the isotopic enrichment of ^{11}B. The O content was determined by difference, assuming that all elements were in their standard oxidation states. The National Bureau of Standards standard reference material 610 (National Institute of Standards and Technology 610) glass was used as an external standard.

The density of the samples was determined by use of a Micromeritics AccuPyc II 1340 helium gas pycnometer with a 1 cm^3 sample chamber. The glass transition temperatures (T_g) were determined using a Netzsch DSC 404F1 differential scanning calorimeter. Samples were heated from room temperature to 800 °C in a platinum pan at a rate of 10 °C min^{-1}. The T_g value was taken as the point of inflection of the T_g event on the DSC curve.

6.4.3 ^{10}B and ^{11}B NMR

^{11}B MAS and MQMAS NMR spectra were collected on a 16.4 T (224.63 MHz ^{11}B frequency) Bruker Avance NMR spectrometer. MAS spectra were collected at a spinning speed of (25 000 ± 5) Hz using a 2.5 mm outer diameter ZrO_2 rotor. Single pulses of 0.54 µs duration (15° tip angle, ν_{rf} = 77 kHz) and a recycle delay of 5 s were used to ensure quantitative excitation. Recycle delays were high enough to ensure that both three- and four-coordinate sites were fully relaxed. 256 scans were collected for each sample. To compensate for the substantial ^{11}B background, the spectrum of an empty rotor collected under the same conditions was subtracted from the spectrum of each sample, after careful phasing and intensity adjustment. ^{11}B MQMAS spectra were collected at spinning rates of (25 000 ± 5) Hz using a three-pulse sequence with full echo acquisition [240]. Spectra were collected in split-t_1 mode with a 2.37 ms delay between the conversion and selective pulse. Each spectrum was acquired with 166 t_1 increments with 96 transients per increment. All ^{11}B and ^{10}B chemical shifts were referenced to solid $NaBH_4$, with a resonance at −42.1 ppm relative to the primary shift reference ($BF_3 \cdot Et_2O$, 0 ppm) [159]. The MQMAS spectra were referenced using the C_z convention [241]. The DMFIT 20150521 [184] software package was used to analyse the ^{11}B NMR data. REDOR spectra were collected at a spinning speed of (10 000 ± 5) Hz in a 3.2 mm ZrO_2 rotor using a HXY probehead. The conventional REDOR pulse sequence was used [140]. A sample of LBG glass with natural abundance boron was

used to allow for ^{11}B{^{10}B} interactions to be probed. The ^{10}B Larmor frequency at 16.4 T was 75.24 MHz. ^{11}B $\pi/2$ and π pulses were set to 3.10 µs and 6.25 µs, optimized to allow for near-maximum signal from both BO_3 and $[B\emptyset_4]^-$ sites. ^{11}B pulses were optimized via Hahn-echo experiments. ^{10}B π pulses were optimized via maximizing the difference observed when the ^{10}B channel was activated. REDOR pulse powers were 80 kHz for ^{11}B and 40 kHz for ^{10}B. Recycle delays for the REDOR experiments were set to 50 s, optimized to prevent relaxation effects from being mistaken for the REDOR dephasing.

6.4.4 Neutron Diffraction

Time-of-flight neutron diffraction data were collected at the ISIS pulsed neutron source at the Rutherford Appleton Laboratory using the GEM diffractometer [166]. Samples were loaded into thin-walled (25 µm) vanadium foil cans of 8.3 mm internal diameter, with careful consideration to minimize the exposure of the samples to atmospheric water during transport and loading. The samples were in the form of irregular fragments of maximum dimension ranging from 2 mm to 8 mm. Data were normalized by comparison to those from a vanadium-niobium rod and corrected for background signals. The distinct scattering, $i(Q)$, for each sample was combined and processed using the GudrunN [242] and ATLAS [243] program suites. As the very low momentum transfer region ($Q < 0.7$ Å^{-1}) was not directly observed, the distinct scattering for each sample was extrapolated to 0 Å^{-1} by fitting a symmetric function of the form $A+BQ^2$ to the region below 0.9 Å^{-1}. The distinct scattering was then Fourier transformed using a modification function, $M(Q)$; either a Lorch function [63] (to minimize the effects of termination ripples) or a step function (to maximize real-space resolution) was used. All samples were transformed with a maximum momentum transfer $Q_{\max} = 50$ Å^{-1}. The result of the Fourier transform of the distinct scattering is the differential neutron correlation function:

$$D(r) = \frac{2}{\pi}\int_0^\infty Qi(Q)M(Q)\sin(rQ)\,\mathrm{d}Q. \tag{6.1}$$

With the addition of an "average density" term, $T^0(r)$, we obtain the total correlation function $T(r)$:

$$T(r) = T^0(r) + D(r). \tag{6.2}$$

The average density term is a function of the atomic number density of the sample, g^0, and the average coherent neutron scattering length of the sample, $\left\langle \bar{b} \right\rangle_{av}$:

$$T^0(r) = 4\pi r g^0 \left\langle \bar{b} \right\rangle_{av}^2. \tag{6.3}$$

For all $T(r)$ reported in this paper, we followed the renormalization procedure described by Alderman *et al.* [27]. Renormalization constants were on the order of 5 %. Peaks were fitted with resolution-broadened Gaussian functions. Average coordination numbers were calculated using

$$n_{ij} = \frac{r_{ij} A_{ij}}{(2 - \delta_{ij}) c_i \bar{b}_i \bar{b}_j}, \tag{6.4}$$

where n_{ij} is the average coordination number of the element pair i–j, r_{ij} and A_{ij} are the peak position and peak area, respectively, of the resolution-broadened Gaussian function fitting the relevant peak, c_i is the atomic fraction of element i, and δ_{ij} is the Kronecker delta. $T(r)$ correlation functions were fit using the PFIT program [244].

6.5 Results

6.5.1 Sample Characterization

To account for possible variations in composition, and the potentially different interactions between La_2O_3, B_2O_3, and GeO_2, most values are compared to changes in the molar ratio $R = [La_2O_3]/([B_2O_3] + [GeO_2])$. The ratio R is chosen in analogy with alkali borate glasses, where $R = [A_2O]/[B_2O_3]$ [245]. This is intended to capture deviations in the $[GeO_2]/[B_2O_3]$ ratio, which is nominally at a constant ratio of 2:1. The densities, molar volumes, and glass transition temperatures, are presented in Table 6.1. Glass transition temperatures were determined from DSC curves presented in Appendix C (Figs. C.10 to C.15). The densities of the glasses increase with R. The measured density of the 0LaBG sample is consistent with data contained within the

INTERGLAD database [246], which would predict a density of $(2.98 \pm 0.07)\,\mathrm{g\,cm^{-3}}$.

Table 6.1: Density, molar volume, and glass transition temperatures of borogermanate samples.

Sample	Density / $\mathrm{g\,cm^{-3}}$	Molar volume / $\mathrm{cm^3\,mol^{-1}}$	T_g / °C
0LaBG	2.95 ± 0.01	32 ± 1	406 ± 2
20LaBG	4.72 ± 0.01	29.5 ± 0.4	679 ± 2
25LaBG-1	4.96 ± 0.01	30.4 ± 0.4	683 ± 2
25LaBG-2	4.81 ± 0.01	30.7 ± 0.4	679 ± 2
30LaBG-1	5.10 ± 0.01	31.8 ± 0.4	689 ± 2
30LaBG-2	4.88 ± 0.01	32.8 ± 0.4	682 ± 2
25LaBG-X	5.16 ± 0.02	29.8 ± 0.5	

The compositions presented in Table 6.2 were determined by LA-ICP-MS, a technique chosen to avoid the difficulty found in X-ray-based measurements in determining light atom composition.

The reported compositions deviate somewhat from the nominal compositions, typically on the order of 1 mol% to 2 mol% of the component oxides. However, it is difficult to reconcile these compositions with the observed mass loss during melting (approx. 3 % of total sample mass). The combined mass of the starting reagents and crucible was compared to the mass of the resulting glass.

The La_2O_3 and GeO_2 starting reagents were both heated to high temperatures to assess whether the mass loss was caused by hydration or adsorbed water, but no appreciable mass loss was observed. The mass loss was thus attributed to the B_2O_3 starting reagent. The amount of mass lost (approx. 3 % of total sample mass, on the order of 0.5 g) suggests that the B_2O_3 had become partially hydrated and converted to H_3BO_3, a well-known reaction. The presence of H_3BO_3 would both explain the apparent deficiency of B_2O_3 in the final glass (due to less borate being provided in the batched reagents) and the significant mass loss observed upon melting (in the form of H_2O released upon melting of H_3BO_3). The compositions estimated from the mass loss are, on average, within 1 mol% to 2 mol% of the compositions from LA-ICP-MS, and are also reported in Table 6.2. The compositions as estimated from mass loss were used for analysis of the neutron diffraction data. The uncertainty surrounding the composition of the glass samples leads to uncertainty in the coordination numbers

Table 6.2: Nominal and experimental borogermanate sample compositions. Experimental values determined from use of LA-ICP-MS and from mass loss calculations are reported.

	Nominal Composition / mol%			Composition from LA-ICP-MS / mol%			Composition from Mass Loss / mol%			
Sample	La_2O_3	B_2O_3	GeO_2	La_2O_3	B_2O_3	GeO_2	La_2O_3	B_2O_3	GeO_2	R
0LaBG	0.0	33.0	67.0	0	30.3 ± 1.5	69.7 ± 1.5	0	33 ± 1	67 ± 1	0
20LaBG	20.0	26.4	53.6	21.0 ± 0.3	25.2 ± 0.2	53.7 ± 0.2	19.9 ± 0.6	26.8 ± 0.8	53.3 ± 0.8	0.25 ± 0.01
25LaBG-1	25.0	25.0	50.0	25.9 ± 0.2	24.5 ± 0.1	49.6 ± 0.3	24.9 ± 0.7	25.1 ± 0.8	49.9 ± 0.7	0.33 ± 0.02
25LaBG-2	25.0	25.0	50.0	25.2 ± 0.2	26.9 ± 0.3	47.9 ± 0.4	23.9 ± 0.7	28.1 ± 0.8	48.0 ± 0.7	0.31 ± 0.02
30LaBG-1	30.0	23.1	46.9	30.8 ± 0.4	23.1 ± 0.4	46.1 ± 0.8	29.9 ± 0.9	23.5 ± 0.7	46.6 ± 0.7	0.43 ± 0.02
30LaBG-2	30.0	23.1	46.9	30.4 ± 0.5	24.6 ± 0.9	45.1 ± 0.4	29.1 ± 0.9	25.5 ± 0.8	45.4 ± 0.7	0.41 ± 0.02
25LaBG-X	25.0	25.0	50.0	26.3 ± 0.5	22.6 ± 0.4	51.0 ± 0.1	25.8 ± 0.8	22.4 ± 0.7	51.8 ± 0.8	0.35 ± 0.02

derived from neutron diffraction from use of Eq. (6.4) [27].

The pXRD of the 25LaBG-X sample shows mainly the diffraction peaks of crystalline $LaBGeO_5$ with a small amount of an impurity phase tentatively identified as $La_2Ge_2O_7$. As the 25LaBG-X sample is primarily used to establish the behaviour of GeO_4, this impurity does not pose a significant problem: all Ge in $La_2Ge_2O_7$ is in the form of GeO_4. This potentially could cause estimates of the La–O coordination number to be lower than the crystal structure would imply. The presence of $La_2Ge_2O_7$ is consistent with a deficit of B_2O_3 in the sample.

6.5.2 ^{10}B and ^{11}B NMR Results

Selected ^{11}B MAS NMR spectra are shown in Fig. 6.3, with vertical offsets for clarity. The ^{11}B MQMAS spectra of the glass samples are shown in Fig. 6.4. The projections of the MAS and isotropic axes are present on the top and left of the spectra, respectively. The relevant spectral parameters are summarized in Table 6.3. The BO_3 peak is centred between approx. 12 ppm to 16 ppm, while the $[B\emptyset_4]^-$ peak is centred at approx. 1 ppm. The BO_3 peak shows a noticeable shift to higher chemical shifts with lanthanum content. There is not a similar trend with the $[B\emptyset_4]^-$ peak; however, the chemical shift of the $[B\emptyset_4]^-$ peak in each glass sample is significantly more positive than that of crystalline $LaBGeO_5$. There is no evidence of the presence of multiple BO_3 peaks in any of the MQMAS spectra (Fig. 6.5). As the P_Q of the $[B\emptyset_4]^-$ environment is very small (as is common in borate glasses), it is difficult to precisely quantify it via MQMAS. The P_Q of the $[B\emptyset_4]^-$ environment in all glass samples is less than 600 kHz.

Table 6.3: Selected ^{11}B MAS and MQMAS NMR parameters.

	BO_3			$[B\emptyset_4]^-$		
Sample	δ_{iso}^{CS*}/ ppm	$P_Q{}^{\dagger}$/ MHz	$\delta^{MQ\ddagger}$/ ppm	δ_{iso}^{CS} / ppm	$P_Q{}^{\dagger}$/ MHz	n_{BO}
0LaBG	15.5 ± 0.5	2.6 ± 0.1	66 ± 1	2.1 ± 0.2	N.A.	3.01 ± 0.03
20LaBG	17.6 ± 0.5	2.6 ± 0.1	74 ± 1	2.1 ± 0.2	0.5 ± 0.5	3.46 ± 0.03
25LaBG-1	18.1 ± 0.5	2.6 ± 0.1	76 ± 1	2.0 ± 0.2	0.6 ± 0.6	3.37 ± 0.03
25LaBG-2	17.8 ± 0.5	2.6 ± 0.1	76 ± 1	1.9 ± 0.2	0.4 ± 0.4	3.41 ± 0.03
30LaBG-1	18.6 ± 0.5	2.7 ± 0.1	78 ± 1	2.2 ± 0.2	0.5 ± 0.5	3.25 ± 0.03
30LaBG-2	18.2 ± 0.5	2.6 ± 0.1	76 ± 1	2.0 ± 0.2	0.5 ± 0.5	3.31 ± 0.03
25LaBG-X	18.8 ± 0.2			1.4 ± 0.2	0.4 ± 0.3	3.98 ± 0.04

* Isotropic chemical shift as determined by MQMAS

† Quadrupolar product $P_Q = C_Q\sqrt{1 + \frac{\eta_Q{}^2}{3}}$

‡ Location of the peak maximum in the isotropic dimension of the MQMAS experiment (using the C_z convention at 16.4 T) [134].

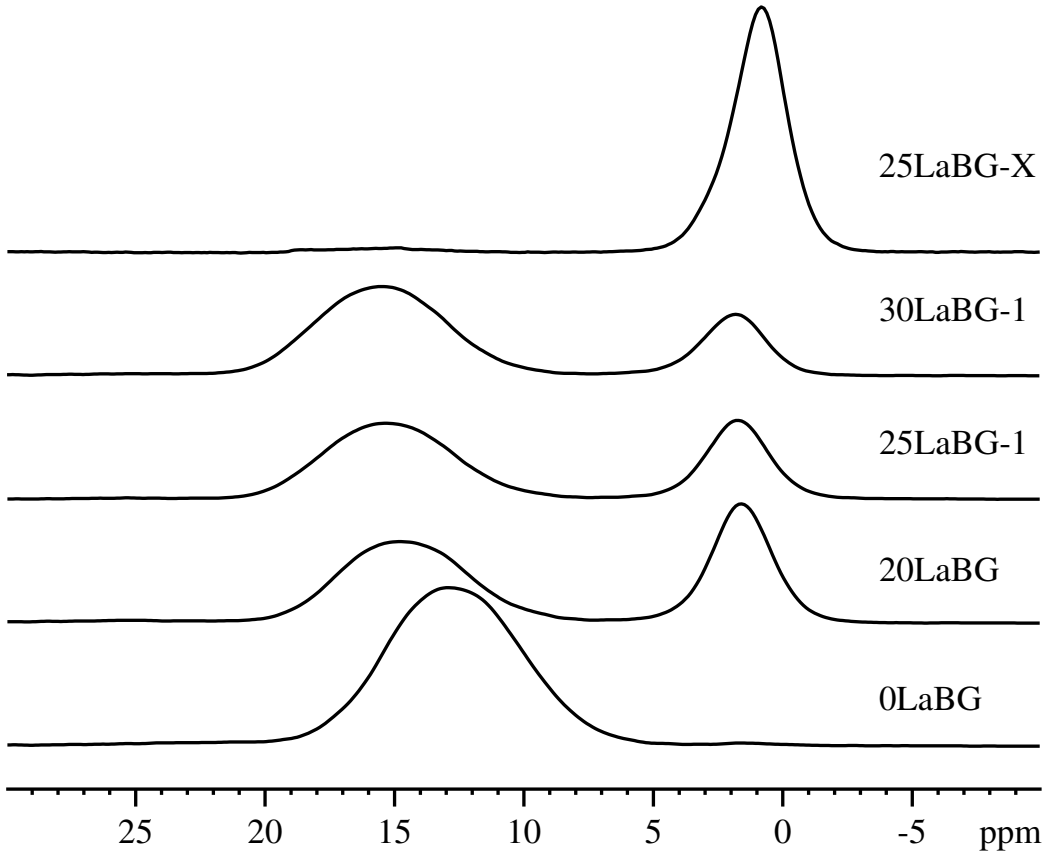

Figure 6.3: ^{11}B MAS NMR spectra of selected glass samples. Spectral limits are set to emphasize the central transition.

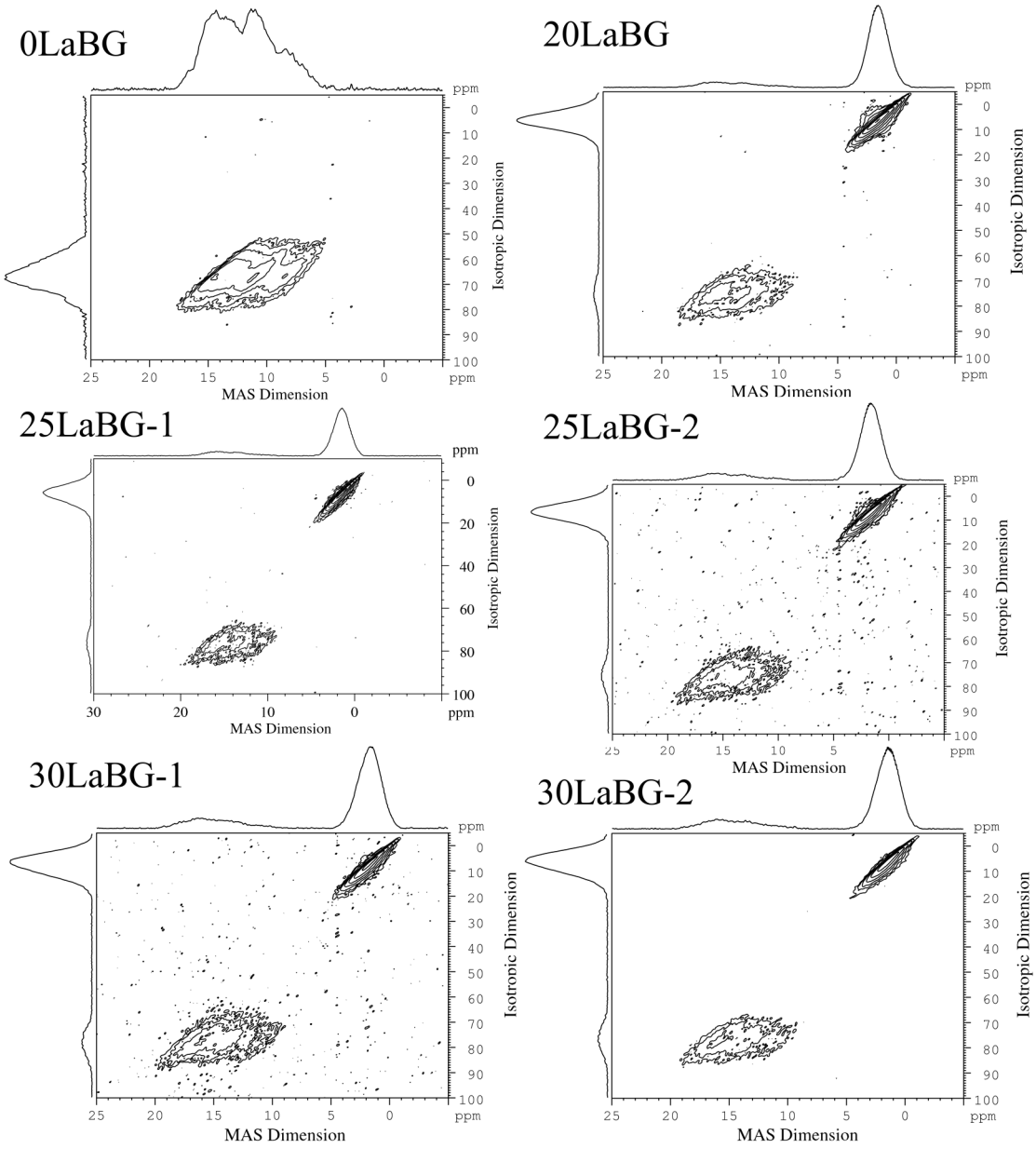

Figure 6.4: ^{11}B MQMAS spectra of the glass samples. The projections of the MAS (horizontal) and isotropic (vertical) axes are presented at the top and the left of the figure, respectively. The spectra are of, from top-left to bottom-right: 0LaBG; 20LaBG; 25LaBG-1; 25LaBG-2; 30LaBG-1; 30LaBG-2. The isotropic dimension of all spectra are referenced per the C_z convention [134].

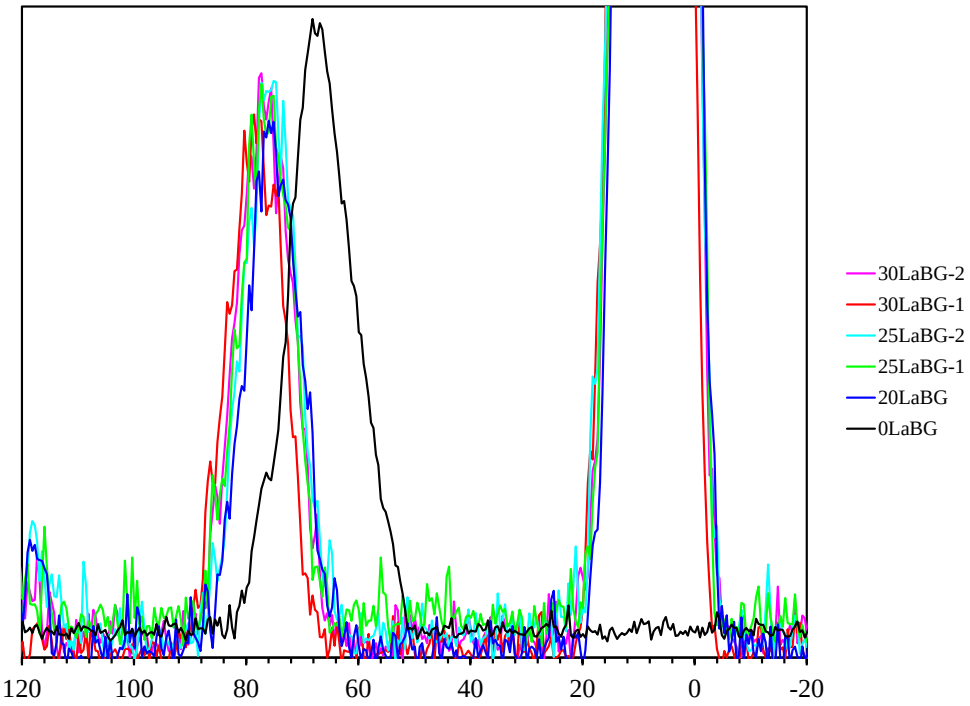

Figure 6.5: The isotropic projections of the ^{11}B MQMAS NMR spectra of the glass samples presented in Fig. 6.4. The projections are scaled to have approximately equal intensity of the BO_3 peak. The $[B\emptyset_4]^-$ peaks are truncated. Aside from the dramatic difference between the 0LaBG sample and the rest, there is little difference between the BO_3 peaks. The reader is directed to the online version for colour.

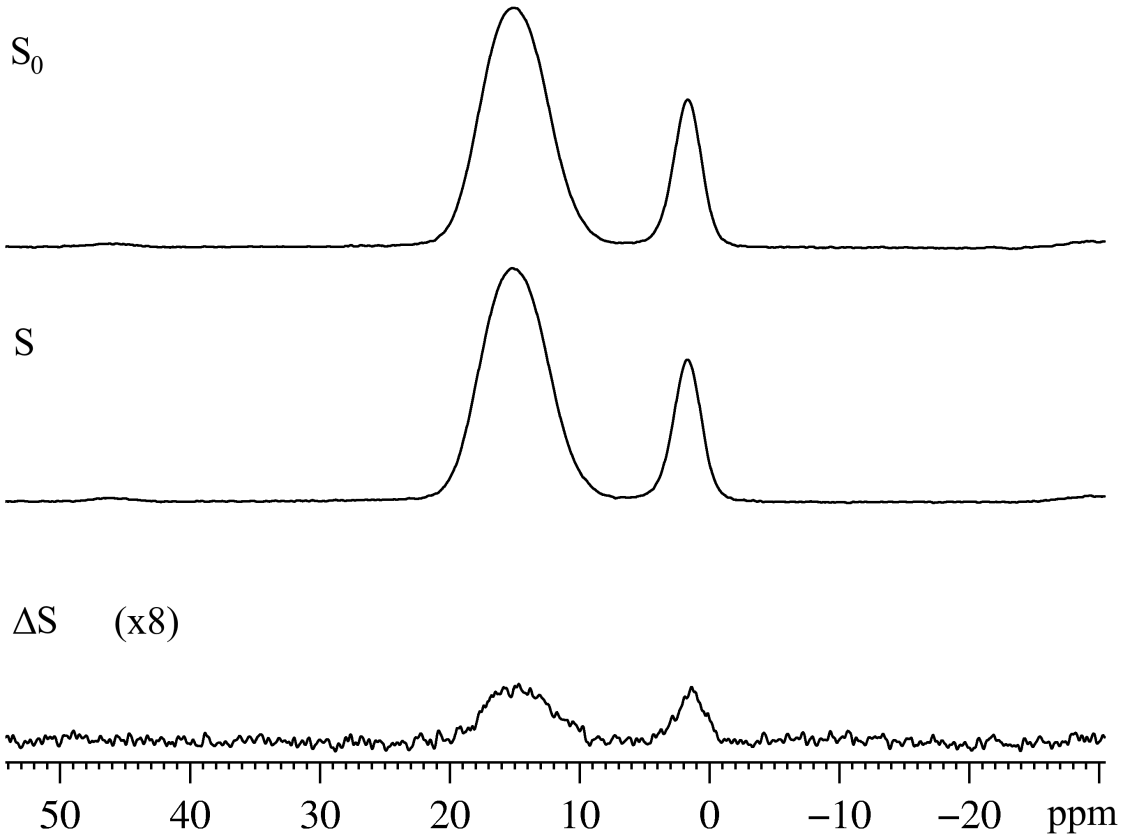

Figure 6.6: ^{11}B{^{10}B} REDOR NMR spectra of a natural-abundance $LaBGeO_5$ glass. The top spectrum (S_0) is the ^{11}B Hahn-echo spectrum. The middle spectrum (S) is the ^{11}B spectrum with ^{11}B{^{10}B} dipolar recoupling. The bottom spectrum (ΔS) is the difference between the two. The difference spectrum is increased in scale by a factor of 8 for clarity. This set of spectra corresponds to a $\Delta S/S_0$ value of approx. 0.03 and Hahn-echo delay of 49 ms, and is within the $\Delta S/S_0$ range where the REDOR behavior is expected to be independent of geometry [144].

A set of ^{11}B{^{10}B} REDOR spectra are presented in Fig. 6.6. ^{10}B and ^{11}B are chemically identical, but spectroscopically distinct. ^{11}B{^{10}B} REDOR spectra of sodium and lithium borate glasses have been previously reported [52]. ^{10}B, with integer spin quantum number $I = 3$, does not exhibit a sharp central transition. Therefore, due to the large quadrupole coupling of the BO_3 environment, it cannot be readily excited and observed using ^{10}B NMR. Hence, ^{11}B{^{10}B} REDOR experiments selectively probe the proximity of $[B\emptyset_4]^-$ environments to both BO_3 and $[B\emptyset_4]^-$ environments. The spectrum labelled S_0 is the experiment without the reintroduction of the dipolar coupling, while the spectrum labelled S is affected by the ^{11}B{^{10}B}

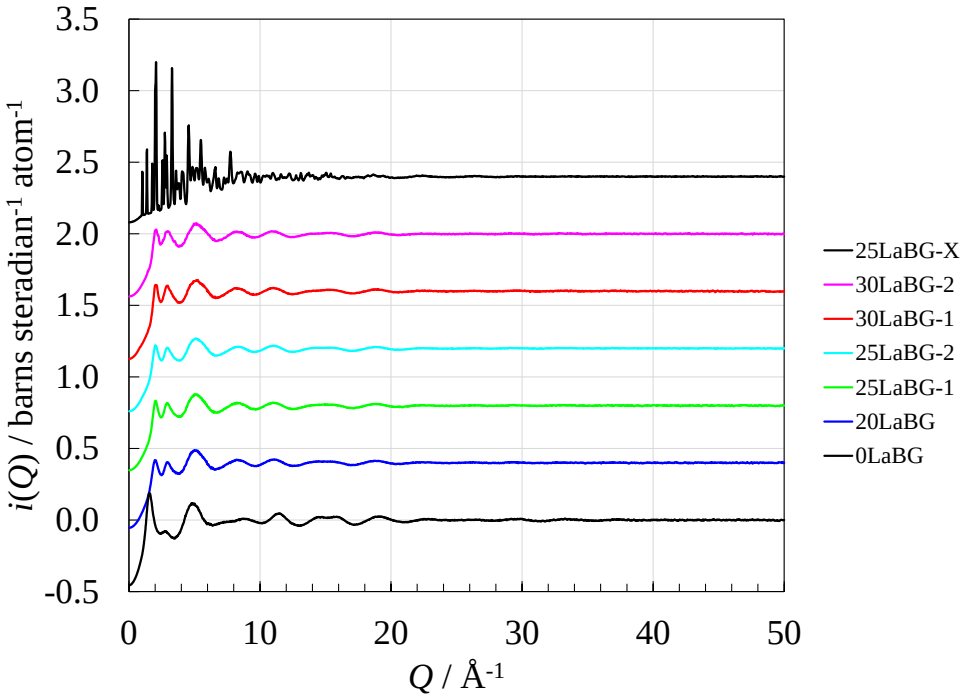

Figure 6.7: The distinct scattering, $i(Q)$, of lanthanum borogermanate glass and crystalline samples, with vertical offsets of $0.4\,\mathrm{b\,sr^{-1}\,atom^{-1}}$. The error bars are smaller than the data points. The most substantial differences are observed for Q values less than $6\,\mathrm{Å}^{-1}$.

dipolar coupling of the $[B\emptyset_4]^-$ environment. ΔS is the difference between the two. In Fig. 6.6 the difference is vertically scaled by a factor of 8. Both BO_3 and $[B\emptyset_4]^-$ environments exhibit significant dephasing, indicating that both environments are close in space to $[B\emptyset_4]^-$ [41, 247].

6.5.3 Neutron Diffraction Results

The distinct scattering for selected glass samples is shown in Fig. 6.7. While there is an obvious difference in the scattering of the $x = 0$ sample and the rest of the series, the $x = [0.20, 0.25, 0.30]$ samples appear largely similar.

We present selected $T(r)$ total correlation functions in Fig. 6.8. While the region from $r = 0\,\mathrm{Å}$ to the first real peak should in principle have a value of 0, small

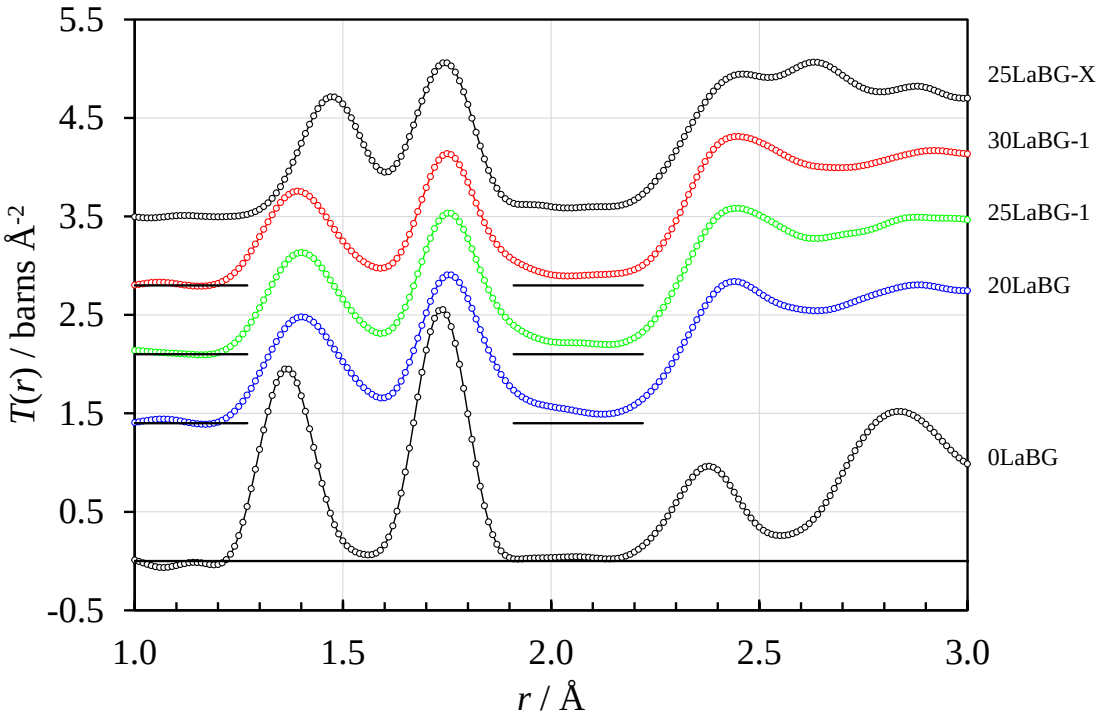

Figure 6.8: The $T(r)$ total correlation functions, in the region of interest ($r = 1\,\text{Å}$ to $3\,\text{Å}$). The functions are vertically offset by $1\,\text{b}\,\text{Å}^{-2}$ for clarity. Horizontal lines indicate the horizontal axis for the respective functions. The presented functions were Fourier transformed from the distinct scattering in Fig. 6.7 using Lorch modification functions.

experimental errors and truncation effects lead to ripples in the measured correlation functions (see Fig. C.4).

The first real peak, generally centred at a distance of about 1.40 Å, is due to B–O bonds. In 0LaBG and 25LaBG-X, this peak is symmetric, as the former contains only BO_3 units, while the latter contains only $[B\text{Ø}_4]^-$ units. In all other compositions a distinct asymmetry can be observed in this peak; a long distance shoulder is observed regardless of choice of modification function. In order to properly fit this asymmetric peak, we use two resolution-broadened Gaussian functions with fixed positions: one peak for BO_3, with $r = 1.367\,\text{Å}$; and one for $[B\text{Ø}_4]^-$, with $r = 1.473\,\text{Å}$. The positions for the BO_3 and $[B\text{Ø}_4]^-$ peaks are based upon those obtained by fitting the $T(r)$ functions of 0LaBG and 25LaBG-X, respectively, as these samples separately contain almost entirely BO_3 and $[B\text{Ø}_4]^-$.

The second peak, centred at approx. 1.75 Å, is assigned to Ge–O interactions. In

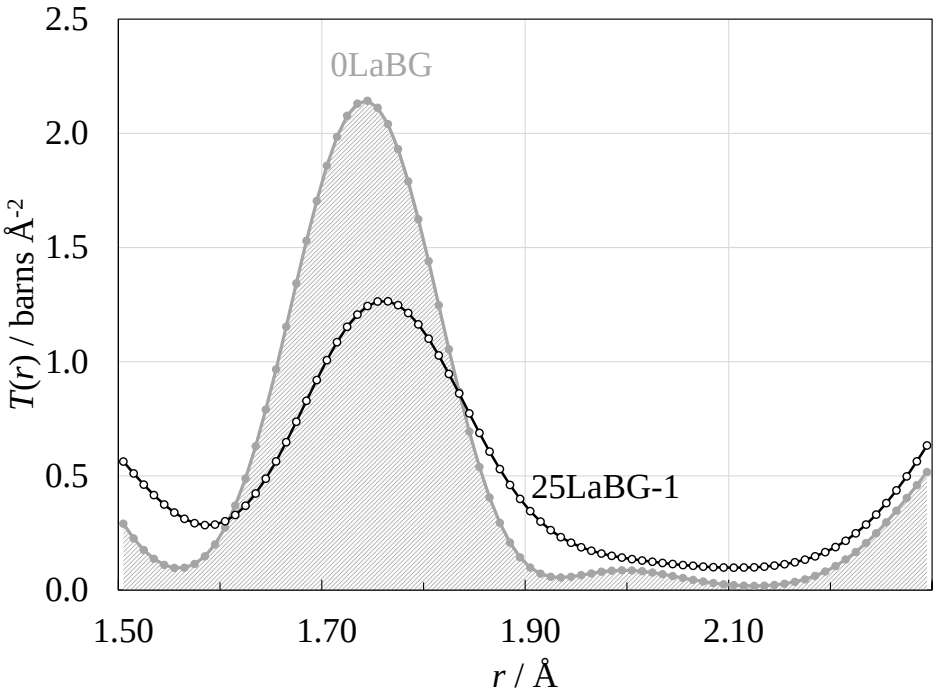

Figure 6.9: The $T(r)$ correlation functions of 0LaBG (in grey) and 25LaBG-1 (open circles). The 0LaBG sample contains only GeO_4. The Ge−O peak in 25LaBG-1 is notably shifted in position and less symmetric than the Ge−O peak in 0LaBG. The change in total intensity is expected, as 25LaBG-1 contains significantly less Ge than does 0LaBG.

0LaBG this peak is symmetric. The addition of La_2O_3 to the glass produces substantial changes in the behaviour of this peak in the $x = [0.20, 0.25, 0.30]$ samples. This change is highlighted in Fig. 6.9, where the $T(r)$ functions of 0LaBG and 25LaBG-1 are overlaid with no vertical offset. The peak shows both a move to higher r values, and a distinct asymmetric tail that extends towards high-r values. This high-r tail is attributed to the formation of longer Ge−O bonds, consistent with the formation of high-coordinate germanium-oxygen polyhedra, *i.e.*, GeO_5 and GeO_6 [27, 28, 42, 64]. Our data do not have the ability to unambiguously assign this intensity to a particular species, nor to preclude a combination of the two species being present.

In order to fit this asymmetric peak which overlaps at low r with the B−O peak,

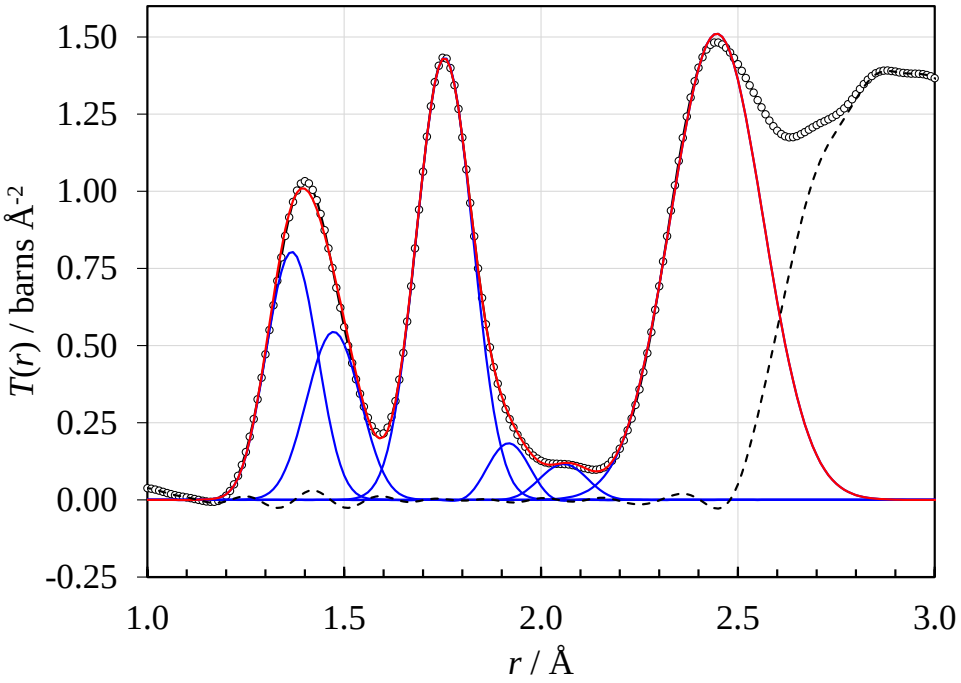

Figure 6.10: An example peak fit of $T(r)$ for 25LaBG-1. The total fit (red line) is overlaid on the experimental data (open circles). The individual peaks, in blue, are in order attributed to BO_3, $[B\emptyset_4]^-$, three Ge–O peaks, and a final peak resulting from La–O, O–O, and B–B interactions. The fit residual is displayed as a dashed line.

and at high r with the subsequent peak at ∼2.4 Å, we follow a similar approach to Alderman *et al.* in their fitting of neutron diffraction data of calcium germanate glasses [12]. We first fit the B–O peak (as above) and the leading edge of the Ge–O peak, between 1.20 Å to 1.80 Å. The residual is then fitted up to 1.95 Å with a single additional peak. The leading edge of the subsequent peak (at ∼2.4 Å) is fitted from 2.2 Å to 2.5 Å. The final residual of the above 5 peaks consistently yields some remaining intensity at approximately 2.07 Å. This final intensity is fit with a single additional peak, and is assigned to the Ge–O interaction. An example of the fit resulting from this process is shown in Fig. 6.10.

The third peak at ∼2.4 Å arises from a combination of several different atom pairs and structural correlations, as will be discussed below. The fit to the leading edge of

this peak, performed as part of the procedure to determine the Ge–O coordination number, does not in itself provide structurally meaningful information.

Mean B–O coordination numbers, n_{BO}, and mean Ge–O coordination numbers, n_{GeO}, as calculated using Eq. (6.4) are reported in Table 6.4. n_{BO} and n_{GeO} of 0LaBG and 25LaBG-X were found to be approximately 3 % below nominal values. Slight underestimation of coordination numbers from neutron diffraction is common, and can occur for various reasons, including Q-resolution, inadequate normalization, or errors in the multiple scattering correction [248]. The complete list of fitting parameters can be found in Table C.1.

Table 6.4: Selected mean bond lengths and coordination numbers from neutron diffraction.

Sample	r_{BO} / Å	n_{BO}	r_{GeO} / Å	n_{GeO}
0LaBG	1.367 ± 0.001	2.9 ± 0.1	1.737 ± 0.001	3.9 ± 0.1
20LaBG	1.414 ± 0.004	3.2 ± 0.1	1.787 ± 0.004	4.4 ± 0.1
25LaBG-1	1.411 ± 0.004	3.2 ± 0.1	1.785 ± 0.004	4.4 ± 0.1
25LaBG-2	1.411 ± 0.004	3.1 ± 0.1	1.788 ± 0.005	4.4 ± 0.1
30LaBG-1	1.404 ± 0.004	3.2 ± 0.1	1.788 ± 0.005	4.3 ± 0.1
30LaBG-2	1.408 ± 0.004	3.1 ± 0.1	1.784 ± 0.005	4.1 ± 0.1
25LaBG-X	1.474 ± 0.001	3.8 ± 0.1	1.744 ± 0.001	3.9 ± 0.1

6.6 Discussion

6.6.1 ^{10}B and ^{11}B NMR

Gupta *et al.* [34] have previously performed ^{11}B MAS NMR measurements on $LaBGeO_5$, in both glass and crystalline states, and also on a partially crystallized sample. Their spectra show that the glass contains "about equal concentration" of BO_3 and $[B\emptyset_4]^-$ units, but a quantitative determination of the concentration was not reported, and thus we give the first such quantitative report. Selected ^{11}B NMR spectra are presented in Fig. 6.3, and selected parameters are presented in Table 6.3. The ^{11}B MAS NMR spectra consist of two peaks: the broad BO_3 peak, with maxima at approximately 15 ppm; and the narrow $[B\emptyset_4]^-$ peak, at approximately 2 ppm. The slight asymmetry apparent in the crystalline 25LaBG-X $[B\emptyset_4]^-$ peak is attributed to the 3/2→1/2 satellite transition, which is not resolved from the central transition. The same

transition can be observed in the BO_3 peaks of the glass samples, where the resolution is sufficient to fit the satellite peak separately (see Fig. C.1).

The lanthanum-free 0LaBG sample contains overwhelmingly three-coordinate boron, while the crystalline 25LaBG-X sample contains only four-coordinate boron. The lanthanum-containing glass samples, even those with the same composition as the crystal, have a mixture of three- and four-coordinate boron. The proportions of $[B\emptyset_4]^-$ decreases in response to R. The change in n_{BO} is consistent with the expected evolution of the boron-oxygen environment in response to increasing modifier oxide, as displayed in Fig. 6.2. The addition of modifier oxide, in this case La_2O_3, converts $B\emptyset_3$ to $[B\emptyset_4]^-$, which will in turn convert to $B\emptyset_2O^-$ and eventually $B\emptyset O_2{}^{2-}$ [22]. Identification of the type of three-coordinate species is important to assess the likelihood of whether the glass is homogeneous, or possibly contains heterogeneous regions. The isotropic chemical shift, δ_{iso}^{CS}, has been correlated with the amount of non-bridging oxygen in BO_3 units in crystalline materials [48]. Based upon the values from crystalline systems, the δ_{iso}^{CS} value of the 0LaBG sample is consistent with either individual $B\emptyset_3$ units or boroxol rings, while the lanthanum-containing glasses are consistent with either $B\emptyset_2O^-$ units or borate ring structures containing non-bridging oxygen (*e.g.*, di-triborate) [20]. Our ^{11}B MAS NMR spectra have insufficient resolution to distinguish between these possibilities, largely due to the inherent structural broadening present in glassy materials. ^{11}B MQMAS NMR was used to examine the possibility of multiple coexisting BO_3 species. The isotropic dimension of the MQMAS spectrum is free from quadrupolar broadening. While this does not mitigate the structural broadening that is present in the glass, the increase in resolution has been used to evaluate BO_3 speciation in high-alkali borate glasses [49], as well as to evaluate ring and non-ring BO_3 proportions in binary borogermanate glasses [53]. For all samples studied in this work, the BO_3 peak in the isotropic dimension is easily modelled by a single Gaussian lineshape. There is no indication of multiple coexisting BO_3 environments in any sample, either via rings or varying amounts of non-bridging oxygen. In the study by Lee *et al.*, boroxol rings cease to be apparent in MQMAS in binary borogermanate glasses as the GeO_2/B_2O_3 ratio rises above 3:2 [53]; hence it is unsurprising that our 0LaBG glass, with a GeO_2/B_2O_3 molar ratio of 2:1, does not show the presence of ring structures. Aguiar and Kroeker present ^{11}B MQMAS spectra of alkali borate glasses

with multiple coexisting BO_3 units, and observe substantial asymmetric broadening in the isotropic projections of the MQMAS spectra [49]. The broadening we observe is symmetric around a mean isotropic chemical shift (Table 6.3). The significant width of the peaks in the isotropic dimension indicates the presence of a distribution of chemical shifts in the BO_3 environments. The width of the isotropic peaks of the lanthanum-containing glasses are significantly narrower than that of the lanthanum-free 0LaBG sample, indicating that the lanthanum-containing glasses have less short-range disorder. The isotropic chemical shifts of each sample (Table 6.3, as derived per Millot and Man [134]) are assigned to their likely BO_3 environments by comparison to literature values [48, 49]. The lanthanum-containing samples have mean δ_{iso}^{CS} values in the range of 17.6 ppm to 18.6 ppm, which is most consistent with $B\emptyset_2O^-$ units, and inconsistent with either $B\emptyset_3$ or $B\emptyset\,O_2{}^{2-}$ units.

The change in the $[B\emptyset_4]^-$ peak is much less drastic, and more difficult to assign. No trend is observed with the change in the δ_{iso}^{CS} of the $[B\emptyset_4]^-$ peak with response to R in the glass samples. However, the $[B\emptyset_4]^-$ δ_{iso}^{CS} for each peak is, on average, (0.7 ± 0.3) ppm more positive than the equivalent value in crystalline 25LaBG-X. While there is insufficient information available to identify the exact change in the $[B\emptyset_4]^-$ environment responsible for this consistent change in δ_{iso}^{CS}, it is plausibly attributed to the presence of BO_3 in the second coordination sphere of the $[B\emptyset_4]^-$ unit. Attaching BO_3 units to $[B\emptyset_4]^-$ tetrahedra has been previously shown to increase the $[B\emptyset_4]^-$ δ_{iso}^{CS} by approximately 0.5 ppm [50]. This structural motif can be observed in the LaB_3O_6 and LaB_5O_9 crystals [249, 250]. However, while the effects of silicon and phosphorus substitution on the $[B\emptyset_4]^-$ δ_{iso}^{CS} have been established [50, 251, 252], to our knowledge there have been no similar studies on the effects of germanium substitution. Therefore, we cannot discount the possibility that the observed shift in $[B\emptyset_4]^-$ δ_{iso}^{CS} is due to changing connectivity between germanium and $[B\emptyset_4]^-$.

While our ^{11}B MAS experiments are insufficient to identify the nature of the connectivity of the borate species, our $^{11}B\{^{10}B\}$ REDOR experiment provides additional evidence regarding connectivity. The REDOR pulse sequence reintroduces dipolar coupling which would otherwise be averaged away by MAS. Dipolar coupling is a through-space interaction, and is proportional to the inverse cube of the separation between nuclei. REDOR is commonly used in the study of glasses. It has been used to

characterize cation clustering in mixed-alkali silicates [253], selective site connectivity in sodium boroaluminate glasses [142], degree of polymerization in sodium tungsten phosphate glasses [254], and the number of B−O−P links in lithium borophosphate glasses [255]. As both ^{11}B and ^{10}B are quadrupolar, and ^{10}B is of integer nuclear spin, exact distances cannot be extracted from our data [41]. However, for small values of $\Delta S/S_0$, the dipolar dephasing is expected to reflect only short length scales, and the effect has been shown to be independent of geometry [144]. As we present spectra where $\Delta S/S_0$ is small, this implies that any dephasing observed in the ^{11}B spectrum is due to the presence of a $[B\emptyset_4]^-$ species in close proximity to either BO_3 or $[B\emptyset_4]^-$. Both the BO_3 and $[B\emptyset_4]^-$ peaks show significant dephasing, and are dephased in similar proportions. From this we conclude that both species are in close proximity to $[B\emptyset_4]^-$, and that neither BO_3–$[B\emptyset_4]^-$ nor $[B\emptyset_4]^-$–$[B\emptyset_4]^-$ links are preferred over the other. This supports a glass network where the borate subnetwork is not segregated, and is homogeneous.

6.6.2 Neutron Diffraction

B-O and Ge-O Coordination

Average bond lengths and mean coordination numbers determined via neutron diffraction are shown in Table 6.4. Coordination numbers were determined by the use of Eq. (6.4) applied to the resolution-broadened Gaussian functions used to fit the $T(r)$ functions. Average bond lengths were determined by integration of $rT(r)$.

The experimental values of both n_{GeO} and n_{BO} for the crystalline sample, 25LaBG-X, are consistent with the nominal values (4 and 4, respectively) for the reported structure of $LaBGeO_5$ [78], and similarly the experimental coordination numbers for the La-free glass, 0LaBG, are consistent with expectation (3 and 4, respectively) based on the ^{11}B MAS NMR results, albeit with some uncertainty reflecting the uncertainty in the sample compositions. For the La-containing glass samples, n_{BO} values determined by neutron diffraction are consistently lower than those determined by ^{11}B MAS NMR within uncertainty (Fig. 6.11 and Fig. 6.13), and the NMR values are preferred, since they are not affected by compositional uncertainty, and these are plotted in Fig. 6.12a, together with the neutron diffraction values for n_{GeO} in Fig. 6.12b. We attribute the uncertainty in n_{BO} to composition, rather than fitting

errors or truncation effects in the $T(r)$ functions or relaxation effects in the ^{11}B MAS NMR, for several reasons. The maximum momentum transfer used for Fourier transformation of the distinct scattering is quite large ($Q_{\max} = 50\,\text{Å}^{-1}$), allowing for substantial real-space resolution and minimizing the possibility of truncation. The regions of the $T(r)$ functions before the B–O region (*e.g.*, $r \geq 1\,\text{Å}^{-1}$) have minimal baseline effects when compared to the size of the B–O peaks (Fig. C.4). Additionally, the ^{11}B MAS spectra were collected such that both BO_3 and $[B\emptyset_4]^-$ environments were allowed to completely relax between scans, preventing saturation effects that could cause errors in n_{BO}.

All of the La-containing glass samples show a mean germanium coordination number which is significantly greater than 4, and this result is evidence of the presence of high-coordinate (*i.e.*, 5-coordinate or 6-coordinate) germanium polyhedra. This conclusion is supported by the asymmetric shape of the Ge–O peaks in the $T(r)$ correlation functions (see Figs. 6.8 to 6.10).

The r-scale of neutron diffraction data is more accurate and precise than the intensity scale [27, 69], and as such we do not expect it to have particular errors affecting the coordination number. Indeed, the average B–O bond length (r_{BO}) behaves as we would predict from the trend of the B–O coordination number according to ^{11}B NMR: the mean peak position moves to shorter distances in samples with lower boron-oxygen coordination numbers (Fig. 6.13). The positions of the B–O peaks in both 0LaBG and 25LaBG-X are consistent with the bond lengths expected from bond-valence calculations for 3- and 4-coordinated boron respectively [256–258], and with similar structures from the literature [78]. The positions of the Ge–O peaks in both control samples are also consistent with the expectations for their structures. The position of the Ge–O peak in 0LaBG [(1.737 ± 0.001) Å] is consistent with GeO_4 units with all bridging oxygen. The position of the Ge–O peak in 25LaBG-X [(1.744 ± 0.001) Å] is in reasonable agreement with the average Ge–O bond length in the reported $LaBGeO_5$ crystal structure (1.753 Å) [78].

For all of the La-containing glasses, the B–O peak occurs at a longer distance compared to the La-free glass, 0LaBG, consistent with an increase in the B–O coordination number, due to the formation of some $[B\emptyset_4]^-$ when La_2O_3 is added to the glass. Furthermore, the addition of La_2O_3 leads to the Ge–O peak shifting

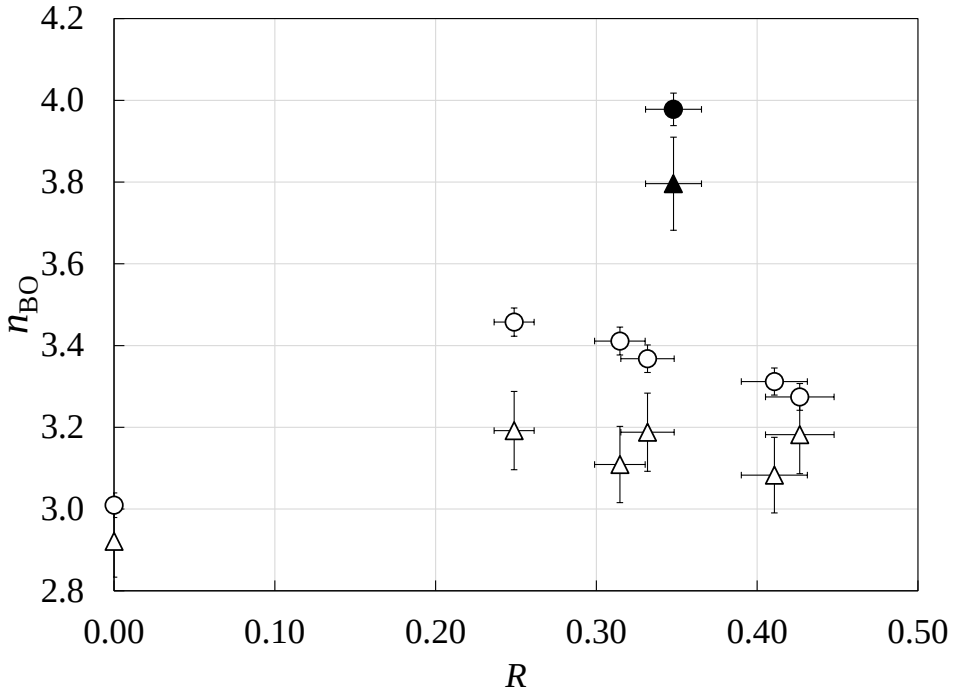

Figure 6.11: The mean B–O coordination number as determined by ^{11}B MAS NMR (circles) and the mean B–O coordination number as determined by neutron diffraction (triangles) as a function of the molar ratio $R = [La_2O_3]/([B_2O_3]+[GeO_2])$. The filled markers correspond to the crystalline $LaBGeO_5$ sample 25LaBG-X, while the open markers denote glass samples. In principle, all of these values should agree. However, the neutron values are usually substantially lower than those observed through NMR. This is likely due to uncertainty in the composition of the samples.

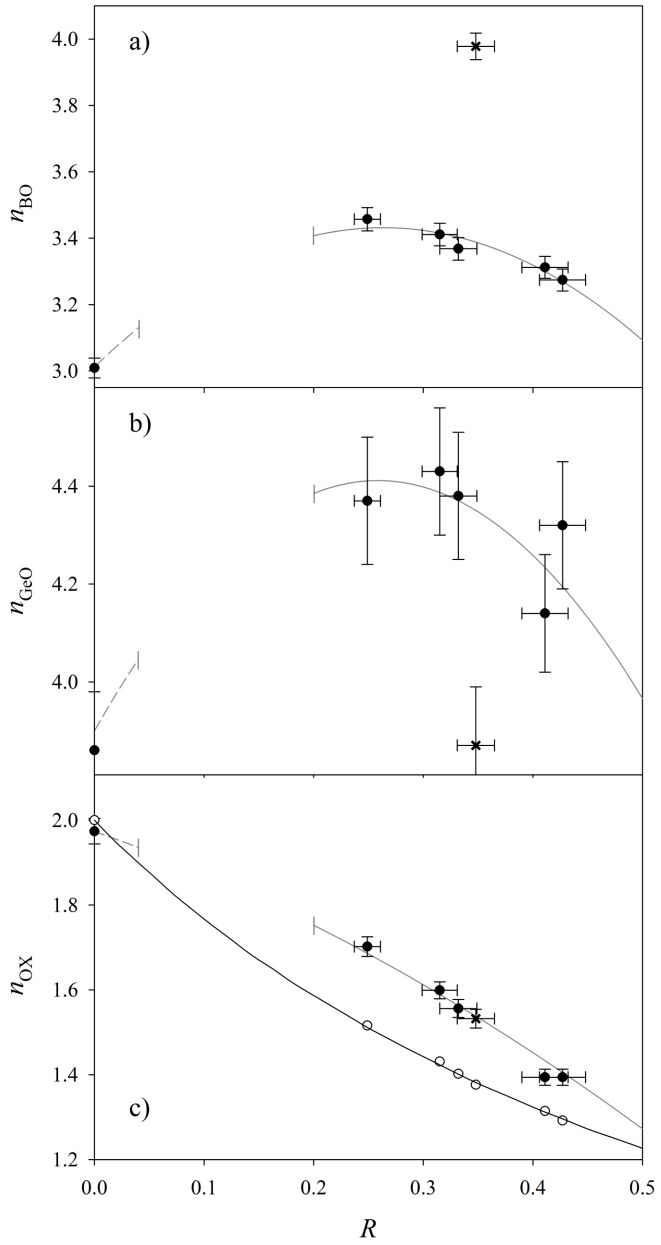

Figure 6.12: Mean coordination numbers, n_{ij}, as a function of the molar ratio $R = [La_2O_3]/([B_2O_3]+[GeO_2])$, with closed circles for the glass samples, and a cross for the crystalline sample. The grey lines represent a guide to the eye, with a break in the region of no glass formation [238]. a) n_{BO}, as determined by ^{11}B MAS NMR. b) n_{GeO}, as determined by neutron diffraction. c) n_{OX} ($=n_{OB}+n_{OGe}$, where X represents any glass former cation, B or Ge), as determined from the data shown in parts a) and b). The open circles and black line are the theoretical coordination number that would be obtained for a network of corner-sharing BO_3 and GeO_4 units, with no increase in n_{BO} or n_{GeO}.

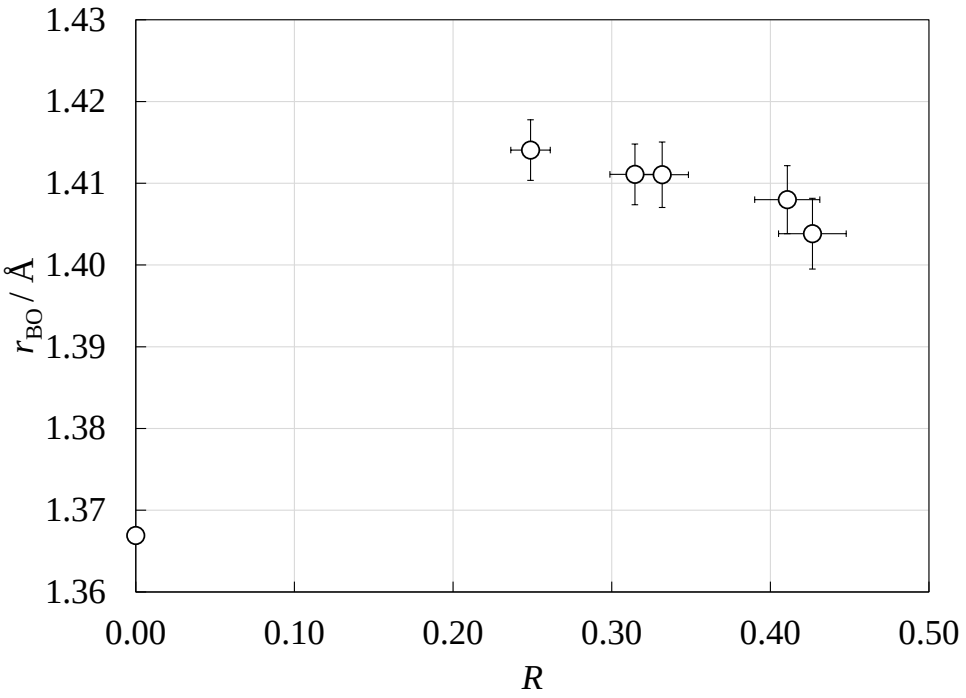

Figure 6.13: The average B−O bond length, r_{BO}, at determined by neutron diffraction as a function of the molar ratio $R = [La_2O_3]/([B_2O_3]+[GeO_2])$. The average B−O bond length decreases as R increases, consistent with a reduction in n_{BO}.

to longer distance and becoming asymmetric (Figs. 6.9 and 6.10), compared to the La-free glass. There are also changes in the region above 2.2 Å, due to a number of factors, as discussed below.

The germanium-oxygen peak is substantially different between the La-free and La-bearing glass samples (Fig. 6.9). The average Ge–O bond length (r_{GeO}) increases from (1.737 ± 0.001) Å in 0LaBG to approximately 1.78 Å in the lanthanum-containing samples (Table 6.4). Although the presence of La^{3+} ions leads to some lengthening of the bonds to bridging oxygen (as is observed for the length of the Ge–O bond in the bridge between GeO_4 and $[B\emptyset_4]^-$ tetrahedra in crystalline $LaBGeO_5$), the major cause of lengthening of the mean Ge–O bond length is likely to be the formation of $[GeO_5]^-$ and/or $[GeO_6]^{2-}$ units. These units have longer mean Ge–O bond lengths than GeO_4 tetrahedra, and will likely have a significantly less symmetric distribution of bond lengths. For example, a difference is often observed between equatorial and axial bond lengths in $[GeO_6]^{2-}$ octahedra. The longer bond lengths in these high-coordinate germanate species shifts the peak maxima to larger values of r, while the distribution of bond lengths manifests as a broad tail on the high-r side of the GeO_4 peak [12, 27, 28, 42, 64]. Such a tail is observed in all lanthanum-containing glass samples (Fig. 6.8 and Fig. 6.9), and persists when the data are Fourier transformed using a step modification function, rather than a Lorch modification function (Fig. C.7).

Each lanthanum-containing glass sample has a mean value of n_{GeO} that is significantly above 4 (Table 6.4). However, whereas tetrahedral units are highly symmetric with only small differences in bond lengths, 5- and 6-coordinated units have a greater degree of asymmetry, and it is not possible to use the observed correlation function to directly differentiate between the two possible higher Ge–O coordination numbers [28, 62]. Regardless, we can still calculate reasonable estimates for the proportion of high-coordinate germanium present in our samples: from 20 % of the total germanium content (assuming only 6-coordinate germanium) to 40 % (assuming only 5-coordinate germanium).

There are many reports in the literature for binary borate [259] and germanate [55, 56, 62] glasses (especially alkali systems), studied over a wide composition range, which show that the coordination number, n_{BO} or n_{GeO}, increases and then declines as increasing amounts of modifier are added to the glass; a behaviour known as the

borate anomaly or the germanate anomaly, respectively. The glass forming range for La-containing glasses is more limited, but nevertheless the guides to the eye shown in Fig. 6.12a and Fig. 6.12b strongly suggest that the two coordination numbers in lanthanum borogermanate glasses also follow an anomalous composition dependence, which we may term a *borogermanate* anomaly.

La-O Coordination

The germanium and boron coordination numbers in crystalline $LaBGeO_5$ are both four [78], and these coordination numbers are markedly different to those in the glasses, as confirmed by our experimental results (see Fig. 6.12a and Fig. 6.12b). A comparison of the crystalline correlation function with that for the glass with closest composition gives further evidence that the glass structure differs significantly from the crystal structure (see Fig. 6.14). In particular, the distance range $r{\sim}2.2\,\text{Å}$ to $2.75\,\text{Å}$ (which is typical of La–O bond lengths) shows significant differences between crystal and glass. This region of the correlation functions, $T(r)$, is markedly more complex than the region of the first two (B–O and Ge–O) peaks, because it involves contributions from several different atom pairs and types of structural correlation. Nevertheless, it is of particular interest because it contains information about the La–O coordination. For example, in the determined structure of crystalline $LaBGeO_5$, four different types of distance can be identified as contributing to this region of the correlation function: 1) the O–O distance in $[B\emptyset_4]^-$ tetrahedra, $r_{OO(B4)} \approx 2.41\,\text{Å}$; 2) the La–O bond lengths, which are more widely distributed, from $2.40\,\text{Å}$ to $2.74\,\text{Å}$, with a total coordination number, n_{LaO}, of 9; 3) the B–B distance of $2.65\,\text{Å}$, arising from a B–O–B bridge between two $[B\emptyset_4]^-$ tetrahedra; and 4) the O–O distance in GeO_4 tetrahedra, $r_{OO(Ge4)} \approx 2.84\,\text{Å}$. For the crystal, the B–B contribution in this region of $T(r)$ is small ($\sim 5\,\%$ of the area), whilst the O–O and La–O contributions are of similar magnitudes.

For information on the La–O coordination in the glasses to be derived, it is necessary to model the other contributions to the relevant region of the correlation function. Generally speaking, this distance range includes La–O, O–O and X–X contributions (where X represents a network forming cation), but no X–O contributions. The approach used here is firstly to show that this region can be modelled well for the La-free

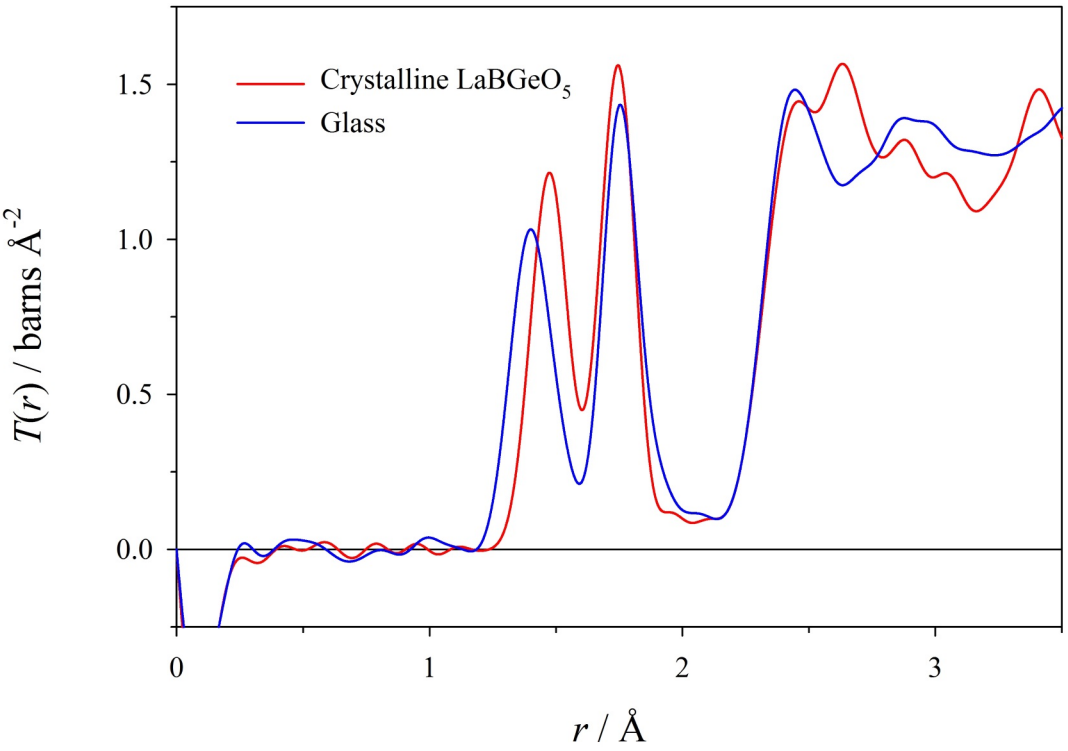

Figure 6.14: Comparison of the neutron correlation functions measured for crystalline $LaBGeO_5$ and for the glass sample of closest composition (samples 25LaBG-X and 25LaBG-1 respectively).

glass, secondly to show that the modelling approach yields a reasonable estimate of the La–O distribution and coordination number, n_{LaO}, for the crystal, and then to use the same method to estimate the value of n_{LaO} for the La containing glasses. It is necessary to note that our model is not unique; and, as with the Ge–O peaks above, the La–O peaks are not intended to imply physically exact distributions of bond lengths, but simply a means of modelling the intensity in a convoluted function. However, as we will demonstrate, by applying constraints informed by our analysis of the B–O and Ge–O environments, we can obtain reasonable estimates of the La–O coordination in the glass.

For the glasses, the presence of BO_3 units leads to an additional O–O distance from the borate units, $r_{\mathrm{OO(B3)}} = 2.3677\,\text{Å} (= \sqrt{3}\, r_{\mathrm{BO(B3)}})$, which does not occur in the crystal. If the B–O coordination number is known, then for a sample of composition $x\mathrm{GeO_2} \cdot y\mathrm{B_2O_3} \cdot z\mathrm{La_2O_3}$ it can be shown that the coordination numbers for the two O–O distances in borate units are given by

$$n_{\mathrm{OO(B3)}} = \frac{12(4 - n_{\mathrm{BO}})}{2x + 3y + 3z} \tag{6.5}$$

$$n_{\mathrm{OO(B4)}} = \frac{24(n_{\mathrm{BO}} - 3)}{2x + 3y + 3z} \tag{6.6}$$

It should be emphasised that these are identities that follow directly from the B–O coordination number and the geometry of the BO_3 and $[B\emptyset_4]^-$ units, with no additional assumptions.

Similarly, the presence of higher coordinated GeO_m (m=5 and/or 6) in the glasses leads to additional O–O distances from the germanate units, but consideration of germanate units is more complex than for borate units. Firstly, it is unknown whether the higher germanium coordination number is 5 or 6, or a mixture thereof. Secondly, whereas the higher coordinated borate unit has a simple geometry (the $[B\emptyset_4]^-$ tetrahedron) with a very narrow distribution of O–O distances, higher coordinated germanate units are more complicated with more than one type of O–O distance (*e.g.*, in a regular $[GeO_6]^{2-}$ octahedron, there are two O–O distances, which are $\sqrt{2}$ and 2 times the Ge–O distance). Nevertheless, if it is assumed that the higher germanium coordination is octahedral, the O–O coordination numbers for the GeO_4

unit ($r_{\mathrm{OO(Ge4)}} \approx 2.8365\,\text{Å} = \sqrt{8/3}\, r_{\mathrm{GeO(Ge4)}}$) and for the first distance in the $[GeO_6]^{2-}$ unit ($r_{\mathrm{OO(Ge6)}} \approx 2.68\,\text{Å}$) are given by

$$n_{\mathrm{OO(Ge4)}} = \frac{6x(6 - n_{\mathrm{GeO}})}{2x + 3y + 3z} \tag{6.7}$$

$$n_{\mathrm{OO(Ge6)}} = \frac{12x(n_{\mathrm{GeO}} - 4)}{2x + 3y + 3z} \tag{6.8}$$

In the α-quartz form of GeO_2 [260], the Ge–Ge distance that arises from Ge–O–Ge bridges between GeO_4 tetrahedra is 3.15 Å, which is markedly longer than the distance range of interest, and hence this correlation need not be considered at this stage. However, both B–B and B–Ge distances are shorter, and need to be taken into account: a neutron diffraction study of pure B_2O_3 glass shows two B–B distances of 2.364 Å inside boroxol groups (B–$\hat{\mathrm{O}}$–B bond angle 120°) and 2.474 Å outside boroxol groups (bond angle 130°) [261]. The B–Ge distances in the reported structure of crystalline $LaBGeO_5$ [78] are 2.87 Å and 2.89 Å (with B–$\hat{\mathrm{O}}$–Ge bond angles of 121.0° and 123.9°, respectively), and in fact we have found that a successful model of the correlation function of the La-free glass requires that the B–Ge distance is shorter than this.

The measurements of the B–O and Ge–O coordination numbers for the La-free glass support a structural model comprised of only BO_3 and GeO_4 units. In this case, there are only two O–O contributions to the relevant region of the correlation function, with coordination numbers of $n_{\mathrm{OO(B3)}} = 1.700$ and $n_{\mathrm{OO(Ge4)}} = 3.451$.

The correlation function for the La-free glass was fitted in the region of interest using four peaks, as shown in Fig. 6.15, and the parameters for the fit are given in Table 6.5. The positions of the two O–O peaks were fixed at the values calculated from the fitted B–O and Ge–O bond lengths, whilst the positions of the B–B and B–Ge peaks were allowed to vary. The widths of all of the peaks except the B–B peak were allowed to vary. The B–B peak is the smallest peak, and it was found to be necessary to constrain its width; a value of 0.07 Å was used, as found in pure B_2O_3 glass [261]. All of the coordination numbers were fixed; the O–O coordination numbers were fixed to values calculated using Eqs. (6.5) and (6.7), whilst the B–B and B–Ge coordination numbers were fixed to those for a chemically random network.

The fit is shown in Fig. 6.15, and it is apparent that the model assumptions that were used give a good account of this region of the measured correlation function. The fitted B–B distance corresponds to a B–$\hat{\text{O}}$–B bond angle of 124.4°, typical of bond angles in borates, and similar to the B–$\hat{\text{O}}$–B bond angle of 129.6° in $LaBGeO_5$. The fitted B–Ge distance corresponds to a B–$\hat{\text{O}}$–Ge bond angle of 121.3°; this value is very similar to the corresponding bond angles in crystalline $LaBGeO_5$, and hence the main reason that the B–Ge distance in the glass is shorter than in this crystal is that the B–O bond length is shorter (due to the smaller B–O coordination number). The fitted peak widths are typical of the values found in oxide glasses [62, 261]. Since the B–B and B–Ge coordination numbers were fixed at the values for a chemically random network, the closeness of the fit is also evidence that there is not a strong chemical ordering of the network.

Table 6.5: The parameters for a fit to the region from 2.19 Å to 2.73 Å of the correlation function for the La-free glass. Errors for the parameters that were varied in the fit are given.

Atom pair i-j	r_{ij} / Å	u_{ij} / Å	n_{ij}
O–O_{B3}	2.3677	0.0701 ± 0.0009	1.700
B–B	2.419 ± 0.004	0.07	1.275
O–O_{Ge4}	2.8365	0.078 ± 0.011	3.451
B–Ge	2.712 ± 0.010	0.085 ± 0.009	1.725

The fit to the correlation function for the La-free glass shows that it is possible to use reasonable modelling assumptions to give a good account of the O–O and X–X correlations in the region of interest, and it yields parameters that can be applied to the La-containing samples. The same modelling approach was then used to simulate the non-La correlations in this region for the crystalline sample, as shown in Fig. 6.16a, and the parameters for this simulation are given in the upper part of Table 6.6. For the simulation, the peak widths (u_{ij}) determined from fitting the correlation function of the La-free glass (Table 6.5) were used. For the $LaBGeO_5$ crystal structure, both O–O coordination numbers are 2.4 (as predicted by Eq. (6.6) and Eq. (6.7)), whilst both X–X coordination numbers are 2.0. The O–O distance in $[B\text{Ø}_4]^-$ tetrahedra was calculated as $\sqrt{8/3}\, r_{BO(B4)}$, using a value for the B–O bond length in $[B\text{Ø}_4]^-$ tetrahedra, $r_{BO(B4)}$, predicted using a bond-valence calculation [258].

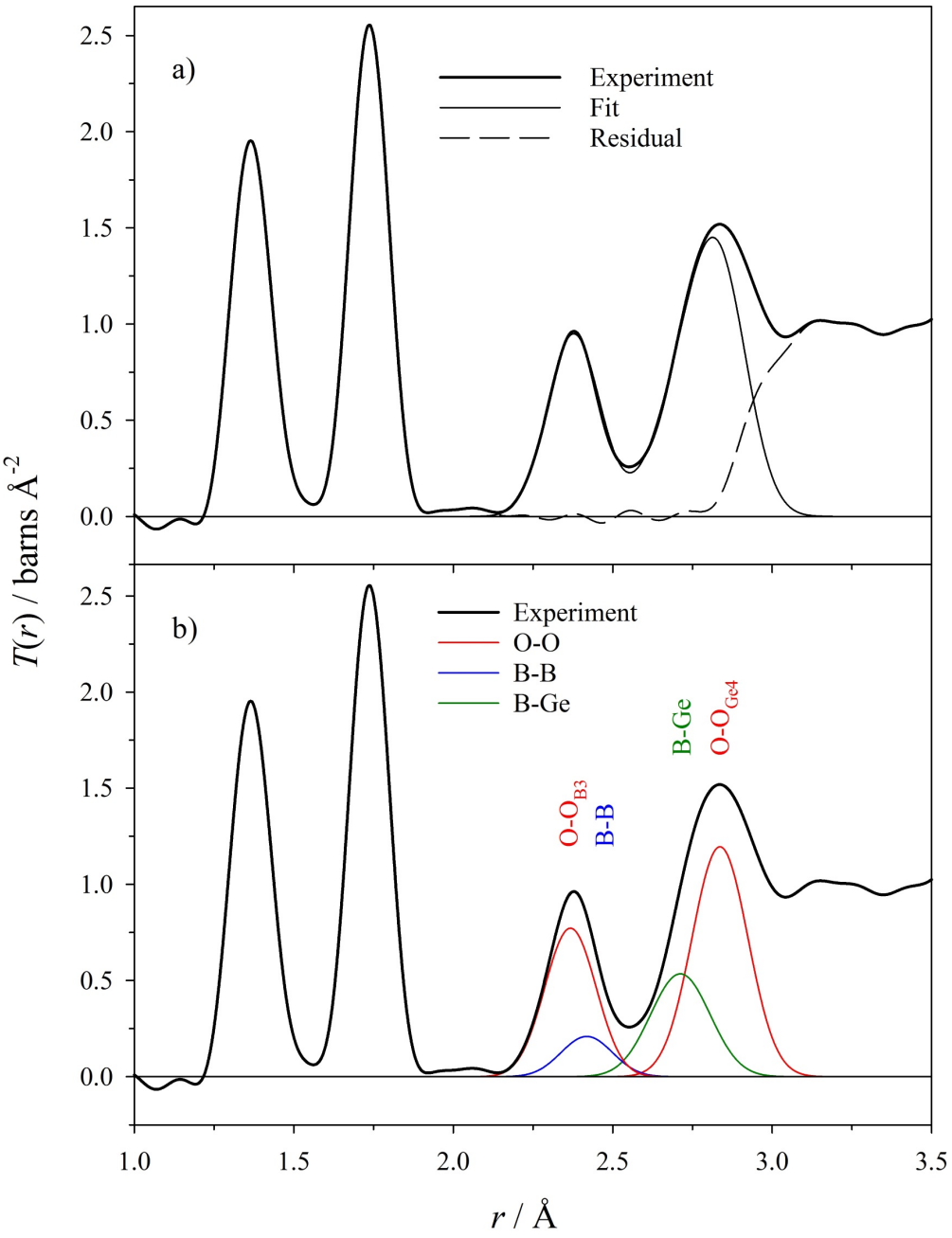

Figure 6.15: The fit to the region of interest of the correlation function of the La-free glass. a) The total fit (thin line) is shown together with the experimental result (thick line) and the residual (dashed line). b) The components of the fit (red for O−O peaks, blue and green for B−B and B−Ge peaks respectively) together with the experimental result (black).

In both borates and germanates, X–$\hat{\text{O}}$–X bond angles are typically in the range from 120° to 130°, and hence the X–X distances were calculated from the bond lengths on the assumption of a bond angle of 125°. The non-La simulation was then subtracted from the experimental correlation function, to yield the difference shown in Fig. 6.16b. In the region of interest, this difference is a measure of the distribution of La–O bond lengths. As in the detailed crystallographic structural model [78], there is a smaller number of short La–O bonds (involving non-bridging oxygen), and a larger number of long La–O bonds. In fact there is an asymmetry to the larger peak, and hence the distribution was fitted with a total of three peaks to give the parameters in the lower part of Table 6.6. These fitted peaks are a means of parametrising the La–O distribution, rather than being an accurate determination of the precise bond lengths in the crystal. The total value of n_{LaO} estimated in this way is 8.2; the value is a little less than, but similar to value of 9 obtained from a full crystallographic analysis [78]. The exact value obtained by this method is sensitive to the choice of parameters for the non-La simulation, especially the parameters for the O–O_{Ge4} and B–Ge peaks; if these peaks are moved to longer distance (either by increasing the assumed interatomic distance, or by decreasing the assumed width), then a larger value of n_{LaO} is obtained. Nevertheless, a bond-valence calculation [257] of the valence corresponding to the fitted peaks yields a total of 2.91 (see Table 6.6); this value is close to the formal La^{3+} valence, indicating that the result is reasonable.

Table 6.6: Parameterisation of the region of interest of the correlation function for the crystalline sample (see Fig. 6.16). The first four sets of values were used to simulate the non-La contributions (see text for details), which were subtracted from the experimental function. The resultant difference was then fitted to give the final three sets of values for the La–O coordination, and the valence corresponding to these fit components is also given [257].

Atom pair *i*-*j*	r_{ij} / Å	u_{ij} / Å	n_{ij}	Valence
O–O_{B4}	2.412	0.0701	2.4	
B–B	2.615	0.07	2.0	
O–O_{Ge4}	2.8365	0.078	2.4	
B–Ge	2.857	0.085	2.0	
La–O	2.286 ± 0.002	0.051 ± 0.004	0.78 ± 0.04	0.58
La–O	2.58 ± 0.01	0.10 ± 0.01	5.85 ± 0.74	1.94
La–O	2.682 ± 0.002	0.05 ± 0.01	1.57 ± 0.73	0.40
Total La–O	$\bar{r}_{\text{LaO}}=$ 2.57		8.2	2.91

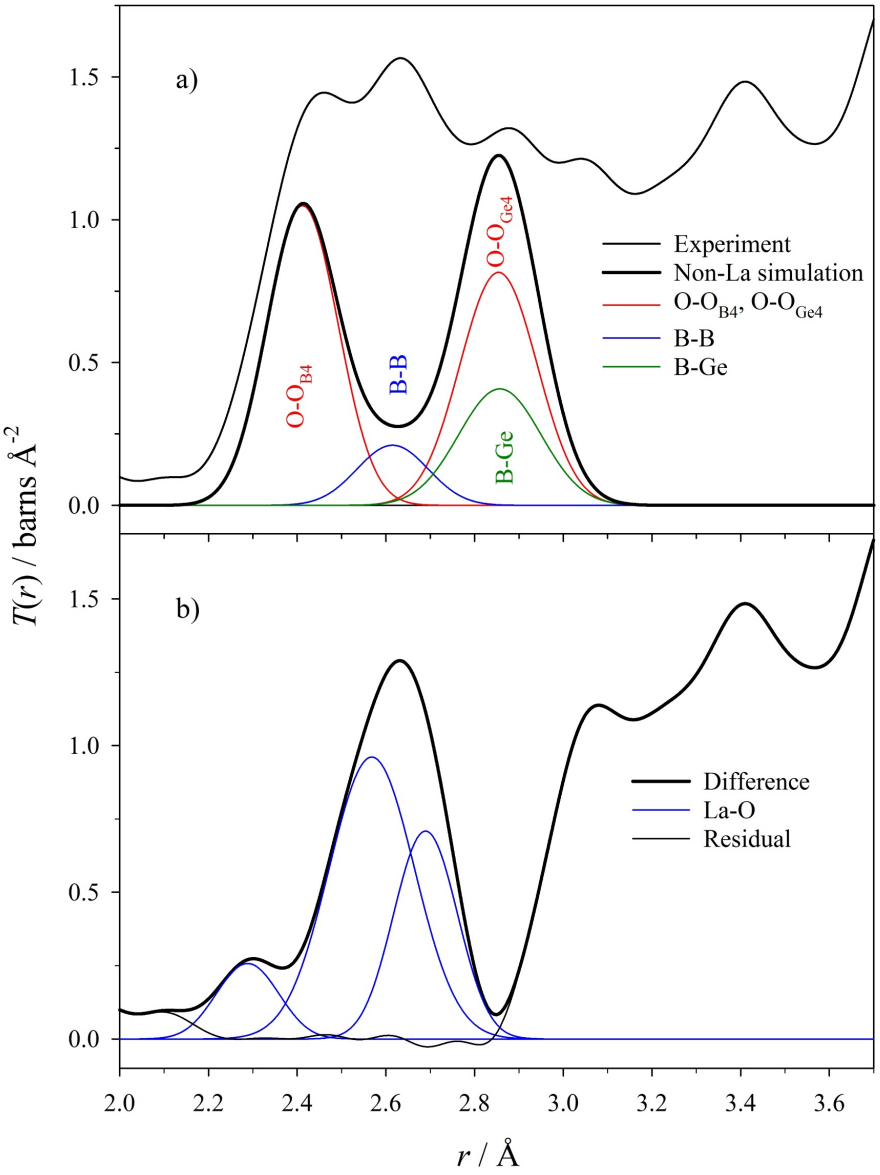

Figure 6.16: The region of interest of the correlation function for the crystalline sample. a) The experimental correlation function (thin black line) together with a simulation of the non-La contributions in this region (thick black line). The individual components of the simulation are also shown; red lines are the peaks for O – O distances in $[B\emptyset_4]^-$ and GeO_4 tetrahedra, whilst blue and green lines are respectively the B – B and B – Ge peaks for distances arising from corner-sharing between these tetrahedra. b) The difference between experiment and the non-La simulation (thick black line), together with the components of a fit to the difference (blue lines), and the residual for the fit (thin black line).

This method of estimating the La–O correlation (simulation of non-La contributions, followed by fitting of the remainder) yields a reasonable result for the crystalline sample, and it was applied to the glasses too (see Figs. 6.17 and 6.18).

However, the non-La simulation for the glasses is more complicated. Firstly, the glasses contain more different types of structural unit (BO_3, $[B\emptyset_4]^-$, GeO_4, and GeO_m; it was assumed that m=6), leading to a greater number of different O–O contributions. The n_{OO} coordination number for each of these was calculated using Eq. (6.5) to Eq. (6.8). As for the La-free glass, the O–O distances in BO_3 and GeO_4 units were calculated from the measured B–O and Ge–O bond lengths respectively. The O–O distances in regular $[B\emptyset_4]^-$ and $[GeO_6]^{2-}$ units were calculated from bond-valence predictions of the B–O and Ge–O bond lengths (note that the O–O distance in a $[GeO_6]^{2-}$ octahedron is shorter than in a GeO_4 tetrahedron) [258]. The widths for the four O–O peaks were assumed to be the same as determined from fitting the correlation function for the La-free glass (see Table 6.5). Secondly, the region of interest also contains X–X contributions (where X = network forming cation), and there are ten of these in total, arising from the four different structural units. The X–X coordination numbers were calculated by assuming that the NBOs are statistically distributed on the BO_3 and GeO_4 units (not the $[B\emptyset_4]^-$ or $[GeO_6]^{2-}$ units [20, 62]), and by assuming a random distribution of the different types of oxygen bridge between the units (a chemically disordered network). These are reasonable assumptions, because there is no evidence from the REDOR NMR data for an ordering of borate species, and thus there is no reason to suspect an ordering of germanate species, or between borate and germanate species. The X–X distances were calculated from the X–O bond lengths with an assumption of a X–$\hat{O}$–X bond angle of 125°. The widths for the three B–B and four B–Ge peaks were taken from the fit for the La-free glass (Table 6.5), whilst a width $u = 0.10$ Å was assumed for the three Ge–Ge peaks. In Fig. 6.17, which shows the simulations for the samples with the least and most La_2O_3, the four simulated O–O peaks are all shown, whilst a single peak is shown for the sums of all B–B, B–Ge and Ge–Ge peaks respectively. Thus the X–X peaks in Fig. 6.17 are broader than the O–O peaks because they each include several contributions with different distances.

In the region of interest, the difference between the simulation and the experimental

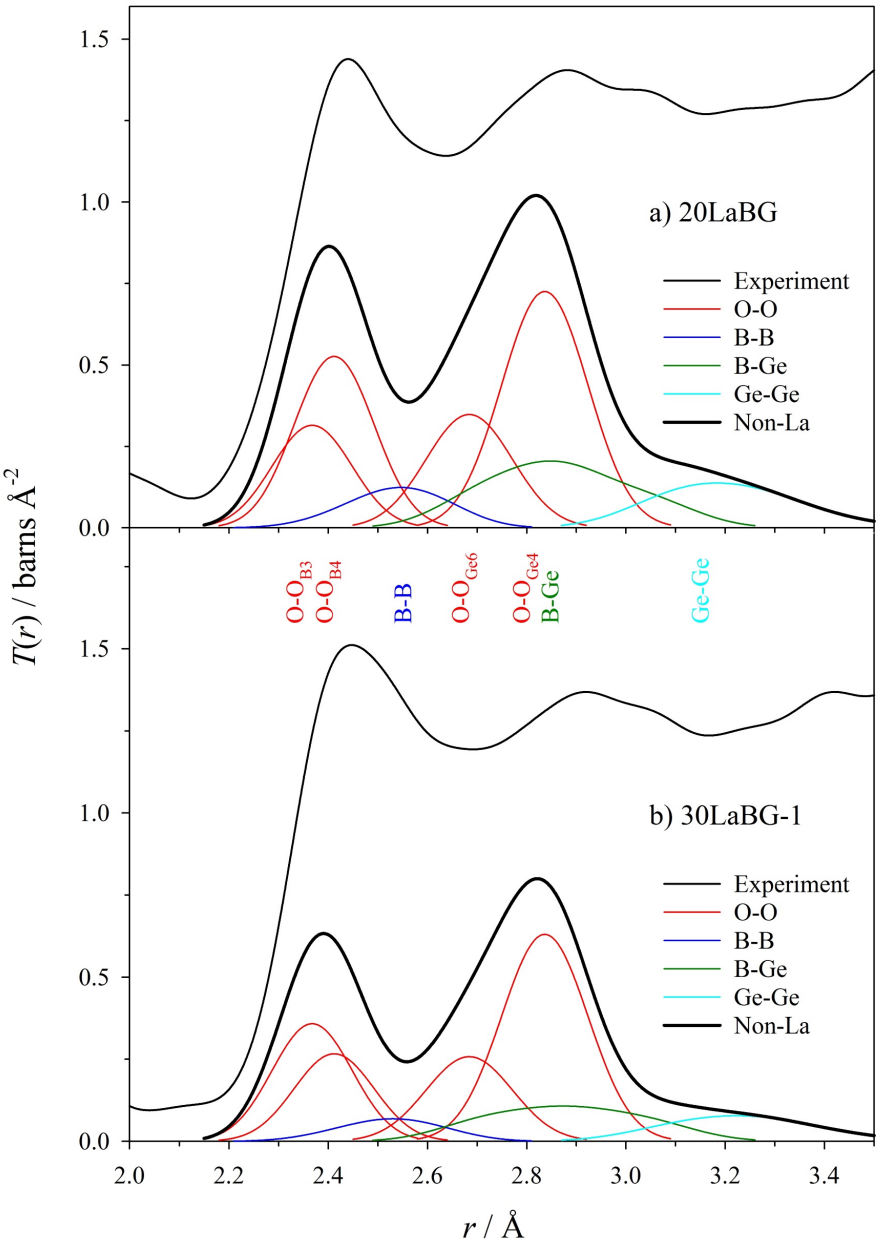

Figure 6.17: The region of interest of the correlation functions for glass samples with low and high La_2O_3 content, a) 20LaBG, and b) 30LaBG-1. The thin black line is the experimental correlation function, whilst the thick black line is the total simulation of all contributions in the region of interest, other than La-O. The simulation includes component peaks due to O–O (red lines), B–B (blue line), B–Ge (green line) and Ge–Ge (cyan line) correlations.

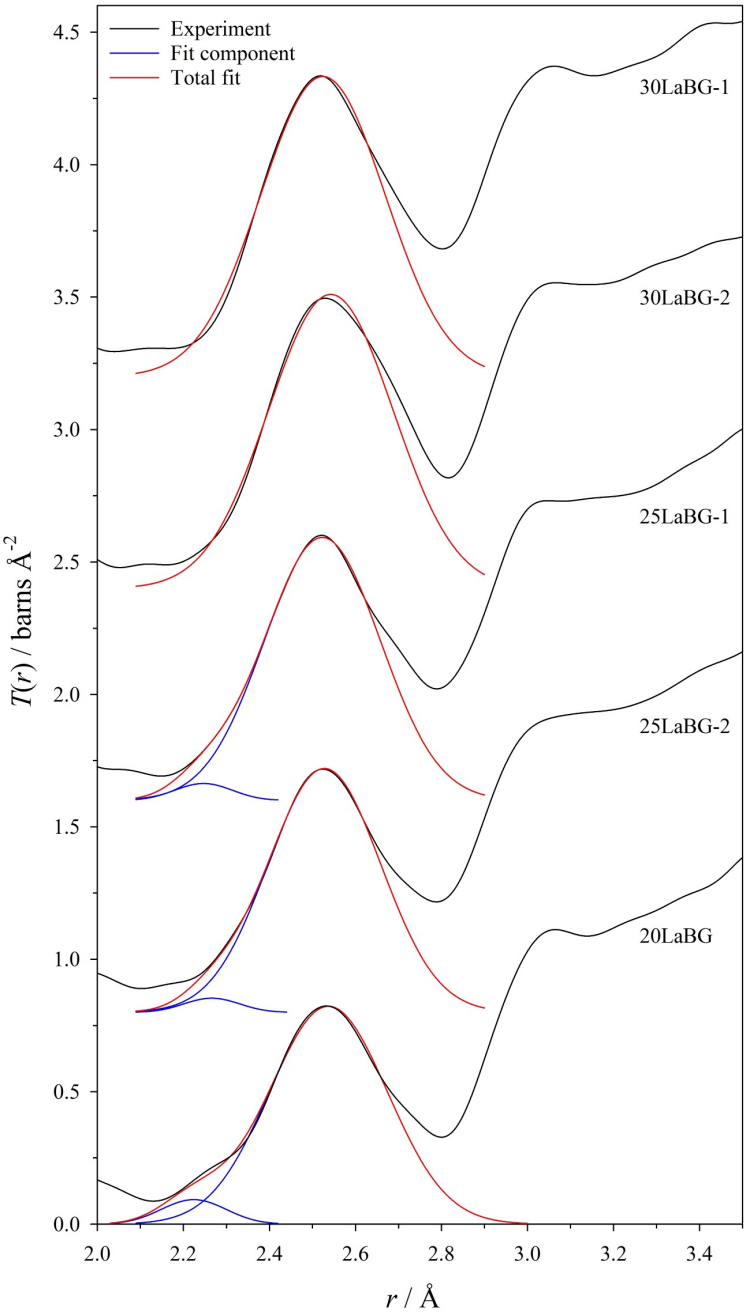

Figure 6.18: The difference between the experimental correlation function and the simulation of the non-La contributions in the region of interest. Results for the glass samples are plotted with suitable vertical displacements, and with the La_2O_3 content increasing towards the top of the figure. The fit to the La−O peak is shown as a red line, and the individual components of the fit are shown as blue lines.

correlation function is due to La–O correlations, and this difference is larger for higher La_2O_3 content (Fig. 6.17b). For each glass, the simulation was subtracted from the experimental correlation function to yield the estimates of the La–O distribution shown in Fig. 6.18. As for the crystalline sample (Fig. 6.16), there is a main La–O peak at longer distance, with a smaller peak at shorter distance; the shorter distance peak decreases as the La_2O_3 content increases. As shown in Fig. 6.18, the estimates of the La–O distribution were fitted, yielding the results given in Table 6.7. The

Table 6.7: The parameters for fits to the La–O correlation in the glasses (errors are not given, because these values are essentially estimates). $\bar{r}$ is the average La–O bond length. Σn is the total La–O coordination number over all components of the fit. Σ is the total La valence over all components of the fit.

Glass sample	r_{LaO} / Å	u_{LaO} / Å	n_{LaO}	Valence
20LaBG	2.22	0.06	0.40	0.35
	2.54	0.13	7.42	2.77
	$\bar{r} =$ 2.52		$\Sigma n =$ 7.82	$\Sigma =$ 3.11
25LaBG-1	2.25	0.05	0.19	0.16
	2.52	0.13	7.10	2.75
	$\bar{r} =$ 2.52		$\Sigma n =$ 7.30	$\Sigma =$ 2.91
25LaBG-2	2.27	0.05	0.17	0.13
	2.53	0.13	6.75	2.58
	$\bar{r} =$ 2.52		$\Sigma n =$ 6.92	$\Sigma =$ 2.71
30LaBG-1	2.52	0.14	7.36	2.84
30LaBG-2	2.54	0.14	7.53	2.77

La–O bond lengths are typically 2.52 Å, whilst the values obtained for the total La–O coordination number vary haphazardly around a mean value of 7.4. The variation in values for n_{LaO} is probably an indication of the limit of reliability of this method of estimating the correlation, but nevertheless the valence values are close to the formal valence of La^{3+}, indicating that the results are reasonable. The values obtained for n_{LaO} are consistently smaller than the value of 8.2 obtained for the crystal using the same method (Table 6.6). The values obtained for the average La–O bond length ($\bar{r}$ in Table 6.7) are also consistently shorter than the average value for crystalline $LaBGeO_5$, 2.605 Å [78], as is expected for a smaller coordination number [258].

In crystalline $LaBGeO_5$ [78], there is one short O–O distance of 2.766 Å in the La coordination shell for a pair of oxygen that are not in the same borate or germanate

unit. This possibility has not been included in the preceding analysis, but it is worth noting that if the La–O coordination number in the glasses is smaller than in the crystal then the oxygen around a La atom are not packed as closely and hence such a short O–O distance may be less likely than in the crystal, and furthermore its statistical weight is small even for the crystal structure.

La–O coordination numbers and bond lengths in crystal structures show a wide variability; the bond lengths are usually in the range 2.3 Å to 2.9 Å, with coordination numbers varying from 7 to 12 [177, 219, 262, 263], though values as low as 6 have been observed [264]. In lanthanum borate and germanate crystals, coordination numbers from 7 to 10 are usually found [265, 266], with mean bond lengths from 2.54 Å to 2.66 Å. La–O bond lengths as short as those we have observed in the range 2.2 Å to 2.3 Å (Tables 6.6 and 6.7) have not previously been reported in crystal structures, and merit future investigation.

To summarize, while the difficulty in precisely determining the composition of our samples results in some uncertainty in our quantitative results, the general reliability of neutron diffraction allows us to make the following structural conclusions:

1. High-coordinate germanium, in the form of [GeO_5] and/or [GeO_6], is present in all lanthanum-containing glasses.

2. The fraction of germanium in the form of [GeO_5] and/or [GeO_6] is substantial, between 20 % to 40 % in most glass samples.

3. The lanthanum-oxygen coordination number in the $LaBGeO_5$ glass is lower than that of the crystal.

6.6.3 Density, T_g, and Molar Volume

The variation in the glass transition temperature of the samples is very small, and not clearly related to any individual composition or structural parameter (Table 6.1). The glass transition temperature increases as the B–O coordination number decreases. This trend is contrary to what would be expected in binary alkali borate glass, where T_g reaches a maximum at approximately the same composition as n_{BO}, and either decreases or remains constant as n_{BO} continues to decrease [267, 268]. The behaviour

is also different from binary lanthanum borate glasses, which experience a maximum in T_g at about 25 mol% La_2O_3 [238]. The glass transition temperatures of the lanthanum borogermanate system are of similar magnitude to those of the binary lanthanum borate glasses. The binary lanthanum germanate glass composition is not well-studied, and reported composition ranges have lanthanum concentrations significantly lower than present in this work [269]. However, given the substantially higher field strength of the lanthanum cation compared to alkali or alkaline earth cations, and given the significantly narrower glass-forming region of this composition, it is unlikely that we would observe behaviour substantially similar to these simpler compositions.

The comparison of the molar volumes of the lanthanum-free glass and the lanthanum-bearing glasses is worth noting (Table 6.1). The addition of lanthanum significantly reduces the molar volume of the 20LaBG glass compared to the 0LaBG composition. The molar volume increases as the lanthanum content of the glass increases. As there is no observed trend of n_{GeO} with composition, the most plausible explanation for this change is the decrease in n_{BO} as $[La_2O_3]$ increases.

6.6.4 Electrostatic Bond Strength Analysis

The ^{11}B NMR and neutron diffraction data above suggest certain bonding arrangements: the presence of $[B\emptyset_4]^-$ and $B\emptyset_2O^-$; the presence of non-bridging oxygen on GeO_4 tetrahedra; the presence of high-coordinate germanium; and a mean lanthanum-oxygen coordination number of ∼7.4. We turn to EBS analysis to attempt to model the lanthanum borogermanate glass network [258, 270]. In EBS analysis, we consider the electrostatic bond strength, s, for each cation and coordination. s is defined as z/n, where z is the formal charge of the cation and n is the number of coordinated anions (in this case oxygen). Likely oxygen environments are those for which the summation of the s values of its neighbours is *close* to 2, the magnitude of the formal charge of oxygen. In our analysis we consider *close* to mean EBS sums (Σ) ranging from 1.8 to 2.2, *i.e.*, ±10 % of the formal charge. This can somewhat account for varying bond lengths and angles, which are not considered in this simple model [271, 272]. We also restrict oxygen to no more than 4 nearest neighbours, as numbers greater than this are geometrically unlikely in lanthanum oxide-based materials. Given the local structural units that we have observed experimentally, we can provide reasonable

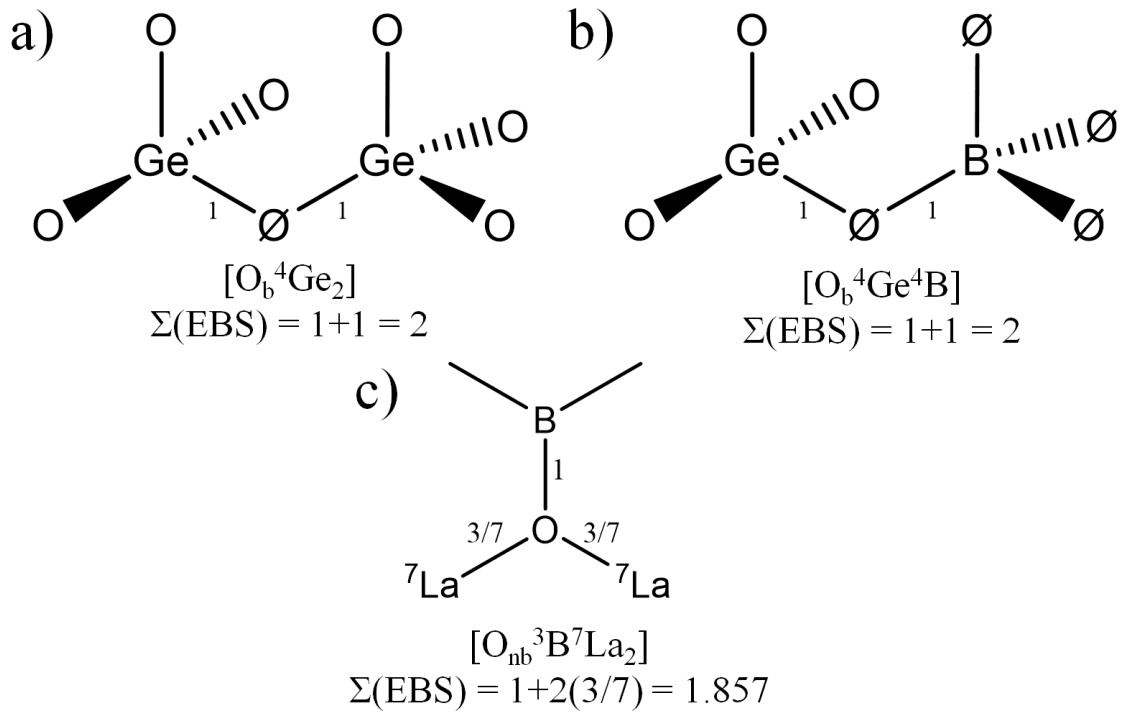

Figure 6.19: Examples of the EBS analysis and the notation being used to describe oxygen sites. a) $[O_b{}^4Ge_2]$: a bridging oxygen connecting two GeO_4 units; b) $[O_b{}^4Ge^4B]$: a bridging oxygen connecting a GeO_4 unit and a $[B\emptyset_4]^-$ unit; c) $[O_{nb}{}^3B^7La_2]$: a non-bridging oxygen connected to a $B\emptyset_2O^-$ unit and two lanthanum with n_{LaO}= 7.

estimates as to EBS values. We first consider the values of s for each network forming species. The boron and germanium values are straightforward to calculate, given the limited range of available coordination numbers. Although La may occur with a range of possible coordination numbers, the range in s values is actually rather small. For the likely n_{LaO} range from 7 to 9, the change in s for La–O bonds is from 0.43 to 0.33; hence, even large changes in the lanthanum-oxygen coordination number have smaller changes in s compared to those for boron or germanium. In the notation we use, superscript prefixes denote coordination number, while subscript suffixes indicate the number of atoms of the given coordination present in the oxygen environment. O_b and O_{nb} indicate bridging and non-bridging oxygen, respectively. For example, $[O_b{}^4Ge_2]$ describes a bridging oxygen environment coordinated to two GeO_4 units (see Fig. 6.19a). For the purposes of this analysis, any oxygen bonded to only one B atom, or to only one Ge atom, is considered to be non-bridging.

There are many possible combinations of bonding environments to be considered. Some are perfectly charge-balanced in the absence of lanthanum, such as $[O_b^4Ge_2]$, $[O_b^3B_2]$, or $[O_b^3B^4Ge]$. Most others require coordination to at least one lanthanum ion for effective charge compensation. In Table 6.8 we present the Σ values for the potential bonding environments in a lanthanum borogermanate glass. While it is difficult to say which of these environments would be more or less likely on EBS analysis alone, it is notable that a very wide range of environments are plausible. $[B\emptyset_4]^-$ units can plausibly be bridged to BO_3 units, or to any of GeO_4, $[GeO_5]^-$, or $[GeO_6]^{2-}$. The germanium bonding units are similarly versatile. This view is similar across all plausible values of n_{LaO}. There are very few potential environments that can be excluded through the use of EBS analysis; nevertheless it is of note that a $[O_b^3B^4B^6La]$ oxygen site would be substantially overbonded, with $\Sigma = 2.25$. As ^{11}B MAS NMR suggests the presence of $B\emptyset_2O^-$ in the second coordination sphere of $[B\emptyset_4]^-$, this suggests that the minimum La–O coordination number is greater than 6, consistent with the neutron diffraction analysis. It is worthwhile to note that there are a few plausible oxygen environments that meet our criteria above that are bonded to three network-forming cations, but require no lanthanum for charge compensation. All of these environments, *e.g.*, $[O_b^6Ge_3]$, require the presence of either $[GeO_5]^-$, $[GeO_6]^{2-}$, or both. While we cannot probe the oxygen environment directly in this experiment, the presence of such "three-coordinate oxygen" would provide additional evidence of the presence of high-coordinate germanium.

EBS analysis is of most use to us in discussing the possible environments around the non-bridging oxygen. Table 6.9 contains the EBS sums for several likely values of n_{LaO}. We discount the possibility of non-bridging oxygen on four-coordinate boron, as this structure has not been generally observed [20]. The non-bridging oxygen on BO_3 and GeO_4 species is considered equivalent in EBS analysis, as both have s values of 1. There are plausible non-bridging oxygen configurations for all values of n_{LaO} between 7 to 9. All configurations require at least two O–La bonds (*e.g.*, $[XO_{nb}^7La_2]$) with the higher coordination numbers ($n_{LaO} \geq 8$) requiring three. In the $LaBGeO_5$ crystal, detailed at the bottom of Table 6.9, each non-bridging oxygen is a corner of the $Ge\emptyset_2O_2^{2-}$ tetrahedron shared with two LaO_9 polyhedra. However, according to the EBS analysis, these non-bridging oxygen are substantially underbonded in the

Table 6.8: Electrostatic bond strengths of various bridging oxygen environments in lanthanum borogermanates. The n_{LaO} which results in a value of Σ closest to 2 is included for applicable environments.

O Site	Σ without La / EBS	Best n_{LaO}	Σ with best n_{LaO} / EBS
$[O_b{}^4B_2{}^6Ge]$	2.167		
$[O_b{}^5Ge_2{}^6Ge]$	2.133		
$[O_b{}^4B^6Ge_2]$	2.083		
$[O_b{}^6Ge_3]$	2.000		
$[O_b{}^3B_2]$	2.000		
$[O_b{}^3B^4Ge]$	2.000		
$[O_b{}^4Ge_2]$	2.000		
$[O_b{}^3B^6Ge]$	1.667	9	2.000
$[O_b{}^4Ge^6Ge]$	1.667	9	2.000
$[O_b{}^5Ge_2]$	1.600	8	1.975
$[O_b{}^4B^5Ge]$	1.550	7	1.979

crystal. In practice, this apparent underbonding is avoided mainly by a shortening of the relevant La–O bonds, so that their valence is increased [257]. The analysis in Table 6.9 implies that non-bridging oxygen in the glass are coordinated to either two or three lanthanum ions, and our estimate that the mean La–O coordination number is ∼7.4 implies that a NBO–La coordination number of two is the most common. Furthermore, our observation of a small number of very short La–O bonds suggests the possibility of a small number of non-bridging oxygen that are bonded to only one La^{3+} ion.

Table 6.9: Electrostatic bond strengths of various non-bridging oxygen environments. Sites are arranged in order of $|2-\Sigma|$. Superscript prefixes indicate coordination number, while subscript suffixes indicate the number of a given species. X indicates either ^{4}Ge or ^{3}B; the electrostatic bond strength of their non-bridging oxygen environments are the same. Non-bridging oxygen on ^{5}Ge or ^{6}Ge are not included in the table. The site at the bottom of the table corresponds to the non-bridging oxygen environment in crystalline $LaBGeO_5$.

O Environment	Σ / EBS	Number of La^{3+}
$[XO_{nb}{}^9La_3]$	2.000	3
$[XO_{nb}{}^8La_3]$	2.125	3
$[XO_{nb}{}^7La_2]$	1.857	2
$[^4GeO_{nb}{}^9La_2]$	1.666	2

The EBS analysis, when combined with the ^{11}B MAS NMR, MQMAS NMR, and neutron diffraction data, implies a reasonably homogeneous glass structure. All three-coordinate boron is in the form of $B\emptyset_2O^-$, implying a substantial level of connectivity within the glass network. All four-coordinate boron is in proximity to lanthanum, and the change in the δ_{iso}^{CS} of the $[B\emptyset_4]^-$ peak suggests that $[B\emptyset_4]^-$ may be connected to $B\emptyset_2O^-$, in which case there may be an interconnected boron network. The presence of interconnected $[B\emptyset_4]^-$ and $B\emptyset_2O^-$ also suggests a mean value of n_{LaO}>6, according to our EBS analysis. The amount of positive charge introduced into the system by the addition of La_2O_3 is insufficiently compensated by the observed boron species. Our neutron diffraction data indicate that germanium polyhedra compensate for this remaining charge via a combination of non-bridging oxygen and coordination numbers greater than four. Since the bond strengths for Ge and B are similar, there is nothing in the EBS analysis that precludes mixing of the two elements at the microscopic level, leading to a homogeneous structure. This is consistent with the work of Lee *et al.* [53], who reported no indications of network segregation in B_2O_3–GeO_2 glasses. Despite the potential for the addition of a modifier oxide (such as La_2O_3) to promote either liquid-liquid phase separation or crystallization, our EBS analysis is consistent with a homogeneous network.

6.7 Conclusions

$LaBGeO_5$ is of importance as a ferroelectric nanocomposite, which crystallizes isochemically from a glass of the same composition. A knowledge of the differences and similarities between the $LaBGeO_5$ glass and crystal structures is important for determining the underlying mechanism of formation of the $LaBGeO_5$ transparent ferroelectric nanocomposite material. We have performed both ^{11}B MAS NMR and neutron diffraction measurements on lanthanum borogermanate glasses and crystalline $LaBGeO_5$, combined with electrostatic bond strength analysis, allowing us to construct a coherent structural model of the lanthanum borogermanate glass system. These NMR spectra show the presence of both three- and four-coordinate borate units, and suggest the significant presence of the $[O_b{}^3B^4B^nLa]$ oxygen environment, *i.e.*, that the three- and four-coordinate borate units are frequently neighbours. ^{11}B MQMAS spectra support a model where there are only single types of three- and four-coordinate

environments, and that all BO_3 is in the form of $B\emptyset_2O^-$, *i.e.*, singly-nonbridging trigonal borate units. Our REDOR results support the presence of both BO_3–$[B\emptyset_4]^-$ and $[B\emptyset_4]^-$–$[B\emptyset_4]^-$ connections, and that they exist in similar proportions. This suggests that the borate network does not preferentially group together similar bonding units. Neutron diffraction data provide evidence for the presence of a significant fraction of germanium atoms with a coordination number greater than four, as either $[GeO_5]^-$, $[GeO_6]^{2-}$, or a combination of both, as well as the presence of non-bridging oxygen on the germanium tetrahedra. A detailed modelling approach is shown to work well for the longer range region (∼2.2 Å to 2.75 Å) of the neutron correlation functions of La-free glass and crystalline $LaBGeO_5$. This approach is applied to the glass correlation functions, leading to an estimate of 7.4 for the La–O coordination number, with a typical La–O bond length of 2.52 Å. Our EBS analysis suggests the presence of multiple La^{3+} ions in proximity to non-bridging oxygen sites, as well as a high degree of flexibility in network former mixing. It also constrains the $[O_b^3B^4B^nLa]$ environment to values where n is 7 or greater, and hence the mean lanthanum-oxygen coordination number is greater than 6.

The structure of the $LaBGeO_5$ glass composition differs substantially from the $LaBGeO_5$ crystal; the average oxygen coordination numbers of all three cations are different from the crystal. Furthermore, the composition-dependence of the boron and germanium coordination numbers provides evidence that both boron and germanium undergo an anomaly.

6.8 Acknowledgements

Financial support from NSERC (Canada Grant Number RGPIN 261987) is gratefully acknowledged. We thank Dr. Mark Obrovac and Dr. Daniel Boyd of Dalhousie University for access to an X-ray diffractometer and helium gas pycnometer, respectively.

Chapter 7

Network Connectivity and Crystallization in the Transparent Ferroelectric Nanocomposite Material $LaBGeO_5$

7.1 Context

Through the use of ^{11}B MQMAS and neutron diffraction (Chapter 6) we have established the local structure of the La, B, and Ge components of the $LaBGeO_5$ glass. However, determining the local order is only part of constructing a model of the structure of the glass. After establishing which short-range bonding units are present (*i.e.*, $B\emptyset_2O^-$, $[B\emptyset_4]^-$, GeO_4, $^{5/6}Ge$, and on average LaO_7), the next step is to determine how these units are connected. The techniques used in previous chapters are ill-suited to determine glass network connectivity, especially in the structurally complex $LaBGeO_5$ system. Hence we turn instead to ^{17}O NMR spectroscopy and $^{11}B\{^{10}B\}$ REDOR NMR spectroscopy.

^{17}O MAS and MQMAS NMR is an obvious choice for probing network connectivity in oxide glasses, as all glass structural units are cation-oxygen polyhedra. The ^{17}O NMR spectra we present in this chapter provide significant data on the presence (and absence) of various network connectivities, but, as will be discussed, the spectral resolution is limited. As a complementary technique we turned to $^{11}B\{^{10}B\}$ REDOR NMR spectroscopy, which probes the connectivity between $[B\emptyset_4]^-$ units and both BO_3 and $[B\emptyset_4]^-$ units. With the overall connectivity data from our ^{17}O NMR spectra, and the borate-specific connectivity from our $^{11}B\{^{10}B\}$ REDOR NMR spectroscopy, we can construct a model for the network connectivity of the $LaBGeO_5$ glass.

This chapter also examines the crystallization of the $LaBGeO_5$ glass-ceramic. ^{17}O NMR is equally effective in crystals and in glasses, and as such it is particularly well-suited for the study of glass-ceramic composites. Through the use of ^{17}O NMR, along with pXRD and ^{11}B and ^{139}La NMR, we probe potential structural changes in either the crystalline or glass forms of $LaBGeO_5$ during the crystallization of the

$LaBGeO_5$ glass.

This chapter was originally prepared for submission in The Journal of Physical Chemistry C. The contributions of the authors to the text are as follows. ALP synthesized all of the experimental samples, conducted all of the experiments and DFT calculations, performed the analysis of the data, and wrote the manuscript. UWZ provided significant technical support with the optimization of the ^{17}O and $^{11}B\{^{10}B\}$ REDOR NMR spectroscopy, assisted in the evaluation of the ^{17}O and $^{11}B\{^{10}B\}$ REDOR data, and provided editorial contributions to the manuscript. JWZ provided significant contributions to the experimental design and substantial editorial contributions to the manuscript.

7.2 Abstract

The $LaBGeO_5$ glass-ceramic composite is a TFN material that has come under attention for its ferroelectric properties, and for its straightforward synthesis. The $LaBGeO_5$ crystals-in-glass can be formed through controlled devitrification of the glass, as well as through laser irradiation. While previous structural models of the glass have been reported, they have only considered differences in the borate environment between the glass and the crystal. We present here a comprehensive NMR study of the short-range order of crystalline $LaBGeO_5$ and $LaBGeO_5$ glass. Through a combination of ^{11}B, $^{11}B\{^{10}B\}$, ^{17}O, and ^{139}La NMR spectroscopies we identify specific structural motifs in the glass. In particular, structures not present in the crystal (*e.g.*, $B\emptyset_2O^-$, $B\emptyset_2O^-$–$[B\emptyset_4]^-$, GeO_6) are positively identified in the glass. We present evidence in support of the presence of both $^{5/6}Ge-O-{}^{4}Ge$ and $^{5/6}Ge-O-B$ structures, as well as the possibility of O_{666} triclusters. Quantitative ^{11}B and ^{17}O MAS NMR spectroscopies provide data in support of a revised equation to determine the crystallization fraction of a partially cerammed sample via moderate-field ^{11}B NMR spectroscopy.

7.3 Introduction

Ferroelectric glass-ceramics are composite materials in which a ferroelectric crystalline phase is nucleated within a glass matrix. One example of a ferroelectric glass-ceramic is the $LaBGeO_5$ composition. As the $LaBGeO_5$ glass can be congruently

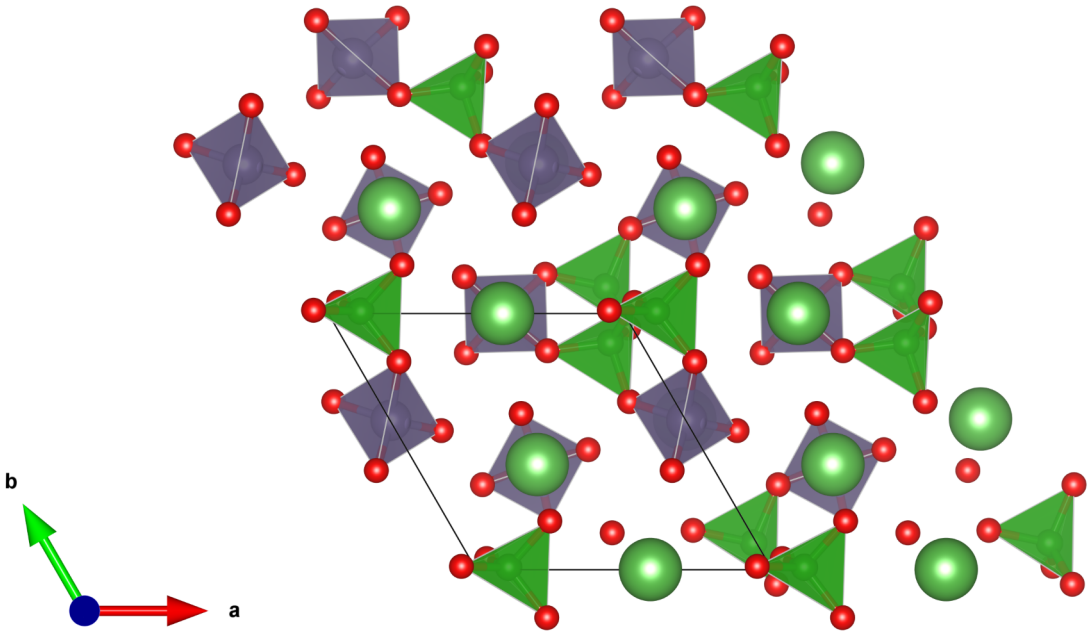

Figure 7.1: The room-temperature crystal structure of $LaBGeO_5$ [78]. The presented view is down the crystallographic c axis. The unit cell is indicated by black lines; a 2×2×2 supercell is shown in order to highlight the helical $[B\emptyset_4]^-$ chain at the centre. $[B\emptyset_4]^-$ tetrahedra are coloured dark green, while $Ge\emptyset_2O_2^{2-}$ tetrahedra are purple. LaO_9 polyhedra are omitted for clarity. Lanthanum ions are light green.

(*i.e.*, isochemically) crystallized, it has become a particular target for investigation into transparent ferroelectric nanocomposite materials. Many different compositions (*e.g.*, $LiNbO_3$, $BaTiO_3$) can produce glass-ceramics that are transparent (*i.e.*, with crystals with diameters less than the wavelength of visible light) with ferroelectric crystallites [273, 274]. However, many of these compositions produce multiple distinct crystalline phases upon devitrification, complicating their characterization and analysis. The apparently simple crystallization behaviour of $LaBGeO_5$ has made it the target of many investigations. The $LaBGeO_5$ crystal has been well-characterized, with its structure (Fig. 7.1) [78, 79], second-harmonic generation efficiency [232, 233], ferroelectric moment [88], and Curie temperature [88, 233, 275] having been reported in the literature. Similar efforts have been undertaken with regards to the glass and glass-ceramic composite, and various physical properties of both have been reported [96]. Recently, laser-written single-crystal $LaBGeO_5$ architectures in $LaBGeO_5$ glass have

been reported [107, 108]. To fully understand the mechanism and dynamics of single-crystal formation within a glassy matrix, it is necessary to have a thorough understanding of the glass structure and how it relates to the crystal structure.

There are a number of structural studies of the $LaBGeO_5$ glass reported in the literature. In 2000, Kratochvílová *et al.* reported Raman spectra of the glass [74]. Based upon comparison to the crystal, they concluded that the structure of the glass was similar to the crystal, albeit disordered. In 2004 Gupta *et al.* reported the first NMR study of the $LaBGeO_5$ glass, presenting ^{11}B MAS NMR spectra definitively proving the presence of both BO_3 and $[B\emptyset_4]^-$ units in the glass, whereas the crystal only has $[B\emptyset_4]^-$ units [34]. Sigaev *et al.* revisited the Raman spectrum of $LaBGeO_5$ in 2010, concluding that their data confirmed the presence of BO_3, but also that all other structural units were unchanged from the crystal [75]. Further, they concluded that the $LaBGeO_5$ glass is composed of "crystal-like" nanoregions, where the boron is fourfold coordinate, connected by regions where the boron is threefold coordinated.

The above studies neglect to consider possible structural changes in either the germanium or lanthanum environments. Five- and six-coordinate germanium-oxygen polyhedra are known to form in germanate crystals, and have been shown to be present in alkali and alkaline-earth germanate glasses [12, 28, 55, 62]. Via neutron diffraction, we have shown that high-coordinate germanium is present in lanthanum borogermanate glasses [212]. This dramatic change in the germanium environment between the glass and the crystal suggests the possibility of radically different glass and crystal structures, on both the short-range and intermediate-range connectivity. However, only the short-range order of the $LaBGeO_5$ glass has been studied. NMR spectroscopy offers the possibility of probing the connectivity between structural units, including between high-coordinate germanate units.

We present here a study of the structural differences between the glass and crystal phases of the boron, germanium, and lanthanum local environments through a combination of ^{11}B, $^{11}B\{^{10}B\}$, ^{17}O, and ^{139}La NMR spectroscopies. ^{11}B NMR spectroscopy is a mature technique for the study of borate glasses [49, 276, 277]. $^{11}B\{^{10}B\}$ REDOR experiments can probe the connectivity of the borate network in borate glasses [52]. ^{139}La NMR spectroscopy has become more accessible with the advent of the WCPMG pulse sequence [126], but no comprehensive model of

the relationship between glass spectra and properties has yet been reported in the literature. ^{17}O NMR spectroscopy is a very powerful technique for the study of oxide glass structure, and has previously been used to establish the presence of high-coordinate germanium in sodium germanate glasses [54–56]. ^{73}Ge NMR studies of glass are not generally considered to be feasible, as previous attempts have produced inconclusive results [25]. With this comprehensive probe into the short-range order of the glass we intend to produce reasonable constraints on the structure of the glass in order to inform future mechanistic studies of the formation of $LaBGeO_5$ glass-ceramics.

7.4 Experimental Procedures

7.4.1 Sample Synthesis

Crystalline $Ge^{17}O_2$ was synthesized by hydrolysing germanium ethoxide ($Ge(OC_2H_5$, $\geq 99.95\,\%$, Sigma-Alrich) with 40 % ^{17}O-enriched $H_2{}^{17}O$ (Cortecnet). The ethoxide and enriched water were combined under nitrogen at a molar ratio of 1:2 in a sealed container and allowed to react for 3 d. The product was then heated to 350 °C under nitrogen for approximately 3 d for improved crystallinity. The identity of the crystalline product was confirmed to be trigonal (quartz structure) GeO_2 via pXRD. Crystalline $H_3B^{17}O_3$ was synthesized by hydrolysing a 1 mol dm^{-3} solution of borane tetrahydrofuran (THF) ($BH_3OC_4H_8$, Sigma-Aldrich) with 40 % ^{17}O-enriched $H_2{}^{17}O$. The enriched $H_2{}^{17}O$ was slowly added to 0 °C borane THF solution under dry nitrogen atmosphere. Excess THF and evolved hydrogen gas were removed under vacuum. The final polycrystalline product was verified to be H_3BO_3 via both pXRD and ^{11}B MAS NMR spectroscopy. $LaBGeO_5$ glass was synthesized by combining stochiometric amounts of the enriched $Ge^{17}O_2$ and $H_3B^{17}O_3$ powders with La_2O_3 (99.99 %, Sigma-Aldrich), thoroughly grinding the mixture in a mortar and pestle, and then melting the mixture in a 95/5 Pt/Au crucible at 1250 °C in a box furnace in air. The melt was quenched by pouring it onto a brass plate preheated to 400 °C. Partially crystallized samples were produced by placing the powdered sample in a furnace pre-heated to 765 °C for short lengths of time (approx. 4 min). Observations (*i.e.*, pXRD, NMR) were taken, and afterwards the sample was returned to the furnace for further crystallization. ^{17}O NMR spectra were collected when sufficient crystallization was observed in the

powder via ^{11}B MAS NMR. Reported samples are labelled LBG-G, for the original glass, and LBG+8, LBG+12, LBG+24, and LBG+60, where the number in the label is the total time spent crystallizing, in minutes. An additional sample was prepared by heating the LBG+60 sample for an additional 3 d; this further increased the crystal fraction, but removed the ^{17}O, preventing the collection of ^{17}O NMR spectra. This sample is labelled LBG+3d. LaB_3O_6 crystal powder was synthesized by combining stoichiometric amounts of La_2O_3 and B_2O_3 and heating in a platinum crucible for 12 h at 850 °C. $LaBGeO_5$ samples were produced with natural abundance reagents (La_2O_3 (99.99 %), GeO_2 ($\geq$ 99.99 %), B_2O_3 ($\geq$ 98 %), all from Sigma Aldrich) for ^{11}B{^{10}B} NMR experiments, but otherwise followed the synthesis described above.

7.4.2 Sample Characterization

PXRD was carried out using a Rigaku Ultima IV X-ray diffractometer equipped with a copper anode X-ray tube, a diffracted beam monochromator, and a scintillation detector. Diffractograms were collected from finely-ground samples in air at room temperature. 2θ was incremented with steps of 0.05° and a 2 s dwell time. Density of the glass sample was measured using Archimedes' method, using absolute ethanol as the working fluid. Density measurements were controlled for variations in temperature.

7.4.3 Nuclear Magnetic Resonance Spectroscopy

^{11}B MAS NMR spectra were collected on a 16.4 T (224.63 MHz ^{11}B frequency) Bruker Avance NMR spectrometer. Spectra were collected at a spinning speed of (25 000 $\pm$ 5) Hz using a 2.5 mm ZrO_2 rotor. Single pulses of 0.54 µs duration (15° tip angle, ν_{rf} = 77 kHz) and an optimized recycle delay of 5 s were used to ensure quantitative excitation. 512 scans were collected for each sample. ^{11}B background from the probe was subtracted from the experimental spectrum after careful phasing and intensity adjustment. Probe background spectra were collected immediately following the collection of sample spectra, using the same experimental conditions. ^{11}B chemical shifts were referenced to solid $NaBH_4$, with a resonance at $-$42.1 ppm relative to the primary shift reference ($BF_3 \cdot Et_2O$, 0 ppm) [159].

^{10}B MAS NMR spectra were collected on a 16.4 T (75.24 MHz ^{10}B frequency) Bruker Avance NMR spectrometer. Spectra were collected using a HXY 3.2 mm

probehead operating in HX mode. ^{10}B Hahn echo spectra were collected at a spinning speed of $(10\,000 \pm 5)$ Hz to allow for the observation of many spinning sidebands. Pulse lengths for the $\pi/2$ and π pulses were optimized to be 6 µs and 10 µs. Spectra were collected using a 20 s recycle delay and 256 scans.

^{17}O MAS and triple quantum magic angle spinning (3QMAS) NMR spectra were collected on both 9.4 T (54.24 MHz ^{17}O frequency) and 16.4 T (94.91 MHz ^{17}O frequency) Bruker Avance NMR spectrometers. All spectra were collected at a spinning speed of $(14\,000 \pm 5)$ Hz using 4 mm ZrO_2 rotors. MAS spectra at 16.4 T were collected using single pulses of 0.52 µs duration (10° tip angle, $\nu_{rf} = 53$ kHz) and optimized relaxation delays of 0.5 s. MAS spectra at 9.4 T were collected using single pulses of 0.83 µs duration (12° tip angle, $\nu_{rf} = 40$ kHz). ^{17}O MAS spectra generally required between 8192 and 16384 scans to yield spectra of sufficient quality.

3QMAS spectra were collected using a three-pulse sequence with full echo acquisition [240]. Split-t_1 spectra at 16.4 T were collected using optimized excitation and conversion pulses of 6.0 µs and 1.5 µs ($\nu_{rf} = 53$ kHz) and a 22 µs 180° selective pulse ($\nu_{rf} = 22$ kHz). The same parameters were used for crystalline and glassy samples. 24 slices in the F1 dimension were collected, with 1152 transients per slice. All ^{17}O NMR spectra were referenced to tap water (0 ppm). The 3QMAS spectra were referenced using the C_z convention [134, 241].

Static ^{139}La spectra were collected at 16.4 T (98.91 MHz ^{139}La frequency) and 9.4 T (56.52 MHz ^{139}La frequency) using the WCPMG pulse sequence [129]. The WCPMG sequence combines WURST [124] shaped pulses with the CPMG signal enhancement protocol [130, 131]. 50 µs WURST-80 pulses were swept over 500 kHz at a rate of 10 MHz ms^{-1}. Between 100 and 200 echoes were collected per transient, depending on the spin-spin relaxation time (T_2) of the sample. Due to the breadth of the peaks, spectra were collected piecewise by moving the transmitter in increments of 100 kHz, *i.e.*, VOCS collection [127, 128]. Each subspectrum was collected by coadding 512 transients, with an optimized relaxation delay of 0.5 s. ^{139}La spectra were referenced to a 1 mol dm^{-3} solution of $LaCl_3$ (0 ppm).

^{11}B{^{10}B} REDOR spectra were collected using the conventional pulse sequence [140]. Spectra were collected using a 3.2 mm HXY probehead, with ZrO_2 rotors spinning at $(10\,000 \pm 5)$ Hz. REDOR experiments were conducted on a sample with natural

abundance oxygen. ^{11}B $\pi/2$ and π pulses were set to 3.10 µs and 6.25 µs and were optimized to provide a reasonable balance between optimum excitation for the BO_3 and $[B\emptyset_4]^-$ environments. ^{11}B pulses were optimized using Hahn echo experiments. ^{10}B π pulses were optimized via maximizing the REDOR difference, resulting in a 12.5 µs pulse length. REDOR pulse powers were 80 kHz for ^{11}B and 40 kHz for ^{10}B. Recycle delays were optimized via spin-lattice relaxation (T_1) saturation recovery experiments, and were set to five times the longest T_1 observed in a given sample. These delays ranged from 50 s to 225 s. The number of scans collected varied depending on the sample, and ranged from 8 to 48.

Spectra of all nuclides studied were fitted using the INT2QUAD module of the DMFIT 20150521 [184] software package. Fits were broadened using Lorentzian functions for crystalline environments, and Gaussian functions for amorphous environments. The glass components of ^{139}La spectra were fitted using the Czjzek distribution [135, 136, 139], which is discussed in more detail below.

7.4.4 Density Functional Theory Calculations

First-principles DFT calculations were performed using the QUANTUM ESPRESSO code (https://www.quantum-espresso.org/), version 5.1.3 [162, 163]. In order to calculate NMR observables, the GIPAW method as implemented in version 5.1 of the QE-GIPAW package was used [156, 157]. Custom PAW datasets using the PBE exchange and correlation functional [192], based upon the JTH set [191], were constructed to avoid the issue of PAW sphere overlap [155]. PAW datasets were generated using ATOMPAW [165]. An optimized plane-wave cutoff energy of 60 Rydberg was used with a shifted $6 \times 6 \times 6$ Monkhorst-Pack k-point grid. The latter corresponds to a k-point spacing of 0.025 Å^{-1}. Results from calculations on the experimental structure [78] are presented. For the EFG calculations, nuclear quadrupole moments were taken from Pyykkö [57]. To convert the chemical shielding values provided by GIPAW to experimentally-observable chemical shifts, calculated shielding values were compared to experimental shifts for known systems. Details of the conversion are reported in Appendix D.

7.4.5 Raman Spectroscopy

Unpolarized Raman spectra were collected using a Nicolet NXR 9600 Fourier-transform Raman spectrometer. A 1064 nm laser was used to excite the samples. The spectra were collected with a spectral resolution of $2\,\mathrm{cm}^{-1}$. The glass spectrum was collected by summing 256 scans at a power of 400 mW. The crystal spectrum was collected by summing 128 scans at a power of 70 mW. The glass spectrum is of a single piece of glass, while the crystal spectrum was collected from a powdered sample.

7.5 Results

7.5.1 X-Ray Diffraction

The X-ray diffraction results for LBG-G, LBG+12, and LBG+60 are shown in Fig. 7.2. The diffractogram for the glass sample, LBG-G, shows no sharp diffraction peaks, consistent with an amorphous material. The diffraction patterns of LBG+12 and LBG+60 are consistent with the diffraction pattern of $LaBGeO_5$ as reported by Rulmont and Tarte [278]. Despite the substantial difference in the level of crystallization between these two samples (*vide infra*), the diffractograms appear similar. Both show diffraction peaks from a single crystalline phase, identified as $LaBGeO_5$, though there is some slight variation in both peak intensity and position. Based on Rietveld refinement of the diffractograms (Appendix D.2), both the a and c lattice constants are somewhat lower in the partially crystallized samples than what is reported in the literature [78, 79, 278]. As amorphous materials are not effective in constructively scattering X-rays, it is expected that the crystallites will provide the majority of the pXRD signal regardless of the level of crystallization. The density of the LBG-G glass sample was found to be $(4.89 \pm 0.02)\,\mathrm{g\,cm}^{-3}$, consistent with previous literature reports on this composition [96, 212]. However, one must be cautious when comparing physical properties of the $LaBGeO_5$ glass with those in the literature, as Al_2O_3 contamination of the melt from corundum crucibles is known to be an issue [98].

7.5.2 ^{11}B NMR Spectroscopy

^{11}B MAS NMR spectra of LBG-G, LBG+12, and LBG+60 are shown in Fig. 7.3. The spectrum of the glass sample, LBG-G, has two peaks: one centred around

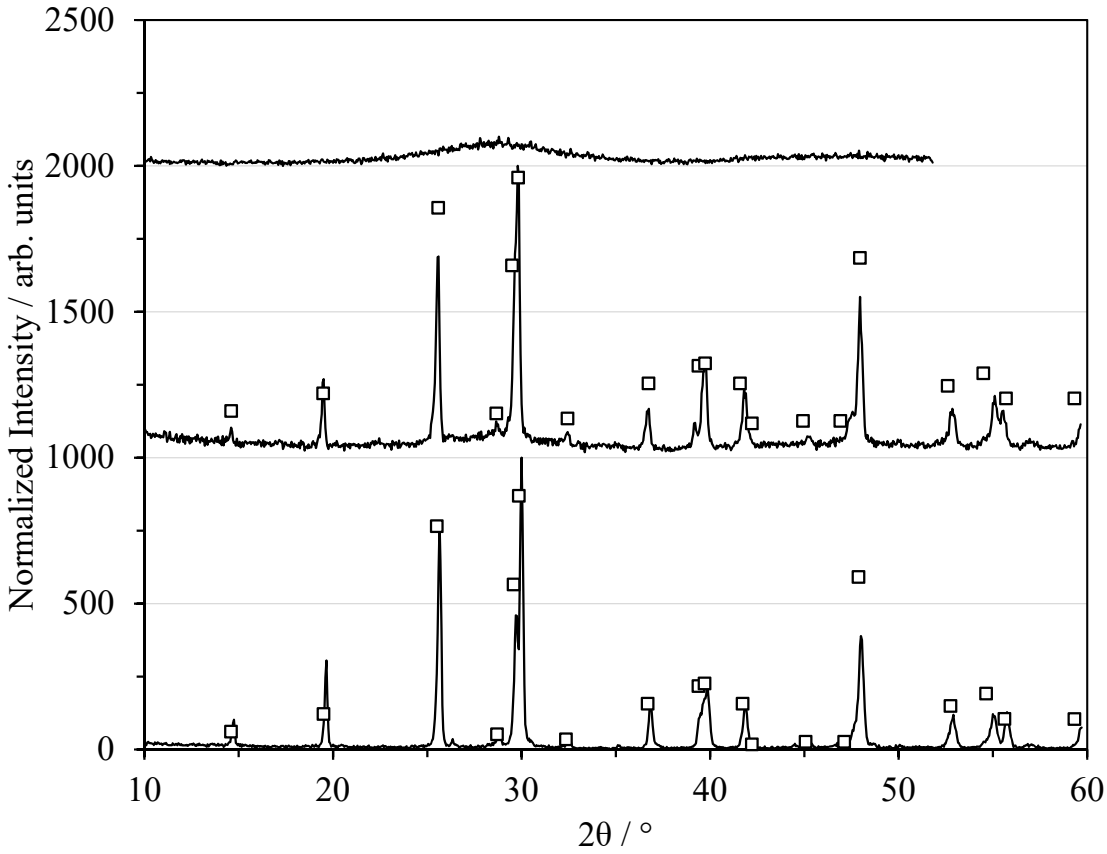

Figure 7.2: X-ray diffractograms of: glassy LBG-G, top; partially crystallized LBG+12, middle; and mostly crystallized LBG+60, bottom. Diffractograms are offset by 1000. The intensities of the LBG+12 and LBG+60 diffractograms are normalized such that the most intense peak has a value of 1000. The intensity of the LBG-G diffractogram is normalized to 100 for ease of comparison to the partially crystallized samples. The expected position and intensities of the reflections of crystalline $LaBGeO_5$ are marked with squares (PDF 41-0659) [278].

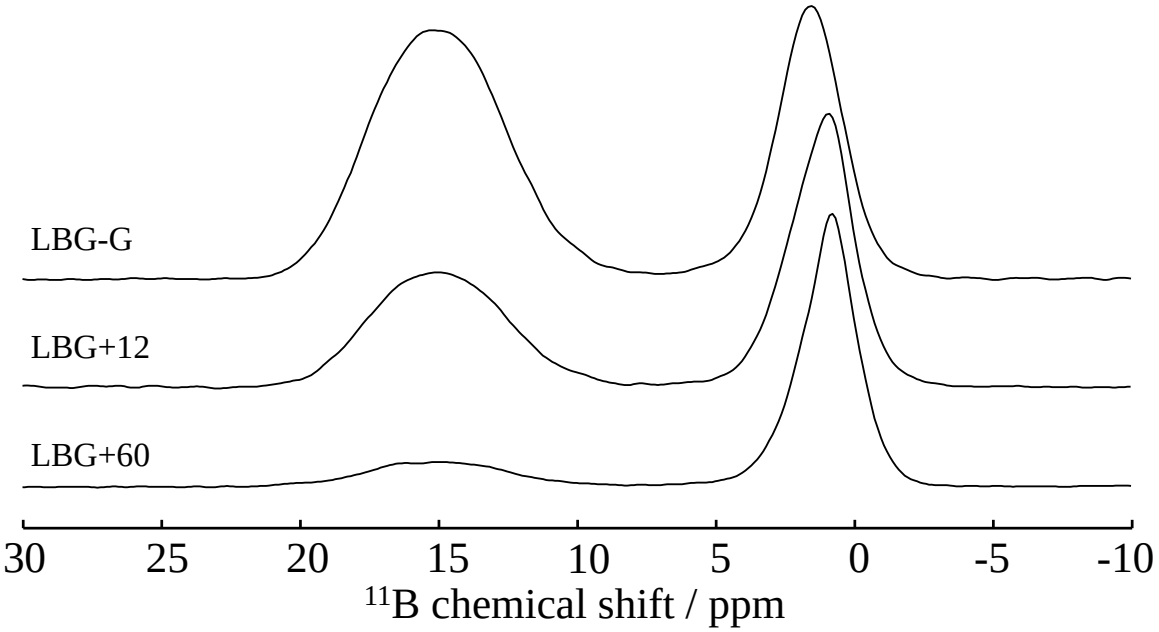

Figure 7.3: ^{11}B MAS NMR spectra of: glassy LBG-G, top; partially crystallized LBG+12, middle; and mostly crystallized LBG+60, bottom.

15 ppm, and a second peak centred around 1 ppm. The position, breadth, and relative intensity of these peaks are consistent with previous reported spectra from this composition [34, 212]. The peak centred around 15 ppm is consistent with the presence of BO_3 units, while the peak centred around 1 ppm is consistent with the presence of $[B\emptyset_4]^-$ units [51]. In order to identify the specific BO_3 species that is likely to be present, we compare the isotropic chemical shift of the observed peak to that of similar environments in crystalline samples. The isotropic chemical shift of the BO_3 peak is obtained by fitting the peak with a single quadrupolar environment, subject to Gaussian broadening. It should be noted that as ^{11}B is a quadrupolar nucleus, the isotropic chemical shift of a given peak will be somewhat more positive than its centre of gravity. The parameters used to fit the glass are reported in Table 7.1.

The chemical shift of the BO_3 peak in the glass, $\delta_{\mathrm{iso}}^{\mathrm{CS}} = (18.3 \pm 0.2)$ ppm, is consistent with the chemical shift of the $B\emptyset_2O^-$ peak in crystalline LaB_3O_6, $\delta_{\mathrm{iso}}^{\mathrm{CS}} = (17.9 \pm 0.2)$ ppm (Fig. D.5), as well with literature reports of chemical shifts of three-coordinate borate units [48]. Based upon 3QMAS spectra of lanthanum borogermanate glasses, we have previously identified this three-coordinate boron species as $B\emptyset_2O^-$ [212]. It is less straightforward to determine the precise environment of the

Table 7.1: ^{139}La, ^{10}B, ^{11}B and ^{17}O NMR parameters of environments in the glass. ^{139}La and ^{11}B values are from experiments on the LBG-G sample, and parentheses next to these values indicate experimental uncertainties. ^{17}O values are either means taken from our experiments on the $LaBGeO_5$ crystal (Table 7.2), or means taken from the literature. For experimental data, experimental uncertainties are indicated. For literature data, standard deviations are indicated.

Nucleus	Environment	3QMAS Label	δ_{iso}^{CS} / ppm	P_Q / MHz	Sources
^{139}La			$437 \pm 30^{*}$	$4.2 \pm 0.2^{**}$	
^{10}B	BO_4		0.8 ± 0.8	1.0 ± 0.4	
^{11}B	BO_3		18.3 ± 0.2	2.6 ± 0.2	
	BO_4		2.0 ± 0.3	0.8 ± 0.4	
^{17}O†					
	^{4}Ge–O–^{4}Ge	a	63 ± 12	6.7 ± 0.7	[54, 55]
	^{4}Ge–O–B	b	88 ± 5	5.2 ± 0.2	This work
	^{4}B–O–^{4}B	c	95 ± 2	6.1 ± 0.3	This work
	^{4}Ge–O–$^{5/6}$Ge	d	124 ± 30	6.5 ± 0.5	[54, 55]
	O_{666} (rutile GeO_2)	e	156 ± 6	7.35 ± 0.02	[54, 55]
	^{4}Ge–O–La	f	189 ± 4	5.2 ± 0.2	This work
	B–O–La	g	220 ‡	3 ± 1	[279]
	O_{666} ($Na_4Ge_9O_{20}$)	h	246.5 ± 0.5	3.75 ± 0.05	[55]

* This value is the position parameter of the peak, and does not correspond directly to δ_{iso}^{CS} for ^{139}La. It is expressed in ppm and corresponds to Δ_{offset} in Chapter 5, Table 5.2.

** This value is the Czjzek distribution parameter σ, not P_Q . Both are expressed in MHz. See also Chapter 5, Table 5.2.

† ^{17}O values for environments not observed in the $LaBGeO_5$ crystal are averages from literature reports. The uncertainties reported are an estimate of the precision of these values, and not an estimate of the range, which can vary.

‡ Average of the calculated δ_{iso}^{CS} values of the two B–O–La environments in $LaBO_3$.

$[B\emptyset_4]^-$ units. The chemical shift range of the $[B\emptyset_4]^-$ environment only exhibits small changes in response to changes in composition, typically on the order of 2 ppm to 3 ppm [280]. Furthermore, structural disorder in the glass results in broadening of the NMR peak, which makes observing small changes in chemical shift difficult. However there is a significant change in the position of the $[B\emptyset_4]^-$ peak between the glass and crystal spectra. The chemical shift of the $[B\emptyset_4]^-$ peak in the glass is more positive than that in the crystal, with a difference of 0.7 ppm. Our REDOR results, discussed below, provide additional insight into the changes in the $[B\emptyset_4]^-$ environment.

The spectrum of the crystalline sample, LBG+60, shows a dominant peak in the region attributed to $[B\emptyset_4]^-$ units, consistent with the crystal structure of $LaBGeO_5$ [78]. There is residual BO_3 and $[B\emptyset_4]^-$ intensity due to the glass, but the change in the symmetry and breadth of the $[B\emptyset_4]^-$ peak allows the parameters of the crystalline $[B\emptyset_4]^-$ peak to be determined. The NMR parameters of this peak are reported in Table 7.2. The chemical shift of the $[B\emptyset_4]^-$ peak in the glass is slightly more positive than that in the crystal, with a difference of 0.7 ppm.

The spectrum of a sample with intermediate crystallization, LBG+12, is a combination of the spectra of LBG-G and LBG+60. The fitted ^{11}B MAS NMR spectrum of LBG+12 is shown in Fig. 7.4. All partially crystallized samples can be fitted with three peaks: two from LBG-G and one from LBG+60. Furthermore, the ratio of $BO_3/[B\emptyset_4]^-$ in the glass, α, does not appear to change due to crystallization. The crystalline fraction of the partially crystallized samples can be determined by subtracting the spectrum of the glass, LBG-G, and integrating the residual signal, or by fitting the crystalline and glass contributions of the $[B\emptyset_4]^-$ peak directly. Other than the relative intensity of the glass component and the crystal component, no fitting parameters are required to be changed. This suggests that there are no changes to the structure of the bulk glass during crystallization, and that α can be considered to be constant for a given sample. The level of crystallization of the samples is reported in Table 7.3.

7.5.3 ^{139}La NMR Spectroscopy

^{139}La WCPMG NMR spectra of LBG-G, LBG+12, and LBG+60 are shown in Fig. 7.5. The spectrum of the most crystalline sample, LBG+60, is consistent with our previously

Table 7.2: Parameters used to fit experimental data, and parameters from DFT calculations, for ^{139}La, ^{11}B, and ^{17}O NMR of crystalline $LaBGeO_5$. Chemical shift anisotropy parameters are not reported, but generally are expected to be a minor contribution to the lineshape of the peak. For MAS and WCPMG spectra uncertainties derived from the fit are provided; for 3QMAS spectra, fundamental uncertainty due to the resolution of the experiment are provided.

	MAS or WCPMG				3QMAS		Calculated			
Site	δ_{iso}^{CS*}/ ppm	C_Q / MHz	η_Q	P_Q / MHz	δ_{iso}^{CS*}/ ppm	P_Q / MHz	δ_{iso}^{CS*}/ ppm	C_Q / MHz	η_Q	P_Q / MHz
La†	210 ± 25	85.5 ± 0.5	0.3 ± 0.2	86.7 ± 0.5			215	−87.1	0.32	−88.6
B	1.3 ± 0.2	0.8 ± 0.4	0.8 ± 0.2	0.9 ± 0.4			2	0.4	0.97	0.5
Ge‡								41.3	0.84	45.8
O1	85 ± 2	5.0 ± 0.2	0.50 ± 0.04	5.2 ± 0.2	86 ± 3	5.3 ± 0.5	111	−5.1	0.60	−5.4
O2	92 ± 2	5.0 ± 0.2	0.54 ± 0.05	5.2 ± 0.2	93 ± 3	5.4 ± 0.5	116	−5.1	0.52	−5.3
O3	186.4 ± 0.5	5.2 ± 0.1	0.22 ± 0.03	5.2 ± 0.1	185 ± 3	5.1 ± 0.5	233	−4.5	0.14	−4.5
O4	192.5 ± 0.5	5.1 ± 0.1	0.20 ± 0.03	5.2 ± 0.1	191 ± 3	5.3 ± 0.5	239	−4.6	0.19	−4.7
O5	95 ± 2	5.6 ± 0.2	0.75 ± 0.06	6.1 ± 0.3	96 ± 3	5.6 ± 0.5	98	−5.8	0.77	−6.4

* Experimental ^{139}La, ^{11}B, and ^{17}O chemical shifts are referenced to 1 mol dm^{-3} $LaCl_3$ (0 ppm), $NaBH_4$ (−42.1 ppm), and tap water (0 ppm), respectively. Details on the referencing of the chemical shifts obtained from DFT calculations are provided in Appendix D.

† ^{139}La NMR parameters are consistent with those reported in the literature [126].

‡ ^{73}Ge NMR experiments were not carried out. Calculated values are included for completeness.

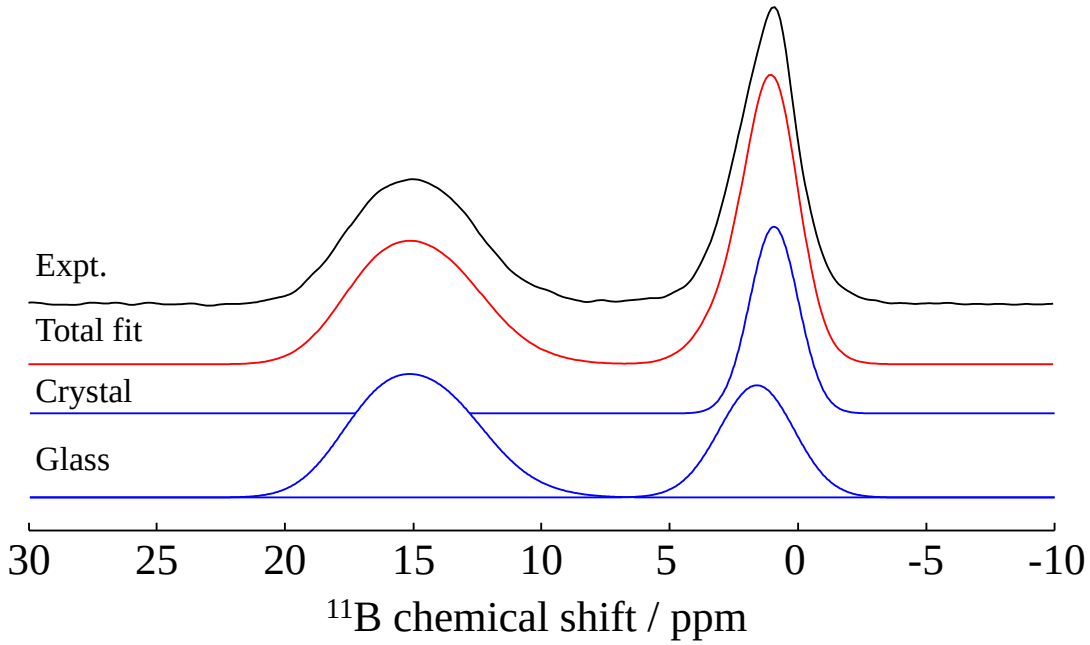

Figure 7.4: ^{11}B MAS NMR spectrum of partially crystallized LBG+12. The parameters for the crystal fit are found in Table 7.2, while the parameters for the glass fit are found in Table 7.1.

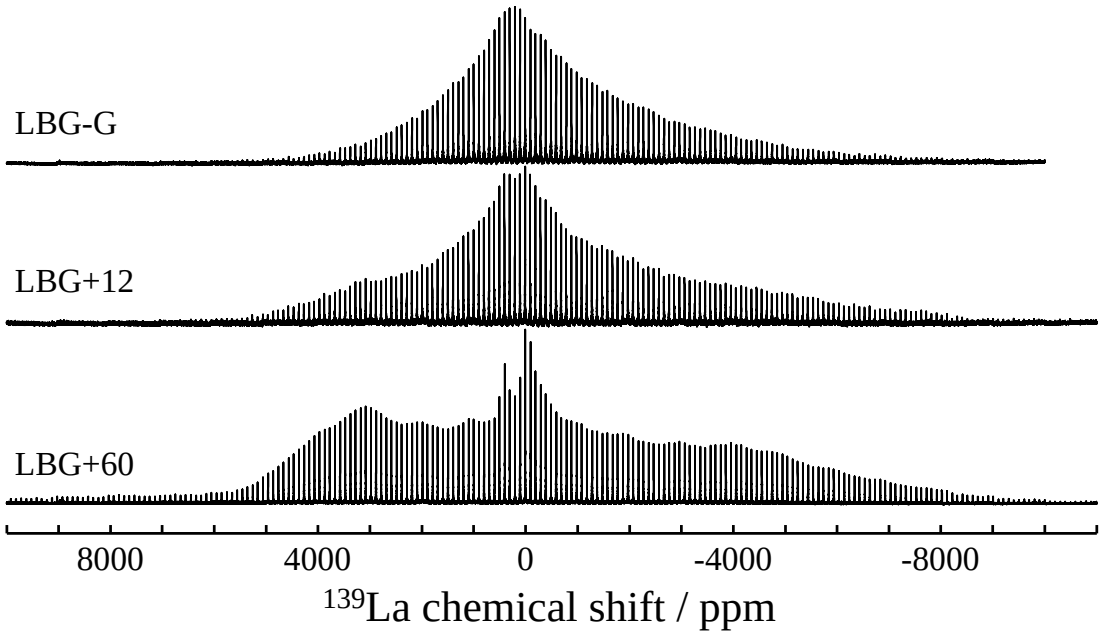

Figure 7.5: ^{139}La WCPMG NMR spectra of: glassy LBG-G, top; partially crystallized LBG+12, middle; and mostly crystallized LBG+60, bottom. As the spectra were collected using WCPMG, the signal intensity is concentrated into spikelets. The intensity envelope of the spikelets recreates the powder pattern of the static NMR spectrum.

Table 7.3: Fraction of the sample composed of $LaBGeO_5$ crystallites as determined by various means. Integrated BO_3 and $[B\emptyset_4]^-$ intensities are reported, as well as intensities determined by peak fitting. Values of c as determined by fitting ^{11}B MAS NMR and integrating ^{17}O MAS NMR data are compared to calculated values.

		Integration		Fit		c			
Sample	Time / min	$[BO_3]$	$[BO_4]$	$[BO_3]$	$[BO_4]$	^{11}B Fit	^{17}O Integration	Gupta *et al.* [34]	Eq. (7.7)
LBG-G	0	0.65 ± 0.03	0.35 ± 0.03	0.63 ± 0.01	0.37 ± 0.01	0	0	0.0 ± 0.3	0.00 ± 0.06
LBG+8	8.0 ± 0.5	0.55 ± 0.03	0.45 ± 0.03	0.54 ± 0.01	0.46 ± 0.01	0.15 ± 0.01	0.13 ± 0.05	0.3 ± 0.2	0.15 ± 0.05
LBG+12	12 ± 1	0.46 ± 0.03	0.54 ± 0.03	0.44 ± 0.01	0.56 ± 0.01	0.29 ± 0.01	0.26 ± 0.05	0.5 ± 0.2	0.28 ± 0.05
LBG+24	24 ± 2	0.34 ± 0.03	0.66 ± 0.03	0.33 ± 0.01	0.67 ± 0.01	0.48 ± 0.01	0.55 ± 0.05	0.7 ± 0.1	0.47 ± 0.04
LBG+60	60 ± 3	0.18 ± 0.03	0.82 ± 0.03	0.17 ± 0.01	0.83 ± 0.01	0.72 ± 0.01	0.78 ± 0.05	0.88 ± 0.07	0.73 ± 0.03

reported spectrum of the $LaBGeO_5$ crystal [126] (Chapter 4). However, the spectrum shows poor definition of the quadrupolar features, indicating that the crystallites have limited long-range order. Furthermore, there is a substantially narrower impurity peak present in the spectrum of LBG+60, LBG+12, and all other partially crystallized samples. This peak is consistent with that of $LaBO_3$ [126]. Relative intensities are not quantitative in WCPMG spectra, as the signal enhancement due to the CPMG loops depends on the T_2 of each different environment. However, the signal due to $LaBO_3$ is consistently quite small, and no indication of $LaBO_3$ is seen in either the pXRD diffractograms (Fig. 7.2) or ^{11}B MAS NMR spectra (Fig. 7.3). As such, we conclude that the amount of $LaBO_3$ present in these samples is very small ($\leq 3\,\%$). This is consistent with our Rietveld refinements of or pXRD data (Appendix D.2) and will generally neglect it as a factor in our analysis. The ^{139}La WCPMG spectrum of the glass sample, LBG-G, is fit with a Czjzek distribution [135, 136, 139]. A fit of the ^{139}La WCPMG spectrum of LBG+12, processed such that the CPMG spikelets form a continuous lineshape, is presented in Fig. 7.6. It is important to note that the breadth parameter of the Czjzek distribution, σ, is not directly comparable to the well-defined C_Q, η_Q, or P_Q of crystalline materials. In binary lanthanum phosphate glasses, σ has been shown to be sensitive to changes in the Q^n species making up the second coordination sphere of the La^{3+} ions (Section 5.6). An increase in the diversity of the Q^n species correlates to an increase in σ. If there were significant changes to the second coordination sphere of the $LaBGeO_5$ glass during crystallization, we would expect to observe changes in either σ or the position parameter. No change in the ^{139}La peak attributed to the glass is observed during crystallization, and so we conclude that the bulk glass does not undergo significant changes during the crystallization process.

7.5.4 ^{11}B{^{10}B} REDOR NMR Spectroscopy

As has been previously reported, BO_3 environments cannot be effectively excited in ^{10}B NMR spectroscopy [52]. The nuclear spin of ^{10}B is integer ($I = 3$). Hence there is no "central transition" which is unaffected by the first-order quadrupolar broadening. Observing the spectra of integer-spin nuclei is similar to observing the satellite transitions of non-integer-spin nuclei [47]. For environments with small quadrupolar coupling constants (*e.g.*, $[B\emptyset_4]^-$), this is not particularly challenging.

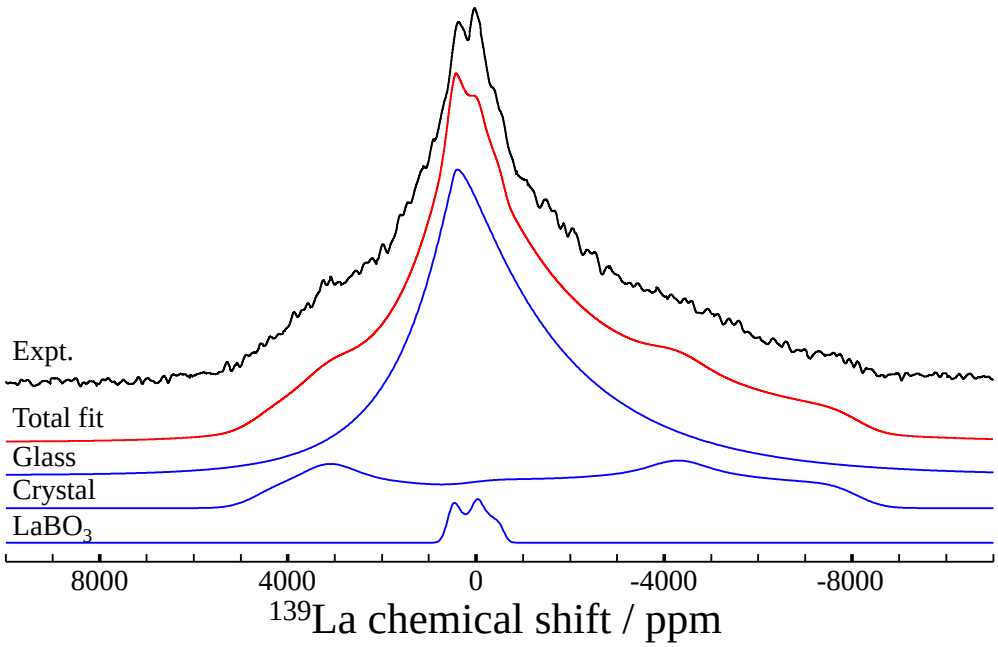

Figure 7.6: ^{139}La WCPMG NMR spectrum of partially crystallized LBG+12. The experimental data is identical to that shown in Fig. 7.5, but by summing the CPMG echoes the spectrum becomes a continuous lineshape. Fitting parameters for the crystal $LaBGeO_5$ peak are reported in Table 7.2, and for the glass in Table 7.1. The spectral parameters for both $LaBGeO_5$ and $LaBO_3$ are previously reported in the literature [126].

However, for environments with large quadrupolar coupling constants (*e.g.*, BO_3), it is quite difficult to produce appreciable excitation using a single pulse. A single pulse, centred on the $[B\emptyset_4]^-$ resonance, will effectively excite the $[B\emptyset_4]^-$ peak without exciting the BO_3 peak. Hence $^{11}B\{^{10}B\}$ REDOR can be used to selectively probe $[B\emptyset_4]^-$–$[B\emptyset_4]^-$ and BO_3–$[B\emptyset_4]^-$connectivity in crystals and glasses.

We present $^{11}B\{^{10}B\}$ REDOR curves of LBG-G, crystalline $LaBGeO_5$ (LBG-X), and LaB_3O_6 in Fig. 7.7. The REDOR curves of the $[B\emptyset_4]^-$–$[B\emptyset_4]^-$ environment of crystalline LBG-X and the BO_3–$[B\emptyset_4]^-$ environment of LaB_3O_6 are used to interpret the behaviour of the similar environments in $LaBGeO_5$ glass.

Typical analysis of REDOR spectra of amorphous samples involves fitting $\Delta S/S_0$ in the region $0 \leq \Delta S/S_0 \leq 0.2$ to extract the value of the van Vleck second moment [41, 52, 142–144]. This analysis relies on the indirect nucleus (in this case ^{10}B) being consistently excited between samples, and on the low-$\Delta S/S_0$ region of the REDOR curve following the universal REDOR lineshape [41, 52]. When we attempt to fit the curves in Fig. 7.7 to extract the van Vleck second moment, we find that the extracted value depends very strongly on the choice of points to fit, and is not reliably transferable. Our curves are effectively linear at both long and short time scales, rather than approximating the "universal" lineshape [41]. This may be due to the $^{11}B\{^{10}B\}$ spin pair being $I = 3/2$ and $I = 3$, respectively. REDOR of quadrupolar spin pairs is inherently less quantitative than REDOR where one spin is $I = 1/2$, due to factors including the quadrupolar splittings of the indirect nuclei [41]. Beyond the quadrupolar nature of both nuclei, as discussed above ^{10}B is of integer spin, and lacks a narrow central transition. This raises concerns about the consistency and homogeneity of the excitation of the $[B\emptyset_4]^-$ environments, as well as the ability to approximate the behaviour of a spin-1/2 nuclide. Hence we do not attempt a quantitative analysis of the REDOR curves, and rely on a more qualitative analysis.

The rate of change of a REDOR curve is indicative of the strength of the dipolar interaction between the observed and indirect nuclide. For an ensemble of spins such as a glass, this strength is affected both by the distance between the nuclides and by the number of nuclides in proximity. Hence a decrease in the rate of change of the REDOR curve can be attributed to a decrease in the dipolar interaction, which in turn is attributed to a decrease in the proximity of the indirect and the observe nuclides.

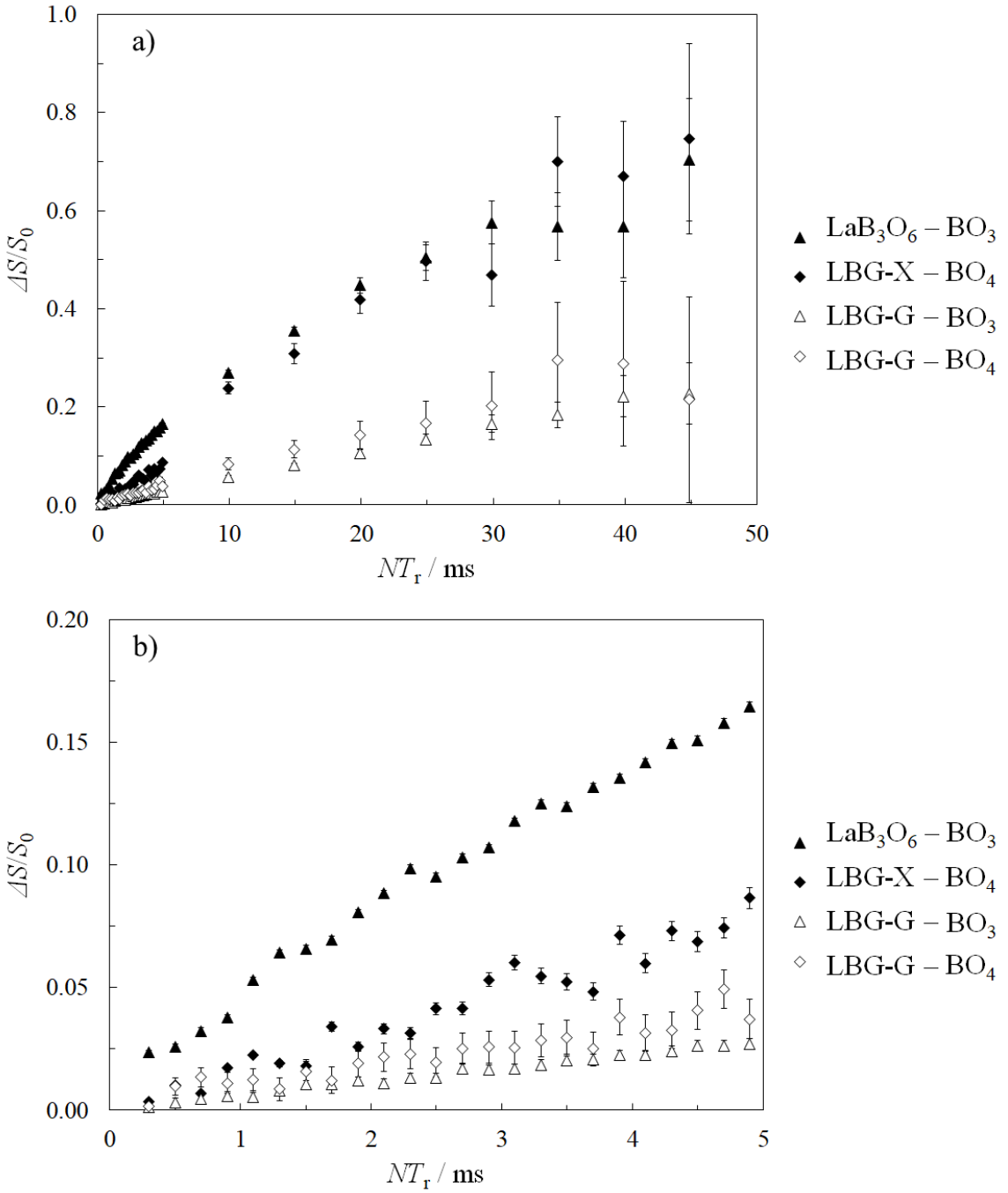

Figure 7.7: $^{11}B\{^{10}B\}$ REDOR NMR curves for crystalline LaB_3O_6, crystalline $LaBGeO_5$ and $LaBGeO_5$ glass. Filled data points indicate data from crystals. Open data points indicate data from the glass. Diamonds indicate $[B\emptyset_4]^-$–$[B\emptyset_4]^-$ environments. Triangles indicate BO_3–$[B\emptyset_4]^-$ environments. a) The REDOR curves at long time scales. b) The REDOR curves at short time scales.

For this interpretation to be reliable between different systems, the proportion of excited spins must be similar. This is not difficult to achieve for ^{11}B at 16.4 T, but it is not obviously true for ^{10}B at the same field strength. Our ^{10}B Hahn echo NMR spectra of our samples (Figs. D.6 to D.8) are of similar breadth, and are fitted with similar values of C_Q (reported in Table D.3). We conclude that the ^{10}B $[B\emptyset_4]^-$ environment is consistently excited across our three samples, and hence can meaningfully interpret qualitative differences in intensity between the REDOR curves.

The REDOR curves of the BO_3–$[B\emptyset_4]^-$ and $[B\emptyset_4]^-$–$[B\emptyset_4]^-$ environments in the LBG-G sample are significant and persistent over long length scales (50 ms), but of lower magnitude than the curves for the equivalent environments in the LBG-X and LaB_3O_6 samples. From this we conclude that the $[B\emptyset_4]^-$ environment in $LaBGeO_5$ has both BO_3 and $[B\emptyset_4]^-$ neighbours. We also conclude that due to the reduced magnitude of the $\Delta S/S_0$ curve for the $[B\emptyset_4]^-$ environment in LBG-G, the $[B\emptyset_4]^-$–$[B\emptyset_4]^-$ environment is less likely to occur in LBG-G than in LBG-X. In LBG-X, the single crystallographic $[B\emptyset_4]^-$ site has two $[B\emptyset_4]^-$ neighbours; hence in the glass we expect that $[B\emptyset_4]^-$ has, on average, significantly fewer than two $[B\emptyset_4]^-$ neighbours. Similarly, in the LaB_3O_6 crystal structure, both crystallographic BO_3 sites have two $[B\emptyset_4]^-$ neighbours, and so we conclude that due to the reduced magnitude of the BO_3–$[B\emptyset_4]^-$ curve in LBG-G that, on average, BO_3 has significantly fewer than two $[B\emptyset_4]^-$ neighbours. With the relative magnitudes of the BO_3–$[B\emptyset_4]^-$ and $[B\emptyset_4]^-$–$[B\emptyset_4]^-$ $\Delta S/S_0$ curves in the LBG-G glass being similar at all time scales, it seems likely that the BO_3 and $[B\emptyset_4]^-$ environments have similar numbers of $[B\emptyset_4]^-$ neighbours; however, given the complicated behaviour of REDOR curves at long time scales, we cannot be certain of this interpretation.

7.5.5 ^{17}O NMR Spectroscopy

^{17}O MAS NMR spectra of LBG-G, LBG+12, and LBG+60 collected at 16.4 T are shown in Fig. 7.8. The ^{17}O MAS spectrum of the most crystalline sample, LBG+60, shows a small amount of residual glass intensity. The ^{17}O MAS spectrum of the LBG-G glass sample can be subtracted from any of the spectra of the partially crystallized samples, with the glass spectrum scaled to match the intensity of the shoulder at approximately 250 ppm. When subtracting the ^{17}O MAS spectrum of the LBG-G

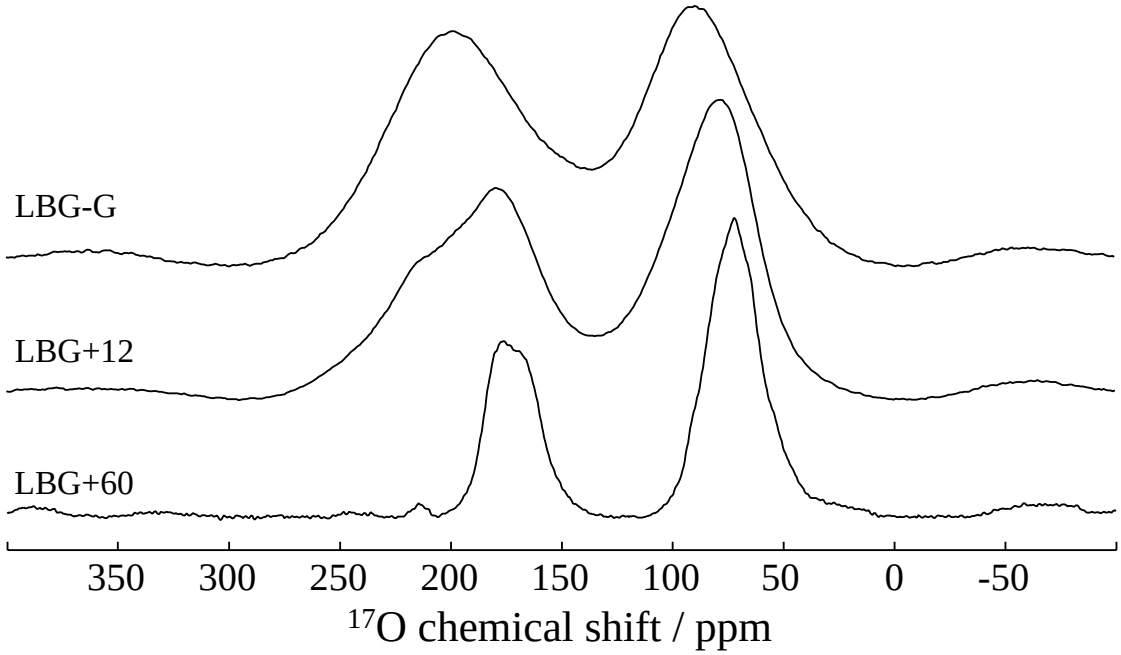

Figure 7.8: ^{17}O MAS NMR spectra of: glassy LBG-G, top; partially crystallized LBG+12, middle; and mostly crystallized LBG+60, bottom.

glass from any of the spectra of the partially crystallized sample, the same difference plot is recovered in each case. This difference plot agrees very well with the spectrum of the most crystallized sample, LBG+60. This is also true for the ^{11}B MAS NMR spectra. That the portion of the spectrum attributed to $LaBGeO_5$ crystallites shows no change with level of crystallization in both ^{17}O and ^{11}B MAS NMR spectra indicates that neither the bulk glass structure nor the crystallite structure change during the crystallization process. Hence, in order to minimize error during the fitting of the ^{17}O NMR spectrum of the $LaBGeO_5$ crystal, we subtract the spectrum of the glass sample from the spectrum of LBG+60 and fit the difference.

There are five crystallographically distinct oxygen sites in the $LaBGeO_5$ crystal structure [78]. O1 and O2 link GeO_4 and $[B\emptyset_4]^-$ tetrahedra, and are considered BO, as they link two glass-forming elements (Ge and B). O1 and O2 are four-coordinate, singly bound to B and Ge, and loosely bound to two different La. O3 and O4 link GeO_4 tetrahedra with LaO_9 polyhedra, and are three-coordinate: singly bound to Ge, and singly bound to two different La. O3 and O4 are considered NBO, as they link a network former (Ge) with La, which often acts as a network modifier. O5 links two corner-sharing $[B\emptyset_4]^-$ tetrahedra, is three-coordinate (one La and two different B

neighbours), and is considered a BO. The occupancy of all oxygen sites is one.

The ^{17}O MAS spectrum of LBG+60 shows two major peaks with maxima at 72 ppm and 170 ppm. Integrating the two major peaks returns a 3:2 intensity ratio. Hence the peak centred at 72 ppm is attributed to the three BO sites, while the peak centred at 170 ppm is attributed to the two NBO sites. The two NBO peaks are not resolved from one another; similarly, all three of the BO peaks are strongly overlapping. Subtracting the spectrum of LBG-G from the ^{17}O MAS spectra of the partially crystallized samples returns difference plots that are identical in all ways save their intensities. The fraction of intensity of each spectrum that is due to crystalline environments can be determined by integration of these difference plots, and these estimates are reported in Table 7.3. The crystallite fraction determined by ^{17}O NMR independently agrees with that from ^{11}B NMR (Table 7.3).

The 3QMAS spectrum of LBG+60 is presented in Fig. 7.9. As in the MAS spectrum, the NBO peak pair is resolved from the BO triplet. The 3QMAS spectrum has somewhat improved resolution with respect to the two NBO sites. The resolution of the three BO sites in the 3QMAS spectrum is poor. For poorly resolved 3QMAS peaks, the P_{Q} and $\delta_{\mathrm{iso}}^{\mathrm{CS}}$ values of a given environment can be extracted via the procedure described by Millot and Man [134]. These values are limited in precision due to the limited resolution of the spectrum, but they do provide a reasonable estimate (and upper bound) on the P_{Q} and $\delta_{\mathrm{iso}}^{\mathrm{CS}}$ of any particular site. While not wholly resolved, the extracted values of the two NBO sites support that the sites have similar C_{Q}, η_{Q}, and $\delta_{\mathrm{iso}}^{\mathrm{CS}}$ values. The extracted values of the three BO sites are not substantially different from one another. Resolution of the 3QMAS spectrum was limited by the fairly rapid decay of the 3QMAS echo.

To aid in the interpretation of the ^{17}O NMR spectra of the $LaBGeO_5$ crystal, first principles calculations were carried out on the experimental structure [78]. The results of the calculations for the ^{17}O NMR parameters (as well as for the ^{139}La and ^{11}B parameters) are presented in Table 7.2. DFT calculations returned EFG parameters in good accord with experiment. The absolute calculated isotropic chemical shifts do not agree with experiment, but the relative calculated shifts do agree with our observations. The relative shift of the NBO and BO calculated chemical shifts is correct (with $\delta_{\mathrm{iso}}^{\mathrm{CS}}(\mathrm{NBO}) > \delta_{\mathrm{iso}}^{\mathrm{CS}}(\mathrm{BO})$), but the calculated values of $\delta_{\mathrm{iso}}^{\mathrm{CS}}(\mathrm{NBO})$ is at least

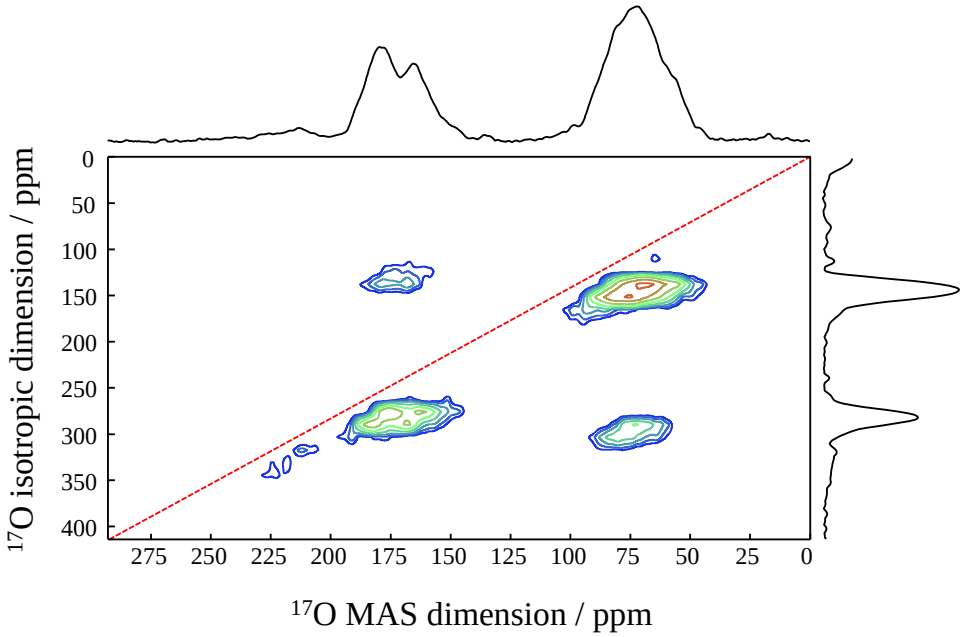

(a) Without fit.

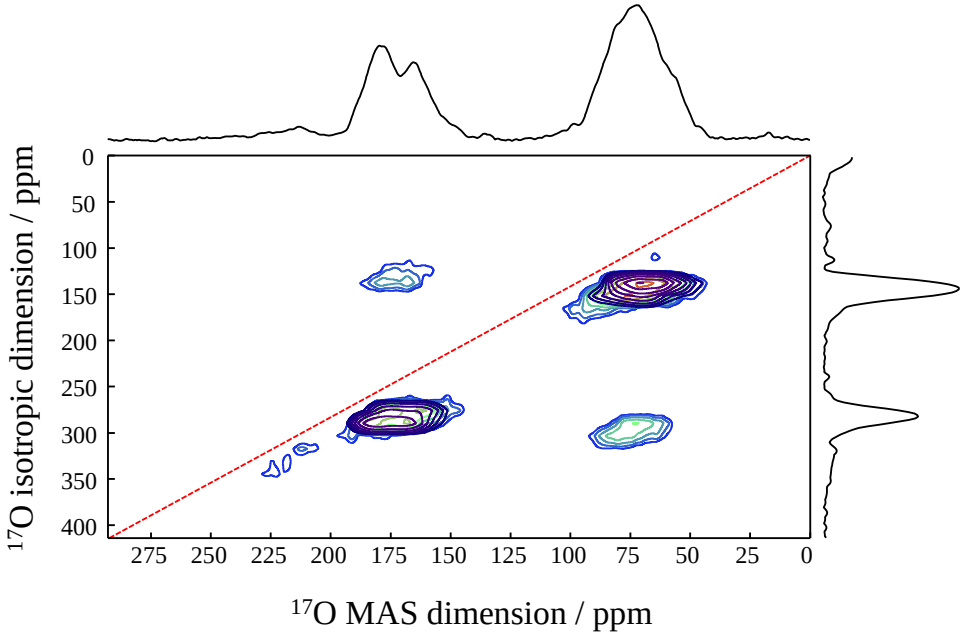

(b) With fit.

Figure 7.9: ^{17}O 3QMAS NMR spectrum of mostly crystallized LBG+60. The diagonal is the correspondence between the MAS and isotropic dimensions, and indicates the position where peaks free from the quadrupole interaction would appear. Fitted peaks are overlaid on experimental data; the parameters of the fitted peaks are reported in Table 7.2. The top left and bottom right peaks are spinning sidebands. The projection of the isotropic dimension (y axis) is processed to remove the contributions from the spinning sidebands.

20 ppm greater than any possible experimental value. Similarly, the calculated values of $\delta_{\mathrm{iso}}^{\mathrm{CS}}$(BO) are at least 10 ppm greater than any possible experimental value, and a 20 ppm difference would be very plausible. The calculated $\delta_{\mathrm{iso}}^{\mathrm{CS}}$ values for the BO sites are within 20 ppm of each other, with the two Ge–O–B sites having similar values. The relative separation of the two Ge–O–La sites is 6 ppm. Similarly, the relative separation of the two Ge–O–B sites is 5 ppm. This is lower than the resolution limit of our 3QMAS spectrum, and hence it is unsurprising that there is difficulty in resolving individual environments.

The results of our GIPAW calculations imply that we should expect similar values of $\delta_{\mathrm{iso}}^{\mathrm{CS}}$, C_{Q}, and η_{Q} for a given pair of Ge–O–B or Ge–O–La sites. The calculated C_{Q} and η_{Q} values of the Ge–O–La sites are quite similar, as are those of the Ge–O–B sites. Both the C_{Q} and η_{Q} values of the B–O–B site are greater than of any other sites. The η_{Q} values of the NBO sites are much lower than those of the BO sites. For all sites, the CSA contribution to the breadth of the peak is expected to be substantially less than the quadrupolar contribution, hence we neglect it in our fits.

With these trends, we can generate a reasonable set of fitting parameters that simultaneously fit the 16.4 T and 9.4 T MAS, Hahn echo, and 3QMAS spectra. The fit of the 16.4 T 3QMAS spectrum, and of the 16.4 T and 9.4 T MAS spectra, are shown in Figs. 7.9 and 7.10. The parameters for this fit are reported in Table 7.2. It bears mentioning that this fit is unlikely to be unique. Even with the assumption that the CSA contribution to the spectrum is negligible, there are still six independent parameters ($\delta_{\mathrm{iso}}^{\mathrm{CS}}$, C_{Q}, η_{Q} for the two individual sites) fitting the NBO peak, and similarly nine independent parameters fitting the BO peak. However, with the significant number of constraints on the fitting process (similar integrated intensities of the peaks, simultaneously satisfying low- and high-field 1D and 2D experiments), we consider our reported parameters to be a reasonable estimate.

No similar fit can be constructed for the ^{17}O MAS NMR spectrum of the $LaBGeO_5$ glass. There are simply too many possible environments, and insufficient resolution, to provide a quantitative estimate of any parameter. However, based upon the 3QMAS spectrum of the glass (Fig. 7.11) a qualitative model of the glass structure can be constructed. The presence of some structural elements are known to be present in the glass from other experiments (*i.e.*, B–O–La); others are expected due to the

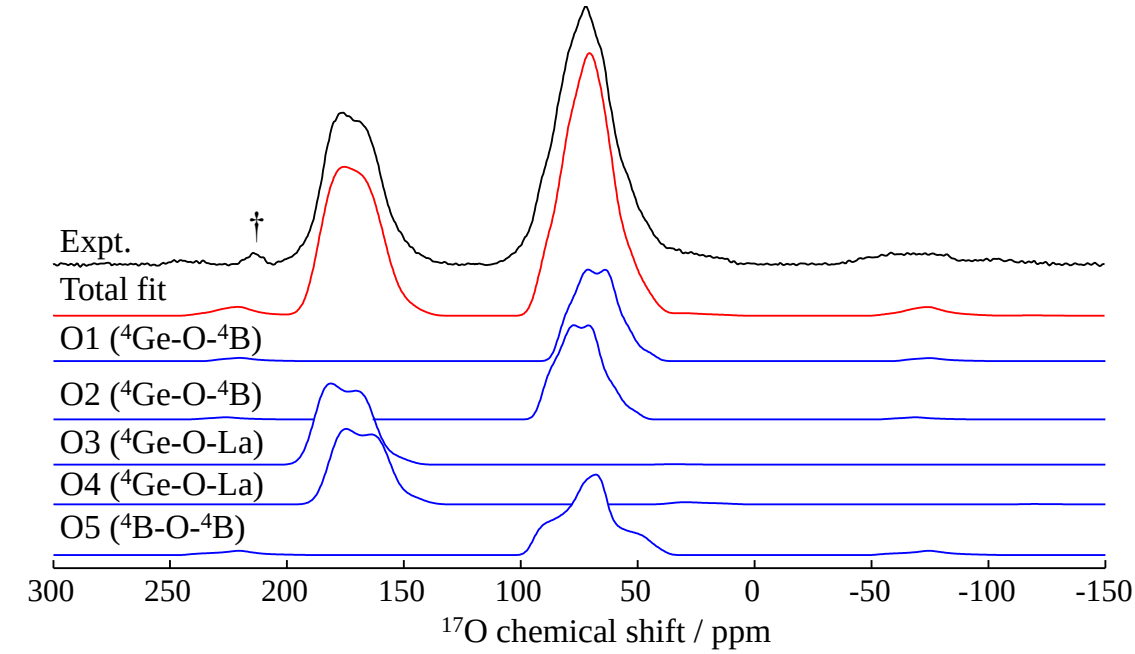

(a) Spectrum at 16.4 T.

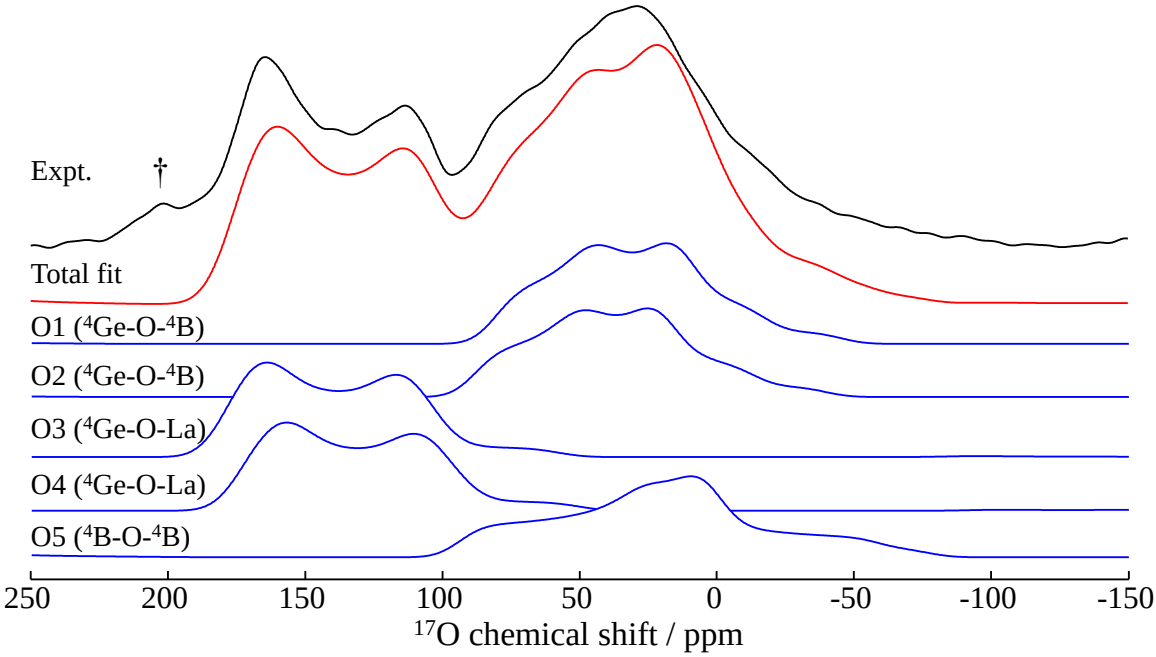

(b) Spectrum at 9.4 T.

Figure 7.10: ^{17}O MAS NMR spectra of the mostly crystallized LBG+60. The parameters of each peak are provided in Table 7.2. A small impurity is marked with †, and is consistent with the presence of $LaBO_3$.

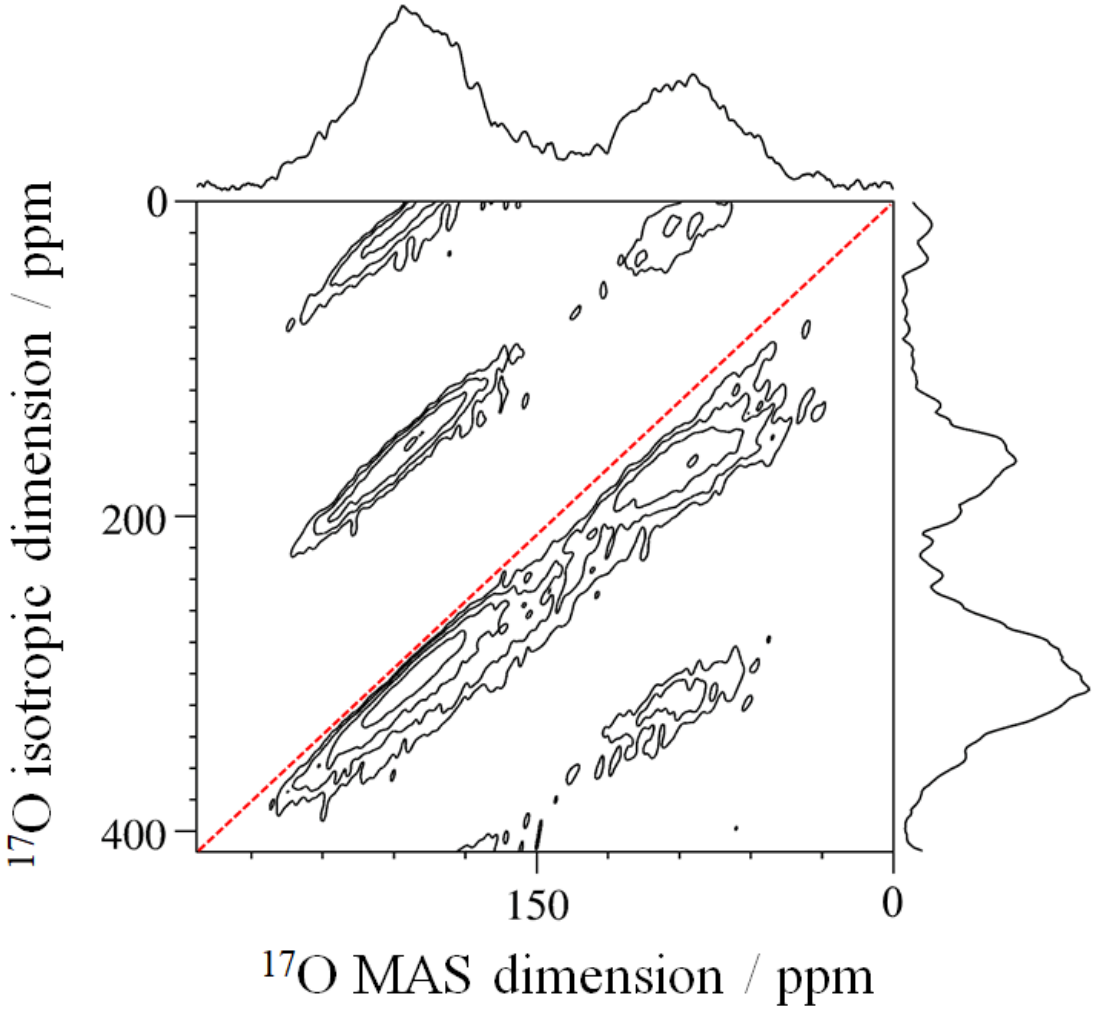

Figure 7.11: ^{17}O 3QMAS NMR spectrum of the glass LBG+G. The diagonal is the correspondence between the MAS and isotropic dimensions, and indicates the position where peaks free from the quadrupole interaction would appear. The projection of the isotropic dimension (y axis) is processed to remove the contributions from spinning sidebands.

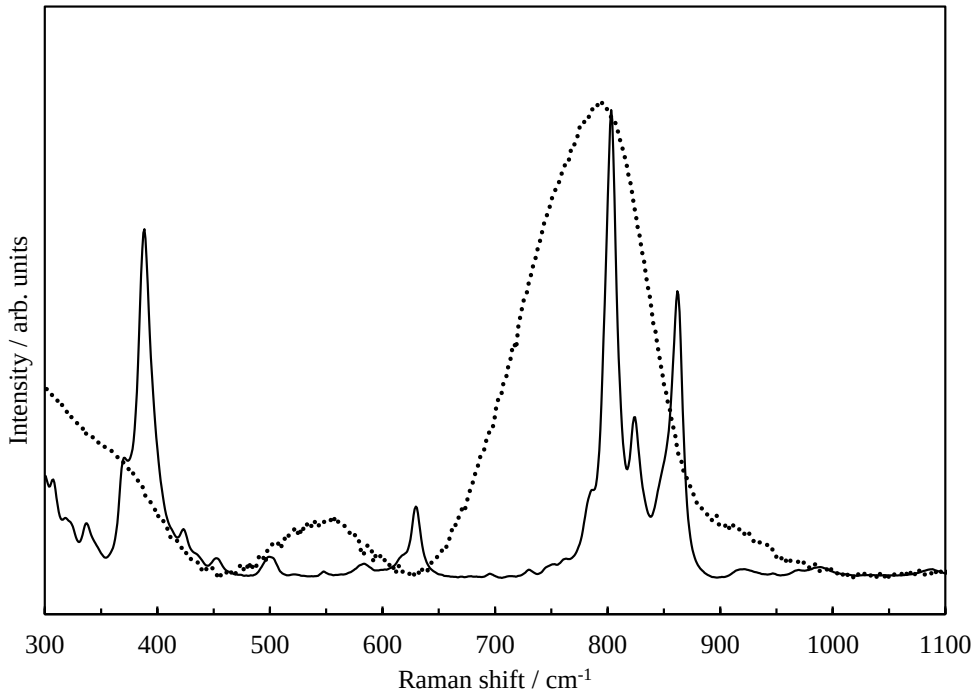

Figure 7.12: Raman spectra of the $LaBGeO_5$ crystal (solid line) and $LaBGeO_5$ glass (dotted line). Some of the Raman intensity in the glass corresponds to crystal modes, in particular the sharp mode at approx. 803 cm^{-1}. However, the glass also has substantial intensity which does not correspond to known $LaBGeO_5$ environments.

structure of the $LaBGeO_5$ crystal (*i.e.*, Ge–O–La, Ge–O–B); yet others can be inferred based upon data in the literature. The resulting qualitative interpretation of the glass structure is discussed in detail below.

We do not observe any ^{17}O intensity in the 450 ppm to 600 ppm region in any spectrum. Intensity in this region would indicate the presence of OLa_4 or OLa_6 environments as in crystalline La_2O_3 [281]. The presence of these environments could indicate partitioning of the glass into La-rich regions [282]. As we do not observe any such intensity, we conclude that La^{3+} is regularly distributed in the glass.

7.5.6 Raman Spectroscopy

The Raman spectra of the $LaBGeO_5$ crystal and glass are presented in Fig. 7.12. The

spectrum of the $LaBGeO_5$ crystal is very similar to previous literature reports, and its peaks have been assigned to various vibrational modes [75, 95, 109, 278, 283]. The particular region of interest for this study is between 775 cm^{-1} to 900 cm^{-1}, which has been assigned to both $[B\emptyset_4]^-$ and GeO_4 tetrahedral vibrations. Notably, there is no significant Raman intensity in the crystal between 630 cm^{-1} to 775 cm^{-1}. The Raman spectrum of the $LaBGeO_5$ glass has a broad, asymmetric, and featureless peak spanning 630 cm^{-1} to 950 cm^{-1}. Like the spectrum of the crystal, this spectrum is consistent with literature reports [75, 109]. The large peak in the glass encompasses the intensity found in the crystal, but also has significant intensity centred at approximately 745 cm^{-1}; the crystal has no corresponding vibrational modes in this region.

7.6 Discussion

7.6.1 Crystallization

The pXRD, ^{11}B MAS NMR, ^{139}La WCPMG NMR, and ^{17}O MAS and 3QMAS results all support a common conclusion regarding the formation of $LaBGeO_5$ crystals from the glass: there are no substantial structural changes in either the glass or the crystal in the partially crystallized samples. In other words, the glass fraction of a partially crystallized $LaBGeO_5$ sample has the same structure as the parent glass, while the crystalline fraction is unmodified $LaBGeO_5$ crystal. The quantitative ^{11}B and ^{17}O MAS NMR results provide the same crystallization fraction (within error), with partially crystallized spectra being combinations of the crystal and glass spectra.

There are some noticeable differences in the pXRD and ^{139}La WCPMG NMR results. Both become somewhat sharper as the crystallization fraction increases. This change is indicative of larger crystallites, but not of a substantial change in either the short-range order (NMR) or long-range order (pXRD) of the $LaBGeO_5$ structure. At the highest crystallization levels, a small amount of $LaBO_3$ is observed, first by ^{139}La WCPMG NMR, then by pXRD at the highest level of crystallization (Appendix D.2). The LBG-G glass likely has a small excess of B_2O_3, allowing for non-stoichiometric crystallization in small quantities. However, $LaBO_3$ is only detected when the sample is already substantially crystallized. Finally, in the partially crystallized samples, the a and c lattice constants are somewhat lower than those reported in the literature.

Based upon the amount of strain determined by our Rietveld refinement (Table D.1), along with the elastic tensor of the $LaBGeO_5$ crystal (Table 8.2) [283], we conclude that the $LaBGeO_5$ crystallites are under some amount of compressive stress, on the order of about 4 GPa.

The data above provide insight into the end result of the nucleation and growth of the $LaBGeO_5$ crystallites, but cannot effectively probe the dynamics of the nucleation mechanism. The most interesting structural evolution during nucleation and growth occurs at the interface between the glass and the nucleus. By definition the nuclei are extremely small, with radii on the order of nanometres. The faction of the total sample volume made up by the interface between nuclei and glass is extremely small, and hence effectively undetectable via either NMR or pXRD. While we cannot directly probe the changes in structure during nucleation, knowledge of the structure of the resulting glass-ceramic has practical significance.

The ability to estimate the degree of crystallization of a $LaBGeO_5$ glass-ceramic composite via NMR spectroscopy is desirable, as estimating volume fraction via techniques such as optical microscopy may prove difficult if the crystallites are sufficiently small such that the material is transparent. Gupta *et al.* have previously reported a model which, through the use of ^{11}B MAS NMR spectroscopy, allows for an estimate of the crystallite fraction [34]. However, when we apply their model to our ^{11}B MAS NMR results, the model disagrees with our direct modelling of the $[B\emptyset_4]^-$ peak, as well as with the crystallization fraction estimated by our ^{17}O MAS results. A small correction to the model of Gupta *et al.*, when applied to our presented samples, leads to values which agree very well with our experimental results. The details of the correction follow.

We use the same notation as Gupta *et al.*, where square brackets indicate the relative intensity of the species within. In the $LaBGeO_5$ crystal, $[BO_3] = 0$ and $[BO_4] = 1$. In the glass, both species will be present, though the precise ratio will depend on the exact composition (*e.g.*, an excess of La_2O_3 will increase BO_3 at the expense of $[B\emptyset_4]^-$) [212]. In a partially crystallized sample,

$$[BO_3]_{\text{expt}} + [BO_4]_{\text{expt}} = 1 \tag{7.1}$$

and

$$[\mathrm{BO_4}]_{\mathrm{expt}} = [\mathrm{BO_4}]_{\mathrm{cryst}} + [\mathrm{BO_4}]_{\mathrm{glass}}. \tag{7.2}$$

As the crystal contains no BO_3 units,

$$[\mathrm{BO_3}]_{\mathrm{expt}} = [\mathrm{BO_3}]_{\mathrm{glass}}. \tag{7.3}$$

We assume that the ratio of $BO_3/[B\emptyset_4]^-$ in the glass, $\alpha = \frac{[\mathrm{BO_3}]_{\mathrm{glass}}}{[\mathrm{BO_4}]_{\mathrm{glass}}}$, does not change as crystallization progresses. This assumption is well-founded based on our ^{11}B, ^{139}La, and ^{17}O NMR data, none of which show any change in the structure of the $LaBGeO_5$ bulk glass during crystallization (Section 7.5). With the assumption that α is constant, the fraction of the four-coordinate boron intensity attributed to the crystallites can be calculated knowing only the fraction of the overall intensity attributed to the three-coordinate site. The fraction of the crystallites in the partially crystallized sample, c, is given by

$$c = \frac{[\mathrm{BO_4}]_{\mathrm{cryst}}}{[\mathrm{BO_4}]_{\mathrm{cryst}} + [\mathrm{BO_4}]_{\mathrm{glass}} + [\mathrm{BO_3}]_{\mathrm{glass}}}. \tag{7.4}$$

With Eq. (7.2), this can be rewritten to remove the (potentially) inaccessible $[\mathrm{BO_4}]_{\mathrm{cryst}}$ term:

$$\begin{aligned} c &= \frac{[\mathrm{BO_4}]_{\mathrm{expt}} - [\mathrm{BO_4}]_{\mathrm{glass}}}{[\mathrm{BO_4}]_{\mathrm{expt}} - [\mathrm{BO_4}]_{\mathrm{glass}} + [\mathrm{BO_4}]_{\mathrm{glass}} + [\mathrm{BO_3}]_{\mathrm{glass}}} \\ c &= \frac{[\mathrm{BO_4}]_{\mathrm{expt}} - [\mathrm{BO_4}]_{\mathrm{glass}}}{[\mathrm{BO_4}]_{\mathrm{expt}} + [\mathrm{BO_3}]_{\mathrm{glass}}} \end{aligned} \tag{7.5}$$

As $[\mathrm{BO_3}]_{\mathrm{glass}}$ and $[\mathrm{BO_4}]_{\mathrm{glass}}$ are related by α, Eq. (7.5) can be written as

$$c = \frac{[\mathrm{BO_4}]_{\mathrm{expt}} - \frac{[\mathrm{BO_3}]_{\mathrm{glass}}}{\alpha}}{[\mathrm{BO_4}]_{\mathrm{expt}} + [\mathrm{BO_3}]_{\mathrm{glass}}} \tag{7.6}$$

With Eqs. (7.1) and (7.3), Eq. (7.6) is reduced to

$$c = [\mathrm{BO_4}]_{\mathrm{expt}} - \frac{[\mathrm{BO_3}]_{\mathrm{expt}}}{\alpha}. \tag{7.7}$$

Equation (7.7) is used to generate the crystallite fraction reported in Table 7.3. It

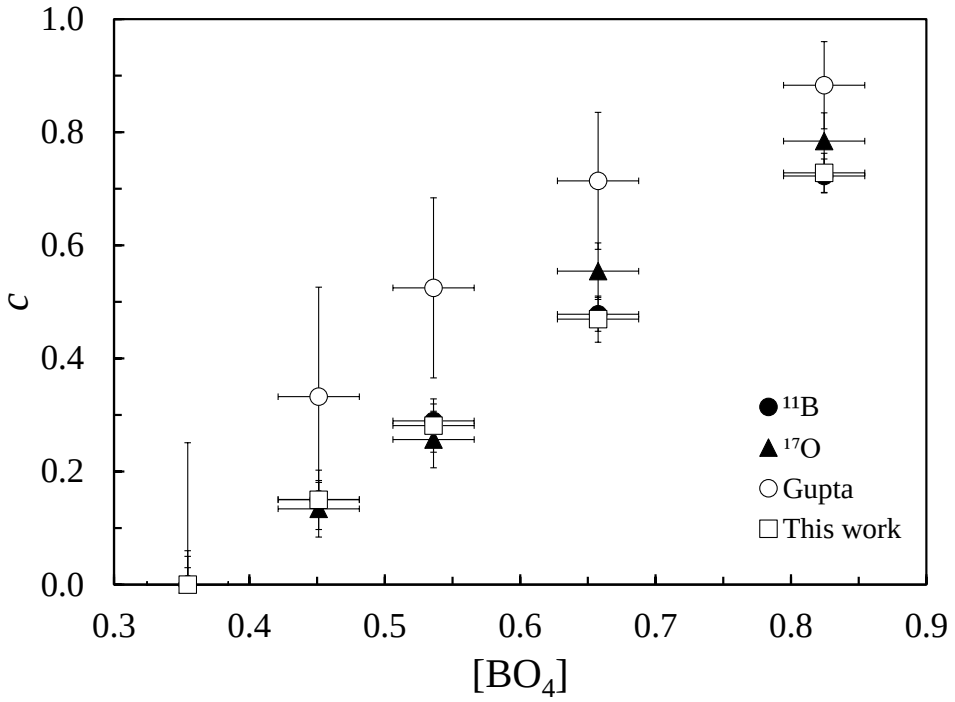

Figure 7.13: A comparison of the crystal fraction, c, of the partially crystallized samples, as determined from both ^{11}B and ^{17}O MAS NMR data, and the crystal fraction predicted by model calculations. Solid points represent experimental data, while open points represent calculated values. Open circles are values calculated using the equation of Gupta *et al.* [34], while open squares are calculated using Eq. (7.7).

agrees very well with the fraction determined by fitting the $[B\emptyset_4]^-$ peak directly, and by integration of ^{17}O MAS spectra. The only difference between our derivation and the derivation of Gupta *et al.* is the introduction of the $[BO_3]_{glass}$ term in Eq. (7.4). However, this term is required to accurately account for the total intensity of the glass, and prevent an overestimation of the crystal fraction. For comparison, our experimental results, the results of our equation, and the results from the equation of Gupta *et al.* are plotted in Fig. 7.13.

The utility of Eq. (7.7) is primarily in the (relatively) accessible data it requires. Fitting the $[B\emptyset_4]^-$ peak directly may not be possible except at high magnetic field strengths and spinning speeds, while the ^{17}O enrichment required for ^{17}O MAS NMR

is prohibitively expensive for routine studies. The ratio of BO_3 to $[B\emptyset_4]^-$ can be quickly determined through ^{11}B MAS NMR at moderate field strengths and spinning speeds, or potentially by Raman spectroscopy, allowing for routine characterization of the crystal fraction of $LaBGeO_5$ TFN materials.

7.6.2 Glass Structure

The structure of the $LaBGeO_5$ crystal is well-understood. Three structural units are present: $[B\emptyset_4]^-$ tetrahedra, $Ge\emptyset_2O_2{}^{2-}$ tetrahedra, and LaO_9 polyhedra. From this, three oxygen bonding motifs are apparent: the two bridging oxygen B–O–B and Ge–O–B; and the non-bridging oxygen Ge–O–La. These three motifs are observed in the ^{17}O MAS and 3QMAS spectra of the $LaBGeO_5$ crystal. The ^{17}O 3QMAS spectrum of the LBG-G glass shares some similarities to that of the LBG+60 crystal, but also has substantial differences. In particular, the 3QMAS intensity in the glass has spread to more positive chemical shift values. By comparison to the crystal, some of the glass intensity can be assigned to the Ge–O–B environment ($\delta_{iso}^{CS} \approx 88$ ppm), the B–O–B environment ($\delta_{iso}^{CS} \approx 95$ ppm), and the Ge–O–La environment ($\delta_{iso}^{CS} \approx 189$ ppm). However, this only accounts for a small portion of the intensity displayed.

Beyond homonuclear (*e.g.*, Ge–O–Ge) and heteronuclear (*e.g.*, Ge–O–B) environments, we must also consider potentially observable differences in coordination number. For example, in binary sodium germanate crystals Du and Stebbins have observed differences in the ^{17}O parameters between $^4Ge-O-{}^4Ge$ and $^4Ge-O-{}^6Ge$ oxygen sites [55], where the leading superscript indicates coordination. They also observe environments in binary sodium germanate glasses which are consistent with the $^4Ge-O-{}^6Ge$ seen in similar crystals [55, 56]. Intensity in this region has been attributed to five- and/or six-coordinate germanium in various sodium germanate glasses [55]. Six-coordinate germanium in glass cannot be distinguished from a possible five-coordinate germanium environment by either spectroscopic or diffraction-based techniques, and hence both five- and six-coordinate germanium must be considered [28, 56, 73]. The notation $^{5/6}Ge$ indicates either or both environments.

In addition to observing $^4Ge-O-{}^{5/6}Ge$ environments in sodium germanate glasses, Du and Stebbins have observed differences between the $^3B-O-{}^3B$ and $^3B-O-{}^4B$ environments, as well as the $^3B-O-Si$ and $^4B-O-Si$ environments, in sodium borosilicate

glasses [51]. Lee *et al.* have reported ^{17}O 3QMAS spectra of binary borogermanate glasses, establishing the relative positions of ^{4}Ge–O–^{4}Ge, ^{4}Ge–O–^{3}B, and ^{3}B–O–^{3}B environments [53]. Oxygen "triclusters" (*i.e.*, oxygen triply bonded to network forming cations such as Ge^{4+}, labeled O_{666}) are known to exist in the rutile crystal phase of GeO_2. With the above literature data, we can establish several trends which we will use to inform our analysis of the LBG-G ^{17}O 3QMAS spectra. In binary germanate glasses, the BO ^{17}O chemical shift increases as the neighbouring germanate coordination increases (*i.e.*, $\delta_{\text{iso}}^{\text{CS}}(^{4}\text{Ge–O–}^{4}\text{Ge}) < \delta_{\text{iso}}^{\text{CS}}(^{4}\text{Ge–O–}^{5/6}\text{Ge}) < \delta_{\text{iso}}^{\text{CS}}(\text{O}_{666})$). The opposite is true with borates, with the BO ^{17}O chemical shift increasing as the neighbouring borate coordination decreases (*i.e.*, $\delta_{\text{iso}}^{\text{CS}}(^{4}\text{B–O–}^{4}\text{B}) < \delta_{\text{iso}}^{\text{CS}}(^{3}\text{B–O–}^{4}\text{B}) < \delta_{\text{iso}}^{\text{CS}}(^{3}\text{B–O–}^{3}\text{B})$). The ^{17}O chemical shift of borates is generally greater than that of germanates for both BO and NBO.

With known oxygen environments identified by the ^{17}O spectra of the $LaBGeO_5$ crystal, we can identify the residual intensity present in the glass. Our identification of the species present in the $LaBGeO_5$ glass is shown in Fig. 7.14. Parameters used in generating this figure are reported in Table 7.1.

The ^{4}Ge–O–B site from the crystal lies very close to the top-right edge of the glass spectrum. If ^{4}Ge–O–^{4}Ge was present in significant quantity in the glass, we would expect more intensity in this region. We therefore conclude that ^{4}Ge–O–^{4}Ge links are not a substantial contributor to the glass network.

The resolution of our 3QMAS spectrum is insufficient to separate the subtle differences between the differently coordinated borate units, which are expected to vary by less than 10 ppm [51]. Given that we know that BO_3 units are present in the glass, we expect Ge–O–B and B–O–B peaks to broaden towards greater $\delta_{\text{iso}}^{\text{CS}}$ values. The intensity region between 100 ppm to 120 ppm can be attributed in part to ^{4}B–O–^{3}B links, which we expect to be present from our REDOR results. It is also possible for ^{3}B–O–^{3}B environments to be present; as our ^{11}B{^{10}B} REDOR experiment only probes species with connectivity to $[B\emptyset_4]^-$, it cannot detect such an environment. Hence our ^{11}B MAS spectra, and our ^{11}B{^{10}B} REDOR experiments, are consistent with the ^{17}O 3QMAS spectrum, but are insufficient to explain the intensity present between 120 ppm to 150 ppm.

The species reported in the literature which can best explain the intensity from

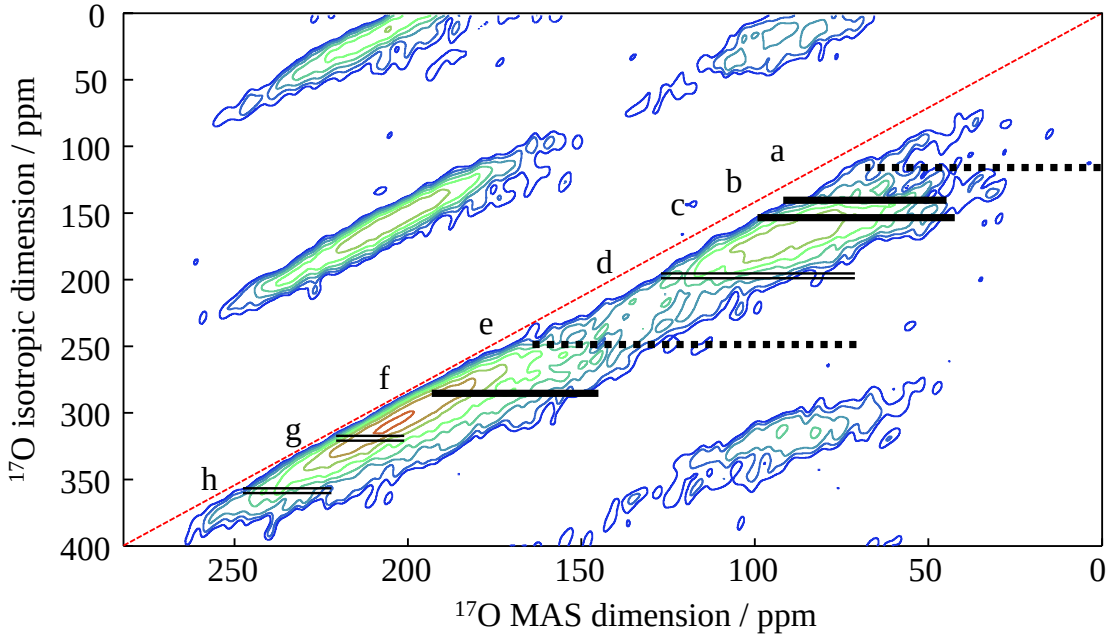

Figure 7.14: Labelled ^{17}O 3QMAS NMR spectrum of the glass LBG-G. Horizontal lines indicate mean expected positions, as well as approximate expected widths in the MAS dimension, of oxygen environments which are expected to be present in $LaBGeO_5$. Parameters for each environment are discussed in Table 7.1. Solid lines are environments present in the $LaBGeO_5$ crystal. Double lines are environments which are plausibly or possibly present based upon data from the literature. Dotted lines are environments which are unlikely to be present, again based upon data from the literature. The environments shown are: a) typical ^{4}Ge–O–^{4}Ge, from literature [54, 55]; b) ^{4}Ge–O–B, from Table 7.2; c) ^{4}B–O–^{4}B, from Table 7.2; d) ^{4}Ge–O–$^{5/6}$Ge, from literature [54, 55]; e) O_{666} as in rutile GeO_2, from literature [54, 55]; f) ^{4}Ge–O–La, from Table 7.2; g) expected B–O–La environment; h) O_{666} as in $Na_4Ge_9O_{20}$, from literature [55].

120 ppm to 150 ppm is $^{5/6}$Ge–O–X, where X is another glass-forming species. The δ_{iso}^{CS} values of $^{5/6}$Ge–O–^{4}Ge in various sodium germanate crystals fall between 80 ppm to 150 ppm [55]. Intensity in this region has been attributed to five- and/or six-coordinate germanium in various sodium germanate glasses [55]. $^{5/6}$Ge–O–X environments, where X is either Ge or Si, have been observed in sodium germanosilicate glasses using ^{17}O NMR spectroscopy [284]. While $^{5/6}$Ge–O–B environments have not been reported in the literature (in part due to a dearth of structural studies on borogermanates), it is plausible that they would appear in a similar chemical shift range to $^{5/6}$Ge–O–^{4}Ge. As the ^{17}O δ_{iso}^{CS} of borates is generally more positive than that of germanates, it is also possible that $\delta_{iso}^{CS}(^{5/6}\text{Ge–O–}^{4}\text{Ge}) < \delta_{iso}^{CS}(^{5/6}\text{Ge–O–B})$. This is consistent with the intensity present between 120 ppm to 150 ppm.

There is a substantial presence of non-bridging oxygen. The peak centred at 199 ppm in the 16.4 T MAS spectrum can be partially, but not wholly, explained by a Ge–O–La NBO peak similar to that seen in the spectrum of the crystal. Assuming that the Ge–O–La NBO peak in the glass can be described by a peak near the same position as the similar peak in the crystal, an additional peak centred at approximately 215 ppm can describe the increased intensity. This is consistent with the position of the impurity peak present in the ^{17}O MAS spectra of LBG+60 which is attributed to $LaBO_3$. Additionally, this chemical shift is consistent with the B–O–La environments predicted by DFT calculations on $LaBO_3$ and LaB_3O_6, and is consistent with the general trend of borate ^{17}O shifts being more positive than germanate shifts. The presence of the B–O–La environment is expected due to the ^{11}B NMR results discussed above.

There is an additional environment which must be considered: the oxygen tricluster. In the rutile phase of GeO_2, this environment is located at $\delta_{iso}^{CS} = (152.2 \pm 0.5)$ ppm, with a P_Q of (7.36 ± 0.02) MHz [55]. While there is intensity in this region of the 3QMAS spectrum of LBG-G glass, the mean P_Q of this region is far lower than what would be required for rutile-like O_{666}. It is unlikely that oxygen triclusters similar to those in rutile GeO_2 exist in the glass. However, an oxygen tricluster geometry has also been observed in $Na_4Ge_9O_{20}$. In $Na_4Ge_9O_{20}$, the tricluster is located at significantly more positive chemical shift ($\delta_{iso}^{CS} = (246.5 \pm 0.5)$ ppm) and with a much lower P_Q ((3.75 ± 0.05) MHz) [55]. While there is intensity in this region in the LBG-G spectra,

it overlaps quite strongly with the expected B–O–La environment. Therefore these data cannot be used to draw a definite conclusion regarding the presence of O_{666} triclusters in the glass. However, if O_{666} triclusters are present, they are likely present in low amounts, as the chemical shift consistent with their presence is near to the leftmost edge of the glass signal in the quantitative MAS spectrum.

The NMR results support a $LaBGeO_5$ glass structure that is both radically different than that of the crystal and highly interconnected. The ^{11}B and ^{17}O NMR spectra of the glass support the presence of many species not featured in the crystal, *i.e.*, $B\emptyset_2O^-$, ($^{5/6}Ge-O-{}^{4}Ge$), and ($^{5/6}Ge-O-B$). The change in position and breadth of the ^{139}La peak in the glass support structural changes in the La environment, though the nature of these changes is not currently certain. The $[B\emptyset_4]^-$ glass peak is of more positive chemical shift than that of the crystal, implying changes in the nature of its neighbours. Our $^{11}B\{^{10}B\}$ REDOR experiments support this interpretation, indicating that there are fewer $[B\emptyset_4]^-$–$[B\emptyset_4]^-$ links in the $LaBGeO_5$ glass than in the crystal, as well as the presence of BO_3–$[B\emptyset_4]^-$ links. The absence of $^{4}Ge-O-{}^{4}Ge$ and La–O–La environments, and the presence of both $^{4}Ge-O-B$ and plausibly $^{5/6}Ge-O-B$ environments, support a highly interconnected glass network. There are no indications of ordered, "crystal-like" environments present in the glass.

Direct NMR probes of internuclear distances are difficult to carry out for this composition, due to the spectroscopic properties of ^{139}La and ^{73}Ge. The presence of high-coordinate germanium provides a plausible explanation for the difference in glass-forming ability between the $LaBGeO_5$ and the $LaBSiO_5$ compositions. The $LaBSiO_5$ crystal is isostructural to the $LaBGeO_5$ crystal [83], but its precise composition has recently been shown to be outside the lanthanum borosilicate glass forming region when alumina contamination is avoided [97]. If six-coordinate germanium were not present, there would be no obvious structural difference between the $LaBGeO_5$ and $LaBSiO_5$ compositions to explain this difference in behaviour.

Our Raman results support the presence of high-coordinate germanium in the glass. Henderson *et al.* have reported a Raman band attributed to $^{5/6}Ge$ in alkali germanate glasses at a Raman shift of approx. $744\,cm^{-1}$ [73]. While there is no resolved peak observed at this shift in our Raman spectrum of the $LaBGeO_5$ glass (Fig. 7.12), there is substantial intensity present. No intensity is observed at this shift in the spectrum

of the crystal. Hence the substantial intensity at approx. 744 cm^{-1} in the glass can plausibly be attributed to the presence of high-coordinate germanium species.

7.7 Conclusions

We present ^{11}B MAS, ^{11}B{^{10}B} REDOR, ^{139}La WCPMG, ^{17}O MAS and ^{17}O 3QMAS NMR spectra to provide insight regarding the structure of the glass and to probe possible structural changes during crystallization. All NMR spectra indicate substantial structural differences between the glass and the crystal. The crystal is composed of $[B\emptyset_4]^-$ tetrahedra, $Ge\emptyset_2O_2{}^{2-}$ tetrahedra, and LaO_9 polyhedra, with three oxygen environments: ^{4}B–O–^{4}B, ^{4}Ge–O–^{4}B, and ^{4}Ge–O–La. Certain structural units not present in the crystal (*e.g.*, $B\emptyset_2O^-$, $B\emptyset_2O^-$–$[B\emptyset_4]^-$, GeO_6) are positively identified in the glass. Other environments (*e.g.*, $^{5/6}$Ge–O–B) are plausibly present as well, while others still (*i.e.*, La–O–La and ^{4}Ge–O–^{4}Ge) are absent. The diverse range of Ge–O–B environments, as well as the absence of La–O–La and ^{4}Ge–O–^{4}Ge environments, suggests a highly interconnected and homogeneous glass network. Insufficient resolution precludes a quantitative analysis of the proportions of different environments. No structural changes in either the glass or crystal were observed for a range of partially-crystallized samples. A revised equation for calculating the crystallite fraction, c, from moderate-resolution ^{11}B MAS NMR data is presented, supported by high-resolution ^{11}B and ^{17}O MAS NMR spectra.

7.8 Acknowledgements

Financial support from NSERC (Canada Grant Number RGPIN 261987) is gratefully acknowledged. We thank Prof. Mark Obrovac and Prof. Alex Speed of Dalhousie University for access to an X-ray diffractometer and for the synthesis of $H_3B^{17}O_3$, respectively. Compute Canada is thanked for access to computational resources.

Chapter 8

Anisotropic Stress in Laser-Written $LaBGeO_5$ Glass-Ceramic Composites

8.1 Context

This chapter describes the results of DFPT calculations on the $LaBGeO_5$ crystal structure. Due to the complicated thermal dynamics of the laser-writing process, it is expected that laser-written $LaBGeO_5$ glass-ceramics will have some residual stress. The stresses during writing are so significant that the process needs to take place at elevated temperatures, in this case 400 °C [103]. Knorr *et al.* attempted to characterize this stress through analysis of micro-Raman spectra of a $LaBGeO_5$ laser-written line [108]. They informed their analysis using the data of Coussa *et al.*, who collected Raman spectra of the $LaBGeO_5$ glass and crystal under isotropic compressive stress [109]. However, there is no reason to expect that the stress on the laser-written $LaBGeO_5$ glass-ceramic composite will be isotropic. Furthermore, Coussa *et al.* only reported the response of two $LaBGeO_5$ crystal Raman modes to stress. Knorr *et al.* report data on two modes, only one of which which was described by Coussa *et al.* Hence we conducted DFPT calculations on the $LaBGeO_5$ crystal to examine the response of all its Raman modes to stresses, both isotropic and anisotropic. This allowed us to construct a more physically meaningful model of the stresses present in laser-written $LaBGeO_5$ glass-ceramics.

This chapter was originally published as Paterson, A.L. and Zwanziger, J.W., Anisotropic Stress in Laser-Written $LaBGeO_5$ Glass-Ceramic Composites, *J. Appl. Phys.* 124 (8) (2018) 083106, with permission of AIP Publishing [283]. The content below has been reproduced from the preprint version of the article, with minor modifications for style and clarity. Copyright permissions for this use are contained in Appendix E. The contributions of the authors to the text are as follows: ALP synthesized all samples, collected all novel experimental data, conducted all DFT

calculations and data analysis, and wrote the majority of the manuscript. JWZ provided substantial insights to the analysis of the data, and made significant editorial contributions to the manuscript.

8.2 Abstract

$LaBGeO_5$ glass-ceramic composite materials are of interest because the $LaBGeO_5$ crystal phase is ferroelectric, and can be grown in single-crystal form within the glass by localized heating from femtosecond laser irradiation. The crystals formed are expected to exhibit residual stress, due to the different mechanical properties of the glass and crystal phases. Recent micro-Raman data on these crystals have been interpreted as showing an isotropic stress field in the crystals. Here we reinterpret these data in light of detailed density functional perturbation calculations of the Raman spectra of the crystal phase under different stress conditions. Our results support a model where the stress in the *ab* plane of the $LaBGeO_5$ crystal is compressive and the stress along the *c* axis of the crystal is tensile. This model is consistent with the linear thermal expansion coefficients of the $LaBGeO_5$ crystal, which are anisotropic and of differing sign. These results indicate complexity of crystal formation in this system and possible limitations of using it in optical devices where a uniform stress state would be required.

8.3 Introduction

TFN materials are a class of glass-ceramics that combine the transparency of glass with ferroelectric properties, which can only be found in crystalline structures [1]. While there are many examples of TFN materials with widely varying compositions [274, 285], perhaps one of the most interesting is the $LaBGeO_5$ glass-ceramic. $LaBGeO_5$ is a synthetic form of the stillwellite mineral, and both the germanate and its isostructural silicate analogue are ferroelectric [88, 286]. Part of the interest in the $LaBGeO_5$ TFN system stems from its congruent crystallization, *i.e.*, the glass and crystal have the same stoichiometry. Given that many TFN composites can contain multiple chemically distinct crystalline phases [1], the $LaBGeO_5$ system is attractive for its relative simplicity. All forms of the $LaBGeO_5$ system have come under substantial

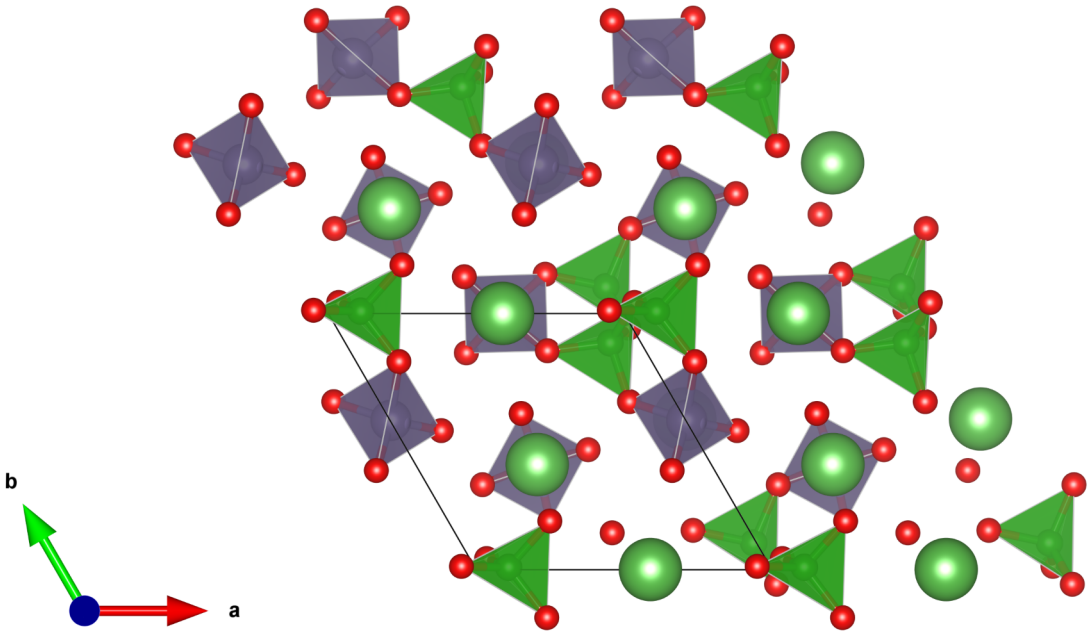

Figure 8.1: The room-temperature crystal structure of $LaBGeO_5$ [78]. The presented view is down the crystallographic c axis with a $2 \times 2 \times 2$ supercell. $[B\emptyset_4]^-$ tetrahedra are coloured dark green, while $Ge\emptyset_2O_2{}^{2-}$ tetrahedra are purple. LaO_9 polyhedra are omitted for clarity. Lanthanum ions are light green.

investigation, including determinations of the crystal structures [78, 79] (Fig. 8.1), studies of the glass structure [34, 75], studies of the nonlinear optical properties of the system [232, 233], and studies on the crystallization of the nanocomposite material [34, 98, 287]. Perhaps one of the most interesting properties of the $LaBGeO_5$ system is the formation of $LaBGeO_5$ crystals within the bulk of the glass through the application of laser irradiation. Laser-written $LaBGeO_5$ crystals have been formed via both continuous-wave and femtosecond lasers, with the latter being used to create complex three-dimensional architectures [2, 103, 104, 288]. Recent evidence has also suggested that these laser-written crystals-in-glass maintain single-crystal character over macroscopic distances [105].

While the glass and crystal have the same chemical composition, they do not have the same structure and would not be expected to have the same mechanical properties. Therefore, the crystals induced in the glass would be expected to form under possibly significant stress fields, due to the different elastic properties of the glass host and the

crystal. Knorr *et al.* have provided some insight into the environment of both undoped and Er-doped $LaBGeO_5$ laser-written crystals in glass, based upon space-resolved Raman spectroscopy, and conclude that the crystal experiences isotropic compressive stress [108]. Coussa *et al.* report Raman spectra of both $LaBGeO_5$ glass and crystal under isotropic pressures up to 18.3 GPa [109]. However, Coussa *et al.* only report the response of two high-frequency peaks for the crystal, while Knorr *et al.* report data on both high- and low-frequency modes [108]. Furthermore, the data presented by Coussa *et al.* for the $LaBGeO_5$ crystal are not reported to be controlled for the orientation of the crystal [109]. The intensities and peak shifts observable in the Raman spectrum of the $LaBGeO_5$ crystal depend on both the orientation and polarization of the incident laser [95, 198]. Moreover, recent work has shown that the crystals themselves grow anisotropically [104], and in addition crystalline $LaBGeO_5$ exhibits both anisotropic and negative thermal expansion [79]. Thus the crystals, even if annealed, when cooled to ambient temperature in the glass matrix would be expected to show complex residual stress.

In order to provide a comprehensive examination of the stresses experienced by $LaBGeO_5$ laser-written crystals in glass at ambient conditions, we report DFPT-based calculations of the Raman spectra of the $LaBGeO_5$ crystal in response to changes in stress and strain, and compare them to the existing experimental data [108, 109]. Both isotropic and anisotropic stresses are considered. We also consider our results in the context of the Selsing model of stresses present in glass-ceramics [289]. The Selsing model requires knowledge of the thermal expansion coefficients of both the glass and crystal. The linear coefficient of thermal expansion of the $LaBGeO_5$ glass has been reported in the literature [96], but the thermal expansion behaviour of the $LaBGeO_5$ crystal is more complicated and the coefficients of thermal expansion of the crystal have not been previously reported. We extract the volumetric coefficient and the two linear coefficients of thermal expansion of the $LaBGeO_5$ crystal from the temperature-dependent neutron diffraction data of Belokoneva *et al.* [79]. The Selsing model also requires the knowledge of various elastic moduli of the glass and of the crystal. We report experimental values for the elastic moduli of the $LaBGeO_5$ glass, as well as elastic moduli for the $LaBGeO_5$ crystal derived from DFT calculations.

8.4 Theory

8.4.1 Raman Intensities from DFPT

Raman scattering consists of an incoming light wave interacting inelastically with an atomic displacement, resulting in a scattered outgoing light wave, and thus from a density functional theory standpoint can be reduced to the computation of the third derivative of the total energy with respect to two interactions of the electric field and an atomic displacement. A key result of DFPT, known as the $2n + 1$ theorem, is that such third-order terms can be computed from knowledge of only the ground and 1st-order perturbed wavefunctions [290, 291]. This result makes the *ab initio* computation of Raman spectra as (relatively) simple as computing the Γ-point phonons and the optical dielectric response. The reduction of the bare DFPT derivatives to experimentally relevant geometries is described in detail by Caracas and Cohen [292].

We briefly restate the relevant equations, and the context in which we interpret the results. Via DFPT, we calculate the Raman susceptibility tensor β_{ij}, with $i, j = x, y, z$. β_{ij} is a second-rank tensor which is the derivative of the electric polarizability tensor χ_{ij} with respect to the atomic displacements $r_{\alpha\tau}$ associated with the phonon eigenvector $u_{\alpha\tau}$, scaled by the unit cell volume Ω such that:

$$\beta_{ij} = \sqrt{\Omega} \sum_{\alpha,\tau} \frac{\partial \chi_{ij}}{\partial r_{\alpha\tau}} u_{\alpha\tau}, \tag{8.1}$$

where

$$\chi_{ij} = \frac{\epsilon_{ij}^{\infty} - \delta_{ij}}{4\pi}, \tag{8.2}$$

and ϵ_{ij}^{∞} is the high-frequency dielectric tensor. The Raman intensity of a given phonon mode at a given polarization will be proportional to ${\omega_{\mathrm{L}}}^4 \beta_{ij}^2$, where ω_{L} is the frequency of the incident laser. However, this requires linearly polarized incident light and the selection of polarized scattered light. In a system where the incident and scattered light are unpolarized we would expect to observe averages of the possible orientations. The equations describing the Raman intensity of a powder, in which the intensity from crystallites is averaged, should serve as a sufficient approximation for our purposes. The total Raman intensity of a powder is the sum of the orientational averages of the

parallel ($I_{\parallel}^{\text{powder}}$) and perpendicular ($I_{\perp}^{\text{powder}}$) components of the crystal:

$$I_{\text{Total}}^{\text{powder}} = I_{\parallel}^{\text{powder}} + I_{\perp}^{\text{powder}}. \tag{8.3}$$

The parallel and perpendicular components of the intensity can be calculated from the rotational invariants of the susceptibility tensor:

$$\begin{aligned} I_{\parallel}^{\text{powder}} &= C\left(10G^{(0)} + 4G^{(2)}\right), \\ I_{\perp}^{\text{powder}} &= C\left(5G^{(1)} + 3G^{(2)}\right). \end{aligned} \tag{8.4}$$

The rotational invariants are

$$\begin{aligned} G^{(0)} &= \frac{1}{3}(\beta_{xx} + \beta_{yy} + \beta_{zz})^2 \\ G^{(1)} &= \frac{1}{2}\left[(\beta_{xy} - \beta_{yx})^2 + (\beta_{yz} - \beta_{zy})^2 + (\beta_{zx} - \beta_{xz})^2\right] \\ G^{(2)} &= \frac{1}{2}\left[(\beta_{xy} + \beta_{yx})^2 + (\beta_{yz} + \beta_{zy})^2 + (\beta_{zx} + \beta_{xz})^2\right] \\ &\quad + \frac{1}{3}\left[(\beta_{xx} - \beta_{xx})^2 + (\beta_{yy} - \beta_{yy})^2 + (\beta_{zz} - \beta_{zz})^2\right]. \end{aligned} \tag{8.5}$$

C is the prefactor

$$C = (\omega_{\text{L}} - \omega)^4 \frac{1 + n(\omega)}{30\omega}. \tag{8.6}$$

As mentioned above, ω_{L} is the frequency of the incident light (*i.e.*, the laser frequency). ω is the frequency of the phonon mode under consideration. $n(\omega)$ is the Bose-Einstein factor $n(\omega) = [\exp(\hbar\omega/k_{\text{B}}T) - 1]^{-1}$ at temperature T. Once the Raman response for each phonon mode has been calculated for a given temperature and laser frequency, the total spectrum can be plotted via convolution with an appropriate damping function, such as a Lorentzian.

8.4.2 Directional Dispersion of Raman Modes in Polar Crystals

The $LaBGeO_5$ crystal is a member of the polar $P3_1$ space group [78]. For polar space groups, the phonon mode frequencies depend not only on the specifics of the crystal structure, but also the relative orientation of the incident laser and the crystallographic axes. We present a brief discussion of the practical consequences of this effect in the context of Raman spectroscopy on a single crystal of $LaBGeO_5$. For a comprehensive

discussion of this phenomenon, the reader is directed to the literature [150, 293].

The $LaBGeO_5$ unit cell contains 24 atoms [78], and hence has 69 optic phonon modes, all of which are Raman-active [95]. The 69 optic modes of the $LaBGeO_5$ crystal can be decomposed into 23 A modes and 23 E modes. As a member of the trigonal polar $P3_1$ space group, the $LaBGeO_5$ crystal structure is uniaxial, and hence contains an "optically isotropic" plane and an orthogonal optic axis. The optic axis is coincident with the crystallographic c axis; our choice of Cartesian coordinates places the z axis in this direction. The optically isotropic xy plane is hence in the crystallographic ab plane. Dependent on the orientation of the phonon wavevector, $\mathbf{q}$, relative to the c axis, the phonon modes of the crystal can be classified as purely longitudinal optic (LO) or transverse optic (TO). The angle between $\mathbf{q}$ and c is denoted by θ. For $\mathbf{q} \parallel c$ (*i.e.*, $\theta = 0°$), there will be a set of A(LO) modes and doubly-degenerate E(TO) modes. Conversely, for $\mathbf{q} \perp c$ (*i.e.*, $\theta = 90°$), the degeneracy of the E modes is broken, and three distinct symmetries can be observed: A(TO), E(TO), and E(LO) modes. One set of E(TO) modes is transverse for any θ, and these modes are referred to as ordinary modes. The ordinary modes are of constant frequency for any value of θ. All other modes have frequencies that depend on θ; these modes are referred to as extraordinary modes. The frequencies of the extraordinary modes vary continuously and monotonically with θ, and frequencies at intermediate values of θ couple two fundamental modes at $\theta = 0°$ and $\theta = 90°$. The symmetries of the fundamental modes do not need to be the same; A modes can couple with E modes, and TO modes can couple with LO modes. Any modes so linked are coupled by "directional dispersion" [293]. While the symmetries of the fundamental modes at the extremes of θ are well-defined, the same cannot be said for modes at intermediate values of θ. These "oblique" modes can be of complex mixed A, E, LO, and TO character. The directional dispersion of the extraordinary modes can be calculated via the roots of

$$\left| ({\omega_i}^2 - \omega^2)\delta_{ij} + \frac{(\hat{\boldsymbol{q}} \cdot \boldsymbol{M}_i)\,(\hat{\boldsymbol{q}} \cdot \boldsymbol{M}_j)}{\epsilon_0 \epsilon_\infty\,(\hat{\boldsymbol{q}})} \right| = 0, \tag{8.7}$$

where

$$\epsilon_\infty\,(\hat{\boldsymbol{q}}) = \epsilon_\infty^{\parallel} \cos^2\theta + \epsilon_\infty^{\perp} \sin^2\theta. \tag{8.8}$$

In the above equations, ω is the frequency of the extraordinary mode, ω_i is the

transverse phonon frequency of mode i, $\hat{\boldsymbol{q}}$ is the unit vector of the direction of propagation, and $\boldsymbol{M}_i$ is the reduced dielectric polarization vector of mode i [95, 294].

The practical consequences of the directional dispersion of the $LaBGeO_5$ crystal are threefold. The first is that care must be taken when choosing the direction of non-analyticity of the $\boldsymbol{q} \to \boldsymbol{0}$ limit in our DFPT calculations [295]. The second is that through careful analysis of the experimentally observable modes, the relative orientation of the crystal can be determined [95]. The third is that it is possible for the directional dispersion to depend on the stress experienced by the system. As such, any study of the response of the phonon frequencies of a polar crystal to stress must carefully consider the orientation of the crystal.

8.4.3 The Selsing Model

The Selsing model [289] is a simple model for estimating the isotropic thermal stress present in a glass-ceramic composite. It predicts that the stress inside the ceramic phase is given by

$$P = \frac{\Delta\alpha\Delta T}{\frac{1+\nu_\mathrm{G}}{2E_\mathrm{G}} + \frac{1-2\nu_\mathrm{X}}{E_\mathrm{X}}}, \tag{8.9}$$

where subscripts G and X refer to glass and crystal values, respectively. Furthermore, $\Delta\alpha$ is the mismatch between the volumetric thermal expansion coefficients of the glass and the crystal, such that $\Delta\alpha = \alpha_\mathrm{X} - \alpha_\mathrm{G}$; ΔT is the difference between the glass transition temperature and room temperature; and E and ν are the elastic moduli and the Poisson's ratios of the crystal and glass, respectively. The Selsing model was derived for systems where the crystallites are spherical, isotropic, and rarefied such that their stress fields do not overlap; the latter condition typically requires a crystallized volume fraction of less than 10 % [296]. In the system under investigation these conditions do not rigorously hold, but nevertheless, we use the Selsing model to provide an estimate of the order of magnitude of the stress experienced by the $LaBGeO_5$ crystals-in-glass.

8.5 Methods

8.5.1 Density Functional Perturbation Theory Calculations

All electronic structure calculations were performed using the ABINIT 8.6.3 software package [161]. NCPPs were generated using the ONCVPSP code [164]. The pseudopotentials were generated using parameters as provided from the ABINIT website (https://www.abinit.org/), except that the exchange-correlation functional was changed to the local-density approximation (LDA). The LDA with the Teter rational polynomial parametrization fit to Ceperley-Alder data was used to enable the calculation of Raman intensities. The valence spaces of the pseudopotentials were as follows: La($5s^2 5p^6 s^1 5d^2$); B($2s^2 2p^1$); Ge($3d^{10} 4s^2 4p^2$); O($2s^2 2p^6$). A plane-wave energy cutoff of 40 hartree was used with a $4 \times 4 \times 4$ shifted Monkhorst-Pack grid of k-points, which resulted in a root mean square (RMS) convergence of $0.8\,\mathrm{cm}^{-1}$ in the phonon frequencies. The choice of k-point mesh corresponds to a grid spacing of approximately $0.035\,\text{Å}^{-1}$. Structural optimizations were carried out using the Broyden-Fletcher-Goldfarb-Shanno algorithm, which was considered converged when the maximum force on any atom was less than 2×10^{-5} hartree per bohr. The initial structural input was generated from data reported by Kaminskii *et al.* [78] using the CIF2CELL program [297]. The crystallographic information file was obtained from ICSD [298]. The relaxed geometry was generated by allowing both cell dimensions and ionic positions to vary. Stressed geometries were generated by straining the unit cell according to the elastic constants calculated from the relaxed geometry for a given stress, and then allowing ionic positions to relax. The space group symmetry was preserved for all calculations. Raman intensities were calculated using Eqs. (8.3), (8.4) and (8.6), using values of $T = 298\,\mathrm{K}$ and $\omega_\mathrm{L} = 488\,\mathrm{nm}$, to match values provided in Knorr *et al.* [108]. Calculated Raman spectra were plotted with a full-width at half-maximum (FWHM) value of $15\,\mathrm{cm}^{-1}$, consistent with widths observed by Knorr *et al.* [108]. Space-resolved Raman shift profiles were extracted from Fig. 6 of Knorr *et al.* [108] through the use of IMAGEJ software [299].

8.5.2 Sample Preparation and Measurements of Physical Properties

Stoichiometric amounts of La_2O_3 (Sigma-Aldrich, 99.99 %), GeO_2 (Sigma-Aldrich, ≥99.99 %), and B_2O_3 (Sigma-Aldrich, ≥98 %) were intimately mixed and then melted in a 95/5 Pt/Au crucible using a 1250 °C box furnace in air for 30 min. The melt was quenched by pouring into an aluminium mould preheated to 500 °C. The resulting glass block was (5.55 ± 0.02) mm thick. Experimental elastic moduli of the glass were derived from measurement of the velocities of longitudinal and transverse ultrasonic waves in the glass. Velocities were determined via use of a Olympus 45MG ultrasonic thickness gauge. Longitudinal and transverse transducers were both operated at 5 MHz. The Poisson's ratio of the glass is $\nu = [1 - 2(v_T/v_L)^2]/[2 - 2(v_T/v_L)^2]$, where v_T and v_L are respectively the transverse and longitudinal velocities. The shear modulus G of the glass is $G = {v_T}^2\rho$, where ρ is the density of the glass. The other moduli can be calculated via the standard relations for a glass [3]. The density of the glass was determined by Archimedes' method using absolute ethanol as the immersion fluid. Density measurements were controlled for temperature.

8.6 Results

The calculated phonon frequencies of the relaxed ($P = 0$ GPa) system, and their comparison to experimental values, are presented in Table 8.1. The experimental phonon frequencies are obtained from Hrubá *et al.* [95], and our calculated frequencies agree with their experimental values within approximately 11 cm^{-1} RMS, or 0.5% less than experiment. As discussed above, the symmetry character of a given mode depends on the orientation of the incoming wavevector, $\boldsymbol{q}$, with the optic axis of the crystal, c. Frequencies for both $\theta = 0°$ (A(LO), E(TO) and $\theta = 90°$ [A(TO), E(TO), ELO] are provided. Calculated Raman spectra of the $\theta = 0°$ orientation for selected stress fields are presented in Fig. 8.2. The relative intensities of the Raman peaks do not dramatically change when stresses of approximately 1 GPa are applied. The relative intensities of the peaks are generally consistent with literature reports on powdered samples [75, 109].

In order to make use of the Selsing model, we require reliable values for the volumetric coefficient of thermal expansion for both the $LaBGeO_5$ glass and crystal, as

Table 8.1: Phonon frequencies from experiment, and from DFPT calculations. Experimental values are obtained from Hrubá *et al.* [95]. Due to their low oscillator strengths, certain modes are not experimentally observable. Calculated values are from the relaxed geometry. All values are in cm^{-1}.

	Experiment [95]		Relaxed			Experiment [95]		Relaxed	
Mode	TO	LO	TO	LO	Mode	TO	LO	TO	LO
A_1	87	89	81.8	81.9	E_1	92	92.7	89.6	89.6
A_2	95	95.5	94.0	95.4	E_2	109	110	110.2	110.7
A_3	117	119	118.6	120.4	E_3	124	125	125.4	125.5
A_4	144	144.5	152.0	152.6	E_4	162	179	159.6	174.3
A_5	173	213	178.9	187.3	E_5	185	200	185.7	195.2
A_6			187.7	209.8	E_6	207	208	202.5	208.1
A_7	215	221.5	211.0	225.3	E_7	233	233.5	231.4	232.0
A_8	273	273	261.5	261.5	E_8	258	262	250.4	255.2
A_9			297.4	298.0	E_9	301	320	287.7	306.8
A_{10}	306	307	304.4	304.6	E_{10}	336	352	330.4	351.9
A_{11}	324	329	319.2	323.0	E_{11}	384	396	379.9	387.9
A_{12}	368	380	360.4	374.6	E_{12}	423	439	415.8	434.3
A_{13}	389	422	383.5	417.7	E_{13}	454	454	449.8	450.1
A_{14}	503	510	499.3	507.0	E_{14}	496	502	496.5	499.8
A_{15}	549	552	544.2	547.5	E_{15}	616	621	619.3	620.6
A_{16}	631	633	625.5	628.3	E_{16}	695	701	692.4	694.9
A_{17}	733	745	731.1	742.5	E_{17}	722	753	718.8	743.5
A_{18}	799	803	791.1	793.9	E_{18}	784	811	773.4	800.8
A_{19}	806	813	802.2	823.4	E_{19}	826	834	820.6	831.6
A_{20}	847	852	848.0	850.3	E_{20}	859	863	870.6	871.4
A_{21}	864	866	871.8	878.3	E_{21}	918	928	926.6	941.8
A_{22}	941	980	990.8	1006.8	E_{22}	975	1042	994.2	1054.1
A_{23}	992	1050	1014.6	1074.9	E_{23}	1088	1098	1119.8	1124.9

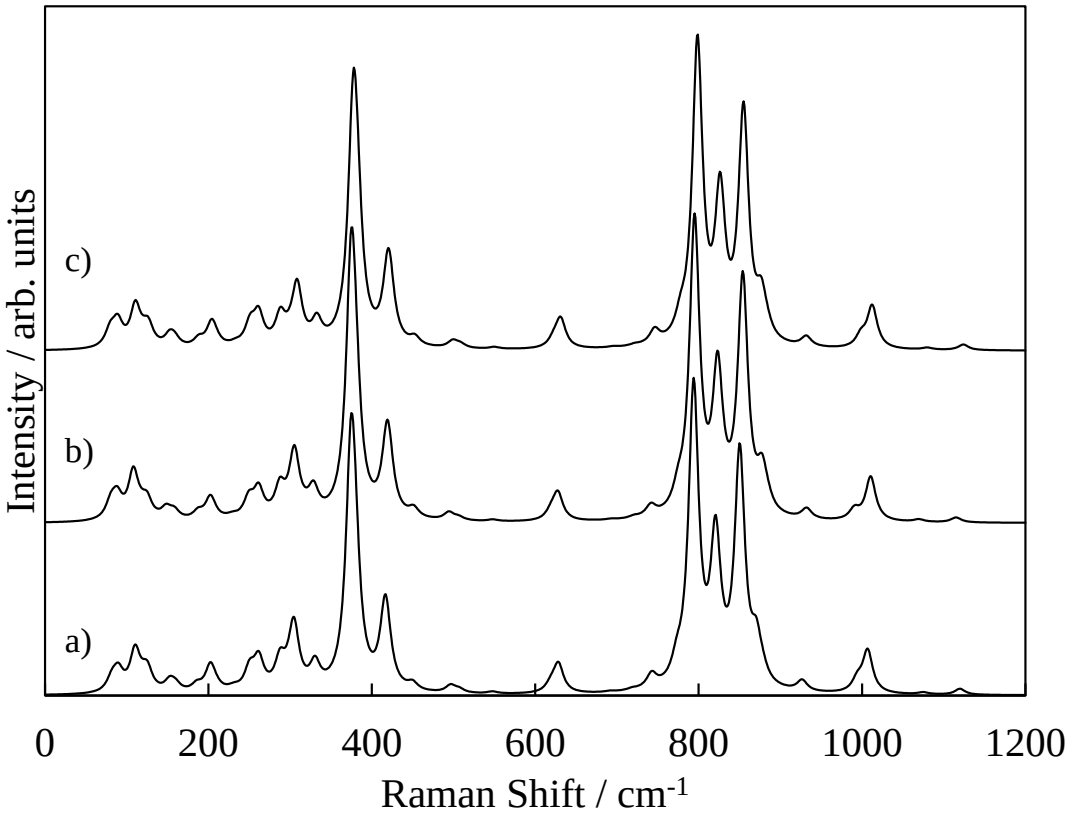

Figure 8.2: Theoretical Raman spectra for $LaBGeO_5$ at different stress fields: a) $P = 0\,\text{GPa}$; b) $\sigma_{xx} = \sigma_{yy} = -\sigma_{zz} = 1\,\text{GPa}$; c) $P = 1\,\text{GPa}$. The spectra are vertically offset for clarity. Intensities are calculated using Eqs. (8.3), (8.4) and (8.6), using a temperature of 298 K. The incident laser wavelength is set to 488 nm, to match the data of Knorr *et al.* [108]. We convolute the spectra with a Lorentzian function with a FWHM of $15\,\text{cm}^{-1}$, consistent with linewidths reported by Knorr *et al.*

Table 8.2: The unique elastic stiffness constants and the elastic moduli of the $LaBGeO_5$ glass and low-temperature crystal. The bulk modulus (K), shear modulus (G), elastic modulus (E), and Poisson's ratio (ν) of the crystal are reported as Voigt-Reuss-Hill averages. All crystal values are derived from DFT calculations on the relaxed ($|P| = 0\,\mathrm{GPa}$) $LaBGeO_5$ structure.

	$P3_1$ Crystal	Glass
C_{11} / GPa	229.9	128 ± 1
C_{12} / GPa	98.3	46 ± 3
C_{13} / GPa	102.1	
C_{14} / GPa	-0.3	
C_{15} / GPa	6.6	
C_{33} / GPa	280.7	
C_{44} / GPa	64.1	41.0 ± 0.8
K / GPa	148.8	73 ± 3
G / GPa	67.4	41.0 ± 0.8
E / GPa	175.0	104 ± 2
ν	0.303	0.26 ± 0.01

well as values for the glass transition temperature, the elastic modulus and Poisson's ratio for the crystal, and the shear modulus for the glass. The glass transition temperature of the $LaBGeO_5$ glass has been reported to be about 670 °C [96, 232]. Our experimental results for the elastic constants and moduli of the $LaBGeO_5$ glass, as well as the Voigt-Reuss-Hill averages [300] of the elastic moduli of the low-temperature phase of the $LaBGeO_5$ crystal, are reported in Table 8.2. The shear, bulk, and elastic moduli require knowledge of the density of the sample. The density of the glass was found to be $(4.98 \pm 0.03)\,\mathrm{g\,cm^{-3}}$. Our value for the shear modulus of the glass [$(41.0 \pm 0.8)\,\mathrm{GPa}$] is close to the values reported in the literature (approx. 39.0 GPa) [246]. To our knowledge, the elastic moduli of the $LaBGeO_5$ crystal have not been reported in the literature.

The linear thermal expansion expansion coefficient of the glass has been reported to be $\alpha_{L,G} = 7.6 \times 10^{-6}\,\mathrm{K^{-1}}$ over the temperature range of 20 °C to 300 °C [96]. As glass is an isotropic material, the volumetric thermal expansion coefficient is simply three times the linear coefficient. Hence the volumetric thermal expansion coefficient of the glass is $\alpha_{V,G} = 23 \times 10^{-6}\,\mathrm{K^{-1}}$. A preliminary value for the linear thermal expansion coefficient of the $LaBGeO_5$ crystal has been reported as $\alpha_{L,X} = 6.5 \times 10^{-6}\,\mathrm{K^{-1}}$ [96]. However, this value does not appear to acknowledge the anisotropy of the $LaBGeO_5$

Table 8.3: Linear (α_a, α_c) and volumetric (α_V) coefficients of thermal expansion for the $LaBGeO_5$ low-temperature crystal phase ($P3_1$), high-temperature crystal phase ($P3_121$), and glass. Crystal coefficients are calculated from high-resolution neutron diffraction data reported by Belokoneva *et al.* [79]. Glass coefficients are from Sigaev *et al.* [96].

Phase	Temperature / °C	α_a / $10^{-6}\,K^{-1}$	α_c / $10^{-6}\,K^{-1}$	α_V /$10^{-6}\,K^{-1}$
$P3_1$	20–300	≈0	14.1 ± 0.7	14.6 ± 0.9
	350–480	-3.6 ± 0.3	27 ± 1	16.5 ± 0.1
	480–530	-18 ± 2	38 ± 3	15.2 ± 0.3
$P3_121$	550–700	61 ± 5	15 ± 1	20.3 ± 0.2
Glass*	20–300	7.6	7.6	23

* For an isotropic material such as a glass, $\alpha_a = \alpha_c = \frac{1}{3}\alpha_V$. The glass values were reported in Ref. [96] without uncertainties.

crystal, nor the negative thermal expansion reported for this system [79]. Based upon the report high-resolution temperature-dependent neutron diffraction data [79], we calculate average linear and volumetric coefficients of thermal expansion for both the high-temperature and low-temperature phases of the $LaBGeO_5$ crystal over a range of temperatures. These values are reported in Table 8.3.

8.7 Discussion

8.7.1 Selsing Model Calculations

Using the Selsing formula (Eq. (8.9)), we can estimate the magnitude and sign of the stress in the laser-written $LaBGeO_5$ crystal-in-glass. Most of the requisite data is presented in Section 8.6. With the ambient temperature assumed to be 25 °C, we calculate the residual internal thermal stress on the $LaBGeO_5$ crystal to be 0.6 GPa. As discussed in Section 8.4.3, there are a number of assumptions made by the model which do not match the system under investigation. Hence we do not expect the stresses we predict from our DFPT calculations to agree perfectly with the value from the Selsing model. We do expect that any physically plausible stress to be of a similar order of magnitude, however.

8.7.2 Crystal Orientation

The observable vibrational modes in the $LaBGeO_5$ crystal depend on the orientation and polarization of the incident light [95, 150, 293]. As such, it is important to consider the possible effects of angular variation on the behaviour of the Raman peaks of the $LaBGeO_5$ crystal in response to stress. The only empirical data on the behaviour of the crystalline $LaBGeO_5$ Raman peaks in response to stress are presented by Coussa *et al.* [109], who did not discuss the orientation of their sample. As such, we discuss the possible interactions of directional dispersion and stress in the sections below. However, there is substantial experimental evidence available regarding the orientation of laser-written $LaBGeO_5$ crystals-in-glass. Based upon polarized micro-Raman measurements of $LaBGeO_5$ laser-written lines, with the laser perpendicular to the direction of crystal growth, Stone *et al.* concluded that the c axis of the crystal is parallel to the direction of crystal growth [2]. Stone *et al.* later confirmed this observation through the use of scanning electron microscopy (SEM) [105]. The SEM data of Stone *et al.* show that there is less than 1° of variation over the face of a laser-written $LaBGeO_5$ crystal. The data presented in Fig. 5 of Knorr *et al.* are consistent with the c axis of the crystal being parallel to the direction of crystal growth [108]. Their unpolarized Raman spectra are collected parallel to the direction of crystal growth. The $A(LO)_{13}$ mode at $422\,cm^{-1}$ and $E(TO)_{19}$ mode at $826\,cm^{-1}$ are resolved from their neighbouring peaks, consistent with a $\theta = 0°$ geometry. If $\theta \neq 0°$, the degeneracy of the E modes is broken, and directional dispersion would lead to a complicated pattern of oblique modes. At the maximum value of $\theta = 90°$, our calculations show that the $E(LO)_{11}$, $E(TO)_{12}$, and $E(LO)_{12}$ modes shift and overlap such that the peak at $422\,cm^{-1}$ is substantially diminished. A similar set of changes occurs around the $E(TO)_{19}$ mode. Therefore, regarding spectral overlap, our calculations are consistent with the conclusion of Knorr *et al.* that $\theta = 0°$.

8.7.3 Isotropic Stress

Coussa *et al.* report that the Raman peak at $803\,cm^{-1}$, identified as the $A(LO)_{18}$ mode, responds to compressive isotropic stress with a slope of $(3.3 \pm 0.2)\,cm^{-1}\,GPa^{-1}$ [109]. Knorr *et al.* observe a difference in the $A(LO)_{18}$ mode of $2.5\,cm^{-1}$ between the centre the and edge of their crystal sample (Fig. 8.3). Based upon the results of Coussa *et*

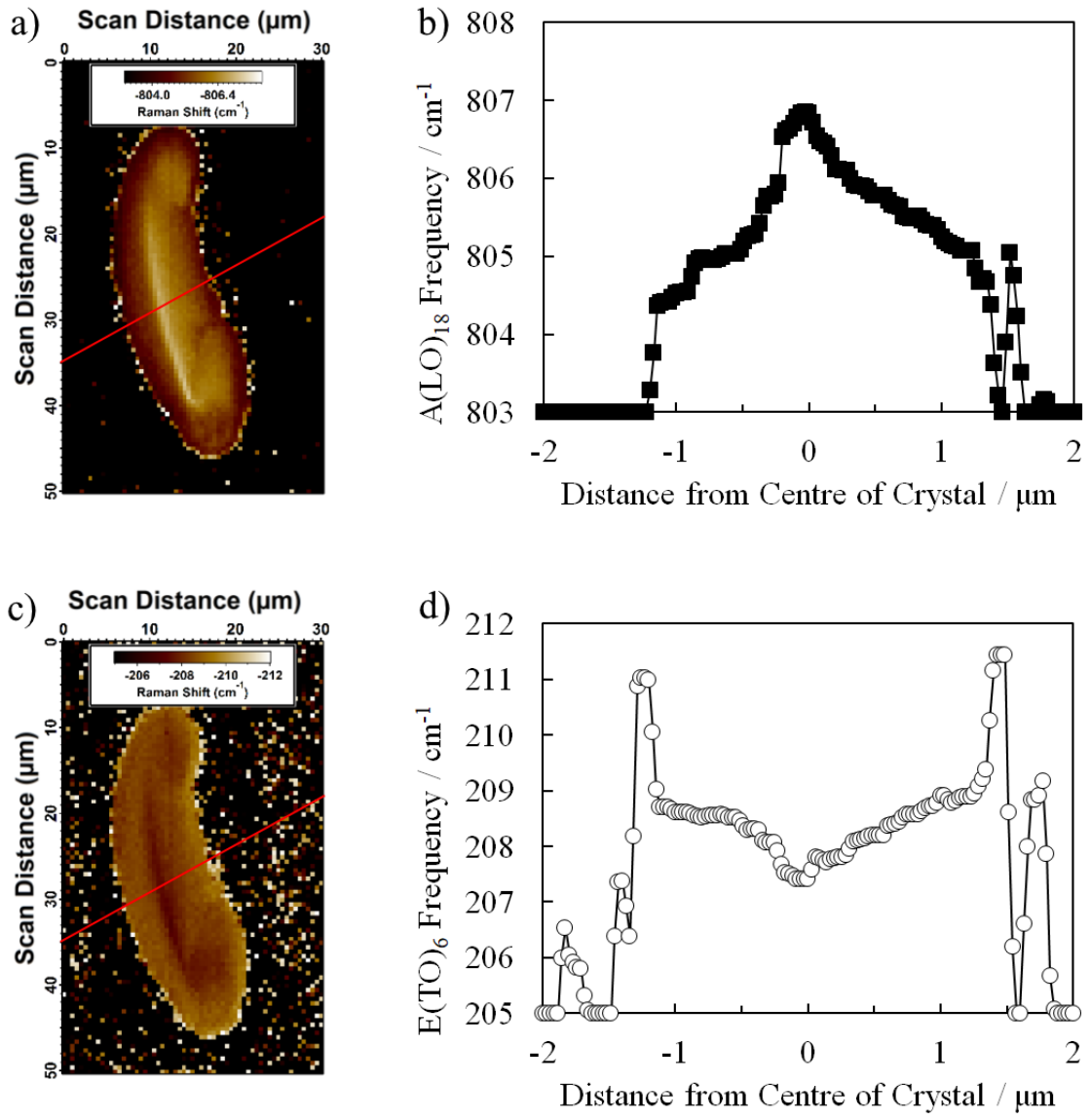

Figure 8.3: Experimental micro-Raman data for the $LaBGeO_5$ crystal-in-glass and extracted Raman shift profiles. a) Micro-Raman data of the $A(LO)_{18}$ mode, adapted from Fig. 6 of Knorr *et al.* [108]. b) The Raman profile of the $A(LO)_{18}$ mode. c) Micro-Raman data of the $E(TO)_6$ mode, adapted from Fig. 6 of Knorr *et al.* [108]. d) The Raman profile of the $E(TO)_6$ mode. The Raman profiles (b,d) are extracted from the micro-Raman data (a,c). The data points extracted from the micro-Raman data are indicated by red lines in (a,c). We set the 0 point of our x axis as the maximum of the $A(LO)_{18}$ mode, which coincides with the minimum of the $E(TO)_6$ mode and is roughly at the centre of the crystal. Positive x axis values move towards the right of the line of the inset, while negative values move toward the left. The profile was chosen to coincide with the "minor" axis of the crystal, approximately parallel with the shortest path through the crystal.

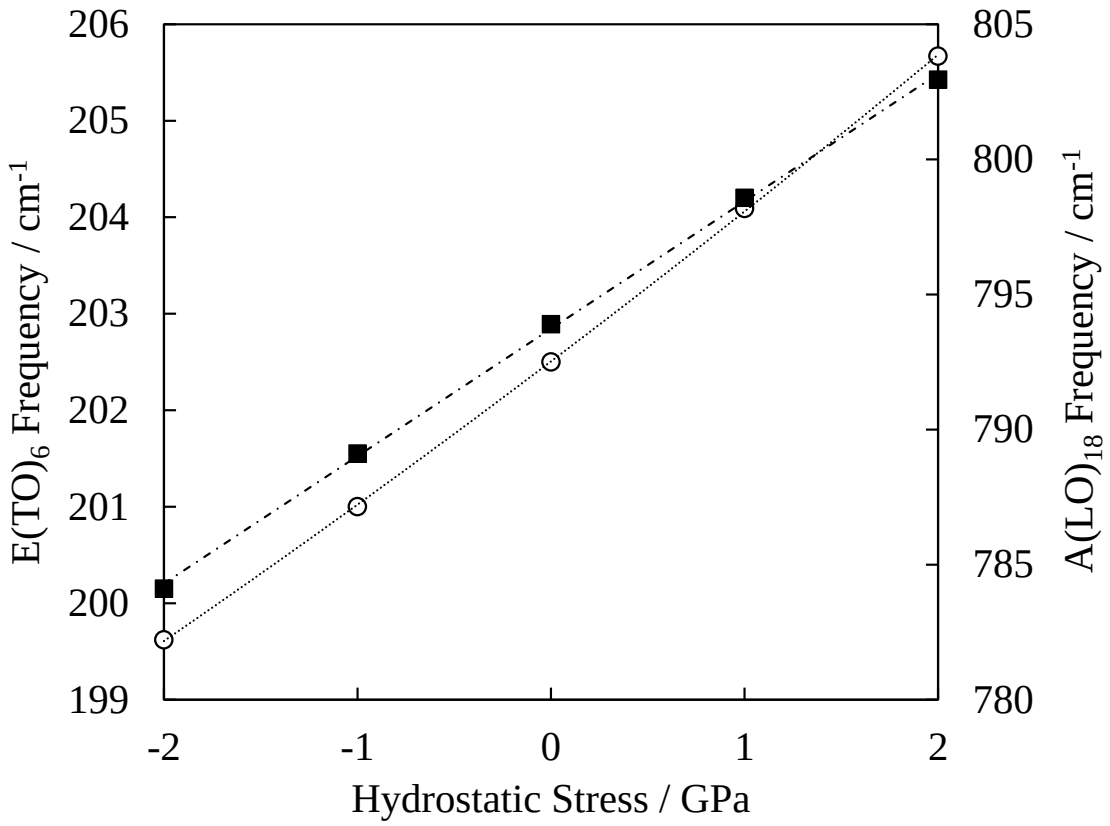

Figure 8.4: The responses of the $E(TO)_6$ (left axis, open circles) and $A(LO)_{18}$ (right axis, filled squares) modes to isotropic stress. The lines are linear fits to the data.

al., Knorr *et al.* conclude that there is a stress differential of 0.75 GPa between the centre and the edge, leading to a stress gradient of 0.168 GPa µm^{-1} over a length of 4.5 µm [108].

Our data for the responses of the $A(LO)_{18}$ and $E(TO)_6$ to changes in isotropic stress are presented in Fig. 8.4. Considering only the $A(LO)_{18}$ mode, our results for systems under isotropic stress are consistent with the data of Coussa *et al.* [109], with a slope for the $A(LO)_{18}$ mode of 4.72 cm^{-1} GPa^{-1}. This would suggest a stress differential of 0.53 GPa between the edge and centre of the crystal, with a stress gradient of 0.11 GPa µm^{-1}. However, Coussa *et al.* do not report on the behaviour of the $E(TO)_6$ mode. Based upon changes induced by isotropic stress, our results predict that a stress differential of 0.5 GPa would result in an $E(TO)_6$ shift of 0.8 cm^{-1} between the edge and centre of the crystal. Knorr *et al.* observe nearly the opposite:

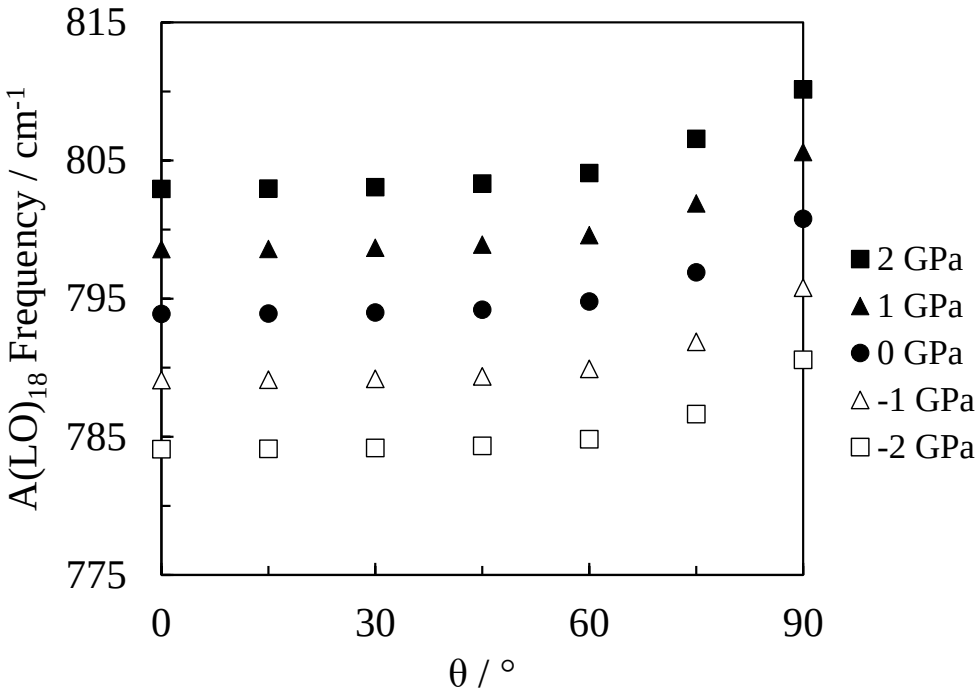

Figure 8.5: Changes in the frequency of the $A(LO)_{18}$ mode in response to changes in θ for various isotropic stresses. There is very little change in frequency for $\theta < 45°$. For $\theta \geq 45°$, the $A(LO)_{18}$ frequency increases at about the same rate regardless of stress.

a shift of $-1.5\,\mathrm{cm}^{-1}$. Our computed slope of the $E(TO)_6$ mode is both linear and positive, with a value of $1.5\,\mathrm{cm}^{-1}\,\mathrm{GPa}^{-1}$. There is no isotropic stress, either tensile or compressive, for $\theta = 0°$ crystal orientation, that can simultaneously explain a positive shift in $A(LO)_{18}$ and a negative shift in $E(TO)_6$, as both respond positively to compression and negatively to tension.

Therefore, explaining the laser-induced crystal growth in this system requires a reconsideration of the conclusions that $\theta = 0°$, and/or that the stress field is isotropic. We consider first the possibility of directional dispersion. The changes in frequency of the $A(LO)_{18}$ mode with response to changes in θ for the stresses studied are presented in Fig. 8.5, and likewise for $E(TO)_6$ in Fig. 8.6. For all stresses studied, an increase in θ leads to a monotonic positive change in $A(LO)_{18}$ and a monotonic negative change in $E(TO)_6$. It is possible to construct a combination of isotropic stress and $\theta \neq 0°$

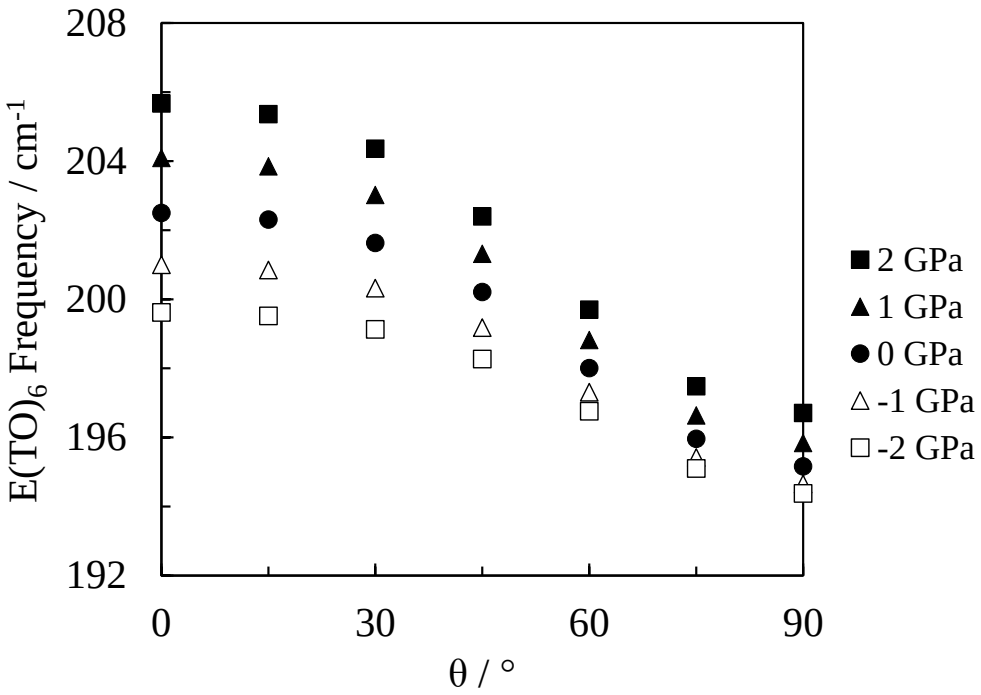

Figure 8.6: Changes in the frequency of the $E(TO)_6$ mode in response to changes in θ for various isotropic stresses. The influence of stress on the frequency of the $E(TO)_6$ mode decreases as θ increases.

which leads to a shift of $2.5\,\mathrm{cm}^{-1}$ in $\mathrm{A(LO)}_{18}$ and $-1.5\,\mathrm{cm}^{-1}$ in $\mathrm{E(TO)}_6$. However, we do not believe such a combination is a physically plausible explanation for the experimental data reported by Knorr *et al.*, for the following reasons.

As discussed in Section 8.7.2, we would expect an observable change in the number of resolvable peaks as θ moved away from 0°; no such change is observed. Furthermore, any such combination of isotropic stress and θ would require $\theta = 0°$ at the edge of the crystal, and $\theta \neq 0°$ at the centre. Were there to be a change in θ as the crystal grows, we would expect $\theta = 0°$ at the centre, and for θ to increase as the distance from the centre increases. Finally, the value of θ required to match the experimentally observed shifts is approximately 40°, while the SEM results of Stone *et al.* suggest that we should expect θ to be small or zero, with little to no variance across the face of the crystal-in-glass [105]. Hence, it is much more likely that a different phenomenon is responsible for the positive shift in $\mathrm{A(LO)}_{18}$ and negative shift in $\mathrm{E(TO)}_6$. A plausible explanation is that the crystal experiences anisotropic stress. Working on a similar system, Stone hypothesized that $\mathrm{LaBGeO_5}$ laser-written lines experience significant tensile stress parallel to the c axis of the crystal [106]. We now consider the possible effects of anisotropic stresses on the $\mathrm{LaBGeO_5}$ crystal.

8.7.4 Anisotropic Stress

Anisotropic stresses are generally more complicated and more computationally expensive to calculate than isotropic stresses, as the former may break the symmetry of the crystal. However, the $\mathrm{LaBGeO_5}$ crystal has $P3_1$ symmetry, *i.e.*, lattice constants $a = b \neq c$. If the stresses on the system are applied in a similar fashion, that is $\sigma_{xx} = \sigma_{yy} \neq \sigma_{zz}$, then the symmetry of the system is preserved. As this seems to be a plausible approximation of the system under investigation, where the constraints in the xy plane are different than the constraints along the z axis, we have exploited this symmetry in our calculations. The responses of the frequencies of the $\mathrm{A(LO)}_{18}$ and $\mathrm{E(TO)}_6$ modes to anisotropic stresses are presented in Fig. 8.7. The stresses applied are such that $\sigma_{xx} = \sigma_{yy} = -\sigma_{zz}$, *i.e.*, compressive stress in the xy plane and tensile stress along the z axis, or vice versa. The behaviour of the $\mathrm{A(LO)}_{18}$ mode in response to this anisotropic stress is generally similar to its response to isotropic stress. For positive xy stresses where $\sigma_{xx}, \sigma_{yy} \leq 2\,\mathrm{GPa}$, the $\mathrm{A(LO)}_{18}$ frequency becomes

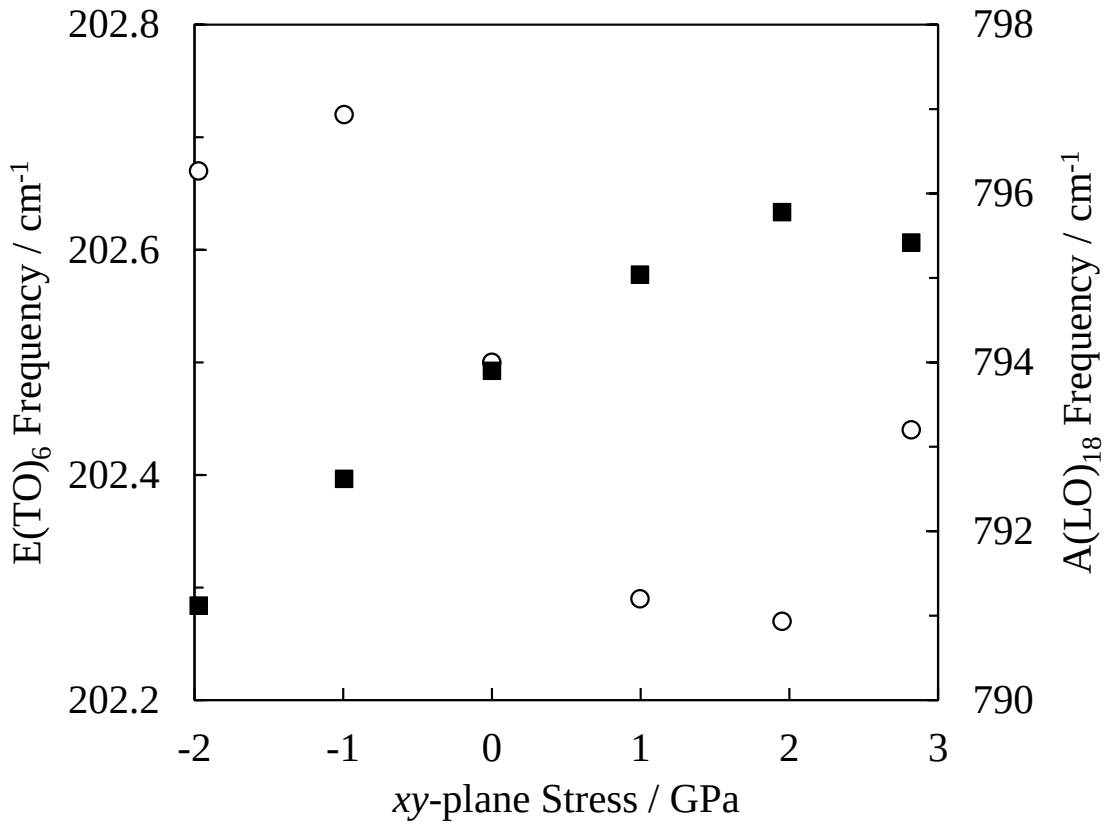

Figure 8.7: The responses of the $E(TO)_6$ (left axis, open circles) and $A(LO)_{18}$ (right axis, filled squares) modes to anisotropic stress. The data are arranged according to the stress applied to the xy plane. The stresses on the z axis at a given xy plane stress are of approximately equal magnitude and opposite sign of the the xy plane stress.

more positive, and vice versa for negative xy stresses. However, when the stress is increased further ($\geq 2\,\text{GPa}$), the $A(LO)_{18}$ shift reverses direction. The magnitude of the change in $A(LO)_{18}$ in the anisotropic case is lower than that of the isotropic case. The behaviour of the $E(TO)_6$ mode in the anisotropic case is very different than in the isotropic case. The most obvious change is that in the anisotropic case, the sign of the shift of the $E(TO)_6$ mode in response to changing stress is generally opposite that of the $A(LO)_{18}$ mode; in the isotropic case, both the $E(TO)_6$ mode and the $A(LO)_{18}$ mode have shifts of the same sign. The changes of the $E(TO)_6$ mode are very non-monotonic, with the shift reversing direction at the extremes of the strains studied. Like the $A(LO)_{18}$ mode, the magnitude of the change in $E(TO)_6$ is lower in the anisotropic case than in the isotropic case.

There are two possible combinations of anisotropic stresses which could explain the experimental observations of Knorr *et al.* The first is compressive stress in the xy plane and tensile stress along the z axis, with the stress minimum at the glass-crystal interface. The second is tensile stress in the xy plane and compressive stress along the z axis, with the stress minimum at the centre of the crystal. In order to determine which combination is more likely, we examine the thermal expansion behaviour of the $LaBGeO_5$ glass and $LaBGeO_5$ crystal. The coefficients of thermal expansion of the $LaBGeO_5$ glass and both $LaBGeO_5$ crystal phases are reported in Table 8.3.

The temperature and crystallization dynamics of the glass-ceramic composite system are expected to be very complex. Indeed, a recent study by Stone *et al.* on the dynamics of laser-writing in the $LaBGeO_5$ system helps explain the preferential alignment of the crystallographic c axis with the direction of laser writing, as well as the "bean" shape of the crystal cross-section [104]. The results of Stone *et al.* demonstrate that the direction of crystal growth can be affected by the change in thermal gradient caused by the translation of the laser beam [104], dividing the growing crystal into two regions: one that undergoes growth tangential to the centre of the laser, and one that undergoes growth radially aligned with the centre. These regions are expected to experience different thermal dynamics and growth patterns while still being crystallographically aligned. However, growth in both of these regions is expected to occur at temperatures in excess of the glass transition temperature, which in $LaBGeO_5$ glass is approximately $670\,^{\circ}\text{C}$ [33]. Knorr *et al.* conducted their

laser writing with the glass sample within a heating chamber held at 500 °C in order to mitigate thermal stresses and resultant cracking of the sample [108]. Many of the stresses from the complex thermal dynamics during laser writing may be mitigated by holding the bulk sample at this elevated temperature. Ultimately, however, it is of interest to consider the stresses in the crystals that remain at ambient conditions, where a device based on this technology would typically be used. Because the crystals grow anisotropically [104], and exhibit anisotropic thermal expansion [79], the ambient stress field could also be expected to be anisotropic. Based upon the coefficients of thermal expansion (Table 8.3) we can provide a justification as to which anisotropic stress combination is more likely.

To form the laser-written $LaBGeO_5$ crystal-in-glass, the sample is initially locally heated by the application of laser irradiation. As the system cools, it will pass through the glass transition temperature (670 °C) [96, 232] and a solid-solid phase transition between the high-temperature ($P3_121$) and low-temperature ($P3_1$) crystal structures (530 °C) [79]. The experimental data for the glass only extend to 300 °C; however, based upon the behaviour of other glasses we do not expect the coefficients of thermal expansion of the glass to vary by more than 50 % [3, 301].

As the composite system cools from the glass transition temperature to the phase transition temperature, both the glass and the crystal contract in all dimensions. The volumetric coefficients of thermal expansion of the glass and the high-temperature phase of the crystal are likely similar, with the glass coefficient being somewhat higher. This would suggest that the residual stress in the crystal is uniformly compressive. However, the linear coefficients of thermal expansion suggest that tensile stress is possible: the linear coefficient of thermal expansion of the crystal c axis is higher than the linear coefficient of thermal expansion of the glass.

Upon passing the phase transition temperature, the a and b axes of the crystal begins to expand as the temperature decreases. While there is no data on the glass coefficient of thermal expansion in this range, the thermal expansion of the glass is expected to remain positive. Hence the ab plane stress experienced by the crystal is expected to remain compressive. In this temperature range the c axis of the crystal continues to contract, and at a higher rate than the glass. Hence we expect the stress in the c axis to remain tensile.

As the system drops below approximately 350 °C, the linear coefficient of thermal expansion of the a axis of the crystal approaches zero, while the c axis and the glass continue to contract. The exact stress dynamics will depend on the precise (and as of yet undetermined) high-temperature behaviour of the glass, as well as the thermal gradient in the system. However, given that it is implausible for the c axis of the crystal to experience anything other than tensile stress, and that even if the linear coefficient of thermal expansion of the glass is greater than expected, the negative thermal expansion present in the ab plane of the crystal provides a source of compressive stress, we conclude that the most likely combination of anisotropic stress is compressive in the ab plane and tensile along the z axis, with a stress maximum at the centre of the crystal.

With the conclusion that the stress in the system is compressive in the ab plane and tensile along the c axis, we can provide an estimate on the amount of stress experienced by the system. The maximum negative shift of the $E(TO)_6$ mode is between $\sigma_{xx}, \sigma_{yy} \approx$ 1 GPa–2 GPa. Above 2 GPa the shift of the mode becomes positive. As the shift of the $E(TO)_6$ mode is monotonically negative, we expect that the magnitude of the maximum stress on the system is 2 GPa or lower. This would correspond to a maximum stress gradient of 0.44 GPa µm^{-1} over the 4.5 µm distance between the edge and centre of the crystal. The direction and relative magnitude of the shift of the $A(LO)_{18}$ mode is consistent with this model.

The model we present above (*i.e.*, compressive ab stress and tensile c stress) correctly returns the directions of the changes in the $A(LO)_{18}$ and $E(TO)_6$ modes, but underestimates the magnitude of the shifts, by 25% and 85% respectively. However, the experimental shifts are quite small: 2.5 cm^{-1} and -1.5 cm^{-1}, respectively. It is difficult using DFT calculations to reproduce such small shifts precisely; hence we believe that the direction of the calculated shift is more reliable than the absolute values. A second point of concern is that there is no particular reason to expect that the stress gradient in the system is linear. Indeed, when the shift of the $E(TO)_6$ mode is examined over the breadth of the crystal, there are indications of non-linear behaviour. Finally, it is certainly possible for the stress gradient of the ab plane to be different than that of the c axis. The thermal expansion dynamics of the ab plane are significantly more complicated than that of the c axis; the former has both positive

and negative thermal expansion in the relevant temperature regime, whereas the latter has only positive thermal expansion. The *ab* plane is also ultimately constrained by glass, while the *c* axis is constrained by neighbouring crystal volumes. This could lead to stresses of different magnitudes between the *ab* plane and the *z* axis.

While the above considerations prevent us from precisely quantifying the stress fields present in the experimental data presented by Knorr *et al.* [108], our results still provides compelling evidence regarding the overall nature of the stresses. Our DFT calculations support a model where the stresses experienced by the laser-written $LaBGeO_5$ crystal-in-glass are anisotropic, and best described by compressive stress in the *ab* plane of the crystal and tensile stress along the *c* axis of the crystal. The magnitude of these stresses is expected to be less than 2 GPa. This stress profile is consistent with the thermal expansion behaviour of the $LaBGeO_5$ glass and crystal phases, which at times undergo negative thermal expansion.

8.8 Conclusions

The observable Raman modes of the $LaBGeO_5$ crystal depend on the relative orientation of the crystal axes and the incident laser. Based upon the modes observed by Knorr *et al.*, we conclude that the angle between the *c* axis of the $LaBGeO_5$ crystal and the incident laser in their experiment is $\theta = 0°$. Our DFPT calculations support a model where the stress in laser-written $LaBGeO_5$ crystals-in-glass is anisotropic. The observed trends in the shifts of the $A(LO)_{18}$ and $E(TO)_6$ modes indicate compressive stress in the *ab* plane of the laser-written crystal and tensile stress along the *c* axis. These stresses are between approximately 1 GPa to 2 GPa in magnitude. This anisotropic stress is supported by qualitative analysis of the relative directions and magnitudes of the coefficients of thermal expansion of the $LaBGeO_5$ glass and crystal in the temperature range of the $P3_121$ to $P3_1$ phase transition. The much simpler Selsing model suggests a compressive stress of a similar magnitude, 0.6 GPa, but note that the Selsing model only can yield isotropic stress. Finally, the directional dispersion of select optical phonon modes of the $LaBGeO_5$ crystal are reported. The $A(LO)_{18}$ and $E(TO)_6$ modes do not show complex changes in directional dispersion in response to stress. Our results show that the stress environment of laser-written $LaBGeO_5$ crystals-in-glass is more complex than previously considered, which will

need to be accounted for in applications requiring homogeneously stressed systems.

8.9 Acknowledgements

Financial support from NSERC (Canada Grant Number RGPIN 261987) is gratefully acknowledged. We thank Compute Canada for access to computational resources.

Chapter 9

Conclusion

9.1 The Goals of this Work

The primary question motivating this work was "*what is the structure of the* $LaBGeO_5$ *glass?*" This is not a simple question, as it encompasses many different experimental approaches and techniques. Accordingly, the central goals of this work were as follows:

- obtain data on the short-range structure of boron in the $LaBGeO_5$ glass via ^{11}B NMR spectroscopy;
- probe for the presence of high-coordinate germanium in the glass via neutron diffraction;
- develop a model relating ^{139}La NMR parameters to short-range lanthanum structure in crystalline materials;
- apply this crystalline model to ^{139}La NMR spectrum of the $LaBGeO_5$ glass to determine the lanthanum-oxygen environment;
- probe the connectivity of the $LaBGeO_5$ glass via ^{17}O NMR spectroscopy;
- test the Sigaev model directly via $^{11}B\{^{10}B\}$ heteronuclear NMR spectroscopy;
- examine the mechanism of crystallization of the $LaBGeO_5$ glass-ceramic composite;
- and evaluate the stress on laser-written $LaBGeO_5$ glass-ceramics via DFT calculations.

These goals were mostly achieved. This chapter will synthesize the data described in Chapters 4 to 8 and present a holistic analysis of the structure of the $LaBGeO_5$ glass.

The structure of the $LaBGeO_5$ glass can be divided into two length scales: short-range, considering only the polyhedra of the first cation-oxygen coordination sphere;

and intermediate-range, considering the connectivity between different short-range polyhedra.

We begin by discussing the crystal. There are three cations present in the $LaBGeO_5$ system: La^{3+}; B^{3+}; and Ge^{4+}. In the crystal, these cations are present as asymmetric LaO_9 polyhedra, $[B\emptyset_4]^-$ tetrahedra, and $Ge\emptyset_2O_2^{2-}$ tetrahedra. This is the short-range order of the system. The intermediate-range order is well-known, but by nature somewhat lengthier to explain.

The intermediate-range order of the $[B\emptyset_4]^-$ tetrahedron is the simplest in the system. Each $[B\emptyset_4]^-$ tetrahedron shares two edges with symmetry-equivalent LaO_9 polyhedra. $[B\emptyset_4]^-$ tetrahedra form a helical chain around the 3_1 crystallographic screw axis (parallel to the c axis), with each $[B\emptyset_4]^-$ unit corner-sharing with two symmetry-equivalent neighbours. Each $[B\emptyset_4]^-$ neighbour pair forms a three-member ring with a $Ge\emptyset_2O_2^{2-}$ tetrahedron.

The $Ge\emptyset_2O_2^{2-}$ tetrahedron is edge-sharing with two symmetry-equivalent LaO_9 polyhedra, shares a corner with a third, and forms a three-membered ring with two symmetry-equivalent $[B\emptyset_4]^-$ tetrahedra. No germanium unit is connected to any other germanium unit.

The LaO_9 polyhedron is edge-sharing with two symmetry-equivalent $[B\emptyset_4]^-$ tetrahedra, two symmetry-equivalent LaO_9 polyhedra, and two symmetry-equivalent GeO_4 tetrahedra. It is also corner-sharing with two additional symmetry-equivalent $Ge\emptyset_2O_2^{2-}$ tetrahedra. Using the notation from Section 6.6.4, there are two distinct $[O_b{}^9La_2{}^4B^4Ge]$ environments with two symmetry-equivalent oxygen, two distinct $[O_{nb}{}^9La_2{}^4Ge]$ environments with two symmetry-equivalent oxygen, and one $[O_b{}^9La^4B_2]$ environment. While there are only two formally non-bridging oxygen in the system, the lanthanum polyhedron is involved with the bonding of all of the bridging oxygen in the system.

In the glass, all three cations display radical differences in both the short-range and intermediate-range order. ^{11}B MAS NMR had previously been used by Gupta *et al.* to establish the presence of BO_3 triangles in the glass, but they did not identify the BO_3 species present [34]. Based upon the ^{11}B MQMAS spectra of the $x La_2O_3 – (100\text{-}x)(0.33\,B_2O_3 – 0.67\,GeO_2)$ samples (where $x = 25$ corresponds to $LaBGeO_5$), we conclude that there is a single BO_3 species present in any appreciable

amount (Section 6.6.1). Using the ^{11}B MQMAS spectra and our own ^{11}B MAS spectra, we obtain the mean δ_{iso}^{CS} values of the BO_3 environment in the glass and correlate them to a crystalline model from the literature [48]. We conclude that the BO_3 units present in the glass are $B\emptyset_2O^-$. $[B\emptyset_4]^-$ units are still present in the $LaBGeO_5$ glass.

The changes in the germanium environment are less precisely known, but no less dramatic. Our neutron diffraction results (Section 6.6.2) support the partial conversion of the $Ge\emptyset_2O_2{}^{2-}$ tetrahedra in the crystal to either $[Ge\emptyset_5]^-$, $[Ge\emptyset_6]^{2-}$, or both. The uncertainty in the coordination numbers determined by neutron diffraction preclude useful numerical modelling. It is not immediately obvious whether the mean number of non-bridging oxygen per GeO_4 unit is changed; however, the ^{17}O MAS and MQMAS spectra of the glass support the presence of Ge–O–La environments, which are not expected to be found on $[Ge\emptyset_5]^-$ or $[Ge\emptyset_6]^{2-}$.

In the glass, the lanthanum-oxygen coordination number is less than it is in the crystal. Neutron diffraction data (Chapter 6) suggest that the mean n_{LaO} in the glass is about 7. Unfortunately, due to differences between δ_{iso}^{CS} and Δ_{offset} in the Czjzek fit of our ^{139}La WCPMG NMR spectra, we cannot obtain an estimate of n_{LaO} via NMR spectroscopy (Chapter 5). However, our ^{139}La WCPMG NMR spectra of $LaBGeO_5$ glass are consistent with a structure where the environment of La^{3+} is disordered, and inconsistent with the presence of periodic structures. Like with the germanium results, the n_{LaO} data are not sufficient to provide an estimate of the exact distribution of La-O polyhedra. However, obtaining an estimate for the mean n_{LaO} in the glass informs the analysis of the intermediate-range order of the glass.

Determining the intermediate-range order of the glass is more difficult than the short-range order, as there are fewer experimental probes which are easily applicable. ^{11}B{^{10}B} REDOR NMR spectroscopy is perhaps the most direct probe of the intermediate range order, at least for the borate species. Our REDOR results support a structure where the $[B\emptyset_4]^-$ units of the glass are approximately equally as likely to be connected to $B\emptyset_2O^-$ units as $[B\emptyset_4]^-$ units. Furthermore, the number of $[B\emptyset_4]^-$–$[B\emptyset_4]^-$ connections is lower in the glass than in the crystal. A change in the $[B\emptyset_4]^-$ environment is supported by the ^{11}B MAS NMR spectra; the $[B\emptyset_4]^-$ environment in the glass has a significantly different δ_{iso}^{CS} than the $[B\emptyset_4]^-$ environment in the glass, consistent with a change in connectivity.

With the data above, we can begin to construct a model of the connectivity of the borate units. The $B\emptyset_2O^-$ species are, on average, expected to have two La^{3+} neighbours, one $[B\emptyset_4]^-$ neighbour, and one other neighbour, likely a germanate. A single La^{3+} neighbour is expected due to the presence of a non-bridging oxygen; the clustering of two La^{3+} is expected due to the mean n_{LaO} value (Section 6.6.4). One $[B\emptyset_4]^-$ neighbour is expected due to the $^{11}B\{^{10}B\}$ REDOR results. The remaining neighbour is not precisely determined, as our REDOR results cannot probe possible BO_3–BO_3 connections. However, the ^{17}O NMR spectra support the significant presence of Ge–O–B environments, and as will be discussed below, the absence of certain Ge–O–Ge environments; additionally, in lanthanum-free borogermanate glasses, $B\emptyset_3$ and $Ge\emptyset_4$ units mix freely ([53], Section 6.6.2). Both of these points increase the likelihood of ^{3}B–O–Ge linkages.

The $[B\emptyset_4]^-$ species are, on average, expected to have about one $B\emptyset_2O^-$ neighbour and about one $[B\emptyset_4]^-$ neighbour. As $[B\emptyset_4]^-$ is not generally expected to contain non-bridging oxygen, its other two neighbours are expected to be germanate units. We might expect that ^{4}B–O–^{4}Ge connections are more likely than ^{4}B–O–$^{5/6}Ge$ connections based upon the respective charges of the units. The $[B\emptyset_4]^-$ species has a formal, non-local negative charge, as do both $[Ge\emptyset_5]^-$ and $[Ge\emptyset_6]^{2-}$. Lowenstein's rule (*i.e.*, tetrahedral avoidance in aluminates) suggests that charged species are less likely to be neighbours [302]. However, for a high field strength cation such as La^{3+}, tetrahedral avoidance has less of an impact on structure [41]. Hence we cannot identify a preference in the germanate neighbours of $[B\emptyset_4]^-$ units.

Determining the connectivity of the germanate units is less straightforward than for the borate units. The most direct probe of the connectivity of germanate units is ^{17}O MAS and MQMAS spectroscopy. Our ^{17}O NMR results support the presence (or absence) of five main Ge–O–X connectivities: ^{4}Ge–O–La, ^{4}Ge–O–^{4}Ge, ^{4}Ge–O–B, ^{4}Ge–O–$^{5/6}Ge$, and $^{5/6}Ge$–O–B. We discuss them in order.

Both the ^{17}O MAS and MQMAS spectra clearly show the presence of Ge–O–La environments (Chapter 7). These NBO environments are not typically associated with high-coordinate germanate species [62], and so we conclude that the Ge–O–La environments are specifically ^{4}Ge–O–La environments. While our ^{17}O NMR are non-quantitative for various reasons, we expect that the average GeO_4 unit will have two

NBO present, *i.e.*, $Ge\emptyset_2O_2^{2-}$. This is due to simple charge compensation: between both $B\emptyset_2O^-$ and $[B\emptyset_4]^-$ species, the average borate unit has a single negative charge. As the number of borate and germanate units are equal, and together they must compensate for the positive charge of the La^{3+} ions, the mean germanate unit must be doubly negatively charged. In four-coordinate germanate units, this would manifest as two non-bridging oxygen per bonding unit.

A connection which appears to be absent in the $LaBGeO_5$ glass is $^4Ge-O-^4Ge$. This environment, which we would expect to be observable via ^{17}O MQMAS NMR, is not observed within our limit of detection. The avoidance of $^4Ge-O-^4Ge$ is not expected from any fundamental rule, but could be due to some combination of dilution or steric effects. However, it must be accounted for in the connectivity model.

The MQMAS results support the presence of $^4Ge-O-B$ environments, where the boron can either be $B\emptyset_2O^-$ or $[B\emptyset_4]^-$; the resolution of the MQMAS spectra is insufficient to separate the two. This supports the $^{11}B\{^{10}B\}$ REDOR results described above, which suggested the presence of $Ge-O-B$ links for both $B\emptyset_2O^-$ and $[B\emptyset_4]^-$. Considering the amount of intra-borate connectivity, even with conservative assumptions regarding the type and amount of high-coordinate germanium, there are more than sufficient germanate units to account for the proposed borate-germanate connectivity. However, due to a lack of quantifiable data, it is difficult to draw further conclusions regarding the $^4Ge-O-B$ connectivity, and whether there exists a bias towards one of the borate units.

Connectivity between ^4Ge and $^{5/6}Ge$ is supported by the ^{17}O MQMAS NMR spectrum. However, due to the inherently non-quantitative nature of MQMAS NMR, and the poor resolution of the ^{17}O MAS spectrum, we cannot speculate on the probability of connectivity between these two units beyond saying that the connection does occur.

The final germanate unit connectivity we explore is $^{5/6}Ge-O-B$. This assignment is based on ^{17}O MQMAS NMR data, and is somewhat speculative (Chapter 7). This connectivity motif has not been previously reported in the literature, but we conclude that this is due to a general lack of data on the structure of borogermanate glasses; in this case, absence of evidence is not good evidence of absence. It is possible that there could be some mutual avoidance of high-coordinate germanium and $[B\emptyset_4]^-$ units, due

to both being non-locally negatively charged, but this would not apply to the $B\emptyset_2O^-$ units; also, as described above, avoidance may not apply with a high field strength cation such as La^{3+}.

Considering all possible connectivities for the germanate units, it becomes apparent that the germanate units are highly interconnected with the borate units, regardless of coordination. There is more connectivity between germanate units in the glass than in the crystal, as the former has $^4Ge-O-^{5/6}Ge$ connectivity while neither has $^4Ge-O-^4Ge$ connectivity. There is no obvious segregation of either borates or germanates of any coordination.

The connectivity of the lanthanum present in the $LaBGeO_5$ glass is largely described by the discussion above, but there remains two important and related points to discuss: namely, lanthanum clustering and the possibility of free oxygen (*i.e.*, La–O–La with no B or Ge neighbour). Our EBS analysis in Section 6.6.4 suggests that, within the assumptions of the EBS model, a single La^{3+} ion is insufficient to compensate NBO on either $B\emptyset_2O^-$ or $Ge\emptyset_2O_2{}^{2-}$. With a mean n_{LaO} of approx. 7, at least two La^{3+} are required. At first, this would appear to imply that La^{3+} are clustered in the glass. However, there is no indication of the presence of free oxygen in the ^{17}O NMR spectra. This limits the potential size of any cluster: no lanthanum can be isolated from the borate or germanate network.

Instead of clustering, it might be more direct to describe La^{3+} as being regularly distributed in the glass. Every borate and germanate structural unit described above requires one or more La^{3+} ions in close proximity. There is no plausible mechanism for phase separation into a La^{3+}-rich phase and a La^{3+}-poor phase, as no plausible borate or germanate units that would support such phase separation are observed.

With the above knowledge of the short-range and intermediate-range order of the $LaBGeO_5$ glass, we can construct an overall model of its structure. The $LaBGeO_5$ glass is highly disordered. Various borate, germanate, and lanthanate polyhedra are intimately connected. Every type of borate unit is connected to every other type of unit. Only connections between the $Ge\emptyset_2O_2{}^{2-}$ tetrahedra appear to be absent. Lanthanum ions are spread evenly throughout the glass network. There are no indications of phase separation of any sort. A plausible pictorial representation of the glass structure is presented in Fig. 9.1.

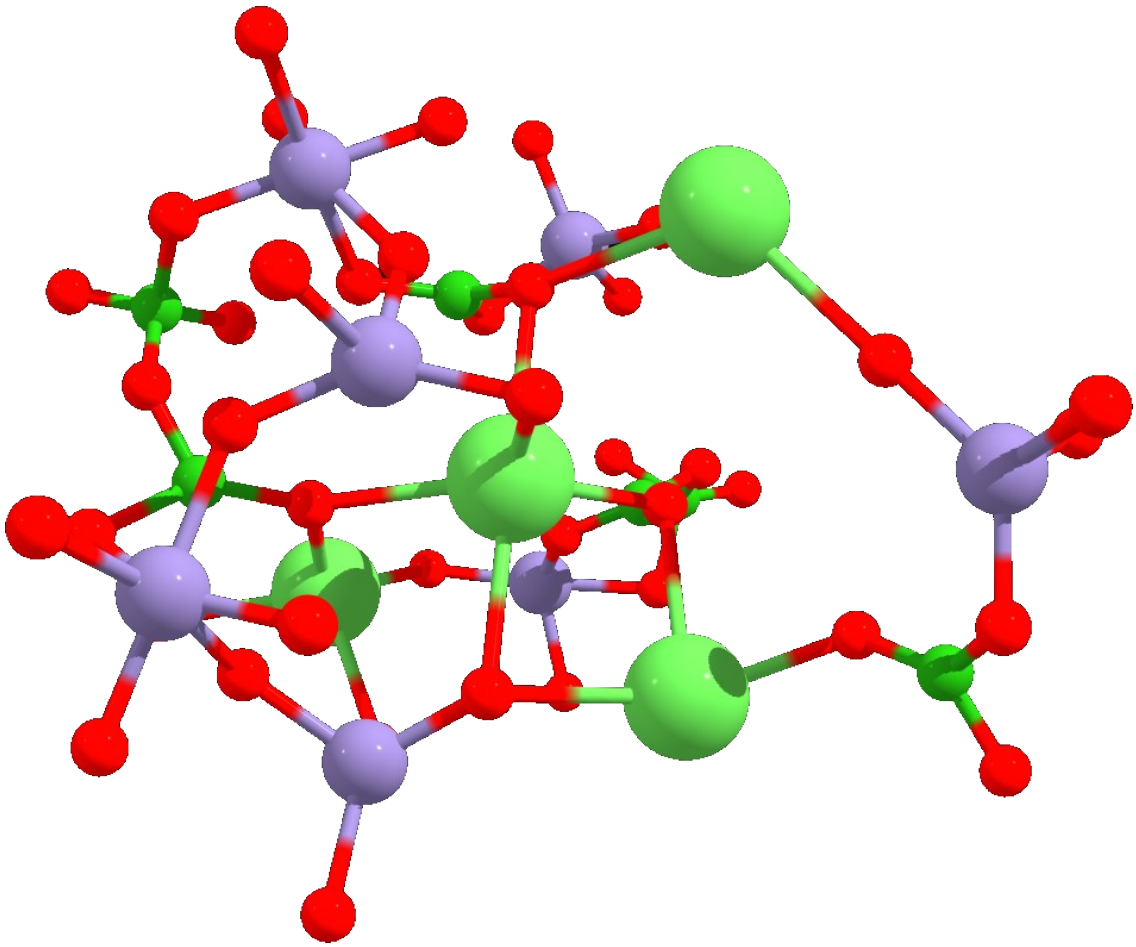

Figure 9.1: A pictorial representation of a plausible configuration of the $LaBGeO_5$ glass structure. The presented structure is manually constructed, and should only be used as a visual aid in interpreting the connectivity of the glass. Germanium ions are purple. Oxygen ions are red. Borate ions are dark green and small. Lanthanum ions are light green and large. The colours are consistent with presentations of the $LaBGeO_5$ crystal (*e.g.*, Fig. 2.5.) Note that lanthanum-oxygen interactions are only presented for non-bridging oxygen, and do not represent the full scale of lanthanum coordination.

Our structural model contradicts the model proposed by Sigaev *et al.* [75]. We observe high-coordinate germanium via several means, a structural unit that was previously discounted. We do not observe "crystal-like" regions in any experiment. We show that the three-coordinate boron and four-coordinate boron are not segregated; in fact, our results indicate that the opposite is true.

Several inferences can be drawn from our model, which may be informative for future work on the $LaBGeO_5$ system and related materials. The homogeneity of the glass structure precludes the formation of clusters or structures that could provide obvious nucleation sites. The presence of high-coordinate germanate units in the $LaBGeO_5$ glass helps to explain why a $LaBSiO_5$ glass cannot be formed; silicate and germanate behaviour is similar when both are four-coordinate, but higher coordinate silicate units do not generally form at standard pressures.

The difference in structure between the $LaBGeO_5$ crystal and glass would suggest a heterogeneous nucleation mechanism [35, 52]. Thermal analysis by Sigaev *et al.* suggest that surface (*i.e.*, heterogeneous) crystallization is dominant in the $LaBGeO_5$ glass [239]. This is supported by the large value for T_{gr} in the $LaBGeO_5$ system; with $T_g = 938\,K$ and $T_m = 1467\,K$, $T_{gr} = 0.64$ [96, 303]. It has been shown that, at least for silicate glasses, systems where $T_{gr} > 0.6$ will only undergo heterogeneous nucleation [32]. What, then, is the source of the nucleation sites in the $LaBGeO_5$ glass? The system has been shown to undergo bulk nucleation, both by bulk thermal heating and by local laser-heating [2, 34]. We suspect that $LaBO_3$ plays a role in the heterogeneous nucleation of $LaBGeO_5$. $LaBO_3$ is a common co-precipitant in the $La_2O_3-B_2O_3-GeO_2$ system, regardless of the precise stoichiometry. Indeed, only three crystals (*i.e.*, $LaBGeO_5$, $LaBO_3$, and $La_2Ge_2O_7$) commonly precipitate from $La_2O_3-B_2O_3-GeO_2$ glasses. We see evidence of $LaBO_3$ in our partially-crystallized samples (Chapter 7), but no trace of $La_2Ge_2O_7$. It is possible that the greater glass-forming ability of the $La_2O_3-B_2O_3$ composition plays a role, as the $La_2O_3-GeO_2$ glass system only forms glasses for quite low ($< 10\,\%$) La_2O_3 contents. Stone has observed $LaBO_3$ occasionally precipitating during the laser-writing process, but not ubiquitously [106]. Lipat'ev *et al.* have recently suggested the possibility of the formation of Ge nanoparticles acting as heterogeneous nucleation sites for $LaBGeO_5$ [304]. The most direct way to test either hypothesis is synchrotron X-ray diffraction with micrometer spatial resolution; no

other technique has the required combination of spatial resolution and crystallographic specificity to definitively address the question of structural changes during nucleation.

9.2 Limitations of the Work

There is much work that could be done to either improve or build upon the results described herein. A major limitation of the structural model that we have constructed is that it is mostly qualitative. There are several reasons for this.

The neutron diffraction data (Chapter 6) are limited in their quantitative precision due to the uncertainty regarding the precise compositions of the samples studied. While the data unambiguously support the presence of $^{5/6}$Ge, they cannot be used to construct a meaningful quantitative model. In principle, repeating the experiment while giving exacting attention to the composition is possible, but the difficulty in accurately quantifying boron in ternary glasses remains a barrier.

The ^{17}O MAS NMR spectra (Chapter 7) do not have sufficient resolution between environments to allow for quantitative fitting; there are simply too many unconstrained or minimally constrained parameters for such a fit to be unique. While the peak resolution in the ^{17}O MQMAS NMR spectra is substantially improved, MQMAS NMR spectra are inherently non-quantitative in intensities. The same is true for the ^{11}B{^{10}B} REDOR experiments, due to the integer nature of the ^{10}B nuclear spin number. Rotational-echo adiabatic passage double-resonance (REAPDOR) NMR spectroscopy, a pulse sequence related to REDOR, has been suggested as an improvement over REDOR, though it is still unclear if precisely quantitative results can be achieved with integer spin nuclides.

The application of ^{139}La NMR to glasses (Chapter 5) is limited by two main factors. The first is that the two fit parameters in the Czjzek model (σ and Δ_{offset}) are not directly comparable to spectral parameters available in crystals. While we can still extract a quantitative indication of the level of disorder in the glass via σ, this parameter is not useful for modelling specific local structural features.

The second limitation is the strength of the ^{139}La NMR crystalline model (Chapter 4). Even if $\delta_{\text{iso}}^{\text{CS}}$ were to be obtained for the Czjzek model in lanthanum oxide-based glasses, any structural information it contained would be from comparison with data

from crystals. There are a limited number of suitable lanthanum oxide-based crystalline compounds for the construction of the crystal model. An ideal model compound would have easily resolved peaks corresponding to crystallographic sites with a range of coordination numbers. Given the extreme breadth of most ^{139}La NMR peaks, this is unlikely to occur. Furthermore, in order to properly assess how δ_{iso}^{CS} responds to changes in CN in samples with differing compositions, a wide composition range in a binary system would be desirable. Unfortunately, there are very few crystal structures within a chemical series; for example, there are only two xLa$_2$O$_3$–(1-x)B$_2$O$_3$ crystal structures which have manageable ^{139}La NMR spectra. The lack of suitable crystal structures and series is a significant barrier to improving on the crystalline model.

The development of the ^{139}La NMR crystalline model would also benefit from a more rigorous statistical approach. An *a priori* analysis of the statistical power of the model would be helpful to estimate the number of samples required for the model to be generally useful, regardless of composition effects. In general, pre-registering the hypothesis of the work and the methodology for the analysis is good practice, and should be considered for studies relying on statistical analysis.

9.3 Future Work

Despite the advances of our model, there are many avenues for further investigation. A major question which remains unanswered is the specific nucleation mechanism of the LaBGeO$_5$ glass-ceramic. While probing the nucleation mechanism of the LaBGeO$_5$ glass was an initial goal of this work, studying the formation of nuclei is quite difficult. The interface between glass and nucleus occupies a very small volume, both in absolute and relative terms. This complicates the study of the nucleation interface via NMR spectroscopy or neutron diffraction, as both techniques require significant sample volume to be effective. While we were unable to directly probe the nucleation of the LaBGeO$_5$ system, our data support a hypothesis where the nucleation is heterogeneous.

Probing the structure of a glass-crystal interface is not straightforward, due to the small size and quantity of the interface. Beyond the synchrotron X-ray diffraction mentioned above, one potentially interesting approach would be to use molecular dynamics simulations to model the interface. This is not a simple undertaking; due to the complexity of the glass structure, the number of atoms present in the simulation

would have to be quite large, on the order of thousands. Substantial validation of the simulation approach would also be required, preferably with direct comparison to experimental diffraction data (that we have conveniently provided). Even if directly modelling the interaction between crystal and glass is too computationally demanding, molecular dynamics simulations of the glass could help evaluate both our proposed structure of the glass, as well as the validity of the application of the Czjzek model to our ^{139}La NMR spectra of the glass.

Beyond the pure $LaBGeO_5$ glass, other examples of the stillwellite system have lingering questions. For example, does doping $LaBGeO_5$ glass (*e.g.*, with Er^{3+}) cause structural changes which are significant to the crystallization process? While the $LaBSiO_5$ composition does not form a glass, other lanthanum borosilicate compositions do; is the behaviour of equivalent lanthanum borogermanates similar up until a critical point, or are there no structural similarities?

Along with the questions about the $LaBGeO_5$ system in particular, our work reveals an under-studied glass composition: the borogermanates. Compared to borosilicate glasses, there are very few structural studies of borogermanates. Our results in Chapter 6 suggest the possibility of a so-called "borogermanate anomaly", but the miscibility gap in the lanthanum borogermanate series we studied prevented this from being thoroughly tested. Speaking generally, how does the presence of borate units affect the evolution of germanium coordination, and vice versa?

The study of the crystallization mechanism of the $LaBGeO_5$ glass-ceramic composite has an obvious route to improve upon it: the direct study of a laser-written sample. The samples studied in Chapter 7 were crushed and ground to powder in order to study them by both ssNMR and pXRD. This is not a precise recreation of the conditions of the laser-writing process. However, reproducing the laser-writing apparatus was beyond the means and scope of this work.

With the benefit of hindsight, many improvements could be made to the work contained herein. Beyond these improvements, however, a number of novel experiments could be attempted to provide new or complementary information.

To improve the experimental model of the glass structure, ^{17}O{^{11}B} REDOR NMR could potentially be useful; by selectively dephasing ^{17}O environments in proximity to ^{11}B, the peaks from Ge–O–Ge and Ge–O–La could be resolved from the

Ge–O–B, B–O–B, and B–O–La environments. This could potentially identify enough constraints to make a fit of the ^{17}O spectrum reasonably quantitative. Additional information on the La–O environment could be obtained via the use of X-ray diffraction (which minimizes O–O interactions), or from neutron diffraction with isomorphic substitution (*e.g.*, replacing La^{3+} with chemically similar, but diffraction-distinct, Ce^{3+}); either would be helpful to clarify precisely which high-r interactions are due to La–O polyhedra.

Exploring the differences between the lanthanum borosilicate and lanthanum borogermanate systems, as well as probing the possibility of a borogermanate anomaly, both require the same approach. Make samples (paying special attention to composition control), collect NMR spectra, collect diffraction data, and evaluate. These experiments do not need novel methods, but they do require due care and attention to ensure that quantitative results can be obtained. To probe a borogermanate anomaly in particular, a ternary borogermanate system with a wide composition range would be preferable; sodium borogermanate glasses seem to be a likely candidate.

9.4 Final Summary

We have produced a model for the structure of the $LaBGeO_5$ glass. This structure was constructed using ^{10}B, ^{11}B, ^{17}O, and ^{139}La NMR spectroscopies in conjunction with neutron diffraction and DFT modelling. The structure of the $LaBGeO_5$ glass is radically different from the structure of the $LaBGeO_5$ crystal, with changes in both the local structure and connectivity of all constituent elements. The stress environment in $LaBGeO_5$ laser-written crystals-in-glass is expected to be anisotropic. Our results strongly support the hypothesis of heterogeneous nucleation in this system. We hope to see this work built upon in the future.

Appendix A

PAW and Pseudopotential Generation

A.1 Software

Both PAW datasets and NCPPs were used over the course of this work. PAW datasets were generated from input based upon version 0.2 of the JTH set [191]. PAW datasets were altered to avoid PAW sphere overlap, which is disallowed by the PAW formalism [155]. Version 4.0.0.12 of the ATOMPAW computer program was used to generate the PAW datasets [165]. NCPPs were generated from input based upon the ONCVPSP set of NCPPs distributed by the ABINIT project [164]. The NCPP were based upon the ONCVPSP-PBE-PDv0.3 set, and were converted to the LDA exchange-correlation (XC) functional using version 3.3.0 of the ONCVPSP code [165].

A.2 PAW Datasets

The details of the construction of the datasets for each atom used are described below. They are accompanied by the ATOMPAW input script used for their generation. If an atom is omitted, then for all structures studied involving that element the default JTH radius was sufficient to avoid overlap. In oxide materials, PAW sphere overlap is most likely to occur between oxygen and its neighbours, particularly lighter elements such as boron.

A.2.1 Boron

Our boron dataset significantly decreases the PAW radius, from the default value of 1.7 bohr to 1.2 bohr. This is required due to the length of the typical B−O bond length, which is approximately 2.7 bohr. The boron dataset treats the $2s^2 2p^1$ electrons as the valence space.

```
B 5
GGA-PBE loggrid 700
2 2 0 0 0 0
2 1 1
0 0 0
c
v
v
1
1.20
y
0
n
y
1
n
custom rrkj
2 0 ultrasoft
1.2
1.2
1.2
1.2
```

A.2.2 Oxygen

Our oxygen dataset uses a decreased PAW radius of 1.30 bohr, down from the default value of 1.41 bohr. This helps resolve the many PAW overlaps which occur with the default radius.

```
O 8
GGA-PBE loggrid 700
2 2 0 0 0 0
2 1 4
0 0 0
c
v
v
1
1.30
y
-0.664
n
y
-1.757
n
custom rrkj
2 0 ultrasoft
1.30
1.30
1.30
1.30
```

A.2.3 Silicon

Our silicon dataset uses a decreased PAW radius of 1.55 bohr, down from the default value of 1.90 bohr.

```
Si 14
GGA-PBE loggrid 1000
3 3 0 0 0 0
3 1 2
0 0 0
c
c
v
c
v
1
1.55 1.55 1.0 1.55
y
1
n
y
2
n
custom rrkj
bessel
1.55
1.55
1.55
1.55
```

A.2.4 Phosphorus

Our phosphorus dataset uses a decreased PAW radius of 1.50 bohr, down from the default value of 1.9 bohr.

```
P 15
GGA-PBE loggrid 1201
3 3 0 0 0 0
3 1 3
0 0 0
c
c
v
c
v
1
1.50
y
1.5
n
y
2
n
custom rrkj
2 0 ultrasoft
1.5
1.5
1.5
1.5
```

A.2.5 Germanium

Our germanium dataset uses a decreased PAW radius of 1.85 bohr, down from the default value of 2.30 bohr.

```
Ge 32
GGA-PBE scalarrelativistic loggrid 2000
4 4 3 0 0 0
4 1 2
0 0 0
c
c
c
v
c
c
v
c
1
1.85 1.85 1.5 1.85
y
4
n
y
2
n
custom rrkj
bessel
1.85
1.85
1.85
1.85
```

A.3 Optimized Norm-Conserving Vanderbilt Pseudopotentials

NCPPs were generated from the ONCVPSP-PBE-PDv0.3 set. This set uses the PBE XC functional. In order to convert a NCPP from the PBE XC functional to the LDA XC functional, we change the `iexc` flag in the input file from `4` (for PBE) to `3` (for LDA). As we did not further modify the NCPPs, we do not provide the input for their generation. The boron NCPP was obtained from the ABINIT website. The lanthanum, germanium, and oxygen NCPPs were taken as is from the *ONCVPSP*-3.3.0 distribution.

Appendix B

Supporting Information for Chapter 4: Relating ^{139}La Quadrupolar Coupling Constants to Polyhedral Distortion in Crystalline Structures

B.1 Context

This appendix was originally published as supporting information to Chapter 4, published as as Paterson, A.L., Hanson, M.A., Werner-Zwanziger, U., and Zwanziger, J.W., *Relating ^{139}La Quadrupolar Coupling Constants to Polyhedral Distortion in Crystalline Structures*, J. Phys. Chem. C 119 (45) (2015) 25508–25517 [126]. The content below has been reproduced from the preprint version of the supporting information, with minor modifications for style and clarity.

B.2 Powder X-ray Diffractograms

The X-ray diffractograms are compared to PDFs obtained from the PDF-2 2002 database.

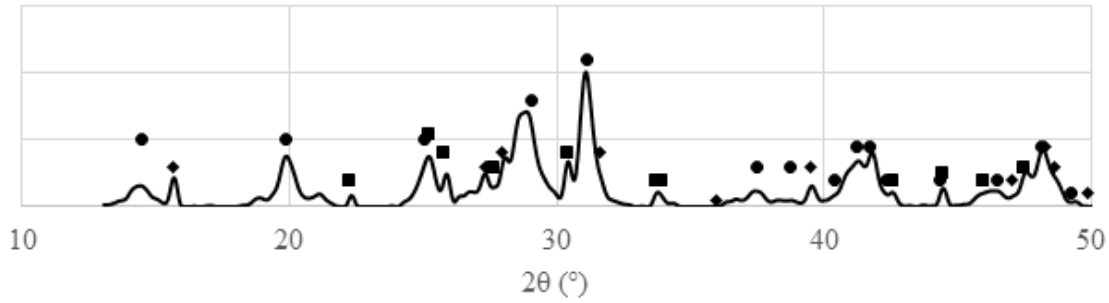

Figure B.1: PXRD diffractogram of $LaPO_4 \cdot 1.8\,H_2O$. Circles indicate peaks from $LaPO_4 \cdot 0.5\,H_2O$ (PDF 46-1439). Squares indicate peaks from $La_2O_2CO_3$ (PDF 84-1963). Diamonds indicate peaks from $La(OH)_3$ (PDF 36-1481).

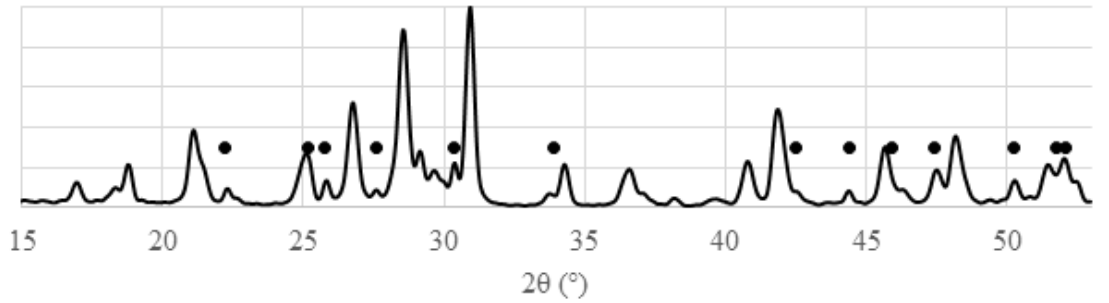

Figure B.2: PXRD diffractogram of $LaPO_4$. Circles indicate peaks from $La_2O_2CO_3$ (PDF 84-1963). All other peaks are from $LaPO_4$ (PDF 83-651).

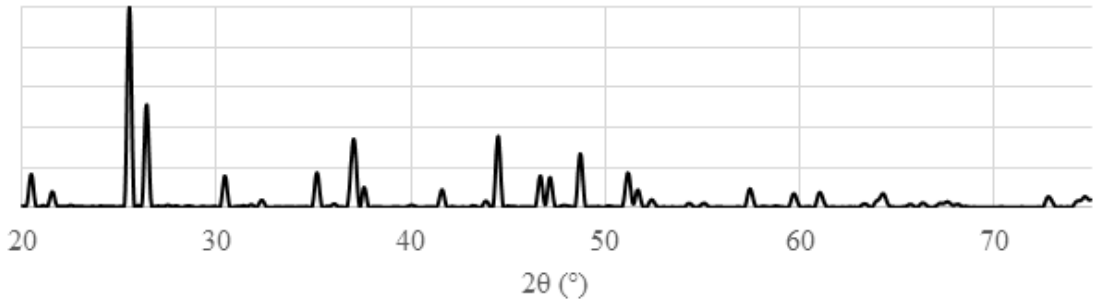

Figure B.3: PXRD diffractogram of $LaBO_3$. All observed peaks are from $LaBO_3$ (PDF 12-0762).

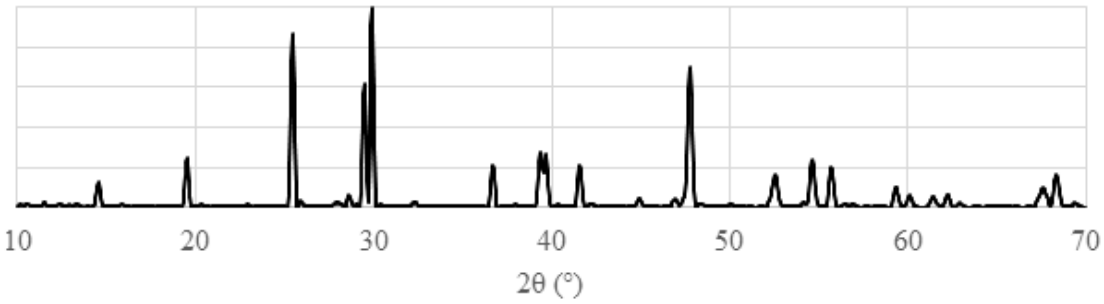

Figure B.4: PXRD diffractogram of $LaBGeO_5$. All observed peaks are from $LaBGeO_5$ (PDF 41-659).

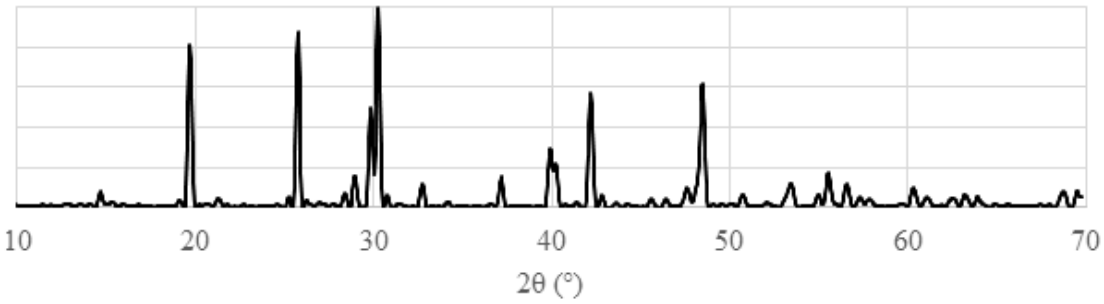

Figure B.5: PXRD diffractogram of $LaBSiO_5$. All observed peaks are from $LaBSiO_5$ (PDF 50-237).

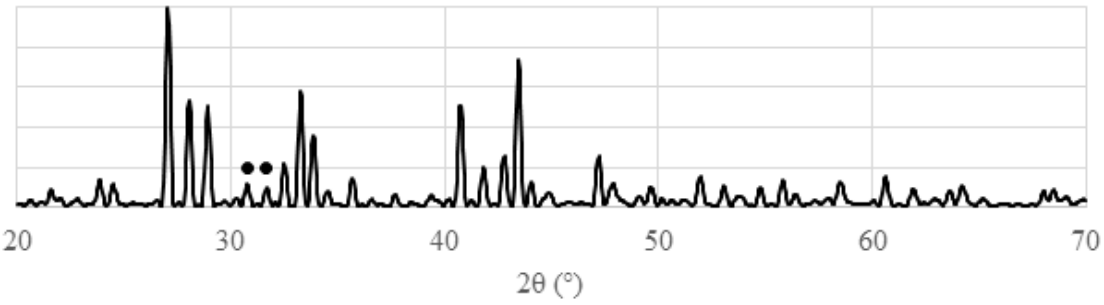

Figure B.6: PXRD diffractogram of $La_2(SO_4)_3 \cdot 9\,H_2O$ (PDF 89-6401). Circles indicate peaks from an unidentified impurity.

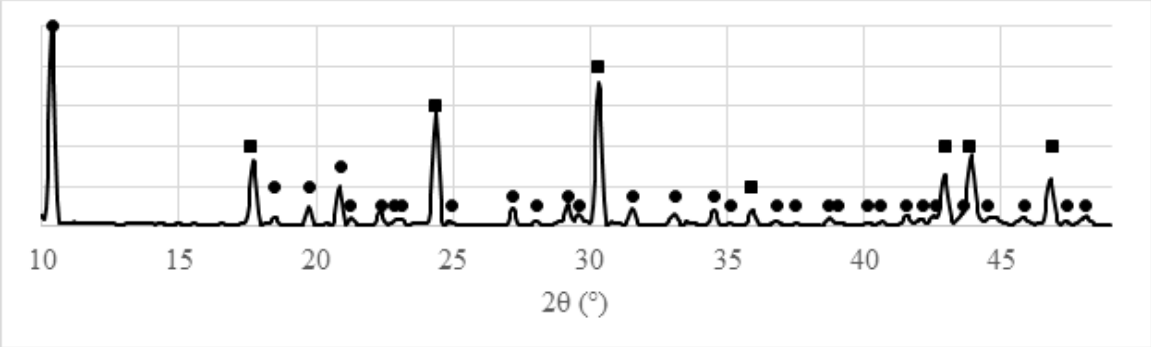

Figure B.7: PXRD diffractogram of $La_2(CO_3)_3 \cdot 8\,H_2O$. Circles indicate peaks from $La_2(CO_3)_3 \cdot 8\,H_2O$ (PDF 73-439). Squares indicate peaks from $La(CO_3)(OH)$ (PDF 26-815).

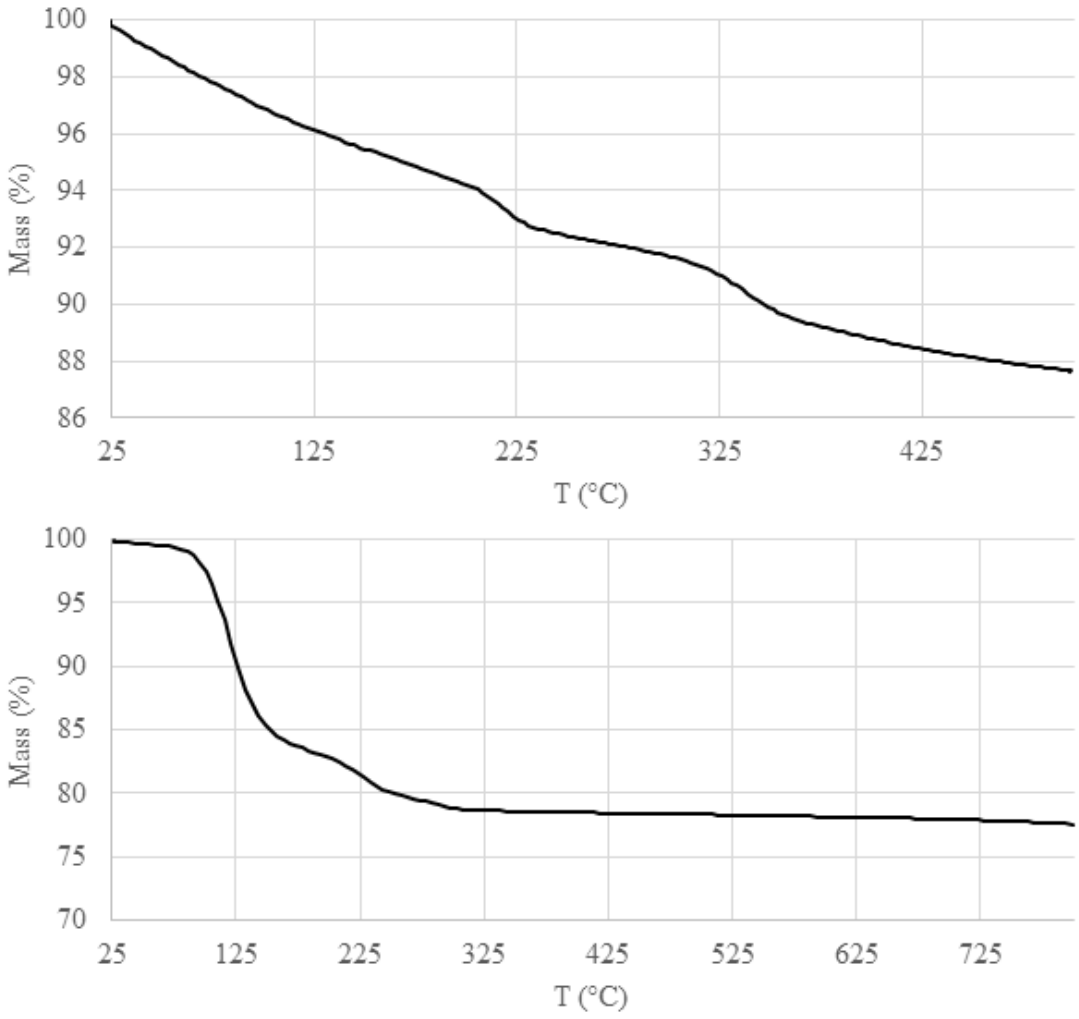

Figure B.8: Top: TGA thermogram of $LaPO_4 \cdot nH_2O$. Bottom: TGA thermogram of $La_2(SO_4)_3 \cdot nH_2O$.

B.3 Thermogravimetric Analysis

TGA was carried out using an aluminium crucible in a NETSZCH TG 209 F3 instrument under nitrogen atmosphere. 33.05 mg of $LaPO_4 \cdot nH_2O$ was heated from room temperature to 500 °C based upon previous literature studies [305]. 31.71 mg of $La_2(SO_4)_3 \cdot nH_2O$ was heated from room temperature to 800 °C based upon previous literature studies [306]. Based upon these plots (with 12.37 % and 22.44 % mass loss, respectively), we calculate n of $LaPO_4 \cdot nH_2O$ to be 1.84, and n of $La_2(SO_4)_3 \cdot nH_2O$ to be 9.08.

B.4 Density Functional Theory Calculations

Table B.1: Atomic parameters used in this study. The electronic valence of each atom is given, along with the configuration of the PAW projectors. The PAW radius is provided in atomic units. All nuclear quadrupole moment were taken from the literature [57]. Any atom not mentioned here was taken without alteration from the JTH PAW dataset table.

Atom	Valence	Projected	Radius / bohr	Q / b
H	$1s^1$	3s	0.5	0
B	$2s^2 2p^1$	2s, 2p	1.2	0.040 59
O	$2s^2 2p^4$	2s, 2p	1.3	−0.025 58
Si	$3s^2 3p^2$	2s, 2p	1.55	0
P	$3s^2 3p^3$	2s, 2p	1.5	0
S	$3s^2 3p^4$	2s, 2p	1.45	−0.0678
Ge	$4s^2 4p^2$	2s, 2p, 1d	1.85	−0.196

Table B.2: Specific details regarding the calculations performed in this study. Both the plane-wave cutoff and the PAW fine grid cutoff are in hartree. All calculations save $LaScO_3$ and $LaNbO_4$ used shifted Monkhorst-Pack grids of the dimensions below; $LaScO_3$ and $LaNbO_4$ used grids not parallel to the reciprocal lattice vectors.

System	ecut	pawecutdg	k-point Grid	Grid Spacing / $Å^{-1}$
La_2O_3	30	140	$10 \times 10 \times 7$	0.03
$LaPO_4 \cdot 0\,H_2O$	45	150	$6 \times 6 \times 6$	0.03
$LaPO_4$	45	150	$4 \times 4 \times 5$	0.04
$LaBO_3$	45	150	$7 \times 4 \times 6$	0.03
$LaBGeO_5$	45	105	$6 \times 6 \times 6$	0.02
$LaBSiO_5$	45	150	$5 \times 5 \times 5$	0.03
$La_2(SO_4)_3 \cdot 9\,H_2O$	25	75	$3 \times 3 \times 4$	0.03
$La(OH)_3$	40	150	$7 \times 7 \times 12$	0.02
$LaAlO_3$	35	110	$8 \times 8 \times 8$	0.02
$LaCoO_3$	40	150	$9 \times 9 \times 9$	0.02
$LaCrO_3$	45	150	$6 \times 6 \times 4$	0.03
$LaScO_3$	20	40	0 5 3 5 0 3 5 5 0	0.03
$LaNbO_4$	30	90	-4 0 4 -4 -8 12 4 4 -4	0.04

B.5 Crystal Analysis

B.5.1 Lanthanum Oxide

La_2O_3 has been previously investigated by ^{139}La ssNMR: first by Bastow in 1994, using a frequency-swept spin-echo technique [59]; and more recently by Spencer *et al.* using a WURST echo [60]. Given the thorough understanding of La_2O_3 in the literature, it is a good choice as a test compound for the implementation of WCPMG and VOCS, as well as for validating computational methods. La_2O_3 crystals are hexagonal and of space group $P\bar{3}m1$ with 1 formula unit per unit cell [219]. The lanthanum environment in La_2O_3 is the simplest of all of the compounds investigated in this work, described by Spencer *et al.* as "pseudo-octahedral". The LaO_7 coordination polyhedron is more precisely referred to as a face-capped octahedron, with two sets of three La–O bonds and the "cap" bond with lengths of 2.37 Å, 2.73 Å, and 2.46 Å respectively.

Our measured C_Q for La_2O_3 is (58.6 ± 0.3) MHz with an η_Q of 0.00 ± 0.03, shown in Fig. B.9, in excellent agreement with the most recent literature values as reported by Spencer *et al.* [60]. We used the same CSA values as Spencer *et al.* in fitting both our 9.4 T and 16.4 T (Fig. B.10) spectra to good effect.

DFT calculations of the EFG at the La^{3+} site using the experimental geometry [219] yielded a C_Q of 60.5 MHz and an η_Q of 0.0, which is in good agreement with the experimental results. When examining the calculated EFG tensor, the largest component V_{zz} is aligned with the La–O bond of the cap oxygen, and is parallel to the c axis of the unit cell as shown in Fig. B.11. The c axis in La_2O_3 possesses threefold rotational symmetry, which is consistent with both the observed and calculated η_Q of 0.

The least-squares ellipsoid that is fit to the LaO_7 polyhedron in La_2O_3 is a prolate spheroid, with semi major axes $e_a = e_b = (2.481 \pm 0.002)$ Å and $e_c = (2.731 \pm 0.002)$ Å and ellipsoid character of 1.00 ± 0.01. There is a moderate departure from spherical symmetry, with $\epsilon = 0.098 \pm 0.002$. The ellipsoid is aligned with the EFG tensor, with the largest semi major axis e_c parallel with V_{zz}, and the two other semi major axes in the plane defined by V_{xx} and V_{yy}, perpendicular to V_{zz}.

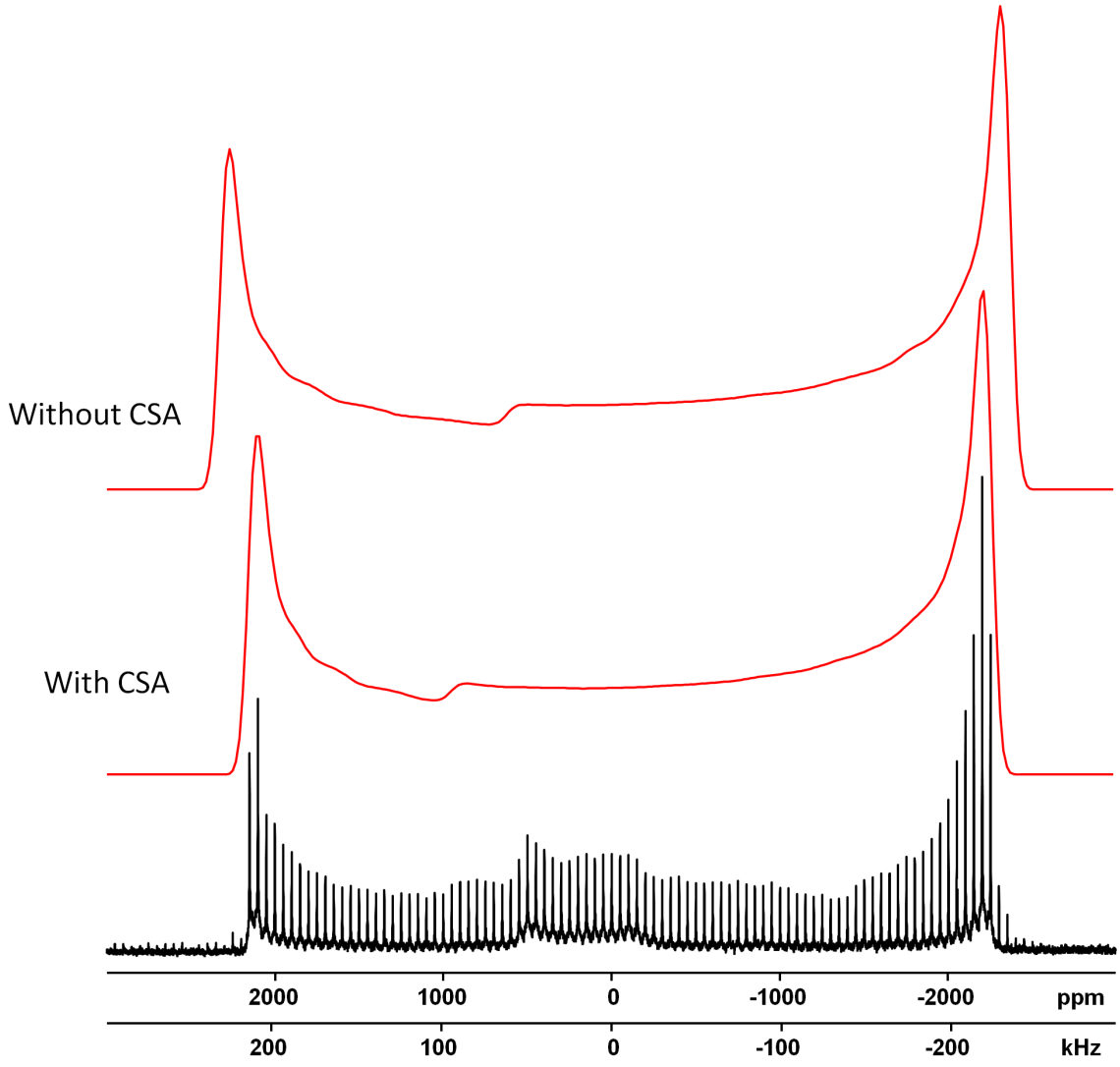

Figure B.9: Static ^{139}La NMR spectrum of La_2O_3. Analytical simulation is show in red. The EFG and CSA parameters used are given in Table 4.1.

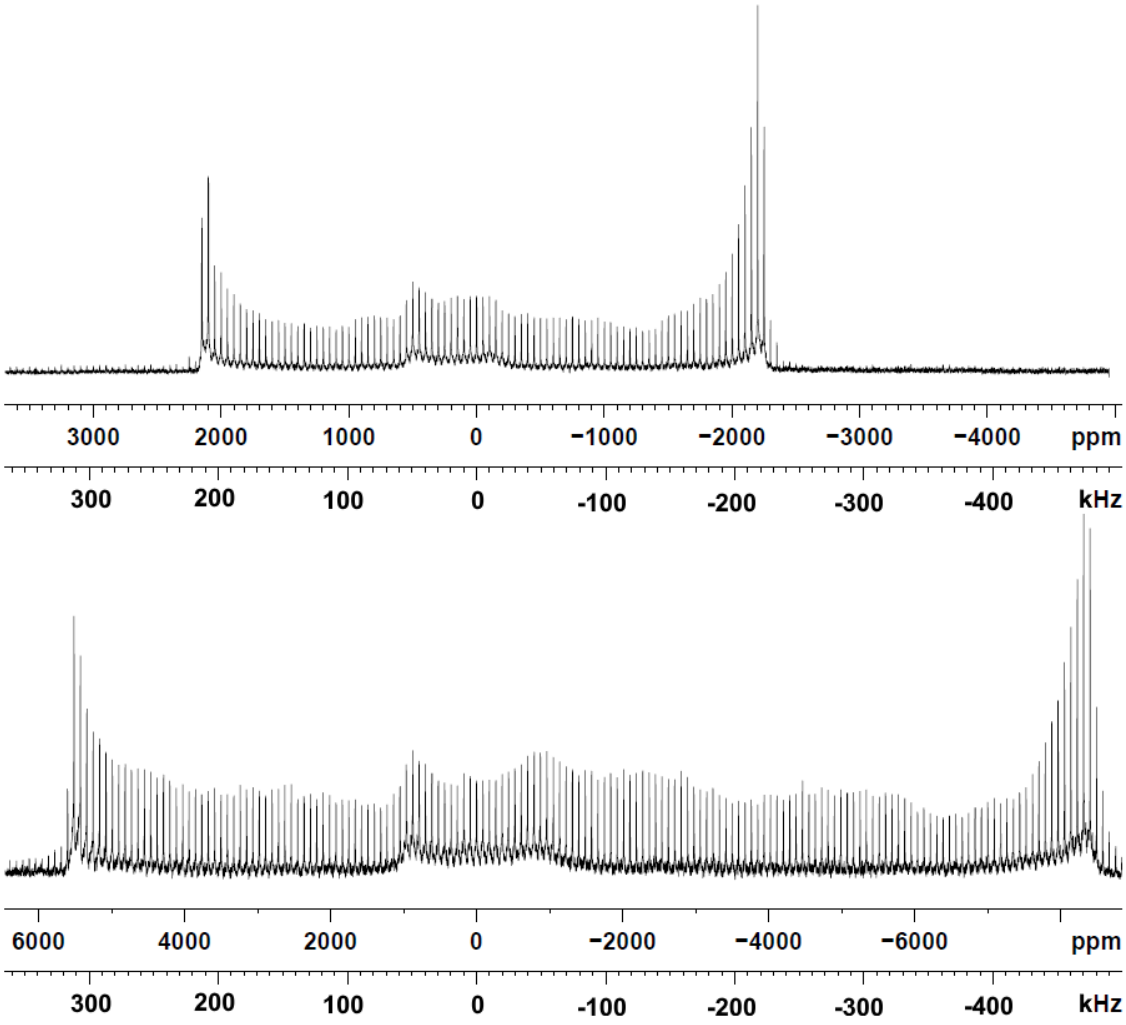

Figure B.10: Static ^{139}La NMR spectra of La_2O_3. Both spectra are set to the same frequency scale. Top: Spectrum collected at 16.4 T. Bottom: Spectrum collected at 9.4 T.

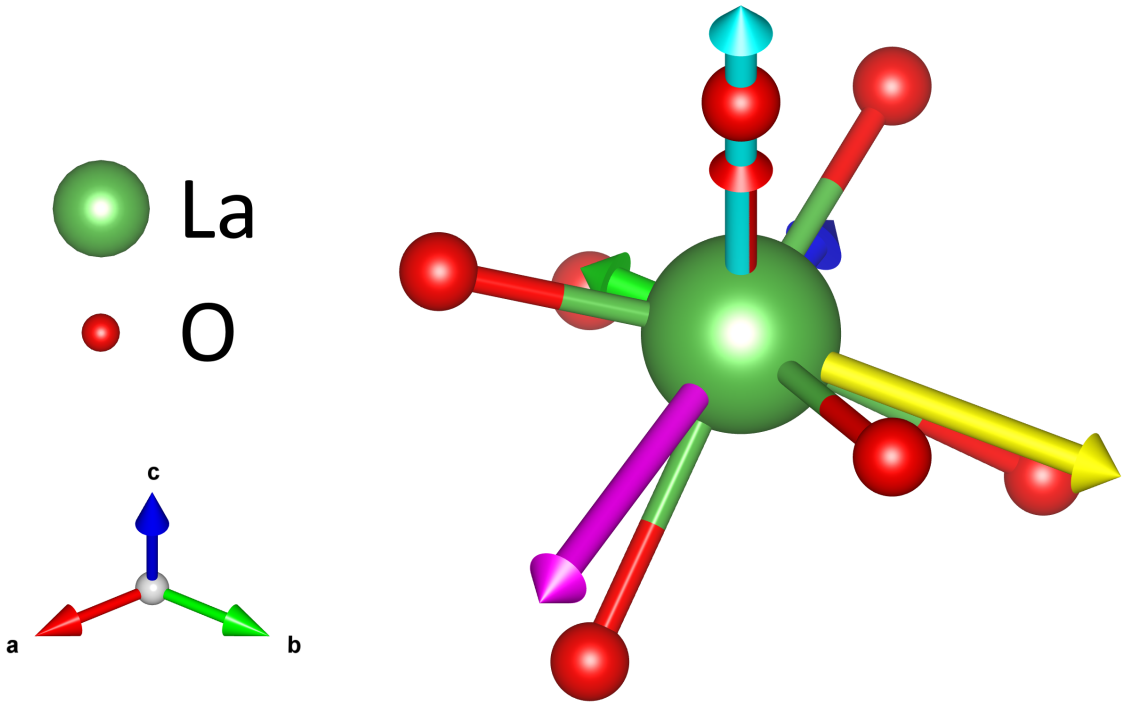

Figure B.11: First coordination sphere of LaO_7 in La_2O_3. The V_{xx}, V_{yy}, and V_{zz} components are displayed as blue, green, and red, respectively. The e_a, e_b, and e_c semi major axes are in yellow, magenta, and teal respectively.

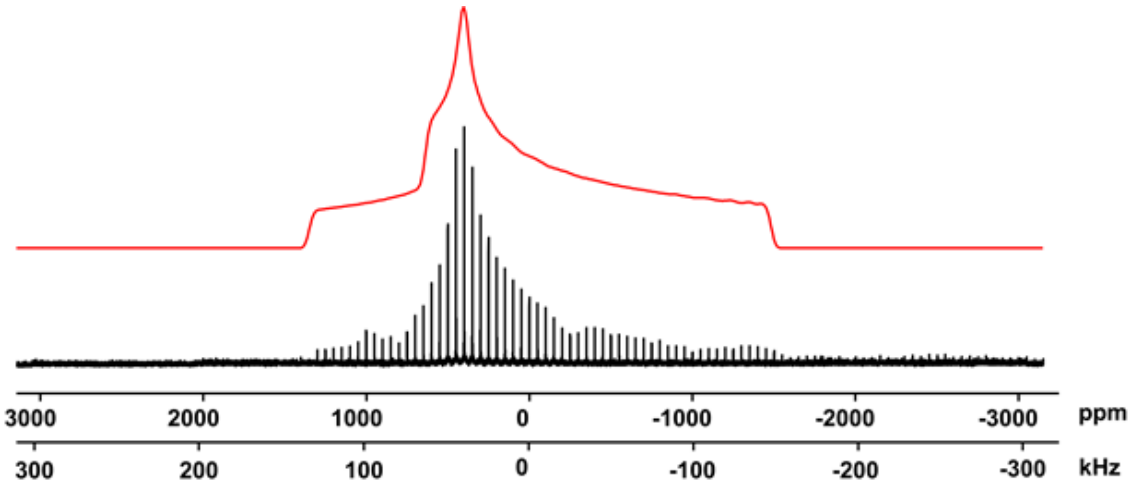

Figure B.12: Static ^{139}La NMR spectrum of $LaPO_4 \cdot 1.8\,H_2O$. Analytical simulation is show in red. The EFG and CSA parameters used are reported in Table 4.1.

B.5.2 Lanthanum Phosphate Hydrate

$LaPO_4 \cdot nH_2O$, also known as rhabdophane, is a rare-earth phosphate mineral that has been proposed for use in environmental phosphate sequestration [172]. The structure of rhabdophane was first proposed by Mooney in 1950 [307]. Rhabdophane is reported to be of the hexagonal $P6_222$ space group, with zeolitic channels parallel to the c axis and 3 formula units per cell. The lanthanum environment is eightfold coordinate to oxygen, with bond lengths reported: four bonds of length 2.34 Å and four of length 2.66 Å. The reported bond lengths, however, do not include any possible zeolitic water contributions. There are no obvious symmetry elements in the LaO_8 polyhedron that would force a particular value of η_Q.

The sample of $LaPO_4 \cdot nH_2O$ used was determined to be $LaPO_4 \cdot 1.8\,H_2O$ through the use of TGA (Fig. B.8). Our ^{139}La NMR spectrum of this sample is fit using a C_Q of (33 ± 1) MHz with an η_Q of 1.00 ± 0.05 (Figure S12). This conflicts with the spectrum reported by Dithmer *et al.* [172], where they observed a broad, largely featureless resonance. The difference may result from different methods of preparation, resulting in dramatically differing crystallinity.

The DFT calculations conducted on the experimental geometry provided by Mooney [307] yield a C_Q of -136 MHz and an η_Q of 0.5, which is significantly at odds with the experimental results. While the difference can be explained in part by the absence of zeolitic water in the structure used for the calculation, it is unlikely for a

small amount of water to cause such a large disparity in C_Q. It has been suggested by Mesbah *et al.* that the structure of $LnPO_4 \cdot nH_2O$, including $LaPO_4 \cdot nH_2O$, is in fact monoclinic [308]. However, the structure proposed by Mesbah *et al.* contains six unique lanthanide sites, which are not resolved in the spectrum of $LaPO_4 \cdot 1.8\,H_2O$. Due to the extreme difference between experimental and calculated results, we place little stock in the orientation of the EFG tensor determined through our DFT calculations.

The LaO_8 polyhedron in $LaPO_4 \cdot nH_2O$ as reported by Moody is poorly fit by either a sphere or an ellipsoid, and as such is not included in any structural models.

B.5.3 Lanthanum Phosphate

Anhydrous $LaPO_4$ is better known as the mineral monazite [223]. Monazite was historically a commercial source of lanthanides, but it fell into disuse in part due to the presence of the radioactive daughter ions of thorium. The lanthanum environment in $LaPO_4$ is more complicated than the hydrated equivalent: the lanthanum site is ninefold coordinate, with significant variation in bond lengths. La–O bond lengths range from 2.47 Å to 2.78 Å, with an average bond length of 2.58 Å.

The experimental ^{139}La ssNMR spectrum of $LaPO_4$ is presented in Fig. B.13. The spectrum was fit using two sites: one site with a C_Q of (46.7 ± 1.0) MHz and an η_Q of 0.75 ± 0.05, which is consistent with the values reported by Dithmer *et al.* ((46.7 ± 10.0) MHz and 0.75 ± 0.03, respectively) [172]; and one using the parameters reported above for $LaPO_4 \cdot 1.8\,H_2O$. The sample appears to have undergone hydration between heating and collection of the spectrum. There is no appreciable CSA contribution visible in the lineshape at 16.4 T.

DFT calculations of $LaPO_4$ using the experimental geometry [223] yield a C_Q of 53.6 MHz and an η_Q of 0.56. The calculations somewhat overestimates C_Q and underestimates η_Q, but are consistent with the experimental results. Both the higher C_Q and lower η_Q than experiment can both be explained by an overestimation of V_{zz} in the theoretical results. None of the tensor components are oriented toward any particular feature of the LaO_9 polyhedron.

The ellipsoid fitting the LaO_9 polyhedron is triaxial in nature, with $e_a = (2.415 \pm 0.001)$ Å, $e_b = (2.574 \pm 0.001)$ Å, and $e_c = (2.796 \pm 0.001)$ Å. There is significant deviation from spherical symmetry, with $\epsilon = (0.147 \pm 0.001)$ Å and a

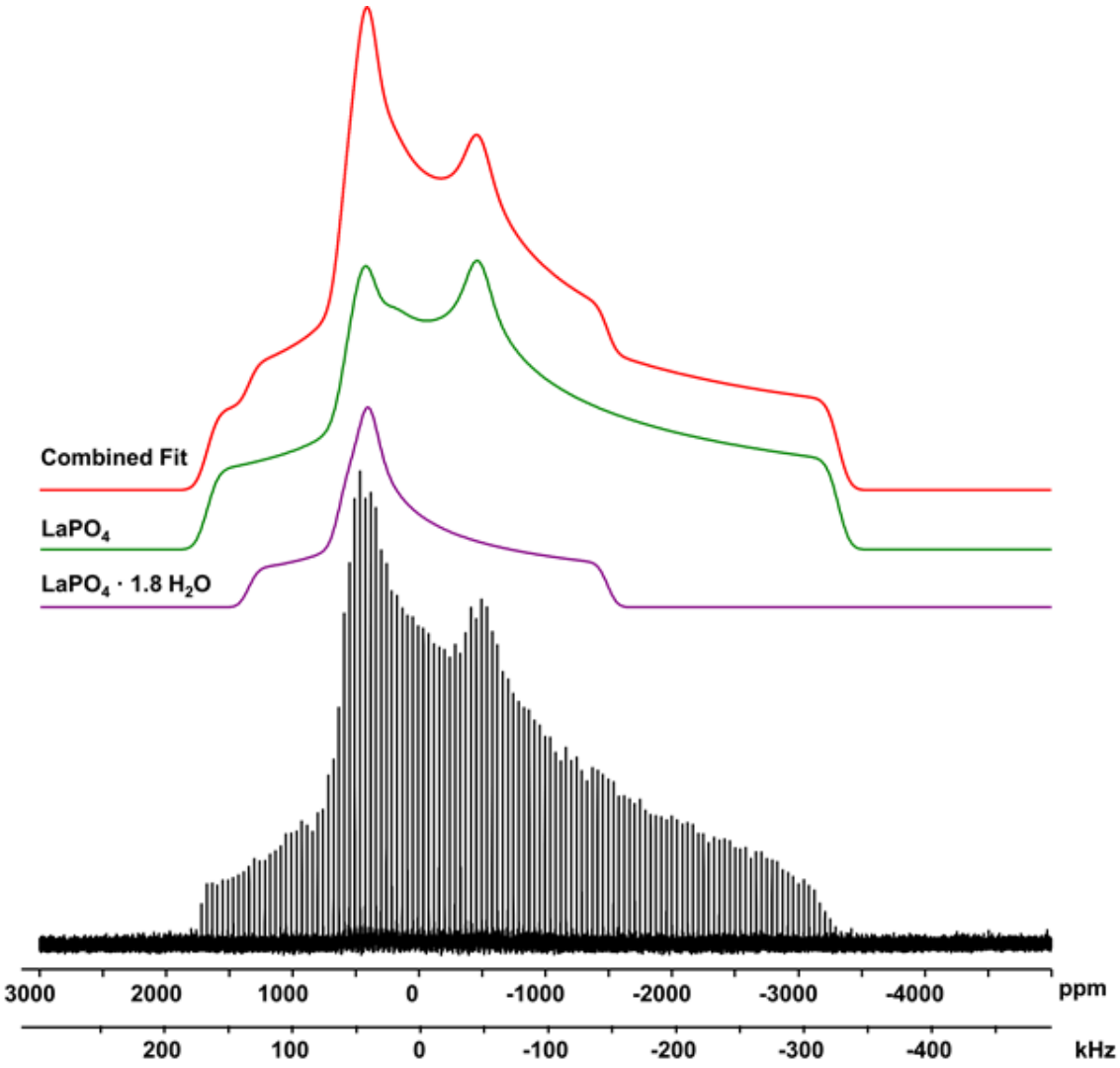

Figure B.13: Static ^{139}La NMR spectrum of $LaPO_4$. Total analytical simulation is show in red. The simulations of the individual sites are in green ($LaPO_4$) and purple ($LaPO_4 \cdot 1.8\,H_2O$). The EFG and CSA parameters used are reported in Table 4.1.

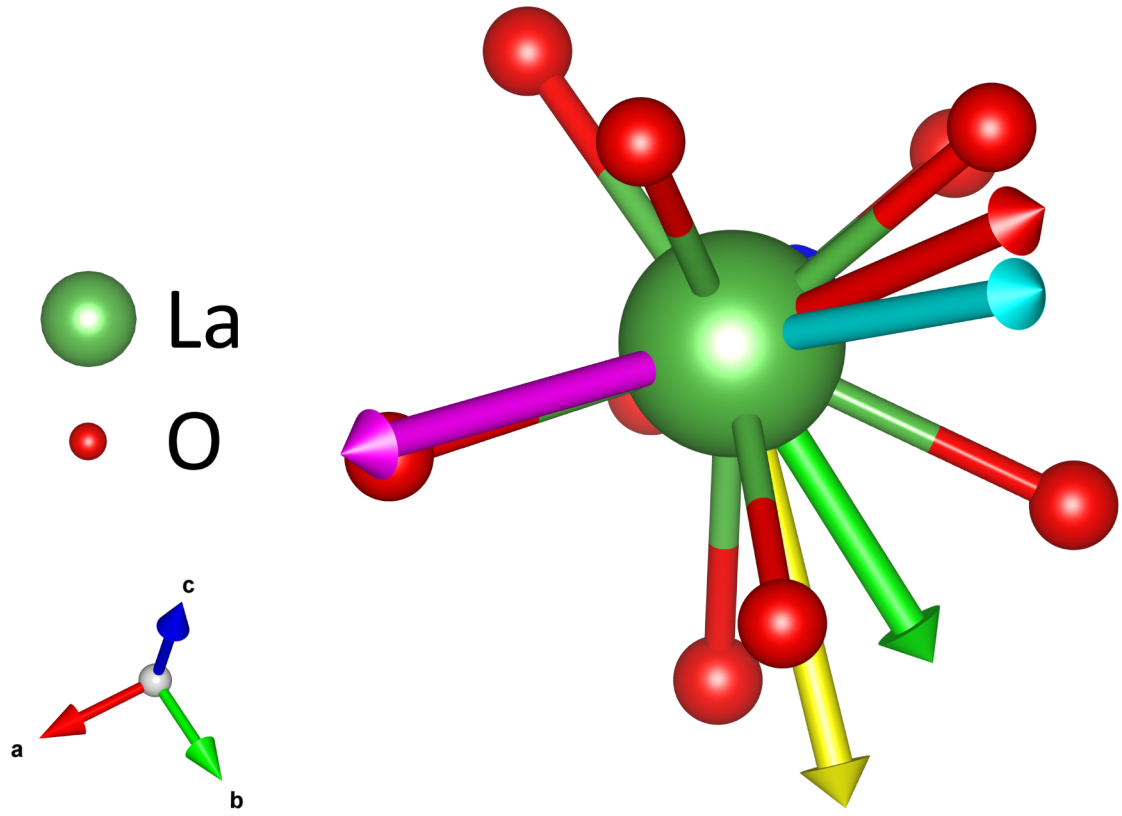

Figure B.14: First coordination sphere of LaO_9 in $LaPO_4$. The V_{xx}, V_{yy}, and V_{zz} components are displayed as blue, green, and red, respectively. The e_a, e_b, and e_c semi major axes are in yellow, magenta, and teal respectively.

character of 0.05 ± 0.01. The V_{zz} component is nearest to the e_c axis, but the EFG tensor is generally not aligned with the ellipsoid of best fit (Fig. B.14).

B.5.4 Lanthanum Borate

$LaBO_3$ has previously been investigated using ^{11}B ssNMR by Kroeker and Stebbins [48], but has not been probed by ^{139}La ssNMR. $LaBO_3$ is a possible side product in the synthesis of $LaBGeO_5$ and $LaBSiO_5$ [286], as well as the primary phase to crystallize out of La_2O_3–B_2O_3 glasses. The room temperature phase of $LaBO_3$ is orthorhombic, with space group *Pnma* and 4 formula units per cell [309]. The lanthanum environment is ninefold coordinate to oxygen, with four La–O bond pairs of lengths 2.41 Å, 2.49 Å, 2.77 Å, and 2.80 Å, and one La–O bond of length 2.38 Å. The average La–O bond

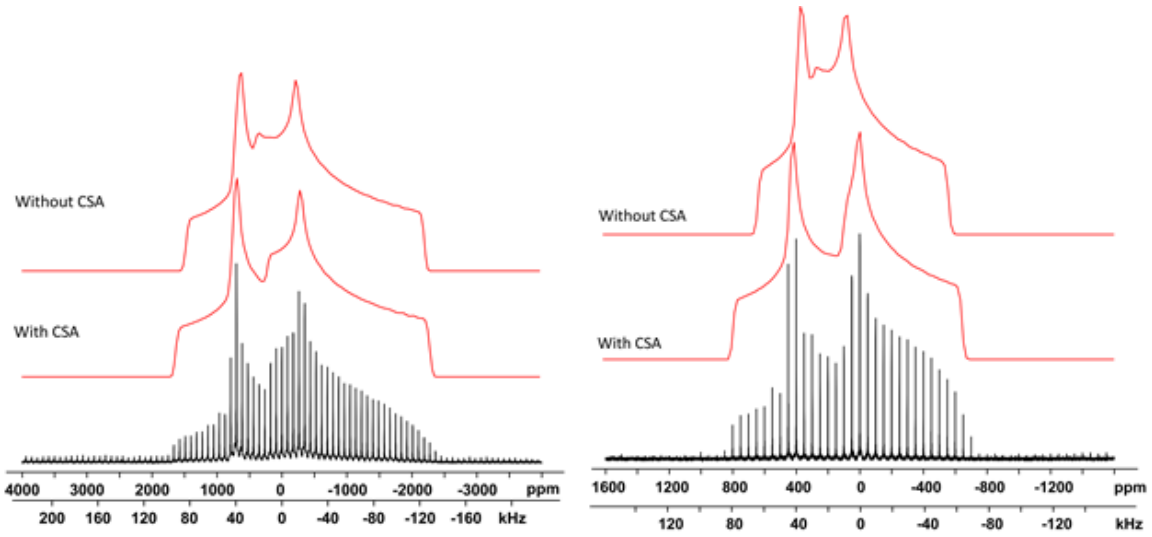

Figure B.15: Static ^{139}La NMR spectra of $LaBO_3$. Analytical simulations are shown in red. The EFG and CSA parameters used are reported in Table 4.1. Left: Spectrum collected at 9.4 T. Right: Spectrum collected at 16.4 T.

length is 2.59 Å. There is a mirror plane bisecting the LaO_9 polyhedron, with the independent La–O bond parallel to the plane.

Using the ^{139}La ssNMR spectra of $LaBO_3$ measured at 9.4 T and 16.4 T (Figs. B.15 and B.16), the quadrupole and chemical shift parameters could be determined. The quadrupole coupling has a value of C_Q of (23.4 ± 0.4) MHz with an η_Q of 0.68 ± 0.05. There is a significant CSA contribution to the lineshape, with $\Omega = (350 \pm 30)$ ppm, $\kappa = 0.3 \pm 0.1$, and Euler angles $\alpha = (15 \pm 5)°$, $\beta = (0 \pm 5)°$, and $\gamma = (165 \pm 10)°$. The magnitude of the CSA parameters is significant when compared to the quadrupolar influence on the lineshape: the measured span for the La^{3+} site of $LaBO_3$ is comparable to La_2O_3 or $LaScO_3$, while the ^{139}La C_Q of La^{3+} in $LaBO_3$ is significantly less than that in La_2O_3 or $LaScO_3$.

DFT calculations of $LaBO_3$ on the experimental geometry [309] yielded a C_Q of -28.8 MHz with an η_Q of 0.57. Both values agree reasonably well with experiment, though the C_Q is overestimated. Calculations carried out on a different $LaBO_3$ structure [201] using the same parameters reported a C_Q of -84 MHz and η_Q of 0.05, which are even further from experiment. The ^{139}La C_Q of $LaBO_3$ appears to be extremely sensitive to structure, which should be considered when comparing experimental and computational values.

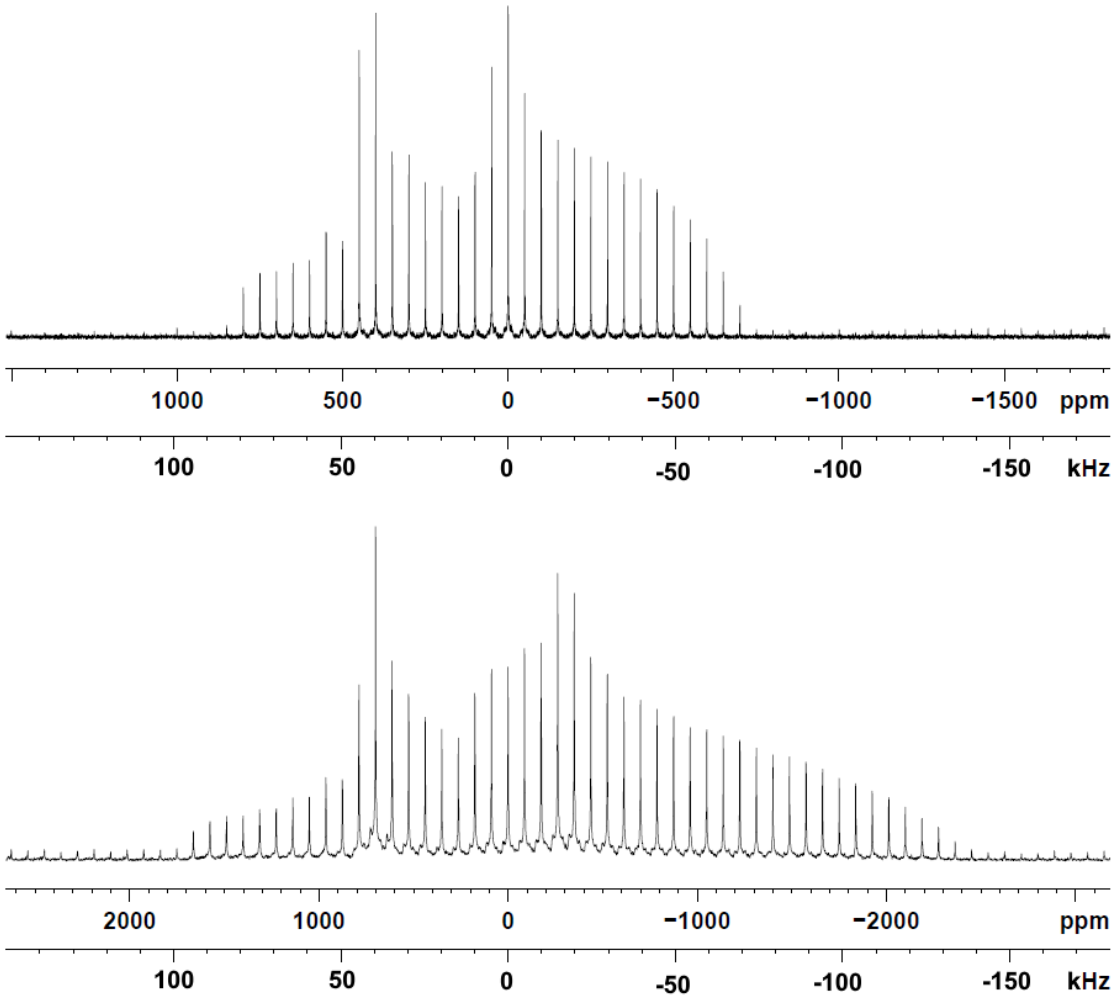

Figure B.16: Static ^{139}La NMR spectra of $LaBO_3$. Both spectra are set to the same frequency scale. Top: Spectrum collected at 16.4 T. Bottom: Spectrum collected at 9.4 T.

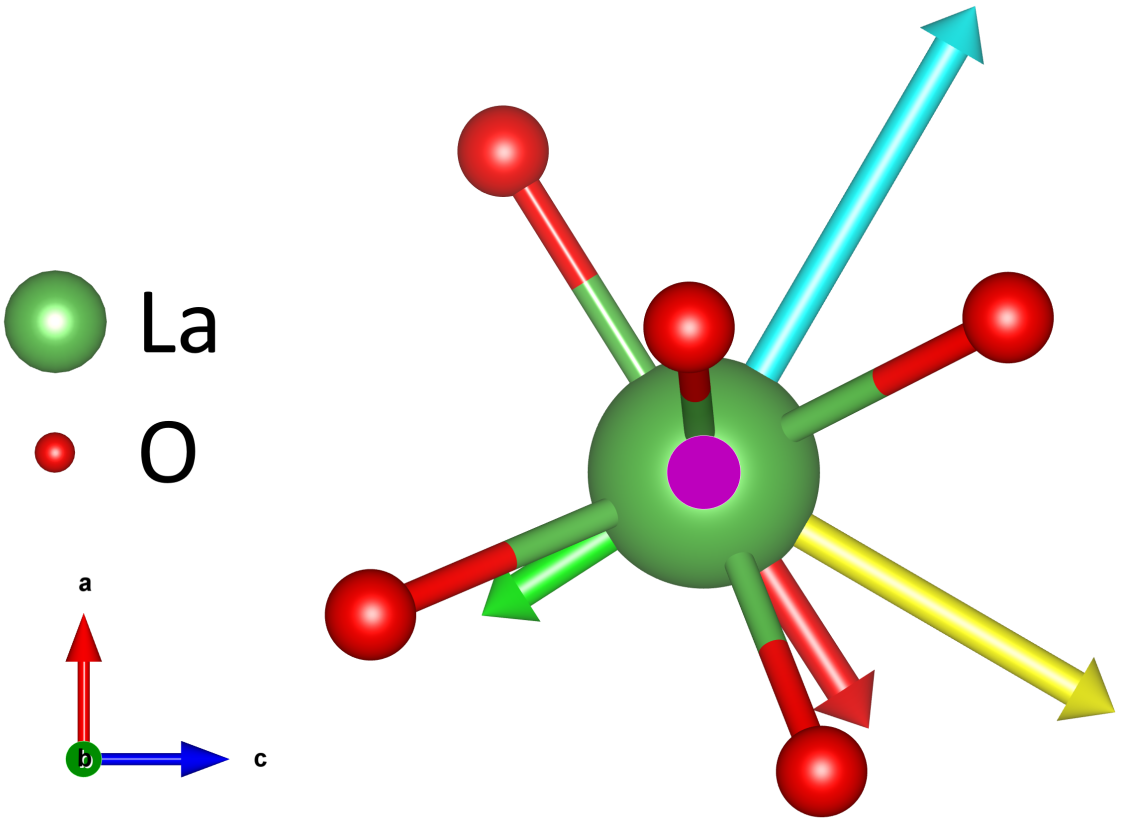

Figure B.17: First coordination sphere of LaO_9 in $LaBO_3$. The V_{xx}, V_{yy}, and V_{zz} components are displayed as blue, green, and red, respectively. The e_a, e_b, and e_c semi major axes are in yellow, magenta, and teal respectively.

The least-squares ellipsoid which fits the LaO_9 polyhedron in $LaBO_3$ is significantly distorted, with $\epsilon = 0.157 \pm 0.001$ and semi major axes $e_a = (2.331 \pm 0.001)$ Å, $e_b = (2.721 \pm 0.001)$ Å, and $e_c = (2.741 \pm 0.001)$ Å. The character is nearly wholly oblate at -0.92 ± 0.01. This is at odds with the experimental η_Q, as a small value of η_Q would be expected when the system is nearly axially symmetric. The V_{xx} EFG component is antiparallel to the e_b semi major axis, and the V_{zz} component is close to the e_a axis (Fig. B.17).

B.5.5 Lanthanum Borosilicate

Another member of the stillwellite family, $LaBSiO_5$ is the silicate analogue of $LaBGeO_5$, and is isostructural to $LaBGeO_5$ [220]. Also of space group $P3_1$, the lanthanum

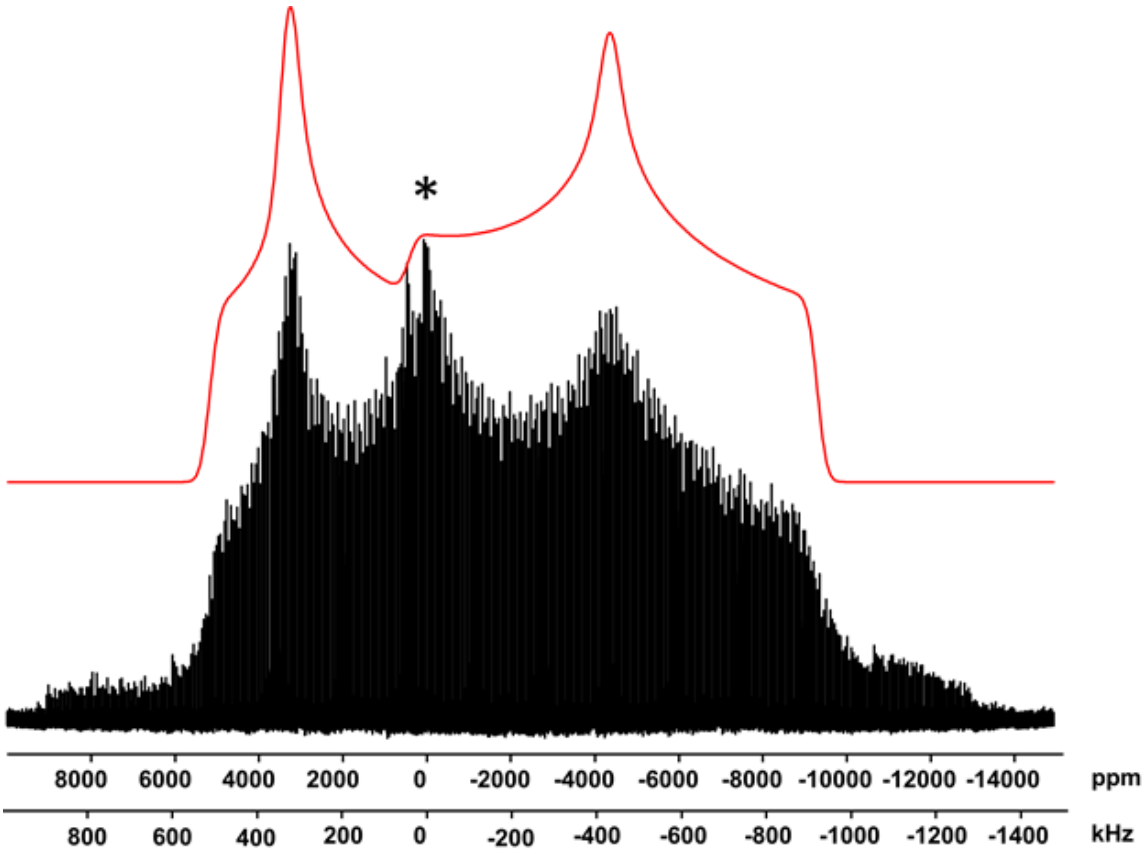

Figure B.18: Static ^{139}La NMR spectrum of $LaBSiO_5$. Analytical simulation is show in red. The EFG parameters used are reported in Table 4.1. The presence of an impurity is indicated with an asterisk.

environment of $LaBSiO_5$ is of slightly higher coordination, forming a LaO_{10} polyhedron. This difference is attributed to the difference in size between the GeO_4 and SiO_4 tetrahedra [310]. La–O bonds range in length from 2.39 Å to 2.86 Å, with an average of 2.64 Å. Like $LaBGeO_5$, there are no obvious symmetry elements present in the lanthanum polyhedron of $LaBSiO_5$.

The ^{139}La ssNMR spectrum of $LaBSiO_5$ is presented in Fig. B.18. The lineshape is fit with a C_Q of (90.0 ± 0.5) MHz and η_Q of 0.35 ± 0.02. The spectrum of $LaBSiO_5$ is the broadest presented in this study, and among the broadest reported in the literature [174]. While similar in shape to the spectrum of $LaBGeO_5$, the spectrum of $LaBSiO_5$ is slightly broader and slightly less axially symmetric, likely a consequence of the higher coordination number.

The coordination ellipsoid of lanthanum in $LaBSiO_5$ is quite oblate, with $e_a =$

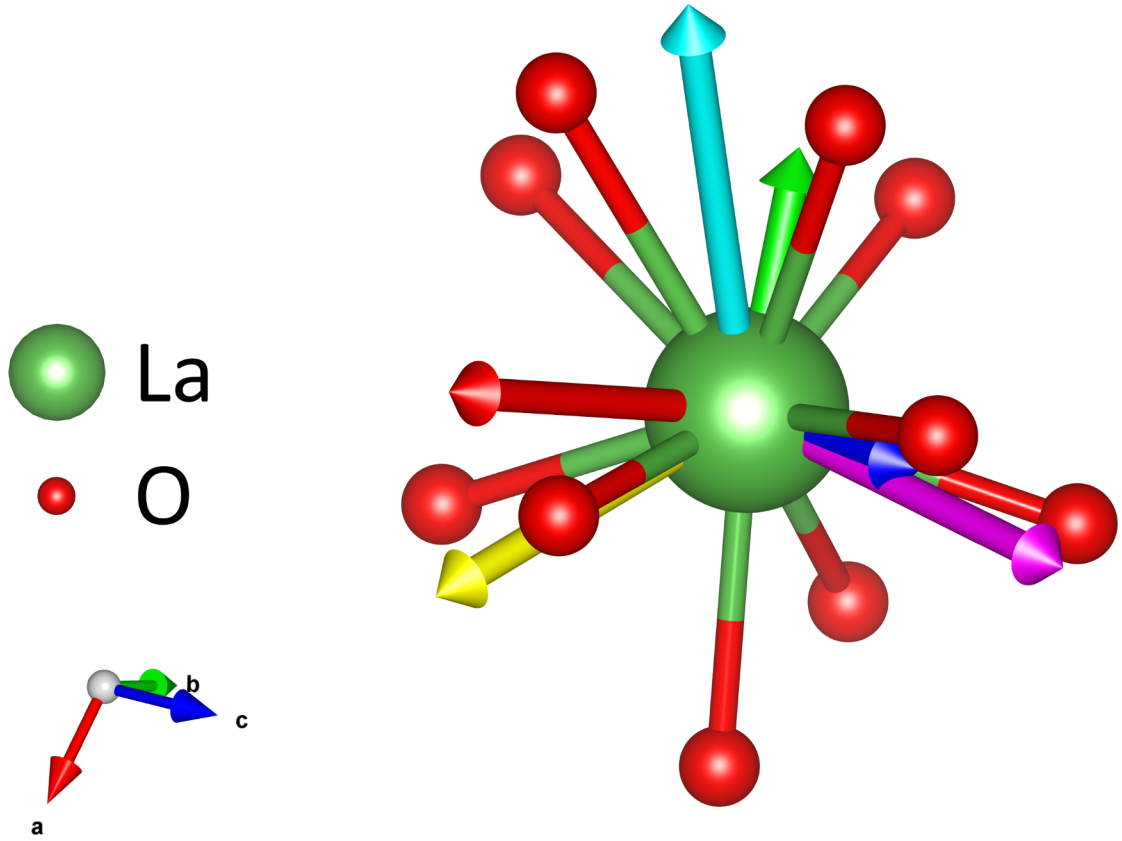

Figure B.19: First coordination sphere of LaO_{10} in $LaBSiO_5$. The V_{xx}, V_{yy}, and V_{zz} components are displayed as blue, green, and red, respectively. The e_a, e_b, and e_c semi major axes are in yellow, magenta, and teal respectively.

(2.350 ± 0.001) Å, $e_b = (2.713 \pm 0.001)$ Å, $e_c = (2.808 \pm 0.001)$ Å, with a character of -0.67, lower than that of $LaBGeO_5$. The span of this ellipsoid is quite large at 0.175. The semi major axis e_b is very nearly aligned with the V_{yy} EFG component, and the V_{zz} EFG component is close to the e_a axis (Fig. B.19).

B.5.6 Lanthanum Sulfate Nonahydrate

$La_2(SO_4)_3 \cdot 9\,H_2O$ is a commercially available lanthanum compound with a defined crystal structure, making it a good model compound for this investigation.
$La_2(SO_4)_3 \cdot 9\,H_2O$ is of the hexagonal $P6_3/m$ space group with two formula units per unit cell [218]. There are two lanthanum sites in $La_2(SO_4)_3 \cdot 9\,H_2O$: site La(1), with twelvefold coordination; and site La(2), with ninefold coordination. Both sites have highly symmetric polyhedra with C_3 rotation axes parallel to the crystallographic c

axis. La(1) is best described as a distorted LaO12 icosahedron, and La(2) as a LaO9 tricapped trigonal prism. As a result, both sites are predicted to have η_Q values of 0, but will have non-zero C_Q values. La(1) has two sets of bonds: three pairs of La–O bond length 2.59 Å, and three pairs of length 2.80 Å, with an average length of 2.70 Å. La(2) has two different bond lengths: the equatorial La–O bonds of length 2.51 Å, and the non-equatorial bonds of length 2.55 Å. The second coordination sphere of the two sites also has significant variation. The La(1) icosahedron edge-shares with six SO_4 tetrahedra, where the La(2) site corner-shares with three SO_4 tetrahedra which cap the rectangular faces of a trigonal prism. This trigonal prism is formed by water oxygen coordinating to lanthanum. La(1) has no H_2O in its near proximity, whereas the environment of La(2) is dominated by it.

The difference in the local structure of the two sites is reflected in the spectrum of $La_2(SO_4)_3 \cdot 9\,H_2O$ (Fig. B.20). Two peaks are observed: peak 1, with isotropic chemical shift $\delta_{iso}^{CS} = (-175 \pm 25)$ ppm, $C_Q = (52.5 \pm 0.5)$ MHz, and $\eta_Q = 0.00 \pm 0.02$; and peak 2, with $\delta_{iso}^{CS} = (-75 \pm 25)$ ppm, $C_Q = (36.5 \pm 0.5)$ MHz, and $\eta_Q = 0.00 \pm 0.03$. Peak 1 is assigned to La(1) and peak 2 to La(2) based upon the computational results discussed below.

DFT calculations were based on the experimental geometry [218] of $La_2(SO_4)_3 \cdot 9\,H_2O$, but there are no experimentally reported values for the position of the hydrogen atoms. We manually placed hydrogen atoms at reasonable starting locations and optimized their positions, holding the position of all other atoms (*i.e.*, La, S, and O) constant. Our calculations yield a C_Q of −59.1 MHz and η_Q of 0.0 for La(1) and C_Q of −36.5 MHz and η_Q of 0.0 for La(2). The asymmetry parameters are confined by symmetry, but the magnitudes of the quadrupolar coupling constants agree reasonably well with the fit proposed above. The difference in the calculated C_Q of the two sites is used as a basis for assigning peak 1 to site La(1) and peak 2 to site La(2). The V_{zz} component of the EFG at La(1) is collinear to the crystallographic c axis, and as such is directed towards the neighbouring LaO_{12} icosahedron. In site 2, V_{zz} is also collinear to the crystallographic c axis, with V_{xx} and V_{yy} consequentially in the crystallographic ab plane.

Both sites can be fit independently by least-squares ellipsoids. Both are spheroids, as expected due to their axial symmetry. The ellipsoid of La(1) is oblate, with $e_a =$

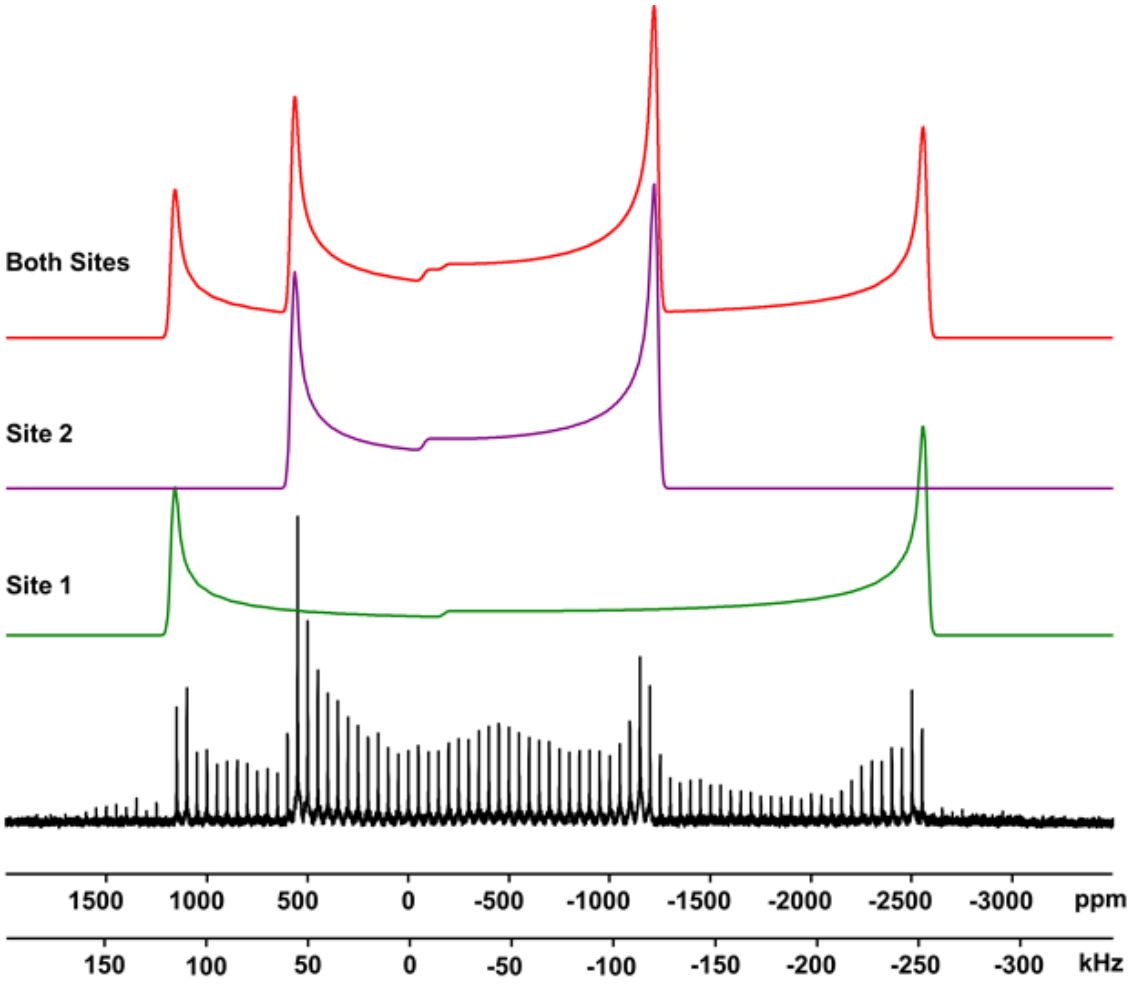

Figure B.20: Static ^{139}La NMR spectrum of $La_2(SO_4)_3 \cdot 9\,H_2O$. Analytical simulation is show in red. The EFG parameters used are reported in Table 4.1.

(2.463 ± 0.001) Å and $e_b = e_c = (2.837 \pm 0.001)$ Å. Despite the icosahedral nature of the LaO_{12} polyhedron, there is significant distortion from spherical symmetry with $\epsilon = 0.138 \pm 0.001$. The character of the ellipsoid is -1.00 ± 0.01, as expected from an oblate spheroid. Considering the LaO_{12} ellipsoid, the shortest semi-major axis is aligned with the crystallographic c axis, and hence collinear with V_{zz}. The ellipsoid of La(2) is prolate, with $e_a = e_b = (2.514 \pm 0.001)$ Å and $e_c = (2.585 \pm 0.001)$ Å. The La(2) ellipsoid is significantly less distorted than the La(1) ellipsoid, with $\epsilon = 0.028 \pm 0.001$. As a prolate spheroid, the character of the ellipsoid is 1.00 ± 0.01. The largest semi major axis is parallel to both V_{zz} and the crystallographic c axis. As a spheroid, the direction of the degenerate semi major axes is not unique, and like V_{xx} and V_{yy} they also lies in the ab plane (Fig. B.21).

B.5.7 Lanthanum Carbonate Octahydrate

Despite pXRD suggesting that the sample of $La_2(CO_3)_3 \cdot nH_2O$ was crystalline, and with $n = 8$, it was not possible to obtain a spectrum with sufficient resolution to separate the multiple sites present. The collected spectrum, presented in Fig. B.22, is believed to be a combination of the two sites [311] of $La_2(CO_3)_3 \cdot 8\,H_2O$ and the three sites [312] of lanthanum carbonate oxide ($LaCO_3OH$), the presence of which is suggested by pXRD (Fig. B.7).

Given the multi-phase nature of the sample, along with the poor spectral resolution, DFT calculations on the lanthanum carbonate octahydrate system were not attempted.

B.5.8 Lanthanum Hydroxide

La_2O_3 will easily convert to $La(OH)_3$ under exposure to atmospheric water [313]. It has influenced previous ^{139}La NMR studies, and as a consequence has been well-studied using ^{139}La ssNMR [60]. We did not collect further $La(OH)_3$ spectra in this work.

$La(OH)_3$ is in the $P6_3/m$ space group, as confirmed by both X-ray and neutron diffraction studies [217, 314]. The unit cell of $La(OH)_3$ contains two formula units. The lanthanum environment is ninefold coordinate, with only oxygen in the first coordination sphere. Like site La(2) of $La_2(SO_4)_3 \cdot 9\,H_2O$, the LaO_9 polyhedron in $La(OH)_3$ is a tricapped trigonal prism, with a threefold rotation axis parallel to the crystallographic c axis. This predicts an η_Q of 0, which is confirmed by a previous

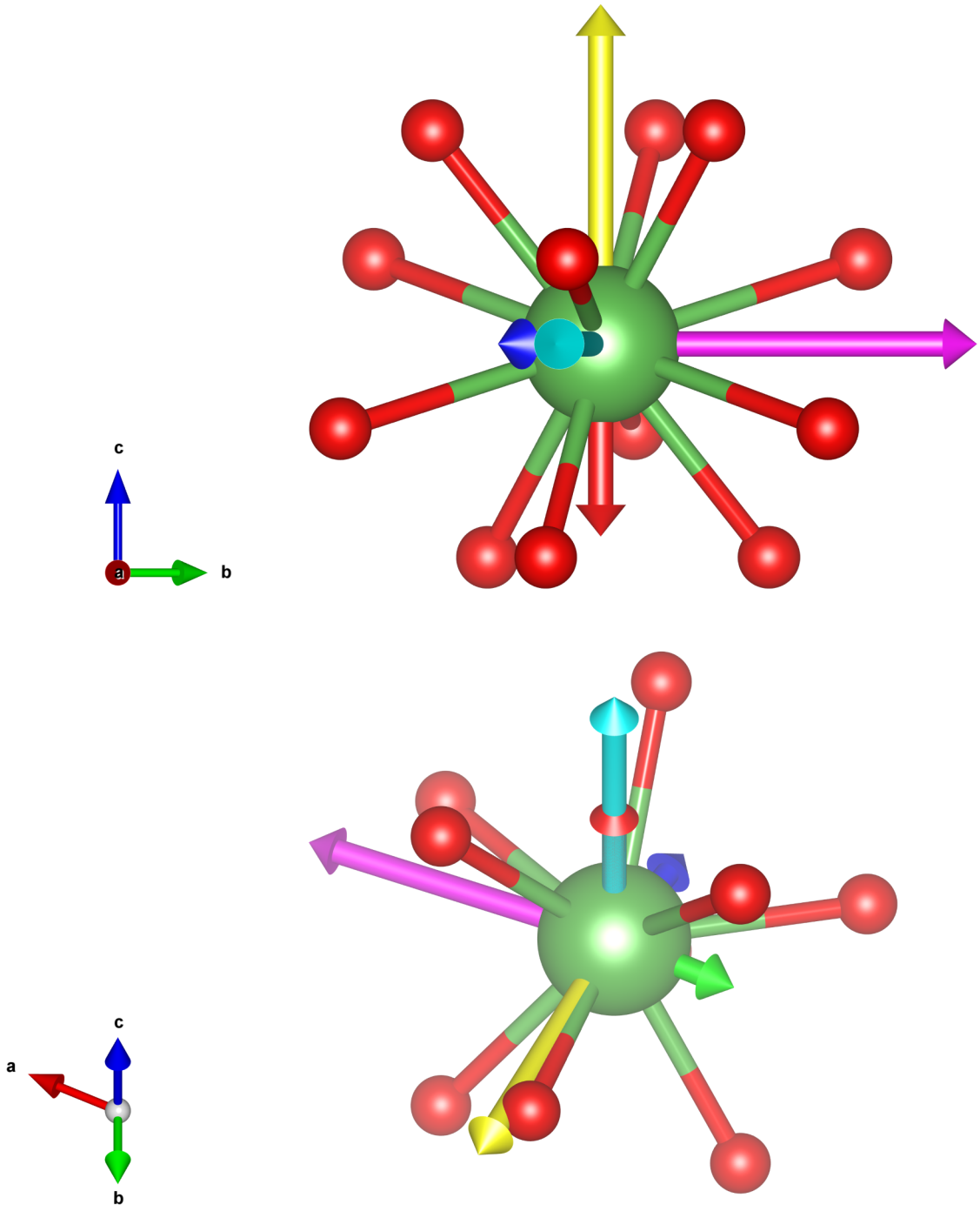

Figure B.21: Top: First coordination sphere of LaO_{12} in $La_2(SO_4)_3 \cdot 9\,H_2O$. Bottom: First coordination sphere of LaO_9 in $La_2(SO_4)_3 \cdot 9\,H_2O$. The V_{xx}, V_{yy}, and V_{zz} components are displayed as blue, green, and red, respectively. The e_a, e_b, and e_c semi major axes are in yellow, magenta, and teal respectively.

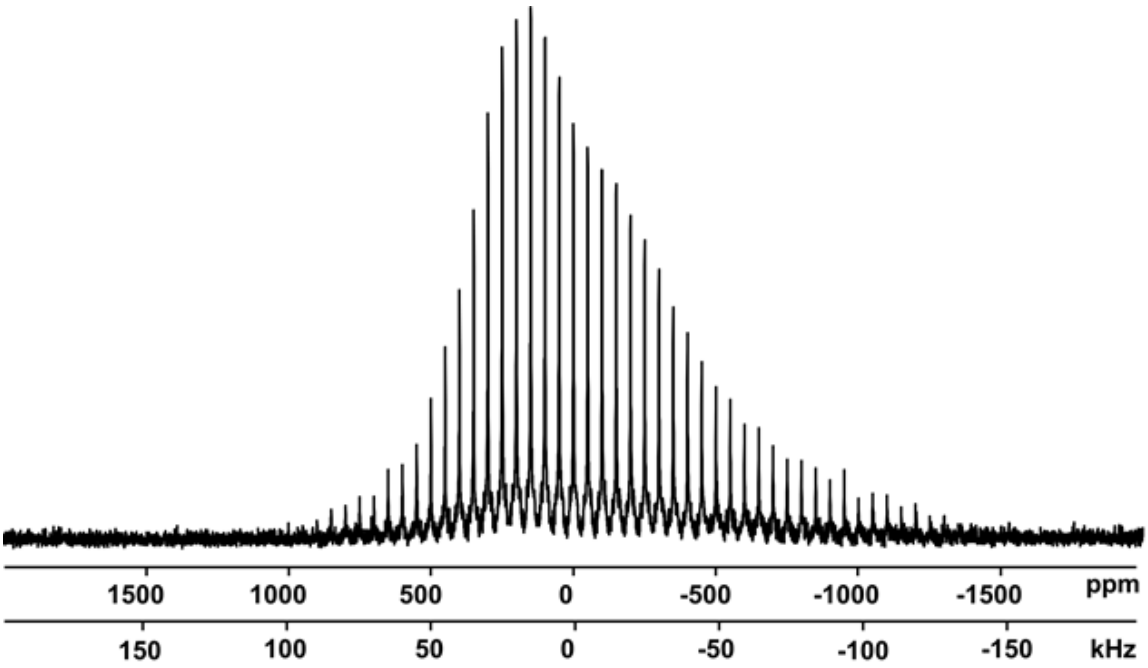

Figure B.22: Static ^{139}La NMR spectrum of sample of nominal composition $La_2(CO_3)_3 \cdot nH_2O$.

study of $La(OH)_3$ [60].

We conducted DFT calculations on $La(OH)_3$ using the experimental geometry [217], with the positions of the hydrogen atoms determined through neutron powder diffraction. Our DFT calculations yield a C_Q of -29 MHz and an η_Q of 0.0, consistent with the experimental results reported by Spencer *et al.*, who report an experimental C_Q of (22.0 ± 0.5) MHz and an η_Q of 0.050 ± 0.025. The V_{zz} component is collinear the crystallographic c axis, and is hence oriented to face the nearest neighbouring LaO_9 polyhedron.

The ellipsoid used to fit the LaO_9 polyhedron of $La(OH)_3$ is a prolate spheroid, with $e_a = e_b = (2.551 \pm 0.001)$ Å and $e_c = (2.620 \pm 0.001)$ Å. It is very nearly spherical, with $\epsilon = 0.027 \pm 0.010$ and a character of 1.00 ± 0.01. The longest semi major axis is parallel to the crystallographic c axis and hence collinear with V_{zz} (Fig. B.23).

B.5.9 Lanthanum Aluminate

$LaAlO_3$ is a rhombohedral perovskite of space group $R\bar{3}c$ with six formula units per unit cell. $LaAlO_3$ is remarkable in the NMR community for possessing one of the

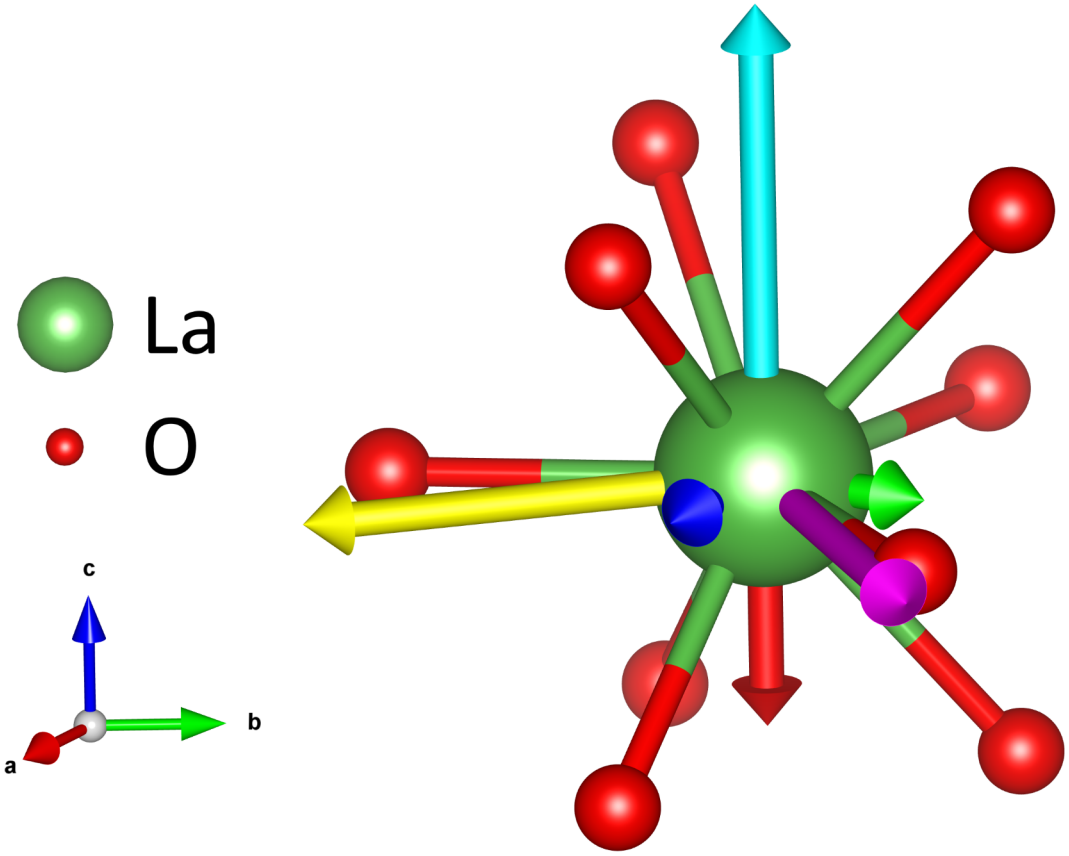

Figure B.23: First coordination sphere of LaO_9 in $La(OH)_3$. The V_{xx}, V_{yy}, and V_{zz} components are displayed as blue, green, and red, respectively. The e_a, e_b, and e_c semi major axes are in yellow, magenta, and teal respectively.

smallest reported ^{139}La C_Q values [58]. The coordination environment of lanthanum in $LaAlO_3$ is twelvefold coordinate, with the LaO_{12} polyhedron assuming a slightly distorted cuboctahedron geometry [262]. Despite the distortion, there is a C_3 rotation axis parallel to the crystallographic c axis, which enforces an η_Q of 0.

The ^{139}La ssNMR spectrum of $LaAlO_3$ was first observed by Dupree *et al.*, where they fit the lineshape with a C_Q of 6 MHz and an η_Q of 0 [58]. Given that the peak is narrow enough to be collected through MAS NMR, these values are quite reliable. We conducted DFT calculations on the experimental geometry [262] which yielded a C_Q of 8.4 MHz and an η_Q of 0.0. This is in good agreement with the experimental results of Dupree *et al.*The V_{zz} component of the EFG is parallel to the crystallographic c axis.

The ellipsoid of LaO_{12} in $LaAlO_3$ is the most spherical of all the compounds examined in this study, with $\epsilon = 0.01 \pm 0.01$. As is consistent with an η_Q of 0, the ellipsoid is a spheroid; in particular it is an oblate spheroid, with $e_a = (2.67 \pm 0.01)$ Å and $e_b = e_c = (2.70 \pm 0.01)$ Å. The shortest semi major axis is parallel to both V_{zz} and the crystallographic c axis (Fig. B.24).

B.5.10 Lanthanum Cobaltite

$LaCoO_3$ is a member of the perovskite family, and is of the rhombohedral space group $R\bar{3}c$ with two formula units per cell [263]. $LaCoO_3$ has been previously studied using ^{139}La ssNMR by Bastow [59]. The lanthanum environment in $LaCoO_3$ is twelvefold coordinate to oxygen, forming a distorted cuboctahedron. There are three different La–O bond lengths in the LaO_{12} polyhedron: three of length 2.43 Å; six of length 2.69 Å; and three of length 2.99 Å; together with an average of 2.70 Å. There is a C_3 rotation axis parallel to the crystallographic c axis, enforcing an η_Q of 0 on the lanthanum site.

Our DFT calculations of $LaCoO_3$ using the experimental geometry [263] yield a ^{139}La C_Q of 20.99 MHz and η_Q of 0.00, in reasonable agreement with the experimental results of Bastow. Due to the resolution limits imposed by the frequency-stepped spin-echo technique used, Bastow estimated the C_Q to be 23.8 MHz by the separation of the satellite transitions, rather than by direct simulation of the central transition. V_{zz} is aligned with the C_3 rotation axis, and directed towards a face of a CoO_6 octahedron.

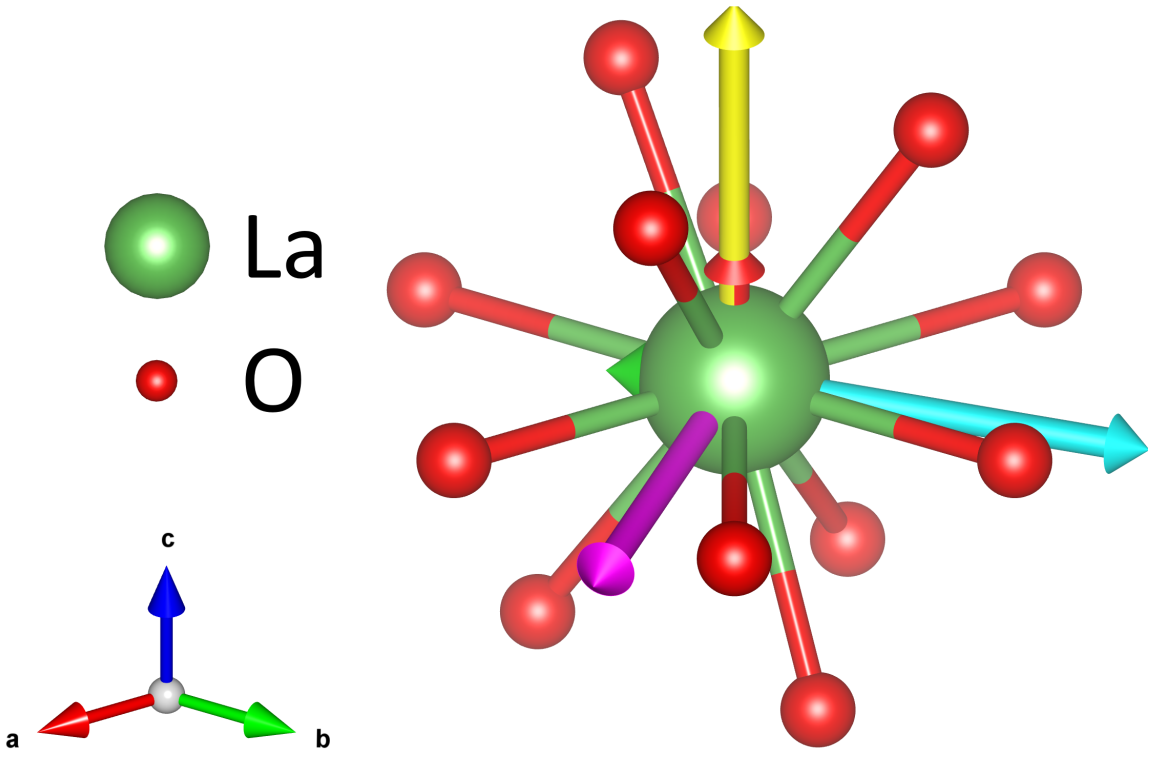

Figure B.24: First coordination sphere of LaO_{12} in $LaAlO_3$. The V_{xx}, V_{yy}, and V_{zz} components are displayed as blue, green, and red, respectively. The e_a, e_b, and e_c semi major axes are in yellow, magenta, and teal respectively.

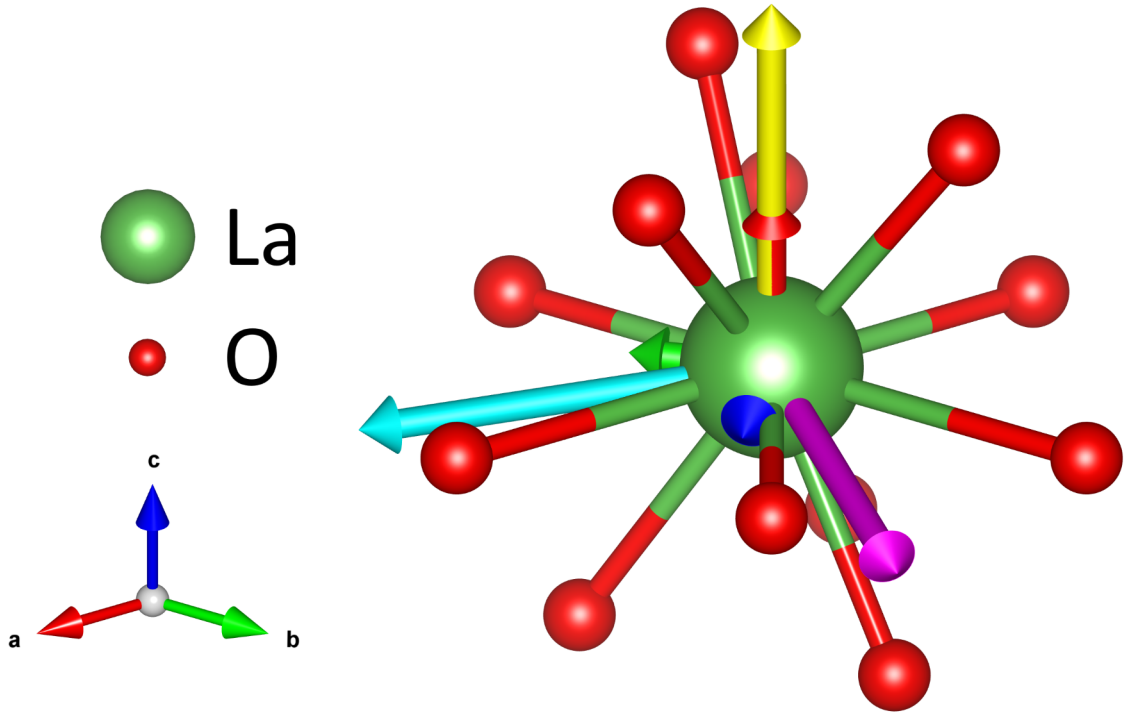

Figure B.25: First coordination sphere of LaO_{12} in $LaCoO_3$. The V_{xx}, V_{yy}, and V_{zz} components are displayed as blue, green, and red, respectively. The e_a, e_b, and e_c semi major axes are in yellow, magenta, and teal respectively.

The ellipsoid fitting the LaO_{12} cuboctahedron is oblate and somewhat distorted, with $\epsilon = 0.04 \pm 0.03$ and a character of -1.00 ± 0.01. The semi major axes are $e_a = (2.67 \pm 0.04)$ Å and $e_b = e_c = (2.78 \pm 0.04)$ Å. As has been observed with other compounds fit by a spheroid, the non-degenerate semi major axis is parallel to the proper rotation axis of the polyhedron (Fig. B.25). The large uncertainty in the ellipsoid span indicates that the oxygen positions are not easily fit by a triaxial ellipsoid; this is a consequence of the square (or in this distorted case, diamond) faces of the cuboctohedral geometry.

B.5.11 Lanthanum Chromite

At room temperature, $LaCrO_3$ is in the orthorhombic *Pbnm* space group with four formula units per cell [315]. It experiences an antiferromagnetic phase transition at approximately 286 K [316], The lanthanum environment is twelvefold coordinate, forming a severely distorted LaO_{12} cuboctahedron. The distortion is sufficiently severe

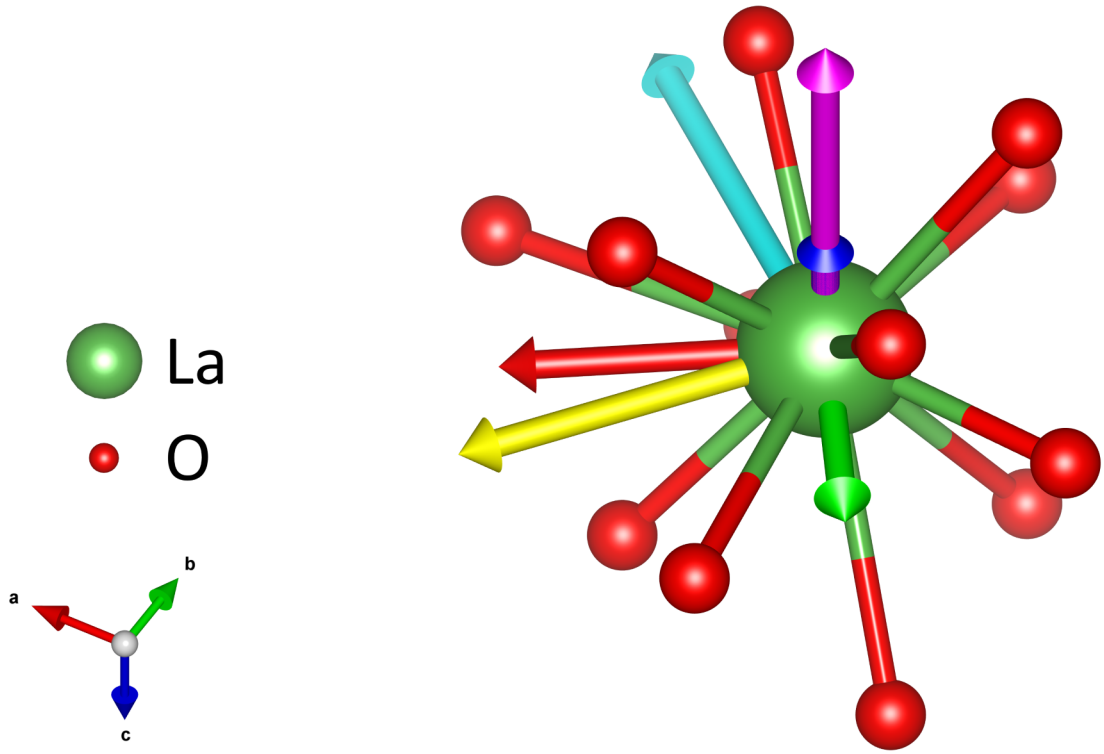

Figure B.26: First coordination sphere of LaO_{12} in $LaCrO_3$. The V_{xx}, V_{yy}, and V_{zz} components are displayed as blue, green, and red, respectively. The e_a, e_b, and e_c semi major axes are in yellow, magenta, and teal respectively.

that there are no obvious symmetry elements prescribing particular NMR behavior. The La–O bond lengths in the LaO_{12} polyhedron range from 2.43 Å to 3.12 Å.

$LaCrO_3$ has been previously studied using ^{139}La ssNMR spectroscopy by Bastow, in which he fits the $LaCrO_3$ peak with a C_Q of 48 MHz and an η_Q of 0.15 [59]. Our DFT calculations on the experimental structure [315] yield a C_Q of −47.2 MHz with an η_Q of 0.32. While the C_Q is in good agreement with experiment, our calculations overestimate the asymmetry parameter as reported by Bastow. However, given the relatively low resolution provided by the frequency-swept spin echo technique used, it is possible that the experimental η_Q was underestimated. The V_{xx} axis is parallel to the crystallographic c axis, while the V_{yy} and V_{zz} components of neighbouring LaO_{12} polyhedra are nearly aligned (Fig. B.26).

The ellipsoid fitting the LaO_{12} cuboctahedron is triaxial, reflecting the level of distortion from spherical symmetry. The span is moderately high at $\epsilon = 0.16 \pm 0.05$,

and the character of the ellipsoid is -0.14 ± 0.01, reflecting a slightly oblate nature. The semi major axis e_b is parallel to both the V_{xx} component and the crystallographic c axis, while V_{zz} is closely adjacent to e_a (Fig. B.26). Like $LaCoO_3$, the coordination polyhedron is poorly fit by an ellipsoid; this is also attributed to the strongly distorted cuboctahedral geometry of the local lanthanum coordination.

B.5.12 Lanthanum Titanate

$LaTiO_3$ has been studied for its role as an antiferromagnet [194] as well as for its application in the battery material lithium lanthanum titanate [317]. $LaTiO_3$ is in the orthorhombic *Pbnm* space group with 4 formula units per unit cell. The lanthanum environment is eightfold coordinate in a distorted square antiprismatic configuration, with bonds ranging from 2.43 Å to 2.77 Å, with an average of 2.60 Å. $LaTiO_3$ has been experimentally observed through low-temperature ^{139}La ssNMR by Furukawa *et al.*They reported a quadrupole resonance frequency of 3.8 MHz and an η_Q of 0.6 [194]. A ^{139}La quadrupole resonance frequency of 3.8 MHz is equivalent to a ^{139}La C_Q of 53.2 MHz. The value of η_Q remains unchanged. The measurement of the quadrupolar coupling constant was verified through nuclear quadrupole resonance [194] and a previous computational study [318].

DFT calculations of $LaTiO_3$ are complicated by the strong electron correlation at the La^{3+} and Ti^{3+} sites. This requires a special approach (LDA+U) [318] that is inconsistent with the rest of the DFT calculations reported in this work, and hence DFT calculations of $LaTiO_3$ were not performed.

The ellipsoid fitting the LaO_8 polyhedron is triaxial, with $e_a = (2.384 \pm 0.001)$ Å, $e_b = (2.462 \pm 0.001)$ Å, and $e_c = (2.872 \pm 0.001)$ Å. The ellipsoid is quite distorted from spherical symmetry, with $\epsilon = 0.190 \pm 0.001$, and a prolate character of 0.59 ± 0.01. The largest semi major axis is parallel with the crystallographic c axis, and is directed towards neighbouring LaO_8 polyhedra (Fig. B.27).

B.5.13 Lanthanum Niobate

$LaNbO_4$ has been thoroughly investigated using ^{139}La ssNMR by Spencer *et al.* [60]; we will not duplicate their efforts here. $LaNbO_4$ has a monoclinic crystal structure of space group $C2/c$ with 4 formula units per unit cell [221]. The lanthanum environment

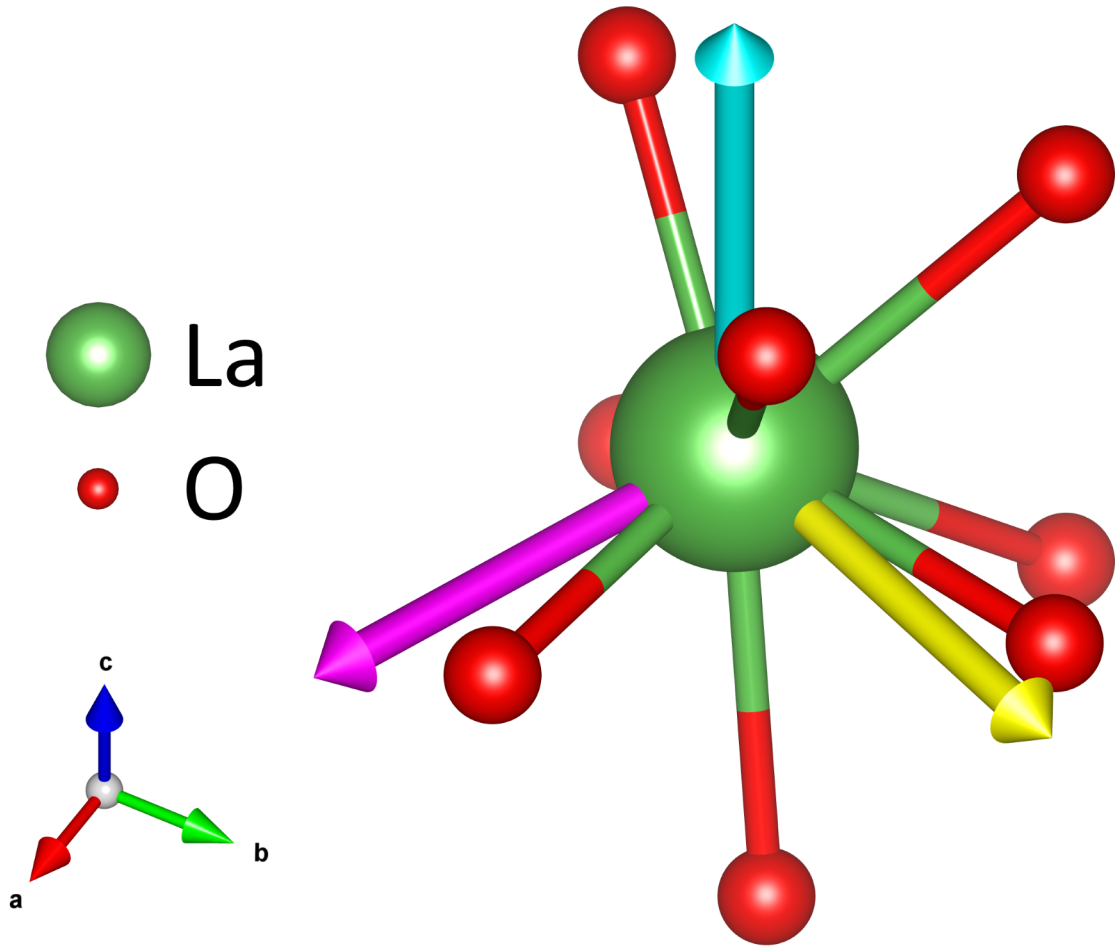

Figure B.27: First coordination sphere of LaO_8 in $LaTiO_3$. The e_a, e_b, and e_c semi major axes are in yellow, magenta, and teal respectively.

in $LaNbO_4$ is eightfold coordinate, with four pairs of La–O bonds with lengths 2.48 Å, 2.49 Å, 2.50 Å, and 2.58 Å. The average La–O bond length is 2.50 Å. The lanthanum coordination polyhedron is a distorted square antiprism.

We performed DFT calculations on the room-temperature monoclinic $LaNbO_4$ crystal structure [221]. Our DFT calculations yield a C_Q of 39.5 MHz and η_Q of 0.50, in good agreement with the experimental values reported by Spencer *et al.* ($C_Q = (36 \pm 2)$ MHz, $\eta_Q = 0.44 \pm 0.05$) [60]. Our computed EFG parameters have approximately the same deviation from experiment as the computed values reported by Spencer *et al.* (calculated $C_Q = 33.8$ MHz, $\eta_Q = 0.38$), albeit in the opposite direction.

The ellipsoid used to fit the LaO_8 coordination polyhedron is triaxial, with $e_a = (2.419 \pm 0.001)$ Å, $e_b = (2.478 \pm 0.001)$ Å, and $e_c = (2.606 \pm 0.001)$ Å. The ellipsoid span indicates a moderate level of distortion with $\epsilon = 0.075 \pm 0.001$. The ellipsoid is somewhat prolate, with a character of 0.32 ± 0.01. While the longest semi major axis of the ellipsoid is parallel to the crystallographic b axis, the other semi major axes are not aligned with any particular structural feature (Fig. B.28).

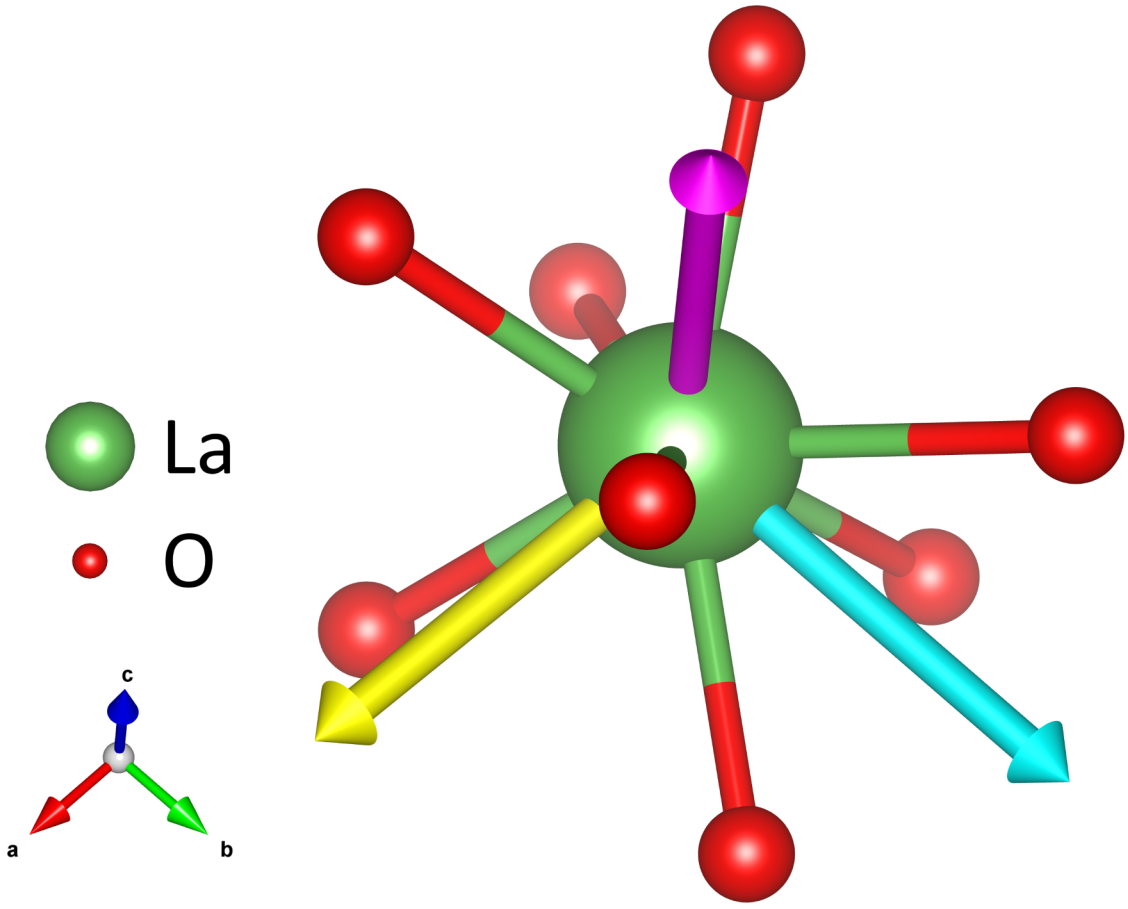

Figure B.28: First coordination sphere of LaO_8 in $LaNbO_4$. The e_a, e_b, and e_c semi major axes are in yellow, magenta, and teal respectively.

B.6 Additional Figures

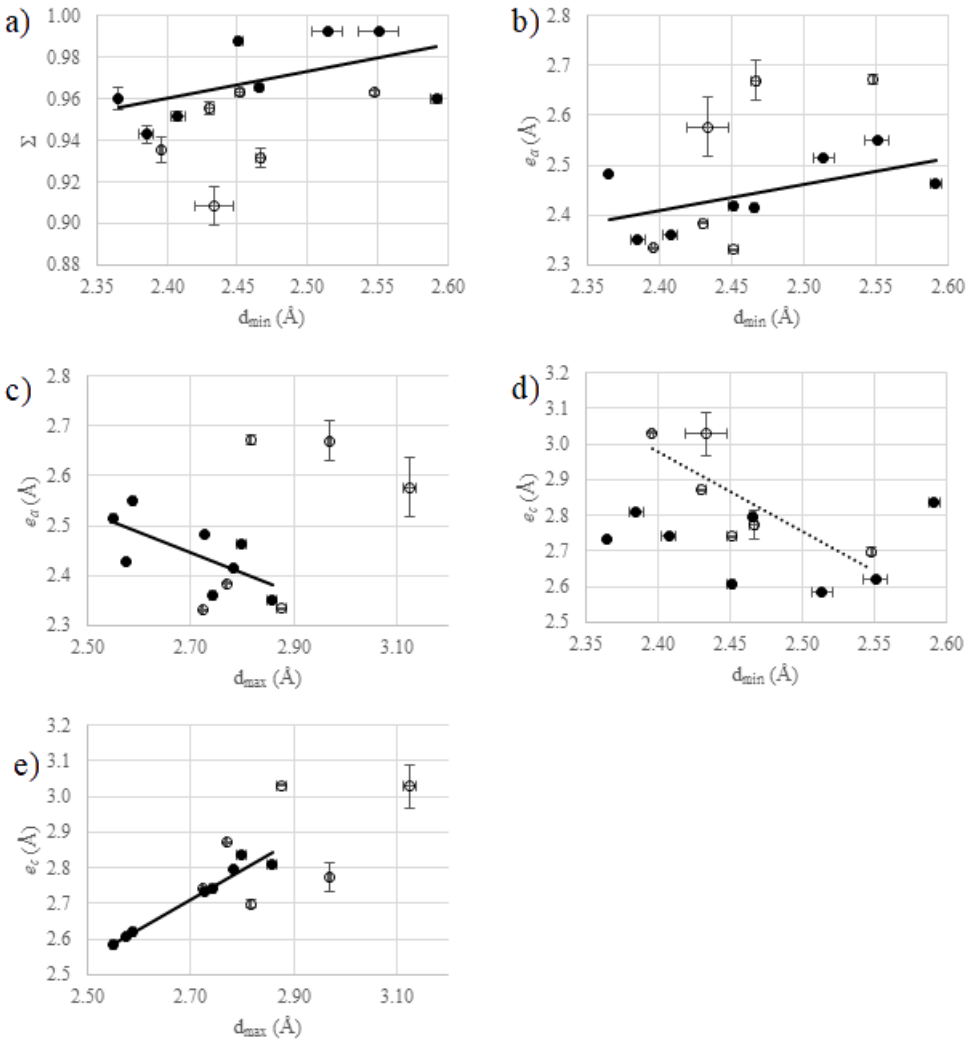

Figure B.29: Relationship between sphericity Σ, ellipsoid span ϵ, the shortest ellipsoid semi major axis e_a, and the longest semi major axis e_c and: $d_{\min}$ (a), b), d)); and $d_{\max}$ (c), e)). Filled circles indicate compounds of the non-$LaMO_3$ family, while open circles indicate $LaMO_3$ compounds. The solid lines indicate the relationship between the respective distortion parameter and the bond length of the non-$LaMO_3$ family, with: a) $\Sigma = 2.78\text{Å}^{-1} \cdot d_{\min} + 0.23$ ($R^2 = 0.38$); b) $e_c = 0.67 \cdot d_{\min} + 0.81\,\text{Å}$ ($R^2 = 0.36$); c) $e_a = -1.08 \cdot d_{\max} + 5.35\,\text{Å}$ ($R^2 = 0.44$); e) $e_c = 1.14 \cdot d_{\max} - 0.39\,\text{Å}$ ($R^2 = 0.95$). The dotted line in d) indicates the relationship between e_c and the minimum La–O bond length of the $LaMO_3$ family, with $e_c = -0.28 \cdot d_{\max} + 3.25\,\text{Å}$ ($R^2 = 0.62$).

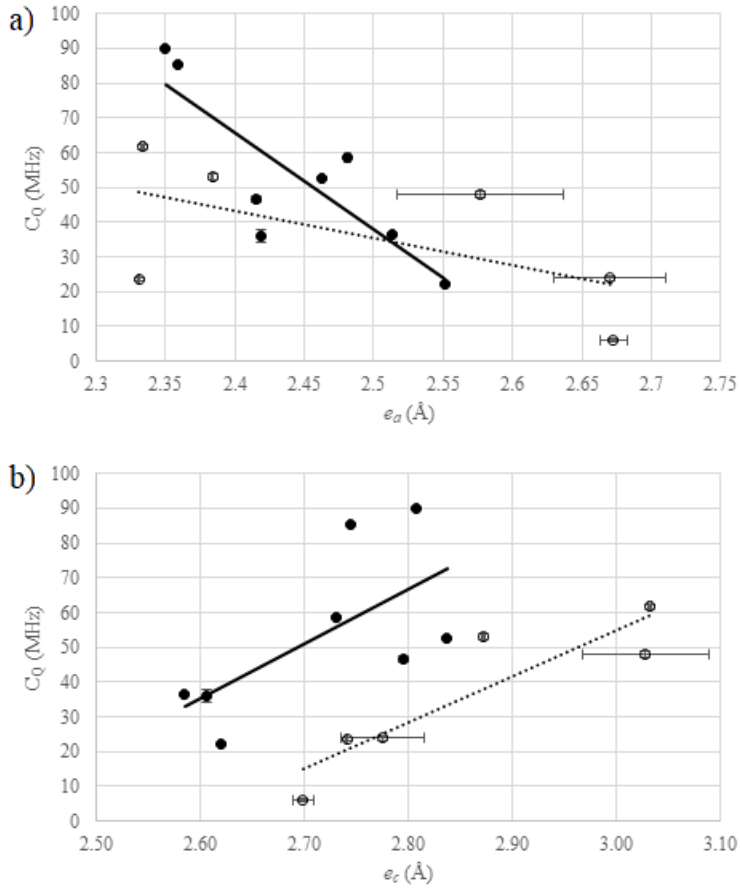

Figure B.30: Relationship between ^{139}La C_Q and: a) shortest ellipsoid semi major axis e_a; b) longest semi major axis e_c. Filled circles indicate compounds of the non-$LaMO_3$ family, while open circles indicate $LaMO_3$ compounds. The solid lines in indicate the relationship between ^{139}La C_Q and the respective distortion parameter of the non-$LaMO_3$ compounds, with: a) $C_\mathrm{Q} = -278\,\mathrm{MHz\,Å^{-1}} \cdot e_a + 734\,\mathrm{MHz}$ ($R^2 = 0.69$); b) $C_\mathrm{Q} = 157\,\mathrm{MHz\,Å^{-1}} \cdot e_c - 373\,\mathrm{MHz}$ ($R^2 = 0.42$). The dotted lines indicate the relationship between ^{139}La C_Q and the respective distortion parameter of the $LaMO_3$ compounds, with: a) $C_\mathrm{Q} = -78\,\mathrm{MHz\,Å^{-1}} \cdot e_a + 230\,\mathrm{MHz}$ ($R^2 = 0.35$); and b) $C_\mathrm{Q} = 133\,\mathrm{MHz\,Å^{-1}} \cdot e_c - 344\,\mathrm{MHz}$ ($R^2 = 0.81$).

Appendix C

Supporting Information for Chapter 6: Structural Differences between the Glass and Crystal Forms of the Transparent Ferroelectric Nanocomposite $LaBGeO_5$, from Neutron Diffraction and NMR Spectroscopy

C.1 Context

The contents of this appendix were published as supporting information for the manuscript making up Chapter 6, published as Paterson, A.L., Hannon, A.C., Werner-Zwanziger, U., and Zwanziger, J.W., Structural Differences between the Glass and Crystal Forms of the Transparent Ferroelectric Nanocomposite $LaBGeO_5$, from Neutron Diffraction and NMR Spectroscopy, *J. Phys. Chem. C* 122 (36) (2018) 20963–20980 [212]. Some minor changes have been made to the text for style and consistency. Copyright permissions for this use are contained in Appendix E.

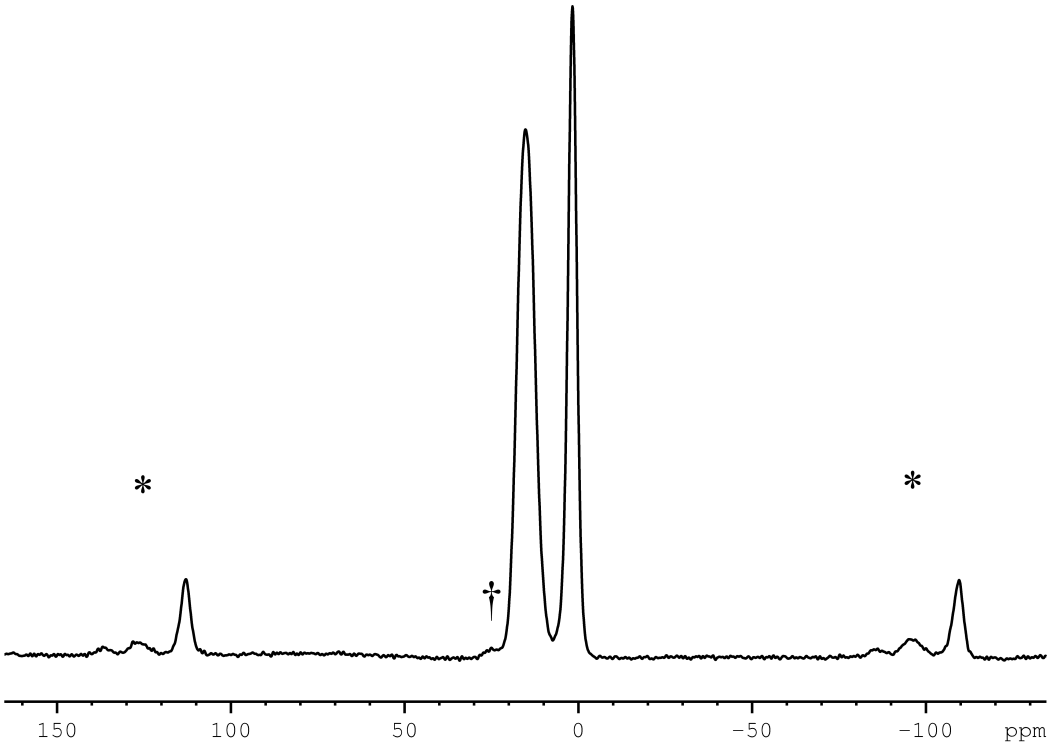

Figure C.1: ^{11}B MAS NMR spectrum of 25LaBG-2. Spectral limits are set to display the first set of spinning sidebands on either side of the central transition. The spinning sidebands are indicated by *. The slight shoulder on the positive side of the BO_3 peak, indicated by †, is the $3/2 \rightarrow 1/2$ satellite transition. Its spinning sideband is resolved from the spinning sideband of the central transition.

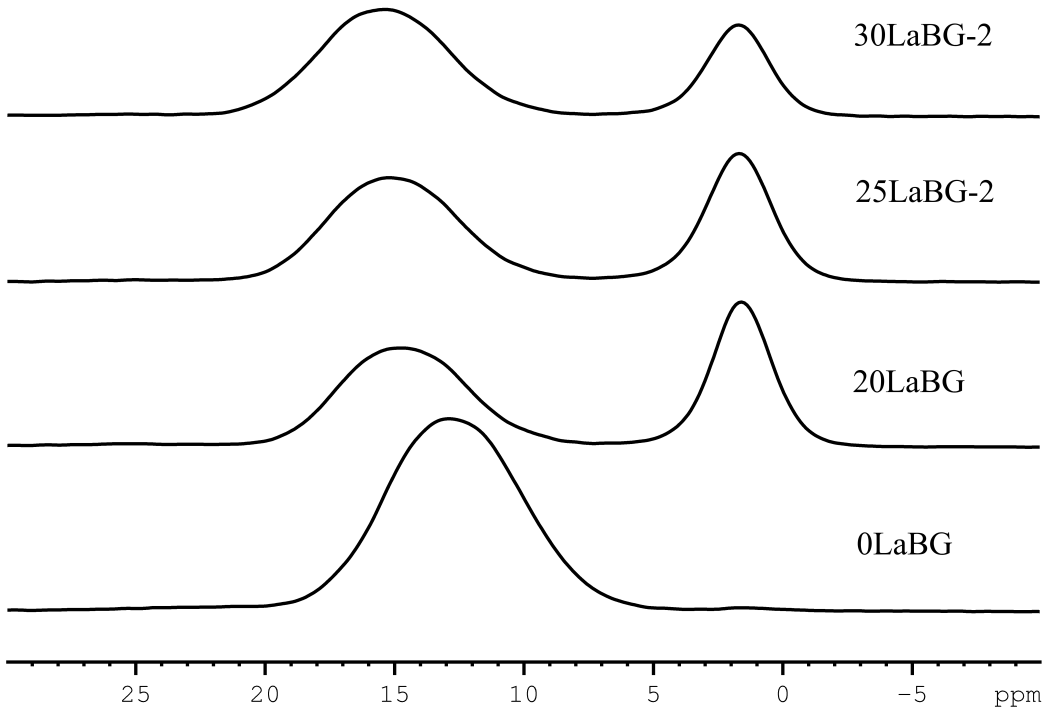

Figure C.2: ^{11}B MAS NMR spectra of samples not displayed in Chapter 6. The 0LaBG and 20LaBG spectra are included for visual reference.

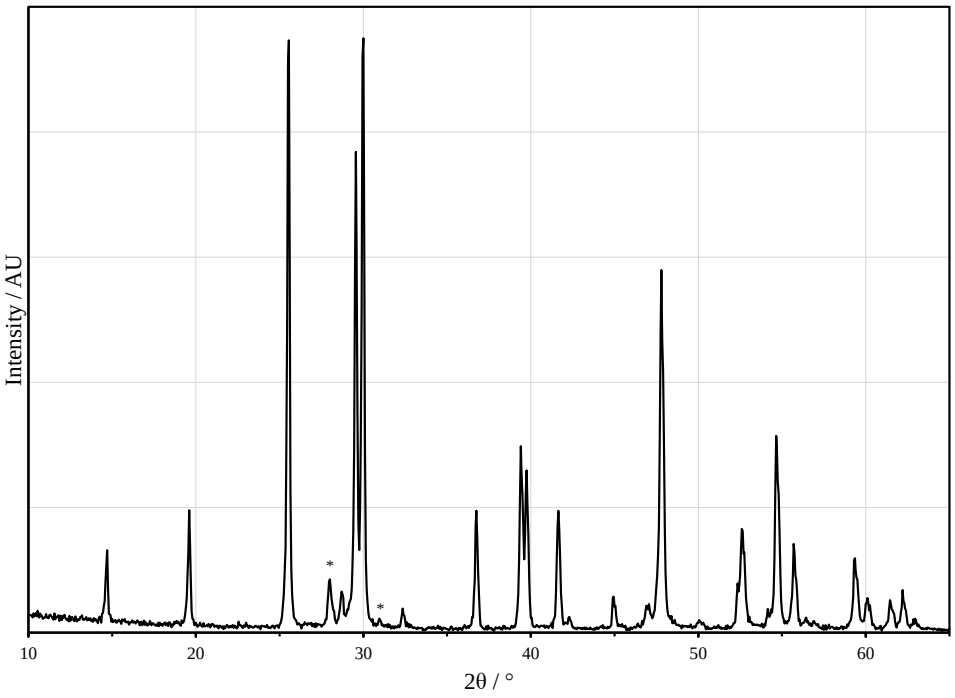

Figure C.3: Powder X-ray diffractogram of the 25LaBG-X sample. The sample is identified as $LaBGeO_5$ by comparison to the diffraction pattern reported by Rulmont and Tarte [278]. Impurity peaks are marked with asterisks (*). The impurity is tentatively identified as $La_2Ge_2O_7$ by comparison with the diffraction pattern calculated from the crystal structure reported by Vetter and Queyroux [265].

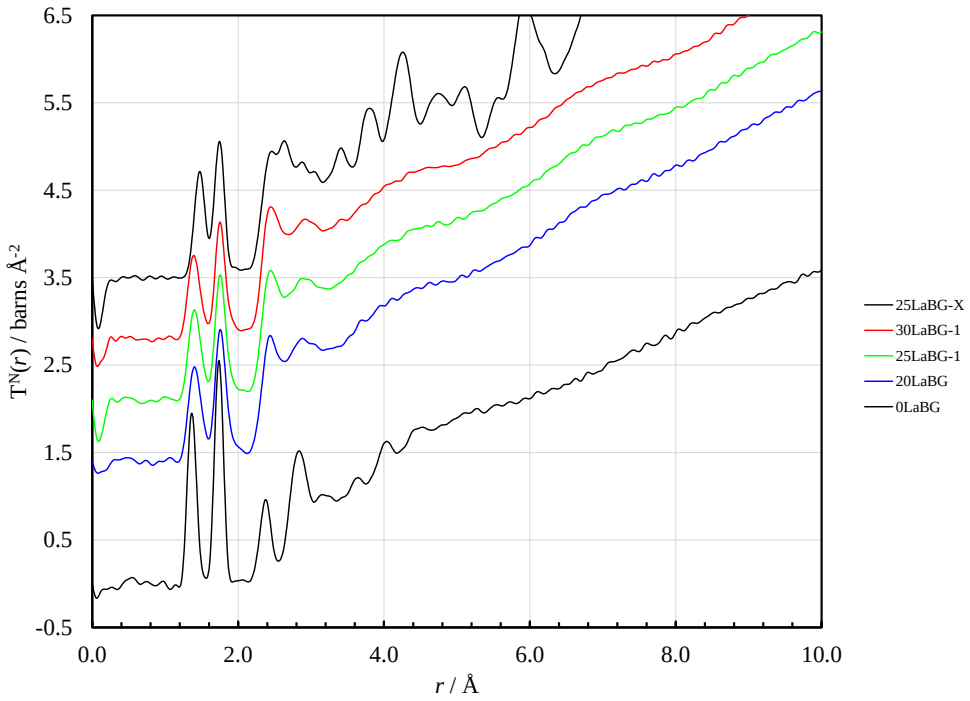

Figure C.4: The $T(r)$ total correlation functions of selected glass and crystal samples. The functions are vertically offset for clarity. A Lorch modification function with $Q_{\max} = 50\,\text{Å}^{-1}$ was used for the Fourier transformations. Error bars are contained within the data points.

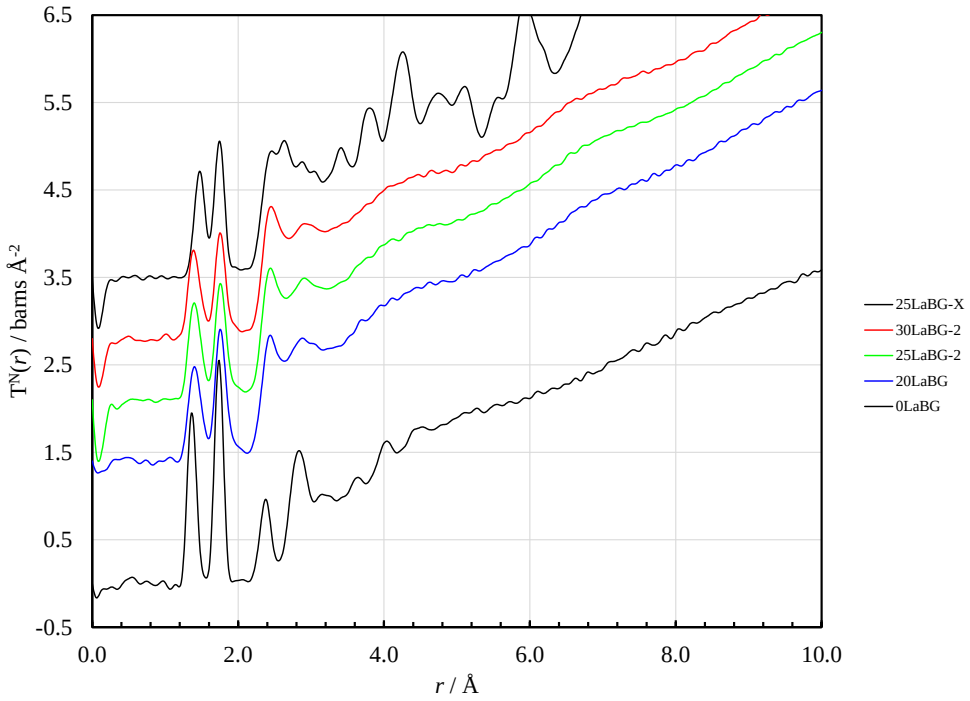

Figure C.5: The $T(r)$ total correlation functions of selected glass and crystal samples. The functions are vertically offset for clarity. A Lorch modification function with $Q_{\max} = 50\,\text{Å}^{-1}$ was used for the Fourier transformations. The $T(r)$ functions of 25LaBG-2 and 30LaBG-2 replace those of 25LaBG-1 and 30LaBG-01, as compared to Fig. C.4 above.

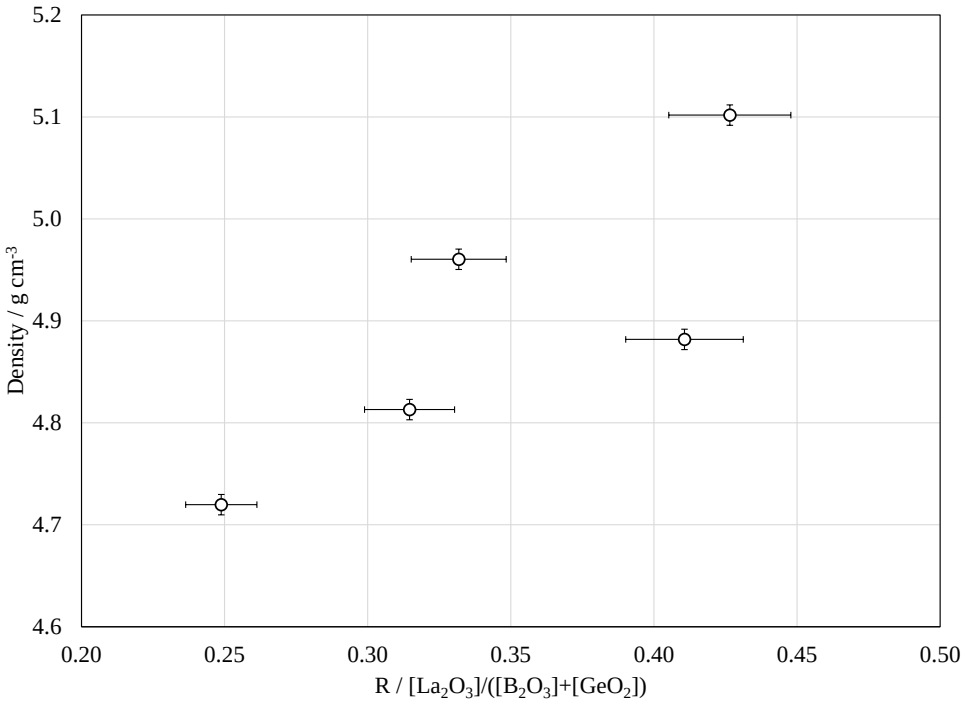

Figure C.6: The density of the lanthanum-containing borogermanate glass samples, as determined through the Archimedes method, as a function of the $R = [La_2O_3]/([B_2O_3]+[GeO_2])$ molar ratio. The $R = 0$ sample, 0LaBG, is omitted to allow for the change in density with molar ratio to be visible. The omitted data can be found in Table 6.1.

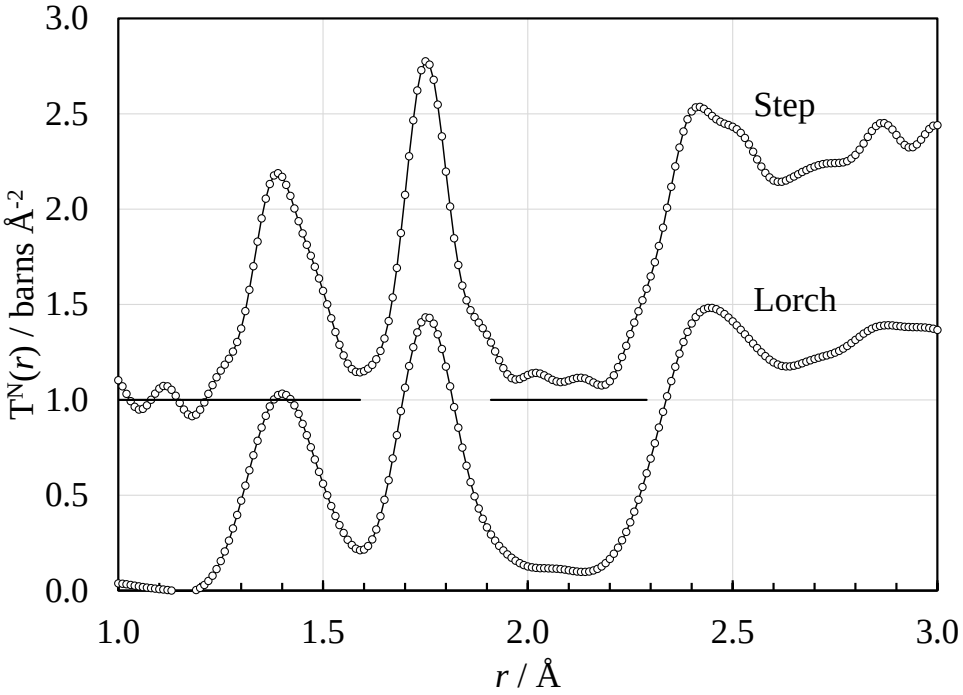

Figure C.7: The $T(r)$ function of 25LaBG-1. Top: as transformed with a step function. Bottom: as transformed with a Lorch function. Both used $Q_{\max} = 50\,\text{Å}^{-1}$. Note the shoulder on the high-r side of the left peak, attributed to the presence of $[\text{B}\text{Ø}_4]^-$. The high-r side of the centre peak shows a tail to high values of r when transformed with a step function. This intensity persists when a Lorch modification function is used, and is attributed to germanium-oxygen coordinations greater than 4.

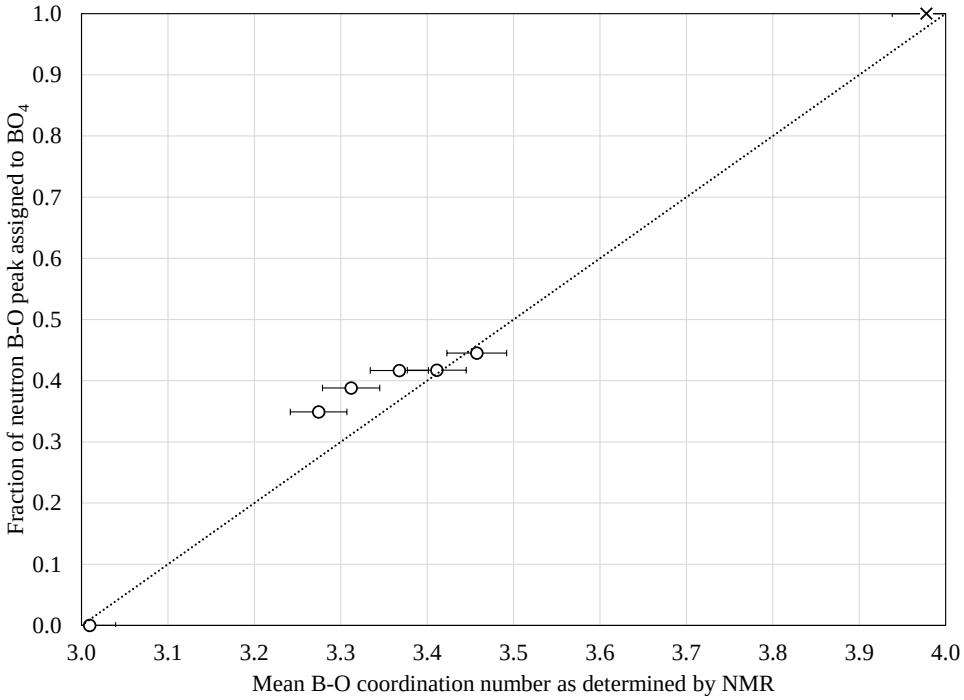

Figure C.8: The fraction of the neutron peak attributed to $[B\emptyset_4]^-$ as a fraction of the total area of the neutron B−O peak, as a function of the B-O coordination number as determined by ^{11}B MQMAS. The data point marked by an X is the crystalline 25LaBG-X sample, while the open circles indicate glass samples. The dotted line is a guide to the eye that indicates correspondence between the proportion of $[B\emptyset_4]^-$ as determined by ^{11}B MQMAS and the $[B\emptyset_4]^-$ fraction as determined by neutron diffraction. While the B−O coordination numbers as determined by neutron diffraction are inconsistent in absolute terms with the more reliable MQMAS values, the proportion of $T(r)$ area attributed to $[B\emptyset_4]^-$ generally follows the same trend as observed through MQMAS.

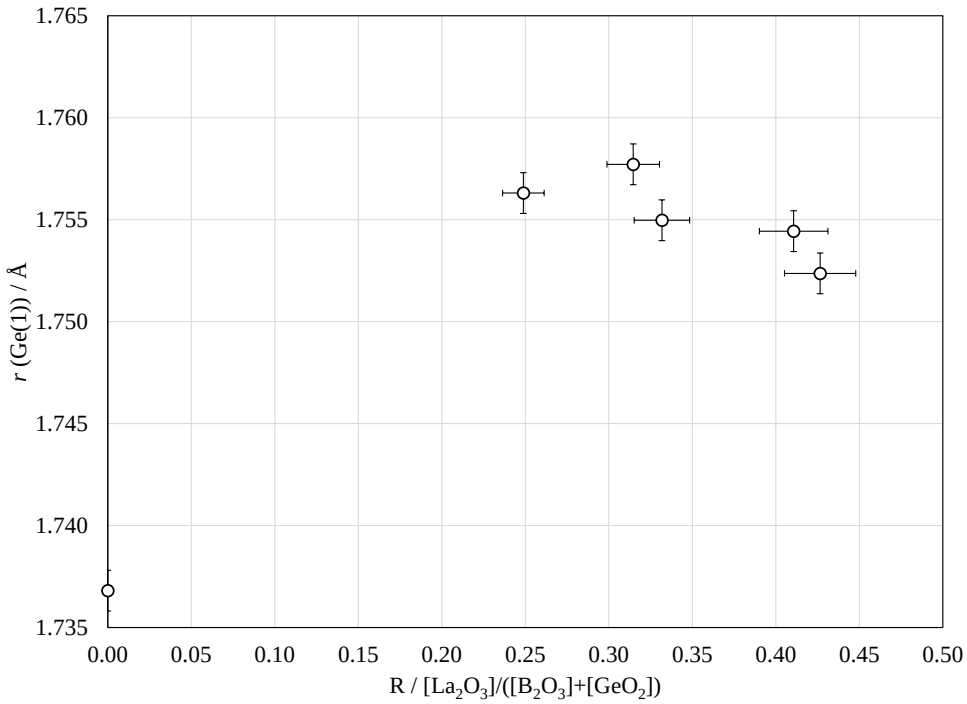

Figure C.9: The position of the fitted Ge(1) peak maximum as a function of the $R = [La_2O_3]/([B_2O_3]+[GeO_2])$ molar ratio.

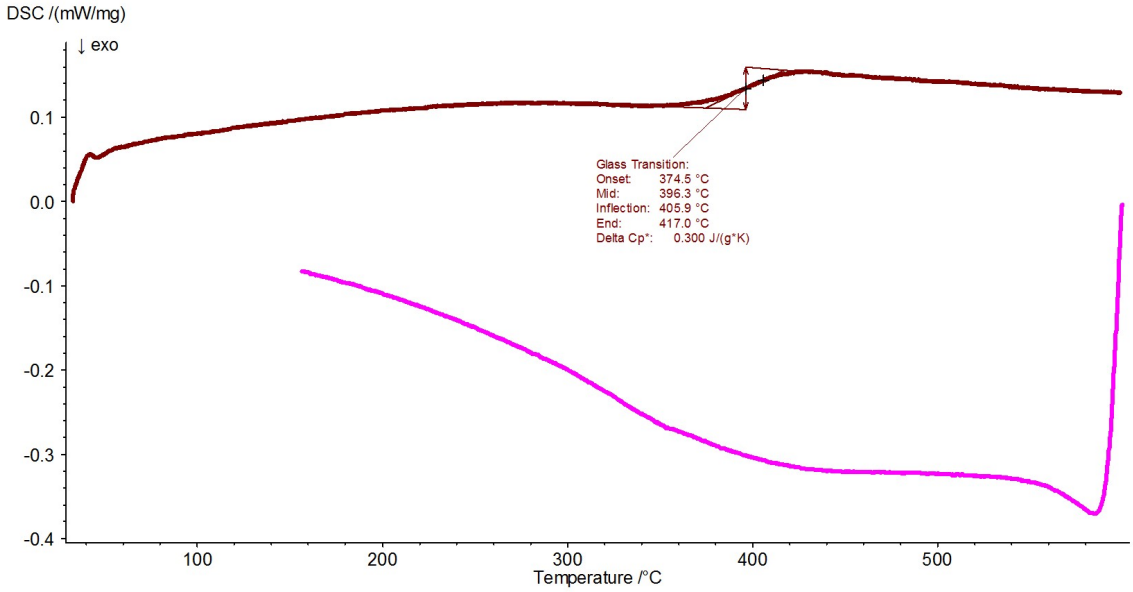

Figure C.10: DSC scan for the 0LaBG sample.

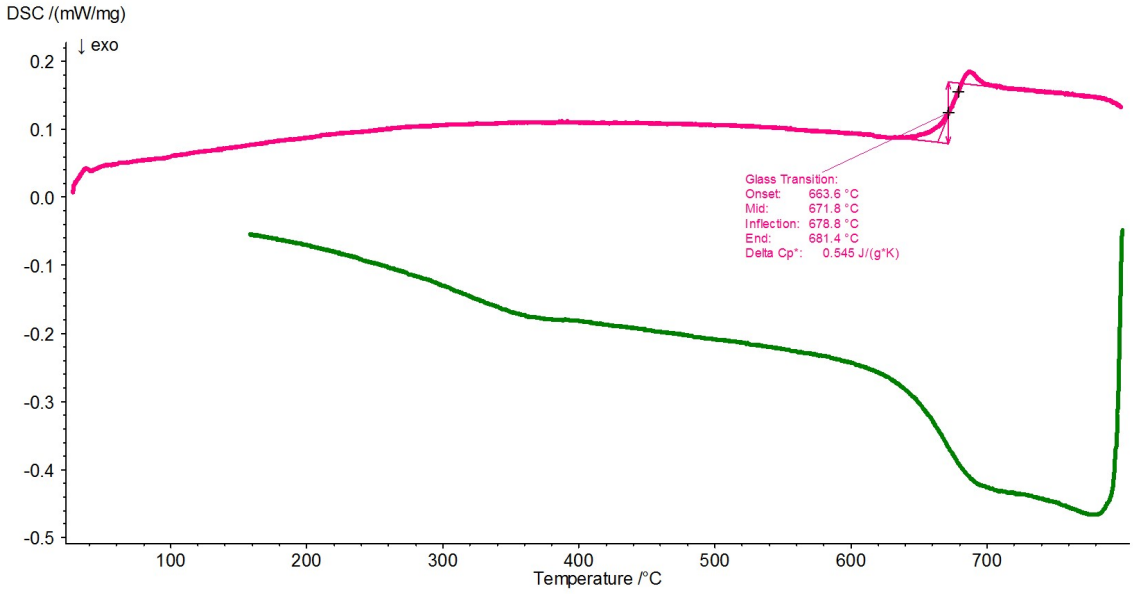

Figure C.11: DSC scan for the 20LaBG sample.

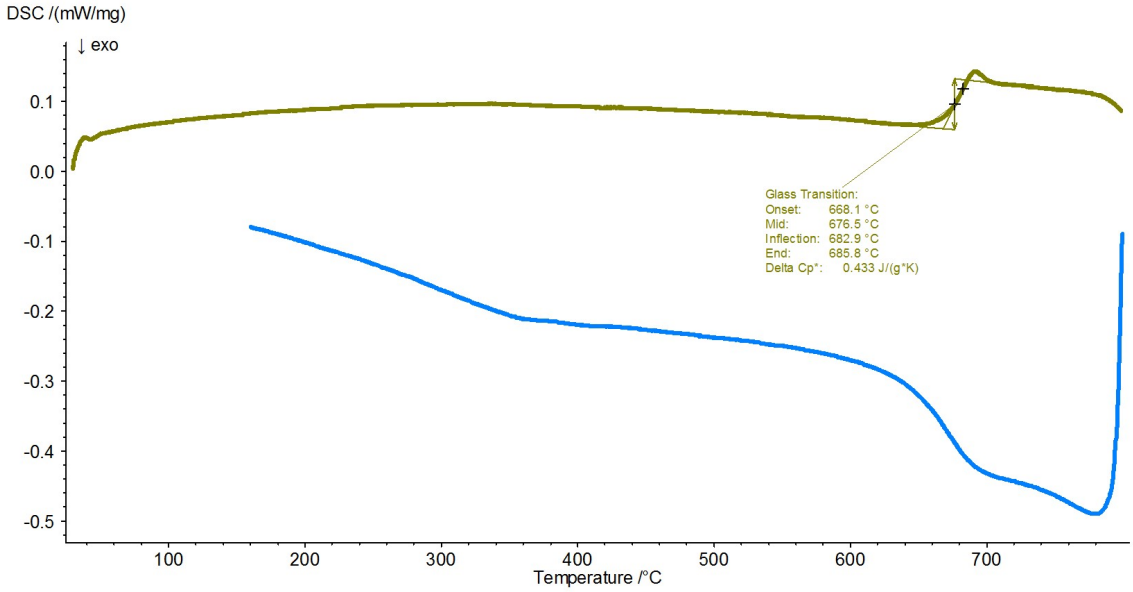

Figure C.12: DSC scan for the 25LaBG-1 sample.

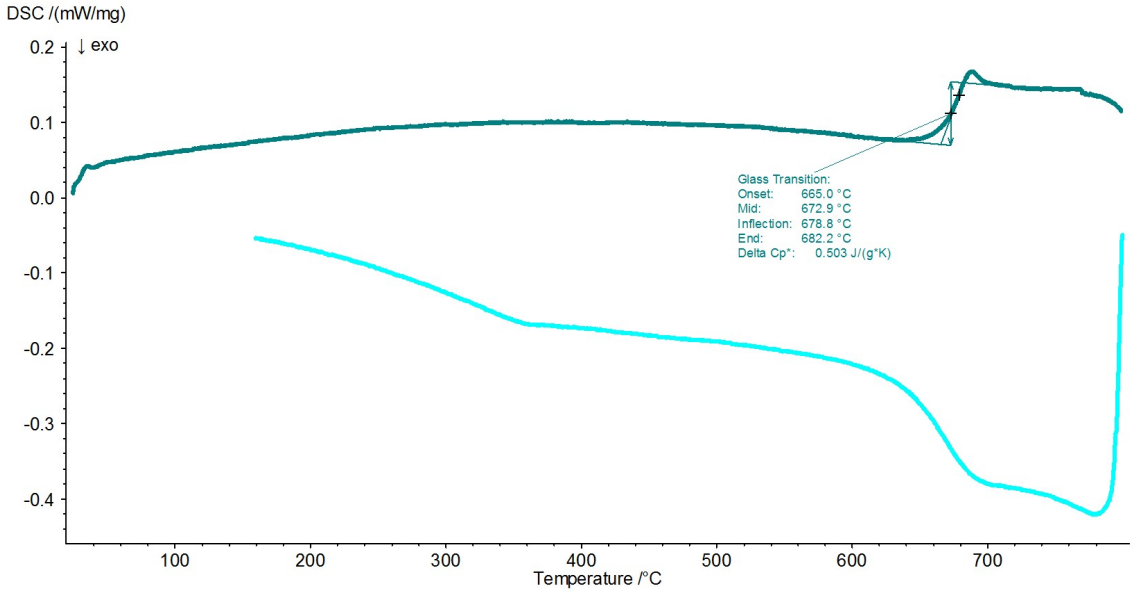

Figure C.13: DSC scan for the 25LaBG-2 sample.

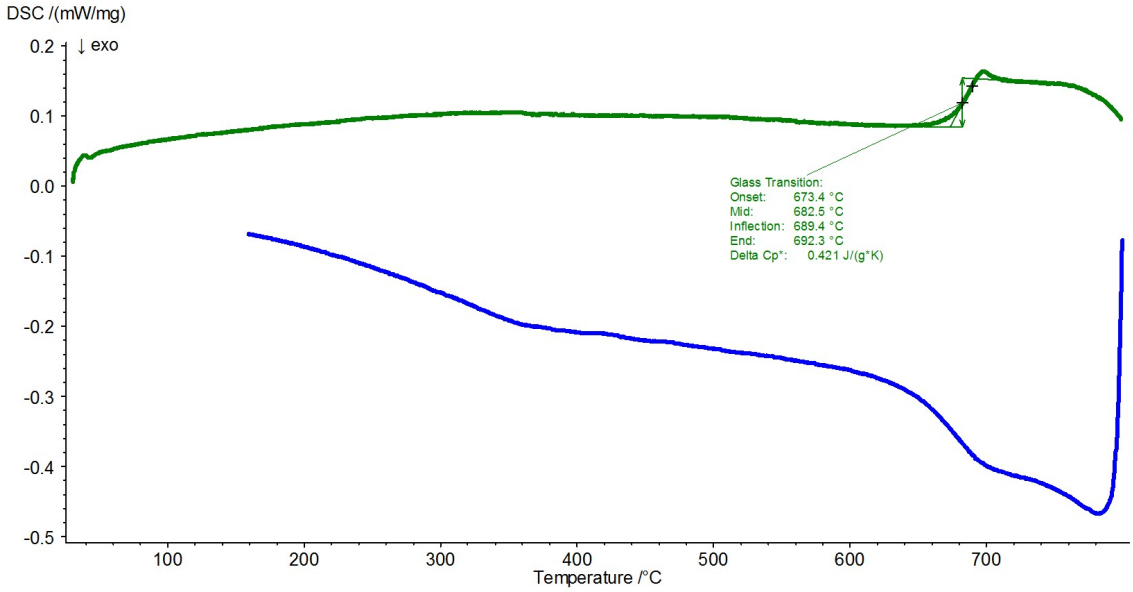

Figure C.14: DSC scan for the 30LaBG-1 sample.

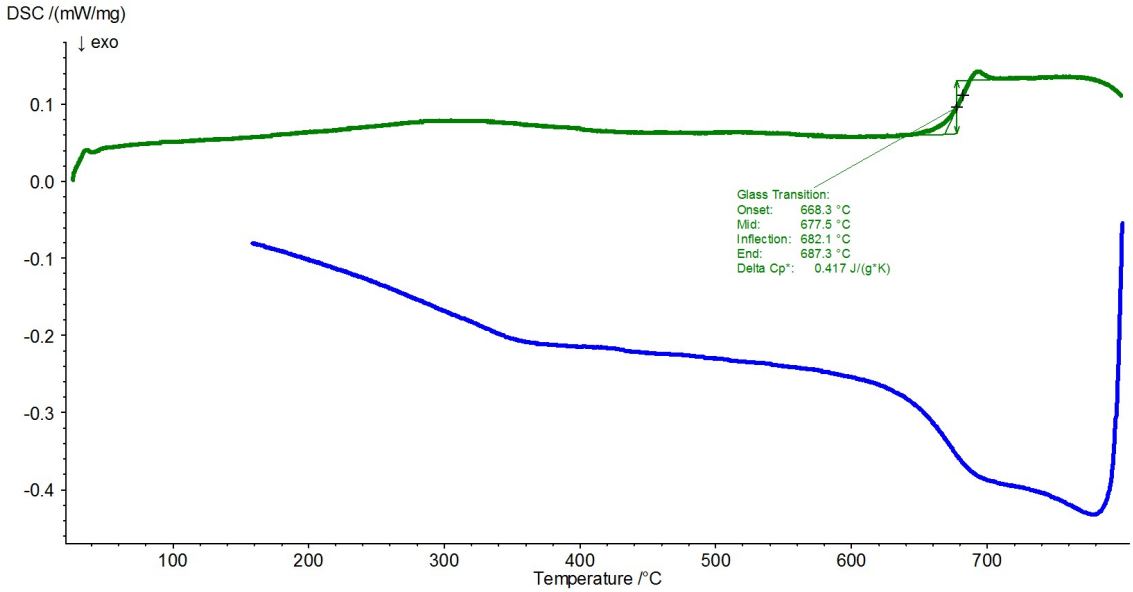

Figure C.15: DSC scan for the 30LaBG-1 sample.

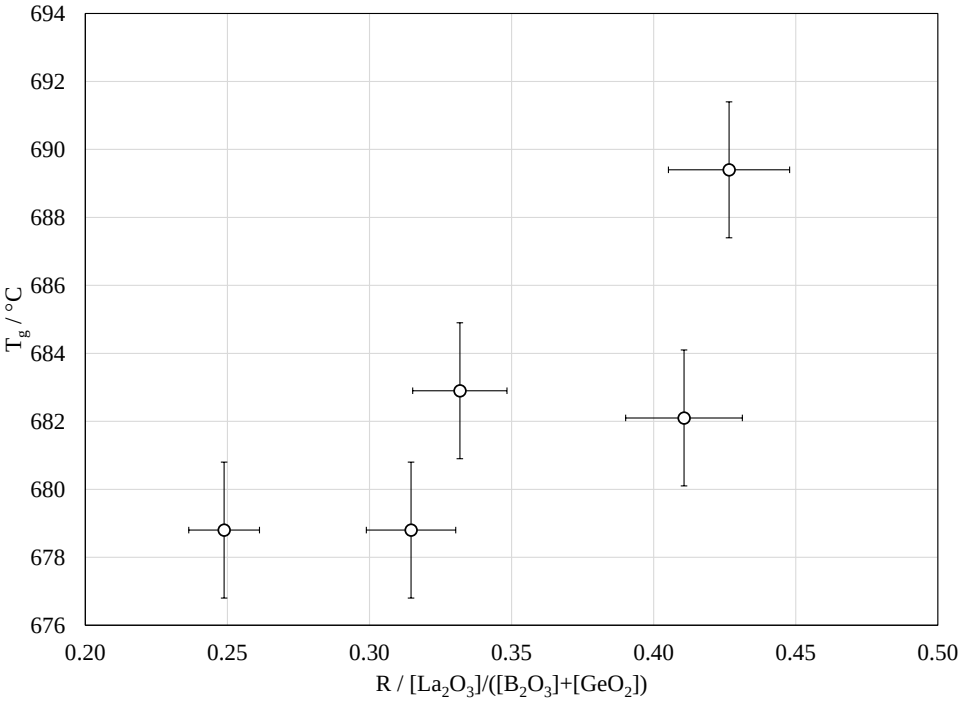

Figure C.16: The glass transition temperature of the lanthanum-containing glass samples, as measured by DSC, as a function of the molar ratio $R = [La_2O_3]/([B_2O_3]+[GeO_2])$. The $R = 0$ sample, 0LaBG, is omitted for clarity.

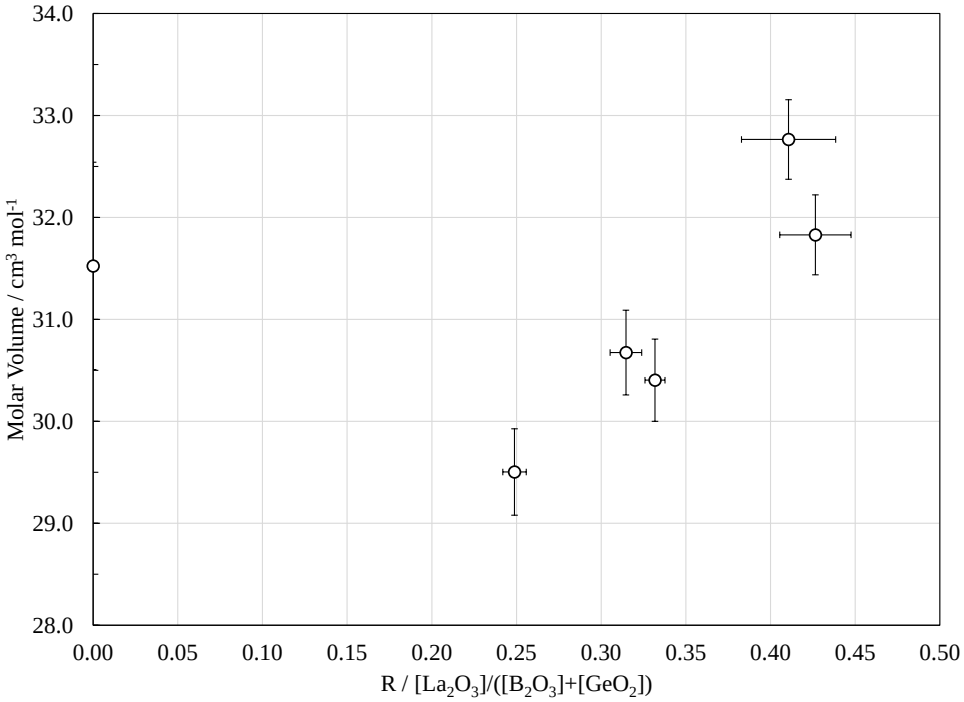

Figure C.17: The molar volume of glass samples as a function of the molar ratio $R = [La_2O_3]/([B_2O_3]+[GeO_2])$. The molar volume is at a maximum within error at both zero lanthanum content ($R = 0$) and maximum lanthanum content ($R = 0.446$).

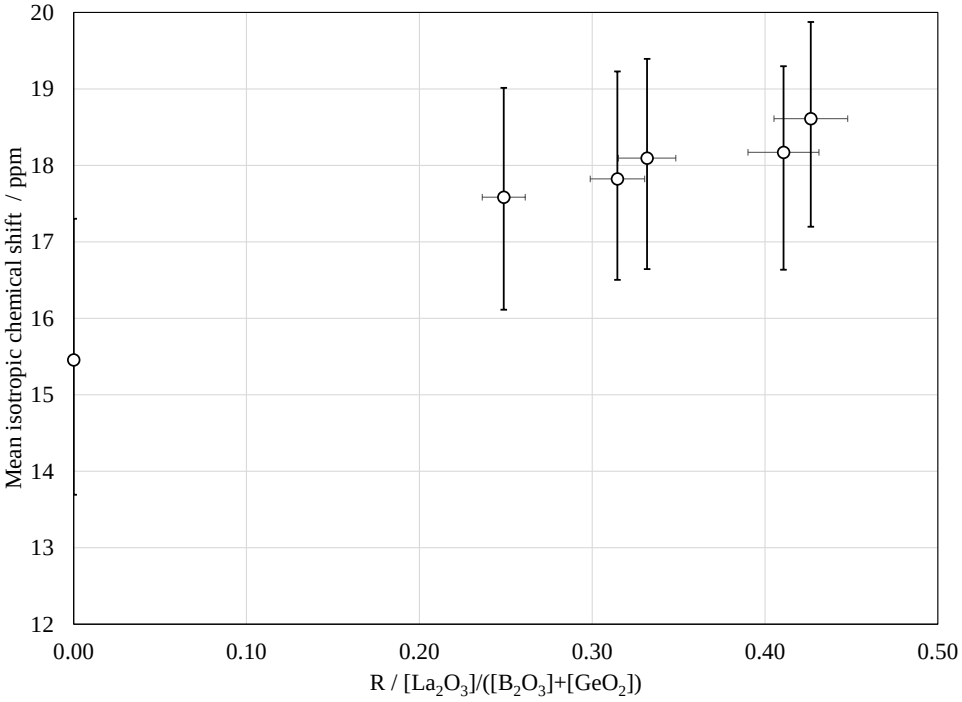

Figure C.18: Isotropic chemical shifts of BO_3 units in the glass samples. The data points indicate the isotropic chemical shifts derived from the centres of gravity of the MQMAS spectra [134]. The error bars along the y axis indicate the breath of the distribution of chemical shifts corresponding to the full-width at half-maximum of the peak in the isotropic axis of the MQMAS spectra. These values are consistent with the $\delta_{\text{iso}}^{\text{CS}}$ values for $B\emptyset_2O^-$ reported in the literature [48, 49]. Error bars along the x axis indicate the uncertainty in R.

Tables

Table C.1: Collected neutron diffraction parameters. r values are peak positions. u values are the widths of the peak in $T(r)$. A values are peak areas in $T(r)$.

		Sample						
Peak	Parameter	0LaBG	20LaBG	25LaBG-1	25LaBG-2	30LaBG-1	30LaBG-2	25LaBG-X
B(3)	r / Å	1.367	1.367	1.367	1.367	1.367	1.367	
	u / Å	0.047	0.052	0.050	0.049	0.053	0.049	
	A / b Å^{-1}	0.300	0.131	0.127	0.137	0.131	0.128	
B(4)	r / Å		1.473	1.473	1.473	1.473	1.473	1.473
	u / Å		0.060	0.054	0.054	0.059	0.061	0.063
	A / b Å^{-1}		0.105	0.091	0.098	0.070	0.081	0.223
Ge(1)	r / Å	1.737	1.756	1.755	1.758	1.752	1.754	1.744
	u / Å	0.045	0.060	0.059	0.062	0.054	0.059	0.059
	A / b Å^{-1}	0.383	0.269	0.252	0.242	0.223	0.214	0.274
Ge(2)	r / Å		1.916	1.918	1.927	1.911	1.943	
	u / Å		0.033	0.0267	0.038	0.023	0.041	
	A / b Å^{-1}		0.026	0.022	0.020	0.022	0.020	
Ge(3)	r / Å		2.046	2.057	2.060	2.071	2.094	
	u / Å		0.043	0.042	0.055	0.057	0.039	
	A / b Å^{-1}		0.019	0.017	0.017	0.018	0.011	
Residual	r / Å		2.445	2.446	2.444	2.448	2.451	
	u / Å		0.112	0.111	0.108	0.107	0.109	
	A / b Å^{-1}		0.429	0.444	0.438	0.440	0.443	

Table C.2: EBS of various oxygen environments in lanthanum borogermanates, not accounting for the contribution of lanthanum. The environments are sorted according to Σ

O Environment	Σ / EBS
$[O_b^4B_2^6Ge]$	2.167
$[O_b^5Ge^6Ge_2]$	2.133
$[O_b^4B^6Ge_2]$	2.083
$[O_b^6Ge_3]$	2.000
$[O_b^3B_2]$	2.000
$[O_b^3B^4Ge]$	2.000
$[O_b^4Ge_2]$	2.000
$[O_b^3B^5Ge]$	1.800
$[O_b^4Ge^5Ge]$	1.800
$[O_b^3B^4B]$	1.750
$[O_b^4B^4Ge]$	1.750
$[O_b^3B^6Ge]$	1.667
$[O_b^4Ge^6Ge]$	1.667
$[O_b^5Ge_2]$	1.600
$[O_b^4B^5Ge]$	1.550
$[O_b^4B_2]$	1.500
$[O_b^5Ge^6Ge]$	1.467
$[O_b^4B^6Ge]$	1.417
$[O_b^6Ge_2]$	1.333
$[O_{nb}^3B]$	1.000
$[O_{nb}^4Ge]$	1.000
$[O_{nb}^5Ge]$	0.800
$[O_{nb}^4B]$	0.750
$[O_{nb}^6Ge]$	0.667

Appendix D

Supporting Information for Chapter 7: Network Connectivity and Crystallization in the Transparent Ferroelectric Nanocomposite Material $LaBGeO_5$

D.1 Context

The contents of this appendix were prepared as supporting information for Chapter 7.

D.2 Powder X-Ray Diffraction

X-ray diffraction data were collected to aid in phase identification of the samples. By process of elimination based upon the sample composition, and the phases known to be present in the composition, the identities of of the crystalline components of the samples were established.

For a more rigorous identification, Rietveld refinements of the pXRD data were conducted. The phase scale, background, zero parameter, and lattice parameters were allowed to vary. Ionic positions were fixed to those reported by Kaminskii *et al.* [78], as those reported by Belokoneva *et al.* have unrealistic bond lengths and angles [79]. When positions or ionic occupancies were allowed to vary, the results were generally unphysical. Peak shape parameters were fixed to the defaults provided in the RIETICA program, as no experimental data from a standard reference material was available for the X-ray diffractometer used. The results of the refinements are presented in Table D.1; an example refinement (for sample LBG+60) is presented in Fig. D.1.

The strains reported in Table D.1 are relative to the averages of the lattice parameters reported by Kaminskii *et al.*, Belokoneva *et al.*, and Rulmont and Tarte [78, 79, 278]. The stresses are obtained from these strains through the use of the elastic stiffness tensor reported in Table 8.2 [283]. They should be considered a rough estimate of the stresses within the system.

Rietveld refinement was also used to quantify the fraction of $LaBO_3$ within the

Table D.1: Results of Rietveld refinements of pXRD data. Strain is reported as the ratio of the refined lattice parameters to the average of the $LaBGeO_5$ lattice parameters reported in the literature. Stresses are obtained using the elastic constants reported in Table 8.2 [283]. The sample 25LaBG-X is described in Chapter 6; all other samples are from Chapter 7.

					Strain		Stress / GPa	
Sample	Crystallinity / %	χ^2	a / Å	c / Å	a	c	σ_{xx}	σ_{zz}
LBG+8	15	3.32	6.914	6.857	0.9870	0.9984	4.4	3.1
LBG+12	29	4.71	6.920	6.862	0.9879	0.9991	4.1	2.7
LBG+24	48	7.36	6.921	6.860	0.9880	0.9989	4.0	2.7
LBG+60	72	4.30	6.924	6.851	0.9885	0.9976	4.0	3.0
LBG+3d	80	8.30	6.997	6.868	0.9988	1.0000	0.4	0.2
25LaBG-X	98	8.30	6.992	6.863	0.9982	0.9993	0.7	0.6

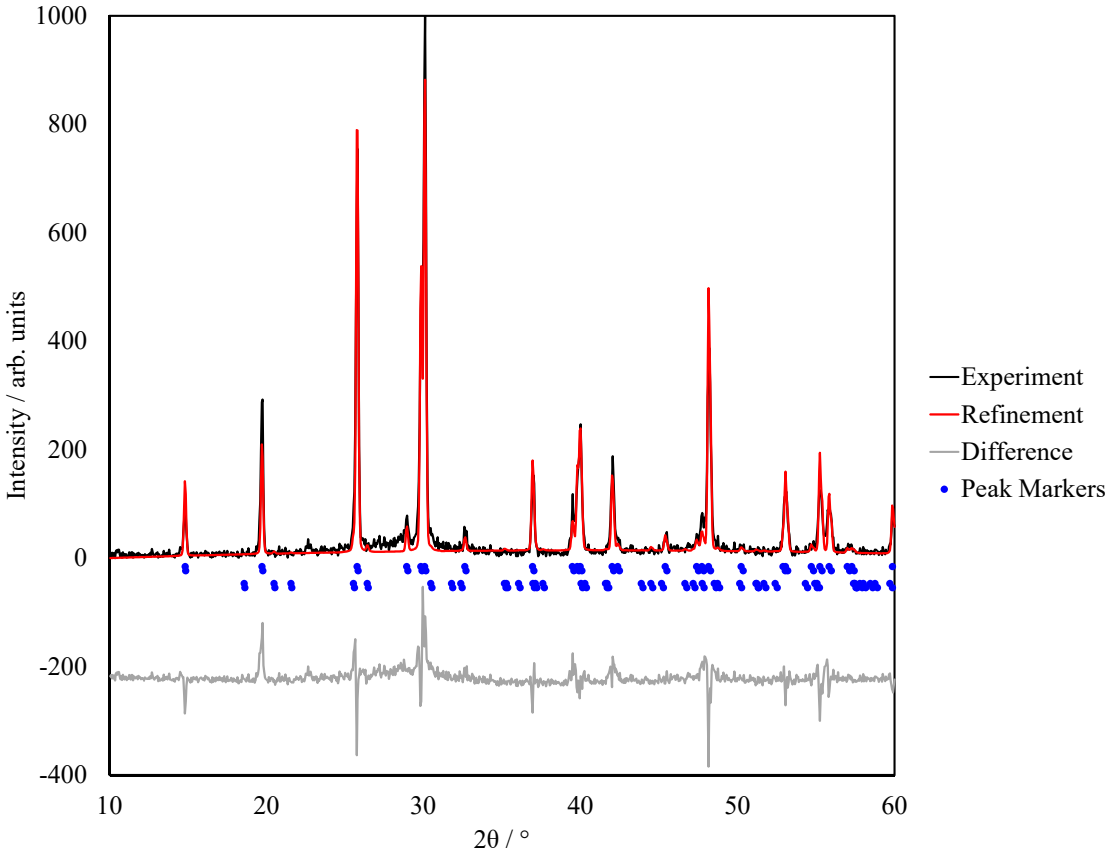

Figure D.1: PXRD diffraction pattern and Rietveld refinement profile for sample LBG+60. The refinement uses lattice parameters somewhat smaller than literature values. The parameters are reported in Table D.1. The top row of peak markers are for $LaBGeO_5$; the bottom row are for the orthorhombic phase of $LaBO_3$.

samples where it was observed. In the LBG+60 sample, room-temperature (*i.e.*, orthorhombic) $LaBO_3$ was observed in the ^{139}La WCPMG NMR spectrum (Fig. 7.5), but not the ^{11}B NMR spectrum (Fig. 7.3). The ^{139}La WCPMG NMR spectrum suggests that $LaBO_3$ makes up 4 % of the sample, or 6.5 % of the crystalline fraction. However, WCPMG is formally non-quantitative in intensities. The Rietveld refinement of LBG+60 suggests that (2.4 ± 0.7) % of the crystalline portion of the sample is made up of $LaBO_3$. However, when the intensity attributable to $LaBGeO_5$ is considered ((98 ± 2) %), along with the signal-to-noise ratio of the diffractogram, it is not plausible to say that $LaBO_3$ has been detected. Hence the fraction of the partially-crystallized samples made up by $LaBO_3$ is thought to be generally less than 3 %.

There is what appears to be a peak at 22.65°, which has been proposed as an indication of high-temperature (*i.e.*, monoclinic) $LaBO_3$. When the data is closely examined, the data points about 22.65° are in fact inconsistent with the behaviour of a real peak. Furthermore, the main peak of monoclinic $LaBO_3$ is located about 22.9°, and does not well fit the data. The ^{139}La WCPMG NMR data may not be quantitative in intensity, but it is quantitative in C_Q, and the data is inconsistent with the monoclinic phase. Finally, the phase transition to monoclinic $LaBO_3$ occurs at (1488 ± 5) °C [214], and that temperature was never reached at any point in this study. The body of evidence suggests that $LaBO_3$ is not detected by pXRD in the LBG+60 sample.

In the LBG+3d sample, room-temperature $LaBO_3$ is detected via ^{139}La WCPMG NMR, ^{11}B MAS NMR, and pXRD. ^{139}La WCPMG NMR suggests 13 % of the La content is in $LaBO_3$; however, the glass fraction of LBG+3d is not detectable in the ^{139}La WCPMG NMR spectrum. ^{11}B MAS NMR suggests that (9 ± 1) % of the B content is in $LaBO_3$; with crystalline $LaBGeO_5$ making up (80 ± 1) % of the overall sample, $LaBO_3$ would make up about (11 ± 1) % of the crystalline content. The crystalline content attributable to $LaBO_3$ by pXRD is 15 %. Of these values, the fraction derived from ^{11}B NMR is perhaps the most reliable, as it fully accounts for the presence of the amorphous $LaBGeO_5$, the crystalline $LaBGeO_5$, and the crystalline $LaBO_3$. The estimate provided by the Rietveld refinement could be improved by a more careful model, though this would require the collection of additional data.

D.3 Density Functional Theory Calculations

The QE-GIPAW package calculates the absolute chemical shielding tensor, from which the isotropic chemical shielding (σ) is calculated. The experimental NMR observable we wish to derive from the isotropic chemical shielding (σ_{iso}) is the isotropic chemical shift ($\delta_{\text{iso}}^{\text{CS}}$). There are two generally accepted techniques used in the literature to predict chemical shift values from calculated chemical shielding values [158]. The first is to calculate the shielding of a reference compound (σ_{ref}) with known $\delta_{\text{iso}}^{\text{CS}}$, and calculate the $\delta_{\text{iso}}^{\text{CS}}$of the compound of interest via

$$\delta_{\text{iso}}^{\text{CS}} = \sigma_{\text{ref}} - \sigma_{\text{iso}}. \tag{D.1}$$

The second is to fit a set of calculated σ to their experimental $\delta_{\text{iso}}^{\text{CS}}$ values for a range of relevant systems, and interpolate the desired $\delta_{\text{iso}}^{\text{CS}}$ values via

$$\delta_{\text{iso}}^{\text{CS}} = a(\sigma_{\text{ref}} - \sigma_{\text{iso}}) \tag{D.2}$$

where a is a constant and σ_{ref} is the y-intercept of the line. We use Eq. (D.2) to reference the ^{139}La and ^{17}O shifts, and Eq. (D.1) with LaB_3O_6 to reference ^{11}B shifts. ^{73}Ge chemical shifts were not referenced, as no ^{73}Ge NMR experiments were conducted. The data used to produce the fit for the ^{17}O and ^{139}La references are listed in Table D.2, and plotted in Figs. D.2 and D.3.

The σ and $\delta_{\text{iso}}^{\text{CS}}$ values for various nuclei for various crystal structures are presented in Table D.2. All calculations were conducted using the experimental crystal structures. Plane-wave cutoffs were generally set to 60 Rydberg, and shifted Monkhorst-Pack k-point grids were used. The density of the k-point grids were set to ensure k-point spacings of less than $0.03\,\text{Å}^{-1}$.

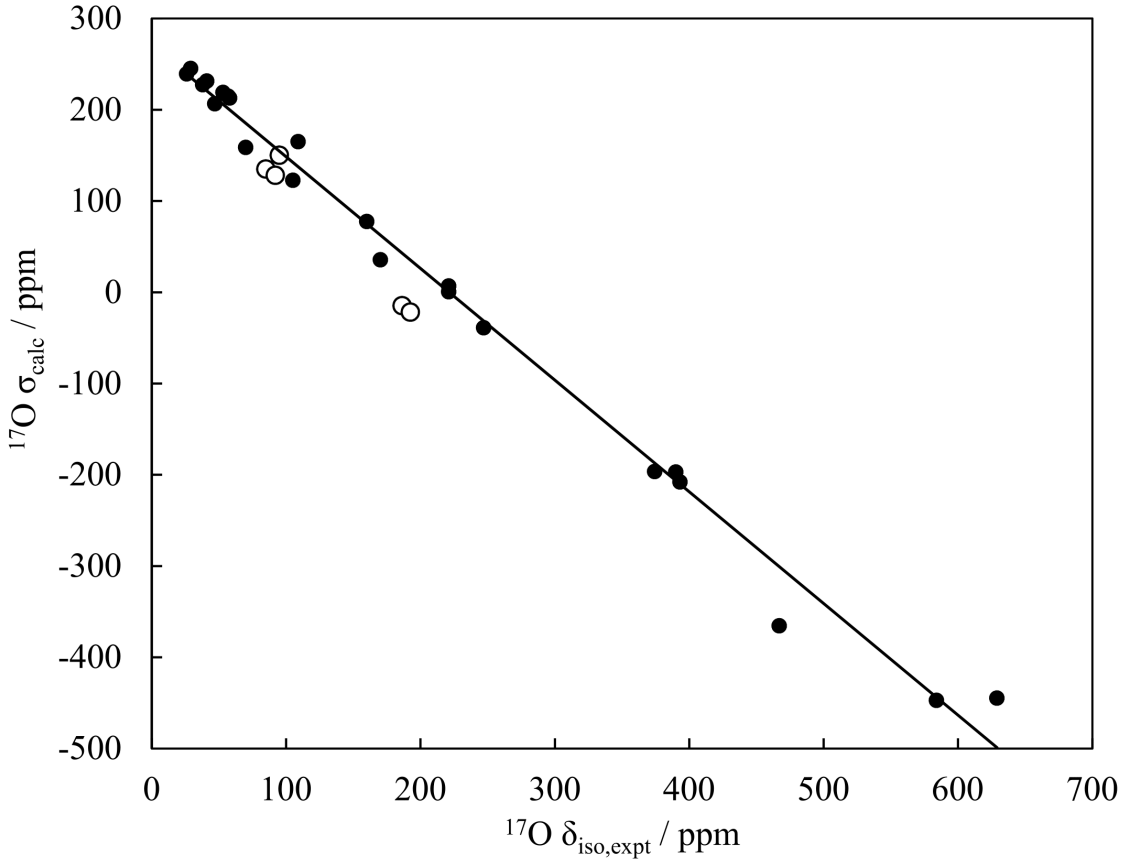

Figure D.2: The data used to convert the calculated chemical shieldings σ to predicted chemical shifts δ_{iso}^{CS} for ^{17}O. The filled circles indicate data from Table D.2. The open circles indicate the O environments in $LaBGeO_5$; their experimental shifts are discussed in Section 7.5. The line is a linear fit to the filled circles.

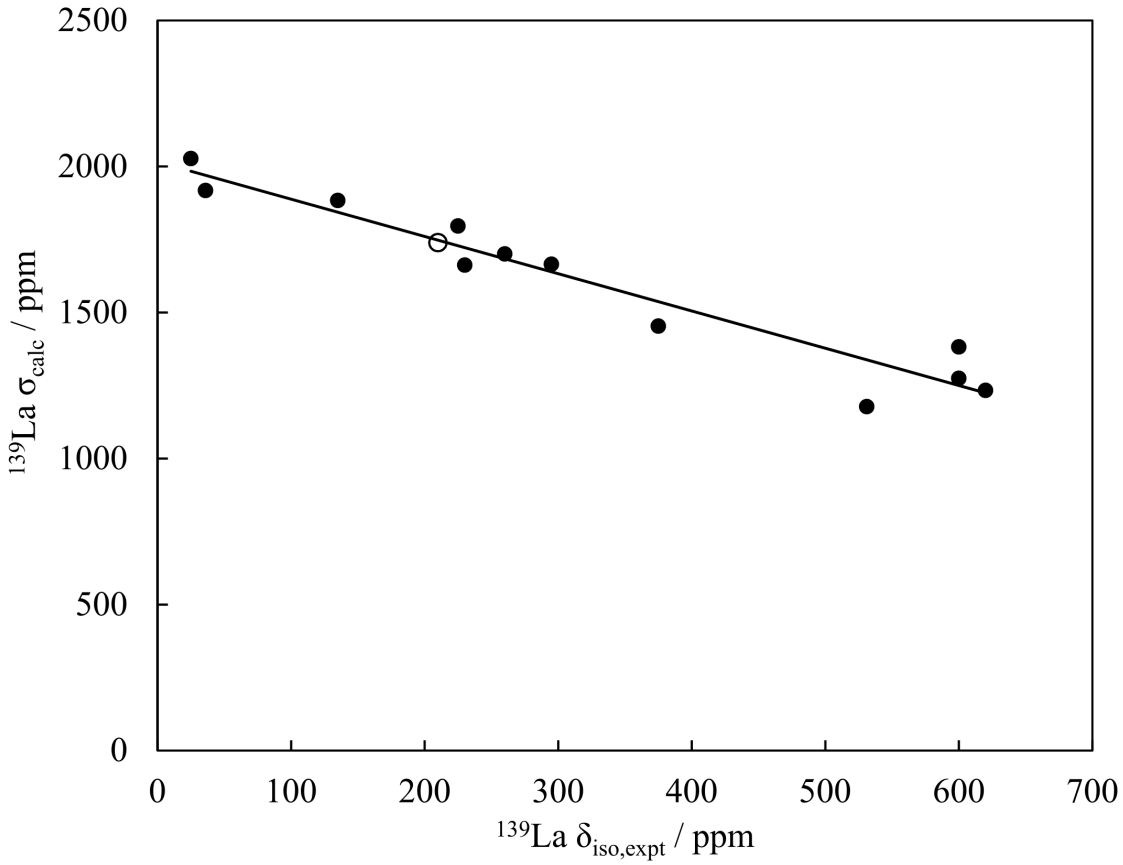

Figure D.3: The data used to convert the calculated chemical shieldings σ to predicted chemical shifts δ_{iso}^{CS} for ^{139}La. The filled circles indicate data from Table D.2. The open circle indicates the La environment in $LaBGeO_5$; their experimental shifts are discussed in Section 7.5. The line is a linear fit to the filled circles.

Table D.2: Comparison between experimental δ_{iso}^{CS} and calculated σ.

		^{139}La / ppm		^{11}B / ppm		^{17}O / ppm		Sources	
	Site	δ_{iso}^{CS}	σ	δ_{iso}^{CS}	σ	δ_{iso}^{CS}	σ	Structure	δ_{iso}^{CS}
La_2O_3	La	620	1233					[219]	[126]
	O1					584	-447		[319]
	O2					467	-365		[319]
$LaAlO_3$		375	1453					[262]	[126]
Quartz GeO_2						70	159	[260]	[55]
Rutile GeO_2						160	78	[260]	[55]
$LaBO_3$	La	230	1662					[309]	[126]
	B			22	73				This work
	O1						14		
	O2						-12		
SnO						246	-39	[320]	[319]
SnO_2						105	123	[321]	[322]
$LaScO_3$	La	600	1275					[177]	[177]
	O1					393	-208		[177]
	O2					374	-196		[177]
Quartz SiO_2						43	227	[323]	[324]
Stishovite SiO_2						109	165	[325]	[326]
Coesite SiO_2	O1					29	245	[327]	[328]
	O2					41	231		[328]
	O3					57	215		[328]
	O4					53	219		[328]
	O5					58	213		[328]
$LaGaO_3$	La	600	1382					[329]	[330]
	O1					221	7		[331]
	O2					221	1		[331]
MgO						47	206	[332]	[333]
BeO						26	239	[334]	[333]
BaO						629	-445	[335]	[333]
SrO						390	-197	[336]	[333]
$LaPO_4$		36	1917					[223]	[126]
LaB_3O_6	La	135	1883					[216]	Unpublished work
	B1			18	77				This work
	B2			-1	96				This work
	O1						145		
	O2						7		
	O3						156		
$LaBSiO_5$		225	1796					[220]	[126]
LaP_3O_9		25	2027					[222]	Unpublished work
$LaNbO_4$		295	1665					[221]	[60]
$La_2Sn_2O_7$		531	1177					[337]	Unpublished work

D.4 NMR Spectra

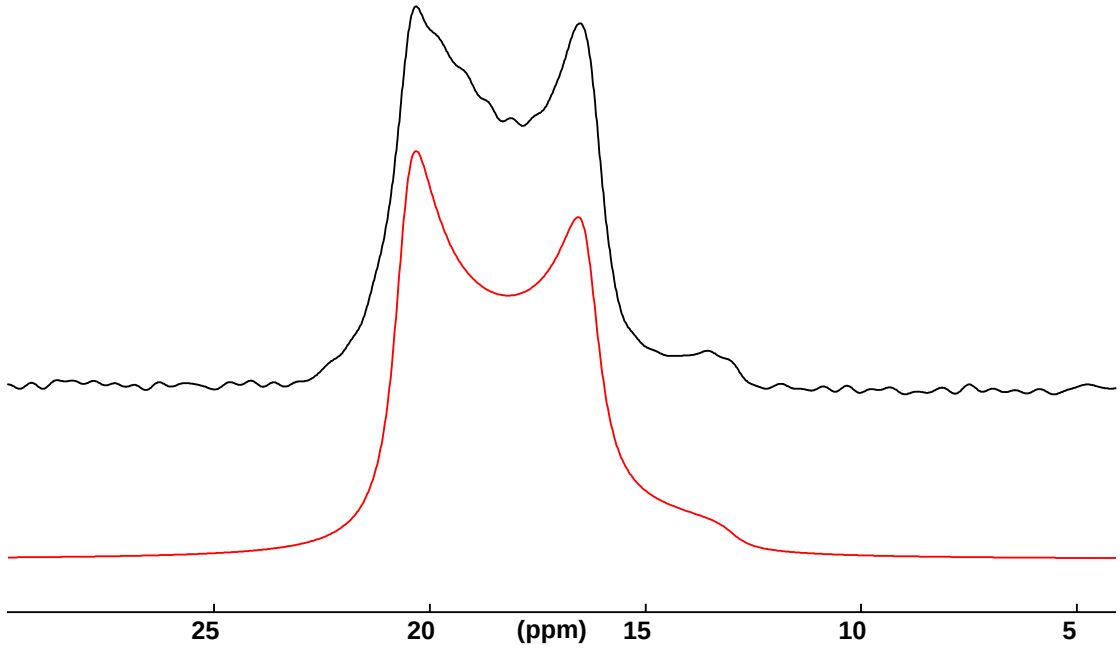

Figure D.4: ^{11}B MAS NMR spectrum of $LaBO_3$. The fit corresponds to the following set of parameters: $\delta_{iso}^{CS} = (22 \pm 1)$ ppm; $C_Q = (2.7 \pm 0.1)$ MHz; η_Q fixed at 0.05. The C_Q value agrees well with the value reported in the literature, but our δ_{iso}^{CS} is 1.4 ppm more positive [48].

Table D.3: ^{10}B NMR parameters for the samples investigated. Parameters were obtained by fitting the spectra. Values in parentheses indicate uncertainties.

Sample	δ_{iso}^{CS} / ppm	C_Q / MHz	η_Q	P_Q / MHz
LBG-G	0.8 ± 0.8	0.9 ± 0.4	1.0 ± 0.4	1.0 ± 0.4
LBG-X	0.9 ± 0.8	0.8 ± 0.4	1.0 ± 0.4	1.0 ± 0.4
LaB_3O_6	-0.5 ± 0.8	0.6 ± 0.4	0.0 ± 0.4	0.6 ± 0.4

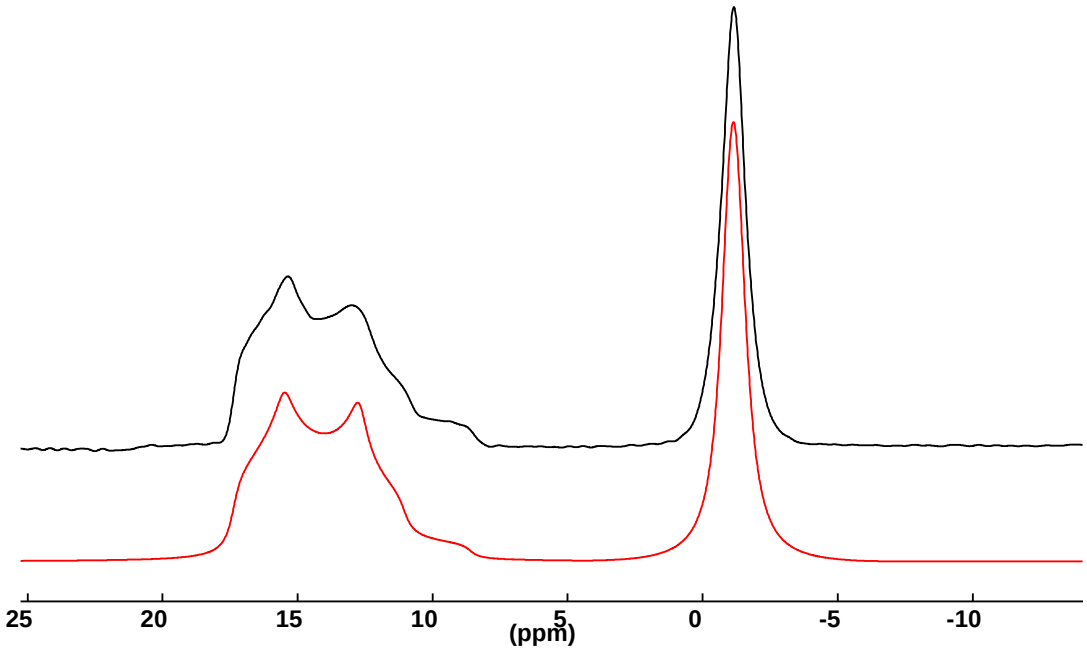

Figure D.5: ^{11}B MAS NMR spectrum of LaB_3O_6. The fit consists of two peaks in a 2:1 intensity ratio. The $B\emptyset_2O^-$ peak uses the following set of parameters: $\delta_{iso}^{CS} = (18 \pm 1)$ ppm; $C_Q = (2.7 \pm 0.1)$ MHz; $\eta_Q = 0.36 \pm 0.02$. The $[B\emptyset_4]^-$ peak parameters are: $\delta_{iso}^{CS} = (-1 \pm 1)$ ppm; $P_Q = (0.8 \pm 0.3)$ MHz. These values agree well with those reported in the literature [97].

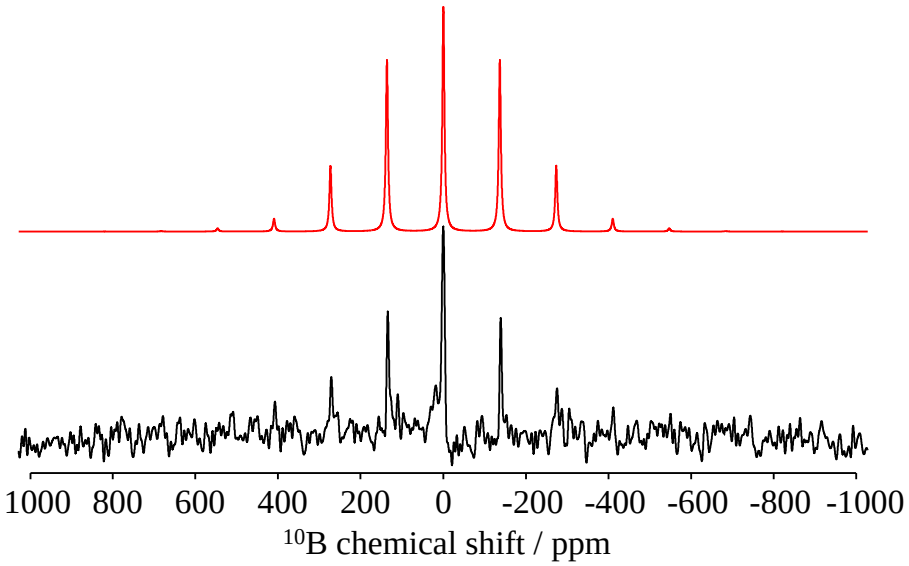

Figure D.6: ^{10}B Hahn echo NMR spectrum of LaB_3O_6. Only the $[B\emptyset_4]^-$ environment is excited. Fit parameters are in Table D.3.

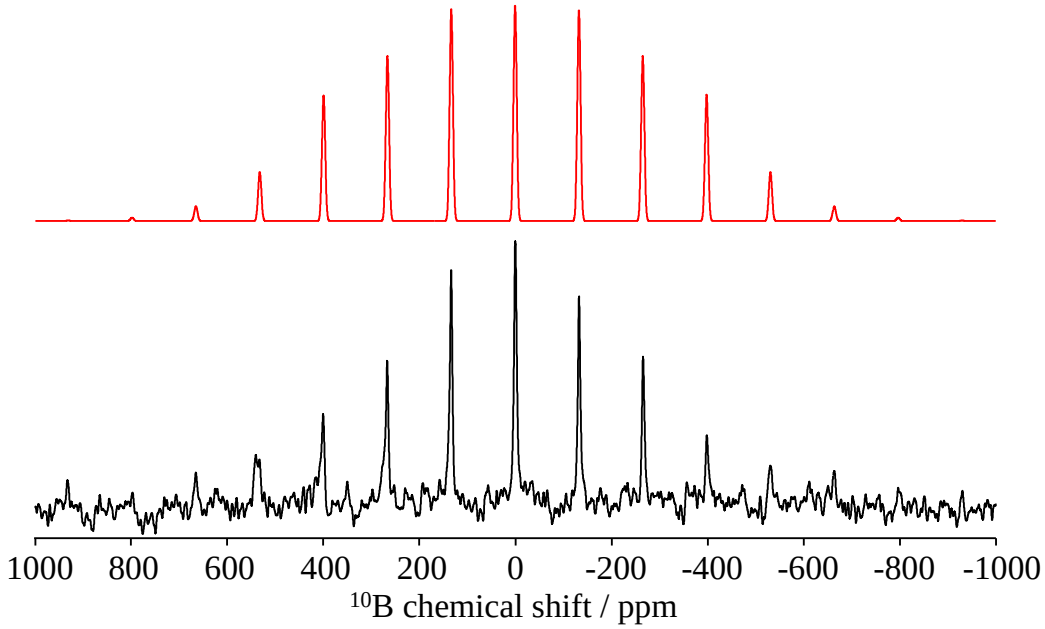

Figure D.7: ^{10}B Hahn echo NMR spectrum of $LaBGeO_5$ glass. Only the $[B\emptyset_4]^-$ environment is excited. Fit parameters are in Table D.3.

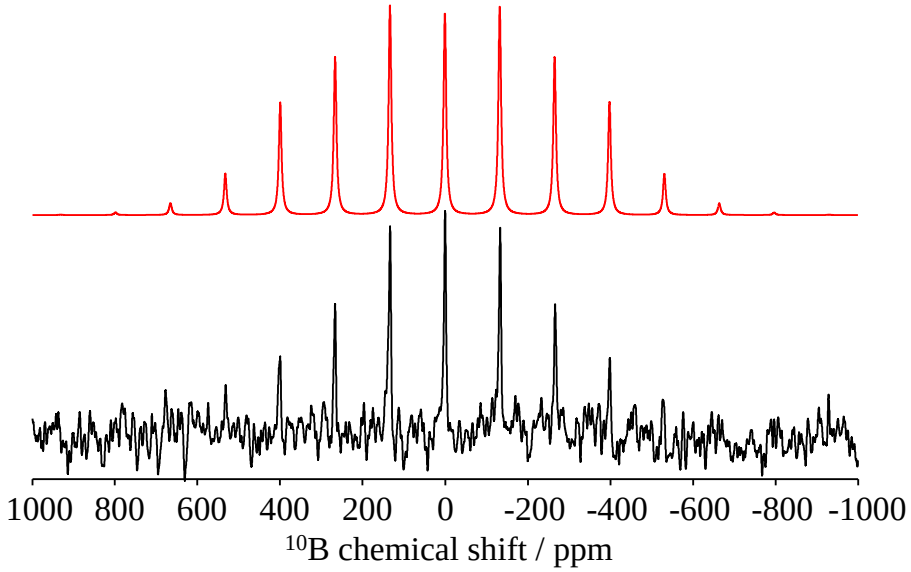

Figure D.8: ^{10}B Hahn echo NMR spectrum of $LaBGeO_5$ crystal. Fit parameters are in Table D.3.

Appendix E

Copyright Permissions

Some of the content in this dissertation is used with the permission of the copyright holders. Copyright permission letters are contained within this appendix. In particular, Figs. 2.1 to 2.3 and 3.8 and Chapters 4, 6 and 8 all contain copyrighted content. Copyright permission letters are presented in the order that the copyrighted material appears in the text. For Fig. 8.3, which contains in part content derived from Knorr *et al.* [108], the original article is published under an Open Access licence which does not require permission for reuse in part.

JOHN WILEY AND SONS LICENSE TERMS AND CONDITIONS

Sep 18, 2018

This Agreement between Mr. Alexander Paterson ("You") and John Wiley and Sons ("John Wiley and Sons") consists of your license details and the terms and conditions provided by John Wiley and Sons and Copyright Clearance Center.

License Number	4432040516577
License date	Sep 18, 2018
Licensed Content Publisher	John Wiley and Sons
Licensed Content Publication	International Journal of Applied Glass Science
Licensed Content Title	My Borate Life: An Enigmatic Journey
Licensed Content Author	Adrian C. Wright
Licensed Content Date	Mar 3, 2015
Licensed Content Volume	6
Licensed Content Issue	1
Licensed Content Pages	19
Type of use	Dissertation/Thesis
Requestor type	University/Academic
Format	Print and electronic
Portion	Figure/table
Number of figures/tables	1
Original Wiley figure/table number(s)	Figure 2
Will you be translating?	No
Title of your thesis / dissertation	Experimental and Theoretical Investigation of Glass Ceramics: The Transparent Ferroelectric Nanocomposite LaBGeO5
Expected completion date	Dec 2018
Expected size (number of pages)	400
Requestor Location	Mr. Alexander Paterson [redacted] Halifax, NS [redacted] Canada Attn: Mr. Alexander Paterson
Publisher Tax ID	EU826007151
Total	0.00 CAD
Terms and Conditions	

TERMS AND CONDITIONS

This copyrighted material is owned by or exclusively licensed to John Wiley & Sons, Inc. or one of its group companies (each a"Wiley Company") or handled on behalf of a society with which a Wiley Company has exclusive publishing rights in relation to a particular work

(collectively "WILEY"). By clicking "accept" in connection with completing this licensing transaction, you agree that the following terms and conditions apply to this transaction (along with the billing and payment terms and conditions established by the Copyright Clearance Center Inc., ("CCC's Billing and Payment terms and conditions"), at the time that you opened your RightsLink account (these are available at any time at http://myaccount.copyright.com).

Terms and Conditions

- The materials you have requested permission to reproduce or reuse (the "Wiley Materials") are protected by copyright.

- You are hereby granted a personal, non-exclusive, non-sub licensable (on a stand-alone basis), non-transferable, worldwide, limited license to reproduce the Wiley Materials for the purpose specified in the licensing process. This license, **and any CONTENT (PDF or image file) purchased as part of your order,** is for a one-time use only and limited to any maximum distribution number specified in the license. The first instance of republication or reuse granted by this license must be completed within two years of the date of the grant of this license (although copies prepared before the end date may be distributed thereafter). The Wiley Materials shall not be used in any other manner or for any other purpose, beyond what is granted in the license. Permission is granted subject to an appropriate acknowledgement given to the author, title of the material/book/journal and the publisher. You shall also duplicate the copyright notice that appears in the Wiley publication in your use of the Wiley Material. Permission is also granted on the understanding that nowhere in the text is a previously published source acknowledged for all or part of this Wiley Material. Any third party content is expressly excluded from this permission.

- With respect to the Wiley Materials, all rights are reserved. Except as expressly granted by the terms of the license, no part of the Wiley Materials may be copied, modified, adapted (except for minor reformatting required by the new Publication), translated, reproduced, transferred or distributed, in any form or by any means, and no derivative works may be made based on the Wiley Materials without the prior permission of the respective copyright owner.**For STM Signatory Publishers clearing permission under the terms of the STM Permissions Guidelines only, the terms of the license are extended to include subsequent editions and for editions in other languages, provided such editions are for the work as a whole in situ and does not involve the separate exploitation of the permitted figures or extracts,** You may not alter, remove or suppress in any manner any copyright, trademark or other notices displayed by the Wiley Materials. You may not license, rent, sell, loan, lease, pledge, offer as security, transfer or assign the Wiley Materials on a stand-alone basis, or any of the rights granted to you hereunder to any other person.

- The Wiley Materials and all of the intellectual property rights therein shall at all times remain the exclusive property of John Wiley & Sons Inc, the Wiley Companies, or their respective licensors, and your interest therein is only that of having possession of and the right to reproduce the Wiley Materials pursuant to Section 2 herein during the continuance of this Agreement. You agree that you own no right, title or interest in or to the Wiley Materials or any of the intellectual property rights therein. You shall have no rights hereunder other than the license as provided for above in Section 2. No right, license or interest to any trademark, trade name, service mark or other branding ("Marks") of WILEY or its licensors is granted hereunder, and you agree that you shall not assert any such right, license or interest with respect thereto

- NEITHER WILEY NOR ITS LICENSORS MAKES ANY WARRANTY OR REPRESENTATION OF ANY KIND TO YOU OR ANY THIRD PARTY, EXPRESS, IMPLIED OR STATUTORY, WITH RESPECT TO THE MATERIALS OR THE ACCURACY OF ANY INFORMATION CONTAINED IN THE MATERIALS, INCLUDING, WITHOUT LIMITATION, ANY IMPLIED WARRANTY OF MERCHANTABILITY, ACCURACY, SATISFACTORY QUALITY, FITNESS FOR A PARTICULAR PURPOSE, USABILITY, INTEGRATION OR NON-INFRINGEMENT AND ALL SUCH WARRANTIES ARE HEREBY EXCLUDED BY WILEY AND ITS LICENSORS AND WAIVED BY YOU.

- WILEY shall have the right to terminate this Agreement immediately upon breach of this Agreement by you.

- You shall indemnify, defend and hold harmless WILEY, its Licensors and their respective directors, officers, agents and employees, from and against any actual or threatened claims, demands, causes of action or proceedings arising from any breach of this Agreement by you.

- IN NO EVENT SHALL WILEY OR ITS LICENSORS BE LIABLE TO YOU OR ANY OTHER PARTY OR ANY OTHER PERSON OR ENTITY FOR ANY SPECIAL, CONSEQUENTIAL, INCIDENTAL, INDIRECT, EXEMPLARY OR PUNITIVE DAMAGES, HOWEVER CAUSED, ARISING OUT OF OR IN CONNECTION WITH THE DOWNLOADING, PROVISIONING, VIEWING OR USE OF THE MATERIALS REGARDLESS OF THE FORM OF ACTION, WHETHER FOR BREACH OF CONTRACT, BREACH OF WARRANTY, TORT, NEGLIGENCE, INFRINGEMENT OR OTHERWISE (INCLUDING, WITHOUT LIMITATION, DAMAGES BASED ON LOSS OF PROFITS, DATA, FILES, USE, BUSINESS OPPORTUNITY OR CLAIMS OF THIRD PARTIES), AND WHETHER OR NOT THE PARTY HAS BEEN ADVISED OF THE POSSIBILITY OF SUCH DAMAGES. THIS LIMITATION SHALL APPLY NOTWITHSTANDING ANY FAILURE OF ESSENTIAL PURPOSE OF ANY LIMITED REMEDY PROVIDED HEREIN.

- Should any provision of this Agreement be held by a court of competent jurisdiction to be illegal, invalid, or unenforceable, that provision shall be deemed amended to achieve as nearly as possible the same economic effect as the original provision, and the legality, validity and enforceability of the remaining provisions of this Agreement shall not be affected or impaired thereby.

- The failure of either party to enforce any term or condition of this Agreement shall not constitute a waiver of either party's right to enforce each and every term and condition of this Agreement. No breach under this agreement shall be deemed waived or excused by either party unless such waiver or consent is in writing signed by the party granting such waiver or consent. The waiver by or consent of a party to a breach of any provision of this Agreement shall not operate or be construed as a waiver of or consent to any other or subsequent breach by such other party.

- This Agreement may not be assigned (including by operation of law or otherwise) by you without WILEY's prior written consent.

- Any fee required for this permission shall be non-refundable after thirty (30) days from receipt by the CCC.

- These terms and conditions together with CCC's Billing and Payment terms and conditions (which are incorporated herein) form the entire agreement between you and WILEY concerning this licensing transaction and (in the absence of fraud) supersedes all prior agreements and representations of the parties, oral or written. This Agreement may not be amended except in writing signed by both parties. This Agreement shall be binding upon and inure to the benefit of the parties' successors, legal representatives, and authorized assigns.

- In the event of any conflict between your obligations established by these terms and conditions and those established by CCC's Billing and Payment terms and conditions, these terms and conditions shall prevail.

- WILEY expressly reserves all rights not specifically granted in the combination of (i) the license details provided by you and accepted in the course of this licensing transaction, (ii) these terms and conditions and (iii) CCC's Billing and Payment terms and conditions.

- This Agreement will be void if the Type of Use, Format, Circulation, or Requestor Type was misrepresented during the licensing process.

- This Agreement shall be governed by and construed in accordance with the laws of the State of New York, USA, without regards to such state's conflict of law rules. Any legal action, suit or proceeding arising out of or relating to these Terms and Conditions or the breach thereof shall be instituted in a court of competent jurisdiction in New York County in the State of New York in the United States of America and each party hereby consents and submits to the personal jurisdiction of such court, waives any objection to venue in such court and consents to service of process by registered or certified mail, return receipt requested, at the last known address of such party.

WILEY OPEN ACCESS TERMS AND CONDITIONS

Wiley Publishes Open Access Articles in fully Open Access Journals and in Subscription journals offering Online Open. Although most of the fully Open Access journals publish open access articles under the terms of the Creative Commons Attribution (CC BY) License only, the subscription journals and a few of the Open Access Journals offer a choice of Creative Commons Licenses. The license type is clearly identified on the article.

The Creative Commons Attribution License

The Creative Commons Attribution License (CC-BY) allows users to copy, distribute and transmit an article, adapt the article and make commercial use of the article. The CC-BY license permits commercial and non-

Creative Commons Attribution Non-Commercial License

The Creative Commons Attribution Non-Commercial (CC-BY-NC)License permits use, distribution and reproduction in any medium, provided the original work is properly cited and is not used for commercial purposes.(see below)

Creative Commons Attribution-Non-Commercial-NoDerivs License

The Creative Commons Attribution Non-Commercial-NoDerivs License (CC-BY-NC-ND) permits use, distribution and reproduction in any medium, provided the original work is properly cited, is not used for commercial purposes and no modifications or adaptations are made. (see below)

Use by commercial "for-profit" organizations

Use of Wiley Open Access articles for commercial, promotional, or marketing purposes requires further explicit permission from Wiley and will be subject to a fee.

Further details can be found on Wiley Online Library
http://olabout.wiley.com/WileyCDA/Section/id-410895.html

Other Terms and Conditions:

v1.10 Last updated September 2015

Questions? customercare@copyright.com or +1-855-239-3415 (toll free in the US) or +1-978-646-2777.

ELSEVIER LICENSE
TERMS AND CONDITIONS

Oct 15, 2018

This Agreement between Mr. Alexander Paterson ("You") and Elsevier ("Elsevier") consists of your license details and the terms and conditions provided by Elsevier and Copyright Clearance Center.

License Number	4450270346809
License date	Oct 15, 2018
Licensed Content Publisher	Elsevier
Licensed Content Publication	Journal of Non-Crystalline Solids
Licensed Content Title	Crystallization of glass-forming liquids: Maxima of nucleation, growth, and overall crystallization rates
Licensed Content Author	Jürn W.P. Schmelzer,Alexander S. Abyzov,Vladimir M. Fokin,Christoph Schick,Edgar D. Zanotto
Licensed Content Date	Dec 1, 2015
Licensed Content Volume	429
Licensed Content Issue	n/a
Licensed Content Pages	9
Start Page	24
End Page	32
Type of Use	reuse in a thesis/dissertation
Portion	figures/tables/illustrations
Number of figures/tables/illustrations	1
Format	both print and electronic
Are you the author of this Elsevier article?	No
Will you be translating?	No
Original figure numbers	Figure 4
Title of your thesis/dissertation	Experimental and Theoretical Investigation of Glass Ceramics: The Transparent Ferroelectric Nanocomposite LaBGeO5
Expected completion date	Dec 2018
Estimated size (number of pages)	400
Requestor Location	Mr. Alexander Paterson [redacted] Halifax, NS [redacted] Canada Attn: Mr. Alexander Paterson
Publisher Tax ID	GB 494 6272 12
Total	0.00 CAD
Terms and Conditions	

INTRODUCTION

1. The publisher for this copyrighted material is Elsevier. By clicking "accept" in connection with completing this licensing transaction, you agree that the following terms and conditions apply to this transaction (along with the Billing and Payment terms and conditions established by Copyright Clearance Center, Inc. ("CCC"), at the time that you opened your Rightslink account and that are available at any time at http://myaccount.copyright.com).

GENERAL TERMS

2. Elsevier hereby grants you permission to reproduce the aforementioned material subject to the terms and conditions indicated.

3. Acknowledgement: If any part of the material to be used (for example, figures) has appeared in our publication with credit or acknowledgement to another source, permission must also be sought from that source. If such permission is not obtained then that material may not be included in your publication/copies. Suitable acknowledgement to the source must be made, either as a footnote or in a reference list at the end of your publication, as follows:

"Reprinted from Publication title, Vol /edition number, Author(s), Title of article / title of chapter, Pages No., Copyright (Year), with permission from Elsevier [OR APPLICABLE SOCIETY COPYRIGHT OWNER]." Also Lancet special credit - "Reprinted from The Lancet, Vol. number, Author(s), Title of article, Pages No., Copyright (Year), with permission from Elsevier."

4. Reproduction of this material is confined to the purpose and/or media for which permission is hereby given.

5. Altering/Modifying Material: Not Permitted. However figures and illustrations may be altered/adapted minimally to serve your work. Any other abbreviations, additions, deletions and/or any other alterations shall be made only with prior written authorization of Elsevier Ltd. (Please contact Elsevier at permissions@elsevier.com). No modifications can be made to any Lancet figures/tables and they must be reproduced in full.

6. If the permission fee for the requested use of our material is waived in this instance, please be advised that your future requests for Elsevier materials may attract a fee.

7. Reservation of Rights: Publisher reserves all rights not specifically granted in the combination of (i) the license details provided by you and accepted in the course of this licensing transaction, (ii) these terms and conditions and (iii) CCC's Billing and Payment terms and conditions.

8. License Contingent Upon Payment: While you may exercise the rights licensed immediately upon issuance of the license at the end of the licensing process for the transaction, provided that you have disclosed complete and accurate details of your proposed use, no license is finally effective unless and until full payment is received from you (either by publisher or by CCC) as provided in CCC's Billing and Payment terms and conditions. If full payment is not received on a timely basis, then any license preliminarily granted shall be deemed automatically revoked and shall be void as if never granted. Further, in the event that you breach any of these terms and conditions or any of CCC's Billing and Payment terms and conditions, the license is automatically revoked and shall be void as if never granted. Use of materials as described in a revoked license, as well as any use of the materials beyond the scope of an unrevoked license, may constitute copyright infringement and publisher reserves the right to take any and all action to protect its copyright in the materials.

9. Warranties: Publisher makes no representations or warranties with respect to the licensed material.

10. Indemnity: You hereby indemnify and agree to hold harmless publisher and CCC, and their respective officers, directors, employees and agents, from and against any and all claims arising out of your use of the licensed material other than as specifically authorized pursuant to this license.

11. No Transfer of License: This license is personal to you and may not be sublicensed, assigned, or transferred by you to any other person without publisher's written permission.

12. No Amendment Except in Writing: This license may not be amended except in a writing signed by both parties (or, in the case of publisher, by CCC on publisher's behalf).
13. Objection to Contrary Terms: Publisher hereby objects to any terms contained in any purchase order, acknowledgment, check endorsement or other writing prepared by you, which terms are inconsistent with these terms and conditions or CCC's Billing and Payment terms and conditions. These terms and conditions, together with CCC's Billing and Payment terms and conditions (which are incorporated herein), comprise the entire agreement between you and publisher (and CCC) concerning this licensing transaction. In the event of any conflict between your obligations established by these terms and conditions and those established by CCC's Billing and Payment terms and conditions, these terms and conditions shall control.
14. Revocation: Elsevier or Copyright Clearance Center may deny the permissions described in this License at their sole discretion, for any reason or no reason, with a full refund payable to you. Notice of such denial will be made using the contact information provided by you. Failure to receive such notice will not alter or invalidate the denial. In no event will Elsevier or Copyright Clearance Center be responsible or liable for any costs, expenses or damage incurred by you as a result of a denial of your permission request, other than a refund of the amount(s) paid by you to Elsevier and/or Copyright Clearance Center for denied permissions.

LIMITED LICENSE

The following terms and conditions apply only to specific license types:
15. **Translation**: This permission is granted for non-exclusive world **English** rights only unless your license was granted for translation rights. If you licensed translation rights you may only translate this content into the languages you requested. A professional translator must perform all translations and reproduce the content word for word preserving the integrity of the article.
16. **Posting licensed content on any Website**: The following terms and conditions apply as follows: Licensing material from an Elsevier journal: All content posted to the web site must maintain the copyright information line on the bottom of each image; A hyper-text must be included to the Homepage of the journal from which you are licensing at http://www.sciencedirect.com/science/journal/xxxxx or the Elsevier homepage for books at http://www.elsevier.com; Central Storage: This license does not include permission for a scanned version of the material to be stored in a central repository such as that provided by Heron/XanEdu.
Licensing material from an Elsevier book: A hyper-text link must be included to the Elsevier homepage at http://www.elsevier.com . All content posted to the web site must maintain the copyright information line on the bottom of each image.

Posting licensed content on Electronic reserve: In addition to the above the following clauses are applicable: The web site must be password-protected and made available only to bona fide students registered on a relevant course. This permission is granted for 1 year only. You may obtain a new license for future website posting.
17. **For journal authors:** the following clauses are applicable in addition to the above:
Preprints:
A preprint is an author's own write-up of research results and analysis, it has not been peer-reviewed, nor has it had any other value added to it by a publisher (such as formatting, copyright, technical enhancement etc.).
Authors can share their preprints anywhere at any time. Preprints should not be added to or enhanced in any way in order to appear more like, or to substitute for, the final versions of articles however authors can update their preprints on arXiv or RePEc with their Accepted Author Manuscript (see below).
If accepted for publication, we encourage authors to link from the preprint to their formal publication via its DOI. Millions of researchers have access to the formal publications on ScienceDirect, and so links will help users to find, access, cite and use the best available

version. Please note that Cell Press, The Lancet and some society-owned have different preprint policies. Information on these policies is available on the journal homepage.
Accepted Author Manuscripts: An accepted author manuscript is the manuscript of an article that has been accepted for publication and which typically includes author-incorporated changes suggested during submission, peer review and editor-author communications.
Authors can share their accepted author manuscript:

- immediately
  - via their non-commercial person homepage or blog
  - by updating a preprint in arXiv or RePEc with the accepted manuscript
  - via their research institute or institutional repository for internal institutional uses or as part of an invitation-only research collaboration work-group
  - directly by providing copies to their students or to research collaborators for their personal use
  - for private scholarly sharing as part of an invitation-only work group on commercial sites with which Elsevier has an agreement
- After the embargo period
  - via non-commercial hosting platforms such as their institutional repository
  - via commercial sites with which Elsevier has an agreement

In all cases accepted manuscripts should:

- link to the formal publication via its DOI
- bear a CC-BY-NC-ND license - this is easy to do
- if aggregated with other manuscripts, for example in a repository or other site, be shared in alignment with our hosting policy not be added to or enhanced in any way to appear more like, or to substitute for, the published journal article.

Published journal article (JPA): A published journal article (PJA) is the definitive final record of published research that appears or will appear in the journal and embodies all value-adding publishing activities including peer review co-ordination, copy-editing, formatting, (if relevant) pagination and online enrichment.
Policies for sharing publishing journal articles differ for subscription and gold open access articles:
Subscription Articles: If you are an author, please share a link to your article rather than the full-text. Millions of researchers have access to the formal publications on ScienceDirect, and so links will help your users to find, access, cite, and use the best available version.
Theses and dissertations which contain embedded PJAs as part of the formal submission can be posted publicly by the awarding institution with DOI links back to the formal publications on ScienceDirect.
If you are affiliated with a library that subscribes to ScienceDirect you have additional private sharing rights for others' research accessed under that agreement. This includes use for classroom teaching and internal training at the institution (including use in course packs and courseware programs), and inclusion of the article for grant funding purposes.
Gold Open Access Articles: May be shared according to the author-selected end-user license and should contain a CrossMark logo, the end user license, and a DOI link to the formal publication on ScienceDirect.
Please refer to Elsevier's posting policy for further information.
18. **For book authors** the following clauses are applicable in addition to the above:
Authors are permitted to place a brief summary of their work online only. You are not allowed to download and post the published electronic version of your chapter, nor may you scan the printed edition to create an electronic version. **Posting to a repository:** Authors are permitted to post a summary of their chapter only in their institution's repository.

19. **Thesis/Dissertation**: If your license is for use in a thesis/dissertation your thesis may be submitted to your institution in either print or electronic form. Should your thesis be published commercially, please reapply for permission. These requirements include permission for the Library and Archives of Canada to supply single copies, on demand, of the complete thesis and include permission for Proquest/UMI to supply single copies, on demand, of the complete thesis. Should your thesis be published commercially, please reapply for permission. Theses and dissertations which contain embedded PJAs as part of the formal submission can be posted publicly by the awarding institution with DOI links back to the formal publications on ScienceDirect.

Elsevier Open Access Terms and Conditions

You can publish open access with Elsevier in hundreds of open access journals or in nearly 2000 established subscription journals that support open access publishing. Permitted third party re-use of these open access articles is defined by the author's choice of Creative Commons user license. See our open access license policy for more information.

Terms & Conditions applicable to all Open Access articles published with Elsevier:

Any reuse of the article must not represent the author as endorsing the adaptation of the article nor should the article be modified in such a way as to damage the author's honour or reputation. If any changes have been made, such changes must be clearly indicated.

The author(s) must be appropriately credited and we ask that you include the end user license and a DOI link to the formal publication on ScienceDirect.

If any part of the material to be used (for example, figures) has appeared in our publication with credit or acknowledgement to another source it is the responsibility of the user to ensure their reuse complies with the terms and conditions determined by the rights holder.

Additional Terms & Conditions applicable to each Creative Commons user license:

CC BY: The CC-BY license allows users to copy, to create extracts, abstracts and new works from the Article, to alter and revise the Article and to make commercial use of the Article (including reuse and/or resale of the Article by commercial entities), provided the user gives appropriate credit (with a link to the formal publication through the relevant DOI), provides a link to the license, indicates if changes were made and the licensor is not represented as endorsing the use made of the work. The full details of the license are available at http://creativecommons.org/licenses/by/4.0.

CC BY NC SA: The CC BY-NC-SA license allows users to copy, to create extracts, abstracts and new works from the Article, to alter and revise the Article, provided this is not done for commercial purposes, and that the user gives appropriate credit (with a link to the formal publication through the relevant DOI), provides a link to the license, indicates if changes were made and the licensor is not represented as endorsing the use made of the work. Further, any new works must be made available on the same conditions. The full details of the license are available at http://creativecommons.org/licenses/by-nc-sa/4.0.

CC BY NC ND: The CC BY-NC-ND license allows users to copy and distribute the Article, provided this is not done for commercial purposes and further does not permit distribution of the Article if it is changed or edited in any way, and provided the user gives appropriate credit (with a link to the formal publication through the relevant DOI), provides a link to the license, and that the licensor is not represented as endorsing the use made of the work. The full details of the license are available at http://creativecommons.org/licenses/by-nc-nd/4.0.

Any commercial reuse of Open Access articles published with a CC BY NC SA or CC BY NC ND license requires permission from Elsevier and will be subject to a fee.

Commercial reuse includes:

- Associating advertising with the full text of the Article
- Charging fees for document delivery or access
- Article aggregation
- Systematic distribution via e-mail lists or share buttons

Posting or linking by commercial companies for use by customers of those companies.

20. **Other Conditions**:

v1.9

Gmail Alex Paterson <[redacted]>

GEM Image

Alex Hannon - UKRI STFC <[redacted]> Mon, Aug 13, 2018 at 10:28 AM
To: Alex Paterson <[redacted]>

Dear Alex

Of course you have permission.

I hereby grant you permission to use the figure in any written work or presentation of which you are an author.

Does the attached version work for you?

Let me put in an advance order for a copy of your dissertation.

Cheers,

Alex.

From: Alex Paterson [mailto:[redacted]]
Sent: 13 August 2018 12:34
To: Hannon, Alex (STFC,RAL,ISIS)
Subject: GEM Image

[Quoted text hidden]

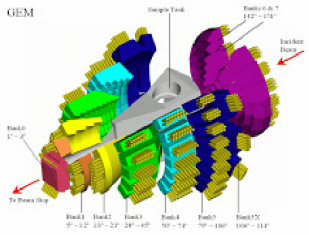

gemdetbcol2_ach3.jpg
450K

Title: Relating 139La Quadrupolar Coupling Constants to Polyhedral Distortion in Crystalline Structures

Author: Alexander L. Paterson, Margaret A. Hanson, Ulrike Werner-Zwanziger, et al

Publication: The Journal of Physical Chemistry C

Publisher: American Chemical Society

Date: Nov 1, 2015

PERMISSION/LICENSE IS GRANTED FOR YOUR ORDER AT NO CHARGE

This type of permission/license, instead of the standard Terms & Conditions, is sent to you because no fee is being charged for your order. Please note the following:

- Permission is granted for your request in both print and electronic formats, and translations.
- If figures and/or tables were requested, they may be adapted or used in part.
- Please print this page for your records and send a copy of it to your publisher/graduate school.
- Appropriate credit for the requested material should be given as follows: "Reprinted (adapted) with permission from (COMPLETE REFERENCE CITATION). Copyright (YEAR) American Chemical Society." Insert appropriate information in place of the capitalized words.
- One-time permission is granted only for the use specified in your request. No additional uses are granted (such as derivative works or other editions). For any other uses, please submit a new request.

Title: Structural Differences between the Glass and Crystal Forms of the Transparent Ferroelectric Nanocomposite, LaBGeO5, from Neutron Diffraction and NMR Spectroscopy

Author: Alexander L. Paterson, Alex C. Hannon, Ulrike Werner-Zwanziger, et al

Publication: The Journal of Physical Chemistry C

Publisher: American Chemical Society

Date: Sep 1, 2018

PERMISSION/LICENSE IS GRANTED FOR YOUR ORDER AT NO CHARGE

This type of permission/license, instead of the standard Terms & Conditions, is sent to you because no fee is being charged for your order. Please note the following:

- Permission is granted for your request in both print and electronic formats, and translations.
- If figures and/or tables were requested, they may be adapted or used in part.
- Please print this page for your records and send a copy of it to your publisher/graduate school.
- Appropriate credit for the requested material should be given as follows: "Reprinted (adapted) with permission from (COMPLETE REFERENCE CITATION). Copyright (YEAR) American Chemical Society." Insert appropriate information in place of the capitalized words.
- One-time permission is granted only for the use specified in your request. No additional uses are granted (such as derivative works or other editions). For any other uses, please submit a new request.

BACK CLOSE WINDOW

AIP PUBLISHING LICENSE
TERMS AND CONDITIONS

Sep 18, 2018

This Agreement between Mr. Alexander Paterson ("You") and AIP Publishing ("AIP Publishing") consists of your license details and the terms and conditions provided by AIP Publishing and Copyright Clearance Center.

License Number	4432040012604
License date	Sep 18, 2018
Licensed Content Publisher	AIP Publishing
Licensed Content Publication	Journal of Applied Physics
Licensed Content Title	Anisotropic stress in laser-written LaBGeO5 glass-ceramic composites
Licensed Content Author	Alexander L. Paterson, Josef W. Zwanziger
Licensed Content Date	Aug 28, 2018
Licensed Content Volume	124
Licensed Content Issue	8
Type of Use	Thesis/Dissertation
Requestor type	Author (original article)
Format	Print and electronic
Portion	Excerpt (> 800 words)
Will you be translating?	No
Title of your thesis / dissertation	Experimental and Theoretical Investigation of Glass Ceramics: The Transparent Ferroelectric Nanocomposite LaBGeO5
Expected completion date	Dec 2018
Estimated size (number of pages)	400
Requestor Location	Mr. Alexander Paterson [redacted] Halifax, NS [redacted] Canada Attn: Mr. Alexander Paterson
Billing Type	Invoice
Billing Address	Mr. Alexander Paterson [redacted] Halifax, NS [redacted] Canada Attn: Mr. Alexander Paterson
Total	0.00 CAD

Terms and Conditions

AIP Publishing -- Terms and Conditions: Permissions Uses

AIP Publishing hereby grants to you the non-exclusive right and license to use and/or distribute

the Material according to the use specified in your order, on a one-time basis, for the specified term, with a maximum distribution equal to the number that you have ordered. Any links or other content accompanying the Material are not the subject of this license.

1. You agree to include the following copyright and permission notice with the reproduction of the Material:"Reprinted from [FULL CITATION], with the permission of AIP Publishing." For an article, the credit line and permission notice must be printed on the first page of the article or book chapter. For photographs, covers, or tables, the notice may appear with the Material, in a footnote, or in the reference list.
2. If you have licensed reuse of a figure, photograph, cover, or table, it is your responsibility to ensure that the material is original to AIP Publishing and does not contain the copyright of another entity, and that the copyright notice of the figure, photograph, cover, or table does not indicate that it was reprinted by AIP Publishing, with permission, from another source. Under no circumstances does AIP Publishing purport or intend to grant permission to reuse material to which it does not hold appropriate rights.
   You may not alter or modify the Material in any manner. You may translate the Material into another language only if you have licensed translation rights. You may not use the Material for promotional purposes.
3. The foregoing license shall not take effect unless and until AIP Publishing or its agent, Copyright Clearance Center, receives the Payment in accordance with Copyright Clearance Center Billing and Payment Terms and Conditions, which are incorporated herein by reference.
4. AIP Publishing or Copyright Clearance Center may, within two business days of granting this license, revoke the license for any reason whatsoever, with a full refund payable to you. Should you violate the terms of this license at any time, AIP Publishing, or Copyright Clearance Center may revoke the license with no refund to you. Notice of such revocation will be made using the contact information provided by you. Failure to receive such notice will not nullify the revocation.
5. AIP Publishing makes no representations or warranties with respect to the Material. You agree to indemnify and hold harmless AIP Publishing, and their officers, directors, employees or agents from and against any and all claims arising out of your use of the Material other than as specifically authorized herein.
6. The permission granted herein is personal to you and is not transferable or assignable without the prior written permission of AIP Publishing. This license may not be amended except in a writing signed by the party to be charged.
7. If purchase orders, acknowledgments or check endorsements are issued on any forms containing terms and conditions which are inconsistent with these provisions, such inconsistent terms and conditions shall be of no force and effect. This document, including the CCC Billing and Payment Terms and Conditions, shall be the entire agreement between the parties relating to the subject matter hereof.

This Agreement shall be governed by and construed in accordance with the laws of the State of New York. Both parties hereby submit to the jurisdiction of the courts of New York County for purposes of resolving any disputes that may arise hereunder.

V1.2

Questions? customercare@copyright.com or +1-855-239-3415 (toll free in the US) or +1-978-646-2777.

Bibliography

[1] H. Jain, Transparent ferroelectric glass-ceramics, Ferroelectrics 306 (1) (2004) 111–127. doi:10.1080/00150190490458446.

[2] A. Stone, M. Sakakura, Y. Shimotsuma, G. Stone, P. Gupta, K. Miura, K. Hirao, V. Dierolf, H. Jain, Directionally controlled 3D ferroelectric single crystal growth in $LaBGeO_5$ glass by femtosecond laser irradiation, Opt. Express 17 (25) (2009) 23284–23289. doi:10.1364/oe.17.023284.

[3] A. K. Varshneya, Fundamentals of Inorganic Glasses, Academic Press, New York, 1994.

[4] J. E. Shelby, Introduction to Glass Science and Technology, Royal Society of Chemistry, 2007.

[5] P. M. Anderson, A. E. Lord, Viscosity of metglas 2826 near the glass transition using rapid heating, J. Non-Cryst. Solids 37 (2) (1980) 219–229. doi:10.1016/0022-3093(80)90153-2.

[6] D. G. Legrand, Crazing, yielding, and fracture of polymers. I. Ductile brittle transition in polycarbonate, J. Appl. Polym. Sci. 13 (10) (1969) 2129–2147. doi:10.1002/app.1969.070131010.

[7] W. H. Zachariasen, The atomic arrangement in glass, J. Am. Chem. Soc. 54 (10) (1932) 3841–3851. doi:10.1021/ja01349a006.

[8] V. Martin, U. Werner-Zwanziger, J. W. Zwanziger, R. A. Dunlap, Correlation of structure and photoelastic response in tin phosphate glass, Int. J. Appl. Glass Sci. 2 (4) (2011) 282–289. doi:10.1111/j.2041-1294.2011.00049.x.

[9] S. Sen, H. Maekawa, G. N. Papatheodorou, Short-range structure of invert glasses along the pseudo-binary join $MgSiO_3$–Mg_2SiO_4: Results from ^{29}Si and ^{25}Mg MAS NMR spectroscopy, J. Phys. Chem. B 113 (46) (2009) 15243–15248. doi:10.1021/jp9079603.

[10] U. Hoppe, E. Metwalli, R. K. Brow, J. Neuefeind, High-energy X-ray diffraction study of La co-ordination in lanthanum phosphate glasses, J. Non-Cryst. Solids 297 (2-3) (2002) 263–274. doi:10.1016/s0022-3093(01)00936-x.

[11] D. A. McKeown, G. A. Waychunas, G. E. Brown, EXAFS and XANES study of the local coordination environment of sodium in a series of silica-rich glasses and selected minerals within the Na_2O–Al_2O_3–SiO_2 system, J. Non-Cryst. Solids 74 (2-3) (1985) 325–348. doi:10.1016/0022-3093(85)90078-x.

[12] O. L. G. Alderman, A. C. Hannon, S. Feller, R. Beanland, D. Holland, The germanate anomaly in alkaline earth germanate glasses, J. Phys. Chem. C 121 (17) (2017) 9462–9479. doi:10.1021/acs.jpcc.6b12372.

[13] X. Xue, J. F. Stebbins, ^{23}Na NMR chemical shifts and local Na coordination environments in silicate crystals, melts and glasses, Phys. Chem. Miner. 20 (5). doi:10.1007/bf00215100.

[14] J. F. Stebbins, S. Kroeker, S. K. Lee, T. J. Kiczenski, Quantification of five- and six-coordinated aluminum ions in aluminosilicate and fluoride-containing glasses by high-field, high-resolution ^{27}Al NMR, J. Non-Cryst. Solids 275 (1-2) (2000) 1–6. doi:10.1016/s0022-3093(00)00270-2.

[15] E. C. Power, A. L. Paterson, U. Werner-Zwanziger, L. D. Ellis, J. W. Zwanziger, Zero stress-optic bismuth oxide-based glass, J. Non-Cryst. Solids 479 (2018) 82–89. doi:10.1016/j.jnoncrysol.2017.10.023.

[16] X. Xue, M. Kanzaki, R. G. Tronnes, J. F. Stebbins, Silicon coordination and speciation changes in a silicate liquid at high pressures, Science 245 (4921) (1989) 962–964. doi:10.1126/science.245.4921.962.

[17] D. R. Uhlmann, R. R. Shaw, The thermal expansion of alkali borate glasses and the boric oxide anomaly, J. Non-Cryst. Solids 1 (5) (1969) 347–359. doi:10.1016/0022-3093(69)90018-0.

[18] A. C. Wright, G. Dalba, F. Rocca, N. M. Vedishcheva, Borate versus silicate glasses: Why are they so different?, Phys. Chem. Glasses: Eur. J. Glass Sci. Technol., Part B 51 (5) (2010) 233–265.

[19] G. S. Henderson, The germanate anomaly: What do we know?, J. Non-Cryst. Solids 353 (18-21) (2007) 1695–1704. doi:10.1016/j.jnoncrysol.2007.02.037.

[20] A. C. Wright, My borate life: An enigmatic journey, Int. J. Appl. Glass Sci. 6 (1) (2015) 45–63. doi:10.1111/ijag.12113.

[21] R. E. Youngman, J. W. Zwanziger, Multiple boron sites in borate glass detected with dynamic angle spinning nuclear magnetic resonance, J. Non-Cryst. Solids 168 (3) (1994) 293–297. doi:10.1016/0022-3093(94)90342-5.

[22] A. C. Wright, N. M. Vedishcheva, B. A. Shakhmatkin, A crystallographic guide to the structure of borate glasses, Mater. Res. Soc. Symp. Proc. 455 (1996) 381. doi:10.1557/proc-455-381.

[23] A. O. Ivanov, K. S. Evstrop'ev, On the structure of simple germanate glass, in: Doklady Akademii Nauk, Vol. 145, Russian Academy of Sciences, 1962, pp. 797–800.

[24] M. K. Murthy, J. Ip, Some physical properties of alkali germanate glasses, Nature 201 (4916) (1964) 285–286. doi:10.1038/201285a0.

[25] V. K. Michaelis, S. Kroeker, ^{73}Ge solid-state NMR of germanium oxide materials: Experimental and theoretical studies, J. Phys. Chem. C 114 (49) (2010) 21736–21744. doi:10.1021/jp1071082.

[26] A. C. Hannon, D. D. Martino, L. F. Santos, R. M. Almeida, A model for the Ge−O coordination in germanate glasses, J. Non-Cryst. Solids 353 (18-21) (2007) 1688–1694. doi:10.1016/j.jnoncrysol.2007.02.046.

[27] O. L. G. Alderman, A. C. Hannon, D. Holland, N. Umesaki, On the germanium–oxygen coordination number in lead germanate glasses, J. Non-Cryst. Solids 386 (2014) 56–60. doi:10.1016/j.jnoncrysol.2013.11.032.

[28] U. Hoppe, R. Kranold, H.-J. Weber, A. C. Hannon, The change of the Ge−O coordination number in potassium germanate glasses probed by neutron diffraction with high real-space resolution, J. Non-Cryst. Solids 248 (1) (1999) 1–10. doi:10.1016/s0022-3093(99)00104-0.

[29] J. W. P. Schmelzer, A. S. Abyzov, V. M. Fokin, C. Schick, E. D. Zanotto, Crystallization of glass-forming liquids: Maxima of nucleation, growth, and overall crystallization rates, J. Non-Cryst. Solids 429 (2015) 24–32. doi:10.1016/j.jnoncrysol.2015.08.023.

[30] P. F. James, Volume nucleation in silicate glasses, in: Glasses and Glass-Ceramics, Springer Netherlands, 1989, pp. 59–105. doi:10.1007/978-94-009-0817-8_3.

[31] E. D. Zanotto, Isothermal and adiabatic nucleation in glass, J. Non-Cryst. Solids 89 (3) (1987) 361–370. doi:10.1016/s0022-3093(87)80278-8.

[32] V. M. Fokin, E. D. Zanotto, J. W. P. Schmelzer, Homogeneous nucleation versus glass transition temperature of silicate glasses, J. Non-Cryst. Solids 321 (1-2) (2003) 52–65. doi:10.1016/s0022-3093(03)00089-9.

[33] Y. Takahashi, Y. Benino, V. Dimitrov, T. Komatsu, Transparent surface crystallized glasses with optical non-linear $LaBGeO_5$ crystals, J. Non-Cryst. Solids 260 (1-2) (1999) 155–159. doi:10.1016/s0022-3093(99)00573-6.

[34] P. Gupta, H. Jain, D. B. Williams, O. Kanert, R. Kuechler, Structural evolution of $LaBGeO_5$ transparent ferroelectric nano-composites, J. Non-Cryst. Solids 349 (2004) 291–298. doi:10.1016/j.jnoncrysol.2004.08.212.

[35] J. G. Longstaffe, U. Werner-Zwanziger, J. F. Schneider, M. L. F. Nascimento, E. D. Zanotto, J. W. Zwanziger, Intermediate-range order of alkali disilicate glasses and its relation to the devitrification mechanism, J. Phys. Chem. C 112 (15) (2008) 6151–6159. doi:10.1021/jp711438v.

[36] B. Chen, U. Werner-Zwanziger, M. L. F. Nascimento, L. Ghussn, E. D. Zanotto, J. W. Zwanziger, Structural similarity on multiple length scales and its relation to devitrification mechanism: A solid-state NMR study of alkali diborate glasses and crystals, J. Phys. Chem. C 113 (48) (2009) 20725–20732. doi:10.1021/jp907259e.

[37] J. W. P. Schmelzer, V. M. Fokin, A. S. Abyzov, Crystallization of glass: What we know, what we need to know, Int. J. Appl. Glass Sci. 7 (3) (2016) 253–261. doi:10.1111/ijag.12212.

[38] J. W. P. Schmelzer, V. M. Fokin, A. S. Abyzov, E. D. Zanotto, I. Gutzow, How do crystals form and grow in glass-forming liquids: Ostwald's rule of stages and beyond, Int. J. Appl. Glass Sci. 1 (1) (2010) 16–26. doi:10.1111/j.2041-1294.2010.00003.x.

[39] I. S. Gutzow, J. W. P. Schmelzer, The Vitreous State, Springer Berlin Heidelberg, 2013. doi:10.1007/978-3-642-34633-0.

[40] A. H. Silver, P. J. Bray, Nuclear magnetic resonance absorption in glass. I. Nuclear quadrupole effects in boron oxide, soda-boric oxide, and borosilicate glasses, J. Chem. Phys. 29 (5) (1958) 984–990. doi:10.1063/1.1744697.

[41] M. Bertmer, L. Züchner, J. C. C. Chan, H. Eckert, Short and medium range order in sodium aluminoborate glasses. 2. Site connectivities and cation distributions studied by rotational echo double resonance NMR spectroscopy, J. Phys. Chem. B 104 (28) (2000) 6541–6553. doi:10.1021/jp9941918.

[42] J. W. Zwanziger, J. L. Shaw, U. Werner-Zwanziger, B. G. Aitken, A neutron scattering and nuclear magnetic resonance study of the structure of GeO_2–P_2O_5 glasses, J. Phys. Chem. B 110 (41) (2006) 20123–20128. doi:10.1021/jp062432n.

[43] M. Feike, C. Jäger, H. W. Spiess, Connectivities of coordination polyhedra in phosphate glasses from double-quantum NMR spectroscopy, J. Non-Cryst. Solids 223 (3) (1998) 200–206. doi:10.1016/s0022-3093(97)00439-0.

[44] J. F. Stebbins, Effects of temperature and composition on silicate glass structure and dynamics: Si-29 NMR results, J. Non-Cryst. Solids 106 (1-3) (1988) 359–369. doi:10.1016/0022-3093(88)90289-x.

[45] B. Tischendorf, J. U. Otaigbe, J. W. Wiench, M. Pruski, B. C. Sales, A study of short and intermediate range order in zinc phosphate glasses, J. Non-Cryst. Solids 282 (2-3) (2001) 147–158. doi:10.1016/s0022-3093(01)00350-7.

[46] F. Fayon, C. Bessada, J.-P. Coutures, D. Massiot, High-resolution double-quantum ^{31}P MAS NMR study of the intermediate-range order in crystalline and glass lead phosphates, Inorg. Chem. 38 (23) (1999) 5212–5218. doi:10.1021/ic990375p.

[47] K. J. D. MacKenzie, M. E. Smith, Multinuclear Solid-State NMR of Inorganic Materials, Elsevier, 2002. doi:10.1016/s1470-1804(02)x8001-8.

[48] S. Kroeker, J. F. Stebbins, Three-coordinated boron-11 chemical shifts in borates, Inorg. Chem. 40 (24) (2001) 6239–6246. doi:10.1021/ic010305u.

[49] P. M. Aguiar, S. Kroeker, Boron speciation and non-bridging oxygens in high-alkali borate glasses, J. Non-Cryst. Solids 353 (18-21) (2007) 1834–1839. doi:10.1016/j.jnoncrysol.2007.02.013.

[50] L. van Wüllen, W. Müller-Warmuth, D. Papageorgiou, H. J. Pentinghaus, Characterization and structural developments of gel-derived borosilicate glasses: A multinuclear MAS-NMR study, J. Non-Cryst. Solids 171 (1) (1994) 53–67. doi:10.1016/0022-3093(94)90032-9.

[51] L.-S. Du, J. F. Stebbins, Solid-state NMR study of metastable immiscibility in alkali borosilicate glasses, J. Non-Cryst. Solids 315 (3) (2003) 239–255. doi:10.1016/s0022-3093(02)01604-6.

[52] B. Chen, U. Werner-Zwanziger, J. W. Zwanziger, M. L. F. Nascimento, L. Ghussn, E. D. Zanotto, Correlation of network structure with devitrification mechanism in lithium and sodium diborate glasses, J. Non-Cryst. Solids 356 (44-49) (2010) 2641–2644. doi:10.1016/j.jnoncrysol.2010.04.053.

[53] S. K. Lee, H. N. Kim, B. H. Lee, H.-I. Kim, E. J. Kim, Nature of chemical and topological disorder in borogermanate glasses: Insights from B-11 and O-17 solid-state NMR and quantum chemical calculations, J. Phys. Chem. B 114 (1) (2010) 412–420. doi:10.1021/jp9093113.

[54] R. Hussin, D. Holland, R. Dupree, Does six-coordinate germanium exist in Na_2O-GeO_2 glasses? Oxygen-17 nuclear magnetic resonance measurements, J. Non-Cryst. Solids 232-234 (1998) 440–445. doi:10.1016/s0022-3093(98)00394-9.

[55] L.-S. Du, J. F. Stebbins, Oxygen sites and network coordination in sodium germanate glasses and crystals: High-resolution oxygen-17 and sodium-23 NMR, J. Phys. Chem. B 110 (25) (2006) 12427–12437. doi:10.1021/jp0615510.

[56] S. K. Lee, B. H. Lee, Atomistic origin of germanate anomaly in GeO_2 and Na-germanate glasses: Insights from two-dimensional ^{17}O NMR and quantum chemical calculations, J. Phys. Chem. B 110 (33) (2006) 16408–16412. doi:10.1021/jp063847b.

[57] P. Pyykkö, Year-2008 nuclear quadrupole moments, Mol. Phys. 106 (16-18) (2008) 1965–1974. doi:10.1080/00268970802018367.

[58] R. Dupree, M. H. Lewis, M. E. Smith, A high-resolution NMR study of the lanthanum-silicon-aluminum-oxygen-nitrogen system, J. Am. Chem. Soc. 111 (14) (1989) 5125–5132. doi:10.1021/ja00196a016.

[59] T. J. Bastow, ^{139}La nuclear magnetic resonance characterisation of La_2O_3 and $La_{1-x}Sr_xMO_3$ where M = Cr, Mn or Co, Solid State Nucl. Magn. Reson. 3 (1) (1994) 17–22. doi:10.1016/0926-2040(94)90047-7.

[60] L. Spencer, E. Coomes, E. Ye, V. Terskikh, A. Ramzy, V. Thangadurai, G. R. Goward, Structural analysis of lanthanum-containing battery materials using ^{139}La solid-state NMR, Can. J. Chem. 89 (9) (2011) 1105–1117. doi:10.1139/v11-049.

[61] U. Hoppe, R. Kranold, D. Stachel, A. Barz, A. C. Hannon, A neutron and X-ray diffraction study of the structure of the LaP_3O_9 glass, J. Non-Cryst. Solids 232-234 (1998) 44–50. doi:10.1016/s0022-3093(98)00396-2.

[62] A. C. Hannon, D. D. Martino, L. F. Santos, R. M. Almeida, Ge−O coordination in cesium germanate glasses, J. Phys. Chem. B 111 (13) (2007) 3342–3354. doi:10.1021/jp066714z.

[63] E. Lorch, Neutron diffraction by germania, silica and radiation-damaged silica glasses, J. Phys. C: Solid State Phys. 2 (2) (1969) 229–237. doi:10.1088/0022-3719/2/2/305.

[64] M. Ueno, M. Misawa, K. Suzuki, On the change in coordination of Ge atoms in Na_2O-GeO_2 glasses, Physica B+C 120 (1-3) (1983) 347–351. doi:10.1016/0378-4363(83)90404-7.

[65] P. Armand, M. Beno, A. J. G. Ellison, G. S. Knapp, D. L. Price, M.-L. Saboungi, Local and intermediate-range order in cesium germanate glass, Europhys. Lett. 29 (7) (1995) 549–553. doi:10.1209/0295-5075/29/7/007.

[66] D. L. Price, A. J. G. Ellison, M.-L. Saboungi, R.-Z. Hu, T. Egami, W. S. Howells, Short-, intermediate-, and extended-range order in rubidium germanate glasses, Phys. Rev. B 55 (17) (1997) 11249–11255. doi:10.1103/physrevb.55.11249.

[67] U. Hoppe, R. K. Brow, D. Ilieva, P. Jóvári, A. C. Hannon, Structure of rare-earth phosphate glasses by X-ray and neutron diffraction, J. Non-Cryst. Solids 351 (40-42) (2005) 3179–3190. doi:10.1016/j.jnoncrysol.2005.08.016.

[68] U. Hoppe, G. Walter, R. Kranold, D. Stachel, Structural specifics of phosphate glasses probed by diffraction methods: A review, J. Non-Cryst. Solids 263-264 (2000) 29–47. doi:10.1016/s0022-3093(99)00621-3.

[69] A. C. Hannon, Neutron diffraction techniques for structural studies of glasses, in: M. Affatigato (Ed.), Modern Glass Characterization, John Wiley & Sons, Inc., 2015, pp. 158–240. doi:10.1002/9781119051862.ch5.

[70] E. I. Kamitsos, Infrared spectroscopy of glasses, in: M. Affatigato (Ed.), Modern Glass Characterization, John Wiley & Sons, Inc., 2015, pp. 32–73. doi:10.1002/9781119051862.ch2.

[71] R. M. Almeida, L. F. Santos, Raman spectroscopy of glasses, in: M. Affatigato (Ed.), Modern Glass Characterization, John Wiley & Sons, Inc., 2015, pp. 74–106. doi:10.1002/9781119051862.ch3.

[72] E. I. Kamitsos, M. A. Karakassides, G. D. Chryssikos, Vibrational spectra of magnesium-sodium-borate glasses. 2. Raman and mid-infrared investigation of the network structure, J. Phys. Chem. 91 (5) (1987) 1073–1079. doi:10.1021/j100289a014.

[73] G. S. Henderson, L. G. Soltay, H. M. Wang, Q speciation in alkali germanate glasses, J. Non-Cryst. Solids 356 (44-49) (2010) 2480–2485. doi:10.1016/j.jnoncrysol.2010.03.023.

[74] I. Kratochvílová, S. Kamba, I. Gregora, J. Petzelt, V. N. Sigaev, E. N. Smelyanskaya, V. I. Molev, Vibration properties of $Pb_5Ge_3O_{11}$ and $LaBGeO_5$ glasses and crystallised glasses, Ferroelectrics 239 (1) (2000) 39–46. doi:10.1080/00150190008213303.

[75] V. N. Sigaev, S. V. Lotarev, E. V. Orlova, N. V. Golubev, V. V. Koltashev, V. G. Plotnichenko, G. A. Komandin, Structure of lanthanum-borogermanate glass with stillwellite composition according to vibrational spectroscopy data, Glass Ceram. 67 (3-4) (2010) 105–108. doi:10.1007/s10717-010-9238-z.

[76] P. J. Hasnip, K. Refson, M. I. J. Probert, J. R. Yates, S. J. Clark, C. J. Pickard, Density functional theory in the solid state, Philos. Trans. R. Soc., A 372 (2011) (2014) 20130270–20130270. doi:10.1098/rsta.2013.0270.

[77] J. McAndrew, T. R. Scott, Stillwellite, a new rare-earth mineral from Queensland, Nature 176 (4480) (1955) 509–510. doi:10.1038/176509b0.

[78] A. A. Kaminskii, B. V. Mill, E. L. Belokonov, A. V. Butashin, Growth, structure and spectroscopy of lanthanum borogermanate crystals $LaBGeO_5$, Neorg. Mater. 26 (5) (1990) 1105–1107.

[79] E. L. Belokoneva, W. I. F. David, J. B. Forsyth, K. S. Knight, Structural aspects of the 530 °C phase transition in $LaBGeO_5$, J. Phys.: Condens. Matter 9 (17) (1997) 3503–3519. doi:10.1088/0953-8984/9/17/002.

[80] H. Klapper, T. Hahn, Point-group symmetry and physical properties of crystals, in: International Tables for Crystallography, International Union of Crystallography, 2006, pp. 804–808. doi:10.1107/97809553602060000521.

[81] Y. Xu, Ferroelectric Materials and Their Applications, North Holland, 1991.

[82] N. A. Spaldin, Analogies and differences between ferroelectrics and ferromagnets, in: Topics in Applied Physics, Springer Berlin Heidelberg, 2007, pp. 175–218. doi:10.1007/978-3-540-34591-6_5.

[83] L. Chi, H. Chen, H. Zhuang, J. Huang, Crystal structure of $LaBSiO_5$, J. Appl. Cryst. 252 (1-2) (1997) L12–L15. doi:10.1016/s0925-8388(96)02625-4.

[84] M. B. Smirnov, A. V. Menschikova, I. Kratochvilova-Hruba, Z. Zikmund, Lattice dynamics and phase transition in $LaBGeO_5$, Phys. Status Solidi B 241 (5) (2004) 1017–1025. doi:10.1002/pssb.200301990.

[85] B. J. Demaske, A. Chernatynskiy, S. R. Phillpot, First-principles investigation of ferroelectricity in $LaBGeO_5$, J. Phys.: Condens. Matter 28 (16) (2016) 165901. doi:10.1088/0953-8984/28/16/165901.

[86] A. Onodera, B. A. Strukov, A. A. Belov, S. A. Taraskin, H. Haga, H. Yamashita, Y. Uesu, Thermal and dielectric properties of a new ferroelectric $LaBGeO_5$, J. Phys. Soc. Jpn. 62 (12) (1993) 4311–4315. doi:10.1143/jpsj.62.4311.

[87] E. V. Milov, B. A. Strukov, Pyroelectric effect and spontaneous polarization in high-temperature ferroelectric $LaBGeO_5$ (LBGO), Phys. Solid State 43 (3) (2001) 513–516. doi:10.1134/1.1356130.

[88] S. Stefanovich, B. V. Mill, A. V. Butashin, Ferroelectricity and phase transitions in stillwellite $LaBGeO_5$, Sov. Phys. Crystallogr. 37 (4) (1992) 513–515.

[89] J. Capmany, J. G. Solé, Second harmonic generation in $LaBGeO_5$:Nd^{3+}, Appl. Phys. Lett. 70 (19) (1997) 2517–2519. doi:10.1063/1.118907.

[90] R. W. Boyd, The nonlinear optical susceptibility, in: Nonlinear Optics, Elsevier, 2008, pp. 1–67. doi:10.1016/b978-0-12-369470-6.00001-0.

[91] A. A. Kaminskii, A. V. Butashin, I. A. Maslyanizin, B. V. Mill, V. S. Mironov, S. P. Rozov, S. E. Sarkisov, V. D. Shigorin, Pure and Nd^{3+}-, Pr^{3+}-ion doped trigonal acentric $LaBGeO_5$ single crystals nonlinear optical properties, Raman scattering, spectroscopy, crystal-field analysis, and simulated emission of their activators, Phys. Status Solidi A 125 (2) (1991) 671–696. doi:10.1002/pssa.2211250227.

[92] S. Kurimura, M. Harada, K.-i. Muramatsu, M. Ueda, M. Adachi, T. Yamada, T. Ueno, Quartz revisits nonlinear optics: Twinned crystal for quasi-phase matching [invited], Opt. Mater. Express 1 (7) (2011) 1367. doi:10.1364/ome.1.001367.

[93] D. Tang, J. Wang, B. Zhou, G. Xie, J. Ma, P. Yuan, H. Zhu, L. Qian, Temperature-insensitive second-harmonic generation based on noncollinear phase matching in a lithium triborate crystal, J. Opt. Soc. Am. B 34 (8) (2017) 1659. doi:10.1364/josab.34.001659.

[94] J. Capmany, D. Jaque, J. G. Solé, A. A. Kaminskii, Continuous wave laser radiation at 524 nm from a self-frequency-doubled laser of $LaBGeO_5$:Nd^{3+}, Appl. Phys. Lett. 72 (5) (1998) 531–533. doi:10.1063/1.120811.

[95] I. Hrubá, S. Kamba, J. Petzelt, I. Gregora, Z. Zikmund, D. Ivannikov, G. Komandin, A. Volkov, B. Strukov, Optical phonons and ferroelectric phase transition in the $LaBGeO_5$ crystal, Phys. Status Solidi B 214 (2) (1999) 423–439. doi:10.1002/(sici)1521-3951(199908)214:2<423::aid-pssb423>3.0.co;2-x.

[96] V. N. Sigaev, S. Y. Stefanovich, P. D. Sarkisov, E. V. Lopatina, Lanthanum borogermanate glasses and crystallization of stillwellite $LaBGeO_5$: I. Specific features of synthesis and physicochemical properties of glass, Glass Phys. Chem. 20 (5) (1994) 392–397.

[97] H. Trégouët, D. Caurant, O. Majérus, T. Charpentier, T. Lerouge, L. Cormier, Exploration of glass domain in the $SiO_2-B_2O_3-La_2O_3$ system, J. Non-Cryst. Solids 476 (2017) 158–172. doi:10.1016/j.jnoncrysol.2017.09.048.

[98] V. N. Sigaev, P. Pernice, A. Aronne, E. Fanelli, S. V. Lotarev, E. V. Orlova, V. Califano, B. Champagnon, D. Vouagner, Influence of alumina addition on crystallization and texturing behavior of $LaBGeO_5$ glass, J. Non-Cryst. Solids 352 (21-22) (2006) 2123–2128. doi:10.1016/j.jnoncrysol.2006.02.049.

[99] V. N. Sigaev, S. Y. Stefanovich, P. D. Sarkisov, E. V. Lopatina, Stillwellite glass-ceramics with ferroelectric properties, Mater. Sci. Eng. B 32 (1-2) (1995) 17–23. doi:10.1016/0921-5107(94)01167-2.

[100] V. N. Sigaev, S. V. Lotarev, E. V. Orlova, S. Y. Stefanovich, P. Pernice, A. Aronne, E. Fanelli, I. Gregora, Lanthanum borogermanate glass-based active dielectrics, J. Non-Cryst. Solids 353 (18-21) (2007) 1956–1960. doi:10.1016/j.jnoncrysol.2007.02.036.

[101] P. Gupta, H. Jain, D. B. Williams, T. Honma, Y. Benino, T. Komatsu, Creation of ferroelectric, single-crystal architecture in $Sm_{0.5}La_{0.5}BGeO_5$ glass, J. Am. Chem. Soc. 91 (1) (2007) 110–114. doi:10.1111/j.1551-2916.2007.02114.x.

[102] V. N. Sigaev, E. A. Alieva, S. V. Lotarev, N. M. Lepekhin, Y. S. Priseko, A. V. Rasstanaev, Local crystallization of glasses in the $La_2O_3-B_2O_3-GeO_2$ system under laser irradiation, Glass Phys. Chem. 35 (1) (2009) 13–20. doi:10.1134/s1087659609010027.

[103] A. Stone, M. Sakakura, Y. Shimotsuma, G. Stone, P. Gupta, K. Miura, K. Hirao, V. Dierolf, H. Jain, Formation of ferroelectric single-crystal architectures in $LaBGeO_5$ glass by femtosecond vs. continuous-wave lasers, J. Non-Cryst. Solids 356 (52-54) (2010) 3059–3065. doi:10.1016/j.jnoncrysol.2010.03.048.

[104] A. Stone, M. Sakakura, Y. Shimotsuma, K. Miura, K. Hirao, V. Dierolf, H. Jain, Femtosecond laser-writing of 3D crystal architecture in glass: Growth dynamics and morphological control, Mater. Des. 146 (2018) 228–238. doi:10.1016/j.matdes.2018.03.016.

[105] A. Stone, H. Jain, V. Dierolf, M. Sakakura, Y. Shimotsuma, K. Miura, K. Hirao, Multilayer aberration correction for depth-independent three-dimensional crystal growth in glass by femtosecond laser heating, J. Opt. Soc. Am. B 30 (5) (2013) 1234–1240. doi:10.1364/josab.30.001234.

[106] A. Stone, Three-dimensional fabrication of functional single crystal waveguides inside glass by femtosecond laser irradiation, Ph.D. thesis, Lehigh University (2014).
URL https://preserve.lehigh.edu/etd/1639/

[107] A. Stone, H. Jain, V. Dierolf, M. Sakakura, Y. Shimotsuma, K. Miura, K. Hirao, J. Lapointe, R. Kashyap, Direct laser-writing of ferroelectric single-crystal waveguide architectures in glass for 3D integrated optics, Sci. Rep. 5 (1) (2015) 10391. doi:10.1038/srep10391.

[108] B. Knorr, K. Veenhuizen, A. Stone, H. Jain, V. Dierolf, Optical properties and structure of Er:$LaBGeO_5$ laser-induced crystals-in-glass, Opt. Mater. Express 7 (11) (2017) 4095–4110. doi:10.1364/ome.7.004095.

[109] C. Coussa, C. Martinet, B. Champagnon, L. Grosvalet, D. Vouagner, V. Sigaev, In situ Raman spectroscopy of pressure-induced changes in $LaBGeO_5$ glass: Hysteresis and plastic deformation, J. Phys.: Condens. Matter 19 (26) (2007) 266220. doi:10.1088/0953-8984/19/26/266220.

[110] S. Feller, Density, thermal properties, and the glass transition temperature of glasses, in: Modern Glass Characterization, John Wiley & Sons, Inc., 2015, pp. 1–31. doi:10.1002/9781119051862.ch1.

[111] R. E. Newnham, Properties of Materials: Anisotropy, Symmetry, Structure, Oxford University Press, 2004.

[112] W. Voigt, Lehrbuch Der Kristallphysik (mit Ausschluss Der Kristalloptik), Leipzig, Berlin, B.G. Teubner, 1910.

[113] D. L. Bish, J. E. Post (Eds.), Modern Powder Diffraction, The Mineralogical Society of America, 1989.

[114] W. H. Bragg, W. L. Bragg, The reflection of X-rays by crystals, Proc. R. Soc. A 88 (605) (1913) 428–438. doi:10.1098/rspa.1913.0040.

[115] V. K. Michaelis, S. Kroeker, Caesium volatilisation in borosilicate glasses: A multinuclear magnetic resonance study, Phys. Chem. Glasses: Eur. J. Glass Sci. Technol., Part B 50 (4) (2009) 249–252.

[116] K. P. Severin, Energy Dispersive Spectrometry of Common Rock Forming Minerals, Springer-Verlag GmbH, 2005.

[117] J. I. Goldstein, D. E. Newbury, D. C. Joy, C. E. Lyman, P. Echlin, E. Lifshin, L. Sawyer, J. R. Michael, Scanning Electron Microscopy and X-ray Microanalysis, Springer Science+Business Media, Inc., 2003.

[118] N. Miliszkiewicz, S. Walas, A. Tobiasz, Current approaches to calibration of LA-ICP-MS analysis, J. Anal. At. Spectrom. 30 (2) (2015) 327–338. doi:10.1039/c4ja00325j.

[119] H. Hamaed, E. Ye, K. Udachin, R. W. Schurko, Solid-state ^{137}Ba NMR spectroscopy: An experimental and theoretical investigation of ^{137}Ba electric field gradient tensors and their relation to structure and symmetry, J. Phys. Chem. B 114 (18) (2010) 6014–6022. doi:10.1021/jp102026m.

[120] R. K. Harris, Nuclear Magnetic Resonance Spectroscopy, Longman Publishing Group, 1986.

[121] M. H. Levitt, Spin Dynamics: Basics of Nuclear Magnetic Resonance, Wiley, 2001.

[122] E. R. Andrew, Magic angle spinning, Int. Rev. Phys. Chem. 1 (2) (1981) 195–224. doi:10.1080/01442358109353320.

[123] E. Kupče, R. Freeman, Adiabatic pulses for wideband inversion and broadband decoupling, J. Magn. Reson. Ser. A 115 (2) (1995) 273–276. doi:10.1006/jmra.1995.1179.

[124] Ē. Kupče, R. Freeman, Stretched adiabatic pulses for broadband spin inversion, J. Magn. Reson. Ser. A 117 (2) (1995) 246–256. doi:10.1006/jmra.1995.0750.

[125] L. A. O'Dell, The WURST kind of pulses in solid-state NMR, Solid State Nucl. Magn. Reson. 55-56 (2013) 28–41. doi:10.1016/j.ssnmr.2013.10.003.

[126] A. L. Paterson, M. A. Hanson, U. Werner-Zwanziger, J. W. Zwanziger, Relating ^{139}La quadrupolar coupling constants to polyhedral distortion in crystalline structures, J. Phys. Chem. C 119 (45) (2015) 25508–25517. doi:10.1021/acs.jpcc.5b09122.

[127] A. Medek, V. Frydman, L. Frydman, Central transition nuclear magnetic resonance in the presence of large quadrupole couplings: Cobalt-59 nuclear magnetic resonance of cobaltophthalocyanines†, J. Phys. Chem. A 103 (25) (1999) 4830–4835. doi:10.1021/jp990410d.

[128] D. Massiot, I. Farnan, N. Gautier, D. Trumeau, A. Trokiner, J. P. Coutures, ^{71}Ga and ^{69}Ga nuclear magnetic resonance study of β-Ga_2O_3: Resolution of four- and six-fold coordinated Ga sites in static conditions, Solid State Nucl. Magn. Reson. 4 (4) (1995) 241–248. doi:10.1016/0926-2040(95)00002-8.

[129] L. A. O'Dell, R. W. Schurko, QCPMG using adiabatic pulses for faster acquisition of ultra-wideline NMR spectra, Chem. Phys. Lett. 464 (1-3) (2008) 97–102. doi:10.1016/j.cplett.2008.08.095.

[130] H. Y. Carr, E. M. Purcell, Effects of diffusion on free precession in nuclear magnetic resonance experiments, Phys. Rev. 94 (3) (1954) 630–638. doi:10.1103/physrev.94.630.

[131] S. Meiboom, D. Gill, Modified spin-echo method for measuring nuclear relaxation times, Rev. Sci. Instrum. 29 (8) (1958) 688–691. doi:10.1063/1.1716296.

[132] A. Medek, J. S. Harwood, L. Frydman, Multiple-quantum magic-angle spinning NMR: A new method for the study of quadrupolar nuclei in solids, J. Am. Chem. Soc. 117 (51) (1995) 12779–12787. doi:10.1021/ja00156a015.

[133] J.-P. Amoureux, M. Pruski, MQMAS NMR: Experimental strategies and applications, in: R. K. Harris, R. L. Wasylishen (Eds.), eMagRes, Wiley Online Library, 2008. doi:10.1002/9780470034590.emrstm0319.pub2.

[134] Y. Millot, P. P. Man, Procedures for labeling the high-resolution axis of two-dimensional MQ-MAS NMR spectra of half-integer quadrupole spins, Solid State Nucl. Magn. Reson. 21 (1-2) (2002) 21–43. doi:10.1006/snmr.2001.0043.

[135] G. Czjzek, J. Fink, F. Götz, H. Schmidt, J. M. D. Coey, J.-P. Rebouillat, A. Liénard, Atomic coordination and the distribution of electric field gradients in amorphous solids, Phys. Rev. B 23 (6) (1981) 2513–2530. doi:10.1103/physrevb.23.2513.

[136] G. Le Caër, R. A. Brand, General models for the distributions of electric field gradients in disordered solids, J. Phys.: Condens. Matter 10 (47) (1998) 10715–10774. doi:10.1088/0953-8984/10/47/020.

[137] G. Le Caër, B. Bureau, D. Massiot, An extension of the Czjzek model for the distributions of electric field gradients in disordered solids and an application to NMR spectra of ^{71}Ga in chalcogenide glasses, J. Phys.: Condens. Matter 22 (6) (2010) 065402. doi:10.1088/0953-8984/22/6/065402.

[138] D. R. Neuville, L. Cormier, D. Massiot, Al environment in tectosilicate and peraluminous glasses: A ^{27}Al MQ-MAS NMR, Raman, and XANES investigation, Geochim. Cosmochim. Acta 68 (24) (2004) 5071–5079. doi:10.1016/j.gca.2004.05.048.

[139] J.-B. d'Espinose de Lacaillerie, C. Fretigny, D. Massiot, MAS NMR spectra of quadrupolar nuclei in disordered solids: The Czjzek model, J. Magn. Reson. 192 (2) (2008) 244–251. doi:10.1016/j.jmr.2008.03.001.

[140] T. Gullion, J. Schaefer, Rotational-echo double-resonance NMR, J. Magn. Reson. 81 (1) (1989) 196–200. doi:10.1016/0022-2364(89)90280-1.

[141] H. Eckert, S. Elbers, J. D. Epping, M. Janssen, M. Kalwei, W. Strojek, U. Voigt, Dipolar solid state NMR approaches towards medium-range structure in oxide glasses, in: Top. Curr. Chem., Springer Berlin Heidelberg, 2004, pp. 195–233. doi:10.1007/b98651.

[142] J. C. C. Chan, M. Bertmer, H. Eckert, Site connectivities in amorphous materials studied by double-resonance NMR of quadrupolar nuclei: High-resolution $^{11}B \leftrightarrow ^{27}Al$ spectroscopy of aluminoborate glasses, J. Am. Chem. Soc. 121 (22) (1999) 5238–5248. doi:10.1021/ja983385i.

[143] J. H. van Vleck, The dipolar broadening of magnetic resonance lines in crystals, Phys. Rev. 74 (9) (1948) 1168–1183. doi:10.1103/physrev.74.1168.

[144] M. Bertmer, H. Eckert, Dephasing of spin echoes by multiple heteronuclear dipolar interactions in rotational echo double resonance NMR experiments, Solid State Nucl. Magn. Reson. 15 (3) (1999) 139–152. doi:10.1016/s0926-2040(99)00050-8.

[145] R. R. Ernst, G. Bodenhausen, A. Wokaun, Principles of Nuclear Magnetic Resonance in One and Two Dimensions, Oxford University Press, 1987.

[146] E. Lippmaa, A. Samoson, M. Magi, High-resolution aluminum-27 NMR of aluminosilicates, J. Am. Chem. Soc. 108 (8) (1986) 1730–1735. doi:10.1021/ja00268a002.

[147] M. E. Smith, E. R. H. van Eck, Recent advances in experimental solid state NMR methodology for half-integer spin quadrupolar nuclei, Prog. Nucl. Magn. Reson. Spectrosc. 34 (2) (1999) 159–201. doi:10.1016/s0079-6565(98)00028-4.

[148] D. Fenzke, D. Freude, T. Fröhlich, J. Haase, NMR intensity measurements of half-integer quadrupole nuclei, Chem. Phys. Lett. 111 (1-2) (1984) 171–175. doi:10.1016/0009-2614(84)80458-3.

[149] J. R. Ferraro, K. Nakamoto, C. W. Brown, Introductory Raman Spectroscopy, Academic Press, 2003.

[150] W. Hayes, R. Loudon, Scattering of Light by Crystals, Courier Corporation, 1978.

[151] D. S. Sholl, J. A. Steckel, Density Functional Theory, John Wiley & Sons, Inc., 2009. doi:10.1002/9780470447710.

[152] T. Helgaker, J. Olsen, P. Jorgensen, Molecular Electronic-Structure Theory, Wiley-Blackwell, 2013.

[153] D. R. Hamann, M. Schlüter, C. Chiang, Norm-conserving pseudopotentials, Phys. Rev. Lett. 43 (20) (1979) 1494–1497. doi:10.1103/physrevlett.43.1494.

[154] P. E. Blöchl, Projector augmented-wave method, Phys. Rev. B 50 (24) (1994) 17953–17979. doi:10.1103/physrevb.50.17953.

[155] J. W. Zwanziger, Computation of NMR observables: Consequences of projector-augmented wave sphere overlap, Solid State Nucl. Magn. Reson. 80 (2016) 14–18. doi:10.1016/j.ssnmr.2016.10.005.

[156] C. J. Pickard, F. Mauri, All-electron magnetic response with pseudopotentials: NMR chemical shifts, Phys. Rev. B 63 (24) (2001) 245101. doi:10.1103/physrevb.63.245101.

[157] M. Profeta, M. Benoit, F. Mauri, C. J. Pickard, First-principles calculation of the ^{17}O NMR parameters in Ca oxide and Ca aluminosilicates: the partially covalent nature of the Ca-O bond, a challenge for density functional theory, J. Am. Chem. Soc. 126 (39) (2004) 12628–12635. doi:10.1021/ja0490830.

[158] T. Charpentier, The PAW/GIPAW approach for computing NMR parameters: A new dimension added to NMR study of solids, Solid State Nucl. Magn. Reson. 40 (1) (2011) 1–20. doi:10.1016/j.ssnmr.2011.04.006.

[159] R. K. Harris, E. D. Becker, S. M. C. D. Menezes, P. Granger, R. E. Hoffman, K. W. Zilm, Further conventions for NMR shielding and chemical shifts IUPAC recommendations 2008, Solid State Nucl. Magn. Reson. 33 (3) (2008) 41–56. doi:10.1016/j.ssnmr.2008.02.004.

[160] J. Herzfeld, A. E. Berger, Sideband intensities in NMR spectra of samples spinning at the magic angle, J. Chem. Phys. 73 (12) (1980) 6021–6030. doi:10.1063/1.440136.

[161] X. Gonze, F. Jollet, F. A. Araujo, D. Adams, B. Amadon, T. Applencourt, C. Audouze, J.-M. Beuken, J. Bieder, A. Bokhanchuk, E. Bousquet, F. Bruneval, D. Caliste, M. Côté, F. Dahm, F. D. Pieve, M. Delaveau, M. D. Gennaro, B. Dorado, C. Espejo, G. Geneste, L. Genovese, A. Gerossier, M. Giantomassi, Y. Gillet, D. R. Hamann, L. He, G. Jomard, J. L. Janssen, S. L. Roux, A. Levitt, A. Lherbier, F. Liu, I. Lukačević, A. Martin, C. Martins, M. J. T. Oliveira, S. Poncé, Y. Pouillon, T. Rangel, G.-M. Rignanese, A. H. Romero, B. Rousseau, O. Rubel, A. A. Shukri, M. Stankovski, M. Torrent, M. J. V. Setten, B. V. Troeye, M. J. Verstraete, D. Waroquiers, J. Wiktor, B. Xu, A. Zhou, J. W. Zwanziger, Recent developments in the ABINIT software package, Comput. Phys. Commun. 205 (2016) 106–131. doi:10.1016/j.cpc.2016.04.003.

[162] P. Giannozzi, S. Baroni, N. Bonini, M. Calandra, R. Car, C. Cavazzoni, D. Ceresoli, G. L. Chiarotti, M. Cococcioni, I. Dabo, A. D. Corso, S. de Gironcoli, S. Fabris, G. Fratesi, R. Gebauer, U. Gerstmann, C. Gougoussis, A. Kokalj, M. Lazzeri, L. Martin-Samos, N. Marzari, F. Mauri, R. Mazzarello, S. Paolini, A. Pasquarello, L. Paulatto, C. Sbraccia, S. Scandolo, G. Sclauzero, A. P. Seitsonen, A. Smogunov, P. Umari, R. M. Wentzcovitch, QUANTUM ESPRESSO: A modular and open-source software project for quantum simulations of materials, J. Phys.: Condens. Matter 21 (39) (2009) 395502. doi:10.1088/0953-8984/21/39/395502.

[163] P. Giannozzi, O. Andreussi, T. Brumme, O. Bunau, M. B. Nardelli, M. Calandra, R. Car, C. Cavazzoni, D. Ceresoli, M. Cococcioni, N. Colonna, I. Carnimeo, A. D. Corso, S. de Gironcoli, P. Delugas, R. A. DiStasio, A. Ferretti, A. Floris, G. Fratesi, G. Fugallo, R. Gebauer, U. Gerstmann, F. Giustino, T. Gorni, J. Jia, M. Kawamura, H.-Y. Ko, A. Kokalj, E. Küçükbenli, M. Lazzeri, M. Marsili, N. Marzari, F. Mauri, N. L. Nguyen, H.-V. Nguyen, A. O.-d. la Roza, L. Paulatto, S. Poncé, D. Rocca, R. Sabatini, B. Santra, M. Schlipf, A. P. Seitsonen, A. Smogunov, I. Timrov, T. Thonhauser, P. Umari, N. Vast, X. Wu, S. Baroni, Advanced capabilities for materials modelling with Quantum ESPRESSO, J. Phys.: Condens. Matter 29 (46) (2017) 465901. doi:10.1088/1361-648x/aa8f79.

[164] D. R. Hamann, Optimized norm-conserving Vanderbilt pseudopotentials, Phys. Rev. B 88 (8) (2013) 085117. doi:10.1103/physrevb.88.085117.

[165] N. A. W. Holzwarth, A. R. Tackett, G. E. Matthews, A projector augmented wave (PAW) code for electronic structure calculations, part I: atompaw for generating atom-centered functions, Comput. Phys. Commun. 135 (3) (2001) 329–347. doi:10.1016/s0010-4655(00)00244-7.

[166] A. C. Hannon, Results on disordered materials from the GEneral materials diffractometer, GEM, at ISIS, Nucl. Instrum. Methods Phys. Res., Sect. A 551 (1) (2005) 88–107. doi:10.1016/j.nima.2005.07.053.

[167] A. C. Wright, Scientific opportunities for the study of amorphous solids using pulsed neutron sources, J. Non-Cryst. Solids 76 (1) (1985) 187–210. doi:10.1016/0022-3093(85)90062-6.

[168] V. F. Sears, Neutron scattering lengths and cross sections, Neutron News 3 (3) (1992) 26–37. doi:10.1080/10448639208218770.

[169] M. Tliha, H. Mathlouthi, J. Lamloumi, A. Percheron-Guegan, AB_5-type hydrogen storage alloy used as anodic materials in Ni-MH batteries, J. Alloy Compd. 436 (1-2) (2007) 221–225. doi:10.1016/j.jallcom.2006.07.012.

[170] S. Kehoe, M. Langman, U. Werner-Zwanziger, R. J. Abraham, D. Boyd, Mixture designs to assess composition–structure–property relationships in $SiO_2-CaO-ZnO-La_2O_3-TiO_2-MgO-SrO-Na_2O$ glasses: Potential materials for embolization, J. Biomater. Appl. 28 (3) (2013) 416–433. doi:10.1177/0885328212455834.

[171] P. C. D'Haese, G. B. Spasovski, A. Sikole, A. Hutchison, T. J. Freemont, S. Sulkova, C. Swanepoel, S. Pejanovic, L. Djukanovic, A. Balducci, G. Coen, W. Sulowicz, A. Ferreira, A. Torres, S. Curic, M. Popovic, N. Dimkovic, M. E. D. Broe, A multicenter study on the effects of lanthanum carbonate (Fosrenol™) and calcium carbonate on renal bone disease in dialysis patients, Kidney Int. 63 (2003) S73–S78. doi:10.1046/j.1523-1755.63.s85.18.x.

[172] L. Dithmer, A. S. Lipton, K. Reitzel, T. E. Warner, D. Lundberg, U. G. Nielsen, Characterization of phosphate sequestration by a lanthanum modified bentonite clay: A solid-state NMR, EXAFS, and PXRD study, Environ. Sci. Technol. 49 (7) (2015) 4559–4566. doi:10.1021/es506182s.

[173] A. R. Thompson, E. Oldfield, Solid-state scandium-45, yttrium-89, and lanthanum-139 nuclear magnetic resonance spectroscopy, J. Chem. Soc. Chem. Comm. (1) (1987) 27–29. doi:10.1039/c39870000027.

[174] H. Hamaed, A. Y. H. Lo, D. S. Lee, W. J. Evans, R. W. Schurko, Solid-state ^{139}La and ^{15}N NMR spectroscopy of lanthanum-containing metallocenes, J. Am. Chem. Soc. 128 (39) (2006) 12638–12639. doi:10.1021/ja0645180.

[175] K. J. Ooms, K. W. Feindel, M. J. Willans, R. E. Wasylishen, J. V. Hanna, K. J. Pike, M. E. Smith, Multiple-magnetic field ^{139}La NMR and density functional theory investigation of the solid lanthanum (III) halides, Solid State Nucl. Magn. Reson. 28 (2-4) (2005) 125–134. doi:10.1016/j.ssnmr.2005.07.002.

[176] M. J. Willans, K. W. Feindel, K. J. Ooms, R. E. Wasylishen, An investigation of lanthanum coordination compounds by using solid-state ^{139}La NMR spectroscopy and relativistic density functional theory, Chem. - Eur. J. 12 (1) (2006) 159–168. doi:10.1002/chem.200500778.

[177] K. E. Johnston, M. R. Mitchell, F. Blanc, P. Lightfoot, S. E. Ashbrook, Structural study of $La_{1-x}Y_xScO_3$, combining neutron diffraction, solid-state NMR, and first-principles DFT calculations, J. Phys. Chem. C 117 (5) (2013) 2252–2265. doi:10.1021/jp310878b.

[178] C. Pan, Y. J. Lee, B. Ammundsen, C. P. Grey, ^{6}Li MAS NMR studies of the local structure and electrochemical properties of Cr-doped lithium manganese and lithium cobalt oxide cathode materials for lithium-ion batteries, Chem. Mater. 14 (5) (2002) 2289–2299. doi:10.1021/cm011623u.

[179] T. Balić Žunić, E. Makovicky, Determination of the centroid or 'the best centre' of a coordination polyhedron, Acta Crystallogr., Sect. B: Struct. Sci. 52 (1) (1996) 78–81. doi:10.1107/s0108768195008251.

[180] E. Makovicky, T. Balić-Žunić, New measure of distortion for coordination polyhedra, Acta Crystallogr., Sect. B: Struct. Sci. 54 (6) (1998) 766–773. doi:10.1107/s0108768198003905.

[181] B. A. Marinkovic, M. Ari, R. R. de Avillez, F. Rizzo, F. F. Ferreira, K. J. Miller, M. B. Johnson, M. A. White, Correlation between AO_6 polyhedral distortion and negative thermal expansion in orthorhombic $Y_2Mo_3O_{12}$ and related materials, Chemistry of Materials 21 (13) (2009) 2886–2894. doi:10.1021/cm900650c.

[182] C. P. Romao, F. A. Perras, U. Werner-Zwanziger, J. A. Lussier, K. J. Miller, C. M. Calahoo, J. W. Zwanziger, M. Bieringer, B. A. Marinkovic, D. L. Bryce, M. A. White, Zero thermal expansion in $ZrMgMo_3O_{12}$: NMR crystallography reveals origins of thermoelastic properties, Chem. Mater. 27 (7) (2015) 2633–2646. doi:10.1021/acs.chemmater.5b00429.

[183] T. Balić Žunić, I. Vicković, IVTON – a program for the calculation of geometrical aspects of crystal structures and some crystal chemical applications, J. Appl. Cryst. 29 (3) (1996) 305–306. doi:10.1107/s0021889895015081.

[184] D. Massiot, F. Fayon, M. Capron, I. King, S. L. Calvé, B. Alonso, J.-O. Durand, B. Bujoli, Z. Gan, G. Hoatson, Modelling one- and two-dimensional solid-state NMR spectra, Magn. Reson. Chem. 40 (1) (2002) 70–76. doi:10.1002/mrc.984.

[185] K. Eichele, R. E. Wasylishen, WSOLIDS1: Solid-state NMR simulations, version 1.19 (2009).

[186] F. A. Perras, C. M. Widdifield, D. L. Bryce, QUEST—QUadrupolar Exact SofTware: A fast graphical program for the exact simulation of NMR and NQR spectra for quadrupolar nuclei, Solid State Nucl. Magn. Reson. 45-46 (2012) 36–44. doi:10.1016/j.ssnmr.2012.05.002.

[187] X. Gonze, B. Amadon, P.-M. Anglade, J.-M. Beuken, F. Bottin, P. Boulanger, F. Bruneval, D. Caliste, R. Caracas, M. Côté, T. Deutsch, L. Genovese, P. Ghosez, M. Giantomassi, S. Goedecker, D. R. Hamann, P. Hermet, F. Jollet, G. Jomard, S. Leroux, M. Mancini, S. Mazevet, M. J. T. Oliveira, G. Onida, Y. Pouillon, T. Rangel, G.-M. Rignanese, D. Sangalli, R. Shaltaf, M. Torrent, M. J. Verstraete, G. Zerah, J. W. Zwanziger, ABINIT: First-principles approach to material and nanosystem properties, Comput. Phys. Commun. 180 (12) (2009) 2582–2615. doi:10.1016/j.cpc.2009.07.007.

[188] M. Torrent, F. Jollet, F. Bottin, G. Zérah, X. Gonze, Implementation of the projector augmented-wave method in the ABINIT code: Application to the study of iron under pressure, Comput. Mater. Sci. 42 (2) (2008) 337–351. doi:10.1016/j.commatsci.2007.07.020.

[189] M. A. L. Marques, M. J. T. Oliveira, T. Burnus, LIBXC: A library of exchange and correlation functionals for density functional theory, Comput. Phys. Commun. 183 (10) (2012) 2272–2281. doi:10.1016/j.cpc.2012.05.007.

[190] J. W. Zwanziger, M. Torrent, First-principles calculation of electric field gradients in metals, semiconductors, and insulators, Appl. Magn. Reson. 33 (4) (2008) 447–456. doi:10.1007/s00723-008-0080-1.

[191] F. Jollet, M. Torrent, N. Holzwarth, Generation of projector augmented-wave atomic data: A 71 element validated table in the XML format, Comput. Phys. Commun. 185 (4) (2014) 1246–1254. doi:10.1016/j.cpc.2013.12.023.

[192] J. P. Perdew, K. Burke, M. Ernzerhof, Generalized gradient approximation made simple, Phys. Rev. Lett. 77 (18) (1996) 3865–3868. doi:10.1103/physrevlett.77.3865.

[193] A. Belsky, M. Hellenbrandt, V. L. Karen, P. Luksch, New developments in the Inorganic Crystal Structure Database (ICSD): Accessibility in support of materials research and design, Acta Crystallogr., Sect. B: Struct. Sci. 58 (3) (2002) 364–369. doi:10.1107/s0108768102006948.

[194] Y. Furukawa, I. Okamura, K. Kumagai, T. Goto, T. Fukase, Y. Taguchi, Y. Tokura, Electronic correlations on the verge of the Mott transition in $La_{1-x}Sr_xTiO_3$ by $^{47/49}$Ti and ^{139}La nuclear magnetic resonance, Phys. Rev. B 59 (16) (1999) 10550–10558. doi:10.1103/physrevb.59.10550.

[195] V. N. Sigaev, A. B. Mamonov, P. Pernice, A. Aronne, S. Y. Stefanovich, A. A. Bush, Pyroelectric composites based on $LaBSiO_5$ stillwellite, J. Eur. Ceram. Soc. 20 (9) (2000) 1225–1229. doi:10.1016/s0955-2219(99)00291-5.

[196] H. K. Juwhari, W. B. White, Luminescence of rare earth borosilicates with the stillwellite and related structures, Mater. Lett. 64 (15) (2010) 1751–1754. doi:10.1016/j.matlet.2010.04.037.

[197] I. Kratochvílová-Hrubá, I. Gregora, J. Pokorný, S. Kamba, Z. Zikmund, J. Petzelt, M. Čerňanský, V. Studnička, V. N. Sigaev, E. N. Smelyanskaya, Vibrational spectroscopy of $LaBSiO_5$ glass and glass–crystal composites, J. Non-Cryst. Solids 290 (2-3) (2001) 224–230. doi:10.1016/s0022-3093(01)00794-3.

[198] R. Shaltaf, H. K. Juwhari, B. Hamad, J. Khalifeh, G.-M. Rignanese, X. Gonze, Structural, electronic, vibrational, and dielectric properties of $LaBGeO_5$ from first principles, J. Appl. Phys. 115 (7) (2014) 074103. doi:10.1063/1.4866357.

[199] R. P. Liferovich, R. H. Mitchell, A structural study of ternary lanthanide orthoscandate perovskites, J. Solid State Chem. 177 (6) (2004) 2188–2197. doi:10.1016/j.jssc.2004.02.025.

[200] J. Mason (Ed.), Multinuclear NMR, Springer US, 1987. doi:10.1007/978-1-4613-1783-8.

[201] G. K. Abdullaev, G. G. Dzhafarov, K. S. Mamedov, Crystal structure of lanthanum orthoborate, Azerb. Khim. Zh. (1976) 117–120.

[202] I. M. Thomas, S. A. Payne, G. D. Wilke, Optical properties and laser demonstrations of Nd-doped sol-gel silica glasses, J. Non-Cryst. Solids 151 (3) (1992) 183–194. doi:10.1016/0022-3093(92)90028-i.

[203] C. C. Santos, I. Guedes, C.-K. Loong, L. A. Boatner, A. L. Moura, M. T. de Araujo, C. Jacinto, M. V. D. Vermelho, Spectroscopic properties of Er^{3+}-doped lead phosphate glasses for photonic application, J. Phys. D: Appl. Phys. 43 (2) (2009) 025102. doi:10.1088/0022-3727/43/2/025102.

[204] T. Kitagawa, K. Hattori, K. Shuto, M. Yasu, M. Kobayashi, M. Horiguchi, Amplification in erbium-doped silica-based planar lightwave circuits, Electron. Lett. 28 (19) (1992) 1818. doi:10.1049/el:19921159.

[205] K. Terashima, S. Tamura, S.-H. Kim, T. Yoko, Structure and nonlinear optical properties of lanthanide borate glasses, J. Am. Ceram. Soc. 80 (11) (1997) 2903–2909. doi:10.1111/j.1151-2916.1997.tb03210.x.

[206] S. Kroeker, Nuclear waste glasses: Insights from solid-state NMR, in: R. K. Harris, R. L. Wasylishen (Eds.), eMagRes, Wiley Online Library, 2007. doi:10.1002/9780470034590.emrstm1223.

[207] D. Caurant, P. Loiseau, O. Majerus, V. Aubin-Chevaldonnet, I. Bardez, A. Quintas, Glasses, Glass-Ceramics and Ceramics for Immobilization of Highly Radioactive Nuclear Wastes, Nova Science, 2007.

[208] A. J. Rossini, R. W. Schurko, Experimental and theoretical studies of ^{45}Sc NMR interactions in solids, J. Am. Chem. Soc. 128 (32) (2006) 10391–10402. doi:10.1021/ja060477w.

[209] C. P. Grey, M. E. Smith, A. K. Cheetham, C. M. Dobson, R. Dupree, Yttrium-89 magic angle spinning NMR study of rare-earth pyrochlores: Paramagnetic shifts in the solid state, J. Am. Chem. Soc. 112 (12) (1990) 4670–4675. doi:10.1021/ja00168a007.

[210] D. Mohr, A. S. S. de Camargo, C. C. de Araujo, H. Eckert, Local environment of scandium in aluminophosphate laser glasses: Structural studies by solid state NMR spectroscopy, J. Mater. Chem. 17 (35) (2007) 3733. doi:10.1039/b705707e.

[211] N. K. Nasikas, S. Sen, G. N. Papatheodorou, Structural nature of polyamorphism in $Y_2O_3-Al_2O_3$ glasses, Chem. Mater. 23 (11) (2011) 2860–2868. doi:10.1021/cm200241c.

[212] A. L. Paterson, A. C. Hannon, U. Werner-Zwanziger, J. W. Zwanziger, Structural differences between the glass and crystal forms of the transparent ferroelectric nanocomposite, $LaBGeO_5$, from neutron diffraction and NMR spectroscopy, J. Phys. Chem. C 122 (36) (2018) 20963–20980. doi:10.1021/acs.jpcc.8b05747.

[213] B. J. Kennedy, B. A. Hunter, C. J. Howard, Structural and bonding trends in tin pyrochlore oxides, J. Solid State Chem. 130 (1) (1997) 58–65. doi:10.1006/jssc.1997.7277.

[214] E. M. Levin, C. R. Robbins, J. L. Waring, Immiscibility and the system lanthanum oxide-boric oxide, J. Am. Ceram. Soc. 44 (2) (1961) 87–91. doi:10.1111/j.1151-2916.1961.tb15356.x.

[215] I. L. Botto, E. J. Baran, Crystal data for the trimetaphosphates of lanthanum, cerium and praseodymium, J. Appl. Cryst. 12 (2) (1979) 257–258. doi:10.1107/s0021889879012358.

[216] J. S. Ysker, W. Hoffmann, Die kristallstruktur des $La[B_3O_6]$, Naturwissenschaften 57 (3) (1970) 129–129. doi:10.1007/bf00600055.

[217] I. Khidirov, V. T. Om, Localization of hydrogen atoms in rare earth metal trihydroxides $R(OH)_3$, Phys. Status Solidi A 140 (2) (1993) K59–K62. doi:10.1002/pssa.2211400231.

[218] E. G. Sherry, The structure of $Pr_2(SO_4)_3 \cdot 8\,H_2O$ and $La_2(SO_4)_3 \cdot 9\,H_2O$, J. Solid State Chem. 19 (3) (1976) 271–279. doi:10.1016/0022-4596(76)90177-8.

[219] G. Schiller, Die kristallstrukturen von Ce_2O_3 (a-form), $LiCeO_2$ und CeF_3-ein bietrag zur kristallchemie des dreiwertigen cers., Ph.D. thesis, Universitaet Karlsruhe (1985).

[220] V. R. Samygina, E. A. Genkina, B. A. Maksimov, N. I. Leonyuk, Crystal structure of La-analog of stillwellite, Kristallografiya 38 (6) (1993) 61–65.

[221] M. Huse, A. W. B. Skilbred, M. Karlsson, S. G. Eriksson, T. Norby, R. Haugsrud, C. S. Knee, Neutron diffraction study of the monoclinic to tetragonal structural transition in $LaNbO_4$ and its relation to proton mobility, J. Solid State Chem. 187 (2012) 27–34. doi:10.1016/j.jssc.2011.12.025.

[222] J. Matuszewski, J. Kropiwnicka, T. Znamierowska, The crystal structure of lanthanum metaphosphate LaP_3O_9, J. Solid State Chem. 75 (2) (1988) 285–290. doi:10.1016/0022-4596(88)90168-5.

[223] Y. Ni, J. M. Hughes, A. N. Mariano, Crystal chemistry of the monazite and xenotime structures, Am. Mineral. 80 (1-2) (1995) 21–26. doi:10.2138/am-1995-1-203.

[224] R. Dupree, A. P. Howes, S. C. Kohn, Natural abundance solid state ^{43}Ca NMR, Chem. Phys. Lett. 276 (5-6) (1997) 399–404. doi:10.1016/s0009-2614(97)00863-4.

[225] M. N. Garaga, U. Werner-Zwanziger, J. W. Zwanziger, ^{125}Te NMR probes of tellurium oxide crystals: Shielding-structure correlations, Inorg. Chem. 57 (2) (2017) 892–898. doi:10.1021/acs.inorgchem.7b02913.

[226] M. Edén, NMR studies of oxide-based glasses, Annu. Rep. Prog. Chem., Sect. C: Phys. Chem. 108 (2012) 177. doi:10.1039/c2pc90006h.

[227] R. K. Brow, E. Metwalli, D. L. Sidebottom, Properties and structure of lanthanum phosphate glasses, in: Proc. SPIE 4102, Inorganic Optical Materials II, 2000. doi:10.1117/12.405272.

[228] S. G. Lu, C. L. Mak, K. H. Wong, Optical studies of transparent ferroelectric strontium–barium niobate/silica nanocomposite, J. Appl. Phys. 94 (5) (2003) 3422–3426. doi:10.1063/1.1599047.

[229] A. Tarafder, K. Annapurna, R. S. Chaliha, V. S. Tiwari, P. K. Gupta, B. Karmakar, Structure, dielectric and optical properties of Nd^{3+}-doped $LiTaO_3$ transparent ferroelectric glass-ceramic nanocomposites, J. Alloy Compd. 489 (1) (2010) 281–288. doi:10.1016/j.jallcom.2009.09.071.

[230] N. S. Prasad, K. B. R. Varma, Evolution of ferroelectric $LiNbO_3$ phase in a reactive glass matrix ($LiBO_2$–Nb_2O_5), J. Non-Cryst. Solids 351 (16-17) (2005) 1455–1465. doi:10.1016/j.jnoncrysol.2005.03.040.

[231] S. G. Lu, C. L. Mak, G. K. H. Pang, K. H. Wong, K. W. Cheah, Blue-shift and intensity enhancement of photoluminescence in lead-zirconate-titanate-doped silica nanocomposites, Nanotechnology 19 (3) (2007) 035702. doi:10.1088/0957-4484/19/03/035702.

[232] Y. Takahashi, Y. Benino, T. Fujiwara, T. Komatsu, Second harmonic generation in transparent surface crystallized glasses with stillwellite-type $LaBGeO_5$, J. Appl. Phys. 89 (10) (2001) 5282–5287. doi:10.1063/1.1360699.

[233] Y. Takahashi, K. Kitamura, Y. Benino, T. Fujiwara, T. Komatsu, $LaBGeO_5$ single crystals in glass and second-harmonic generation, Mater. Sci. Eng. B 120 (1-3) (2005) 155–160. doi:10.1016/j.mseb.2005.02.010.

[234] S. Stefanovich, B. Mill, V. Sigaev, Processing and characterization of ferro/piezoelectrics in the stillwellite family, Ferroelectrics 201 (1) (1997) 285–294. doi:10.1080/00150199708228379.

[235] E. R. Barney, A. C. Hannon, D. Holland, A multi-technique structural study of the tellurium borate glass system, Phys. Chem. Glasses: Eur. J. Glass Sci. Technol., Part B 50 (3) (2009) 156–164.

[236] A. C. Hannon, E. R. Barney, D. Holland, The structure of tin borate based glasses, Phys. Chem. Glasses: Eur. J. Glass Sci. Technol., Part B 50 (5) (2009) 271–283.

[237] R. A. Martin, P. S. Salmon, C. J. Benmore, H. E. Fischer, G. J. Cuello, Structure of lanthanum and cerium phosphate glasses by the method of isomorphic substitution in neutron diffraction, Phys. Rev. B 68 (5) (2003) 054203. doi:10.1103/physrevb.68.054203.

[238] I. N. Chakraborty, J. E. Shelby, R. A. Condrate, Properties and structure of lanthanum borate glasses, J. Am. Ceram. Soc. 67 (12) (1984) 782–785. doi:10.1111/j.1151-2916.1984.tb19700.x.

[239] V. N. Sigaev, E. V. Lopatina, P. D. Sarkisov, A. Marotta, P. Pernice, Non-isothermal crystallization of $La_2O_3 \cdot B_2O_3 \cdot 2GeO_2$ glasses, Thermochim. Acta 286 (1) (1996) 25–31. doi:10.1016/0040-6031(96)02935-8.

[240] S. P. Brown, S. Wimperis, Two-dimensional multiple-quantum MAS NMR of quadrupolar nuclei: A comparison of methods, J. Magn. Reson. 128 (1) (1997) 42–61. doi:10.1006/jmre.1997.1217.

[241] P. P. Man, Scaling and labeling the high-resolution isotropic axis of two-dimensional multiple-quantum magic-angle-spinning spectra of half-integer quadrupole spins, Phys. Rev. B 58 (5) (1998) 2764–2782. doi:10.1103/physrevb.58.2764.

[242] A. K. Soper, Rutherford Appleton Laboratory technical report, RAL-TR-2011-013, Tech. rep., Rutherford Appleton Laboratory (2011).

[243] A. C. Hannon, W. S. Howells, A. K. Soper, ATLAS: A suite of programs for the analysis of time-of-flight neutron diffraction data from liquid and amorphous samples, in: Inst. Phys. Conf. Ser., Vol. 107, 1990, pp. 193–211.

[244] A. C. Hannon, PFIT correlation function fitting software.
URL http://www.alexhannon.co.uk/

[245] V. K. Michaelis, P. Kachhadia, S. Kroeker, Clustering in borate-rich alkali borophosphate glasses: A ^{11}B and ^{31}P MAS NMR study, Phys. Chem. Glasses: Eur. J. Glass Sci. Technol., Part B 54 (1) (2013) 20–26.

[246] K. Suzuki, International glass database system INTERGLAD, New Glass Forum 25 (1) (2010) 61–67.

[247] Y. Pan, T. Gullion, J. Schaefer, Determination of C–N internuclear distances by rotational-echo double-resonance NMR of solids, J. Magn. Reson. 90 (2) (1990) 330–340. doi:10.1016/0022-2364(90)90138-y.

[248] D. I. Grimley, A. C. Wright, R. N. Sinclair, Neutron scattering from vitreous silica IV. Time-of-flight diffraction, J. Non-Cryst. Solids 119 (1) (1990) 49–64. doi:10.1016/0022-3093(90)90240-m.

[249] G. K. Abdullaev, K. S. Mamedov, G. G. Dzhafarov, Refined crystal structure of lanthanum metaborate $La(BO_2)_3$, Kristallografiya 26 (4) (1981) 837–840.

[250] L. Li, X. Jin, G. Li, Y. Wang, F. Liao, G. Yao, J. Lin, Novel rare earth polyborates. 2. Syntheses and structures†, Chem. Mater. 15 (11) (2003) 2253–2260. doi:10.1021/cm030004d.

[251] L.-S. Du, J. F. Stebbins, Nature of silicon-boron mixing in sodium borosilicate glasses: A high-resolution ^{11}B and ^{17}O NMR study, J. Phys. Chem. B 107 (37) (2003) 10063–10076. doi:10.1021/jp0340481.

[252] G. Tricot, A. Saitoh, H. Takebe, Intermediate length scale organisation in tin borophosphate glasses: New insights from high field correlation NMR, Phys. Chem. Chem. Phys. 17 (44) (2015) 29531–29540. doi:10.1039/c5cp02095f.

[253] B. Gee, M. Janssen, H. Eckert, Local cation environments in mixed alkali silicate glasses studied by multinuclear single and double resonance magic-angle spinning NMR, J. Non-Cryst. Solids 215 (1) (1997) 41–50. doi:10.1016/s0022-3093(97)00037-9.

[254] C. C. de Araujo, W. Strojek, L. Zhang, H. Eckert, G. Poirier, S. J. L. Ribeiro, Y. Messaddeq, Structural studies of $NaPO_3-WO_3$ glasses by solid state NMR and Raman spectroscopy, J. Mater. Chem. 16 (32) (2006) 3277–3284. doi:10.1039/b605971f.

[255] B. Raguenet, G. Tricot, G. Silly, M. Ribes, A. Pradel, Revisiting the 'mixed glass former effect' in ultra-fast quenched borophosphate glasses by advanced 1D/2D solid state NMR, J. Mater. Chem. 21 (44) (2011) 17693. doi:10.1039/c1jm12350e.

[256] I. D. Brown, D. Altermatt, Bond-valence parameters obtained from a systematic analysis of the Inorganic Crystal Structure Database, Acta Crystallogr., Sect. B: Struct. Sci. 41 (4) (1985) 244–247. doi:10.1107/s0108768185002063.

[257] N. E. Brese, M. O'Keeffe, Bond-valence parameters for solids, Acta Crystallogr. B 47 (2) (1991) 192–197. doi:10.1107/s0108768190011041.

[258] A. C. Hannon, Bonding and structure in network glasses, J. Non-Cryst. Solids 451 (2016) 56–67. doi:10.1016/j.jnoncrysol.2016.04.035.

[259] A. C. Hannon, D. Holland, A parameterisation for the composition-dependence of n_4 in binary borate glasses, Phys. Chem. Glasses: Eur. J. Glass Sci. Technol., Part B 47 (4) (2006) 449–454.

[260] J. Haines, O. Cambon, E. Philippot, L. Chapon, S. Hull, A neutron diffraction study of the thermal stability of the α-quartz-type structure in germanium dioxide, J. Solid State Chem. 166 (2) (2002) 434–441. doi:10.1006/jssc.2002.9625.

[261] A. C. Hannon, D. I. Grimley, R. A. Hulme, A. C. Wright, R. N. Sinclair, Boroxol groups in vitreous boron oxide: New evidence from neutron diffraction and inelastic neutron scattering studies, J. Non-Cryst. Solids 177 (1994) 299–316. doi:10.1016/0022-3093(94)90544-4.

[262] H. Lehnert, H. Boysen, J. Schneider, F. Frey, D. Hohlwein, P. Radaelli, H. Ehrenberg, A powder diffraction study of the phase transition in $LaAlO_3$, Z. Kristallogr. 215 (9) (2000) 536–541. doi:10.1524/zkri.2000.215.9.536.

[263] G. Thornton, B. C. Tofield, A. W. Hewat, A neutron diffraction study of $LaCoO_3$ in the temperature range 4.2< T <1248 K, J. Solid State Chem. 61 (3) (1986) 301–307. doi:10.1016/0022-4596(86)90035-6.

[264] X. Zhang, J. Yao, X. Jiang, Y. Fu, Z. Lin, G. Zhang, Y. Wu, $K_3LaTe_2O_9$: A new alkali-rare earth tellurate with face-sharing TeO_6 octahedra, Dalton Trans. 44 (35) (2015) 15576–15582. doi:10.1039/c5dt02255j.

[265] G. Vetter, F. Queyroux, Détermination structurale de la forme de haute température du composé $La_4[Ge_3O_{10}][GeO_4]$: Analyse comparative des structures tricliniques des germanates de terres rares de formule globale $Ln_2Ge_2O_7$, J. Solid State Chem. 73 (2) (1988) 287–297. doi:10.1016/0022-4596(88)90112-0.

[266] O. Jarchow, K. H. Klaska, M. Ruks, B. Holtz, Die kristallstrukturen der verbindungen $La_2Ge_3O_9$ und $Ce_2Ge_3O_9$ und ihre strukturelle verwandtschaft zum toernebohmit-typ $RE_2Al(SiO_4)_2(OH)$, Z. Kristallogr. - Cryst. Mater. 211 (1) (1996) 4–7. doi:10.1524/zkri.1996.211.1.4.

[267] M. Kodama, S. Kojima, Anharmonicity and fragility in lithium borate glasses, J. Therm. Anal. Calorim. 69 (3) (2002) 961–970. doi:10.1023/a:1020684712439.

[268] J. C. Mauro, P. K. Gupta, R. J. Loucks, Composition dependence of glass transition temperature and fragility. II. A topological model of alkali borate liquids, J. Chem. Phys. 130 (23) (2009) 234503. doi:10.1063/1.3152432.

[269] A. Trukhin, B. Capoen, Raman and optical reflection spectra of germanate and silicate glasses, J. Non-Cryst. Solids 351 (46) (2005) 3640–3643. doi:10.1016/j.jnoncrysol.2005.09.017.

[270] L. Pauling, The Nature of the Chemical Bond and the Structure of Molecules and Crystals: An Introduction to Modern Structural Chemistry, Vol. 18, Cornell University Press, 1960.

[271] B. C. Bunker, R. J. Kirkpatrick, R. K. Brow, G. L. Turner, C. Nelson, Local structure of alkaline-earth boroaluminate crystals and glasses: II, ^{11}B and ^{27}Al MAS NMR spectroscopy of alkaline-earth boroaluminate glasses, J. Am. Ceram. Soc. 74 (6) (1991) 1430–1438. doi:10.1111/j.1151-2916.1991.tb04124.x.

[272] I. D. Brown, R. D. Shannon, Empirical bond-strength–bond-length curves for oxides, Acta Crystallogr., Sect. A 29 (3) (1973) 266–282. doi:10.1107/s0567739473000689.

[273] K. Tanaka, H. Kuroda, A. Narazaki, K. Hira, N. Soga, Second harmonic generation in $BaTiO_3$ film crystallized on tellurite glass surface, J. Mater. Sci. Lett. 17 (13) (1998) 1063–1065. doi:10.1023/A:1006663512177.

[274] E. Bescher, Y. Xu, J. D. Mackenzie, New low temperature multiphase ferroelectric films, J. Appl. Phys. 89 (11) (2001) 6341–6348. doi:10.1063/1.1364647.

[275] Y. Uesu, N. Horiuchi, E. Osakabe, S. Omori, B. A. Strukov, On the phase transition of new ferroelectric $LaBGeO_5$, J. Phys. Soc. Jpn. 62 (7) (1993) 2522–2523. doi:10.1143/jpsj.62.2522.

[276] L. van Wüllen, G. Schwering, ^{11}B–MQMAS and ^{29}Si–^{11}B double-resonance NMR studies on the structure of binary B_2O_3–SiO_2 glasses, Solid State Nucl. Magn. Reson. 21 (3-4) (2002) 134–144. doi:10.1006/snmr.2002.0054.

[277] S. Prasad, T. M. Clark, T. H. Sefzik, H.-T. Kwak, Z. Gan, P. J. Grandinetti, Solid-state multinuclear magnetic resonance investigation of Pyrex®, J. Non-Cryst. Solids 352 (26-27) (2006) 2834–2840. doi:10.1016/j.jnoncrysol.2006.02.085.

[278] A. Rulmont, P. Tarte, Lanthanide borogermanates $LnBGeO_5$: Synthesis and structural study by X-ray diffractometry and vibrational spectroscopy, J. Solid State Chem. 75 (2) (1988) 244–250. doi:10.1016/0022-4596(88)90163-6.

[279] S. Wang, J. F. Stebbins, Multiple-quantum magic-angle spinning ^{17}O NMR studies of borate, borosilicate, and boroaluminate glasses, J. Am. Ceram. Soc. 82 (6) (1999) 1519–1528. doi:10.1111/j.1151-2916.1999.tb01950.x.

[280] R. Martens, W. Müller-Warmuth, Structural groups and their mixing in borosilicate glasses of various compositions – an NMR study, J. Non-Cryst. Solids 265 (1-2) (2000) 167–175. doi:10.1016/s0022-3093(99)00693-6.

[281] F. Angeli, T. Charpentier, E. Molières, A. Soleilhavoup, P. Jollivet, S. Gin, Influence of lanthanum on borosilicate glass structure: A multinuclear MAS and MQMAS NMR investigation, J. Non-Cryst. Solids 376 (2013) 189–198. doi:10.1016/j.jnoncrysol.2013.05.042.

[282] T. Schaller, J. F. Stebbins, M. C. Wilding, Cation clustering and formation of free oxide ions in sodium and potassium lanthanum silicate glasses: Nuclear magnetic resonance and Raman spectroscopic findings, J. Non-Cryst. Solids 243 (2-3) (1999) 146–157. doi:10.1016/s0022-3093(98)00838-2.

[283] A. L. Paterson, J. W. Zwanziger, Anisotropic stress in laser-written $LaBGeO_5$ glass-ceramic composites, J. Appl. Phys. 124 (8) (2018) 083106. doi:10.1063/1.5046652.

[284] L.-S. Du, L. Peng, J. F. Stebbins, Germanosilicate and alkali germanosilicate glass structure: New insights from high-resolution oxygen-17 NMR, J. Non-Cryst. Solids 353 (30-31) (2007) 2910–2918. doi:10.1016/j.jnoncrysol.2007.05.122.

[285] A. Narazaki, N. Soga, Second harmonic generation in $BaTiO_3$ film crystallized on tellurite glass surface, J. Mater. Sci. Lett. 17 (13) (1998) 1063–1065.

[286] V. N. Sigaev, A. V. Dechev, S. L. Kadyshman, O. L. Al'takh, S. Y. Stefanovich, V. I. Molev, Glasses in the La_2O_3–B_2O_3–SiO_2 system and crystallization of the ferroelectric $LaBSiO_5$ phase, Glass Phys. Chem. 22 (1) (1996) 1–8.

[287] V. N. Sigaev, P. D. Sarkisov, P. Pernice, A. Aronne, A. M. Datsenko, S. Y. Stefanovich, V. I. Fertikov, O. A. Pozhogin, D. A. Zakharkin, Surface and bulk stillwellite textures in glasses of the La_2O_3–B_2O_3–GeO_2 system, J. Eur. Ceram. Soc. 24 (6) (2004) 1063–1067. doi:10.1016/s0955-2219(03)00424-2.

[288] D. Vouagner, C. Coussa, V. Califano, C. Martinet, B. Champagnon, V. Sigaev, UV nanosecond laser-induced birefringence in LBG glasses, Philos. Mag. 87 (3-5) (2007) 535–542. doi:10.1080/14786430600900104.

[289] J. Selsing, Internal stresses in ceramics, J. Am. Ceram. Soc. 44 (8) (1961) 419–419. doi:10.1111/j.1151-2916.1961.tb15475.x.

[290] X. Gonze, Adiabatic density-functional perturbation theory, Phys. Rev. A 52 (2) (1995) 1096–1114. doi:10.1103/physreva.52.1096.

[291] X. Gonze, J.-P. Vigneron, Density-functional approach to nonlinear-response coefficients of solids, Phys. Rev. B 39 (18) (1989) 13120–13128. doi:10.1103/physrevb.39.13120.

[292] R. Caracas, R. E. Cohen, Theoretical determination of the Raman spectra of $MgSiO_3$ perovskite and post-perovskite at high pressure, Geophys. Res. Lett. 33 (12). doi:10.1029/2006gl025736.

[293] R. Claus, L. Merten, J. Brandmüller, Light Scattering by Phonon-Polaritons, Vol. 75, Springer, 1975. doi:10.1007/BFb0048910.

[294] S. M. Shapiro, J. D. Axe, Raman scattering from polar phonons, Phys. Rev. B 6 (6) (1972) 2420–2427. doi:10.1103/physrevb.6.2420.

[295] X. Gonze, C. Lee, Dynamical matrices, born effective charges, dielectric permittivity tensors, and interatomic force constants from density-functional perturbation theory, Phys. Rev. B 55 (16) (1997) 10355–10368. doi:10.1103/physrevb.55.10355.

[296] F. C. Serbena, E. D. Zanotto, Internal residual stresses in glass-ceramics: A review, J. Non-Cryst. Solids 358 (6-7) (2012) 975–984. doi:10.1016/j.jnoncrysol.2012.01.040.

[297] T. Björkman, CIF2cell: Generating geometries for electronic structure programs, Comput. Phys. Commun. 182 (5) (2011) 1183–1186. doi:10.1016/j.cpc.2011.01.013.

[298] M. Hellenbrandt, The Inorganic Crystal Structure Database (ICSD)—present and future, Crystallogr. Rev. 10 (1) (2004) 17–22. doi:10.1080/08893110410001664882.

[299] C. A. Schneider, W. S. Rasband, K. W. Eliceiri, NIH Image to ImageJ: 25 years of image analysis, Nat. Methods 9 (7) (2012) 671–675. doi:10.1038/nmeth.2089.

[300] R. Hill, The elastic behaviour of a crystalline aggregate, Proc. Phys. Soc. A 65 (5) (1952) 349–354. doi:10.1088/0370-1298/65/5/307.

[301] J. Oishi, T. Kimura, Thermal expansion of fused quartz, Metrologia 5 (2) (1969) 50–55. doi:10.1088/0026-1394/5/2/004.

[302] W. Loewenstein, The distribution of aluminum in the tetrahedra of silicates and aluminates, Am. Mineral. 39 (1-2) (1954) 92.

[303] Y. Takahashi, Y. Benino, T. Fujiwara, T. Komatsu, Comprehensive study of crystallization and phase formation in (La,Gd)$BGeO_5$ glass, J. Ceram. Soc. Jpn. 116 (1358) (2008) 1108–1114. doi:10.2109/jcersj2.116.1108.

[304] A. S. Lipat'ev, S. V. Lotarev, T. O. Lipat'eva, E. V. Lopatina, V. N. Sigaev, Early stages of crystallization of lanthanum-borogermanate glass by a femtosecond laser beam, Glass Ceram. 75 (5-6) (2018) 213–216. doi:10.1007/s10717-018-0057-y.

[305] S. Lucas, E. Champion, D. Bregiroux, D. Bernache-Assollant, F. Audubert, Rare earth phosphate powders $RePO_4 \cdot nH_2O$ (Re=La, Ce or Y)—Part I. Synthesis and characterization, J. Solid State Chem. 177 (4-5) (2004) 1302–1311. doi:10.1016/j.jssc.2003.11.003.

[306] J. A. Poston, R. V. Siriwardane, E. P. Fisher, A. L. Miltz, Thermal decomposition of the rare earth sulfates of cerium(III), cerium(IV), lanthanum(III) and samarium(III), Appl. Surf. Sci. 214 (1-4) (2003) 83–102. doi:10.1016/s0169-4332(03)00358-1.

[307] R. C. L. Mooney, X-ray diffraction study of cerous phosphate and related crystals. I. Hexagonal modification, Acta Crystallogr. 3 (5) (1950) 337–340. doi:10.1107/s0365110x50000963.

[308] A. Mesbah, N. Clavier, E. Elkaim, C. Gausse, I. B. Kacem, S. Szenknect, N. Dacheux, Monoclinic form of the rhabdophane compounds: $REEPO_4 \cdot 0.667\,H_2O$, Cryst. Growth Des. 14 (10) (2014) 5090–5098. doi:10.1021/cg500707b.

[309] A. Nakatsuka, O. Ohtaka, H. Arima, N. Nakayama, T. Mizota, Aragonite-type lanthanum orthoborate, $LaBO_3$, Acta Crystallogr., Sect. E: Struct. Rep. Online 62 (4) (2006) i103–i105. doi:10.1107/s1600536806010142.

[310] Y. Ono, K. Takayama, T. Kajitani, X-ray diffraction study of $LaBSiO_5$, J. Phys. Soc. Jpn. 65 (10) (1996) 3224–3228. doi:10.1143/jpsj.65.3224.

[311] D. B. Shinn, H. A. Eick, Crystal structure of lanthanum carbonate octahydrate, Inorg. Chem. 7 (7) (1968) 1340–1345. doi:10.1021/ic50065a018.

[312] K. Michiba, T. Tahara, I. Nakai, R. Miyawaki, S. Matsubara, Crystal structure of hexagonal $RE(CO_3)OH$, Z. Kristallogr. 226 (6). doi:10.1524/zkri.2011.1222.

[313] P. Fleming, R. A. Farrell, J. D. Holmes, M. A. Morris, The rapid formation of $La(OH)_3$ from La_2O_3 powders on exposure to water vapor, J. Am. Ceram. Soc. 93 (4) (2010) 1187–1194. doi:10.1111/j.1551-2916.2009.03564.x.

[314] G. W. Beall, W. O. Milligan, H. A. Wolcott, Structural trends in the lanthanide trihydroxides, J. Inorg. Nucl. Chem. 39 (1) (1977) 65–70. doi:10.1016/0022-1902(77)80434-x.

[315] Z. A. Zaitseva, A. L. Litvin, S. S. Ostapenko, Crystal structure of lanthanum chromite, Dopov. Akad. Nauk Ukr. RSR, Ser. B: Geol., Khim. Biol. Nauki 1977 (1977) 1094–1096.

[316] K. Tezuka, Y. Hinatsu, A. Nakamura, T. Inami, Y. Shimojo, Y. Morii, Magnetic and neutron diffraction study on perovskites $La_{1-x}Sr_xCrO_3$, J. Solid State Chem. 141 (2) (1998) 404–410. doi:10.1006/jssc.1998.7961.

[317] S. Stramare, V. Thangadurai, W. Weppner, Lithium lanthanum titanates: A review, Chem. Mater. 15 (21) (2003) 3974–3990. doi:10.1021/cm0300516.

[318] J. W. Zwanziger, First-principles study of the nuclear quadrupole resonance parameters and orbital ordering in $LaTiO_3$, Phys. Rev. B 79 (3). doi:10.1103/physrevb.79.033112.

[319] T. J. Bastow, S. N. Stuart, ^{17}O NMR in simple oxides, Chem. Phys. 143 (3) (1990) 459–467. doi:10.1016/0301-0104(90)87025-7.

[320] J. Pannetier, G. Denes, Tin(II) oxide: Structure refinement and thermal expansion, Acta Crystallogr. B 36 (11) (1980) 2763–2765. doi:10.1107/s0567740880009934.

[321] W. H. Baur, A. A. Khan, Rutile-type compounds. IV. SiO_2, GeO_2 and a comparison with other rutile-type structures, Acta Crystallogr. B 27 (11) (1971) 2133–2139. doi:10.1107/s0567740871005466.

[322] E. Oldfield, C. Coretsopoulos, S. Yang, L. Reven, H. C. Lee, J. Shore, O. H. Han, E. Ramli, D. Hinks, ^{17}O nuclear-magnetic-resonance spectroscopic study of high-T_c superconductors, Phys. Rev. B 40 (10) (1989) 6832–6849. doi:10.1103/physrevb.40.6832.

[323] G. Will, M. Bellotto, W. Parrish, M. Hart, Crystal structures of quartz and magnesium germanate by profile analysis of synchrotron-radiation high-resolution powder data, J. Appl. Crystallogr. 21 (2) (1988) 182–191. doi:10.1107/s0021889887011567.

[324] F. H. Larsen, I. Farnan, ^{29}Si and ^{17}O (Q)CPMG-MAS solid-state NMR experiments as an optimum approach for half-integer nuclei having long T_1 relaxation times, Chem. Phys. Lett. 357 (5-6) (2002) 403–408. doi:10.1016/s0009-2614(02)00520-1.

[325] W. Sinclair, A. E. Ringwood, Single crystal analysis of the structure of stishovite, Nature 272 (5655) (1978) 714–715. doi:10.1038/272714a0.

[326] X. Xue, J. F. Stebbins, M. Kanzaki, Correlations between ^{17}O NMR parameters and local structure around oxygen in high-pressure silicates: Implications for the structure of silicate melts at high pressure, American Mineralogist 79 (1-2) (1994) 31–42.

[327] J. R. Smyth, J. V. Smith, G. Artioli, A. Kvick, Crystal structure of coesite, a high-pressure form of silica, at 15 and 298 K from single-crystal neutron and X-ray diffraction data: Test of bonding models, J. Phys. Chem. 91 (4) (1987) 988–992. doi:10.1021/j100288a043.

[328] P. J. Grandinetti, J. H. Baltisberger, I. Farnan, J. F. Stebbins, U. Werner, A. Pines, Solid-state ^{17}O magic-angle and dynamic-angle spinning NMR study of the SiO_2 polymorph coesite, J. Phys. Chem. 99 (32) (1995) 12341–12348. doi:10.1021/j100032a045.

[329] M. Lerch, H. Boysen, T. Hansen, High-temperature neutron scattering investigation of pure and doped lanthanum gallate, J. Phys. Chem. Solids 62 (3) (2001) 445–455. doi:10.1016/s0022-3697(00)00078-0.

[330] T. J. Bastow, T. Mathews, J. R. Sellar, ^{69,71}Ga and ^{139}La NMR characterisation of $LaGaO_3$ and $La_{1-x}Sr_xGa_{1-x}Mg_xO_{3-x}$, Solid State Ionics 175 (1-4) (2004) 129–133. doi:10.1016/j.ssi.2004.09.028.

[331] F. Blanc, D. S. Middlemiss, Z. Gan, C. P. Grey, Defects in doped $LaGaO_3$ anionic conductors: Linking NMR spectral features, local environments, and defect thermodynamics, J. Am. Chem. Soc. 133 (44) (2011) 17662–17672. doi:10.1021/ja2053557.

[332] S. Sasaki, K. Fujino, Y. Takéuchi, X-ray determination of electron-density distributions in oxides, MgO, MnO, CoO, and NiO, and atomic scattering factors of their constituent atoms, Proc. Jpn. Acad., Ser. B 55 (2) (1979) 43–48. doi:10.2183/pjab.55.43.

[333] G. L. Turner, S. E. Chung, E. Oldfield, Solid-state oxygen-17 nuclear magnetic resonance spectroscopic study of the group II oxides, J. Magn. Reson. 64 (2) (1985) 316–324. doi:10.1016/0022-2364(85)90356-7.

[334] O. Reckeweg, C. Lind, A. Simon, F. J. DiSalvo, Rietveld refinement of the crystal structure of α-Be_3N_2 and the experimental determination of optical band gaps for Mg_3N_2, Ca_3N_2 and $CaMg_2N_2$, Z. Naturforsch., B: J. Chem. Sci. 58 (1) (2003) 159–162. doi:10.1515/znb-2003-0124.

[335] M. A. Ghebouli, B. Ghebouli, A. Bouhemadou, M. Fatmi, K. Bouamama, Structural, electronic, optical and thermodynamic properties of $Sr_xCa_{1-x}O$, $Ba_xSr_{1-x}O$ and $Ba_xCa_{1-x}O$ alloys, J. Appl. Cryst. 509 (5) (2011) 1440–1447. doi:10.1016/j.jallcom.2010.11.097.

[336] M. C. Verbraeken, E. Suard, J. T. S. Irvine, Structural and electrical properties of calcium and strontium hydrides, J. Mater. Chem. 19 (18) (2009) 2766–2770. doi:10.1039/b820173k.

[337] N. Kumar, R. Tripathi, A. Dogra, V. P. S. Awana, H. Kishan, Effect of Pr doping in La–Sn–Mn–O system, J. Appl. Cryst. 492 (1-2) (2010) L28–L32. doi:10.1016/j.jallcom.2009.11.100.